BNL-108447-2015

A Compilation of Internship Reports

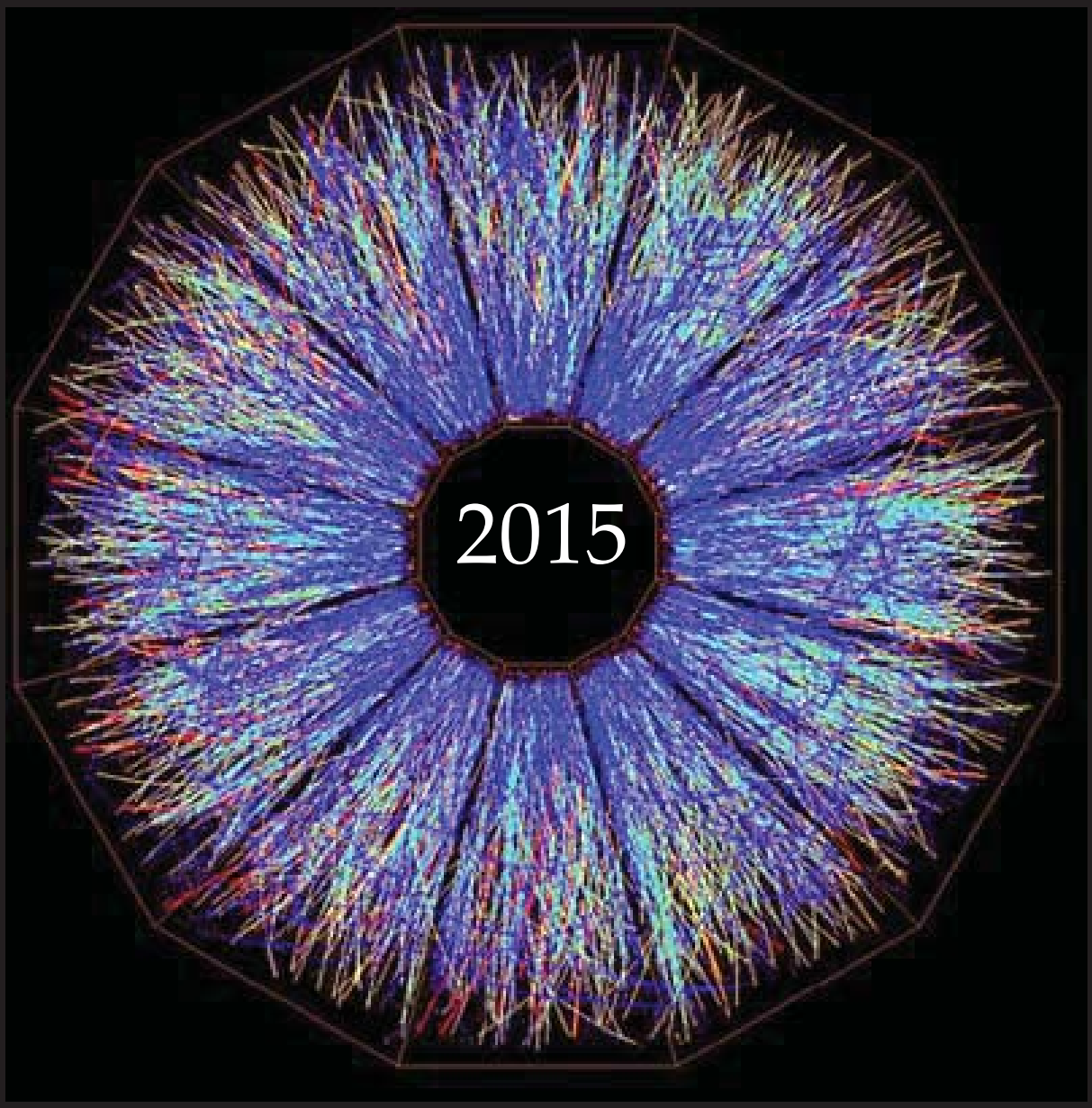

Prepared for The Office of Educational Programs
Brookhaven National Laboratory
Office of Educational Programs

DISCLAIMER

This work was prepared as an account of work sponsored by an agency of the United States Government. Neither the United States Government nor any agency thereof, nor any of their employees, nor any of their contractors, subcontractors or their employees, makes any warranty, express or implied, or assumes any legal liability or responsibility for the accuracy, completeness, or any third party's use or the results of such use of any information, apparatus, product, or process disclosed, or represents that its use would not infringe privately owned rights. Reference herein to any specific commercial product, process, or service by trade name, trademark, manufacturer, or otherwise, does not necessarily constitute or imply its endorsement, recommendation, or favoring by the United States Government or any agency thereof or its contractors or subcontractors. The views and opinions of authors expressed herein do not necessarily state or reflect those of the United States Government or any agency thereof.

BROOKHAVEN
NATIONAL LABORATORY

Table of Contents

Automatically detecting typical failure signatures to improve Sun-photometer data quality 7
Brooke Adams

Examining the water gas shift reaction using Pt-CeO_x-TiO_2 powder catalysts 11
Balal Aslam

Harmonic flow in heavy ion collisions: a search for phase transition and v_2 correlations . . . 16
Mamoudou Ba
Erin O'Brien

Wind farm: feasibility and environmental impacts 20
Matthew Bernard

Acoustic clicktomount: using sound pulses to solve the crystal harvesting bottleneck for high throughput screening applications 25
Mary T. Bollard, Liam McCarthy, Alexander Scalia, et al.

Ionizing Radiation and its Effect on the DNA of the Human Body 33
Nicholas Bonura

Simulating beamline configurations for the Deep Underground Neutrino Experiment 36
Brendon Bullard

Design and analysis of the inner hadronic calorimeter installation fixture for the sPHENIX Project at RHIC 41
Daniel Cacace

Modeling a coating system for photocathodes for Low Energy Relativistic Heavy Ion Collider electron Cooling 47
Patrick Carroll

Using anomaly detection to facilitate intelligence gathering for satellite imagery 50
Daniel Cisek

Replacement cost estimates for overduty electrical panels at the Brookhaven National Laboratory 55
William Clark

Foundation for the processes involved in conducting an energy audit of building 902 59
Keith Combs

Developing a watchdog program to oversee environmental sensors at the Northeast Solar Energy Research Center 61
Lee R. Combs

Maintaining micro climates during nano-liter chemical dispensations using custom designed source plate lids 67
Ashley M. Drozd, Bryan J. Foley, Mary T. Bollard, et al.

Solubility of perfluorocarbons under geothermal conditions 71
Yassien Fadul and Juan Sosa
Characterizing reconstructions in different Liquid Argon Time Projection Chambers 73
Samantha Fortuna
The efficiency of 4-poster tick management stations on three tick species populations within Brookhaven National Laboratory 78
Tayelor Gosselin
The shallow-to-deep transition in convective clouds during the Green Ocean Amazon 2014/5 campaign 83
Cari Gostic
Automated testing of nuclear data using zero- power nuclear reactors 86
Mecheal Greene
Optimization of a fast camera with a twenty-nanosecond resolution 90
Jon Gustafson
Drell-Yan studies and simulations at 500 GeV for pp collisions 95
Samuel George Heppelmann
A study of the performance of non-volatile dual in-line memory 100
Shawn Hoose
Understanding the polarization switching exhibited by Moth-Eye Nanostructures 102
Alexander S. Kaiser
Thick CCD sensor characterization using interferometry techniques 105
Alexander Karlis
Atomic scale investigations of model TiO_2(110) catalysts 108
Alexander Kramer
Developing and optimizing the assembly process to manufacture an electromagnetic caloriometer module for sPHENIX 111
Spencer Laddy-Locks
Simulating electron showers in the Deep Underground Neutrino Experiment far detector . . 114
Jacob Larkin
Effects of laser exposure on the niobium tin surface 117
Zachary Lebens-Higgins
Raft optimization and readout test stand design of the raft electronics board for the Large Synoptic Survey Telescope. 122
Jessica Li
Adding diagnostics to the Relativistic Heavy Ion Collider's main magnet power supply phase-loop lock and silicon controlled rectifier-firing board 125
Raul Martinez
Development and commissioning of tools for measurements and online calculation of electron beam lifetime in the National Synchrotron Light Source - II storage ring . . . 130
Jessica Mele

Identification and location of mutated Arabidopsis genes through map-based cloning 134
Kristina Michta
Construction and analysis of reduced graphene oxide/ ruthenium oxide supercapacitors electrodes using electrophoretic deposition 139
Dakoda W. Mullinax and Z. Amir
Targeting lipid abundant mutants of ***Arabidopsis thaliana*** ***142***
Kimberly Okoli
Visualization of the RHIC Computing Facility 145
Do Om
Development of scientific control and computing capabilities at the Inelastic X-ray Scattering beamline, National Synchrotron Light Source II 147
John Oto
Creation of high charge state lithium and calcium ion beams using laser ablation 151
Kevin Palm
An analysis of understory plant diversity in the Long Island Central Pine Barrens. 154
Ari Rice
Investigating vortex dynamics in trilayer structures of ferromagnetic materials separated by a nonmagnetic spacer layer 163
Angelika Rothberg
The use of EMPIRE to simulate the neutron induced reactions on ^{86}Kr. 170
Elizabeth Rubino
Impacts of white-tailed deer on forest health in the Pine Barrens on Long Island. 177
Taylor Ruhle and Lauren Gazerwitz
Determining meteorological system accuracy using a root sum of squares analysis 181
Megan Safranek
Designing the booster to Alternating Gradient Synchrotron injection lines for the electric dipole moment experiment 186
Michael Severance
What does the future hold for the Nuclear Nonproliferation Treaty? 189
Laura Shanklin
Preliminary tasks for charge coupled device quantum efficiency measurements 194
Thomas Smith
Replacement of the Nd:YAG Chiller 199
Derek Squires
Proton beam production using titanium hydride by means of a laser ion source 203
Cayla Stifler
Investigating the feasibility of instrument comparison as a means for analyzing data on aerosol concentrations. 206
Ariel Stolz

Reduction of photon scattering on the X-ray Powder Diffraction beamline's detector through radiation simulation 211
Dennis Tao
Effects of deer overabundance on bird populations in the Long Island Central Pine Barrens 214
Raffaele Vesia
Self-assembly of magnetite block copolymer nanocomposites 220
Adam Vianna
Single bunch emittance measurements via edge radiation 225
Linnea Zavala
Mechanical metrology testing for the Frontier Macromolecular Crystallography (FMX) Beamline and the Highly Automated Macromolecular Crystallography (AMX) Beamline at NSLS-II 229
Lauren Zipper
Application containers as an alternative to virtualization. 233
Joseph Zuhusky

Automatically detecting typical failure signatures to improve Sun-photometer data quality

Brooke Adams
Department of Physics and Space Sciences, Florida Institute of Technology, Melbourne, FL 32901
Laurie Gregory and Richard Wagener
Environmental Department, Brookhaven National aboratory, Upton, NY 11973

Abstract

Cimel Sun-photometers collect data used to calculate the aerosol optical thickness (AOT), which tells how much light is being reflected by particles in the air and is important for climate change research. Due to the way the AOT data is normalized, a cosine curve will appear in the data when something is obstructing the photometer's tubes. Using Interactive Data Language (IDL), the AOT data was fit with a multiple-linear regression to determine if a cosine curve was present. The resulting coefficients were plotted and a histogram made to see if they can be used to flag problems automatically. The histogram showed the cosine coefficients shifting away from zero, even though it wasn't noticeable by eye, thereby successfully detecting a subtle change in transmission in one of the detectors. More research is needed, however, to verify this method's accuracy and to detect other problems in addition to obstructions.

I. Introduction

Aerosols are particles floating around in our atmosphere that scatter light, including anything from dust, smoke, sea salt, volcanic ash, and many types of human-made pollution. The scattering changes how much energy makes it to the Earth's surface, particularly when the light is scattered back out into space. Since the Industrial Revolution, human-made aerosols have spiked drastically, and areas near a facility that lets off a lot of smoke can experience an overall cooling over time because it consistently gets less light than surrounding areas. Uneven cooling across the globe will affect future climate change, but no one is sure how, therefore instruments such as the Cimel Sun-photometers have been put all over the world to take measurements and monitor various aspects of the atmosphere, including aerosols.[1,2]

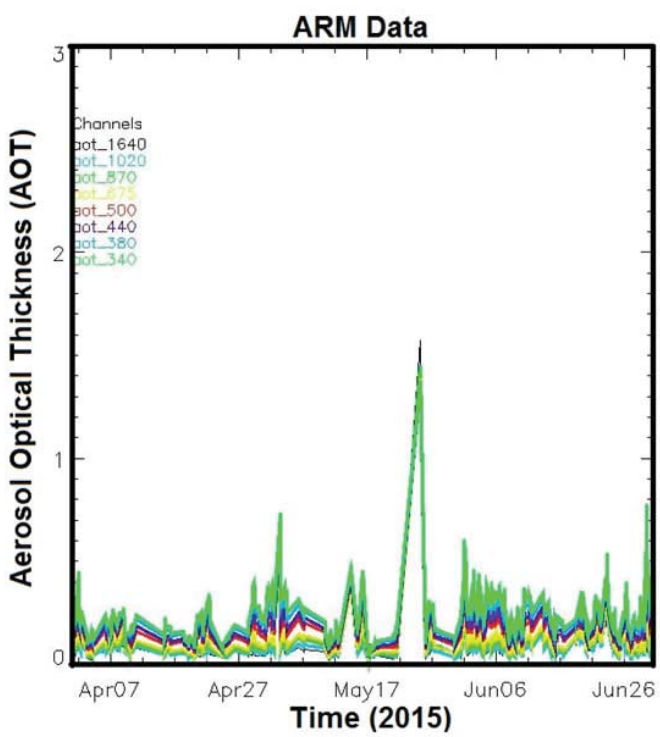

Fig. 1: Example of AOT data plotted on a monthly basis, from the Southern Great Plains (SGP) site.

One calculation made from the Sun-photometer data is the aerosol optical thickness (AOT). The AOT reveals from the scattered light how thickly the aerosols have collected in a region of the atmosphere, where a higher AOT corresponds to the atmosphere being more opaque. The instruments are placed in optimal locations around the world. A problem that commonly occurs with the Sun-photometers, however, is when an obstruction is present in one of the instrument's tubes (i.e. lizards, insects, spider webs, or just dust collecting on one of its many channels). The data reflects this kind of problem with a cosine curve because of the way the AOT data is normalized (light scatter is being measured at all angles, so a $\cos(\theta(t))$ is divided out for normalization to the solar zenith angle).[3]

Employees at Brookhaven National Laboratory check the plots made from the AOT data by NASA's Aerosol Robotic Network (AERONET) for signs of a cosine, along with other visible problems—manually, every day. The automation of such detection will allow for faster identification and resolution of whatever is causing the issue in the data quality.

II. Methods

Using the program Interactive Data Language (IDL), an algorithm was created to begin the automatic detection of a cosine curve in the AOT data. First the data saved by AERONET had to be retrieved from the NetCDF files, which have all the data separated into array variables for every month. The time, zenith-angle, and AOT arrays are found among the other variables, the AOT arrays separated by channel wavelengths (i.e. aot_1640 or aot_500). Each of the AOT variables is checked for bad data that shows up as -999 (usually meaning the instrument tried to take a reading, but nothing was collected, probably due to clouds), and only the channels clear of these values are used for the rest of the analysis. Plots are made of the AOT data versus time for an entire month or more, individual channels being over-plotted in different colors.

But for this algorithm to be more useful and identify problems sooner, it needed to look at the data daily and not just monthly. Using the good channels identified in the monthly plots, the starting date was determined from the converted Julian-date array and the data counted through for the number of days in the file, the data now being restricted by a date index. It was attempted to have each plot saved as a .png file, but the first attempts took too long to convert each image to .png format, possibly due to a problem with computer memory or an incorrect device setting. Richard Wage-

ner has a program already written for this kind of conversion, so that will be incorporated into the algorithm in the future.

For both the monthly and daily routines, the regress function was used to fit a multiple-linear curve to the data, using the equation

$$y = A_0 + A_1 t + A_2 cos(\theta(t))$$

where $A_{0,1,2}$ are calculated coefficients, t is the Julian date, and $\theta(t)$ is the solar zenith angle. The function returns the A coefficients, their uncertainties, goodness-of-fit tests, and an array of y-values calculated with the corresponding times, zenith angle, and coefficients. The y-values are then over-plotted with each AOT channel and any cosine patterns should be visible. Each of the returned values were saved in one array for later use.

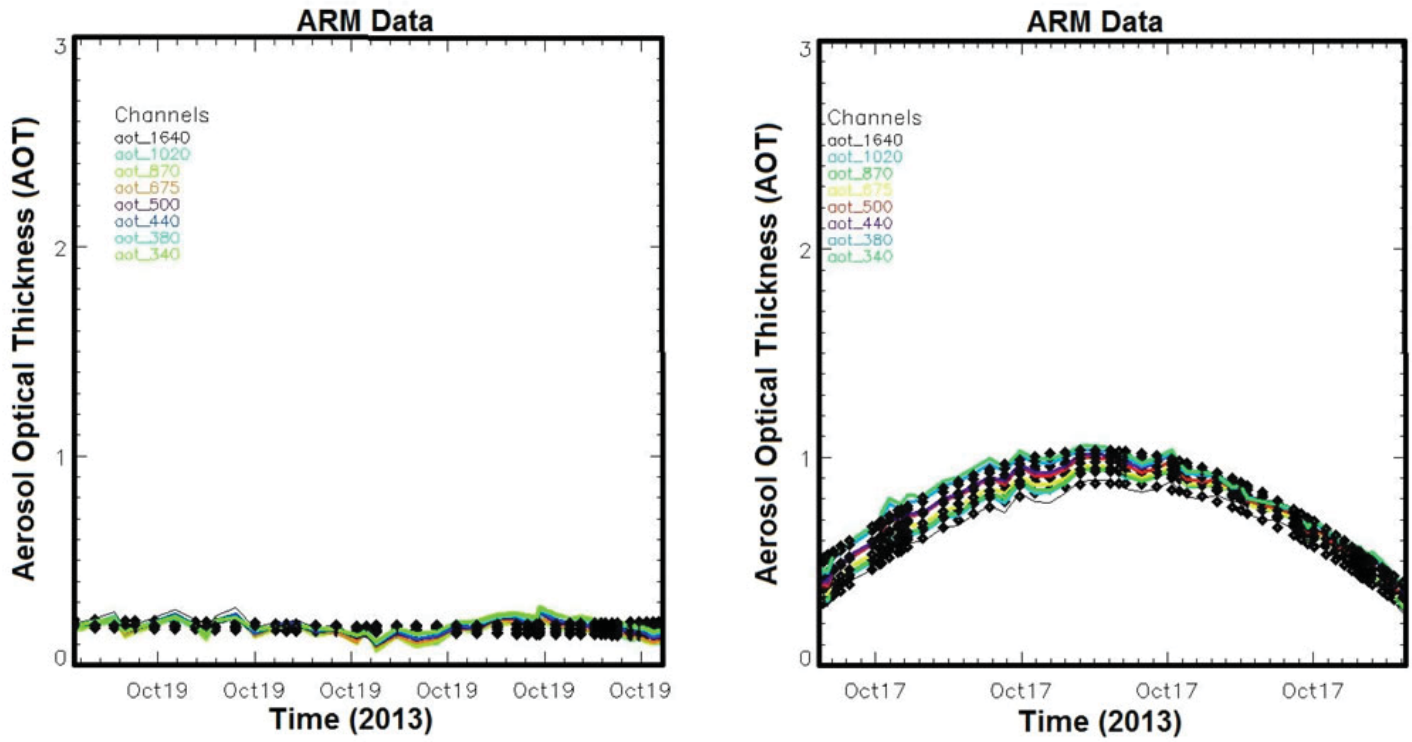

Fig 2: Example over-plots of daily AOT data from the SGP site, fitted by the multiple-linear function (shown by the black symbols). The plot on the left shows when the linear coefficient is high, signifying good data. The one of the right is an example of bad data with a corresponding high cosine coefficient.

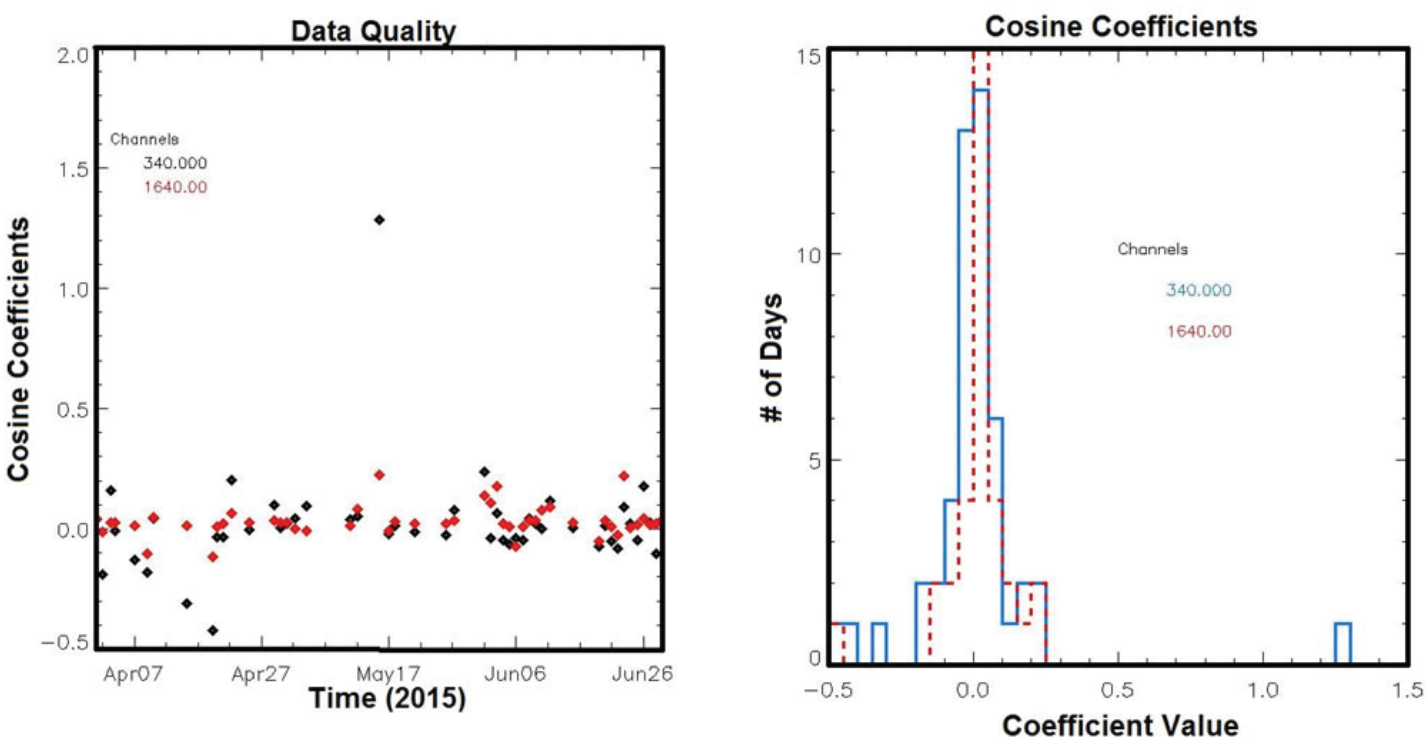

Fig. 3: Example plots for the cosine coefficients calculated for the AOT data of Fig. 1. Note the majority of the coefficients in the left plot are near zero. Only the highest and lowest channels were plotted to keep the plots from being cluttered, but also notice they mostly stay within range of each other, as shown by their peaks overlapping in the histogram.

Once the coefficients had been determined and saved in the array, the cosine coefficients could be used to identify where a cosine curve may be occurring. If the data is good, the linear coefficient (A1) will be larger and the cosine coefficient (A2) will be close to zero, signifying a greater linear significance and an almost non-existent cosine curve. Plotting all the cosine coefficients versus time shows where the A2 values stray too far from zero and, theoretically, that is when a cosine curve is present. To get an even better look at any potential problems, the A2 values were then put into a histogram. Good data should show the majority of the coefficients centered at or around zero, while bad data caused by the Sun-photometer should be shifted.

All of these plots were tests on the algorithm of random data from previous years. The final test was to use it on some data when there was a known instrument malfunction and several data quality reports were filed once the problem was realized. The problem came from the instrument at the Eastern North Atlantic (ENA) site, and the first issues appeared in October 2014 when a problem with the wet sensor was spotted. The issue was thought to be resolved when the sensor was cleaned, but then more data problems cropped up in November. They continued until the instrument was swapped out in April 2015. If this method of using cosine coefficients to pick out bad data is accurate, the data analysis should reflect these reports.

III. Results

In order to determine if the program is successfully detecting the problem from the ENA site, it was necessary to look at the months before, during, and after the reports were filed.

IV. Conclusion

The algorithm has been successful in its preliminary tests, showing a shift in the cosine coefficients during a period when the instrument at the ENA site was having problems with its wet sensor. The final algorithm produces both monthly and daily plots, coefficients and their corresponding uncertainties, a cosine coefficient plot, and a histogram. The first plots are not useful yet because they aren't being saved anywhere, but future work will have them sent to a website so they will be readily available to anyone who needs AOT data. The parameters calculated from these plots are used for the coefficient plot and histogram, which detects the shift in transmission from the Cimel Sun-photometer channels, signifying a problem with the instrument that will affect the data quality.

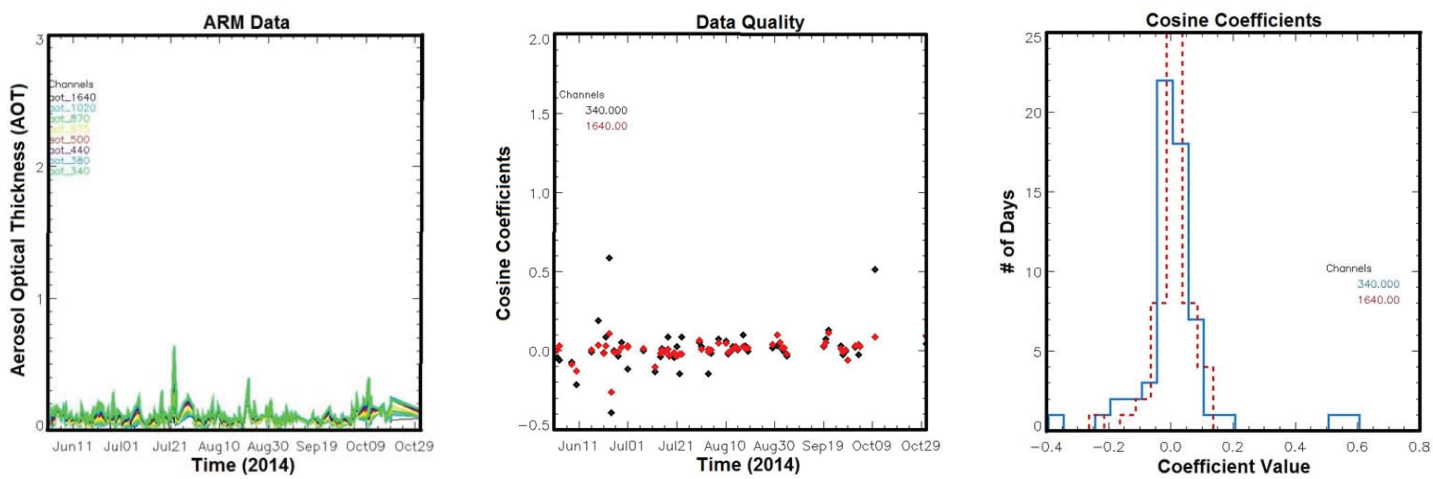

Fig 4: AOT data five months before the ENA instrument malfunctioned. There are a few high cosine coefficients, but for the most part they're all around zero as they should be for an instrument working correctly. The histogram reflects this, as well, the way both channels have the majority of their points in the same area.

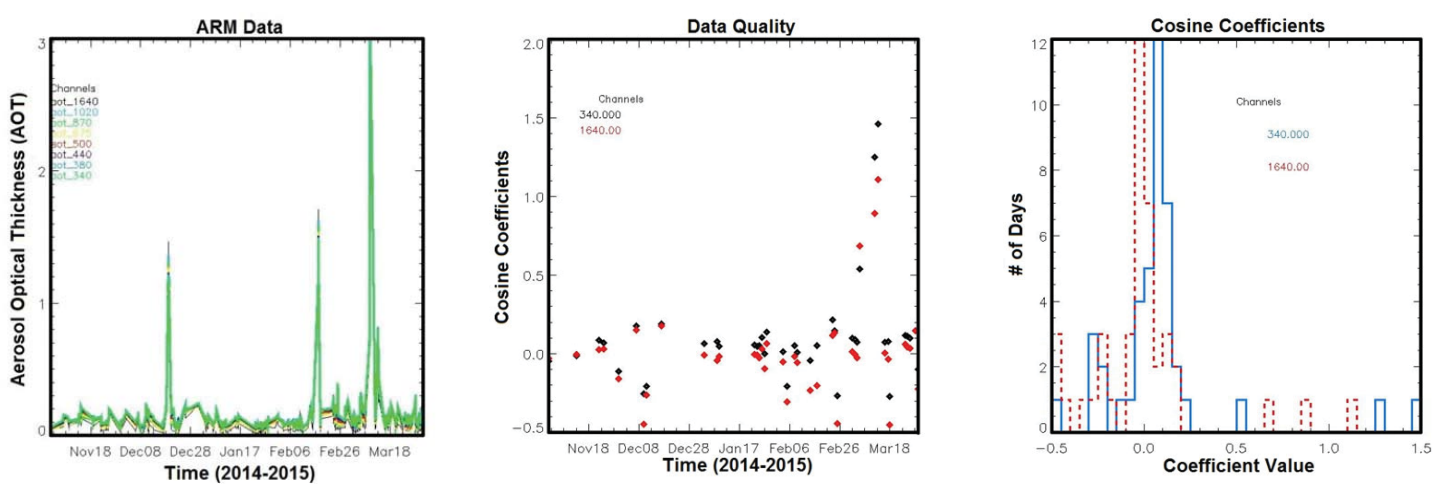

Fig. 5: AOT data for the months the ENA instrument was having problems with the wet sensor. The monthly plot on top doesn't really show anything (the spikes are from cloud cover, not the instrument), but the cosine coefficients are all over the place in comparison to the previous months shown in Fig. 4.. The histogram also shows a shift between the channels, signifying something is wrong with the instrument.

A cosine curve is only one of many problems the Sun-photometers can cause, and while this algorithm proves promising, it still needs to be fine-tuned and tested on more data. There could be false positives in the cosine coefficients—really high coefficients, but no actual curve. If the linear coefficient is just as high, as has been seen quite often, it is unclear if that means a cosine curve is present or not, or why both the linear and cosine components would be so high. Besides the cosine curve, which checks for an obstruction inside the collimator tubes, the separation of channel readings, odd spikes when no clouds are present, and negative curves are all other issues seen in the AERONET plots that need to be added to make the process of fixing data quality completely automatic. A future goal is to incorporate machine learning to this automation instead of giving the computer specific patterns; the shape of the faulty AOT data is not always known, but many problems can be determined just by the plot looking wrong. Machine learning would hopefully get the computer to figure out what "looking wrong" means in the data and to determine patterns from these kind of plots, flagging similar failure signatures in future data.

V. References

[1]"Atmospheric Aerosols: What Are They, and Why Are They So Important?" NASA. Brian Dunbar. August 1, 1996. https://www.nasa.gov/centers/langley/news/factsheets/Aerosols.html

[2]"Aerosols: Tiny Particles, Big Impact". Earth Observatory. Adam Voiland. November 2, 2010. http://earthobservatory.nasa.gov/Features/Aerosols/

[3]"Instrument : Cimel Sunphotometer (CSPHOT)". ARM Climate Research Facility. U.S. Department of Energy, Office of Science. http://www.arm.gov/instruments/csphot

VI. Acknowledgments

Thank you to Laurie Gregory and Rick Wagener for giving me this project.

This project was supported in part by the U.S. Department of Energy, Office of Science, Office of Workforce Development for Teachers and Scientists (WDTS) under the Science Undergraduate Laboratory Internships Program (SULI).

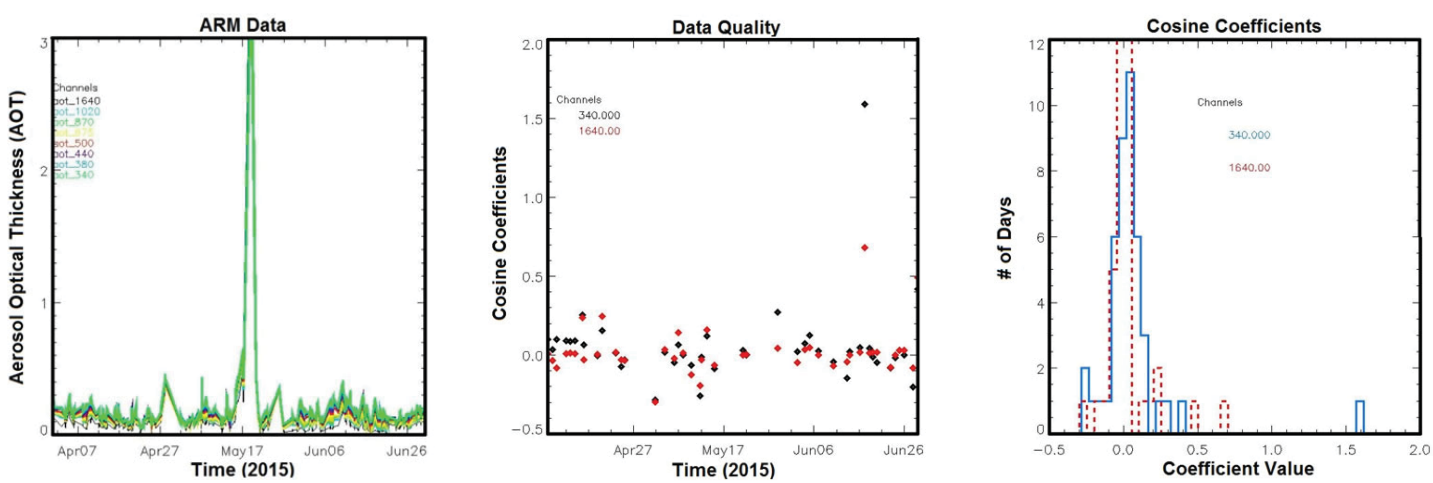

Fig. 6: AOT data for the three months after the instrument was swapped out in mid-April (further data is not available at this time). There still isn't much to see in the monthly (top) plot (again, the spikes are from cloud cover), but the cosine coefficients are noticeably less varied. The histogram shows they are starting to come back together between the channels, too.

Examining the water gas shift reaction using Pt-CeO_x-TiO_2 powder catalysts

Balal Aslam
Chemistry Department, New York Institute of Technology, New York, NY 10023
Dimitriy Vovchok
Department of Chemistry, Stony Brook University, Stony Brook, NY 11794
Sanjaya Senanayake and Jose Rodriguez
Chemistry Department, Brookhaven National Laboratory, Upton, NY 11973
Aaron Johnston-Peck, Andrew Gamalski, and Eric Stach
Center for Functional Nanomaterials, Brookhaven National Laboratory, Upton, NY 11973

Abstract

This study was aimed at unraveling the nature of a series of novel 0.5% Pt-CeO_x-TiO_2 catalysts for the water gas shift reaction (WGS: CO + + H_2O -> H_2 + CO_2). The water gas shift reaction is an important industrial purification reaction that can be used as a source of pure hydrogen for fuel production, ammonia synthesis and polymer synthesis. The activity of these catalysts was examined using mass spectrometry and gas chromatography techniques. High Resolution Transmission Electron Microscopy (HRTEM), Scanning Transmission Electron Microscopy (STEM) and Energy Dispersive Spectroscopy (EDS) was used to examine the local morphology of the catalysts. This study is part of a continued effort to develop better catalysts that can perform with high stability under milder conditions than Cu/ZnO catalysts commonly used in industry. The Pt-CeO_x-TiO_2 catalysts proved to be active for the WGSR, with a complex role of Pt, CeO_x and TiO_2. The qualitative data obtained from mass spectrometry gave us a relative idea of the activity of our catalysts. Activity decreases as the Ceria doping increased from 1wt% to 3 wt% and then to 6 wt%. We observed that the small low dimensional structures present at the CeO_x-TiO_2 interfaces in the 1 wt% Ceria were important for the increased activity for WGS. Future efforts can be geared towards optimizing the structure-activity relationship of such catalysts for the WGS and related H_2 producing reactions.

I. Introduction

The water gas shift reaction (WGSR: CO + H_2O -> H_2 + CO_2) is an important industrial reaction that can be used as a source of pure hydrogen for fuel cell applications, ammonia synthesis and polymer synthesis. The majority of hydrogen produced today is derived from steam reforming of hydrocarbons (CH_4 + H_2O -> CO + $3H_2$).1 The hydrogen obtained from steam reformation contains 1-10% of CO, which degrades the performance of industrial platinum based catalysts and electrodes. 1 The WGSR is essentially used to provide a clean source of molecular Hydrogen by removing the CO from these reformate gas feeds.

In industry, the WGSR is typically performed in two stages, a high temperature stage (HTS) and a low temperature stage (LTS) .1To take advantage of the positive kinetics at high temperatures, the HTS is carried out between 350 °C and 500 °C, with catalyst composed of Fe-Cu or Fe-Cr oxides. This is followed by a thermodynamically driven stage carried out between 200°C and 300 °C using a catalyst composed of Cu-Zn oxides. This process maximizes the conversion of CO in the reformate gas feed. Reformate gas initially contains up to 10% CO, it is brought down between 2-4% after the HTS, and finally below 1% after the LTS. Catalysts currently being used are pyrophoric and require complex activation steps prior to usage.[1]

CeO_2 has been investigated for use in several catalytic reforming processes including the photo catalytic splitting of water due to its low cost, relative earthly abundance, and its distinct redox chemistry (Ce4+ ↔ Ce3+ easily interchangeable).[2] Previous studies have shown that combining TiO_2 with CeO_2 drastically promotes catalytic activity, and this is likely due to the role of TiO_2 as a chemical, thermal, and mechanical stabilizer of nano-CeO_2 particles. [2,3]

A previous study that used STEM imaging revealed that Ceria exists in a hierarchal structure with clusters, chains and nanoparticles on the titania support.[3] There is a lattice mismatch between the Ceria and titania that influences the growth of Ceria on the Titania support. The migration of Ti4+ into the lattice at the Ceria-Titania interface enables the formation of Ce3+ sites, which are very useful in catalytic processes.[2] The existence of Ce3+ in M/CeO_x/TiO_2 (M = Cu, Au, Pt) enables the dissociation of water, which makes this system an outstanding catalyst for the WGSR.[2] Density functional theory (DFT) calculations have shown that the interface layer is the most preferential site for oxygen vacancies.[2] Oxygen vacancies at the interface are favorable because their presence leads to greater amount of Ce3+ at the interface than at the surface layer.[2] Greater concentrations of Ce3+ at the interface is preferential for catalytic activity.[2] When studying the nature of catalysts it is of upmost importance to understand these metal-oxide interfaces.[2] The active nature of a specific interface can give us information as to where the WGS is initiated and how we can maximize production of products from the reaction.

The focus of this study was to examine the nature of the phenomena responsible for the activity of Pt/CeO_x-TiO_2 during the water gas shift reaction (WGSR). Three Pt/CeO_x-TiO_2 samples were studied, each with .5% wt Pt and 1, 3, and 6% wt Ceria on TiO2, a systematic increase in ceria loading.

An SRS RGA 300 quadrupole probe mass spectrometer was used to study the relative activity of these catalysts. Quadrupole mass spectrometers contain ionizers that bombard atoms with electrons which then travel between four parallel rods that are giving off an electric current. Certain atoms will continue to the ion detector based on their mass to charge ratio. This technique allowed us to analyze the products of our reactions after running WGS, by specific titration of mass fragments. To gain insight into the local morphology of our catalysts we used STEM and EDS techniques. STEM is a technique in which electrons are passed

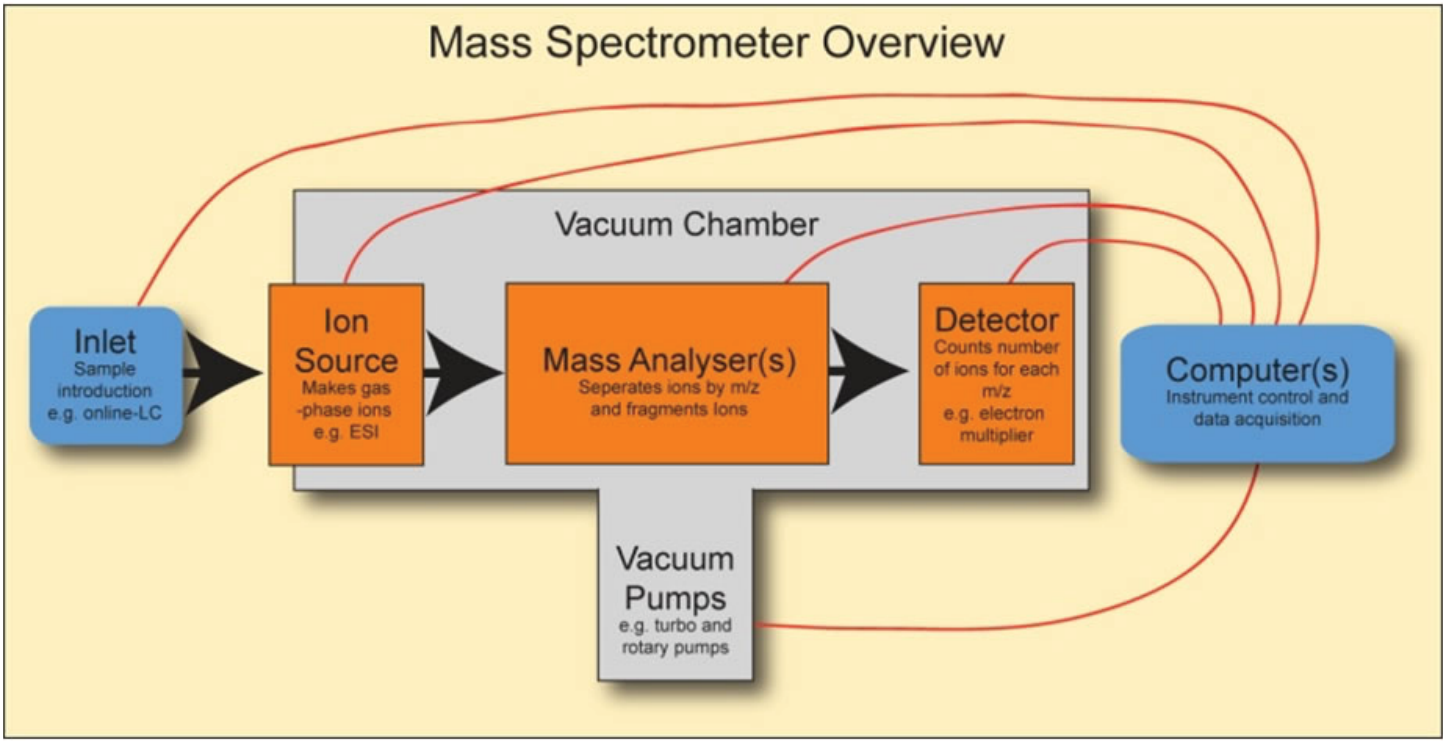

Figure 1: Mass spectrometer overview

through a very thin sample and interaction with it. An image is formed based on the interactions of the electrons with the sample. Through TEM we were able to see the structure of the catalyst and the interfaces that are important to understanding how and where the WGSR occurs. Energy dispersive X-Ray Spectroscopy (EDS) was used for the chemical characterization of STEM images.

II. Design of Activity Testing Reactor

Mass spectrometry was the principal method used to test activity of our catalysts for the WGSR. Figure 1 is a schematic of the portion of our system that was under vacuum conditions (1x10-7-10-8Torr). The RGA detector, mass analyzer, and ion source were connected to a rough pump and a turbo pump. The rough pump brought the pressure of the system down to 10-3 Torr and the turbo pump brought the pressure down to 10-7 Torr. An effort was made to minimize the volume of the ultra high vacuum components of the setup. Lowering the volume helped lower the pressure and reduced the risk of leaks. It is difficult to interpret mass spectrometry results when a leak is present especially if the species being tracked for are found in air, like CO_2. Residual gases and water that are stuck inside of the mass spectrometer can also skew the mass spectrum. To clean the system of such impurities we wrapped it in heating tape and aluminum foil and heated it above 200 °C. The scan performed after this bake out process lacked impurities like water.

Figure 2 shows the Clausen reactor cell that was used for our experiment. As shown by the arrows in the figure gas flowed through the reactor cell through a 1 mm quartz capillary containing our sample, the gas then flowed out towards the mass spectrometer and exhaust. A power supply controlled by a Eurotherm 3504 temperature supply was used to heat the catalyst samples. A thermocouple was connected to our reactor cell and the Euro-

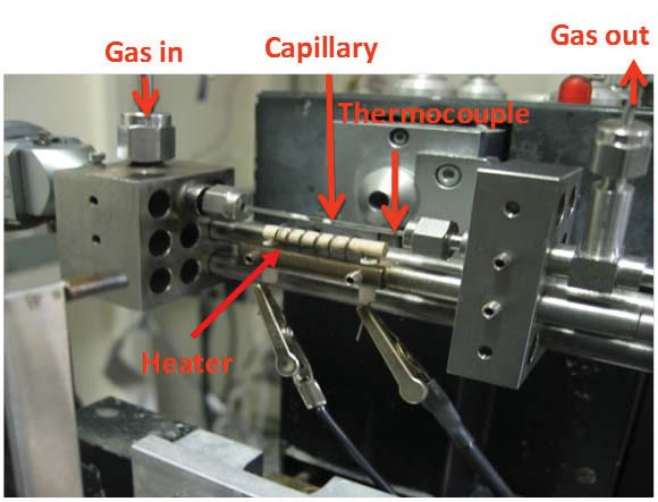

Figure 2: Clausen reactor cell

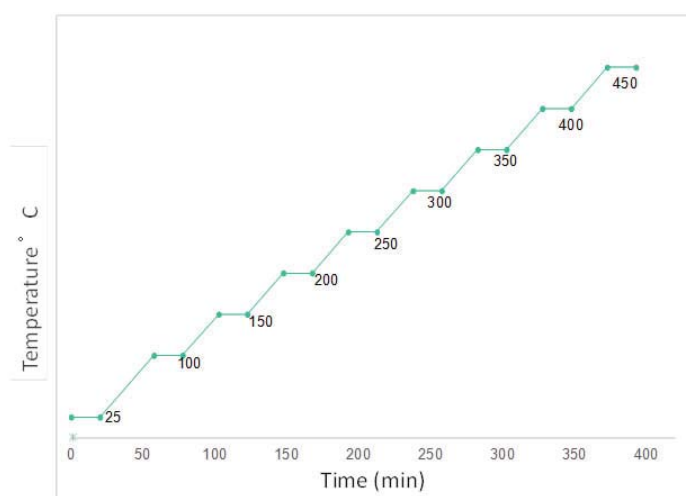

Figure 3: Heating profile

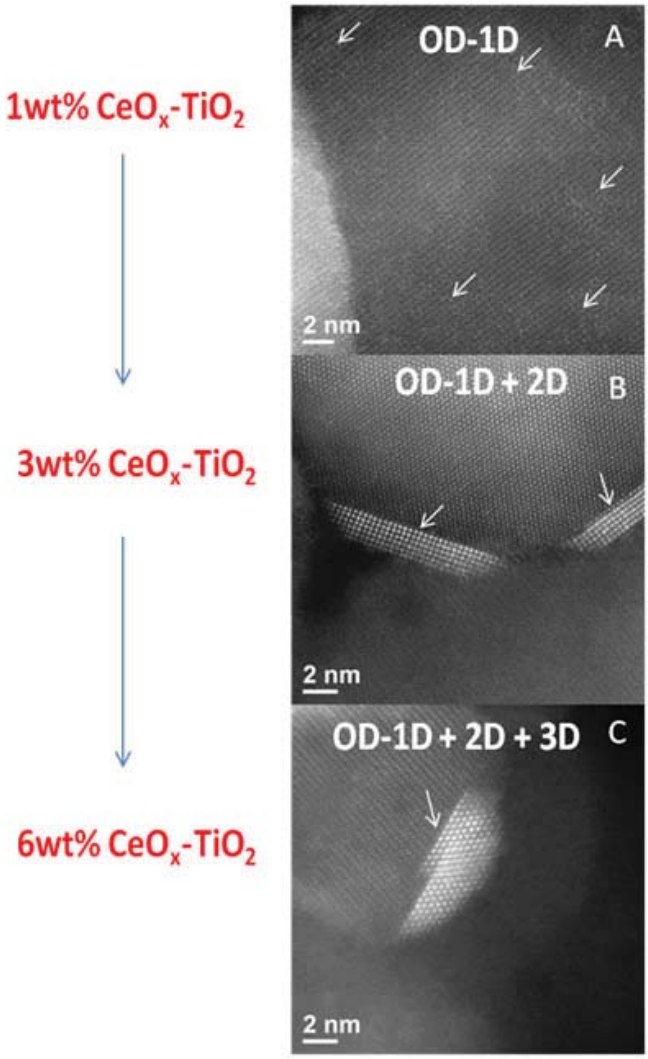

Figure 4: TEM images of 1, 3, and 6 wt% CeOx-TiO2

therm controller to regulate and monitor temperature.

Initially the temperature controller was very erratic; the program was not heating our sample slowly with precision. The temperature would escalate quickly to 300 degrees with erratic jumps in temperature. The problem was solved simply by wrapping the klausen cell in aluminum foil. The erratic jumps in temperature were likely due to the capillary being cooled by air.

Figure 3 shows the heating plan used in our experiment. This plan consisted of 20 minute holds at 25 °C, 100 °C, and 50 degree intervals up to 450 °C. The temperature was ramped at a rate of 5 degrees per minute between holds. This program was inputted into the Eurotherm 3504 temperature controller.

The reactant gases for the WGS are water and CO. Our gas flow setup started with two tanks of gas one containing 5% CO and Helium the other containing pure helium. Helium played no importance in the reaction this tank was used to flush out the system of any excess air before running the WGS. Our tanks were connected to two gas flow meters, which were linked to a water bubbler and finally our Clausen cell. 5% CO and 3% water flowed in helium and travelled inside of our capillary reacting with catalyst samples while the products of the reaction were recorded on our mass spectrometer.

A. STEM

A Scanning Transmission Electron Microscope (STEM) at the center for functional nanomaterials (CFN) was used to take high resolution images of our catalyst samples. These techniques were performed at an accelerating voltage of 200 kV, when performing EDS the sample was tilted 15 degrees to the detector. Images were taken of the three Pt/CeO_x-TiO_2 catalysts. The sample was ground up and placed on lacey carbon. STEM analysis involves passing a beam of electrons through a very thin sample and creating an image based off of the interaction with these electrons and our sample. The image is magnified and displayed on a computer screen.

In a previous study that used STEM to observe the different morphologies of Ceria on Titania, (with weight percentages of 1, 3, and 6% Ceria) it was found that there were 0D-1D clusters in the 1%, 2D chains/plates in the 3%, and 3D nanoparticles present in the six percent.3 These morphologies are significant because the properties of the Ceria in the system reflect the range of morphologies present.

Ceria particles (shown by the arrows) appear brighter in the samples due to the large difference in atomic number between Cerium and Titanium. Figure 3A is 1CeO_x-TiO_2, 0d and 1D ceria particles are present on the titania substrate.

Figure 3B shows two-dimensional chains and ceria aggregates that appear in addition to small clusters when the ceria loading is increased to 3 wt%.3 In Figure 3C the Ceria doping is increased to 6 wt% we can see large three dimensional ceria nanoparticles along with ceria chains and clusters.3 Unique interfaces which are crucial to catalytic activity are created from different size and dispersion of Ceria particles. STEM images of the Pt-3CeO_x-TiO_2 sample showed us that Ceria and Platinum were scattered in some areas and formed aggregates in certain areas. The aggregates of Pt were difficult to find in the Pt-3CeO_x-TiO_2 and even more so in the Pt-6CeO_x-TiO_2.

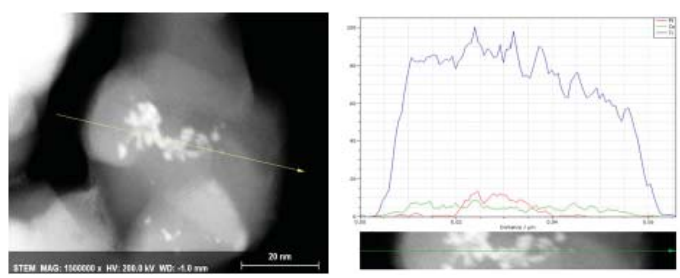

Figure 5: EDS line scan of Pt-3CeO_x-TiO_2 Right: EDS spectrum

This EDS line scan and the accompanying spectrum show an aggregation of Pt particles. Particles like these were very sparsely distributed.

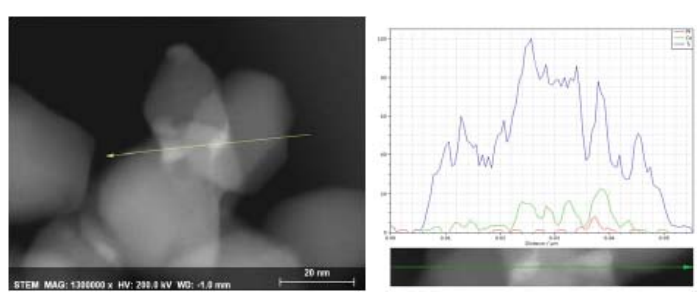

Figure 6: EDS line scan of Pt-3CeO_x-TiO_2 Right: EDS spectrum

This line scan shows an area with an aggregation of Ceria particles, these particles were sparsely distributed as well. The majority of Ceria and Platinum particles were atomically scattered over TiO_2.

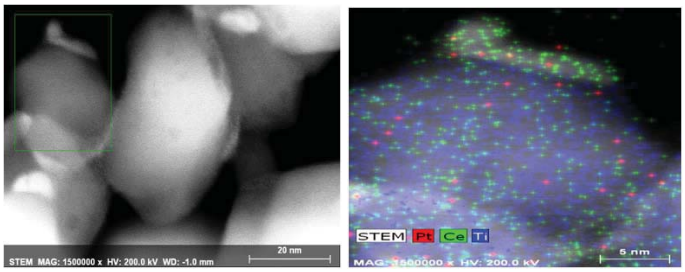

Figure 7: STEM scan of Pt-3CeO$_x$-TiO$_2$ Right: EDS map

The STEM scan and EDS map above shows us what we typically found, sparsely distributed Ceria and Pt and mainly TiO2 support.

B. Mass spectrometry

Mass spectrometry data was collected from experiments performed at the chemistry building in Brookhaven National Laboratory. Approximately 0.5 cm of sample was placed in a 1.0 mm diameter capillary between two pieces of glass wool. The capillary was then placed in a Klausen cell and surrounded by a heating coil to ensure uniform heating of the sample. Our gas setup consisted of a water bubbler and two tanks of gas. The gas tanks contained 5% CO in helium and pure Helium. The gases traveled through two mass flow controllers and then through the bubbler before making it to the reactor cell, we also installed a valve to bypass the water bubbler. The gas flow rate was set at 20cc per minute and was controlled by a Brooks instrument read out and controller. A vacuum system brought the pressure down to 10-7 Torr. The gases and water were allowed to flow through the reactor cell and the gaseous products were recorded by an SRS residual gas analyzer 300. We recorded spectra using SRS computer software for windows and later analyzed the spectra using Excel.

Five experiments were performed using our RGA mass spectrometer. The samples were 3CeO$_x$-TiO$_2$, Pt-1CeOX-TiO$_2$, Pt-3CeO$_x$-TiO$_2$, Pt-6CeO$_x$-TiO$_2$ and Puristar a Cu-ZnO industrial catalyst. We tested all these samples for the water gas shift reaction.

The Puristar catalyst reacted tremendously as we expected it to, this catalyst has been optimized for industrial use in the WGS. We used this catalyst as a benchmark because we knew it would react well and ensure that our mass spectrometer was working properly. The orange line represents the production of H_2 and the blue CO_2 the lines are almost identical as they should be since this is a one to one reaction. Temperature was held steady for 20 minutes after every increase in temperature and during this hold we expected the reactivity to stay constant, however there were small fluctuations in activity.

Figure 9 compares the production of CO2 for the Pt-CeO$_x$-TiO$_2$ catalysts. Catalytic activity decreased as we increased the percent doping of Ceria, the 1 Wt% sample was most reactive for WGS. The 1 wt% sample was also most active for photocatalytic splitting of water. 2 We only observe CO_2 production for these catalysts because the RGA has a high detection limit for H_2, none of the samples met the limit. We can still look at CO_2 for reactivity because the production of CO_2 and H_2 is stoichiometrically equivalent. The 3CeO$_x$-TiO$_2$ sample showed no activity, telling us that the presence of Pt is crucial for reactivity. In terms of activity for the WGS, the interfaces created by Pt and 0D and 1D Ceria clusters are better than those created by chains and 3D nanoparticles.

III. Conclusions

Pt-CeO$_x$-TiO$_2$ catalysts proved to be active for the WGSR. Mass spectrometry data showed us the relative activity of our catalysts. Activity was shown to decrease as the Ceria doping increased from 1wt % to 3 wt% and then to 6 wt%. We analyzed the interfaces present in the 1 wt% Ceria to understand why this sample had greater activity for WGS. STEM data showed us that Pt was generally scattered well, but it aggregated in a few areas. Ceria was also scattered in many areas and small aggregates were found. Further analysis is required to gain a better understanding of these samples. In Situ DRIFTS can help us understand the surface chemistry of this reaction. Knowing which parts of the catalyst participate in the forming and breaking of bonds is crucial to understanding and optimizing catalysts for future use. Using a quantitative technique like gas chromatography can give us accurate information on the amount of CO2 and H2 produced. This study was a good starting point, but future analysis is required to understand this catalyst.

IV. Acknowledgments

This project was supported in part by the U.S Department of Energy, Office of Science, Office of Workforce Development for teachers and Scientists (WDTS) under the Science Undergraduate Laboratory Internships Program (SULI).

V. References:

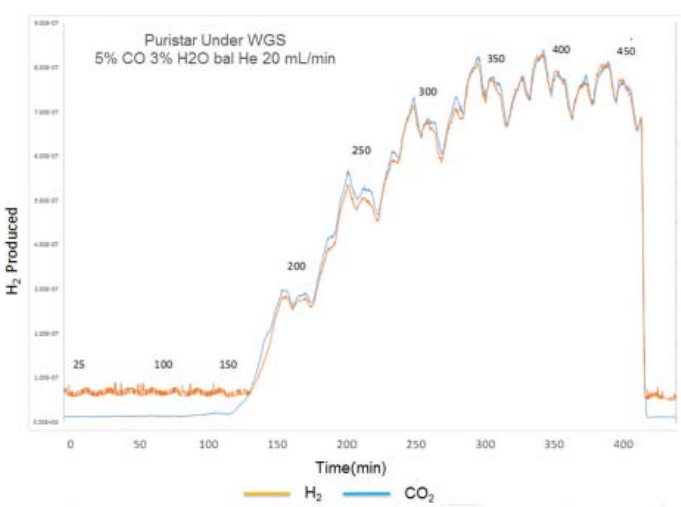

Figure 8: Activity of Puristar catalyst

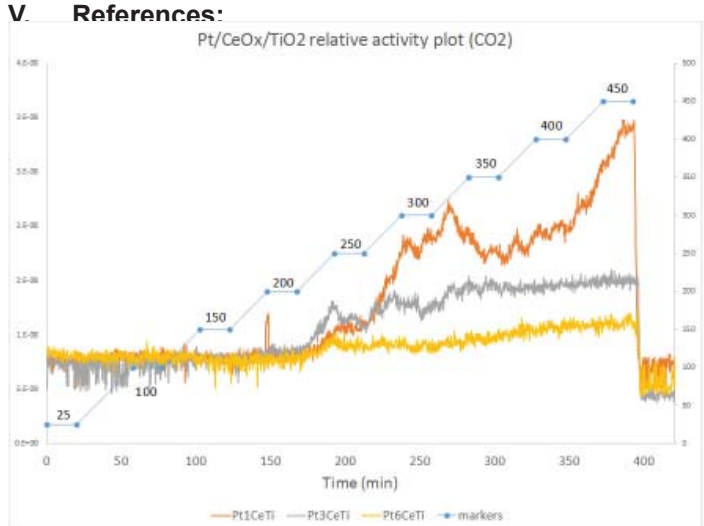

Figure 9: Activity of Pt-CeO$_x$-TiO$_2$ catalysts

[1]Rodriguez, J.A., J.C Hanson, Dario Stacchiola, S.D Senanayake, "In situ/operando studies for the production of hydrogen through the water-gas shift on metal oxide catalyst" Physical Chemistry Chemical Physics (2013), 15 (29): 12004-25

[2]Johnston-Peck, A.C, S.D Senanayake, J.J Plata, Shankhamala Kundu, Wenqian Xu, Laura Barrio, Jesus Graciani, J.F. Sanz, R.M Navarro, J.G Fierro, E.A Stach, J.A Rodriguez "Nature of the Mixed-Oxide Interface in Ceria−Titania Catalysts: Clusters, Chains, and Nanoparticles." The Journal of Physical Chemistry C (2013), 117 (28): 14463-14471

[3]Luo, Si, Thuy-Dong Nguyen-Phan, A.C Johnston –Peck, Laura Barrio, Shawn Sallis, D.A. Arena, Shankhamala Kundu, Wenqian Xu, Louis F.J. Piper, E.A. Stach, D.E. Polyansky, Etsuko, Fujita, J.A. Rodriguez, S.D. Senanayake "Hierarchical Heterogeneity at the CeOx−TiO2 Interface: Electronic and Geometric Structural Influence on the Photocatalytic Activity of Oxide on Oxide Nanostructures." J. Phys. Chem. C (2015), 119 (5): 2669–2679

Harmonic flow in heavy ion collisions: a search for phase transition and v_2 correlations

Mamoudou Ba
Department of Physics and Astronomy, SUNY at New Paltz, New Paltz, NY 12561
Erin O'Brien
Department of Physics, James Madison University, Harrisonburg, VA 22807
Paul Sorensen
Department of Physics, Brookhaven National Laboratory, Upton, NY 11973

Abstract

In heavy ion collisions, like those that occur about 50,000 times per second at the Relativistic Heavy Ion Collider (RHIC) at Brookhaven National Laboratory (BNL), a state of matter called quark-gluon plasma (QGP) is sometimes created. In this state of matter, quarks and gluons are no longer confined to their hadronic states, much like the early stages of the universe microseconds after the Big Bang. The theory of Quantum Chromodynamics (QCD) predicts that close to the transition to a QGP the particles will be strongly interacting. In this case, the viscosity of the QGP may be very small and the space distributions could be preserved and reflected in the momentum distributions. In this analysis, we study the observables that define the azimuthal particle distributions' post-kinetic freeze-out, taking into account the initial geometry of the collision. We look for a reported minimum in the viscous coefficient β" as collision energy is increased; If found, this minimum signals a phase transition in the heavy ion collision. We use Au+Au data of center of mas energies (collision energies) 7, 11, 14, 20, 27, 39, 62 and 200 GeV from RHIC and Pb+Pb at 2.76 TeV from the Large Hadron Collider (LHC). The anisotropic coefficients we study are v_2, which is called elliptic, and v_3, which is called triangular flow. We use a Monte Carlo (MC-) Glauber Model to calculate the eccentricities ($\varepsilon_2$and ε_2) and take into account the sensitivity of v_2 and v_3. The collisions produce and emit particles, whose asymmetry of transmission can be quantified in terms of elliptic flow, v_2. It is expected that the process in which particles are produced depends on the momentum of the particles. Due to this disparity, the null hypothesis of a collision must be modeled using varying sources for each momentum range. We test the independent source model for both low momentum and high momentum particles and found that the null hypothesis fails.

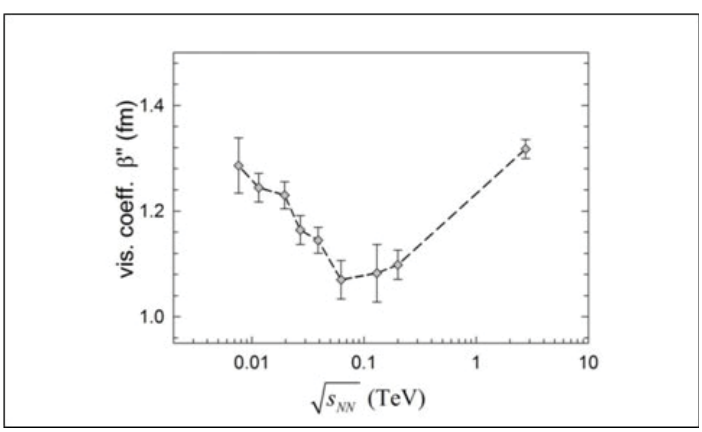

Figure 1. Viscous coefficient reported in Ref[1].

I. Introduction

At the Relativistic Heavy Ion Collider, beams of nuclei of various elements such as gold, and uranium, are accelerated around two rings at 99.9% of the speed of light. At such speeds, Albert Einstein's theory of special relativity predicts Lorentz contraction of length in the direction of motion. Thus a circular nucleus is no longer circular, but deformed. The nucleus of a gold atom is non- circular to begin with. The shape of this element is described as oblate, which means that one of the three coordinates is smaller than the other two. When these nuclei collide at very high energies, thousands of particles are created. As these particles fly out into the detector, they ionize the gas chamber. The STAR detector at RHIC can retrace the path of these particles and determine their origin. According to theory, this distribution of particles in the momentum space reflects their previous state. This state was discovered at RHIC as the quark- gluon plasma. A state of matter so exotic, it can only be created at very high temperature and pressure, much like what happened at the beginning of the universe, millionth of a second after the Big Bang. This is the primordial plasma that filled the universe long before matter particles were created.

II. Search for a phase transition

In this research, we search for a minimum in the viscous coefficient of anisotropic flow which if found signals a point near a phase transition. The data we use in this study is from the latest analysis of $v_n^2\{2\}$ as reported in the beam energy scan of v_3 paper currently in God Parent Committee review. In a previous study by Dr. R. Lacey and his colleagues, an exponential growth was

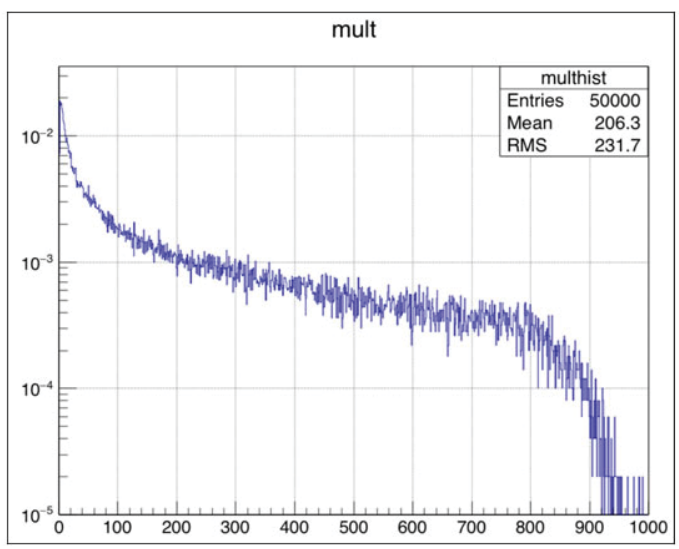

Figure 2. A multiplicity distribution for Au+Au collision at 200 GeV.

observed in the viscous correction of v_n/ε_n, which led to the search for a minimum in the viscous damping. Since the anisotropic coefficients v_2 and v_3 are sensitive to their respective eccentricities ε_2 and ε_3, we use a simple Monte Carlo Glauber model to extract these parameters for each centrality bin. Thereof, we take the ratios between v_n and ε_n. A multiplicity distribution is shown in Figure 2 for 200 GeV. This is close to what we would expect for Au+Au system at the before mentioned center of mass energy. This figure is a sample similar to what we would expect from all the energies, lest differing multiplicity.

Figure 3 shows the linearized exponential relationship in the viscous correction, where n is the harmonic number (2 or 3) and $\overline{R}$ is the initial state transverse size of the collision zone. We observe very small errors, which were calculated using the equation below.

$$\partial f = \sqrt{\left(\frac{\partial f}{\partial v_n^2}\partial v_n^2\right)^2 + \left(\frac{\partial f}{\partial \varepsilon_n^2}\partial \varepsilon_n^2\right)^2}$$

In our case, $f = \ln\left(v_n/\varepsilon_n\right)$ and δf is the error in f, ∂v_n^2, $\partial \varepsilon_n^2$,are errors in v_n^2 and ε_n^2 respectively. Furthermore, $\frac{\partial f}{\partial v_n^2}$ is the partial derivative of the function f with respect to v_n^2. We ignored the second term in the function above because $\partial \varepsilon_n^2$ decrease with the number of events. We run the model for 50,000 events, so the error in the eccentricity does not make much difference.

Similar analysis were conducted for Au+Au at discrete RHIC energies 7, 11, 14, 20, 27, 39, 62, and 200 GeV and using data from the Alice Collaboration, we did a study for Pb+Pb at 200 GeV. Then we extracted the slopes of the linear fits. These slopes are the viscous coefficients, -β" for each energy listed above. Figure 4 shows the viscous coefficient as a function of collision energy for both elliptic flow v_2 and triangular flow v_3.

A major observation from Figure 4 is that it does not quite replicate the reported results of Figure 1. For both 7 GeV and 20 GeV, the value we obtained is too low compared to the reported value. This means that we cannot reproduce the trend observe in Professor R. Lacey et al paper. One of the reasons for this is that for many of the energies, the linear fits do not represent the data very well.

Thus, we obtain very large χ^2. The elliptic flow tends to curve outward, while the triangular flow curves inward. In addition, the data we used in this analysis differs significantly from that in Ref[1] for peripheral collisions, while the central collisions are very similar; this is because now, STAR has better ability to suppress non-flow.

Our new objective was to find upper and lower boundaries, between which the curve in Figure 1 should lie, instead of attempting to replicate the same curve. Figure 5 Show $\ln v_n/\varepsilon_n$ as a function of $1/R$ for 200 GeV with two linear fits. The blue fit is for central collisions, and the red fit is for peripheral collisions.

The fits have very different slopes, suggesting one viscous coefficient for central and another for peripheral collisions. We conducted similar procedures for all energies and plotted the results in Figure 6.

In Figure 6, we observe that the results from Figure 1 do not match our results. The v_2 (right) plot is all over the place, but Ref[1] did not incorporate v_3 analysis. The v_2 analysis (left) for the peripheral collisions (red) resembles the reported results in Ref[1], with the exception of fluctuations in energies from 11 to

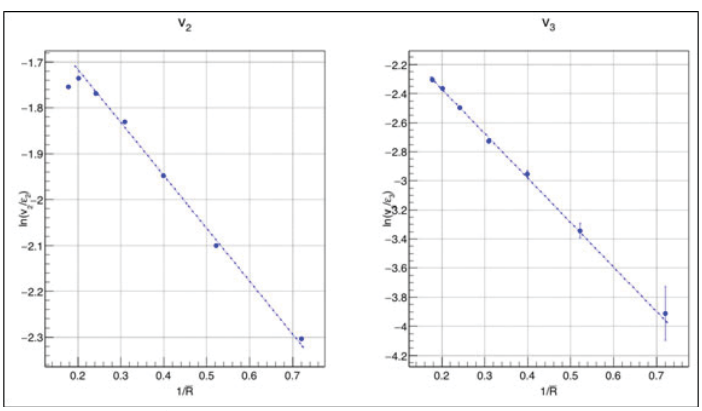

Figure 3. In v_n/ε_n as a function of $1/R$ for 14 GeV.

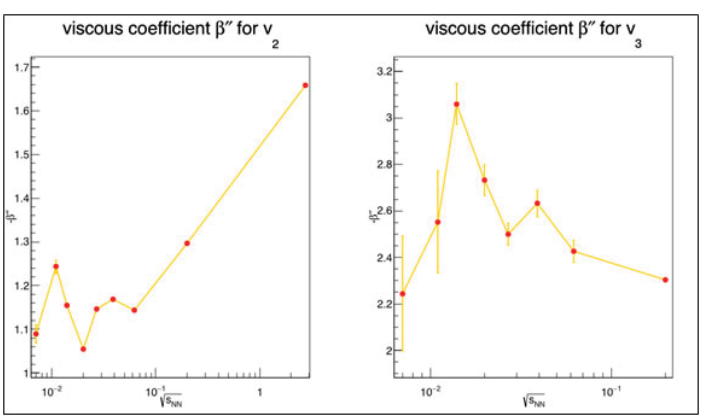

Figure 4. Viscous coefficient, −β", as a function of center of mass energy, $\sqrt{S_{NN}}$ in TeV.

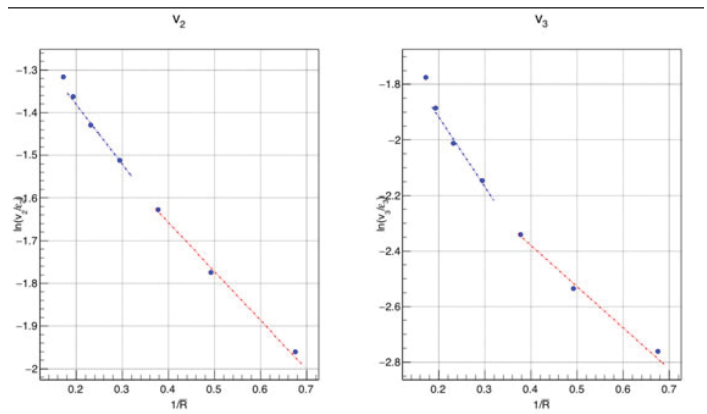

Figure 5. In (v_n/ε_n) as a function of $1/R$ for 200 GeV. The blue linear fit is for central collisions and the red is for peripheral collisions.

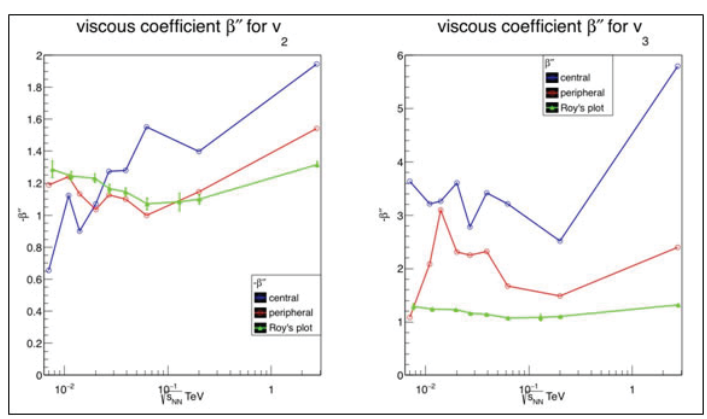

Figure 6. The viscous coefficient, −β", for central collisions (blue), peripheral collisions (red) and the results from Ref[1] (green).

20 GeV. For the v_2 analysis of central collisions (blue), the results are unreliable. The main trend in this analysis is an increase from 200 GeV to 2.76 TeV. This trend was also cited in the paper at an indicative sign of dropping in the viscous coefficient from high energies to mid energies (around 62 GeV), however an increase is not observed in this analysis from 62 GeV to 7 GeV. In this analysis, we do not observe the reported minimum in -β" that would imply a minimum in the viscous damping in $v_{2,3}$ Such results could have signaled a critical point.

III. V_2 correlations and the independent source model

Within the heavy ion collisions, there exists an overlap region, which contains the particles produced. Given the pressure gradient of the system, the emitted particles should mainly flow along the shortest axis, as opposed to having a random distribution of paths (pictured below FIG. 7).

The centrality of the collision refers to the amount of overlap between the nuclei and can range from central (0-5%) to peripheral (80-99%). We produced an individual plot of v_2 values over an array of transverse momentum, p_t for each centrality range. As seen in figure 8 below, within each plot a v_2 value is drawn from low p_t (green), the peak (blue), and using the slope from a flat fit over a high p_t range (red).

For two p_t ranges, the v_2 values were then plotted against N_{part} and N_{bin} (blue) (pictured in figure 9). If the trajectories of emitted particles were trivial, the proportionality between v_2 and N_{bin} or N_{part} would have the equation as stated below, which is known as the independent source model (represented in red).

That is, once created, it is as if the particles do not interact with their surroundings. In the QGP there are interactions such as pressure gradients, which creates the deviation of our data from the model. High momentum and low momentum particles are produced in different processes. High p_t particles are proportional to the number of binary collisions and low p_t to the number of participant pairs. Therefore, It is expected in the null hypothesis that at high p_t, correlation should follow an independent source model with N_{bin} as the number of sources, while a low p_t model would use N_{part}. For this reason it is appropriate to construct an independent source model based on N_{part} for low p_t (FIG. 9 left) and one based on N_{bin} for high p_t (FIG. 9 right).

Independent Source Model:

$$v_n = \frac{A}{\sqrt{N_{bin}}} = \frac{A}{\sqrt{N_{part}}}$$

Represented below in figure 10 are scaled values of v_2 compared with N_{bin} and N_{part} for each p_t range. Plotted in this format, the independent source model would give a constant value. These plots include all sets of data for a complete comparison of results. In bold is the set which is known to be relevant for the independent source model of both p_t ranges.

In peripheral collisions the pressure gradient is very small and in central collisions the difference in pressure gradients between the vertical and horizontal is very small due to the impact geometry. For mid-central collisions, the pressure gradient becomes larger than peripheral collisions and the difference in pressure gradients becomes larger than central collisions. Therefore at mid-centrality, emitted particles should have an increased anisotropy in their trajectories. The peak values plotted (FIG. 10) come from mid-central collisions; this data set aptly has the greatest deviation from the independent source model. The null hypothesis fails to describe the data both at high momentum and low momentum for the relevant source model, either N_{bin} or N_{part}. Our results coincide with what is expected for a strongly interacting quark-gluon plasma.

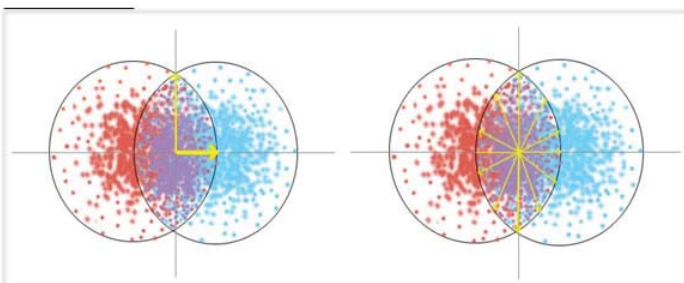

Figure 7. Pressure gradients (yellow) of the overlap region (purple) of two colliding ions (red and blue).

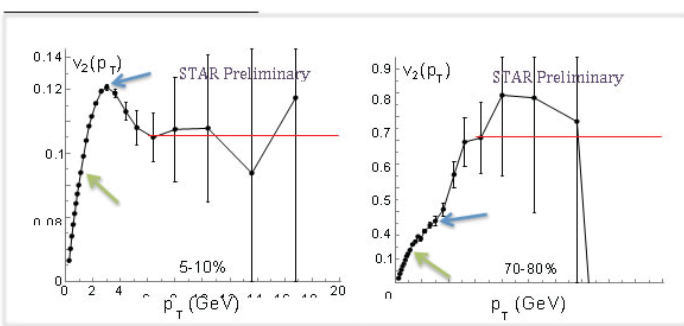

Figure 8. Values of v_2 over a range of transverse momentum for each centrality range.

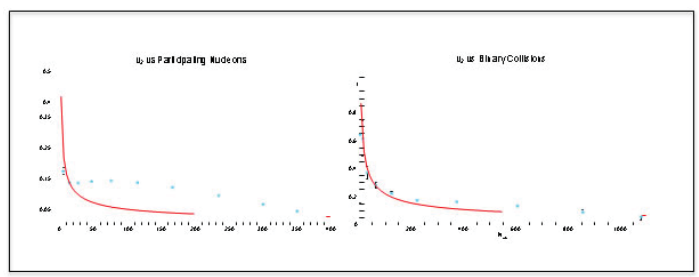

Figure 9. Values of v_2 plotted against the number of participating nucleons and the number of binary collisions. Our data is represented by the blue points and the independent source model is represented by the red line.

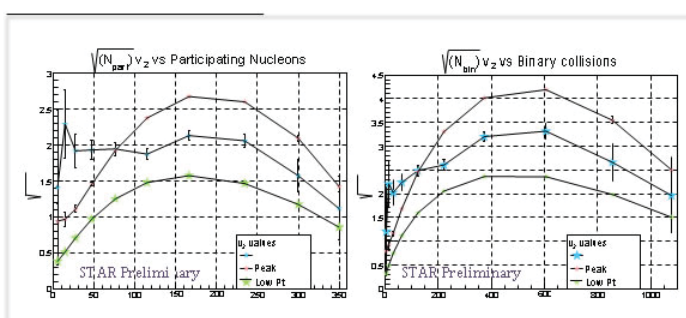

Figure 10. Scaled values of v_2 plotted against the number of participating nucleons and the number of binary collisions. Each momentum ranged pictured by color: high momentum (blue), peak v_2 value at medium momentum range (pink), and low momentum (green).

IV. References

[1]Lacey R. et al. Beam energy dependence of viscous damping of anisotropic flow. arXiv:1305.3341v3, 2013.

[2]ALICE http://hepdata.cedar.ac.uk/view/ins900651, Tables 1 and 2.

[3]Sorensen P., Mócsy A. The Sound of the Little Bangs. ArXiv:1008.3381v2 [hep-ph] 2010.

Wind farm: feasibility and environmental impacts

Matthew Bernard
Department of Mathematical Sciences, University of Massachusetts Lowell, Lowell, MA, 01854
Tim Green
Environmental Health and Safety, Brookhaven National Laboratory, Upton, NY, 11973
Fred Rispoli
Mathematics Department, Dowling College, Oakdale, NY, 11769
John Heiser
Biological, Environmental & Climate Sciences, Brookhaven National Laboratory, Upton, NY, 11973

Abstract

The renewable energy currently available at Brookhaven National Laboratory (BNL) is not adequate. I believe that with the installation of a wind turbine on site, BNL will be at the forefront of energy research and development as well as offsetting some daily energy use. I have taken a statistical approach to figuring out the feasibility of installing a wind turbine on site for energy production and research. I used wind speed data recorded over the last 20 years at the met field, a parcel of land located next to the BNL firehouse. The data sets for each year were very large, due to the fact that they had data for every minute of the year. I analyzed this data using the graphing and analysis capabilities of Excel and Minitab. Next, I was able to find the potential power production of a wind turbine using a well known formula and the average daily wind speeds in a given year, taking into account the 42% efficiency of wind turbines. Knowing the efficiency and conversion formula, I converted wind speed to power. These results showed me that the power potential of the windiest day is only slightly more than half a megawatt. The lowest power production potential is 441.30 kW/day, and the highest power production potential is 661.67 kW/day, similar to the output of the solar research array. From these results I realized that the installation of a wind turbine on site would provide a great tool for research by exploring mechanical improvements to the turbine hub and for analyzing the power produced. As a result of my work so far this summer, I have gained a much better appreciation for the differences between different types of renewable resources as well as gaining incredible knowledge on the use of statistical programs.

I. Background

The scope of the energy infrastructure is changing. The new wave of energy innovation is heavily focused on the use of renewable energy systems. Wind power is growing steadily in the United States as well as around the world. In 2008 only 79 countries had renewable energy and CO_2 emission reduction targets and as of 2013 there were 144 countries with similar targets. [1] Also, the global production of renewable energy in 2012 was 13.2% but in 2013 it rose to 22% a 5% increase in just one year. [2] Globally the installed wind power was 282,482 MW at the end of 2012. [2] New York State has set an ambitious goal of 80% Carbon Dioxide emission reduction by 2050. [3] When Governor Andrew Cuomo was elected in 2010 the total renewable energy production was 22% and by 2014 it was at 23%. [3] Although, the installed wind power production was increased significantly from 1275 MW to 1875 MW from 2010 to 2014. [3] To reach these goals the use of solar power and wind power has to continue on a steady upward trajectory each year. If New York could achieve a 30% growth rate of renewables or better and sustain it each year, there will be no problem reaching the renewable power production goals and carbon dioxide reduction goals by 2050 or sooner. Brookhaven National Laboratory (BNL) currently produces less than 1 MW per day from the solar research array on site, not even producing 1/80th of its daily power consumption from renewable energy sources as seen in Figure 6B. I will show that the installation of another type of renewable energy onsite will be worth while and explore the feasibility of installing a wind turbine and wind farm onsite at BNL. Globally there has been an increase of 383,000 GWH of renewable energy production from 1980 to 2006. [4] Even though there was an increase in non renewables and global energy usage. [4] The demand for energy increases every year and only a limited amount of renewable energy systems can be installed each year. However, as long as the demand for clean and renewable energy stays steady, a clean energy future is within our reach.

II. Methods

The research I am conducting is done in order to find the feasibility of installing wind turbines on the BNL site. In order to do this I needed information on the wind that is here at BNL. This information was given to me by Dr. John Heiser an employee of the Biological, Environmental and Climate Sciences Department. The data included relative humidity, temperature, barometric pressure, wind speed, wind direction, and wind gusts, at 10, 50,and 85 meters as well as the year, month, day, minute, and second. The information I focused on was the wind speeds for each minute at the 85 meter height. I did this because this is the height at which there would be the strongest winds and would provide the most power. For comparative measures I analyzed the wind speeds at 10 meters for 2014 and 2002, which are the lowest and highest levels of recorded wind speeds respectively. When I analyzed the data I used a program called Minitab. This allowed me to import the data which was stacked in a row of 525,600 points in Excel and Minitab would take those points and organize them into rows and columns. These where separated by the 1440 minutes each day and 365 days in each year as seen in Figure 5.

Once I had this data organized for each of the 21 years from 1994 – 2014 I found the average of the days, months and years. Also, by going down the column I was able to find the minute averages. These minute averages were used in many of my future analyses. The reason I found this average to be so important was because it gave you an absolute average day of wind, which can give a much more accurate future prediction. I used this information to find the power production potential. I assumed the wind turbine has a blade diameter of 10 feet, about 3 meters, and a swept area of 80 square feet or exactly 7.4322432 square me-

ters. [5] This formed my power conversion equation (in Watts), W = 0.625 *(7.4322432)*6^3. [5] Using the formula I converted all my average wind speed measurements to watts and then to kilowatts and megawatts.

Although, I realized something was wrong and after a few weeks, I found out that my assumed efficiency of a turbine was 100%, when in actuality the efficiency is only 42%. As I wanted the most accurate results I multiplied all my power production potential values by .42. To put the data in perspective the most power that I found a wind turbine could create is 661.67 kW/day and the least is 441.30 kW/day. So using this data I found a wind turbine that had cut-in speeds within reasonably expected wind speeds and found a type of wind turbine that would best suit the wind speeds at BNL. Using this I could calculate the cost of installing the wind turbine and the payback period. Working with the Environmental Health and Safety department at BNL it was important that I research the impact of the wind turbines on the fragile bird and bat species. All aspects of installing a wind turbine need to be considered first as to make the best decision for BNL.

III. Data and Results

A. Bird and bat effects

The research and analysis I did gave me some very interesting results. The location of BNL is along the Atlantic Flyway which stretches from Canada along the east coast and down into the Caribbean islands. [6] This causes trouble for migratory birds and given the height of 100 meters at the highest or about 328 feet the birds will be impacted. Although, I have learned that birds tend to fly well above 328 feet and on very rare occasions will fly at 328 feet or below. While this will not cause a significant impact on the bird or bat population, as there are only a small amount of animals that are killed by wind turbines each year, there are alternative less fatal wind turbines available. There was a recent installation of a wind farm in Texas which was installed in the direct path of a major bird migratory path and they used avian radar technology developed and used by NASA and US air force that could sense the approaching birds as far out as four miles. [7] When this happened the turbine would lock the turbines and allow the birds to pass. [7] Once these birds passed the turbine would unlock itself and resume normal operation. [7] If upon further research it is found that BNL is in a major hotspot for bird activity then a type of wind turbine with avian radar could be considered. Another possible factor in the bird fatality rate is the fact that on average the wind speeds are stronger from fall to spring as seen in the box plot below.

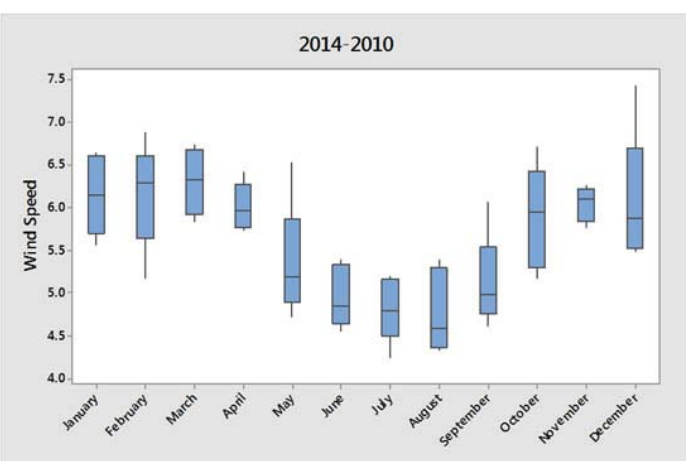

This Box Plot shows the average wind speeds for 5 years from 2010-2014 for each month of the year.

I found the time of the day when there is the least wind is late afternoon with the highest peak at night. This is good for the bird population but not good for the fragile bat population. Since the wind is usually the weakest during daylight hours and strongest at night the bird activity will be less affected during their most active times of the day. Although at night when the bats are most active so are the wind turbines, but with the bats echolocation the reported impact on bats has been significantly lower than that of birds. The one risk that has been reported with many wind turbines has been the current it creates which can pull bats into the turbine and kill them. The chance of death of bats and birds are very rare and only a small amount of fatalities occur each year, which is not enough to wipe out a species.

B. Power production potential and pay back period

There is readily available wind for the wind turbines to function and produce power. The only viable source of wind here at BNL is at 85 meters or higher. During my analysis of the wind data I was given I used primarily the data of the wind speeds at 85 meters. The data was recorded at the met field, a parcel of land located next to the BNL firehouse. Upon analyzing this data I found that the windiest year on record was 2002 and the least windy year was 2014, as shown in Figure 3 and 2 respectively. To analyze the data I had to find a wind turbine to use. This is because every turbine has different cut-in, rated, and cut-off speeds. Cut-in speed refers to the minimum speed needed to start turning the turbines and producing limited power. Rated speed is the speed needed to produce the amount of power the turbine is capable of producing. Cut-out Speed is the speed that when maintained for 10 minutes will cause the turbine to lock up and stop producing energy. I found the Enercon E53 500 KW wind turbine and used this for further analysis. The cut-in speed starts at 2.5 m/s which even on the least windy of days we are able to achieve. The rated speed starts at 10 m/s which can be achieved, and the cut-out speed is 25 m/s which in the 21 years of data was never reached. This means we would on average make between 200 kW and 500kW. Although the amount of power is relatively small the location is very important. The locations I was given as a possible location for installation were the former landfill, the met field, and when the smoke stack is taken down installation in its place. I found that the former landfill does not have the size needed to fit a wind turbine. The location of the smokestack and the met field are two reasonable locations. The area allotted has to allow for a 300 foot buffer zone in all directions around the turbine. Also, I used a boxplot to analyze the daily average wind speeds for all 21 years and a scatter plot to compare 5 years of potential power production per minute, as shown in Figures 1 and 4 respectively. Due to the fact that the Enercon E53 500 kW, which has a hub height of 73 meters and blade length of 27 meters and produces maximum power at up to 10 m/s I calculated how many continuous days in a year the turbine could produce maximum power given wind speeds at BNL. The results showed that the best year was 1996 with 32.68 days and the worst year was 2013 with 15.97 days and the average was 24.14 days. Finally, I was able to calculate the amount of time it would take for BNL to payback the installation of a wind turbine considering rebates and incentives. This cost of installing one wind turbine I found to be $627,500. Then using the Enercon E53 500 kW model, the return on investment each year is 18.8%

which would allow for the system to be paid for in 5-7 years. Also there is an incentive that can be applied by the New York State Energy Research and Development Authority (NYSERDA), which for our specific installation would give us about $174,000. With this Incentive the wind turbine would be paid for in as little as 3-5 years.

C. Noise and health impacts

The implications that come with installing a wind turbine very minimally affect a person's everyday life. These include most notable shadow flicker and noise pollution. Shadow Flicker refers to the constant shadow that the turbine casts during the day time. This constant flicker of light has rarely had a substantial affect on people. Although in rare cases it has been reported to cause epileptic seizures and symptom, mental illness, and irritability. The other noticeable affect is noise and visual pollution. The noise emitted at 300 meters is 43 decibels, which is more than a refrigerator at 40 decibels and less than an air conditioner at 50 decibels. [8] When I see a wind turbine I get excited as so do others but for many the sight of a wind turbine is just visual pollution. This can sometimes make the installation of wind turbines more difficult because of the people who do not want to see it. A recent example of this was with the Cape Wind offshore wind turbine project in long island sound. There were a select few people who were upset about their view being obstructed by these wind turbines and eventually these people derailed the project from coming into fruition.

IV. Wind Pattern Forecast

The use of forecasting models are important when analyzing wind turbine power production potential. This can be done by plotting all the recorded wind speeds for a day in a scatterplot and then trying to find a polynomial trend line that is most accurate. If the trend line has an r^2 value of 80 % or higher then you can accurately predict when the most wind will be available and the most power would be produced. An r^2 value is a percentage given to show the accuracy of a polynomial trend line when applied to a scatterplot. This can be especially important for the wild life that shares the air space with the wind turbine blades. For example if it is found that during the times that birds are most active the wind is lowest the turbine could be locked out, therefore reducing the bird fatalities and when the wind speeds are strongest the wind turbine will be unlocked to harness the energy. Although the forecasting of wind speeds don't just apply to individual days, forecasting models using trend lines can be used for monthly forecasts as well. They could be instrumental into deciding the feasibility of a wind turbine project. This is because you could predict the windiest months and determine to what degree it will interfere with the migrating birds. The 1996 scatterplot was found to have a 93% r^2 value when compared with a 6th degree polynomial trend line as shown in the figure below. Given that the model was so accurate I was able to predict when there will be the strongest and weakest winds throughout the year on a daily basis. This model showed me that late evening until early morning the wind speeds were the strongest and at around noon time they dropped until the lowest wind speed was reached at about sunset. Assuming there were no extreme deviations in the wind speeds then you could reasonably predict when during the day the most and least wind will be available. The use of a scatterplot and trend line for forecasting in Excel is instrumental in wind energy analysis.

V. Conclusion and Recommendations

The installation of a wind farm on BNL site would go a long way to offset carbon emissions and provide vital research opportunities as the new wave of energy production takes root. When the wind farm is installed it would be very powerful in the daily energy offset at BNL, shown in figure 6A. As there are limit-

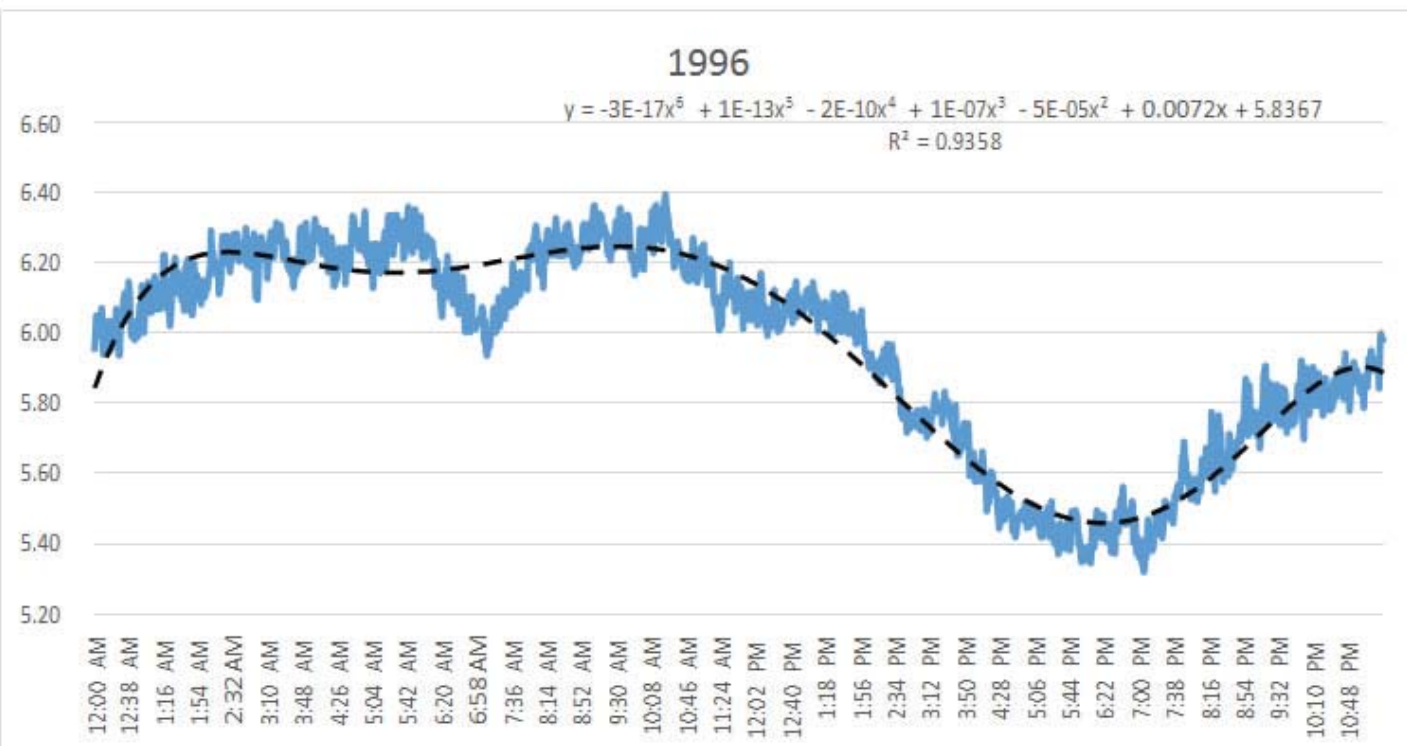

This scatter plot is 1996 average minute wind speeds in one day compared to the 6th degree polynomial trend line (Black).

ed places available for installation realistically only one turbine would be able to be installed. Also, the bird and bat population would need to be steady and not in decline as the inevitable fatalities of the wind turbine could damage a declining bird or bat population. Also, I used a 500 kW system to do my analysis so that the energy production could be similar to that of the solar research array that is currently used for BNL energy offset. For a steadier output though BNL could consider a smaller system. The wind speeds are the best higher up and with the Enercon E53 500 kW wind turbine its highest point reaches 100 meters, so it can be provided with the strongest wind available. I enjoy seeing wind turbines installed and running, and I hope others at BNL do to because a project with so much potential as this one has, would be a shame to see falter because of visual unattractiveness. A vast area of farm land in North Carolina is getting a wind farm installed with low wind speeds. [9] This is possible with taller wind turbines that catch more powerful wind and also the construction of larger blades that can catch stronger and weaker wind and spin the blades faster producing more energy with lower wind speeds. [9] There are a multitude of options for wind turbine installation from the use of avian radar to stop a turbine when birds or bats are flying nearby to taller turbines with bigger blades to catch more wind. The research opportunities associated with the installation of even one wind turbine are so great given such a short payback period and a useful life of 20 years, that BNL should not pass up the opportunity to be a leader in turbine hub research or wind power analysis. The wind energy and renewable energy industries are rapidly growing and BNL can be a part of it, all we have to do is make the next step.

VI. References

1 "Renewable Energy." Wikipedia. Wikimedia Foundation, 20 July 2015. Web. 27 July 2015.

<https://en.wikipedia.org/wiki/Renewable_energy>.

2 "FAQs: Renewable Energy." International Energy Agency. 2015. Web. 27 July 2015.<http://www.iea.org/aboutus/faqs/renewableenergy/>.

3 Waldman, Scott. "Slow Going, so Far, on Ambitious State Renewables Plan." Capital. Capital, 1 Dec. 2014. Web. 27 July 2015. <http://www.capitalnewyork.com/article/albany/2014/12/8557506/slow-going-so-far-ambitious-state-renewables-plan>.

4 De Decker, Kris. "How (not) to resolve the energy crisis." Resilience. Low-tech Magazine, 24 November 2009. Web. 28 July 2015. <http://www.resilience.org/stories/2009-11-24/how-not- resolve-energy-crisis>

5 "The Bottom Line about Wind Turbines." Otherpower. Buckville Publications LLC. 2012. Web. 27 July 2015. <http://otherpower.com/bottom_line.html>.

6 "North American Migration Flyways." Bird Nature. 2001. Web. 27 July 2015. <http://www.birdnature.com/flyways.html>.

7 "Impact of Wind Energy on Environment, Agriculture, Birds, Bats, Climate and Humans." Powered by Wind. Republic of South Africa Department of Energy, and the Embassy of Denmark. Web. 27 July 2015. <http://www.poweredbywind.co.za/dl/english/factsheet2.pdf>.

8 "How Loud Is A Wind Turbine?" GE Reports. General Electric Company, 2 Aug. 2014. Web. 3 Aug. 2015. <http://www.gereports.com/post/92442325225/how-loud-is-a-wind-turbine>.

9 Dearen, Jason. "South Getting Its First Wind Farm Soon as Bigger Turbines Make the Region Viable." US News. U.S. News & World Report, 12 July 2015. Web. 27 July 2015.

<http://www.usnews.com/news/us/articles/2015/07/12/apnewsbreak-south-getting-its-first-big- wind-farm-soon>.

VII. Acknowledgements

This project was supported in part by the U.S. Department of Energy, Office of Science, Office of Workforce Development for Teachers and Scientists (WDTS) under the Science Undergraduate Laboratory Internships Program (SULI).

VIII. Appendixes

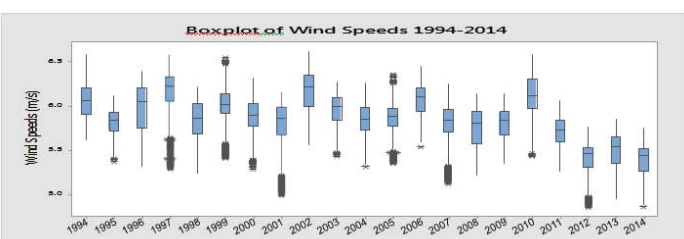

Figure 1: This box plot shows the average daily wind speeds for each of the 21 years from 1994-2014.

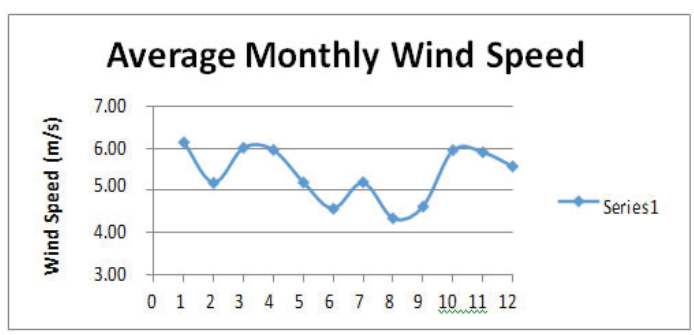

Figure 2: this line chart shows the average monthly wind speeds for 2014, the least windy year.

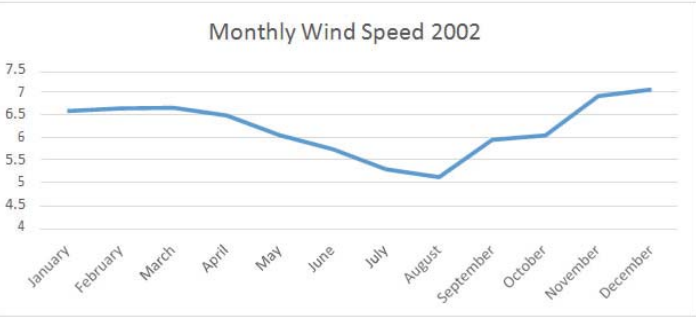

Figure 3: This line chart shows the average monthly wind speeds for 2002, the windiest year.

Date	1/1/2010	1/2/2010	1/3/2010	1/4/2010
Number	WSM88_1	WSM88_2	WSM88_3	WSM88_4
1	2.9	6.2	11.2	9.7
2	3.1	6.8	12	10.8
3	3.1	6	10.5	11.6
4	3.3	5.8	11.2	12.6
5	3.4	6.2	12	12.2
6	3.4	6.2	12.5	10.4
7	3.4	5.5	9.3	11.9
8	3.4	5.9	9.7	11.9
9	3.4	5.3	13.2	11.2
1440	6.3	12.3	9.4	6.5

Figure 5: This picture shows the way I used Minitab and Excel to organize the wind data I was given.

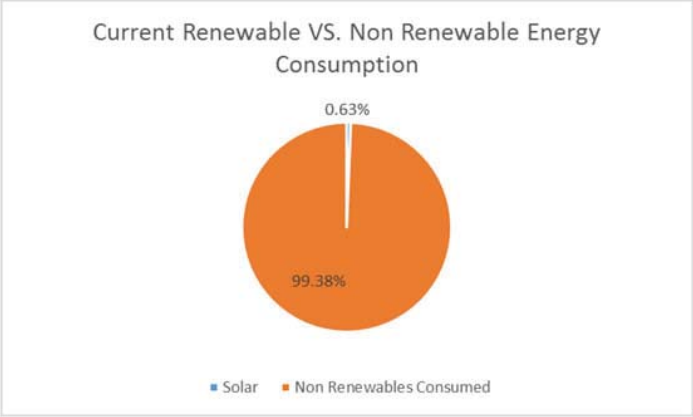

Figure 6B: This Pie chart shows the current renewable energy production on the BNL site.

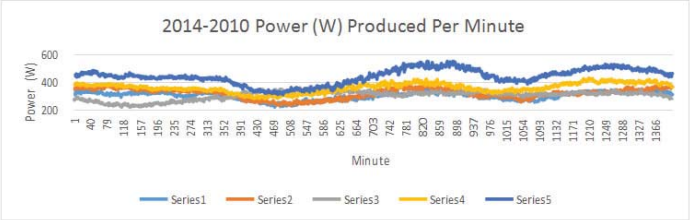

Figure 4: These scatter plots compare the average power production potential per minute in one given day for 5 years from 2014-2010. 2014 (Light Blue), 2013 (Orange), 2012 (Grey), 2011 (Yellow), 2010 (Blue)

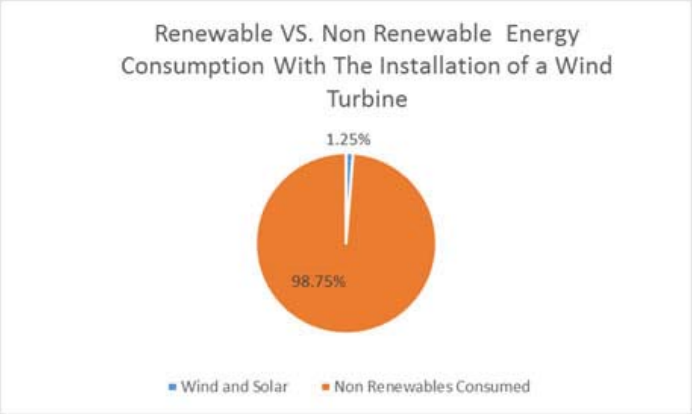

Figure 6A: This Pie chart shows the potential renewable energy production with the installation of a wind turbine on the BNL site.

Acoustic clicktomount: using sound pulses to solve the crystal harvesting bottleneck for high throughput screening applications

Yasmin Nessim Samara[1,4]‡, Liam McCarthy[1,5]‡, Ludmila Leroy[1,4]‡, Mary T. Bollard[1,6]‡, Denise Laspina[1,7]‡, Alexander Scalia[1,8], Daniel L. Ericson[1,9], Christian Roessler[2], Allen M. Orville[2,3], Robert M. Sweet[2,3], and Alexei S. Soares[2]†
† Correspondence: soares@bnl.gov
‡ The three cofirst authors all contributed equally to this work; the order of names was determined at random.

[1]Office of Educational Programs, Brookhaven National Laboratory, Upton, NY, 119735000, USA
[2]Photon Sciences Directorate, Brookhaven National Laboratory, Upton, NY, 119735000, USA
[3]Biosciences Department, Brookhaven National Laboratory, Upton, NY, 119735000, USA
[4]CAPES Foundation, Ministry of Education of Brazil, Brasilia, DF, Zip Code 70.040020, Brazil
[5]Suffolk County Community College, 533 College Rd, Selden, NY 11784, USA
[6]Department of Biology, York College of Pennsylvania, 441 Country Club Rd, York, PA 17403, USA
[7]Department of Biology, Stony Brook University, NY, 117945215, USA
[8]Department of Biological Sciences, 4400 Vestal Parkway East, Binghamton University, NY, 13902, USA
[9]Department of Biomedical Engineering, University at Buffalo, SUNY, 12 Capen Hall, Buffalo, NY, 14260, USA

Keywords: Crystal harvesting, acoustic droplet ejection, crystal mounting, automation, crystallography, microcrystals, high throughput screening, drug discovery.

Abstract

Crystal harvesting has proven difficult to automate and remains the rate limiting step for many structure determination and high throughput screening projects. This has resulted in crystals being prepared faster than they can be harvested for Xray data collection. Fourth generation synchrotrons will support extraordinarily rapid rates of data acquisition, putting further pressure on the crystal mounting bottleneck. Here, we report progress towards a simple solution whereby crystals can be harvested directly from MiTeGen crystallization plates using clicktomount technology. This technology uses an acoustic pulse to eject each crystal out of its crystallization well, through a short air column, and onto a MiTeGen micromesh. We first tested our harvesting equipment by transferring separately grown crystals to fragments of various crystallization plates. We then grew and harvested crystals from intact MiTeGen plates, which we found to be acoustically compatible. Crystals can be individually harvested, or serially combined with a chemical library such as a fragment library.

I. Introduction

Acoustic droplet ejection (ADE) is an automated, keyboard-driven technology for growing protein crystals (Villasenor et al., 2012), improving the quality of protein crystals (Villasenor et al., 2010) and transferring protein crystals onto data collection media (Soares et al., 2011) such as MiTeGen MicroMesh™ sample holders ("micromeshes" hereafter). ADE can also be used to screen chemical libraries using either cryocooled crystals (Yin et al., 2014) or room temperature crystals (Teplitsky et al., 2015). All of these methods use momentum from a sound pulse to move liquids and/or suspended crystals from the source location, through a short air column, to the destination with high precision (Figure 1). Acoustic crystal transfer is gentle (no hand tools are required) and fast (2.33 ± 0.04 crystals harvested per second). The equipment is simple to use and does not require a high level of training or manual dexterity.

Commercial ADE equipment achieves high volume transfer accuracy (±5% v/v) and precise droplet trajectory (± 20 µm) in part by using specialty labware with exactly specified composition and fabrication (Ellson et al., 2003). There is currently no purposebuilt, acoustically transparent crystallization plate that is constructed from acoustically compatible (impedance matched) plastic.

We have previously demonstrated[1] that protein crystals can be grown in and harvested from acoustically compatible 384well polypropylene microplates™ (Labcyte Inc., Sunnyvale, CA) that can be adapted for protein crystallization (Cuttitta et al., 2015). However, some researchers may prefer to grow their crystals in conventional crystallization labware such as a MiTeGen in situ-1™ crystallization plate. Even though in situ MiTeGen crystallization plates are not constructed from materials that are designed to be acoustically transparent, this approach is possible because their plastic bases are sufficiently thin that they do not obstruct acoustic ejection.

A recent review of protein crystal harvesting approaches categorized different technologies based on the level of human involvement and on the extent of contact between the harvesting apparatus and the specimen (Deller & Rupp 2014).

Robotic technologies require a harvesting tool that prods the specimen and are becoming increasingly operator independent (Viola et al, 2011). Contact free crystal harvesting is possible using laser tweezers (Wagner et al., 2013) or magnetic convection (Tung et al., 2014) with the assistance of experienced human operators. Liquid handling assisted harvesting is a promising alternative for minimizing solvent background in cases where the crystals are sufficiently robust to endure the solvent removal process (Luft et al., 2014; Kitago et al., 2010).

Here we describe a bridging technology that combines acoustic equipment with conventional crystallization plates ("nonacoustic labware" hereafter). We demonstrate that a commercially available Echo 550 liquid handling instrument (Labcyte Inc., Sunnyvale, CA) can be used to harvest protein crystals from MiTeGen plates onto micromeshes. At present, the harvesting process is laborious and clumsy because crystallization plates are not designed with acoustic compatibility in mind. This necessitates the assembly of a "plate chimera" that contains some components from an Echo compatible plate (to satisfy the plate verification step performed by the Echo 550) and some components from conventional crystallization plates (to grow the protein crystals). High throughput screening applications may warrant the effort needed to set up this crystal transfer apparatus. We demonstrate this utility by screening a small library of 304 fragments. In the discussion, we propose modest technical improvements that could make this system simple to use. The most important improvement is to design an acoustically compatible crystallization plate. Crystal visualization inside the acoustic injection apparatus would also be helpful.

II. Materials and methods

To demonstrate crystal harvesting from nonacoustic labware onto micromeshes, we used the Echo 550 to transfer three types of test protein crystals (thermolysin, lysozyme, and trypsin) onto micromeshes (Cuttitta et al., 2015). The crystals were harvested from MiTeGen in situ plates and from CrystalDirect plates. Thermolysin was used for proof of principle because it is simple to mount acoustically.

Lysozyme is a dense material that can be challenging to mount acoustically. Trypsin has been studied as a model target for development of new drug discovery technologies (Newman et al., 2009).

To demonstrate acoustic crystal mounting from nonacoustic labware, crystals of thermolysin, lysozyme, and trypsin were grown using conventional hanging drop techniques on MiTeGen plates that are suitable for in situ data collection[2] (Table 1). Thermolysin crystals were grown by equilibrating 330 mg/mL thermolysin (SigmaAldrich® T7902) in 1.45 M calcium chloride, 50 mM Tris pH 7.5, and 45% DMSO over a reservoir solution containing pure water (crystals cryoprotected by 20% ethylene glycol). Lysozyme crystals were grown by equilibrating 120 mg/mL lysozyme (SigmaAldrich® L4919) in 100 mM sodium acetate pH 4.6 and 2% sodium chloride over a reservoir solution containing 8% sodium chloride (crystals cryoprotected by 20% glycerol). Trypsin crystals were grown by dissolving 30 mg/mL trypsin (SigmaAldrich® T1426) with 10 mg/mL benzamidine and 10 mM calcium chloride in 20 mM HEPES (pH 7.0) with 3.75% PEG 3350 and 5% glycerol; this was equilibrated over 15% PEG 3350 and 20% glycerol (no additional cryoprotection needed). To facilitate the harvesting of large crystals (> 50Å) the mother liquor was made into a Bingham fluid by adding 0.3% agarose (a Bingham fluid can be acoustical ejected like a liquid but prevents large crystals from settling to the bottom of the crystallization well).

Modifying a polypropylene plate: Five commonly used crystallization plates were cut into pieces that were one crystallization chamber wide and five crystallization chambers long ("plate sections" hereafter). Each of the five plate sections was transferred to an acoustically transparent plate that was modified to couple the nonacoustic labware to our acoustic system. The middle section of a 384 well polypropylene microplate™ (Labcyte Inc) was modified by grinding down the honeycomb structure to a total height of 1.7 mm. The top of the modified polypropylene plate was coated with ~ 3 mm thick agarose pillow (see below) to acoustically couple the MiTeGen plate fragment with the crystal containing drops to the Echo 550. Without further preparation, the plate sections (from nonacoustic labware) were carefully deposited onto the agarose pillow (Figure 2a), and this completed the structure of the "modified polypro". Care was taken to avoid any air gap between the plastic and the agarose pillow. This apparatus was used both to examine the acoustic properties of nonacoustic labware (§2.1) and to harvest crystals from the plate sections, either one crystal at a time (§2.2) or rapidly for high throughput screening (§2.3& §2.4). Crystals were harvested onto micromeshes for Xray data collection. The apparatus and specimens were photographically documented at each stage of the crystal transfer procedure.

To prepare the agarose pillow that is used to couple the labware, 1% agarose was heated in deionized water to 100°C for 1 minute. A 1000 µL pipette was used to fill each well in the honeycomb structure of the modified polypro plate with the agarose (SigmaAldrich® A6877). An additional 2.0 mm layer of agarose was carefully layered on top of the honeycomb, taking care to prevent bubbles (Figure 2a). The nonacoustic labware was pressed into the agarose layer (while the agarose was still soft, just before the agarose began to supercoil into a hydrogel) until it contacted the honeycomb structure.

Fabricating a hybrid MiTeGen plate: An entire 384 well polypropylene microplate™ (Labcyte Inc) was modified by grinding down the honeycomb structure to a total height of 1.7 mm. The top of the modified polypro was coated with a 3 mm thick agarose pillow (see paragraph above) to acoustically couple the entire MiTeGen plate with the crystal containing drops to the Echo 550 (Figure 2b). This apparatus was used to harvest crystals that were grown in the hybrid MiTeGen plate and mounted onto micromeshes for Xray data collection (§2.5).

The apparatus and specimens were photographically documented at each stage of the crystal transfer procedure.

Diffraction data were collected at the National Synchrotron Light Source (NSLS) beamline X25, Cornell High Energy Synchrotron Source (CHESS) beamline A1, and the Stanford Synchrotron Radiation Lightsource (SSRL) beamline BL141.

Data sets were processed with HKL2000 (Otwinowski et al., 2001) and further processed using CTRUNCATE in the CCP4i suite (Winn et al., 2011). Structures were obtained by molecular substitution from published models and refined using REFMAC (Winn et al., 2003) and ArpWarp (Perrakis et al., 2001) (starting models 4tlnthermolysin, 1lyzlysozyme, 4ncytrypsin) (Holmes et al., 1981; Diamond 1974; Yin et al., 2014). Structures were visually inspected using coot (Emsley et al., 2004).

A. Acoustic properties of nonacoustic labware

We used the Echo WellPing (Labcyte Inc., Sunnyvale, CA) software to examine the acoustic properties of five designs of nonacoustic labware. Each design was placed on an agarose pillow that was deposited on a custom modified source plate (Figure 2a). We then recorded the acoustic signature of each of the nonacoustic labware designs.

B. Visualizing and harvesting protein crystals

A Leica microscope with a polarizing lens was used to discover the location of promising trypsin crystals in a MiTeGen plate section (Figure 2a). The trypsin crystals were colored with a red dye for clarity. After a crystal was selected for harvesting, its position was adjusted by sliding the MiTeGen plate section over the agarose pillow until the center of the crystal was aligned with the center of one of the wells in the modified polypro. The level of wetness of the agarose pillow was balanced so that there was a good acoustic coupling to the crystal selected for harvesting, while not being so wet that the nonacoustic labware would inadvertently slide out of position. A pin platform base was fitted with micromeshes (no plate lid was needed).

The source plate assembly (consisting of the modified polypro with the MiTeGen plate section on top of it) was carefully placed in the lower tray of the Echo 550. The pin platform box was placed in the destination tray. The Echo Array Maker (Labcyte Inc., Sunnyvale, CA) software was then used to harvest the desired crystal out of the MiTeGen plate section and onto one of the micromeshes in the pin platform base. The micromesh containing the crystal was then manually removed from the pin platform base and inserted into a MiTeGen Reusable BaseTM (model B1AR) and immediately cryocooled in liquid nitrogen.

C. Comparing hand mounted controls with acoustically mounted crystals

The apparatus described in §2.2 was assembled with MiTeGen plate segments containing lysozyme crystals and with CrystalDirect plate segments containing thermolysin crystals. Ten lysozyme crystals and ten thermolysin crystals were acoustically transferred to micromeshes. Additionally, ten lysozyme crystals and ten thermolysin crystals were hand mounted onto micromeshes. All crystals were cryocooled. Xray diffraction data were obtained from each of the acoustically harvested test crystals and similarly from each of the hand harvested control crystals.

D. High throughput screening of fragment libraries

The apparatus described in §2.2 was assembled with MiTeGen plate segments containing lysozyme crystals. The lysozyme crystal had a cuboidal habit with a long axis of approximately 50 µm. The plate segment contained 20 µL of dense crystal slurry with a concentration of approximately 70 crystals per µL. A pin platform box was assembled as described in §2.2, but in this case the pin platform was populated to its full capacity with 96 micromeshes. A polypropylene source plate was prepared containing a minlibrary with 33 chemicals, including two known lysozyme ligands, Nacetyl glucosamine (NAG) and benzamidine. The Echo 550 was used to dispense 20 nL of each of the 33 chemicals to its own distinct micromesh. The solvent around each chemical was then allowed to evaporate (leaving the chemical residue still adhered to the micromesh). The Echo 550 was then used to transfer 20 nL of lysozyme crystal slurry to 36 micromeshes (including three controls without chemicals). All of the crystalcontaining micromeshes were cryocooled and Xray diffraction data were individually obtained from each specimen.

We used the same technique to screen a 304 fragment library for binding to trypsin crystals. The fragment library consisted of 45 cocktails, each of which had between six and ten distinct chemicals solvated in 20 mM HEPES (pH 7.5), 0.15 M sodium chloride, 10% glycerol, and 5 mM DTT (dithiothreitol). We ejected 20 nL of trypsin crystal slurry onto each of 45 micromeshes and combined the crystals with 5 nL of each cocktail (the chemicals were not allowed to dry because some of the chemicals rapidly degrade if desiccated). The trypsin crystals had a rodshaped habit approximately 50 µm long. To facilitate crystal identification and centering, the crystals were dyed with a red colorant before ejection. We estimate that, on average, five crystals were transferred to each mesh.

E. Harvesting protein crystals grown in hybrid MiTeGen plate

This apparatus was used to harvest lysozyme, trypsin, and thermolysin protein crystals that were grown in the hybrid MiTeGen plate. Crystals were acoustically mounted onto micromeshes (similar control crystals were manually harvested).

Xray data were obtained from both the acoustically mounted and control lysozyme crystals (trypsin and thermolysin were visually documented, but no Xray data were obtained).

III. Results

Assembly and testing of the acoustic harvesting apparatus was time consuming. The fit between each plate segment and the modified polypro had to be individually adjusted. However, once the system began to work, the crystal harvesting was reliable and remarkably fast. The high throughput acoustic crystal harvesting for the minilibrary screening that was described in §2.4 was completed in less than half a minute. In the discussion, we describe simple improvements that could make high throughput crystal harvesting convenient and robust.

With some effort it was possible to couple all of the plate segments to the modified polypro as described in §2. In some cases, acoustic harvesting was not possible because too much acoustic energy was lost (see §3.1) so that the momentum transferred to the crystal slurry was insufficient to eject a droplet. However, MiTeGen plates and CrystalDirect plates did not greatly diminish the acoustic signal and it was straightforward to harvest crystals from those two plates.

A. Acoustic signature of nonacoustic labware

The sound pulse must retain sufficient amplitude in order to eject crystals from the slurry. The amplitude is reduced mainly by scattering (loss of energy inside of a bulk material) and by reflection (loss of energy at the interface between two materials). Both of these sources of energy loss played a role in making one or more of the tested plates unable to eject crystals. Figure 3 shows the energy reflected from all of the interfaces in each tested nonacoustic labware, as well as a control measurement with no plate segment present. The acoustic energy reflected from the nonacoustic labware is directly visible. The scattered energy can be computed by comparing the amplitude of the reflection from the liquidair interface with the amplitude obtained when no plate is present. All reflections were scaled using the intensity of the reflection from the bottom of the modified polypro plate (since this component is common to all of the tested systems, and occurs before any of the other materials). The results confirm that the MiTeGen plate and the CrystalDirect plate are moderately acoustically transparent. A custom built acoustically transparent crystallization plate would likely perform even better.

B. Selecting and acoustically mounting one specific crystal

We targeted a small crystal cluster containing two moderate sized trypsin crystals, and ejected those specific crystals onto a micromesh (Figure 4). Successful ejection of specifically targeted crystals required careful alignment of the crystals to the ejection zone (we had many near misses). This process would be greatly simplified if the Echo had an internal visualization system.

C. Diffraction from acoustically mounted crystals is comparable to controls

We observed no significant difference between the diffraction of the acoustically harvested crystals and the hand harvested controls (Table 1). The mean resolution limit ($I/\sigma I = 1.0$) was 1.85 Å (Rsym = 11.53%) compared to 1.89 Å (Rsym = 12.88%) for the 10 lysozyme crystals, and 2.13 Å (Rsym = 13.52%) compared to 1.74 Å (Rsym= 7.69%) for the 10 thermolysin crystals.

D. Fragment libraries

The minilibrary that was combined with lysozyme contained 33 common laboratory chemicals that had no significant hazards (chemical safety is important when working with undergraduate interns and our laboratory was simultaneously used by high school students for the duration of this project). The average molecular weight of our minilibrary chemicals was 159 g/mol, the average molecular volume was 134 Å3, the average cLogP was 2.08. The nominal concentration of chemicals was 100 mM (or the highest room temperature solubility). The only chemicals that were observed to bind to lysozyme were NAG and benzamidine (Figure 5).

Less than one minute was required to harvest 45 crystal-containing droplets from a slurry of trypsin crystals (in a single well of a MiTeGen crystallization plate) onto 45 distinct micromeshes, and to combine each crystal with one of the 45 chemical cocktails. None of the 304 chemicals in the cocktail library were observed to bind to trypsin. In part, this is because the chemicals in cocktail libraries were present at lower concentration than is possible with individually solvated chemicals (hence low affinity reactions are difficult to detect).

E. Acoustically harvested protein crystals grown in a hybrid MiTeGen plate

The Xray data that were obtained from the acoustically mounted lysozyme crystals were comparable with the data collected from the control lysozyme crystals.

IV. Discussion

Full automation of the high throughput macromolecular crystal structure determination pipeline would increase productivity in conventional structural biology, as well as enable novel discovery based solutions to stubborn problems. This goal has been frustrated by the difficulty involved in automating the fast transfer of crystals from growth plates onto supports suitable for Xray data collection. In cases where very high speed is not required, robotic solutions (Viola et al., 2007), laser tweezer assisted mounting (Wagner et al., 2013) and laser assisted recovery on thinfilms (Cipriani et al., 2012) are promising alternatives to manually mounting individual crystals. We have previously demonstrated that fast serial crystal mounting by acoustic methods is simplified by using acoustically transparent media (Cuttitta et al, 2015). Combined with automated protein production (Banci et al., 2006; Graslünd et al, 2008), crystallization (BolanosGarcia & Chayen, 2009), and end station automation (Snell et al., 2004), this will accelerate the output of crystallization facilities to match the data collection speeds available at next generation synchrotrons. In cases where crystals are already present on media that is not optimal for acoustic transfer, fast serial mounting may nevertheless be attempted using the hybrid system described here. We have demonstrated that crystals grown in conventional hanging drop experiments can be acoustically transferred onto micromeshes suitable for Xray data collection.

The harvesting system that we tested required the assembly of an awkward "plate chimera" that combined acoustically compatible components and conventional crystallization plate components. Our intent was to demonstrate proof of concept in support of the eventual goal of an integrated acoustic harvesting system with purpose designed crystallization labware (Figure 6). The most important improvement is a crystallization plate that is not rejected by the Echo software.

High throughput screening applications are a natural first fit for acoustic harvesting; small crystals are particularly suitable because they are easy to mount and because they combine rapidly with chemical libraries (Cole et al., 2014). In contrast, click-to-mount applications will require significant improvements, such as an internal visualization system.

Acoustic specimen preparation is particularly advantageous for operations at low volumes. Conventional pipetting is difficult and error prone when the transferred volumes are very small (Kong et al., 2012). Acoustic transfer eliminates error due to different liquids interacting in different ways with tips and tubing. Variations from the training and skill of individual human operators are also eliminated.

Computer operated mounting of crystals limits damage to crystals from physical contact with transfer materials (Tung et al., 2014), and eliminates contaminants that may leach out of pipette tips, nozzles, and plastic labware (McDonald et al., 2008). Once a crystal is transferred to its desired destination, additional components such as fragments, heavy metal solutions, and cryoprotectants may be added to the same location. In such cases, touchless transfer prevents loss of the additive due to adhesion to the surface of the transfer material (Harris et al., 2010).

Acoustic crystal handling accelerates the rate of specimen preparation to match the rate of specimen consumption at modern synchrotron Xray sources. A fully automated structure determination pipeline (including crystal handling) also allows researchers with limited laboratory access to carry out a complex research program using automated protein production and purification, automated crystal growth, automated crystal handling and data collection. Full automation will also ensure that the metadata for a project is generated by each instrument and then accurately transferred to the next instrument. Furthermore, automated crystal handling enables researchers to access a comprehensive shared chemical library archive (including fragment libraries, heavy-atoms, and cryoconditions).

V. Notes

[1]Labcyte Inc. is currently developing a crystallization plate that is transparent to sound, but the design is not ready at this time.

[2]Using in situ plates, X-ray data can be obtained without having to harvest the crystals, so readers may be confused as to why we selected them for this experiment. The thin and flat crystallization surface that promotes high quality in situ data also facilitates acoustic crystal mounting. We experimented with many other kinds of crystallization trays that proved to be unsuitable for acoustic harvesting.

VI. References

Banci, L., Bertini, I., Cusack, S., De Jong, R. N., Heinemann, U., Jones, E. Y., ... & Moras, D. (2006). Acta. Crys. D62, 1208-1217.

Bolanos-Garcia VM, Chayen NE (2009). Progress in biophysics and molecular biology 101, 3-12. Cipriani F, Rower M, Landret C, Zander U, Felisaz F, Marquez JA (2012) Acta. Crys. D68, 1393-1399.

Cole, K., Roessler, C. G., Mulé, E. A., Benson-Xu, E. J., Mullen, J. D., Le, B. A., ... & Soares, A. S. (2014). PLOS ONE 9, e101036

Cuttitta, C. M., Ericson, D.L., Scalia, A., Roessler, C.G., Teplitsky, E., Joshi, K., Campos, O., Agarwal, R., Allaire, M., Orville, A.M., Sweet, R.M., and Soares, A. S (2015). Acta. Cryst. D71, 94-103.

Diamond, R. (1974). J. Mol. Biol. 82, 371-391.

Ellson, R., Mutz, M., Browning, B., Lee, L., Miller, M. F., & Papen, R. (2003). J. Assn. Lab. Autom. 8, 29-34

Emsley, P., & Cowtan, K. (2004). Acta. Cryst. D60, 2126-2132.

Gräslund, S., Nordlund, P., Weigelt, J., Bray, J., Gileadi, O., Knapp, S., ... & Ming, J. (2008). Nature methods 5, 135-146.

Harris, D., Olechno, J., Datwani, S., & Ellson, R. (2010). Journal of biomolecular screening 15, 86-94.

Hannig G, Makrides SC (1998). Trends in biotechnology 16, 54-60. Holmes, M. A., & Matthews, B. W. (1982). J. Mol. Biol. 160, 623-639.

Kitago, Y., Watanabe, N., & Tanaka, I. (2010). Journal of Applied Crystallography 43, 341-346. Kong, F., Yuan, L., Zheng, Y. F., & Chen, W. (2012). J. Assn. Lab. Autom. 17, 169-185.

Luft, J. R., Grant, T. D., Wolfley, J. R., & Snell, E. H. (2014). Journal of Applied Crystallography, 47, 1158-1161.

McDonald GR, Hudson AL, Dunn SM, You H, Baker GB, Whittal RM, Martin JW, Jha A, Edmondson DE, Holt A (2008). Science 322, 917.

Newman, J., Fazio, V. J., Caradoc-Davies, T. T., Branson, K., & Peat, T. S. (2009). Journal of biomolecular screening 14, 1245-1250

Otwinowski, Z., & Minor, W. (2001). Crystallography of Biological Macromolecules 2, 226-235.

Perrakis, A., Harkiolaki, M., Wilson, K. S. & Lamzin, V. S. (2001). Acta Cryst. D57, 1445-1450. Roessler, C. G., Kuczewski, A., Stearns, R., Ellson, R., Olechno, J., Orville, A. M., ... & Héroux, A. (2013). J. Synchrotron Rad. 20, 805-808.

Snell G, Cork C, Nordmeyer R, Cornell E, Meigs G, Yegian D, Jaklevic J, Jin J, Stevens RC, Earnest T (2004). Structure 12, 537-545.

Soares, AS, Engel, MA, Stearns, R, Datwani, S, Olechno, J, Ellson, R, Skinner, JM, Allaire, M, & Orville, AM (2011). Biochemistry 50, 4399-4401.

Teplitsky, E., Joshi, K., Ericson, D. L., Scalia, A., Mullen, J. D., Sweet, R. M., & Soares, A. S. (2015). J. Struc. Biol. 191, 49–58.

Tung, H. W., Sargent, D. F., & Nelson, B. J. (2014). Journal of Applied Crystallography 47, 692–700. Villasenor AG, Wong A, Shao A, Garg A, Donohue TJ, Kuglstatter A, Harris SF (2012). Acta. Cryst. D68, 893-900.

Viola R, Carman P, Walsh J, Miller E, Benning M, Frankel D, McPherson A, Cudney B, Rupp B (2007) Journal of applied crystallography 40, 539-545.

Wagner, A., Duman, R., Stevens, B., & Ward, A. (2013). Acta. Cryst. D69, 1297-1302.

Winn MD, Ballard CC, Cowtan KD, Dodson EJ, Emsley P, Evans PR, Keegan RM, Krissinel EB, Leslie AG, McCoy A, McNicholas SJ, Murshudov GN, Pannu NS, Potterton EA, Powell HR, Read RJ, Vagin A, Wilson KS (2011). Acta. Cryst. D67, 235-242.

Winn, M. D., Murshudov, G. N., & Papiz, M. Z. (2003). Macromolecular TLS refinement in REFMAC at moderate resolutions. Methods in enzymology 374, 300.

Yin, X., Scalia, A., Leroy, L., Cuttitta, C.M., Polizzo, G.M., Ericson, D.L., Roessler, C.G., Campos, O., Millie Y. Ma, Agarwal, R., Jackimowicz, R., Allaire, M., Orville, A.M., Sweet, R.M., Soares, A.S. (2014). Acta. Cryst. D70, 1177-1189.

VII. Acknowledgments

Personnel for this study were recruited largely through the 2013 summer and fall, and 2014 spring and summer sessions of the Science Undergraduate Laboratory Internships Program (SULI), supported through the U.S. Department of Energy, Office of Science, Office of Workforce Development for Teachers and Scientists (WDTS). Major ongoing financial support for acoustic droplet ejection applications was through the Brookhaven National Laboratory/U.S. Department of Energy, Laboratory Directed Research and Development Grant 11008 and from the Offices of Biological and Environmental Research and of Basic Energy Sciences of the US Department of Energy, and from the National Center for Research Resources (P41RR012408) and the National Institute of General Medical Sciences (P41GM103473) of the National Institutes of Health. Additional funding was granted by CAPES N°17040/124 (Brazil). Data for this study were measured at beamline X25 of the National Synchrotron Light Source. We thank Labcyte Inc., and especially Joe Olechno, Richard Ellson and Richard Stearns, for their technical support and guidance. Author contributions: ASS and LL designed the experiment, ASS wrote the paper. YNS, LM, XY, AS, DLE, LL and ASS grew crystals, obtained data and analyzed data. ASS, AMO, and CGR designed the labware. ASS and RMS trained and supervised student interns.

Table 1: Data collection and model refinement statistics for acoustically vs. hand harvested crystals.

	Lysozyme		Thermolysin	
Labware	MiTeGen *in situ*-1			CrystalDirect
Harvesting method	Acoustic	Hand	Acoustic	Hand
Crystal size (µm)	30		120	

Crystallization Conditions

Protein (mg/mL)	120	330
Buffer	0.1 M NaAc pH 4.6	0.05 M TRIS pH 7.5 + 45% DMSO
Precipitant	8% NaCl	1.45 M CaCl2

Data collection statistics

No. of crystals	10	10	10	10
X-ray source	NSLS X25	NSLS X25	NSLS X25	NSLS X25
Wavelegth (Å)	0.9	0.9	0.9	0.9
Beam WxH (µm)	40x40	40x40	150x150	150x150
Resolution (Å)	1.85 ± 0.30	1.89 ± 0.23	2.06 ± 0.32	1.73 ± 0.07
Rsym or Rmerge (%)	11.53 ± 2.76	12.88 ± 3.17	13.52 ± 3.95	7.69 ± 1.72

Model refienement statistics

No. of reflections	19479 ± 5971	18220 ± 4258	33781 ± 7553	41268 ± 3034
Completeness (%)	98.46 ± 2.22	97.34 ± 2.33	96.95 ± 4.97	99.62 ± 0.35
Rwork (%)	17.25 ± 0.96	17.12 ± 0.77	15.11 ± 1.08	14.38 ± 0.09
Rfree (%)	19.72 ± 1.25	19.55 ± 1.49	17.84 ± 1.59	16.65 ± 0.42
rms deviations				
bond lengths (Å)	0.0117 ± 0.0048	0.0112 ± 0.0037	0.0145 ± 0.0030	0.0108 ± 0.0006
bond angles (°)	1.41 ± 0.27	1.4 ± 0.16	1.56 ± 0.18	1.37 ± 0.03

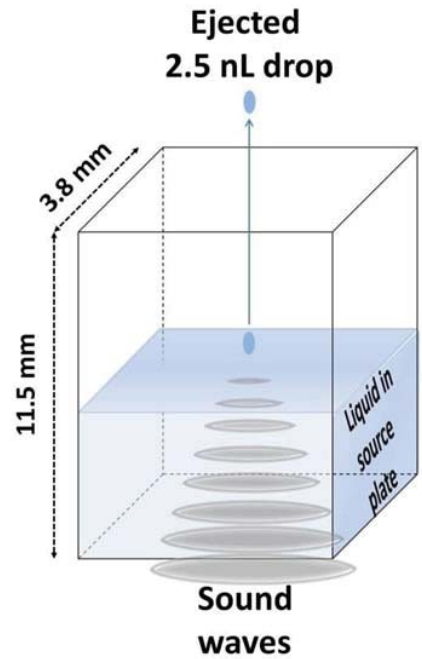

Figure 1: Acoustic droplet ejection.

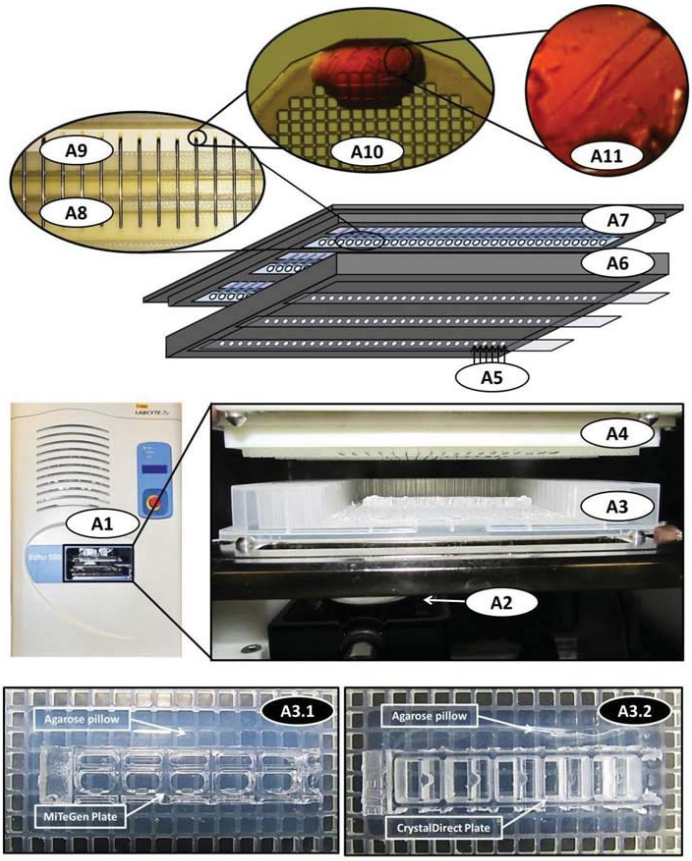

Figure 2: Panel A: Overview of the apparatus for acoustic ejection from nonacoustic labware.

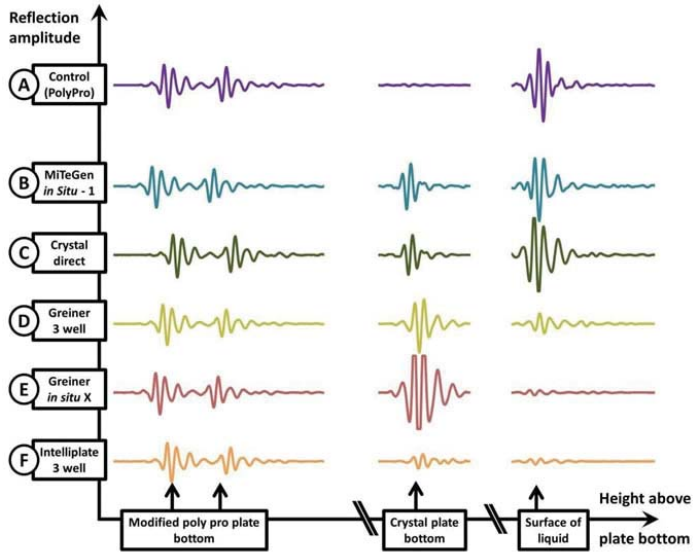

Figure 3: Acoustic signature of diverse plates.

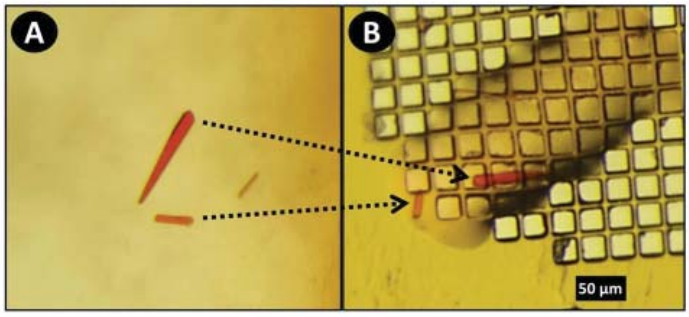

Figure 4: Click to mount: ejecting a selected crystal cluster.

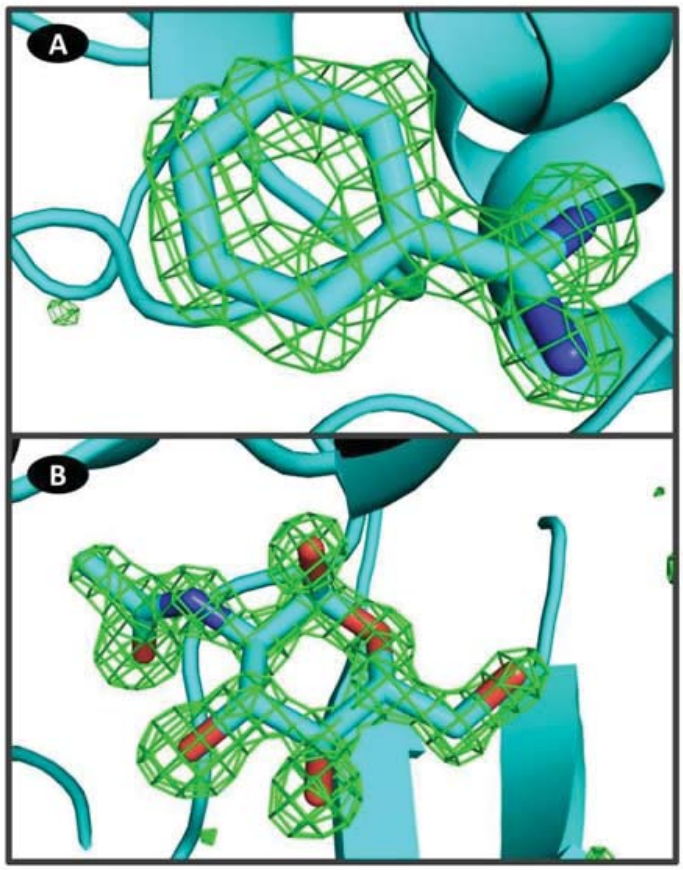

Figure 5: Two known ligands acoustically added to lysozyme

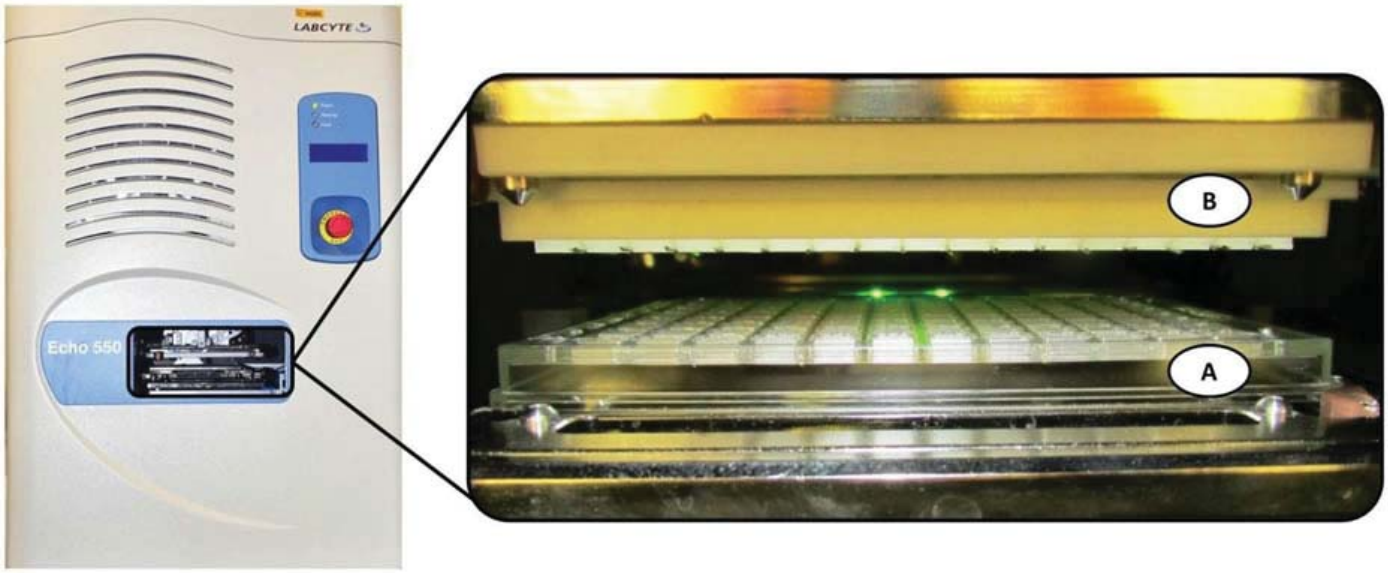

Figure 6: Concept for acoustic transfer of crystals on tobedesigned acoustically compatible crystallization plates.

Ionizing Radiation and its Effect on the DNA of the Human Body

Nicholas Bonura
Chemistry Department, Dowling College, Oakdale, NY 11769
Nicholaos Tsoupas
Collider Accelerator Department, Brookhaven National Lab, Upton, NY 11973

Abstract

Ionizing radiation contains enough energy to release a tightly bound electron from an atom and generate an ionized atom. This radiation is present naturally and we are all exposed to it every single day, but not at dangerous levels. However, the scientists working in close quarters to the particle accelerators here at BNL and other laboratories are exposed to this radiation regularly. This study provides an abundance of information on how the radiation interacts with matter and its impact on human DNA. In order to gather and organize information on these interactions, I have compiled many credible sources into an annotated bibliography. These sources contain an abundance of valuable material and research that can assist anyone interested in performing a study on the interaction of ionizing radiation with matter and DNA. In conducting this study, I have gained valuable research experience as well as the ability to independently perform a study while working with and learning to understand new material and programs.

I. Annotated Bibliography:

Boudaï ffa, B., Cloutier, P., Hunting, D., Huels, M., & Sanche, L. (2000, March 3). Resonant Formation of DNA Strand Breaks by Low-Energy (3 to 20 eV) Electrons. Science Magazine, 1658-1660.

This article, being part of Science Magazine, is extremely credible as it is peer-reviewed before publication takes place. The authors are all part of very reliable departments, research groups, and universities. Their background indicates dependable research and information presented within this article. Ionizing radiation with energy above the threshold is known to have a negative impact on DNA, causing single and double-strand breaks. However, this article explores energies beneath the threshold level, which is also observed to have substantial yields of similar DNA breakage. The purpose of the article is to propose a challenge to the fact that the threshold energy level must be reached in order to affect DNA. This can be very useful in this field of research, studying what effect different energy levels of ionizing radiation can have on human DNA.

Close, D., Nelson, W., & Bernhard, W. (2013). DNA Damage by the Direct Effect of Ionizing Radiation: Products Produced by Two Sequential One-Electron Oxidations. The Journal of Physical Chemistry, 117(47), 12608–12615.

The Journal of Physical Chemistry is a reliable source of information, being composed of an abundance of peer-reviewed articles that are very frequently cited in a great deal of studies. This article is written by credible authors, each being part of a department of physics and other departments. In addition, they have all received an education from prestigious universities. This article portrays a study conducted to challenge the assumption that populations of radicals present within DNA that has been exposed to radiation would account for the lesions that occur. It was found that this was not the case as a result of the theoretical calculations that were performed throughout the study. This article provides the researcher with knowledge on different pathways in which DNA lesions can occur.

Schanz S , Flockerzi E, Schuberth K, Rübe CE (2014) Genetically-Defined DNA Repair Capacity Determines the Extent of DNA Damage Accumulation in Healthy Mouse Tissues after Very Low Doses of Ionizing Radiation. Journal of Carcinogenesis Mutagenesis, 5:196. doi: 10.4172/2157-2518.1000196

This article belongs to the Journal of Carcinogenesis and Mutagenesis, which is a well- known and credible composition of peer-reviewed articles. The authors involved in the publication of this article are all members of the Department of Radiation Oncology and all contributed equally to this manuscript. This article conveys the idea that low doses of ionizing radiation have unclear effects on the genetic factors of the human body. In order to study the effect, mouse strains of varying genetic capacity were exposed to low doses of radiation for different lengths of time. The DNA damage present in each cell population's healthy tissue was then analyzed. This article will allow the researcher to become familiar with the DNA damage that takes place under low doses of ionizing radiation and what health risks it may pose.

Ataian, Y., & Krebs, J. (2006). Five repair pathways in one context: Chromatin modification during DNA repair. Biochemistry and Cell Biology, 84(4), 490-494. doi:10.1139/o06-075

This article is a part of the Biochemistry and Cell Biology Journals, which is a dependable journal consisting of a great deal of peer-reviewed articles. The authors belong to the Department of Biological Sciences at the University of AK Anchorage. This article focuses on the different repair pathways that DNA takes after being faced with more than ten thousand lesions per day. This study is a compilation of recent studies that deal with the necessary enzymes and other factors to repair the damaged site correctly and in a timely fashion. It is explained that DNA repair is a complicated process as features of the genomic DNA hinder the accessibility to the lesion.

Understanding DNA repair is a very significant aspect of this study and this source can help to familiarize the researcher with all possible pathways that can occur.

Effects of Ionizing Radiation on DNA. Retrieved August 4,

2015, from http://teachnuclear.ca/all-things-nuclear/radiation/biological-effects-of-radiation/effects- of-ionizing-radiation-on-dna/

This website is a dependable source to utilize in this study because it is used frequently throughout our educational systems. The Canadian Nuclear Association regulates this website and provides researchers, students, and teachers with an abundance of information on all aspects of nuclear physics. The website also acknowledges the expertise of the nuclear physicists and science educators who have gathered and organized all of the research presented. The section of the website that I found useful in my study was covering the effects of ionizing radiation on DNA. All possible outcomes of what can occur when ionizing radiation comes into contact with a cell are portrayed. In addition, both the direct and indirect pathways of DNA damage are explained including the differences between single and double-strand breaks. This source can be very useful to this study as it explained in detail the basics of the effects that ionizing radiation has on DNA.

DNA Repair. (2015, June 18). Retrieved August 4, 2015, from http://users.rcn.com/jkimball.ma.ultranet/BiologyPages/D/DNArepair.html

This website, known as Kimball's Biology Pages, is a representation of an online biology textbook. The author of the website, John W. Kimball is a retired biology educator and a Harvard University graduate, also receiving his Ph.D. there. His initial text was published in 1965 and has undergone five revisions, making all of the information up to date and reliable. The DNA repair portion was very useful in conducting my study as DNA can utilize numerous pathways to repair itself in response to the effects ionizing radiation. This website explores all possible types of DNA breakage and the side effects that each type of DNA repair can lead to, such as different forms of mutations. This source contributes to this study because it is crucial to understand the various forms of DNA repair after lesions occur as a result of ionizing radiation.

Interactions of Radiation with Matter. Retrieved July 9, 2015, from http://www.columbia.edu/~ejh1/web-rad-train/topic1/print.html#figure2

This website is published by the Center for Radiological Research and affiliated with Columbia University under the World Wide Web-Based Educational Program. The support by such a credible organization and prestigious university reinforces the reliability of the information provided. This website offers the explanation of the interactions of radiation with matter, direct and indirect action of radiation, as well as both single and double DNA strand breaks. The fact that a wide variety of information pertaining to this study is available on this website makes in a very useful source.

Han, W., & Yu, K. (2010). Ionizing Radiation, DNA Double Strand Break and Mutation (K. Urbano, Ed.). Retrieved June 17, 2015, from http://www.cityu.edu.hk/ap/nru/BookAGRhapter7.pdf

This book was published by Nova Science Publishers, a very credible publishing company that handles the publication of many books and journals throughout the world. The authors of this chapter that I utilized in my research are members of the Department of Physics and Material Sciences and are affiliated with the City University of Hong Kong. The authors and publishing company reflect the reliability of the information within this chapter. This chapter deals with the ionizing radiation has been proved to be a major contributor to carcinogenesis. Mutations and misrepairs of damaged DNA are known to be associated with carcinogenesis. This chapter also explores the radiation- induced bystander effect, which has to do with irradiated cells sending off a signal to non-irradiated cells and causing them to suffer strand breaks, mutations, or cell death. This is important in this study because it enables the researcher to understand how radiation can affect cells and how that affect can spread throughout the human body.

Cember, H., & Johnson, T. (2009). Introduction to Health Physics (4th ed.). New York, New York: McGraw-Hill Medical.

This textbook was written by a professor at Northwestern University and an assistant professor and Colorado State University who is also a member of the Department of Environmental and Radiological Health Sciences. The textbook covers health physics from an abundance of different angles, including the interaction of different types of ionizing radiation with matter, as well as with the human body. Many sections of this textbook have great relevance and can be very useful in obtaining information that can be directly related to this study.

Ziegler, James F. "INTERACTIONS OF IONS WITH MATTER." SRIM - The Stopping and Range of Ions in Matter, 2008. Web. 24 July 2015. <http://www.srim.org/>.

This code was developed by James Ziegler, who is a member of the International Electrical and Electronic Engineering Society and the American Physical Society. He also is the author or editor of 20 scientific books and holds 16 patents in the United States. The program he created, "The Stopping and Range of Ions in Matter", allows the user to work with a program that can simulate the behavior of specific particles in different materials. This program receives around 14,000 downloads a year and is renowned for its accuracy and its ability to calculate many features of the transport of ions in matter. This program is extremely useful in this study as it can simulate the use of different types of cancer radiation therapy. This simulation can be done using water as the material due to the fact that the human body is composed mostly of water. The researcher then has the ability to alter the type of particle being used and observe and analyze the differences in scattering and distance traveled in accordance to the energy given to the particle.

Types of Accelerators. (2011). Retrieved August 5, 2015, from http://www.accelerators-for- society.org/

This website is run by the Test Infrastructure and Accelerator Research Area, which is supported by numerous institutions throughout Europe. There are also many partners involved in the work being done, including national and international organizations that manage large research centers, universities, and large industrial companies. The section of this website that was useful in this study fully describes the many different types of accelerators and how they function, as well as the advantages of each type. It also explains what each type of accelerator can be used for and the energy that each is capable of producing. This section is useful in this study because it is important to explore the different types of man-made ionizing radiation as many scientists work in

close proximity to these accelerators, increasing their exposure to radiation. In addition, these accelerators are utilized in radiation therapy, which also exposes patients to ionizing radiation.

Types of Radiation Used to Treat Cancer. (2014, October 10). Retrieved July 29, 2015, from http://www.cancer.org/treatment/treatmentsandsideeffects/treatmenttypes/radiation/radiat iontherapyprinciples/radiation-therapy-principles-types-of-radiation

This website is regulated by the American Cancer Society and contains a great deal of information regarding cancer and treatments to fight it. The website is supported by the National Health Council, which is a standards of excellence certification program, ensuring that the information provided is reliable. The portion of this website that can be related to this study covers the different types of radiation used to treat cancer. This is relevant because while using radiation therapy to battle cancer, the healthy tissue that the beam radiation must pass through is also exposed to the radiation, affecting the DNA that it comes into contact with. This displays the importance of understanding how different forms of beam radiation can impact the healthy cells of the human body.

Simulating beamline configurations for the Deep Underground Neutrino Experiment

Brendon Bullard
Physics, Brandeis University, Waltham, MA 02454
Mary Bishai
Physics, Brookhaven National Laboratory, Upton, NY 11973

The current reference design for the Deep Underground Neutrino Experiment beam- line specifies two double-parabolic horns operating at 230 kA. Recent studies have found an optimized geometry that uses a polycone design for the upstream horn and scaled downstream horn operating at 298 kA. The primary goal of this study is to simulate experimental runs implementing the reference and optimized geometries as well as a three-horn system which separates the upstream horn into two, more easily manufacturable sections. We simulated runs using the latest two versions of G4LBNE and visualized the simulated beamline using HepRep. Beamline performances were judged based on flux of unoscillated neutrinos with energy 0-20 GeV. We found that using 0.5 m of separation between horns 1 and 2 in the three horn system decreased muon neutrino flux by approximately 10% between 1 and 3 GeV and increased flux by up to 30% between 3 and 5 GeV over the optimized horn design. This represents a nonsignificant change in focusing capabilities. Additionally, there is evidence to suggest that changing the position of the second horn along the beam direction alone cannot serve as a mechanism to tune the energy of the peak neutrino flux.

I. INTRODUCTION

A. Neutrino Oscillations

Neutrinos are unique in that the flavor eigenstates ($\nu_e\ \nu_\mu\ \nu_\tau$) and mass eigenstates ($\nu_1\ \nu_2\ \nu_3$) have considerable mixing. The relation between the flavor and mass eigenstates is given by the PMNS matrix1 and is factorized as

$$\left|\nu_a\right\rangle = \sum_{i=1}^{3} U_{ai}\left|\nu_i\right\rangle$$

$$U_{PMNS} = \begin{pmatrix} 1 & 0 & 0 \\ 0 & c_{23} & c_{23} \\ 0 & -s_{23} & c_{23} \end{pmatrix} \begin{pmatrix} c_{13} & 0 & e^{i\delta_{CP}} s_{13} \\ 0 & c_{23} & c_{23} \\ -e^{i\delta_{CP}} s_{13} & 0 & c_{13} \end{pmatrix} \begin{pmatrix} c_{12} & s_{12} & 0 \\ -s_{12} & c_{12} & 0 \\ 0 & 0 & 0 \end{pmatrix} \quad (1)$$

where $s_{ij} = \sin\theta_{ij}$ and $c_{ij} = \cos\theta_{ij}$. The PMNS matrix is determined by four constants: θ_{12}, θ_{13}, and θ_{23} (mixing angles) and a charge-parity (CP) violating term δ_{CP}. CP violation means, roughly, that a particle and its antiparticle have different properties. To date, only the three mixing angles have been measured to good error. The value of δ_{CP} is unknown. If it has a value that is not 0 or π, neutrinos will exhibit CP violation, which would pose a possible mechanism for the matter-antimatter asymmetry in the universe.

Additionally, the ordering of the neutrino mass eigenstates is unknown. We know the magnitudes of Δm^2_{21} and Δm^2_{32} but only the sign of Δm^2_{21} is known, where $\Delta m^2_{ab} = m^2_b - m^2_a$. This leads to the neutrino mass hierarchy problem with two possible orderings: $m_1 < m_2 < m_3$, the normal hierarchy (NH) and $m_3 < m_1 < m_2$, the inverted hierarchy (IH). The former is called the normal hierarchy because it is parallel to the ordering of the charged leptons' mass eigenstates.

B. The DUNE beamline

The Deep Underground Neutrino Experiment (DUNE) is an international collaboration that is currently in development. DUNE is a long baseline neutrino experiment which aims to measure δ_{CP} and the sign of Δm^2_{32}.

When operational, DUNE will extract 60-120 GeV protons from the Main Injector at Fermilab and bend the proton beam downward toward a target. The proton collisions will create many secondary particles, of which pions and kaons are a particular interest. Charged particles will be selectively focused by magnetic horns and decay in a helium-filled decay pipe to produce neutrinos. These neutrinos will travel 1300 km to a massive liquid argon detector at the far site in South Dakota.

DUNE will measure appearance of electron neutrinos and anti-electron neutrinos. Due to the presence of electrons in the atoms of the Earths crust, a matter-antimatter asymmetry is introduced called the matter effect, which aids in the measurement

$$P(\nu_\mu \to \nu_e) \cong P_0 + P_{\sin\delta} + P_{\cos\delta} + P_3 \quad (2)$$

where

$$P_0 = \sin^2\theta_{23}\frac{\sin^2 2\theta_{13}}{(A-1)^2}\sin^2[(A-1)\Delta], \qquad \alpha = \frac{\Delta m^2_{21}}{\Delta m^2_{31}}$$

$$P_3 = \alpha^2\cos^2\theta_{23}\frac{\sin^2 2\theta_{12}}{A^2}\sin^2(A\Delta), \qquad \Delta = \Delta m^2_{31}\frac{L}{4E}$$

$$P_{\sin\delta} = \alpha\frac{8J_{cp}}{A(1-A)}\sin\Delta\sin(A\Delta)\sin[(1-A)\Delta], \qquad A = \sqrt{2}G_F N_e\frac{2E}{\Delta m^2_{31}}$$

$$P_{\cos\delta} = \alpha\frac{8J_{cp}\cot\delta_{CP}}{A(1-A)}\cos\Delta\sin(A\Delta)\sin[(1-A)\Delta], \qquad J_{cp} = \frac{1}{8}\sin 2\theta_{12}\sin 2\theta_{13}\cos\theta_{13}\sin\delta_{CP}$$

of the mass hierarchy[1]. Taking this into account, the appearance probabilities[1] for a beamline of length L and neutrino energy E passing through a medium of electron density N_e are given by the following approximation to second order in α. (See Equation 2.)

The term $P_{sin\delta}$ changes sign between the ν_e and $\overline{\nu_e}$ appearance modes. Equation I is plotted in Figure 1 for three values of δ_{CP} for ν_e and $\overline{\nu_e}$ appearance in both possible mass hierarchies. Taking into account the very low neutrino cross section that increases with energy, the first two oscillation peaks are the most useful in measuring the sought quantities. Thus, we would like to produce ν_μ and $\overline{\nu_\mu}$ with energy Eν < 5 GeV.

Pions main decay mode is a muonic two body decay and also has a much less likely electronic decay mode. Specifically, $\pi^{+(-)} \rightarrow e^{+(-)} + \nu_e(\overline{\nu_e})$ has branching 0.999877 and $\pi^{+(-)} \rightarrow \mu^{+(-)} + \nu_\mu(\overline{\nu_\mu})$ has branching 0.000123. Neutrino energy is related to pion and kaon energy in two body decays[2] by Equation 3, where θ is the small angle between the parent hadron and neutrino momenta and γ is the Lorentz boost of the hadron. This allows us to calculate what energy pions must be produced by the DUNE target.

$$E_\nu = \frac{\left(1 - \frac{m_\mu^2}{2}\right) E_{\pi,K}}{1 + \gamma^2 \theta^2} \tag{3}$$

The DUNE beamline will produce ν_μ and $\overline{\nu_\mu}$ beams by selectively focusing charged pions and kaons with magnetic focusing horns. However, opposite charged pions can travel through the centers of the magnetic horns, leading to a <10% contamination of opposite lepton number neutrinos. The low branching electronic decay of the pion and the electronic decays of kaons contribute to an electronic contamination of <1%.

The reference design[3] for the DUNE beamline uses two double-parabolic magnetic horns. Recent studies[4] have found an optimized design that replaces the first horn with a poly- cone design. The geometric specifications for the reference and optimized designs used are summarized in Tables I, II, and III in Appendix A.

The geometry of Horn 1 in the optimized geometry is difficult to manufacture; we would like to separate the first horn into two horns. From an engineering point of view, the separation can be made anywhere along L_3 of the optimized horn. We decide to make the separation at the end of L_3 so that the two polycone horns resemble the shape of approximate parabolas. Further, the optimized Horn 1 loses neutrino energy tunability that the reference Horn 1 does have[1]. We would like to learn if repositioning Horn 2 in the three horn design can serve as a mechanism to tune the neutrino energy peak.

II. METHODOLOGY Simulation and Analysis

We used G4LBNE (an extension of GEANT45) V2 and V3 to simulate 50 million protons on target (POT) for each beam

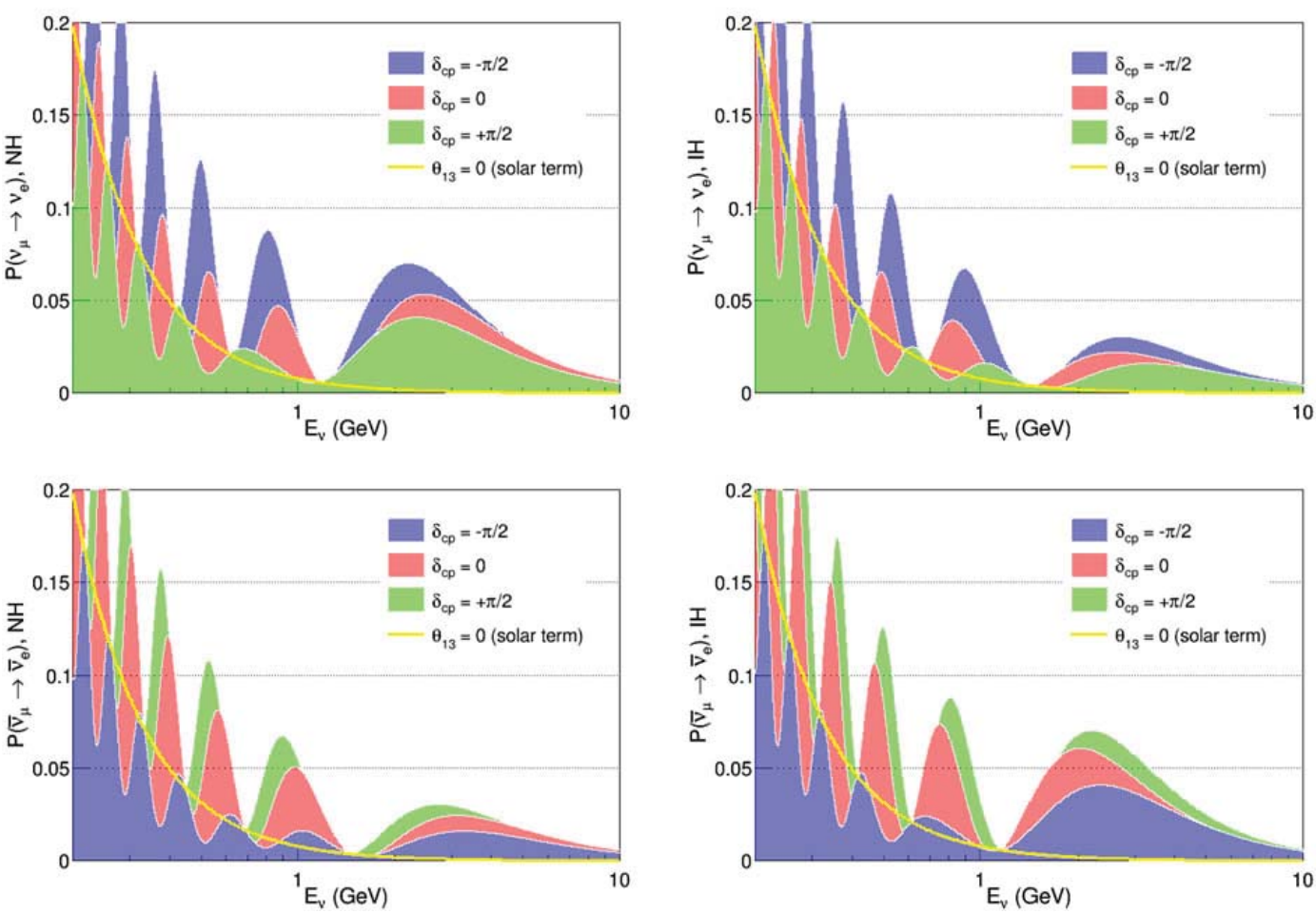

FIG. 1. Appearance probability for ν_e (top) and $\overline{\nu_e}$ (bottom) production in the normal mass hierarchy (left) and inverse mass hierarchy (right) for three possible values of δ_{CP} for L = 1300 km.

cause it constructs beamline hardware such as support structures and generally uses more realistic geometries, V2 is much easier to use because it only requires the user to edit an input text file. To implement custom geometries in V3, source code needs to be altered. Using both versions has the added benefit of ensuring accuracy. I used the HepRep package to visualize pion tracks in beamline configurations. The unoscillated neutrino flux spectra at the far location are collected within the simulation using a virtual detector. G4LBNE outputs the simulation data into a ROOT tree in a .root file.

I ran the reference and optimized designs with proton beam energy 120 GeV and 66 GeV. I ran the three horn design in V2 at 50 million POT for horn separations 0.5, 2.0, 4.0, and 6.0 m. I plotted the neutrino flux for V2 and V3 superimposed as well as a ratio plot for the reference and optimized designs for 66 and 120 GeV proton beams. I also plotted the spectra for a three horn geometry with horn separation 0.5 m superimposed with the optimized design flux in V2 with ratio plots. I plotted the other configurations on a linear scale with the reference, optimized, and 0.5 m configuration.

III. RESULTS AND DISCUSSION

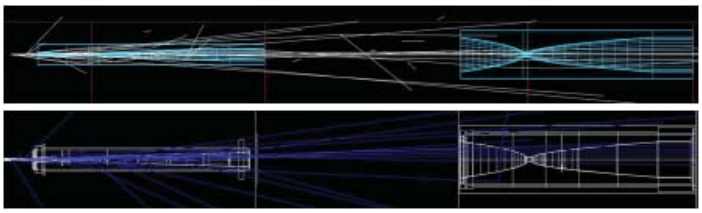

FIG. 2. HepRep visualization (side view) of the reference design horns in G4LBNE/V2 (top) and G4LBNE/V3 (bottom). Protons travel in from the left, passing through the graphite target, producing π^+, which are focused by Horn 1 and subsequently Horn 2. Runs generate 50 POT and include π^+ trajectories with energy 1 GeV ≤ Eπ ≤ 10 GeV.

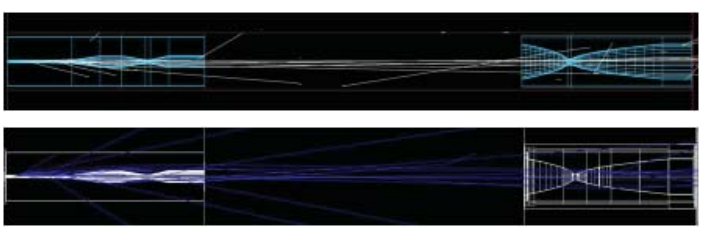

FIG. 4. HepRep visualization (side view) of the optimized design horns in G4LBNE/V2 (top) and G4LBNE/V3 (bottom). Protons travel in from the left, passing through the graphite target, producing π^+, which are focused by Horn 1 and subsequently Horn 2. Runs generate 50 POT and include π^+ trajectories with energy 1 GeV ≤ E_π ≤ 10 GeV

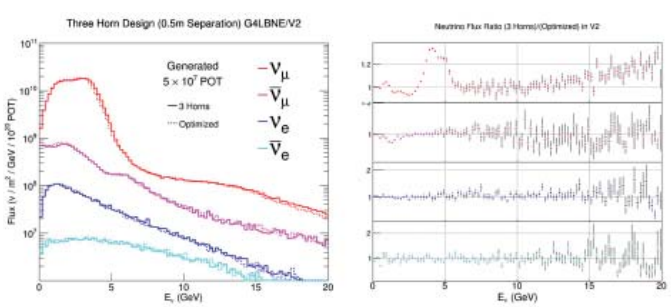

FIG. 6. Simulated far location neutrino flux for a three horn design. The four considered neu- trino flavors are plotted on a log scale (left) along with the bin ratios and associated statistical uncertainties (right)

IV. Conclusions

The ratio plots for the three horn design over the optimized design show that the three horn design decreases muon neutrino flux by approximately 10% between 1 and 3 GeV and increases flux by up to 30% between 3 and 5 GeV. However, by looking at the linear scale muon neutrino flux we see that the increase in flux occurs on the right side drop off. The shape of the flux for the three horn design is, roughly, shifted down and to the right. This is represents a slight decrease in performance for the three horn geometry. However, it is comparable enough to justify building this particular configuration due to the decreased difficulty of manufacturing. Further, by simply increasing the distance between the first two horns, the muon neutrino flux peaks decrease and the widths of the flux distributions increase more than the peaks shift into higher energy ranges. Therefore, this is not a sufficient mechanism to attain useful energy tuning for this type of design.

V. Further Study

The next logical step in investigating the general three horn geometry is to implement the design in G4LBNE/V3 and compare the results to V2. The scientists who worked on the genetic algorithm to generate the optimized geometry could then use the new framework in V3 to run a new algorithm to find an optimal three horn system. Such an algorithm would be able to vary the distance between the first two horns and the outer conductor radius of the second horn. The results of this study suggest that such an optimization would generate a geometry capable of greater fo-

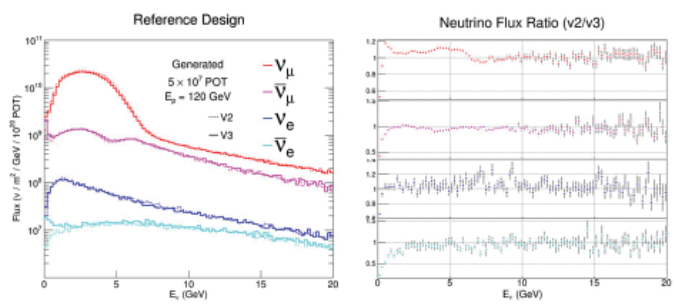

FIG. 3. Simulated far location neutrino flux for the reference design. The four considered neu- trino flavors are plotted on a log scale (left) along with the bin ratios and associated statistical uncertainties (right)

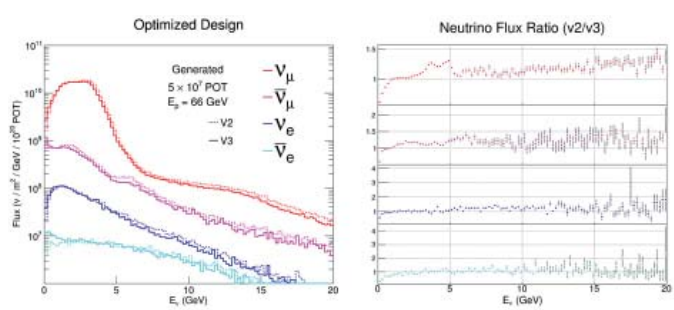

FIG. 5. Simulated far location neutrino flux for the optimized design. The four considered neutrino flavors are plotted on a log scale (left) along with the bin ratios and associated statistical uncertainties (right)

cusing in the neutrino energy range 0 - 5 GeV. DUNE scientists can also try these simulations with opposite current to generate neutrino spectra for anti-muon neutrino beams.

VI. REFERENCES

[1]The LBNE Collaboration, "The Long Baseline Neutrino Experiment," (2013), arXiv:hep- ex/1307.7335.

[2]Z. Pavlovic, Observation of Disappearance of Muon Neutrinos in the NuMI Beam, dissertation, University of Texas at Austin (2008).

[3]P. Adamson (Fermilab) I. et al., "The NuMi Neutrino Beam," (2015), FERMILAB-PUB- 15-253-AD-FESS-ND, arXiv:1507.06690 [physics.acc-ph].

[4]L. Fields and A. Marchionni, "Beam Requirements and Beam Optimization," (2015), presentation.

[5]S. Agnostinelli et al. (GEANT4 Collaboration), "GEANT4: A Simulation toolkit," (2003), 250-303.

VII. ACKNOWLEDGMENTS

This project was supported in part by the U.S. Department of Energy, Office of Science, Office of Workforce Development for Teachers and Scientists (WDTS) under the Science Undergraduate Laboratory Internships Program (SULI).

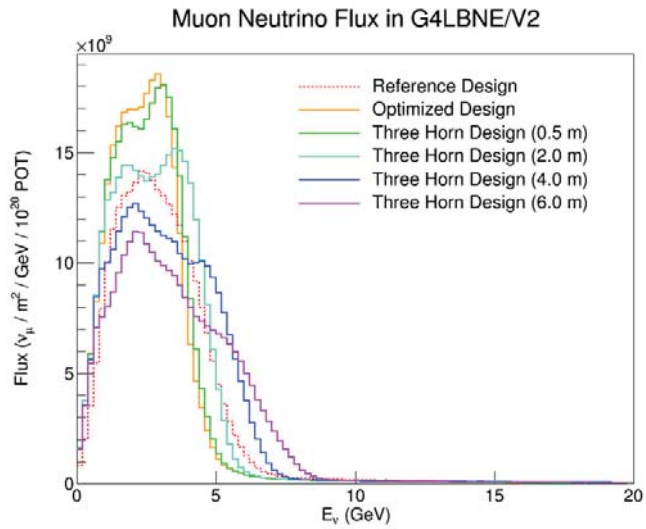

FIG. 7. Simulated far location muon neutrino flux for the reference, optimized, and several three horn designs in G4LBNE/V2

VIII. Appendix A: Beam Specifications

Table III lists the beamline parameters used in simulation for the reference and optimized beamline designs. The three horn geometry is identical to the optimized design with the single modification that Horn 1 is separated between L_3 and L_4. The position of Horn 3 is is the same as Horn 2 in the optimized geometry.

Tables I and II list the parameters that describe the parabolic geometries for Horn 1 and Horn 2 in the reference design, respectively.

	Upstream		Neck	Downstream		
Z(cm)	**0-44.047**	**44.047-80.**	**80.-83.982**	**83.982-95.128**	**95.128-300.**	**300.-354.4**
R_{in}^{IC}	$\sqrt{\frac{92.8484-z}{7.0483}}-0.2$	$\sqrt{\frac{85.7001-z}{7.0483}}$	0.90	$\sqrt{\frac{z-82.2123}{2.1850}}$	$\sqrt{\frac{z-80.}{2.1850}}-0.2$	9.83
R_{out}^{IC}	$\sqrt{\frac{85.7001-z}{7.0483}}$		1.35	$\sqrt{\frac{z-80.}{2.1850}}$		10.03
R_{in}^{OC}	—	—	15.33	—	—	—
R_{out}^{OC}	—	—	16.20	—	—	—

TABLE I. Reference design Horn 1 geometric specifications

	Upstream	Neck	Downstream	
Z(cm)	**0-97.617**	**97.617-104.803**	**104.803-300.**	**300.-354.4**
R_{in}^{IC}	$\sqrt{\frac{100-z}{0.1351}}-0.3$	3.90	$\sqrt{\frac{z-100}{0.2723}}-0.3$	26.80
R_{out}^{IC}	$\sqrt{\frac{100-z}{0.1351}}$	4.40	$\sqrt{\frac{z-100}{0.2723}}$	27.10
R_{in}^{OC}	—	37.0	—	—
R_{out}^{OC}	—	37.87	—	—

TABLE II. Reference design Horn 2 geometric specifications

Parameter	Reference	Optimized
R_1(mm) (Horn 1)	–	37.6
R_2(mm) (Horn 1)	–	162.1
R_3(mm) (Horn 1)	–	54.5
R_4(mm) (Horn 1)	–	166.8
R_{out}^{OC} (mm) (Horn 1)	162	670
L_1(mm) (Horn 1)	–	1811.6
L_2(mm) (Horn 1)	–	796.0
L_3(mm) (Horn 1)	–	593.8
L_4(mm) (Horn 1)	–	676.0
L_5(mm) (Horn 1)	–	140.0
L_6(mm) (Horn 1)	–	524.9
L_7(mm) (Horn 1)	–	997.0
Longitudinal Position (m) (Horn 1)		
Longitudinal Scale (Horn 2)	1	1.32
Radial Scale (Horn 2)	1	1.78
Radial Scale Constant (m) (Horn 2)	0	7.612
Longitudinal Position (m) (Horn 2)	6.61	14.5
Target Length (m)	0.95	2.37
Target Longitudinal Position (m)	-0.42	0.1
Proton Energy (GeV)	120	66
Horn Current (kA)	230	298

TABLE III. Beam specifications for the reference and optimized designs

IX. Appendix B: Neutrino Flux Spectra

Figure 8 shows the reference design spectra run in G4LBNE/V2 and V3 at 66 GeV. Figure 9 shows the optimized design spectra run in G4LBNE/V2 and V3 at 120 GeV.

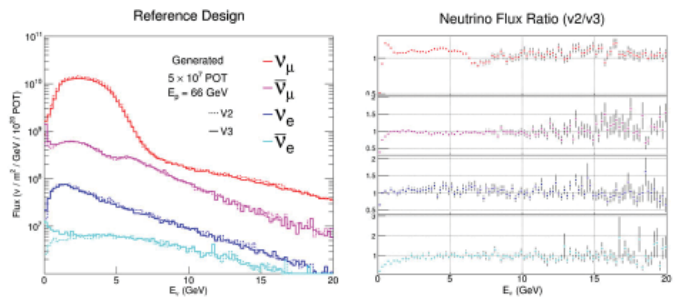

FIG. 8. Simulated far location neutrino flux for the reference design using a nonstandard 66 GeV proton beam. The four considered neutrino flavors are plotted on a log scale (left) along with the bin ratios and associated statistical uncertainties (right)

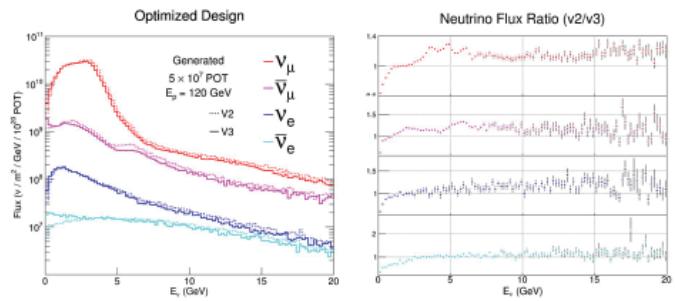

FIG. 9. Simulated far location neutrino flux for the optimized design using a nonstandard 120 GeV proton beam. The four considered neutrino flavors are plotted on a log scale (left) along with the bin ratios and associated statistical uncertainties (right)

Design and analysis of the inner hadronic calorimeter installation fixture for the sPHENIX Project at RHIC

Daniel Cacace
Engineering Department, Stony Brook University, Stony Brook, NY 11790
Donald Lynch
Physics Department, Brookhaven National Laboratory, Upton, NY 11973

Abstract

Every year since the fiscal year 2000 the Relativistic Heavy Ion Collider (RHIC) at Brookhaven National Laboratory (BNL) is operated in a series of experiments lasting about six months. The sPHENIX project, a new detector that is being designed to expand scope of experimentation at RHIC, consists of three main sections including a two-part hadronic calorimeter (HCal) (outer and inner) and an electromagnetic calorimeter which subsequently surround a superconducting magnet. Designing an apparatus to position and install the 32 ton inner HCal for the new detector is a key portion of the current design proposal. The equipment needs to be elevated several feet, rotated for the installation of the modules, and placed within the superconducting magnet, approximately a 20-foot horizontal displacement. Designing and analyzing a mechanism capable of completing the installation is mostly controlled by physical phenomena, but is also influenced by intuition. Development of the installation fixture has proven to be an iterative process consisting of several stages typical of engineering design. Generating designs for the inner HCal installation fixture consisted of conceptualizing potential solutions, fleshing out the details of the more promising ideas, analyzing these results and, creating modifications where necessary to improve the design's capabilities. Creating parts in CAD software, researching commercially available tools and analyzing stress and deformation indicates where the design needs improvement as the process itself reveals potentially superior implementation with the same results.

I. Introduction

sPHENIX is a proposed major upgrade to the current PHENIX detector at RHIC on BNL campus. This proposal is designed to address the fundamental questions regarding the nature of the strongly coupled quark-gluon plasma discovered from PHENIX's experiments at RHIC. In order to achieve the goal of further analyzing this relationship in finer detail the PHENIX infrastructure needs to be updated and modified. In addition to these modifications, new detectors and other sensing equipment needs to be implemented. Part of the implementation process is the installation of the new detectors, specifically the inner hadronic calorimeter (HCal).

The currently proposed set up consists of a pedestal assembly (the primary support structure for the detector assembly), an outer HCal, the sPHENIX (formerly BaBar) superconducting magnet, an inner HCal, and an electromagnetic calorimeter (EMCal). All three of the calorimeters consist of 32 modules (in the EMCal they are called supper modules) which will be installed individually creating hollow cylinders when fully assembled. Figures 1 and 2 show the components and a cross-section of the completed assembly of the new detector. The bottom half of the outer HCal will be installed on the pedestal assembly, thereafter the sPHENIX magnet will be placed into the proper position. Once the sPHENIX magnet is in place the remaining modules for the outer HCal will be installed and subsequently the inner HCal will be assembled and placed inside the superconducting magnet. The EMCal modules will be mounted within the inner HCal, after which the tracker and trigger mechanisms will be installed. Figure 3 shows the assembly procedure. All of the components need to not only be precisely concentric with each other, but also with the interaction region at PHENIX. Given the geometry, size and mass of the detector it's assembly is a complicated and lengthy procedure. The inner HCal poses a particularly difficult problem. A proposed cylindrical cage structure would need to be rotated to install each individual module, then the 32-ton assembly would be elevated approximately 17 feet and horizontally displaced by about 20 feet into the sPHENIX magnet with 2-inch clearance.

II. Methods

A. Cart Mechanism

The initial proposal was to create a cart that would rotate the inner HCal such that individual modules can be installed and traverse an I-beam allowing the assembly to be placed inside the sPHENIX magnet. The I-beam would be supported by a framework that have fine adjustment in its positioning both vertically and horizontally. The first step in designing the cart proposal was to determine an appropriately sized I-beam. The I-beam would need to be able to support over 32 tons and its own weight plus a safety factor with minimal deformation and stress appropriate for steel. Once the steel I-beam is selected the size of the cart can be designed. The cart would need to be able to accommodate rolling mechanism at both ends to traverse the I- beam as well as the flanged roller system to rotate the inner HCal. The flanged rollers would need to be able to rotate the inner HCal via electric motor and thus should be replaced with gears. An internal gear would be installed on the support ring of the inner HCal and six external gears would be installed on the cart to support his weight and allow for its rotation. The electric motor would also need a speed reducer to not only reduce its speed, but to also increase the torque. Figure 4 displays the components of the cart assembly.

The next step in this design would be to take into account the module installation procedure. The idea is to lift each one ton module from each end with wire rope utilizing a crane. Each module be installed individually at the exact same point such that one of its sides is vertical relative to the ground. Figure 5 illustrates the inner HCal's and caps. The Inner HCal cage structure will be rotated such that the installation points create the maximum

symmetry possible. In other words, the first module will be installed, then the cage structure will be rotated 180°, installing the next module at this point, then the partial assembly will be rotated 90° where the next module be installed, etc. Maintaining the symmetry will minimize the moment transferred to the I-beam, thus reducing its angular deflection. Due to one module being installed at a time the I-beam will still experience a moment from a 1 ton module at an approximate radius of 4.5 feet. This suggests the need for an adequate braking system as well as an improvement in stability. Figure 6 displays an improved intermediate design of the cart assembly.

At this point, stress and deformation should be considered. All components, except for those commercially available, are to be made out of steel or stronger materials in order to support the 32 ton detector. Using finite element analysis (FEA) in Autodesk Inventor the maximum deflection due to gravity is approximately a quarter of a millimeter. This deflection should be well within tolerance. The yield strength for steel is about 200 MPa. The computed stress needs to be within an appropriate safety factor determined from the yield strength. Given the complex geometry of a gear FEA is an ineffective tool for computing the likely stress within the teeth.

The load capacity of the gears is given by the manufacturer and is adequate to support the inner HCal.

Now that the majority of the cart mechanism is designed, the support structure should be considered. The initial design consists of three pillar or tower supports. The I-beam that the cart rests on is divided into two segments. The first segment will be supported by one of the end supports and an intermediate temporary support. The first segment is also where the cart will be initially lifted and positioned with a crane. The second segment will be supported by the intermediate support as well as the other end support, making it the portion that is within the outer HCal magnet assembly. The two and supports were later designed to be hexapods intended for six degrees of freedom and fine adjustment of the I-beam supporting the inner HCal. Figure 7 contains images of the hexapods and their displacement.

Then the mechanism for moving the cards along the I-beam should be taken into account.

A wire rope and pulley system should be adequate for the inner HCal to transverse the I-beam. The pulley system, however, would subject the support structure to a significant horizontal

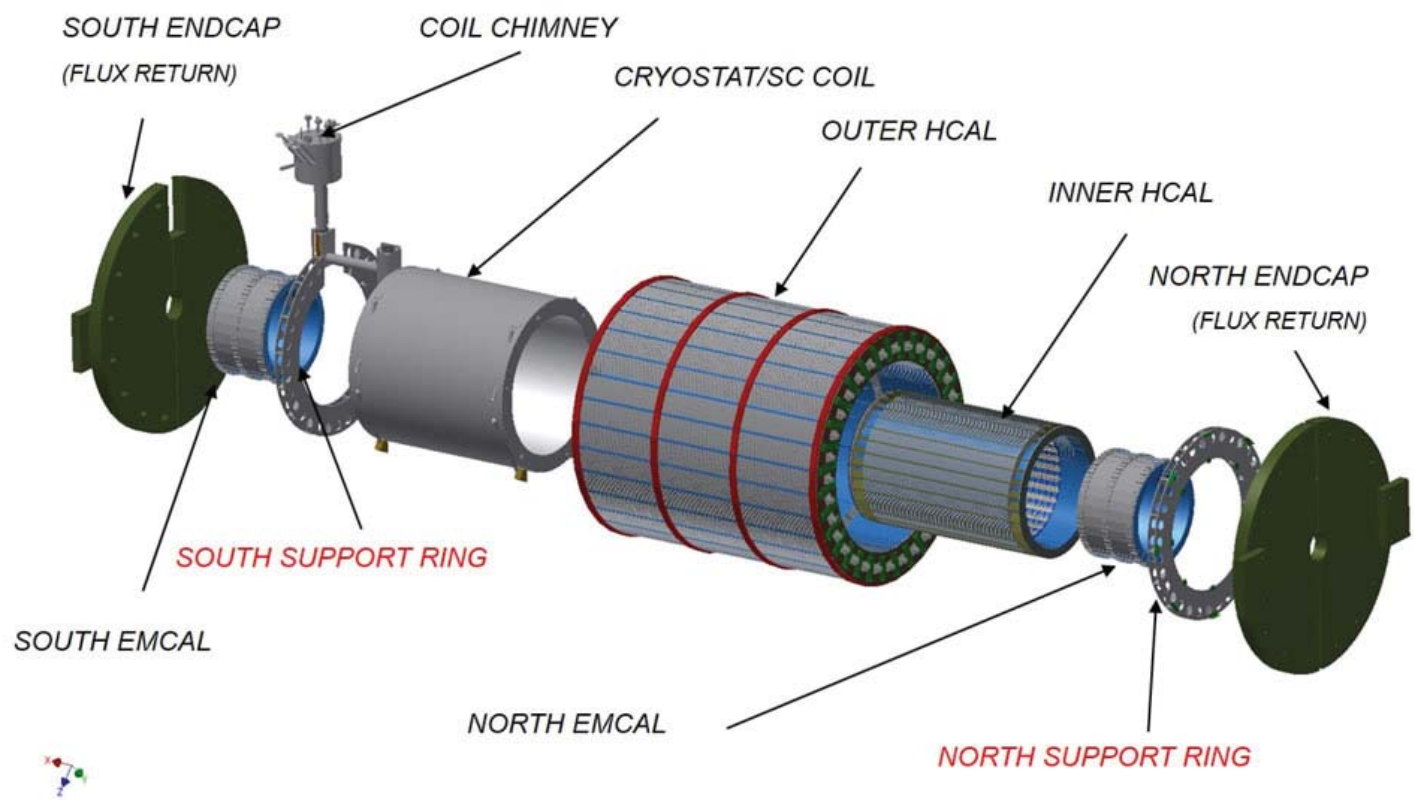

Figure 1. Components of the sPHENIX detector excluding the tracker and trigger.

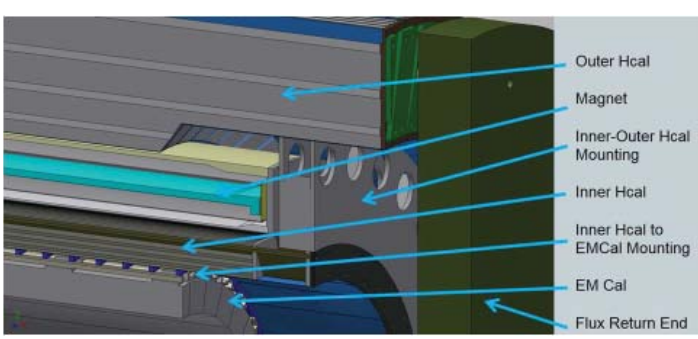

Figure 2. sPHENIX assembly.

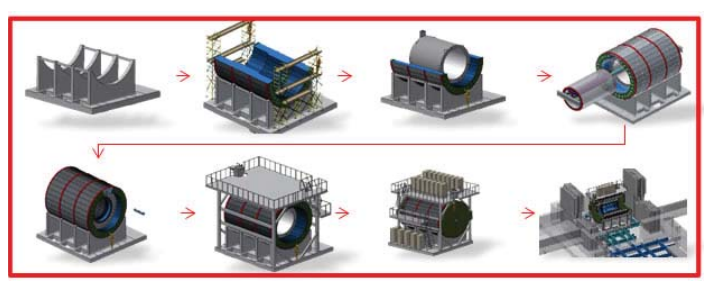

Figure 3. sPHENIX assembly procedure.

loading, thus a framework would be more appropriate. Utilizing a framework for the support structure would increase stability, but would make adjusting the I-beam's position more difficult. After searching for commercially available parts for adjusting the I-beam's position within the outer HCal, hydraulic gantries were discovered and considered. Figure 8 is an image of the design for the framework.

B. Hydraulic Gantry System

Finding hydraulic gantry systems marked a major redesign. Hydraulic gantries would not only be able to lift the inner H Cal, but would also be able to move it into the appropriate position within the magnet. This eliminates the need for the cart structure altogether. Modifying the design to accommodate the gantry system would mean utilizing a two-phase installation process. The inner H Cal could be rotated on a stand supported from the ground and then later lifted and moved into position with hydraulic gantries. This method would not only be safer because it's closer to the ground, but it would also mitigate the concern of the moment created by the installation of one module and it should make it easier to align the inner HCal with the superconducting magnet. Figure 9 is a schematic for the hydraulic gantries.

Designing the stand is the first part of the redesign. It would be similar to the gear mechanism that was used for the cart but it would be external to the inner HCal. The stand would need to accommodate the cylindrical geometry of the inner HCal while offering stability and support for the installation procedure. The geometry of the standard should also be optimized to reduce cost without sacrificing functionality. The components are rotating the inner HCal would be removed before its installation, thereby avoiding any potential clearance conflicts. Figure 10 is an image of the design for the stand.

The second major part of the redesign is the installation fixture. At this point the inner HCal should be completely assembled and thus would only need to be lifted and moved into position. Meaning that the inner HCal could be temporarily, but directly bolted to the I-beam introducing greater stability and precision. The introduction of second I-beam mounting the I- beams together with perpendicular I-beams would also increase accuracy and steadiness via a decrease in deflection and torsion. Fixing perpendicular I-beams to the ends of the structure should prevent further torsion and create a wider base for the hydraulic gantries, again increasing stability. The flange used in bolting the inner HCal to

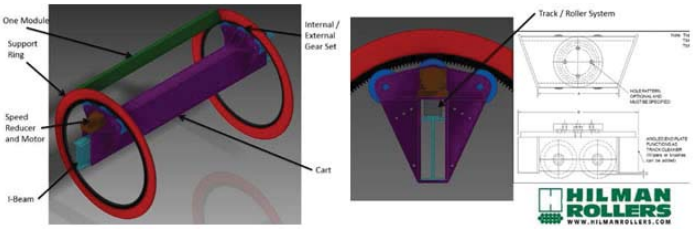

Figure 4. An intermediate design of the installation fixture.

Figure 5. Inner HCal end cap and wire rope installation point.

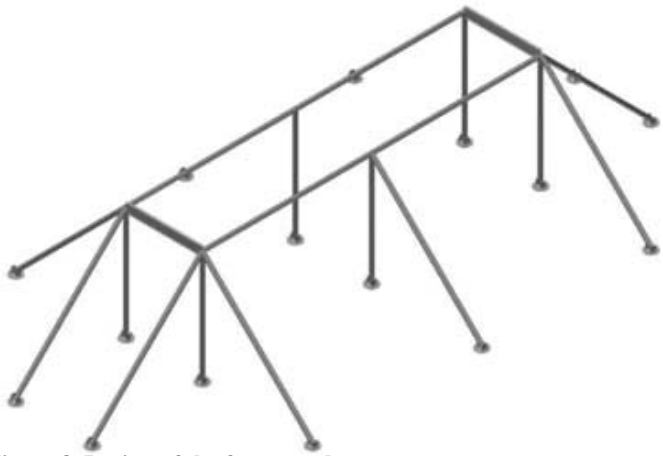

Figure 8. Design of the framework.

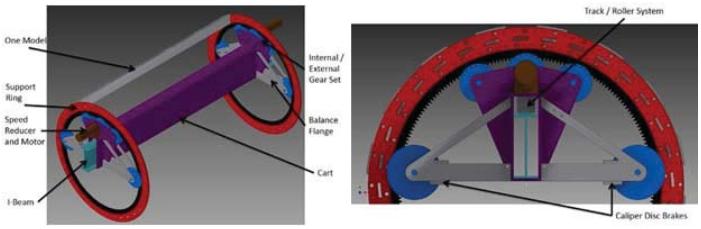

Figure 6. An intermediate design of the installation fixture.

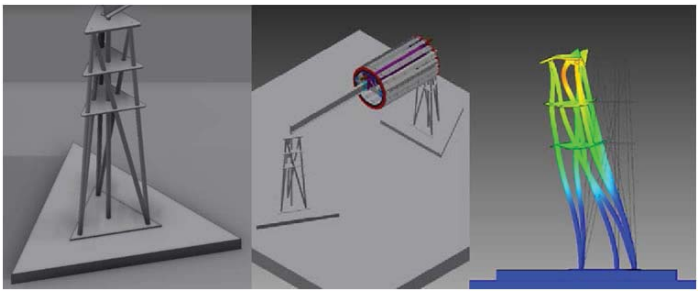

Figure 7. Design and displacment of the hexapods.

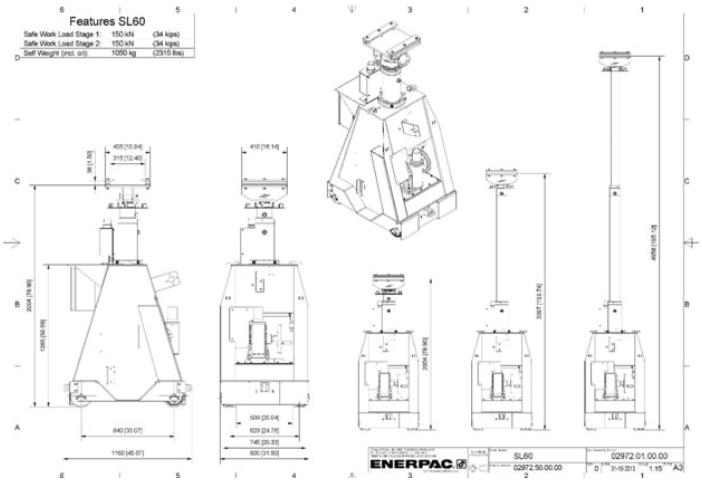

Figure 9. Hydraulic Gantry System schematic.

the I beams is also of particular interest, because, like the stand, the geometry should be optimized to reduce cost without sacrificing functionality. Figure 11 shows the design for the I-beam flange.

III. Results and Discussion

Analyzing the stress and deformation due to loading through finite element analysis is a crucial part of design. Throughout the process of creating both the cart mechanism and the hydraulic gantry system simulations were central to determining the weak points in the structure and what modifications should be made. Please note that the illustrated displacement is exaggerated to show how the part deforms.

A. Cart Mechanism

The cart mechanism is designed in such a way that the only major stress concentration is at the gears. Because the gears would be purchased commercially, the load capacity in the materials yield strength are what need to be considered. The rest of the cart does not experience any major stress. There are stress concentrations on the shaft and the shaft supports for the gears, but they are within an acceptable range for steel. The track and roller system also experience large amount of stress, which is caused by the load distribution being focused at those points. In order to mitigate the stress concentration more rollers could be introduced, however they would need to be equally spaced from the focal points of the application of the force. Creating the symmetry would require a larger cart, thus a larger I-beam and would create more stress due to larger deflections. The largest stress concentration in the cart mechanism assembly is nearly 320 MPa which well exceeds the threshold for suitable stress levels for steel with the yield strength of 200 MPa. The maximum deflection is about

Figure 10. Design of the stand.

Figure 11. Design of the I-Beam Flange.

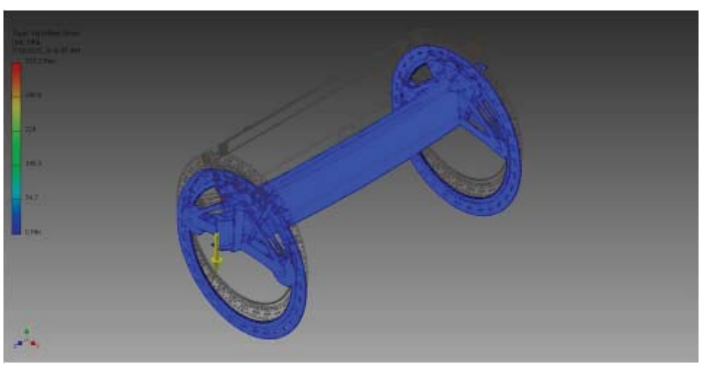

Figure 12. FEA stress analysis of the cart.

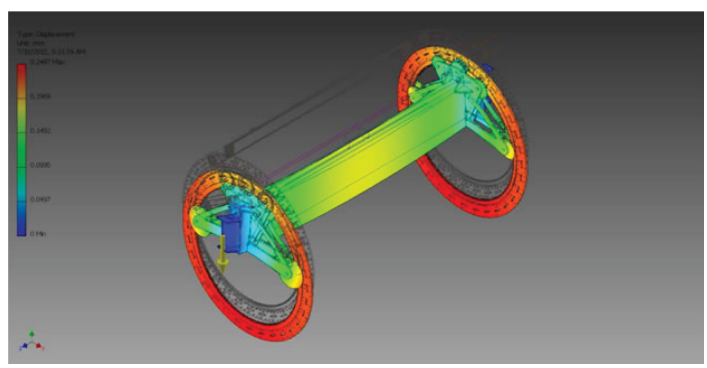

Figure 13. FEA deformation analysis of the cart.

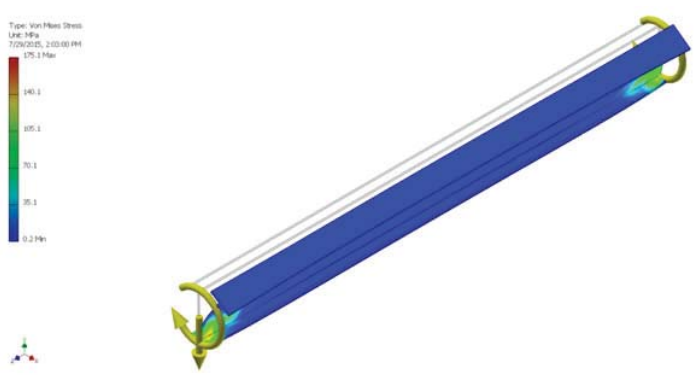

Figure 14. FEA stress analysis of the I-beam.

Figure 15. FEA deformation analysis of the I-beam.

40 mm which is marginally acceptable, although will the assembly will need significant adjustments during the installation process. Figure 12 and 13 show the stress analysis and displacement of the cart experiencing gravity respectively.

The stress and displacement due to the torsion created by the moment from the installation of one module adds to that experienced by the I-beam. The stress created by one module that weighs approximately 1 ton and is at a radius of nearly four and a half feet is slightly over 175 MPa. The stress alone is acceptable, but the I-beam also experiences a maximum of 205 MPa of stress due to the load of 31 modules. The installation of one module also creates a 10 mm deflection to one side causing instability. Rotating the partial assembly with only one module installed will cause further instability, especially when decelerating. Figures 14 and 15 show the stress and displacement of the I-beam experiencing torsion due to the gravitational force of one module respectively.

The framework for the cart mechanism also experiences a notable amount of stress and deflection when under loading. The framework has a maximum stress of approximately 425 MPa, well beyond the acceptable range for steel. An alternate material and/or larger sized I-beam would be required. The framework also experiences a 7 mm deflection, which would need to be accounted for, but is appropriate. Figure 16 and 17 show the stress and displacement of the framework from the inner HCal assembly respectively.

B. Hydraulic Gantry System

Much like the cart mechanism, the stands for the inner HCal have major stress concentrations at the gears. As long as the gears are capable of withstanding this stress due to their material and load capacity, the stress concentration is acceptable. Also like the cart mechanism, there are stress concentrations on the shaft and shaft supports. The semi-complex geometry of the stands is to reduce material, and thus cost, while withstanding the stress created by the 32-ton load and minimize deflection. With the current set up, the stand experiences a maximum of 0.1 mm deflection and a maximum stress concentration of roughly 120 MPa.

Figures 18 and 19 show the stress and displacement of the stand due to the gravitational force of the inner HCal assembly respectively.

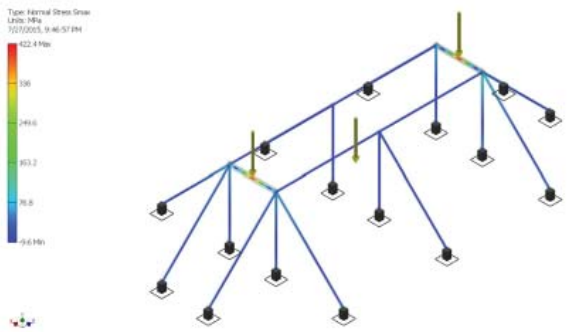

Figure 16. FEA stress analysis of the framework.

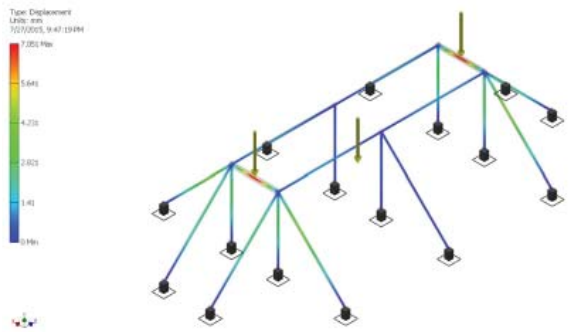

Figure 17. FEA deformation analysis of the framework.

Figure 18. FEA stress analysis of the stand.

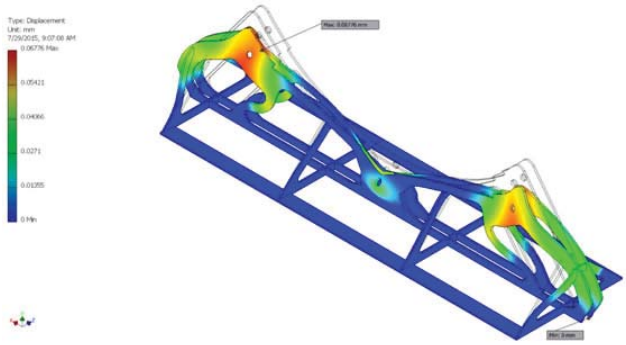

Figure 19. FEA deformation analysis of the stand.

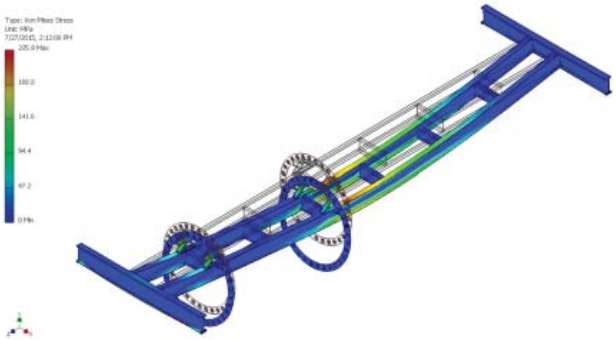

Figure 20. FEA stress analysis of the I-beam and inner HCal.

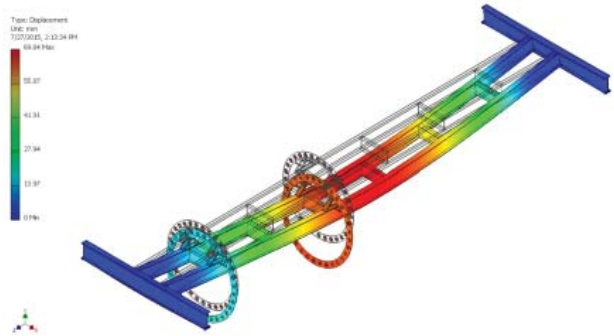

Figure 21. FEA deformation analysis of the I-beam and inner HCal.

The most difficult part of designing the installation fixture was reducing the stress concentrations. The long I-beams inherently create large deflections and deformations and thus stress concentrations. There are two options available to mitigate the issue: either using larger I- beams that will reduce the deflection and thus stress or use a different material for the I-beams that can withstand the necessary stress concentration. The mounting fixture that attaches the inner HCal to the I-beams also experiences large stress concentrations. The fixture experiences 210 MPa of stress. The potential solutions are similar: either the material needs to be able to withstand the stress, or the geometry needs to be redesigned in such a way that the stress distribution creates lesser concentrations. Although the fixture itself does not experience much deflection, the I-beams it is supported on deflect approximately 70 mm. This deflection may seem large, but each of the four towers in the hydraulic gantry system are capable of moving independently. The ability to move independently allows for the back two gantries to be lifted slightly higher, thus making the inner HCal concentric with the outer HCal magnet assembly.

Figures 20 and 21 show the stress and displacement of the I-beam support structure to the gravitational force from the inner HCal assembly respectively.

IV. Conclusion

Utilization of hydraulic gantries affords a superior support structure. The cart apparatus and framework, although potentially more cost-effective, offers less stability, more critical stress points and greater complexity. Ultimately, both methods have high stress for steel; BNL would require a safety factor of two, meaning that stress levels should not exceed 100 MPa. Using hydraulic gantries and the method proposed for the corresponding assembly and installation procedure should provide easier, safer and more accurate results. The hydraulic gantry method experiences fewer and less extreme stress points when compared to the cart fixture method.

Utilization of the gantries does require longer I-beams and thus creates a larger deflection, but because the hydraulic gantries are capable of moving independently the deflection can easily be accommodated for. The capabilities and ease-of-use of the gantry system far exceed that of the cart device, thus making it a more efficient solution.

V. Recommendations and Future Work

Use of hydraulic gantries seems to have many benefits; however further research is needed to determine the stability of the assembly. A Potentially beneficial consideration would be to combine the two ideas. Assembling the HCal on the ground is the best option, but a framework support structure offers better stability and less skepticism concerning safety. It is also worth considering the possibility of moving the pedestal assembly instead of, or in addition to, moving the inner HCal. The pedestal assembly will not have precise movement, but it will allow for coarse adjustment. Currently the proposed gantry track system exceeds the assembly hall dimensions. Moving the pedestal assembly would reduce the required track length, fixing the issue. Both methods pose problematic circumstances that need further consideration. Either the complications need to be solved or an entirely new idea should be proposed.

VI. Acknowledgements

This project was supported in part by the U.S. Department of Energy, Office of Science, Office of Workforce Development for Teachers and Scientists (WDTS) under the Science Undergraduate Laboratory Internships Program (SULI). Also, a special thanks to Don Lynch (sPHENIX Chief Engineer), Rich Ruggiero (sPHENIX Chief Designer), Anatoli Gordeev (sPHENIX HCal Senior Engineer), Ed O'Brien (sPHENIX Project Manager), John Haggerty (sPHENIX Principal Scientist), Jim Mills (sPHENIX Project Engineer) and both the PHENIX and sPHENIX technician and engineering teams for their guidance throughout the duration of the internship.

Modeling a coating system for photocathodes for Low Energy Relativistic Heavy Ion Collider electron Cooling

Patrick Carroll
Mechanical Engineering, University of Rhode Island, Kingston, RI 02881
Joseph Tuozzolo
Collider-Accelerator Department, Brookhaven National Laboratory, Upton, NY 11973
Triveni Rao and John Walsh
Instrumentation Department, Brookhaven National Laboratory, Upton, NY 11973

Abstract

In 2017 the Relativistic Heavy Ion Collider (RHIC) at Brookhaven National Laboratory will commission a 500kV DC electron gun (e gun) which will utilize a photocathode that is excited by laser light to emit high intensity bursts of electrons to be the source for the Low-Energy RHIC electron Cooling (LEReC) project. The photocathode surface material requires an exotic mixture of elements applied in layers through vacuum deposition. Photocathodes must be baked out at temperatures up to 350 °C in a 10^{-8} to 10^{-11} Torr level vacuum and then coated multi-angstrom thick layers of sodium, potassium, and antimony to be suitable for operation in RHIC. During operations, the photocathodes last 24 to 48 hours. With the design constantly changing due to scientific research and testing, my task was to use PTC Creo Parametric to design and model a photocathode preparation system that can fabricate coated photocathodes in volume to meet the RHIC 24 hour/7 days a week operating schedule while staying within the operating parameters. Completion of my project tasks has resulted in the enhancement of my engineering abilities. The opportunities the internship provided have enabled me to become proficient in my ability to think creatively and interact efficiently with other workplace professionals. Most importantly I've acquired the skills to turn abstract design ideas into physical representations using PTC Creo Parametric design software.

I. Introduction

While beam cooling has only been studied for a few decades, it has proven to be highly beneficial to a beam. Cooling can increase beam quality by decreasing the particle sizes and their momentum spread. Many different types of beam cooling have been implemented; electron, stochastic, and laser cooling; Brookhaven National Laboratory's newest project, LEReC, will use electron beam cooling. To generate the electron beam, a laser light strikes a photocathode puck coated with multi angstrom layers of materials. The light will shine at a specific angle which will excite electrons on the cathode. Once excited, the electrons will be emitted horizontally past the anode, as shown in figure 1. Magnets will direct the electron beam to travel towards the storage ring, which will contain a beam of heavy particles. The electron beam will be traveling at the same average velocity as the ion beam where it will "cool" the ion beam.

A key component that starts the cooling process is the photocathode. Meeting the requirements such as the Quantum Efficiency (QE), and photocathode longevity are the top priorities for use in RHIC. It is possible to decrease the laser power needed and maintain sufficient current if a greater QE is attained. For an application such as Low Energy RHIC electron Cooling (LEReC), the electron cooling will require up to 50 mA of current with the laser light having a wavelength of approximately 530nm. Achieving this current level, a high QE, and an ample lifetime can be done by coating a photocathode puck with Na2KSb. When compared to other coating combinations, such as GaAs, CsK2Sb, and CsA; the Na2KSb coating is less sensitive to contaminants, and has a higher tolerance for the expected temperatures the cathode may experience during operations in RHIC. Coated with 100A of antimony, 100A of potassium, and 200A of sodium, the cathodes projected lifetime will be 24 to 48 hours with the QE percentage expected to be in range of 4-6%.

If LEReC runs for 20 weeks without stopping, and the photocathodes last for 48 hours in the e gun means that the minimum number of photocathodes needed for the LEReC project is 140. Lasting for 24 hours on the other hand would result in production of 730 photocathodes. Whether or not the cathode lasts 24 or 48 hours, devising a system to coat the photocathodes must be able to handle the stresses of creating a large quantity of cathodes. This preparation system must meet the substantial volume needs of LEReC; with the objective of preparing 12 cathodes per ¬week. During my internship, I have used PTC Creo Parametric to model and design the photocathode preparation system. A design for the physical deposition system for sodium, potassium and antimony, as well as a basic 3D layout for the preparation system has been completed. The layout will contribute to other engineers and scientists involved.

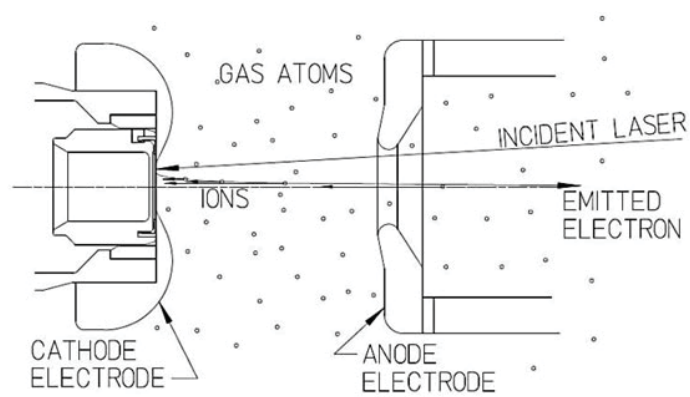

Figure 1.

II. Methods

Modeling a basic layout of the preparation system as well as designing a conceptual 3D model of one part of the preparation system known as the cesiator, has been done using PTC Creo Parametric. The cesiator is a physical deposition system which will apply the layers of sodium, potassium, and antimony to the puck in separate steps at separate stations. Depending on research and development work, the cesiator could be modified as time progresses. However, the preparation process will remain the same.

A 3D model of the preparation system can be shown in figure 2. Preparation of the pucks begins in the container referred to as the vacuum suitcase. It is able to be attached to the preparation system, removed, and reinstalled on the e gun in RHIC. Prior to installation in the e gun, the suitcase must prepare all 12 coated photocathode pucks that are located within it.

Beginning the coating procedure starts by evacuating the system using ion pumps and titanium sublimation pumps. One at a time using a linear manipulator, the photocathode pucks are placed past the transfer station and within the bake out chamber; until 3 pucks are inside of the bake out chamber. Once 3 have been properly situated, the gate valve is closed off from the rest of the system and the bake out starts. After it is sealed, the pucks are heat treated to 350 °C for 8 hours. After 8 hours pass, the 3 cathodes are then individually moved back into the transfer system onto a cart using the same linear manipulator.

The following step is to retract the cart with the 3 heat treated photocathodes into the long linear manipulator. After being retracted, 3 more photocathode pucks from the suitcase will be placed into the bake out chamber. The 3 pucks which were retracted into the translator are then positioned over the sodium. They will be coated one at a time until all 3 have the desired layer of sodium; this is then repeated for potassium and antimony.

A 3D visual of the cesiator design is located in figure 3. The design was collaborated with scientists and engineers in order to meet the scientific and mechanical specifications. The coating process begins with placing an ampule of either sodium or potassium into the ampule holding device. This component is disassembled, and the ampule containing 1 gram of material is placed in a bracket to be held in position where it will stay for nearly a year. Once the component is reassembled, the cesiator will be put to a 10-9 Torr level vacuum. The ampule breaker is comprised of a hydraulically formed bellows, an anvil welded to the upper flange, and bolts that hold the bellows in place. When the bolts are loosened in ambient air, the anvil will be pulled downwards from the vacuum pressures and drive itself into the ampule, which will release the contents (the process for antimony is differed slightly from sodium and potassium by using a crucible instead of an ampule). Once the contents are released, we then must follow the procedure from CEBAF Polarized Electron Source[1]. Modifying this procedure was difficult; the design is vertical instead of oriented horizontally. In addition, our design will not incorporate any copper tubing or crimping. Using electric heating on the tubing will evaporate the alkali metal upwards towards the top of the design, where the photocathode puck will be positioned. The temperature for the material must be consistent throughout the process; 220 °C for sodium; 200 °C for potassium; 170 °C for antimony. This is done by using electrical heaters as well as a gas system which is located within the linear shift. It is comprised of an inlet and outlet pipe, and a gas chamber. Not being under vacuum, the gas chamber will allow the user to use hot gas to heat up the system, or pump in liquid nitrogen in order to halt the evaporation process. Located on the 4.5” conflat cross are an ion pump, and a Non-Evaporable Getter pump (NEG). Included in the rest of the design are one large viewport and one small viewport to accurately align the cathode cart with the cesiator evaporating tube. It also will contain a laser viewport where a laser can be shined onto the photocathode during the evaporation process in order to test the QE and the thickness of the material evaporated. Located on the front of the design is an anode push-pull feedthrough, which is biased to 200V and is used to measure the QE.

Before the contents reach the photocathode however, the photocathode must be positioned above the cesiator system using a linear manipulating device. Once positioned properly, the

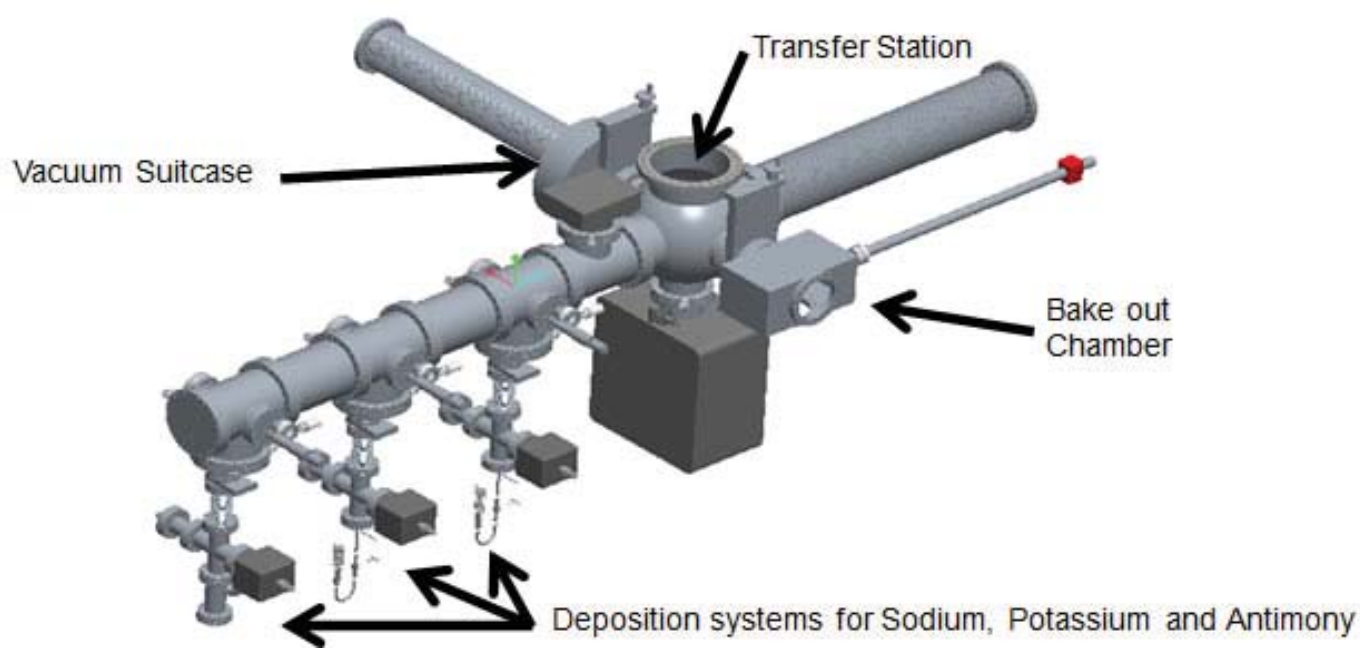

Figure 2: The photocathode preparation system

gate valve is opened which will allow the evaporating tube to be exposed to the deposition chamber which contains the photocathode cart. A linear shift, again shown in figure 3, will compress which results in the tube containing the evaporating material to get within 2 inches of the photocathode. The 3 pucks on the cart will be positioned one puck at a time over the system until all 3 cathodes are coated with sodium. The cart is then moved over to the next station, potassium, where the method is repeated. Finally the pucks will be coated with antimony.

Once the 3 photocathode pucks are coated with the proper amount of sodium, potassium, and antimony; the cart will be retracted back to the transfer station. Next step is to place the 3 pucks back in the suitcase one at a time until all 3 pucks, which will be ready for use in RHIC, are returned. The same processes are then repeated until all 12 photocathode pucks have been coated with their respected materials and are back in the suitcase ready to be transferred to RHIC.

III. Results

After many unsuccessful design iterations, the cesiator system designs for sodium, potassium, and antimony are now completed. Each will include an ion pump; Non Evaporable Getter pump (NEG); viewports for testing Quantum Efficiency (QE) and to properly align the photocathodes; anode feedthrough; and a linear shift. In addition to this, the cesiator system is built from catalog UHV equipment to eliminate any leaks.

The layout shown in figure 2 will include a Residual Gas Analyzer (RGA), large ion pump, transfer station, bake out chamber, turbo pumps, and three linear manipulator systems. The linear manipulators will be able to precisely align the photocathodes into position for baking and the evaporation process. One of the most significant components of this project, which has yet to be fully designed, is the cart which the photocathodes will travel on. This cart will have a crystal monitor, heating and cooling apparatuses, and be electrically biased.

Cornell University's research team has provided us with valuable information on their photocathode pucks and evaporation systems. Taking all of the information they provided into account, the model of the preparation system meets BNL's and Cornell's requirements. Requirements include constraints such as the precision needed under UHV, placement and diameter of the deposition on the photocathode puck, size of systems, and costs. Coating the puck to these dimensions is vital to substantially improve the electron beam, QE, and eliminate any halo beams or ion backstreaming.

While the project was focused on the evaporation process and the cesiator design, it also provided Brookhaven National Laboratory with a basic layout of a preparation system and gave vital information which is being used for the project cost estimate and schedule.

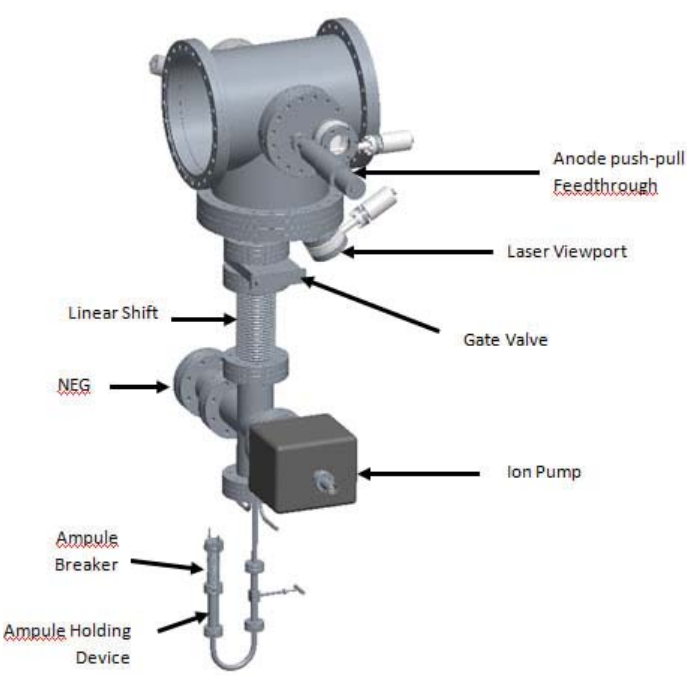

Figure 3: Cesiator system

IV. Conclusions

The conclusion of this project has allowed us to gather more information regarding he preparation process needed for LEReC. In addition, it has provided us with a cesiator design that has nearly all issues and kinks worked out. Modeling this preparation system has proven to be beneficial to me. Completion of the 3D layout and the cesiator has enabled me to acquire knowledge of vacuum systems and components, 3D modeling software, pricing, and the mechanical engineering profession.

V. References

[1]B.M Dunham and C.K. Sinclair "Charging the Cesiator on the Illinois/CEBAF Polarized Electron Source" May, 1990 < https://www.jlab.org/accel/inj_group/docs/NPL-TN/90-9.pdf>

VI. Acknowledgements

This project was supported in part by the U.S. Department of Energy, Office of Science, Office of Workforce Development for Teachers and Scientists (WDTS) under the Science Undergraduate Laboratory Internships Program (SULI). I would also like to thank my mentor Joe Tuozzolo, as well as Triveni Rao, John Walsh, and Ammar Morgan, for their patience and resourcefulness.

Using anomaly detection to facilitate intelligence gathering for satellite imagery

Daniel Cisek
St. Joseph's College, Patchogue, NY 11772
Shinjae Yoo and Susan Pepper
Nonproliferation and National Security Department, Brookhaven National Laboratory, Upton NY 11973

Notice: This manuscript has been authored by employees of Brookhaven Science Associates, LLC under Contract No. DE-AC02-98CH10886 with the U.S. Department of Energy. The publisher by accepting the manuscript for publication acknowledges that the United States Government retains a non-exclusive, paid-up, irrevocable, world-wide license to publish or reproduce the published form of this manuscript, or allow others to do so, for United States Government purposes.

DISCLAIMER

This report was prepared as an account of work sponsored by an agency of the United States Government. Neither the United States Government nor any agency thereof, nor any of their employees, nor any of their contractors, subcontractors, or their employees, makes any warranty, express or implied, or assumes any legal liability or responsibility for the accuracy, completeness, or any third party's use or the results of such use of any information, apparatus, product, or process disclosed, or represents that its use would not infringe privately owned rights. Reference herein to any specific commercial product, process, or service by trade name, trademark, manufacturer, or otherwise, does not necessarily constitute or imply its endorsement, recommendation, or favoring by the United States Government or any agency thereof or its contractors or subcontractors. The views and opinions of authors expressed herein do not necessarily state or reflect those of the United States Government or any agency thereof.

Abstract

The Nonproliferation and National Security Department at Brookhaven National Laboratory works alongside several other agencies to create policy, procedures, and instruments to help combat the threat of nuclear proliferation worldwide. The field of image analysis seeks to extract intelligence information from different types of images, such as maps and seismographs. As part of the nonproliferation regime, imagery analysis is an often-employed tool for the monitoring of proliferation significant sites and the detection of undeclared activities. Recent advances in satellite imaging technology have made this field indispensable in intelligence gathering. However, given the rapid growth of this technology, agencies are still adopting its use. Image analysts are tasked with the surveillance of several sites, each of which must be checked daily for changes. This project seeks to implement an algorithm for anomaly detection, which would serve as a pre-analytic. This would alert analysts to site changes, thus allowing analysts to focus their attention more on analyzing the impor-

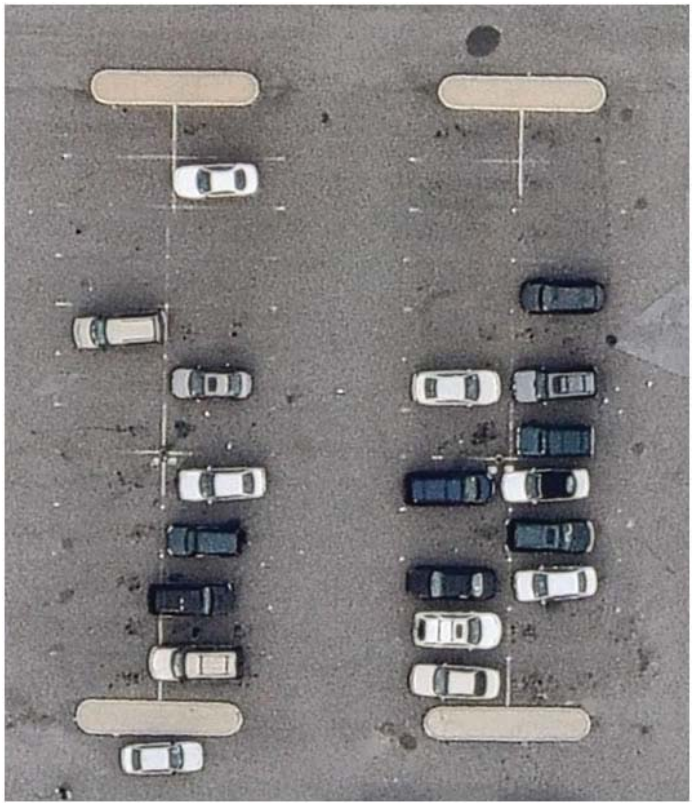

Figure 1: The first image of our chosen data set (a1).

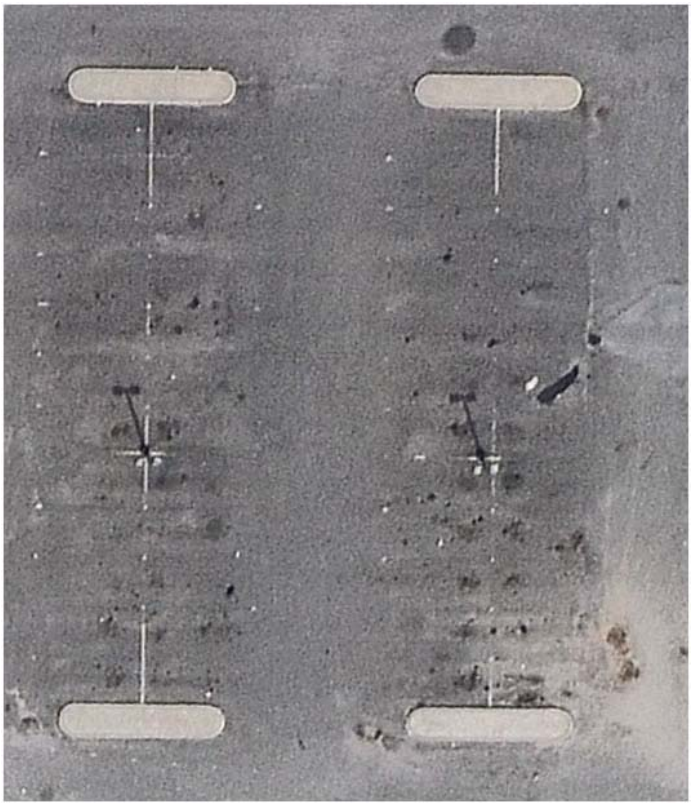

Figure 2: The second image (a2)

tance of changes, rather than wasting time simply looking for differences. We plan to implement this algorithm through the use of MATLAB, a popular data visualization and computing environment that boasts an impressive array of image analysis tools. Through this project we hope to gain an understanding of the use of satellite imagery in intelligence gathering, as well as experience using MATLAB to perform image analysis.

I. Introduction

The Nonproliferation and National Security Department at Brookhaven National Laboratory works alongside several other agencies to create policy, procedures, and instruments to help combat the threat of nuclear proliferation worldwide. Foremost among the organizations that BNL works in conjunction with is the International Atomic Energy Agency (IAEA). The IAEA is an international agency that conducts inspections to ensure that countries are meeting their safeguards agreements under the Nonproliferation Treaty (NPT). The NPT ensures that nuclear material is being used for peaceful purposes, through the application of comprehensive safeguards[1].

The NPT plays a key role in the safeguard system, and helps international efforts to halt the proliferation of nuclear weapons. The NPT is a complex verification system built on states reporting their nuclear material accounts and on-site inspection by the IAEA. The goal of the IAEA is to verify states reports, much like the IRS auditing an individual's taxes. The IAEA can then confirm that all the accounts are "correct" when everything has been reported "correctly" and "completely". From this all nuclear material can be accounted for by the IAEA1. When it comes to verifying what countries report, several approaches are used in conjunction with one another to ensure that any non-compliance on the behalf of member states can be detected quickly. In recent years the IAEA's vigilance has led to the detection of covert nuclear programs both in Iran and Syria[1].

Although in the past verification methods were composed mostly of on-site inspections, the birth of high resolution satellite imagery has given the IAEA and intelligence agencies an invaluable surveillance tool. For many years satellite imagery was expensive and had a low resolution, though in recent years the field has progressed exponentially. Today, we see high resolution satellite imagery being relatively easy to access, with incredible resolution and low revisit time. Recent satellites now offer color images with a spatial resolution, the smallest discernable detail in an image, of less than 1.36 meters with the recently developed GeoEye-2 [2].

Given these huge advances, we see satellite imagery being used to monitor proliferation significant sites where it is suspected that undeclared activates may be taking place. This allows agencies unparalleled access to up-to-date site information and the ability to monitor facility changes. A group at the Monterey Institute of International Studies showed just how important satellite imagery is, when they were able to estimate the plutonium production capabilities of a Pakistani nuclear reactor, using information gleaned from satellite imagery in conjunction with 3D modeling[3]. Because of the utility of such capabilities, groups and organizations in both the intelligence field and the nonproliferation field often keep a group of image analysts on staff. These analysts are usually tasked with monitoring a collection of sites daily, reporting any changes that may occur. Analysts are often looking for anomalies; has anything changed since the last image was taken? For large areas of interest answering this question can take a lot of time, and when you consider that analysts often are assigned several sites, we see what a time-intensive task this can be. This is where BNL's Computational Science Center comes into play. As part of their exploratory research in this area, they seek to address this issue through the development of an anomaly detection pre-analytic. Before an analyst opens a satellite image file the pre-analytic would run, labeling any differences between the newest satellite image, and the most up to date one before that. This would save analysts countless time because instead of spending their time simply looking for changes, they could focus their attention more on analyzing the differences the pre-analytic identifies. As a first step in this process, my project seeks an approach to solving what is known as the "Parking Lot Problem". Solving this involved finding a way of determining how many cars are in a parking lot from a satellite image. This problem is a key element of the anomaly detection process, as it contains many of the same

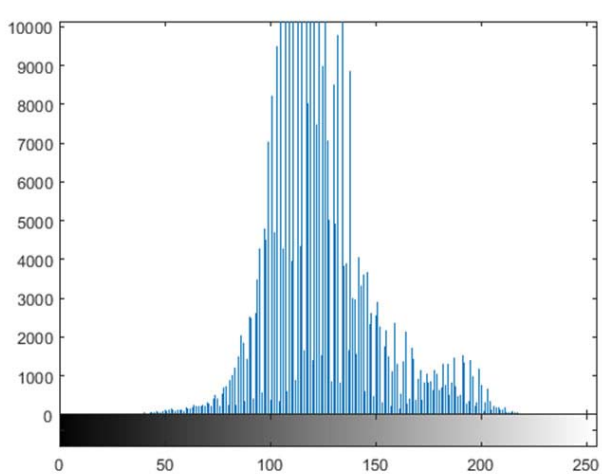

Figure 3: Intensity histogram for our grayscale image

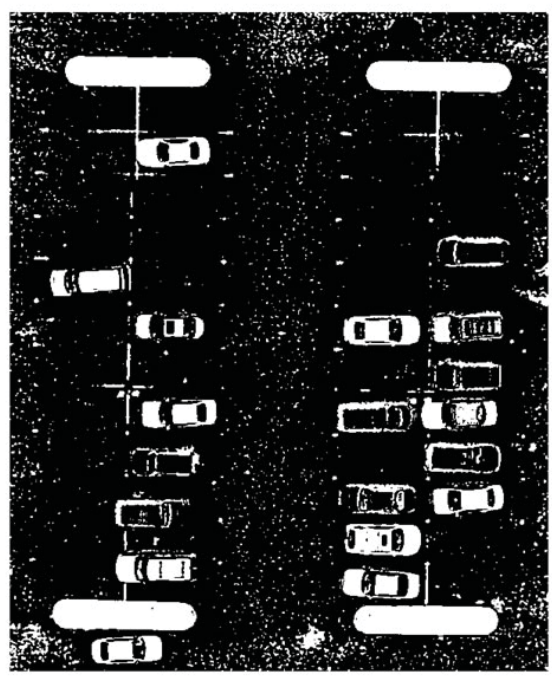

Figure 4: Our image, post-thresholding and equalization

challenges a full anomaly detection algorithm will face, just on a smaller level. Thus, my project attempts to provide a solution to this problem as a first step in the exploratory research the Computational Science Center hopes to conduct.

II. Methods and Results

In order to develop our method of detecting cars, we needed to access high resolution satellite imagery, preferably with multiple photos taken of the same site. Because of this, we settled upon NearMap[4], an international provider of high resolution imagery. Through this site we were able to select a parking lot outside of New York City to serve as the basis for this project, shown below. This spot was chosen because several of the variables we were afraid would greatly complicate the process were minimized. For example, the image is free from harsh shadows, and the concrete is relatively evenly colored, without excessive wear.

We also were able to obtain a second image of the site, taken at a different time. Thankfully this image was free of cars, which made it much easier to use as a base image. Given that we were only able to access two images of the site, this made our process slightly more difficult. Intelligence agencies have access to a far larger collection of images of any given site, which makes anomaly detection much easier. In cases like that, objects that are stationary and unchanging, like the four concrete islands in our images, can be quickly ignored because they remain constant across images.

To process the images themselves, we settled upon Matlab[5], given its comprehensive set of image analysis tools and relative accessibility for new users. We primarily utilized Matlab's Image Processing Toolbox, which contained functions that pertained to every step of the image segmentation process.

Once we obtained the images, we were able to proceed to actually attempting to isolate the cars from their background. Several methods were experimented with, but finally we struck upon one process that seemed to work. This method is discussed in more depth below, including what tools we used to accomplish each step.

The first step was to equalize and threshold our images. Equalizing simply refers to matching the histograms of our two images, both in terms of contrast and brightness, using the imhistmatch command. We added this step to allow us to get the average of our images, which reduces the impact of shadows. Thresholding is an incredibly powerful tool for image segmentation. It allows you to differentiate between the foreground and background of an image, which is very useful, especially with grayscale images. We convert our RGB format images, also known as truecolor images, to grayscale images using the rgb2gray command, in order to facilitate thresholding our image. Thresholding commonly entails selecting a threshold value T, representing an intensity value in our grayscale image. Any gray level values darker than this value T will become black (represented by a value of zero), and any gray level values lighter than this T value will become white (represented by a value of one). Thus, thresholding gives us a way of turning any image into a binary format, meaning all values are composed of either zeros or ones, corresponding to black or white, respectively. In many cases a single threshold value is enough to differentiate between images and their background, but given our project's goal, we found that dual thresholding works better for this task. To better illustrate why this is the case, we consider the below histogram, representing the range of gray level values for our image.

Grayscale histograms visually communicate the number of pixels in an image at each intensity value. This occurs on a scale of zero to two hundred and fifty five, with zero representing black, and two hundred and fifty five representing white. From this histogram we conclude that the concrete, given that it composes the

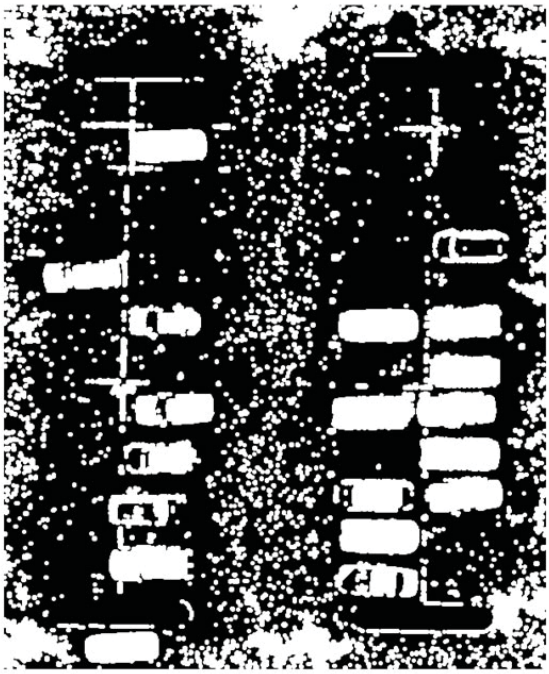

Figure 5: the effects of several morphological functions and the removal of the concrete islands

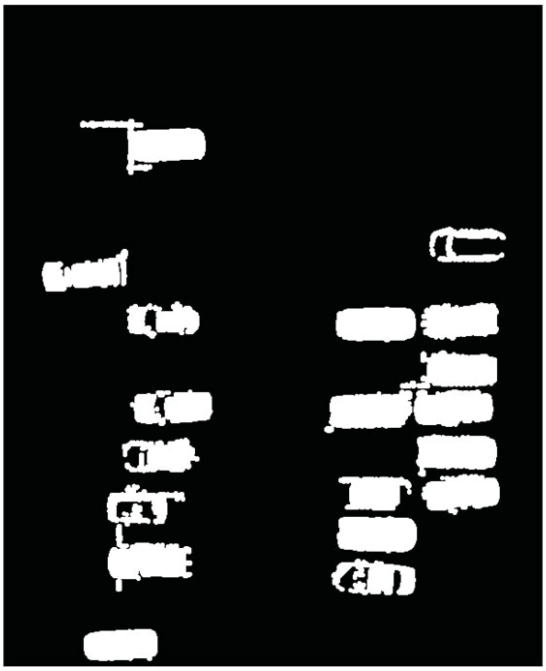

Figure 6: The image with removed background noise

majority of the image, occupies the space from 100 to 150 on our histogram, due to the peak height around these values. If this were simply a single threshold problem, we would simply choose our T value somewhere around a value of 160, and isolate everything from the background. However, cars are tricky because of the variety of colors they come in. In this case we need to consider both cars that are lighter colored than the concrete, and those that are darker colored than the concrete. Because of this, we turn to dual thresholding to isolate colors both lighter and darker than our believed concrete colors. Based on these criteria, it was decided to choose T values of 75 and 150, successfully isolating most of the concrete.

From these steps we get the resulting picture in figure 4.

Our next step used several morphological tools in order to connect nearby objects and fill in empty enclosed areas – in this case, car windshields. We also used Matlab's Image Segmenter app, in order to remove the four concrete islands in the parking lot. As mentioned before, this project serves mainly as a proof of concept for what a more advanced change detection algorithm would accomplish. Given that our focus is change detection, these concrete islands would be ignored because they remain stationary. We simulate this by removing them via the image segmenter tool, mirroring what a more sophisticated algorithm would do automatically. We utilized a variety of morphological tools in order to best distinguish the shape of cars. The first command used was imfill, a tool which fills in enclosed areas. This was used to help fill in the few cars that ended up with a full boundary, thus filling in their windshield. Next we used the bwdist command. Bwdist helps connect objects within a certain distance from each other, further helping us complete the outer boundaries of the cars, in cases where a small distance separates them. These commands yield the following image.

As can be seen from the above picture, this step has helped fill in several more cars, and more clearly distinguish the boundaries of our cars. However, at the same time it has also greatly increased the size of some of the background noise left due to variations of color in the parking lot itself. In this particular case we can remove it without too much trouble, but future projects may encounter trouble if the chosen site has a background that shows more erosion.

To remove the background noise several tools were employed. The first, imclearborder, removes any structures in the image that are connected to the border. By using this command we can clean up much of the image noise, though we use it with the assumption that no cars are on the border of the image. Because of this assumption, choosing our image size is of vital importance. If any car is too near the border of the image it could be erased along with the background noise. This possibility poses more of an issue in high traffic areas or parking lots that exhibit severe erosion, as these two factors contribute to how much noise our image exhibits. However, regardless of the parking lot condition this is something that should be considered when selecting the image used.

To remove all the background noise that the image now contains, the bwareaopen command was used. This command works on binary images to remove shapes of a certain size from the image. In this particular case we used it to remove any object of less than 1500 pixels, a size chosen based upon how big cars were in our image. Picking this value allowed us to leave the cars relatively untouched, while still removing almost all of the background noise. The result of these two commands is shown below:

Given that some of the previous commands tended to slightly bloat the shapes, we used two tools in order to better refine the shapes of the cars. The first, strel, creates what is known as a morphological structuring tool. These can take a variety of shapes. Based upon how we wish to affect the image we settled upon a disk shaped structuring element. After defining our shape, it could

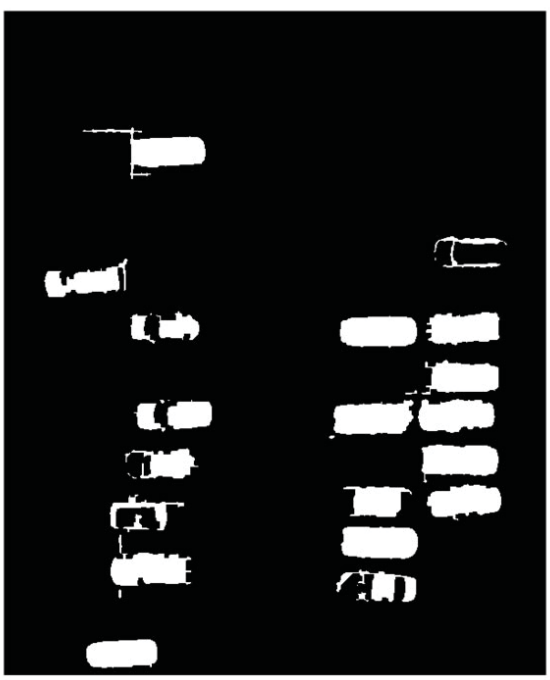

Figure 7: The image after being eroded

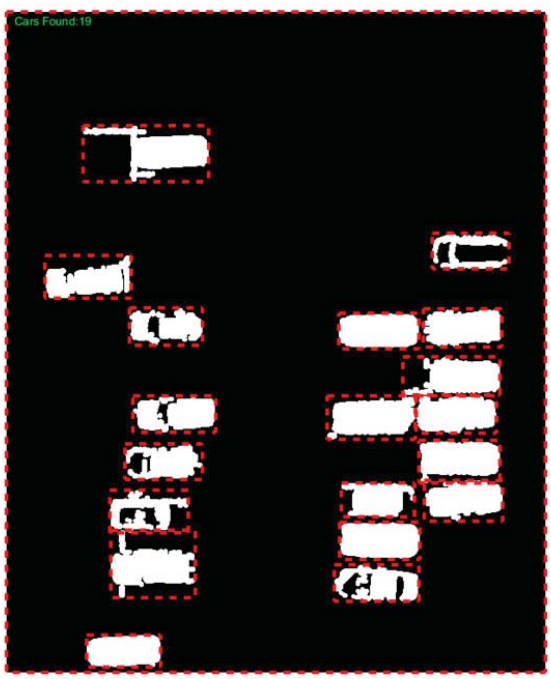

Figure 8: Identified regions are labeled, counted, and outputted.

then be used as the basis of another command, imerode.

This command strips away a layer of pixels from the boundaries of the objects in our image, using the previously defined structuring element. This leaves us with the resultant image:

The third, and final, step of our process involves actually locating the cars in our image. To do this we used the regionprops command, a tool which measures the properties of image objects, and can be used to output a variety of information about any object in an image. As part of this command we used the Bounding Box function to outline any shapes that regionprops identified. Lastly, we outputted the number of objects that were identified, in order to communicate at a glance how many cars were identified. Using the aforementioned commands yields the following image:

This picture shows our final output with the cars identified, labeled, and counted. Through this approach to the Parking Lot Problem we were able to identify every car that was in the chosen parking lot.

III. Complete Code

```
%%Read the image
cd('C:/Users/dcisek/Desktop/dan/data/parking')
pwd
a1 = imread('a1.jpg');
b1 = imread('b1.jpg');
a2=imhistmatch(a1,b1);
A = rgb2gray(a2);
figure, imhist(A)
B = A < 75 | A > 150;
figure, imshow(B)
B = mat2gray(B);
BW = activecontour(B, mask, 50, 'Chan-Vese');

B = B - BW;
figure, imshow(B)
c = imfill(B,'holes');
figure, imshow(c)
g = bwdist(c) <=2.5;
figure, imshow(g)
h = imfill(g,'holes');
figure, imshow(h)
i = bwareaopen(h,1500);
figure, imshow(i)
j = imclearborder(i);
figure, imshow(j)
tr = strel('disk',3);
tt = imerode(j,tr);
figure, imshow(tt)
img =j;
bw = im2bw(img);
stats = [regionprops(bw); regionprops(not(bw))]

imshow(bw);
hold on;
for i = 1:numel(stats)
rectangle('Position', stats(i).BoundingBox, ...
'Linewidth', 2, 'EdgeColor', 'r', 'LineStyle',
'--');
end
Number = bwboundaries(bw);

text(10,10,strcat('\color{green}Cars Found:',num-
2str(length(Number))))
hold on
```

IV. Conclusions and Recommendations

Although this method was able to identify every car in the chosen image, we have to consider the fact that our approach to this problem isn't stable. It works in this specific case, though generalizing this method will likely not produce results with the same degree of accuracy. This discrepancy in accuracy is the result of many variables that may differ between different images and locations. To name but a few, differences in image resolution, shadows, paving material, car color, and time of day can all play a huge role in how well our method can pick out cars from their background. As a proof of concept this method demonstrates that this process can work with relatively high accuracy in certain situations. However, it remains to be seen if an approach can be found that can identify cars successfully, regardless of the different variables mentioned above. Future work should focus on expanding our method to accommodate these variables, as well as investigating the impact that edge detection algorithms could have upon this process.

V. Notes

[1]M. Rosenthal et al., Deterring Nuclear Proliferation: The Importance of IAEA Safeguards, (Brookhaven National Laboratory, 2013)

[2]Satellite Imaging Corporation, GeoEye-2 (WorldView-4) Satellite Sensor (0.34m), http://www.satimagingcorp.com/satellite-sensors/geoeye-2/

[3]Tamara Patton (2012) Combining Satellite Imagery and 3D Drawing Tools for Nonproliferation Analysis: A Case Study of Pakistan's Khushab Plutonium Production Reactors, Science & Global Security: The Technical Basis for Arms Control, Disarmament, and Nonproliferation Initiatives, 20:2-3, 117-140, DOI: 10.1080/08929882.2012.719383

[4] Nearmap, maps.us.nearmap.com/

[5]Matlab, www.mathworks.com/products/matlab/

Replacement cost estimates for overduty electrical panels at the Brookhaven National Laboratory

William Clark
Electrical Engineering, University of New Hampshire, Durham, NH 03824
Raymond Edwards
Modernization Project Office, Brookhaven National Laboratory, Upton, NY, 11973

ABSTRACT

Many of the Brookhaven National Laboratory's (BNL) buildings require large amounts of electrical power, necessitating a large number of electrical panels around the site. A significant number of these panels are overduty. A panel is overduty when a dead short in the panel would exceed its current-handling capabilities, causing a catastrophic failure. The severity of the failure could be reduced by having a correctly-rated panel in place. I have been doing estimates of the cost to replace the overduty panels with properly rated ones. My work has involved many steps; I have been locating the overduty panels by using building plans and an electrical equipment database built by a contractor, assessing wiring configurations and panel conditions, and estimating panel replacement costs. As each panel feeds different circuits, many with different current or voltage requirements, even two seemingly identical panels can have grossly different replacement costs. By getting an idea of how much it will cost to replace the panels, BNL will know how much it will cost to eliminate the overduty panel issue and make the site a safer place to work, allowing scientific research to be carried out with less risk to BNL personnel. By seeking out and estimating the replacement costs for the overduty panels around BNL, I have gained experience working with key plans and seeing how they can differ from the actual physical buildings, as well as seeing how using the blueprints and how the physical configuration of electrical systems can assist electrical engineers in assuring safe designs and installations.

I. BACKGROUND AND INTRODUCTION

One of the most dangerous ways an electrical panel can fail is with an arc flash explosion. When there is a dead short within an electrical panel, an arc flash will occur; current will start to arc between two points, causing what is essentially an explosion as wire, air, and anything else in the panel are vaporized and expands with a ball of light and heat from the arc. Because the amount of current involved in an arc flash is so high, if the panel is not capable of withstanding it the failure will be even more catastrophic. Although they sound rare, there are between 5 and 10 of these incidents per day that send someone to a burn center1. In these incidents, 1-2 people die per day2. Because many of these events are caused by human error3 it isn't possible to completely eliminate the possibility of them occurring; the best that can be done is to reduce the risk from any event as much as possible and use training or safety procedures to attempt to prevent arc flash events from happening.

Every over duty panel at the laboratory was looked at, even if the maximum calculated short circuit current was only 1% over the panel's rating. Although many panels were labeled over duty in the survey (which was done to determine the state of the electrical equipment around BNL; determining if panels or other equipment were over duty was an important part of this), some of these "problem panels" were no longer in service, had been mislabeled in the survey, had been fixed, or simply were nowhere to be found on the building plans or in the building itself. In total, 47 electrical panels had their replacement costs estimated. By replacing over duty electrical panels with higher-rated panels (in terms of short-circuit handling ability, not "normal" current or voltage), the severity of the arc flash incident from a total failure will be reduced as the panels will actually be capable of handling the intense load placed on them; this gives the current interruption devices in the "upstream" circuits (the circuits feeding the panels) the time required to do their job properly, shutting down or eliminating the short circuit safely and as quickly as possible (minimizing the severity of any arc flash incidents) without causing (more) damage to equipment or harm to nearby people.

II. OBJECTIVES

The goal for this project was to get an estimate for the cost to replace every over duty panel around BNL; I was to find the price to replace each individual panel as well as a total cost for all of the panels combined. Knowing how much it would cost to replace everything will allow the work to be budgeted for or it will allow for panels to be replaced alone or in small groups as money allows.

III. MATERIALS AND METHODS

A. Tools

The main tools for this project were the building key plans, the electrical equipment inventory that covers the majority of the site, and an RSMeans Electrical Cost Data book. The key plans generally had an electrical equipment layer that allowed me to locate the panels I was looking for; this layer has various numbers marking different points. These numbers are listed in the electrical equipment database next to the specifics about each piece of equipment- what it is, where it is, what is it rated for; when these numbers are matched, a specific piece of electrical equipment can be located at the position indicated by mark on the key plan. Between these two tools it was possible to locate almost every single panel needed. For panels not found this way, the location could be deduced using the locations of other panels on the electrical plans or by asking people who may have known about them. Once each panel had been found, information about the way each panel was physically installed and configured could be taken down before the RSMeans book was used to assemble a cost estimate for the replacement of each panel.

B. Gathering information

The first step in gathering the requisite information about each panel was to contact someone with authority over the building housing the panel, generally the Facility Project Manager (FPM)

in charge of the building. Making contact with a this person allowed me to get permission to access the buildings, so the people working there could know who I was and why I was there, or parts of buildings with hazards or entry restrictions. Many buildings even required an escort by the FPM or someone in charge of the building. After getting to the panel, I could look into its physical set up; how the panel was mounted, what sort of circuits or breakers it contained, how various conduits fed into it, what the panel was rated for, etc, and note it down in a table. I would also indicate any environmental factors that would make the replacement of the panel any more or less difficult.

C. Estimations

After all of the information has been acquired, the final action is doing the estimates. Using the RSMeans Electrical Cost Data book, it is possible to see how much removing or installing any given part or component of an electrical panel (and its supporting pieces) will cost. After examining an electrical panel's physical configuration, breaking it down into a list of its constituent components and their required ratings is a relatively simple matter. From that list, the price of each part and the price of the labor required to install it can be found and all of the individual prices can be totaled, resulting in a full quote for the replacement of a panel. Any additional factors that could make the panel harder or easier to replace, such as a nearby pipes cramping the panel or a panel being in a radiological area, are also factored into the calculations, adjusting the price of replacement depending on how much of an impact they will have.

IV. RESULTS

In all, I found that the cost to replace every single over duty electrical panel at BNL would be about $901,820. Given that I was not able to locate a couple of the panels or assess some of the others, the "real" total would be slightly higher; using the average price of $19,187.66 to replace each panel, the theoretical cost would be $978,570.64. This is a fairly large amount, but it- and the average price- are both fairly in line with the expected value; even though electrical panels are somewhat simple, it takes a lot of work and some fairly expensive components to fully replace them. Even the panel itself can easily cost several thousand dollars, with prices going up to just under $10,000. Overall, the price of replacement for the panels was fairly evenly spread throughout the range of panel costs; the lower end of the price range is slightly less panel-heavy, but above about a $16,000 replacement cost there's a much more regular distribution.

In general, panels that would be much more expensive to replace were in incredibly tight spaces or involved radiological areas, which would both add significantly to the replacement costs for their own reasons. Outside of a panel's location, having a higher current rating or a higher voltage rating were primary contributors to increasing the cost to replace a given panel; as you get into higher rated panels, they get more expensive, as would be expected. For example, panel 153-PNL-L2, a 120/208 Volt 100 Ampere rated panel (one of the lowest rated panels that can be purchased) was only estimated to be $8,615 to replace where 924-PP-C10-3, a 277/480 Volt 600 Ampere rated panel (one of the highest rated panels that can be purchased), would be about $22,103. Although that seems like a fairly large gap (and it is), these two panels lie on the far ends of the spectrum; In general the replacement costs were fairly centered or clustered around the average.

V. CONCLUSIONS AND RECOMMENDATIONS

The total replacement cost for the over duty electrical panels around BNL is somewhat high, despite the individual panels being fairly cheap. With safety being such a major concern at BNL, going forward with the replacement of the over duty panels, despite the cost, would be a wise course of action. Although having higher-rated, non-over duty electrical panels won't eliminate the risk of arc flash hazards, they will reduce the severity of any arc flash events, potentially saving lives or reducing injuries. Also it is possible to replace panels one at a time as money becomes available; prioritizing panels based on age, condition, and how over duty they are should be a manageable exercise. While this will lead to the same or a slightly higher cost overall (due to prices increasing yearly or every couple of years), it would make the process much more affordable or easy to budget for, since it's small, yearly payments instead of one big lump sum.

VI. REFERENCES

[1]L. K. Fischer, "The Dangers of Arc Flash Incidents", Maintenance Technology.
<http://www.maintenancetechnology.com/2004/02/the-dangers-of-arc-flash-incidents/>Feb 2004

[2]Fischer

[3]L. W. Hilgeman, "Human error often causes arc flash accidents", Safety+Health.
<http://www.safetyandhealthmagazine.com/articles/human-error-often-causes-arc-flash-accidents-2> Aug 2009

VII. ACKNOWLEDGEMENTS

This project was supported in part by the U.S. Department of Energy, Office of Science, and Office of Workforce Development for Teachers and Scientists (WDTS) under the Science Undergraduate Laboratory Internships Program (SULI).

VIII. APPENDIX

Table of panel replacement costs:

Building	Panel	Price	Notes
134	134-DP-AC	23,183	
134	134-DP-P1	25,126	
153	153-PNL-L2	8,615	
153	153-PNL-P2	8,977	
400	400-PP-OA	12,118	
459	459-DP-001	18,878	
459	459-DP-002	28,181	
459	459-DP-004	17,616	
459	459-LP-009	10,557	
459	459-LP-010	9,703	
459	459-PP-002	24,957	
459	459-UPSP-002	-	Unlocated
464	464-PP-1	15,211	Potentially not overduty
480	480W-PNL-Z	19,442	
488	488-LP-1A	12,219	
488	488-PNL-PPL	11,180	
490	490-DP-HV-E-2	-	Can’t access (in a substation) and not in inventory
490	490-PP-HV-1	16,620	
490	490-PP-HV-3	16,532	
490	490-PP-HV-5	20,366	
490	490-PP-HV-8	30,612	
490	490-PP-HV-E-1	21,054	
490	490-PP-HV-E-4	17,604	
493	493-PANEL-A2	24,434	
493	493-PNL-F	16,619	
510	510-DP-5	20,495	
510	510-DP-6	19,822	
510	510-DP-7	17,049	
510	510-DP-8	20,180	
510	510-LDP-E	33,108	Bad position
510	510-LDP-F	20,866	
510	510-LDP-G	22,254	
510	510-LDP-J	22,598	
510	510-PP-1	18,878	
510	510-PP2	19,869	
510	510-PP-3	24,512	
515	515-DP-C	20,602	Unlabeled breakers, in the basement
515	515-DP-C	-	Unlocated
515	515-HVAC-PNL-UPS-1	-	Unlocated
801	801-C-PNL-PP1	21,985	
801	801-H-PNL-PP	34,023	Could not see breakers; in radiological area

830	830-PP-2A	15,596	
860	RCRA-DP-A1	18,589	
860	RCRA-DP-A2	19,879	
902	902-RP-36	10,124	
924	924-PP-C10-3	22,103	
924	924-PP-C10-4	22,278	
933	933-PP-G	18,601	
817A	817-PP-A	13,220	
817A	817-PP-B	13,041	
901A	PANEL N8	22,344	
-	**Total price:**	**901,820**	**Total number of panels: 47**

Foundation for the processes involved in conducting an energy audit of building 902

Keith Combs
Technologies, Three Rivers Community College, Norwich, CT 06360
John Guido
Facility Operations Management, Brookhaven National Laboratory, Upton, NY 11973

Abstract

An energy audit is used to determine the cost effectiveness of optimizing current energy use in a building or upgrading it for more energy efficiency. The main objective was to find out as much information that could be collected by a summer intern to complete the energy audit. This in turn means that not all the data was collected but an idea of what needs to be completed exists. To conduct an energy audit for building 902 at Brookhaven National Laboratory I had to research what was involved in an audit. The main source of information to use for an energy audit came from the Energy & Utilities Division at Brookhaven National Laboratory. They showed me all the information and structure needed to conduct an energy audit through explanation along with a few books. The first step was to figure out the largest energy consuming systems which usually are the lighting and the air circulation. In order to crunch the numbers the total energy use of the building along with the energy data of the equipment had to be collected. Knowing the energy data allows for a cost analysis to estimate the current cost for energy in the building. With knowing the energy cost looking into options to save energy can be looked at next. The options to save energy from research and examination can be as complicated as reworking the structure and layout of the building or as simple as just turning lights off and optimizing equipment operation. The option to be chosen will be based on how economical it is to invest the money with a reasonable time frame of return. Since not all the data was collected an action plan was created to collect the rest of the data to achieve the goal of saving energy in the future.

I. Introduction

The major push for an energy audit was born after the seventies oil crisis. During this period with rising energy costs many companies along with the government had to look for ways to curb costs. This is when an actual organized effort to lower energy costs showed itself as being important but faded shortly after only to come back in the nineties. With the current financial environment any efficient way to save money will be looked at which has increased the prevalence of energy audits.

The purpose to have an energy audit is simple which is to spend money efficiently to save money in the future. In a way it is an investment that when done correctly will have larger payoffs in the future. In order to start this process rolling out an action plan tailored for the current building needs to be created along with what major types of data that would need to be collected. As a summer intern not all the data is easily available to be collected meaning the action plan of what to do for the future for the next person is very important. The progress for this project was not getting goals completed very quickly but more slowly gathering information and consolidating it.

II. Progress

The main approach at first was to collect the needed information. With not knowing what and energy audit is I did research into finding out. An energy audit as it turns out is a series of three main phases. The first phase is a walkthrough of sorts. This requires an inspection of the building or facility to see if any of the systems are working as designed. In a way this is checking the current health of the building and making sure it is working as intended. The second phase gets started if the first phase shows that more can be accomplished to save energy. For this phase collection of energy usage data is quantified to help with the economics of any changes. In order to make economic changes you take specification data of the equipment in existing systems and cross reverencing them with specifications of more energy efficient options. By doing this you get a ball park of what energy saving options are feasible to pursue. The third phase is more long term data collection and analysis. In order to attempt to accurately guess the energy use of a building past just what the equipment and systems operate at, many variables have to be considered. This requires measuring the energy use daily over a year or more to account for variable like the climate, operators, and the physics of the system. For example the energy use of a window air conditioner goes up if the temperature difference between outside and inside air is larger. What makes all this data more easily processed is being able to plug it into simulation software of some kind that can manage it in an understandable manner. This method of data analysis using models are time consuming but accurate by showing energy usage trends which can help make predictions of future energy use. That was one of the categories I had to research but I also had to do research data collection.

What I mean by research data collection is going out and seeing where I can collect the data that I can. I was pointed to the Energy & Utilities Division and the Modernization Project Office. Both of these groups work on making Brookhaven Lab more energy efficient. What data I collected from the Energy & Utilities Division was the total energy use of the building along with books of information on what was involved in an energy audit. They also helped me on figuring out what type of information I should be looking for.

Information I was advised to get was the power consumption of the lights and their associated ballasts along with the energy used to heat and cool the building. The main reaso behind this direct approach is because lighting and environment systems use the most energy. Power for electricity is measure in watts and the ballasts are an associated component that allows the lights to turn on properly. In order to gather power data on the light bulbs in the ceiling I would need to find out what model light bulb they are and that would be how I would find the power draw. Note that all the light bulbs in the ceiling are not the same model and not every fixture has the same amount of bulbs. In addition to power draw

bulbs put out there energy in light which is measured in lumens. You want to get the most lumens for the least amount of watts to have an efficient system. But some areas do not need that much light so by lowering the intensity of light you are lowering the power draw. I was able to closely estimate where and how many bulbs and fixtures are in the ceilings of the building on the other hand the ballasts I was not able to gather their power data along with the lights. I did not gather enough information to fully understand how to measure the air systems however I can make an educated guess. What I guessed is that there is a relation between watts, British thermal units, and cubic feet per minute. A cubic feet per minute measures one cubic foot of air per minute through any form of duct or air flowing system at a given point. One British thermal unit is the amount of energy to heat or cool one pound of water one degree Fahrenheit. The watt is the measurement of electrical power which is voltage multiplied by current. How I guess these measurements tie together in the efficiency of an air system in a building is the amount of electric power is needed to move a certain amount of cubic feet of air per minute along with how much energy is used to cool or heat this air as it is moving through the system to heat or cool the desired space. The data for the air systems I was unable to collect but I did collect a guess value for the area of the space. I collected the raw data of the square footage of rooms and hallways of building 902 using the key plan in Auto CAD software. As long as the key plan is correct the square footage of the building can be estimates fairly accurately along with finding the area of specific locations. This type of raw data is more malleable then having the total because you can include or exclude data as you need it. Just the lighting system in the ceiling and the air flow system have large amounts of data. All this information and then some must be gathered to allow for a decision in the future of how to save energy.

III. Future Work

Future work for this project includes collecting the needed data along with saving energy.

In order to save energy something about the current system needs to be made more energy efficient but that change most likely will cost money. The economics of that change will be decided in the future but options that are available now before the data crunching vary. For instance the lighting during the day can be replaced with ceiling windows that have light collectors on the roof to carry down daylight into the desired space. Besides cloudy days this system would have a high instillation cost and moderate maintenance cost but no operating cost. Another example of an option that has no operating cost but high instillation cost would be building a wind catcher. A wind catcher as in building a tower to be able to collect the wind a draw cool air down into the building along with sucking the hot air out. A drawback is what happens when it's not windy and how does the air move when it is really humid. Those were two structural options but sometimes all that is needed is an operational change. For example letting a building get a little hotter before turning on the air conditioning or turning the air conditioning off at night and turn it on a couple hours before the work day states. There are many more options available in order to make what at first appears to be a simple decision which is save energy really is a complicated decision based on the economics.

IV. Conclusion

In order to make a well-educated decision on what is worth spending money on requires collecting all the data and variables. This concept is to spend x now to save x over y years so that after the y years are over you will have been saving money to spend on other investments that are important. With the ability to have a reasonable return on investment getting the most money back in the shortest amount of time takes a bit of planning along with knowing your data. This projects goal was to gather as much data but more importantly make a plan of action so the project can be completed in the future. The main accomplishment would be so a person in the future looking back and understand what was gathered, how it was gathered, and knowing what needs to be gathered with a general idea of where/how to get it. The major impact from this project is that it will save the lab money to spend in other areas which need money to further research.

V. References

Book in Brookhaven laboratory site library database 119730994835 is the book ID number

Energy-Efficient Operation of Commercial Buildings Redefining the energy Manager's Job

Author-Peter Herzog

Copyright ©1997 by The McGraw-Hill Companies, Inc. From Mark Toscano of the Energy & Utilities Division

Book in Brookhaven laboratory site library database Book id number – 119730722251

Title – Handbook of Energy Audits 3rd edition

Author - Albert Thumann, P.E., C.E.M. Published by The Fairmont Press, Inc. 700 Indian Trail

Lilburn, GA 30247

From Mark Toscano of the Energy & Utilities Division

VI. Acknowledgments

This project was supported in part by the U.S. Department of Energy, Office of Science, Office of Workforce Development for Teachers and Scientists (WDTS) under the Community College Internships Program (CCI)."

VII. Appendix

A. Participants

Name	Institution	Role
Brigitte, Kimble	Modernization Project Office	Gave me information and help in what is in an energy audit.
Mark, Toscano	Energy & Utilities Division	Helped with giving information of what is an energy audit and pointers of what to do for an audit
Ivan, Rodriquez	Facility Operations Office	Help gather a little equipment data
Michael, Paquette	Facility Operations Office	Help point out current building information source material

Developing a watchdog program to oversee environmental sensors at the Northeast Solar Energy Research Center

Lee R. Combs
Electrical Engineering Technology, Three Rivers Community College, Norwich, Connecticut 06360
John Heiser
Department of Environmental Science, Brookhaven National Laboratory, Upton, New York 11973

Abstract

The Northeast Solar Energy Research Center (NSERC) facility built at Brookhaven National Laboratory (BNL), serves as a solar research platform where researchers can study and/or modify components of the array. The facility also helps BNL meet its renewable energy requirements by supplying power to the laboratory. To support the research agenda, a network of meteorological sensors monitor environmental conditions throughout the facility. This network requires a watchdog program to monitor the health of the sensors and send a status report of the sensor array when there is a break or malfunction with a sensor(s). The network includes: pyranometers, which measure global irradiance both in-plane to the solar panels and horizontal to the earth's surface, shaded air-temperature and panel temperature. Currently, there are three sets of such sensors in the NSERC with two more locations planned as the facility expands. Data from the sensor locations is collected and stored in a historian database and is available in real-time. Data from the historian server is ingested into a Microsoft Office Excel (Excel) workbook. The watchdog program, written in Visual Basic Application (VBA) programming language, analyzes the data for missing or not a number (NAN) data and then performs an intercomparison of the sensor values. Under normal conditions, like sensors within the facility should have similar readings (within the sensor error). The program will help mitigate data loss from long periods of unaware malfunctioning or broken sensors. The reduced data loss time will insure a more complete yearly data record for researchers using the facility. Using Excel to collect data from a historian database is a new skill I have learned. I have gained experience in working with VBA programming language in Excel and calibrating sensors which are overseen by the watchdog program.

I. Introduction

The Northeast Solar Energy Research Center (NSERC) facility, built at Brookhaven National Laboratory (BNL), serves as a solar research platform where researchers can study the behavior of the array (e.g., effects of weather and aging, power transmission, etc.) and/or modify componetns of the array (e.g., thin film panels, micro-inverters, etc.). The facility also helps BNL meet its renewable energy requirements by supplying power to the laboratory. To support the research agenda, a network of meteorological sensors monitor environmental conditions throughout the facility. The sensors are monitored by a data logger which collects, transforms and stores the sensor output and also sends a copy of the data to a historian database. The database is then accessible to NSERC researchers. The data loggers are collecting data twenty four hours a day seven days a week, year round. There are times when data is not being recorded correctly which may be due to hardware failure or malfunctions, power outages, historian database problems, etc. The watchdog program is designed to reduce the periods of no data or incorrect data by quickly alerting facility managers of a problem, so repairs/corrections can be made in a timely fashion. The sensors in NSERC that will be monitored are; the pyranometers, which measure global irradiance with one positioned in-plane to the solar panels and another horizontal to the earth's surface, shaded air-temperature and panel temperature. Currently, there are three sets of such sensors in the NSERC with two more locations planned as the facility expands.

Shown in figure 1 is a thermistor temperature sensor stuck to the backside of a solar panel with the adhesive which came with the sensor and electrical tape for added support. Shown in figure 2 is a Platinum Resistance Temperature Probe zip tied to a steel pipe under the shaded area of the array. The sensing part of the probe is at the lower top. Shown in figure 3 are both pyanometers mounted to an aluminum plate that is mounted on top a steel pole position them at the same height as the top of the solar panels.

II. Methods

The NSERC meteorology sensor watchdog program was written in the Visual Basic Application (VBA) language in Microsoft Excel (Excel). Excel has a macro development tab build in so no additional software add-ons are required. Inside the development tab the program code was written using VBA. The code first creates a network connection to the historian database were

Figure 1 (below): Solar Panel Thermistor Sensor.
Figure 2 (right): Air Temperature Probe

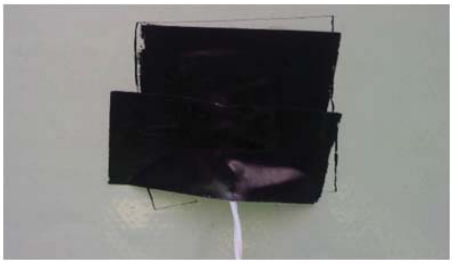

all the meteorology sensor data is stored from the data loggers at the NSERC in real time. When the workbook is first opened the code executes and all requested data for every sensor is collected from the historian database. Every sensor which has data collected is given its own worksheet within the workbook and named according to location and function. The average data for like sensor are compared to one another over a given time interval. The time interval used to determine the average is dependent on the sensor type and is set such that momentary (1 second value) difference are ameliorated. Unique data collection timers are initiated for each sensor type. At the end of each interval the average is recalculated and a new comparison performed. For the air and panel temperature probes a 5 minute timer is set.

The pyranometer sensors are on a 24 hour data collection timer instead of 5 minutes due to how they operate compared to the temperature probes. Air temperature changes slowly, down or up in value, due to things such as weather fronts, passing clouds or sunrise/sunset. Panel temperature changes faster than air temperature when light condition vary as they are a function of air temperature and power production of the panel. Still this change is slower and more dampened than the output from the pyranometers. The pyranometers operate using the sun rays (sun light) to generate power and react quickly to changing light conditions. Power fluctuations on the order of seconds are readily seen and can be hundreds of W/m^2 out of 1200 or less W/m^2. A small cloud could pass over one and not the like sensors, which would result in large differences in the reading between sensors. The watchdog may misread this as a bad sensor and/or operate erratically. For the fast changes over short time spans that are characteristic of pyranomters measuring natural sunlight, a much larger time interval is needed to bring the average of similar sensors into agreement. This is particularly true for cloud filled days. Over the course of one day the average the values of the pyranometers should be closely similar to each other, hopefully within one or two standard deviations in the sensor accuracy. The timers make data analysis more manageable.

When the data import is complete the excel workbook calculates the average value for every sensor separately. The pyranometers have a modified average value, instead of averaging every data point within the 24 hour interval, only data points that fall within the zenith angle to the sun of 70 degrees are utilized. Data outside this range can have artificial variability not attributed to the sensor operations (e.g., zero or slight negative values at night, shading at low sun angles). The Zenith angle has a 0 degree reference when the sun is straight up over your location on the earth's surface. For temperature sensors, all data point values for the time interval are averaged. At the NSERC there are three locations having set of sensors and no reference sensor to compare a given sensor to. To get around having no reference, the sensors are referenced to each other with logic routines. The logic routine is very similar to "AND OR" logic in digital integrated circuits in electronics. The logic begins with each sensor type compared to other like types. If the difference in values exceed a user set threshold the program will notify the user. The threshold is generally set at twice the standard deviation for the sensor. However, due to site specific difference, thresholds alone cannot be used to determine a poor functioning sensor. There may be naturally occurring differences at differing sensor locations. For instance temperature differences due to surface type, nearby equipment, etc. may add an offset and that offset may not be the same for a given time of day or time of year. To account for offsets, the watchdog program calculates the 1 hour average of each sensor which is then subtracted from the other sensors averages to get the offset value. The offset value is added to the threshold value to acquire an accurate representation of the sensor operations. This offset collection happens every hour until the good status changes. At this point it stores the previous offset until and it waits for an hour of good status (sensor is repaired, system is working again, power restored, etc.) to replace the stored offset with a new offset. When a sensor is out of the threshold range on the logic path a domino effect is triggered. Out of threshold conditions elicit an email report to the user detailing current abnormal or out of spec conditions.

In the workbook, two work sheets are used in the threshold comparisons. One sheet is used for all the computations, results, and the analysis while a separate sheet is used to store all the changeable user variables in the VBA code. This is to make it more user friendly for those not familiar with the VBA language and its layout in Excel.

On Sheet1 a table keeps track of all the reports from the sensors with number of counts per status. The statuses are associated to the following colors.

- GREEN indicates the sensor is healthy and no malfunctions.
- RED indicates that the data collected is not a number (NAN) or there was no data collected from a particular sensor.
- YELLOW indicates that the given sensor value is out of

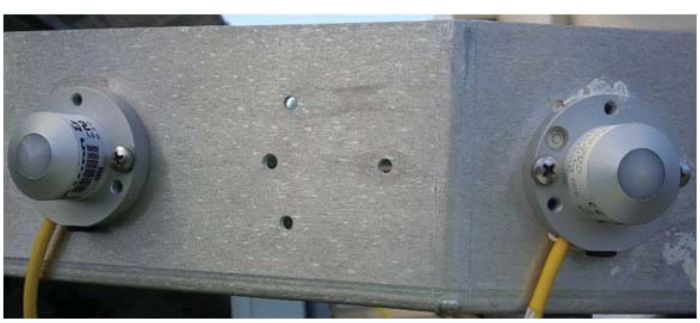

Figure 3: Both Horizontal (Right) and Plane to Array (Left) Pyranometers

	A	B	C	D	E
1	DateTime	TagName	Value		
2	2015-07-21 14:19:52.	NSERC_S1A_ATEMP	30.86		
3	2015-07-21 14:19:53.	NSERC_S1A_ATEMP	30.85		
4	2015-07-21 14:19:54.	NSERC_S1A_ATEMP	30.85		
5	2015-07-21 14:19:55.	NSERC_S1A_ATEMP	30.85		
6	2015-07-21 14:19:57.	NSERC_S1A_ATEMP	30.85		
7	2015-07-21 14:19:58.	NSERC_S1A_ATEMP	30.84		
8	2015-07-21 14:19:59.	NSERC_S1A_ATEMP	30.84		
9	2015-07-21 14:20:00.	NSERC_S1A_ATEMP	30.84		
10	2015-07-21 14:20:01.	NSERC_S1A_ATEMP	30.83		
11	2015-07-21 14:20:02.	NSERC_S1A_ATEMP	30.83		
12	2015-07-21 14:20:03.	NSERC_S1A_ATEMP	30.83		

Figure 4: Data collection to Excel Sheet

range from the others compared to the upper and lower thresholds manually set by the user. Temperature sensor thresholds are degrees Celsius while the pyranometers are in percent.

- BLUE is used for the pyranometers to indicate their soft threshold. The pyranomters have two threshold limits, a soft one to indicate a small change that might indicate calibration is needed or repair may be warranted and a priority threshold when they are deemed in need of immediate change out. The priority threshold uses the color RED.

Every color is given a timer to send a report. If either red, yellow, or blue is counted continuously for one hour a report is sent as an email detailing which sensor and a full copy of the status table of every sensor. After the initial report, a reminder email is sent after 24 hours if the watchdog determines the problem still exists. If the condition of any sensor status is changed to GREEN for 1 hour a good status report is sent. When a good report is sent the timers for each bad status report is reset. The sending report email routines are independent to each individual sensor in the array. If another sensor is indicated as bad in the time it takes to replace the other bad sensor a notification of the newest bad sensor is sent. If the watchdog program does not encounter problems with any of the sensors a timer is tripped every 7 days to send a report detailing all status for each sensor.

The sheet with all changeable variables is named VBA_Variables. The changeable variables include, but not limited to the following: the timing of reporting events, such as 7 day status report; the message contains in individual reports; the time interval for both the 5 minute and 24 hour timer; the solar zenith angle; the send and receive email addresses. The email service required to send emails is Microsoft Office Outlook. The query or data request to the historian for each individual sensor can be modified in accordance to changes in the analysis range. The program structure also allows for easy addition of variables if future expansion is required.

III. Data and Results

All data and results are in the form of an Excel workbook. Figure 4 shows how the data is stored and the excel worksheet from the historian database. The data is collected and stored in numerical order by data with a title of DateTime. The next column is TagName, which is the name given to the particular sensor by the historian database. The last column shown in Value is the sensor value at the given time.

Figure 5 shows the changeable variables in the watchdog program in a user friendly table. The tables are color coded to make it easier to follow. The three sections on top from left to right are the following. The time interval is the clock for the whole workbook with a separate time for the pyranomters and a timer to send weekly reports. The email addresses that the watchdog uses to send and receive reports can be changed. There is a solar calculator intergraded into this workbook from the National Oceanic & Atmospheric Administration (NOAA), this is used in the pyranometers analysis to limit data analysis to a specific zenith angle region. The suns position in the sky changed throughout the year and hence the solar day changed. The calculator determines at what time of day the sun is at the set zenith angles.

The three bigger tables on the lower half of the sheet are the collection of user changeable variables for individual sensors. The table shows the location in NSERC and the sensors at those locations. Also shows what type of error report can be generated for the sensor with a settable timer and message for the email. The query that is sent to the historian database to request data is also in the table and can be changed.

Figure 6 shows how the results are displayed for the end user to analyze. This includes the final results of the data collected from the historian database and the final verdict of whether the

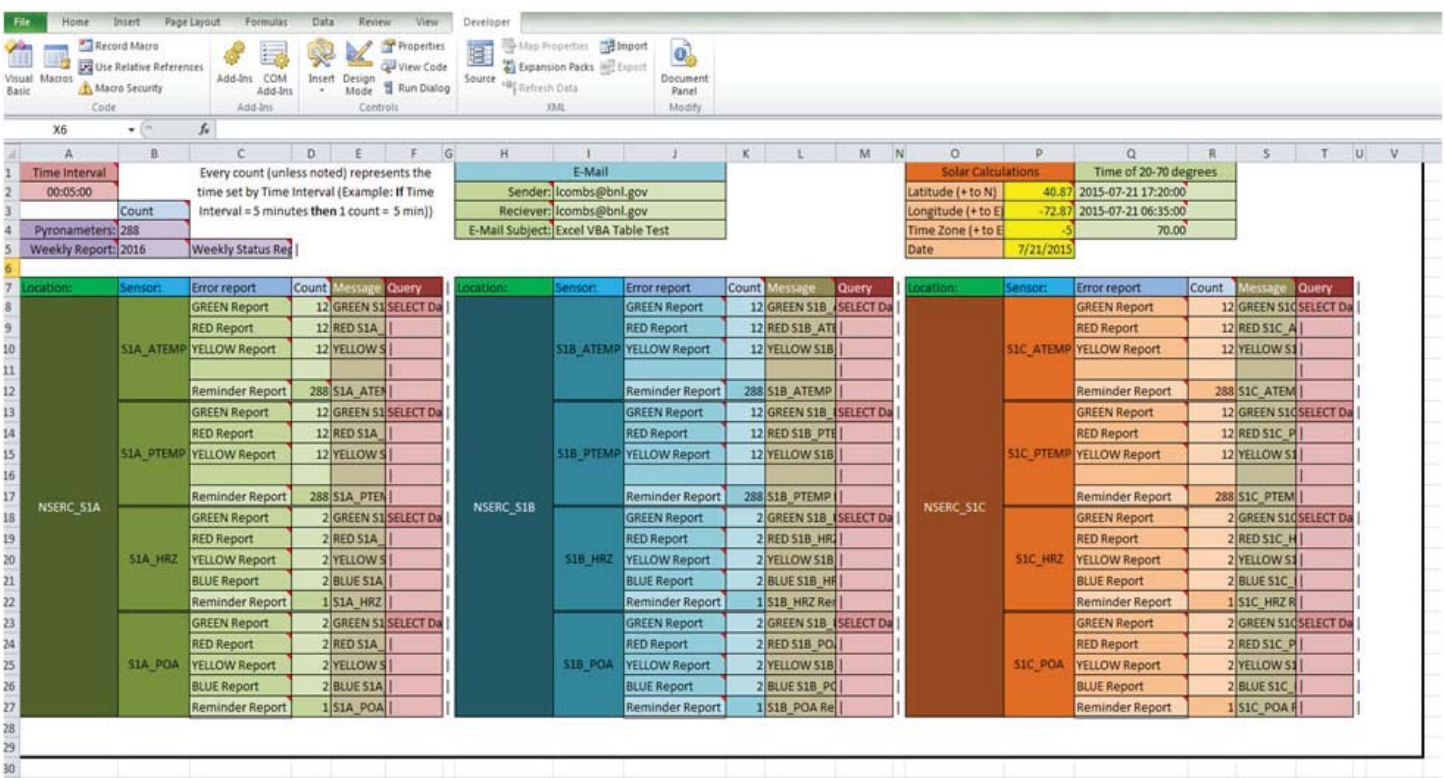

Figure 5: Changeable variables

sensors are good, need to be replaced, or are out of tolerance. In the upper left corner the current date and time is shown with the name of the site being monitored. The time only changes when the workbook completes a cycle of collecting data. This is handy to know when the last or next query will be sent. The three tables in the right upper corner calculate the average value with some conditions in place. The temperature will take an average unless there is data missing, the report contains not a number (NAN), or the value is higher than 100 degrees Celsius or below -50 degrees Celsius. The pyranometer have similar conditions, but instead of a temperature threshold there is a percent difference threshold. The Data is only collected between two specified times of the day determined in the Variables sheet in solar calculations based on the user defined zenith angle. The table in the bottom right corner is a concentrated table containing all the averages from the three tables above, but the table also contains all the user changeable thresholds and calculated offset values for the temperature and pyranometer sensors.

The last two tables at the bottom left contain the results that will be contained in any report sent out from the email protocol. The left table contains every sensor with its status of GREEN, RED, YELLOW, or BLUE. There is also the average reading for each sensor. The right table stores the counts for each status reached by each sensor with a total number of counts on the right. The counts represent how many times the sensors have been at each status. While the total counts represent the number of cycles or the duration the program has been running. The last message box on the most bottom left is reserved for the sensor status message contained in the report email on which sensor has a problem.

IV. Future Work

The watchdog program in the future can be adapted to encompass more sensor arrays and could be adapted for use at the Long Island Solar Farm (LISF) where there are 25 power blocks in 6 areas. Each power block has a single air temperature probe and panel temperature probe. Ten of the power blocks also have relative humidity sensors. Some of the power blocks also have a set of two pyranometers one horizontal and the other plane to array. The watchdog program can be structured to monitor all the sensors at the LISF. This watchdog program can also be structured to monitor other sensors not limited to a solar farm if an array of sensors have a historian database where there data is being stored this program can tap into those data tables and monitor those sensors as well.

V. Conclusion and Recommendations

The NSERC meteorology sensor watchdog program was successfully developed and reduces the workload on the facility operators in monitoring the environmental senor network. This will facilitate a more complete yearly data set. The program can be used in any Excel workbook with no add-ons required for operations. For future improvement the error analysis and VBA code can be optimized to insure increased performance and reliability with more refined routines.

VI. References

[1]Microsoft Office Dev Center. "Getting Started with VBA in Excel 2010." December 2009.

[2]National Oceanic & Atmospheric Administration. "NOAA Solar Calculations.xls" June 2005.

VII. Acknowledgements

This project was supported in part by the U.S. Department of Energy, Office of Science, and Office of Workforce Development for Teachers and Scientists (WDTS) under the Community College Internships Program (CCI). I would like to thank the following people for valuable guidance and assistance: John Heiser (Brookhaven National Laboratory) and Andrew McMahon (Brookhaven National Laboratory)

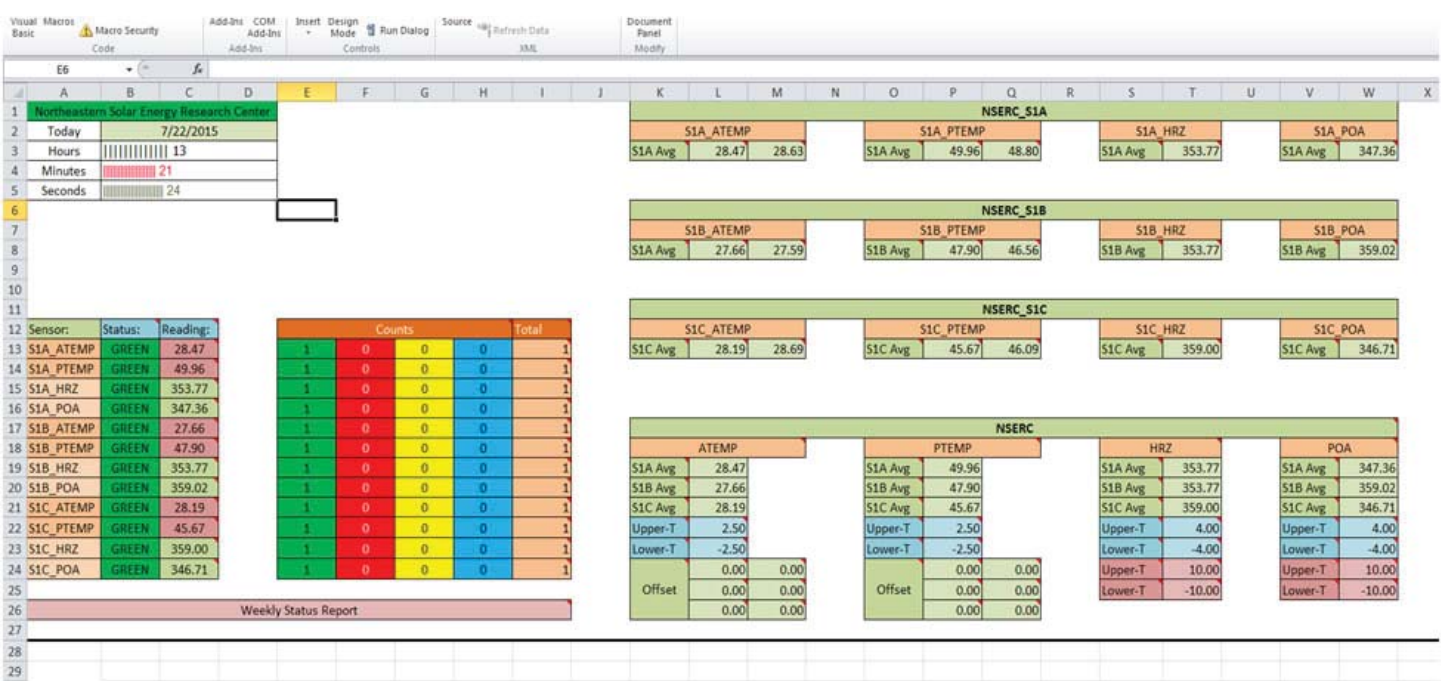

Figure 6: Readable results and analysis

VIII. Appendix

A. Participants:

Names	Institution	Role
Lee Combs	Three Rivers Community College	Intern
John Heiser	Brookhaven National Laboratory	Mentor

B. Notable Outcomes:

Microsoft Excel Visual Basic Application Watchdog Program: (Snippet of Program below)

```
Sub Send_Email() ‘Used to send e-mails from the excel workbook
 Dim Email_Subject, Email_Send_From, Email_Send_To, _
 Email_Cc, Email_Bcc, Email_Body As String
 Dim Mail_Object, Mail_Single As Variant
 Dim Rng As Range

 Email_Subject = Worksheets(“VBA_Variables”).cells(4, 9) ‘Subject Block
 Email_Send_From = Worksheets(“VBA_Variables”).cells(2, 9) ‘Sender E-Mail
 Email_Send_To = Worksheets(“VBA_Variables”).cells(3, 9) ‘Reciever E-Mail
 Email_Cc = “”
 Email_Bcc = “”
 ‘Email_Body = “Testing Testing 1, 2, 3”

 On Error GoTo debugs

 Set Mail_Object = CreateObject(“Outlook.Application”)
 Set Mail_Single = Mail_Object.CreateItem(0)
 Set Rng = Nothing
 Set Rng = Sheets(“Sheet1”).Range(“A12:I26”).SpecialCells(xlCellTypeVisible)
 With Mail_Single
  .Subject = Email_Subject
  .To = Email_Send_To
  .cc = Email_Cc
  .BCC = Email_Bcc
  ‘.Body = Email_Body
  .HTMLBody = RangetoHTML(Rng)
  ‘.Attachments.Add ActiveWorkbook.FullName ‘Attach the full document to the E-Mail
  .Send
 End With
 On Error GoTo 0
 Set OutMail = Nothing

debugs:
 If Err.Description <> “” Then MsgBox Err.Description
End Sub

Function RangetoHTML(Rng As Range) ‘Used by the Send_Email subroutine to create a HTML
 Dim fso As Object    ‘body from a range of table in the excel workbook
 Dim ts As Object
 Dim TempFile As String
 Dim TempWB As Workbook

 TempFile = Environ$(“temp”) & “\” & Format(Now, “dd-mm-yy h-mm-ss”) & “.htm”

 ‘Copy the range and create a new workbook to past the data in
 Rng.Copy
 Set TempWB = Workbooks.Add(1)
 With TempWB.Sheets(1)
 .cells(1).PasteSpecial Paste:=8
 .cells(1).PasteSpecial xlPasteValues, , False, False
 .cells(1).PasteSpecial xlPasteFormats, , False, False
```

```
 .cells(1).Select
 Application.CutCopyMode = False
 On Error Resume Next
 .DrawingObjects.Visible = True
 .DrawingObjects.Delete
 On Error GoTo 0
 End With

 ‘Publish the sheet to a htm file
 With TempWB.PublishObjects.Add( _
  SourceType:=xlSourceRange, _
  Filename:=TempFile, _
  Sheet:=TempWB.Sheets(1).Name, _
  Source:=TempWB.Sheets(1).UsedRange.Address, _
  HtmlType:=xlHtmlStatic)
 .Publish (True)
 End With

 ‘Read all data from the htm file into RangetoHTML
 Set fso = CreateObject(“Scripting.FileSystemObject”)
 Set ts = fso.GetFile(TempFile).OpenAsTextStream(1, -2)
 RangetoHTML = ts.readall
 ts.Close
 RangetoHTML = Replace(RangetoHTML, “align=center x:publishsource=”, _
    “align=left x:publishsource=”)
 ‘Close TempWB
 TempWB.Close savechanges:=False

 ‘Delete the htm file we used in this function
 Kill TempFile

 Set ts = Nothing
 Set fso = Nothing
 Set TempWB = Nothing
End Function
```

Maintaining micro climates during nano-liter chemical dispensations using custom designed source plate lids

Ashley M. Drozd[1,4] ‡, Bryan J. Foley[1,3]‡, Mary T. Bollard[1,5], Nikita Podobedov[1,6], Nicholas Zeniou[1,7], Rick Jackimowicz[2], Robert M. Sweet[2,8], Sean McSweeney[2,8], Alexei S. Soares[2]†
† Correspondence: soares@bnl.gov
‡ The two co-first authors contributed equally to this work
[1]Office of Educational Programs, Brookhaven National Laboratory, Upton, NY, 11973-5000
[2]Photon Sciences Directorate, Brookhaven National Laboratory, Upton, NY, 11973-5000
[3]Fairmont State University, Fairmont, WV 26554
[4]Long Island University, Biology, Brooklyn, NY 11201
[5]York College of Pennsylvania, Biology, York, PA 17403
[6]Ward Melville High School, Setauket- East Setauket, NY 11733
[7]St. Anthony's High School, Huntington Station, NY 11746
[8]Biosciences Department, Brookhaven National Laboratory, Upton, NY, 11973-5000

Abstract

A method is described for using custom snap-on lids to protect chemicals in micro-titer plates from evaporation and contamination. The lids contain apertures (diameter 1.5 mm, 1.0 mm, or 0.5 mm) through which the chemical building blocks can be transferred. The lid with 0.5 mm apertures was tested using a non-contact acoustic liquid handler, the 1.0 mm and 1.5 mm lids were tested using two tip-based liquid handlers. All of the lids reduced the rate at which solvents evaporated to room air, and greatly reduced the rate of contamination by water and oxygen from room air. In steady state measurements the lids reduced the rate of evaporation of methanol, 1-hexene, and water by 33% to 248%. In cycled experiments, the contamination of aqueous solvent with oxygen was reduced below detectability and the rate at which DMSO engorged atmospheric water was reduced by 82%. Our results demonstrate that the lids preserve the integrity of air-sensitive reagents during the time needed for different types of liquid handlers to perform dispensations. Controlling degradation and evaporation of chemical building blocks exposed to the atmosphere is increasingly useful as the reagent volume is reduced by advances in liquid handling technology, such as acoustic droplet ejection.

I. Introduction

Improvements in liquid handling technology (Marx 2014) underlie transformative new capabilities for applications such as bio-assays (Jambunathan et al., 2011) and chemical syntheses (Service 2015). In many cases, the frontier for the miniaturization of fluid phase assemblies has been pushed to volume regimes of just a few nano-liters (Hardy et al, 2012). One challenge is that miniaturization increases the surface area to volume ratio and accelerates both the evaporation of nano-scale solvents into room air as well as their contamination by chemicals in the atmosphere such as water vapor, oxygen, nitrogen containing compounds, and carbon dioxide. Techniques for managing air sensitive and moisture sensitive chemicals on a laboratory scale were established long ago (Stone 1948) and recent reviews of this topic are often somewhat informal (Miller 2013). However, few specialized techniques exist for managing chemicals whose air or moisture sensitivity only becomes problematic at a nanoliter scale (Ellson, R. N. 2009). Recent advances in chemistry and biology continue to uncover useful chemicals that fall into this moderate sensitivity gap (Dinger et al., 2003), though some chemicals are so sensitive that miniaturization plays little role (Fastrup et al., 1992). Quality control is a crucial duty of library curation both because the chemicals are often expensive if not irreplaceable (Yan et al., 2003; Matson et al., 2009) and because their degradation can lead to colossally costly cases of molecular mistaken identities (Screening, 2009). Our group developed miniaturization strategies using acoustic droplet ejection to reduce consumption of fragment libraries (Yin et al, 2014) and heavy metal libraries (Cuttitta et al, 2015) only to discover that chemical integrity was compromised long before the parsimony became useful.

We previously described a simple technique to isolate specific types of experiments from room air (Zipper et al., 2014). Here, we describe a similar but more general approach for using snap-on climate control lids with small apertures to protect chemical building blocks that are located within source plates from the surrounding atmosphere during dispensation (the liquids are transferred through the small apertures in the lid). By greatly reducing both the evaporation and contamination of solvents, the useful life of valuable and fragile chemicals can be greatly extended. The lids are fastened under an inert atmosphere before liquid transfer begins. When all transfers are complete, the lids are replaced with adhesive plate sealant

II. Methods

Depicted in figure 1, an undergraduate engineering intern used the Autodesk Inventor software to design custom plate lids that snap onto two popular 96 and 384 well micro-titer source plates (Nunc™ 96-Well Polypropylene and Echo™ Qualified 384-Well Polypropylene). All of our plate lid designs had circular apertures for liquid transfer located above the center of each micro titer well, and the lids were designed to contact the source plate surface. For lids with 1.5 mm / 1.0 mm / and 0.5 mm apertures, an average of 92.3%/96.9%/99.0% of the total surface area was covered for 384 well micro titer source plates, and an average

of 98.1%/99.2%/99.8% was covered for the 96 well source plates (See table 1).

A. Measuring evaporation rates for methanol, 1-hexene, and water

We used the EchoSurvey software to deduce the volume in each of the 384 wells in a PolyPro source plate by projecting a sound pulse (or "ping") through the plastic bottom of the plate and measuring the time needed until the ping was reflected back from the fluid surface (Harris & Mutz 2006). Using this method, we periodically recorded the volume in each of the wells of PolyPro plates (with no lids) that were initially filled with 50 µL of three test solvents (methanol, 1-hexene, and water). Similar measurements were made for the same three test solvents in plates that were covered with climate control lids with aperture diameters of 1.5 mm, 1.0 mm, and 0.5 mm. We recorded the temperature and humidity in the laboratory during our measurements using a sling psychrometer (Sper Scientific, 20~120F). We noticed that evaporation from plates without lids was non-uniform (with significantly more evaporation occurring in wells near the edges of the plate compared to wells near the interior of the plate). To prevent transient features such as these "edge effects" from influencing our calculated evaporation rates, we took the slope of a linear best fit to the volume change data to be the best estimate of the evaporation rate for each solvent in each plate (Depicted below in figure 2.)

B. Measuring contamination of an aqueous system by oxygen

Although there are many techniques to accurately measure the concentration of oxygen in a test fluid, most of these cannot be used to track the oxygen infiltration into each of the 384 wells of a source plate in real time. We used the oxidation of a reduced form of methylene blue (immobilized by 2% agar) as an indicator of the distance that oxygen penetrated into each of the 384 wells of a source plate (Mills 2005).

We heated 100 mL of 2% w/v agarose to 100 °C in an Erlenmeyer flask for 5 minutes, and then cooled and maintained the solution at 60 °C. We then added 140 mM glucose, 80 mM sodium hydroxide, and 120 µL of 1% methylene blue. During the preparation, nitrogen gas was bubbled through the solution to remove oxygen. The resulting reduced "indicator gel" was colorless and translucent. We transferred 79±11 µL of indicator gel into all 386 source wells of two PolyPro source plates and then allowed the source plates to be fully cleansed of oxygen in an oxygen-free box (apparatus depicted below in figure 3) with a continuous flow

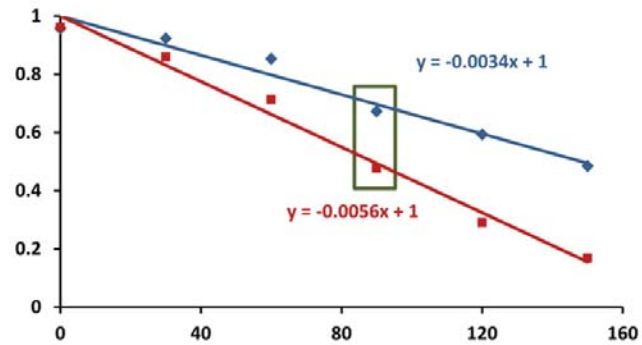

Figure 2.

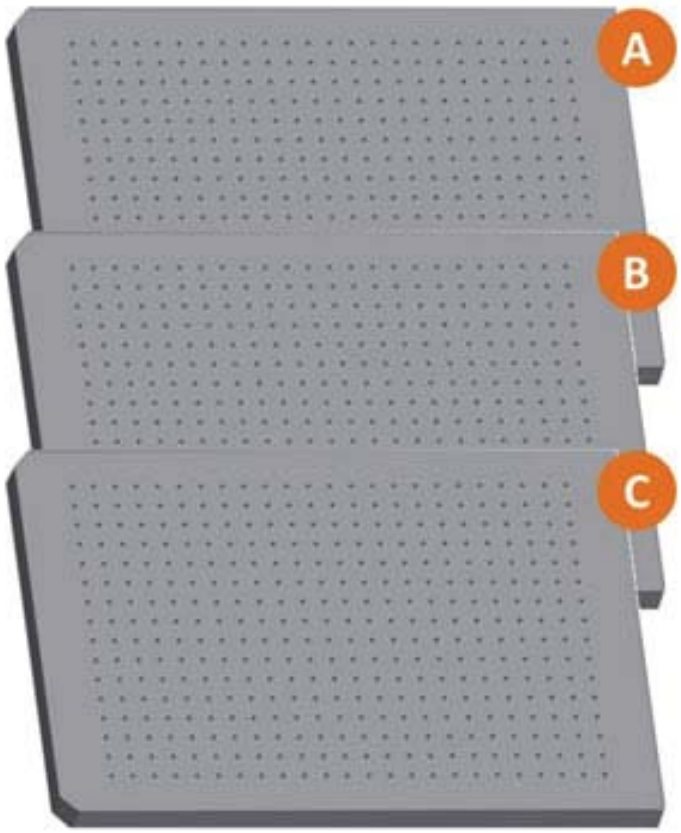

Figure 1.

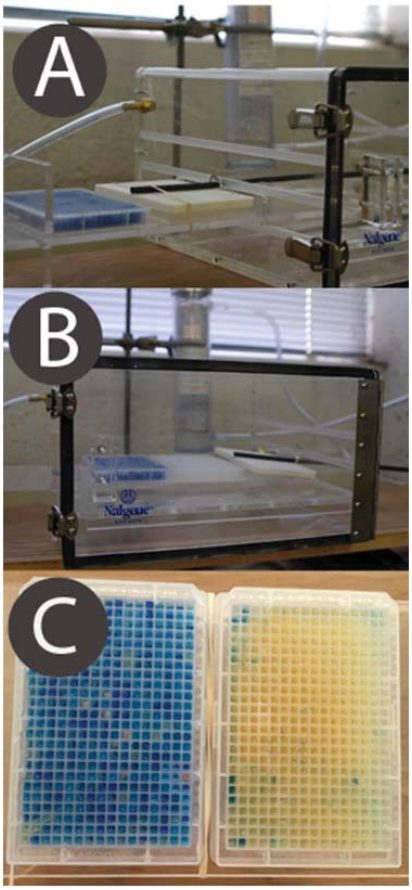

Figure 3.

of 10 L/minute of nitrogen. The oxygen-free acrylic box was part of the apparatus that allowed the plates to be cycled between room air and contaminant-free air.

Both tested plates (covered with a 0.5 mm diameter plate lid and an uncovered control) were cycled into the oxygen-free acrylic box for 0.5 minute and into room air for 5.0 minutes. The plate lid was removed from the covered plate while it was in the acrylic box, and replaced when it was moved to room air (to reproduce the experimental conditions that would be observed if a chemical containing plate were repeatedly used for liquid dispensation and then returned to storage). Every 4 hours during 20 hours of observation one cuboidal indicator gel from the gel containing wells in each of the source plates (control and covered) were individually transferred to water that had been deoxygenated using nitrogen bubbling (as described earlier) for visualization (Leica MZ16 F™).

C. Measuring contamination of DMSO by water

We used the EchoSurvey software to deduce the percentage of DMSO and the percentage of engorged water in each of the 384 wells in two PolyPro source plates (one with lid and one without) that were cycled between a dry nitrogen chamber (for 0.5 minute) and a 100% humidity chamber (for 5 minutes). We used the same apparatus described in section 2.2 with an additional humidity chamber, which surrounded both plates when they were removed from the dry nitrogen chamber. The EchoSurvey software deduces the amount of water that is engorged by DMSO by measuring the force needed to perturb the surface of the liquid (Ellson & Stearns, 2008). Using this method, we periodically recorded the percentage of water engorgement in each of the wells of a PolyPro plate (with no lid) that was initially filled with 60 µL of DMSO. Similar measurements were made for a plate that was covered with a climate control lid with 0.5 mm apertures

III. Data/Results

Our results demonstrate that climate control lids can be instrumental for preserving the integrity of air-sensitive reagents during the time needed for different types of liquid handlers to perform dispensations.

A. Climate control lids reduce evaporation rates for methanol, 1-hexene, and water

The graph depicted below (figure 4) shows that using source plate lids effectively reduced the rate of evaporation of methanol, 1-hexene, and water for all of the tested aperture sizes. The reduction in evaporation rate was well correlated with the volatility of the solvent. The ratio of the average rate of evaporation for methanol and 1-hexene was 1:1.46, which is in good agreement with relative volatilities of the two solvents (1:1.37) (the ratio for water is omitted because it is confounded by room humidity). Consequently, we conclude that the reduction in the evaporation rate of solvents by using climate control lids increases as a function of the volatility of the solvent.

In addition to reducing the average evaporation rate for all wells in a source plate, the climate control lids also improve the uniformity of performance across all wells in the plate.

B. Climate control lids reduce contamination of aqueous system by oxygen

Figure 5 shows that the climate control lid with 0.5 mm diameter apertures significantly reduced the penetration of oxygen into the indicator gel. After 20 hours of cycled exposure to room air, the entire colorless indicator gel was oxidized to a blue color in the control plate, compared to no observable discoloration in the plate that was protected by the climate control lid. Lids with larger aperture sizes slowed the rate of oxygen penetration somewhat, as evidenced by a reduced rate of oxidation of the indicator column (data not shown). However, only the 0.5 mm apertures allowed the indicator column to fully recover from each 5 minute oxygen exposure during the subsequent 0.5 minute in the nitrogen box, allowing the indicator column to remain clear indefinitely.

C. Climate control lids reduce contamination of DMSO by water

We used the EchoSurvey software to demonstrate that climate control lids reduce DMSO engorgement in source plates that were cycled between dry nitrogen and high humidity (the cycling reproduces the environmental changes experienced during repeated liquid dispensations followed by plate storage). We compared the rate of DMSO engorgement of water for source plates with and without lids. During non-rigorous testing we observed that water engorgement was reduced for plates protected by all of our designs, but the reduction was most significant using lids with 0.5 mm apertures (data not shown). The DMSO engorgement experiments were performed in plates covered by lids with 0.5 mm apertures that were cycled between dry nitrogen and high humidity. Overall, the climate control lids reduced the rate of water engorgement by DMSO by 82%. Linear best fits are shown below in figure 6 for both data sets. Only the first three data points were used to determine the best fit for the control plate composition, because of the measurement limits described above (some of the outer-edge wells had engorged 30% water by the fourth measurement). The slopes for the two best fit lines are 0.34% water en-

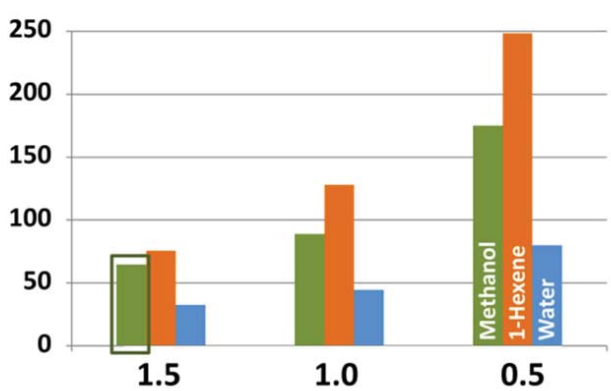

Figure 4.

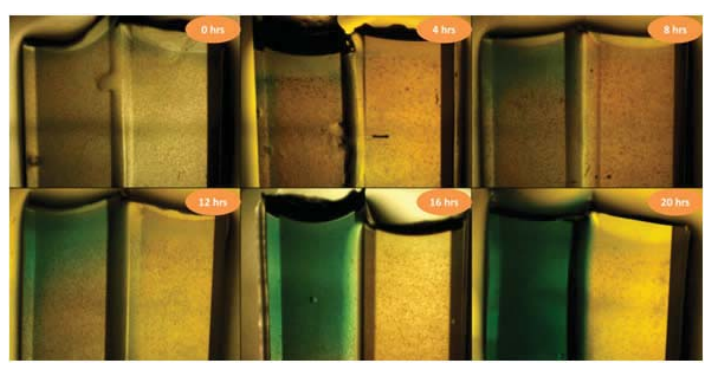

Figure 5.

gorgement per hour (for the plate covered with a ClimateLoc lid) and 1.66% water engorgement per hour (for the control plate).

IV. Conclusion

We have demonstrated that plate lids can greatly reduce the problems commonly encountered when miniaturizing liquid handling that has an air-liquid interface. Evaporation of the solvent is reduced in the steady state, and contamination of the chemicals is reduced when the plate is cycled between dispensation and storage. Rapid advances in advanced liquid handling robots partnered with simple techniques to protect the smaller (and consequently more vulnerable) chemical aliquots may be natural partners to allow the overall quality of assays to be governed by the improvements in liquid handling as opposed to plateauing because of environmental contamination issues (Ekins et al, 2013). These new technologies (in combination with rigorous testing of the performance of liquid handling robots; Taylor et al, 2002) will allow future biological and chemical innovations to probe smaller specimens and to exploit more challenging opportunities.

V. References

Marx, V. Pouring over liquid handling, Nature methods 11 2014 33-38.

Jambunathan, K, et al.: Contact Printing based assay miniaturization to characterize antibody recognition of peptide epitope probes. The FASEB Journal 25 2011 962-3.

Service, Robert F. The synthesis machine, Science 347 2015 1190-1193.

Hardy, N, et al.: New Enabling Technology. Management of Chemical and Biological Samples for Screening Applications. 2012.

Stone, H. W. Storage and Titration with Oxygen-Sensitive Solutions. Analytical Chemistry 20 1948 747-749.

Miller, Sarah. Tips and Tricks for the Lab: Air-Sensitive Techniques. ChemistryViews magazine, May 7 2013

Ellson, R. N. Closures which contain reservoirs and allow acoustic ejection. U.S. Patent Application 2009/0019956. Washington, DC: U.S. Patent and Trademark Office. 2009.

Dinger, M. B., & Mol, J. C. Degradation of the Second-Generation Grubbs Metathesis Catalyst with Primary Alcohols and Oxygen− Isomerization and Hydrogenation Activities of Monocarbonyl Complexes. Eur. J. of Inorganic Chem. 15 (2003) 2827-2833.

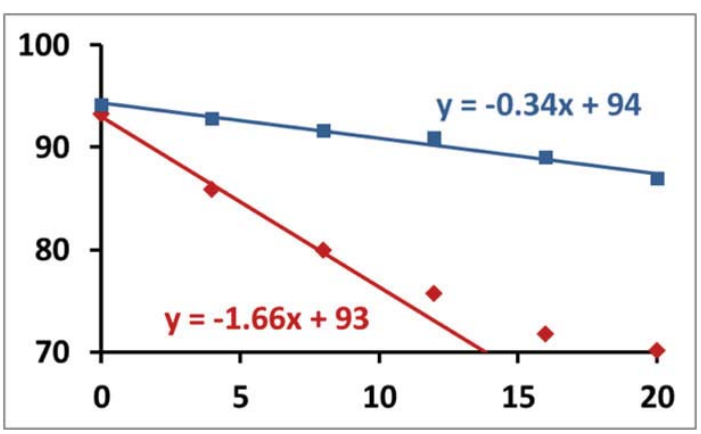

Figure 6.

Fastrup, B., & Nielsen, H. N. On the influence of oxygen on iron catalysts during ammonia synthesis and catalyst characterization. Catalysis letters 14 1992 233-239.

Yan, B, et al.: Quality control in combinatorial chemistry: determination of the quantity, purity, and quantitative purity of compounds in combinatorial libraries. Journal of combinatorial chemistry 5 2003 547-559.

"Screening we can believe in". Nature Chem. Biol. 5 2009 127.

Yin, X, et al.: Hitting the target: fragment screening with acoustic in situ co-crystallization of proteins plus fragment libraries on pin-mounted data-collection micromeshes. Acta Cryst. D70 2014 1177-1189.

Cuttitta, C. M., et al.: Acoustic transfer of protein crystals from agarose pedestals to micromeshes for high-throughput screening. Acta Cryst D71 2014 94-103.

Zipper, L. E, et al.: A simple technique to reduce evaporation of crystallization droplets by using plate lids with apertures for adding liquids. Acta Cryst. F70 2014 1707-1713.

Harris, D. L., & Mutz, M. Debunking the myth: validation of fluorescein for testing the precision of nanoliter dispensing. J. of the Ass. for Labo. Automation 11 2006 233-239.

Mills, A. Oxygen indicators and intelligent inks for packaging food. Chem. Soc. Reviews 34 2005 1003-1011.

Ekins, S., Olechno, J., & Williams, A. J. (2013). PloS one 8, e62325.

Taylor, P. B., Ashman, S., Baddeley, S. M., Bartram, S. L., Battle, C. D., Bond, B. C., ... & Macarron, R. (2002). A standard operating procedure for assessing liquid handler performance in high-throughput screening. J. biomol. screening 7, 554-569.

VI. Acknowledgments

This project was supported in part by the U.S. Department of Energy, Office of Science, Office of Workforce Development for Teachers and Scientists (WDTS) under the Science Undergraduate Laboratory Internships Program (SULI). I would like to give a huge thanks to Alexei Soares for his passion and commitment to this internship program as well as his care for all of his interns' professional growth and development. I would also like to thank Mel Morris, Noel Blackburn, and Ken White –without the help of all of these individuals this experience would not be possible.

Table 1. Characteristics of ClimateLoc source plate lids.

Lid for 384 well plates		
Design aperture (mm)	**Observed aperture (mm)**	**Surface area covered (percent)**
1.5 mm	1.41 ± 0.017	92.3
1.0 mm	0.89 ± 0.029	96.9
0.5 mm	0.50 ± 0.023	99.0
Lid for 96 well plates		
Design aperture (mm)	**Observed aperture (mm)**	**Surface area covered (percent)**
1.5 mm	1.41 ± 0.017	98.1
1.0 mm	0.89 ± 0.029	99.2
0.5 mm	0.50 ± 0.023	99.8

Solubility of perfluorocarbons under geothermal conditions

Yassien Fadul and Juan Sosa
Science, Arts, Physical Education, and Engineering Division,
Mountain View College Community College, Dallas, TX 75211
John Heiser
Environmental Sciences, Brookhaven National Laboratory, Upton, NY 11973

Abstract

Perfluorocarbons-colorless, odorless, dense, non-flammable gases at environmental temperatures-are chemically unreactive. Its chemical properties made it an ideal liquid to use as a tracer, in this case involving geothermal conditions, subterranean steam, and ground water. In our study, we analyzed tracing the movement of ground water and subterranean steam. To mimic geothermal conditions, we assembled a 500mL Autoclave Engineers pressure vessel operating under extreme pressures and temperatures. Moreover, perfluorocarbon tracers in a perfluorocarbon-water mixture inside the autoclave vessel was utilized to detect how much PFC is dissolved in water and steam, under geothermal conditions (200 psi @ 200 °C). From this, determining the solubility of PFC in an aqueous solution, aids in understanding the flow of water under geothermal conditions. As a mechanical engineering major, this research project has helped further my knowledge of how a pressure vessels function and are assembled, as well as the applications of perfluorocarbons. In addition, I am more familiar with how to use a torque wrench, and why specific torques are of importance when operating a pressurized vessel.

I. Introduction

A tracer is an indicator added to a system to detect the movement of mass. Russ Dietz at Brookhaven National Laboratory (BNL) recognized Perfluorocarbon tracers (PFT) in the early 1980s. PFTs are compounds composed solely of carbon and fluorine. They have numerous detecting applications. For example, to detect airflow, detect leaks in underground piping, and in geothermal wells. However, not all PFTs are alike. In our experiment, we used six different PFTs to understand the flow of water under geothermal conditions. The PFTs involved in this research suggest that meticulousness is essential for comparability. Because of their physical characteristics and their presence in the atmosphere at low levels, PFTs make good tracers. According to the Tracer Technology Group at BNL, background concentrations are several part per quadrillion by volume, so the release of small amounts of PFT result in unambiguous signals. The large numbers of fluorine atoms and the structure of these molecules cause them to have high electron affinities. Below are the PFTs abbreviations and nomenclatures: 1) PDCB (Perfluorodimethylcyclobutane, C6F12), 2) PMCP (Perfluoromethylcyclopentane C6F12), 3) PMCH (Perfluoromethylcyclohexane, C7F14), 4) o-PDCH (Perfluorodimethylcyclohexane, C8F16), 5) i-PPCH (Perfluoroisopropylcyclohexane, C9F18) and 6) PTCH (Perfluorotrimethylcyclohexane, C9F18). PFT compounds are appreciably soluble in water, and have been used for dissolving high concentrations of oxygen. They have high densities which make them heavier than water. Other uses of compounds have been, to assist in breathing underwater, in eye surgery, in cosmetics, as a blood substitute and in tracer technology.

II. Methods

Our goal was to get several samples at for different temperatures in a time series for each of the six different PFTs. The purpose of this precise testing of each of the six PFTs is to compare the gas chromatography readings with an electron capture detector (GC/ECD) and examine their solubility curve. First, one copper wire lead from a tank of nitrogen to one slot of a "T" valve, valve C. Another wire made of, iron connected the pressure vessel to the other slot of the "T" valve, valve B. From there both slots led to another iron wire with a valve connected to it allowing us to collect samples, valve A. The vessel was to be filled with 5cc of any PFT assigned, immediately followed by 400cc of distilled water. After ensuring the screws and nuts were torqued down correctly, and the vessel was leak-free, we were ready to begin sampling. The sample bags were all weighed initially. We would create a vacuum in the tube between valve A and the "T". Got our mixture to the desired temperature, and opened the B valve connecting the "T" to inside the vessel. After closing B, we opened valve C and A forcing the condensed vapor and nitrogen into the sample bag. We let the air into the bag at 76 ml/s for 6 minutes and 36 seconds allowing 500ml of air into the bag.

After sampling, we would weigh the sample bags and compare it to the initial weight of the bag. Next, the analytical process begins. A syringe was used to extract 10µL of gas from the bags, which is then inserted into an ambersorb tubes. From there, the ambersorb tube was placed in a gas chromatography detector (GC) to determine the concentration of PFT in the bag. There are two ways to synthesize perfluorocarbons: Fowlers Process and Electrochemical Fluorination. In Fowlers process, they fluorinate hydrocarbons or their partially fluorinated derivatives in the vapor phase over cobalt (III) fluoride. In electrochemical fluorination, a redox reaction occurs when carbon is oxidized and the hydrogen is reduced.

III. Conclusion

When dealing with PMCH, as the temperature increase, the solubility increases to exponentially to a maximum solubility. PDCB decreases solubility as it approaches 110 °C to 150 °C and increases as it approaches 200 °C creating a parabola shape on the graph. PMCH is the best tracer to use when trying to detect the flow of water at geothermal conditions. Also, PDCB will be

more difficult to use as a tracer when monitoring underground water flow due to a vast difference in solubility when analyzing our data. Due to the time period of our research we were not able to analyze the other four PFTs

IV. References

Tom, Watson. "A Really Good Hammer: Quantification of Mass Transfer Using Perfluorocarbon Tracers." Environmental Sciences Department. Environmental Research & Technology Division Tracer Technology Group. , Upton. Lecture

Characterizing reconstructions in different Liquid Argon Time Projection Chambers

Samantha Fortuna
Department of Physics, University of Virginia, Charlottesville, Virginia, 22904
Mary Bishai
Department of Physics, Brookhaven National Laboratory, Upton, New York, 11973

Abstract

The Deep Underground Neutrino Experiment (DUNE) and the Micro Booster Neutrino Experiment (MicroBooNE) are long and short baseline neutrino experiments aimed at demystifying the remaining unknown properties of neutrinos, including their mixing angles, their mass hierarchy, the possible existence of sterile neutrinos, and their charge parity (CP) violation phase. In each experiment, a neutrino beam is fired in a tank of liquid argon, where there are three sets of wire planes set at sixty degree angles to one another that record charge signals from the particle interactions. Using this information, researchers will reconstruct in detail the interactions in the tank. In order to prepare to start taking data, the project created software for different particles that simulate and reconstruct their interactions. This study examined the simulations and their reconstructions for both the MicroBooNE and DUNE Liquid Argon Time Projection Chambers (LArTPCs), and compared the interactions of the particles within each tank. Using scripts that submitted large amounts of jobs to the Fermilab batch system, Fermigrid, we examined different interactions of muons, electrons, neutral pions, and muon neutrinos with an event display that showed their recorded tracks along each of the wire planes. Next, we examined different event reconstruction algorithms and judged their relative efficacies. To do so, we simulated 100 events of neutral current muon neutrino events, and applied the three Liquid Argon Software[2,3] (LArSoft) standard algorithms as well as the Brookhaven-created Wire Cell reconstruction algorithm.[4] We studied both the strengths and weaknesses of each algorithm, and the next steps that need to be taken in order to improve each algorithm. This study will help researchers better understand and reconstruct the particle interactions that will eventually be observed in the LArTPC, and, in doing so, allow researchers to take accurate measurements for the missing neutrino properties.

I. Introduction

This study examined the different methods of reconstruction of the particle interactions within LArTPCs, which will be used for events in both the DUNE 34 kton LArTPC and the smaller MicroBooNE 80 ton LArTPC. With accurately reconstructed particle interactions, researchers will be able to understand and solve for the remaining missing parameters of neutrino interactions, including their mass hierarchy and mixing angles. In addition, MicroBooNE[5] hopes to explain a electron-like excess observed in a previous short-baseline neutrino experiment, the Mini Booster Neutrino Experiment (MiniBooNE)[6]. MiniBooNE observed what might have been an unexpected excess of electron neutrinos, which points to neutrino mixing from muon neutrinos to electron neutrinos over a much shorter distance. If this proves true, the most likely explanation of this mixing is the existence of a much heavier fourth type of neutrino, the sterile neutrino, which would completely change both our understanding of neutrino physics as well as how they fit within the Standard Model. However, MiniBooNE used a Mineral oil Cherenkov detector to record and reconstruct particle interactions, which has difficulty differentiating electrons and photons; therefore, MicroBooNE, using the LArTPC, will serve as much better confirmation of this neutrino mixing over such a short distance. Also, DUNE hopes to find and calculate the amount of CP violation in neutrino reactions; if a large enough amount of CP violation is found within these interactions, it would answer the fundamental question of the preponderance of matter over antimatter in the universe.

Therefore, correctly understanding and reconstructing the data taken from the LArTPCs is crucial to making these discoveries. To do so, the tank of the TPC is filled with liquid Argon, and an electric field of 500 V/cm is run through the tank. As particles travel through the detector, they deposit energy, which ionizes the Argon. This ionization charge drifts along the electric field to a series of three wire planes set at sixty-degree angles to one another. From the signals on the wire planes, the particle tracks are reconstructed. This method is demonstrated in Figure 1 below.

From the signal readout on the wire planes, there are two methods of reconstruction, the LArSoft standard reconstruction[2,3] and Wire Cell reconstruction[4]. In the standard reconstruction, a fit of the data of the wire hits is created to eliminate excess background noise, and from that three two-dimensional wire plane views of the event are reconstructed. Then, these three planes are combined to produce a three dimensional reconstruction of the data. In the Wire Cell reconstruction, all of the data of the wire hits are used, and a large number of small time slices of the YZ wire plane are reconstructed. Then, all of these time slices together are used to reconstruct a three dimensional image of the particle tracks. This study examined the strengths and weaknesses of these

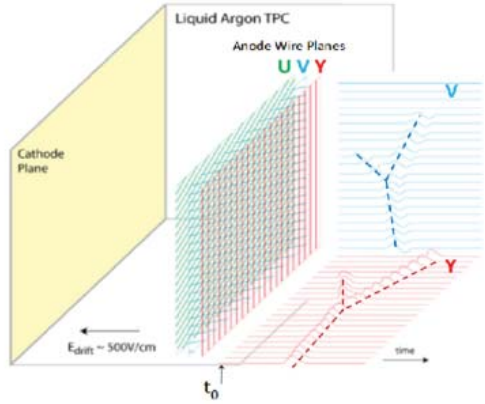

Figure 1 Detector Geometry[1]

two methods, by examining each method of reconstruction for one hundred reconstructed neutral current muon neutrino events.

II. Methods and Results

To begin, we tested the abilities of the simulation software and ran simulated events of muons, electrons, neutral pions, and muon neutrinos through the energy ranges of about 0.5 – 2.0 GeV. To do so more efficiently, we wrote and submitted scripts to the Fermigrid batch computing system to run many simulations at once. In doing so, we were able to confirm the similarities of the particle reconstructions in each detector's software, and therefore data we took from one detector could later be applied to the other. We ran these particle simulations for both the software that simulated the geometry of the DUNE LArTPC as well as the MicroBooNE detector, and compared the results. An example comparison of a 1.5 GeV electron in the DUNE and MicroBooNE detectors, shown with the standard viewer 2D XU, XV, and XY wire plane views (the direction of which in the LArTPC is demonstrated in Figure 1), is shown in Figure 2 below. The x axis of each shows the time and the y axis of each shows the wire number.

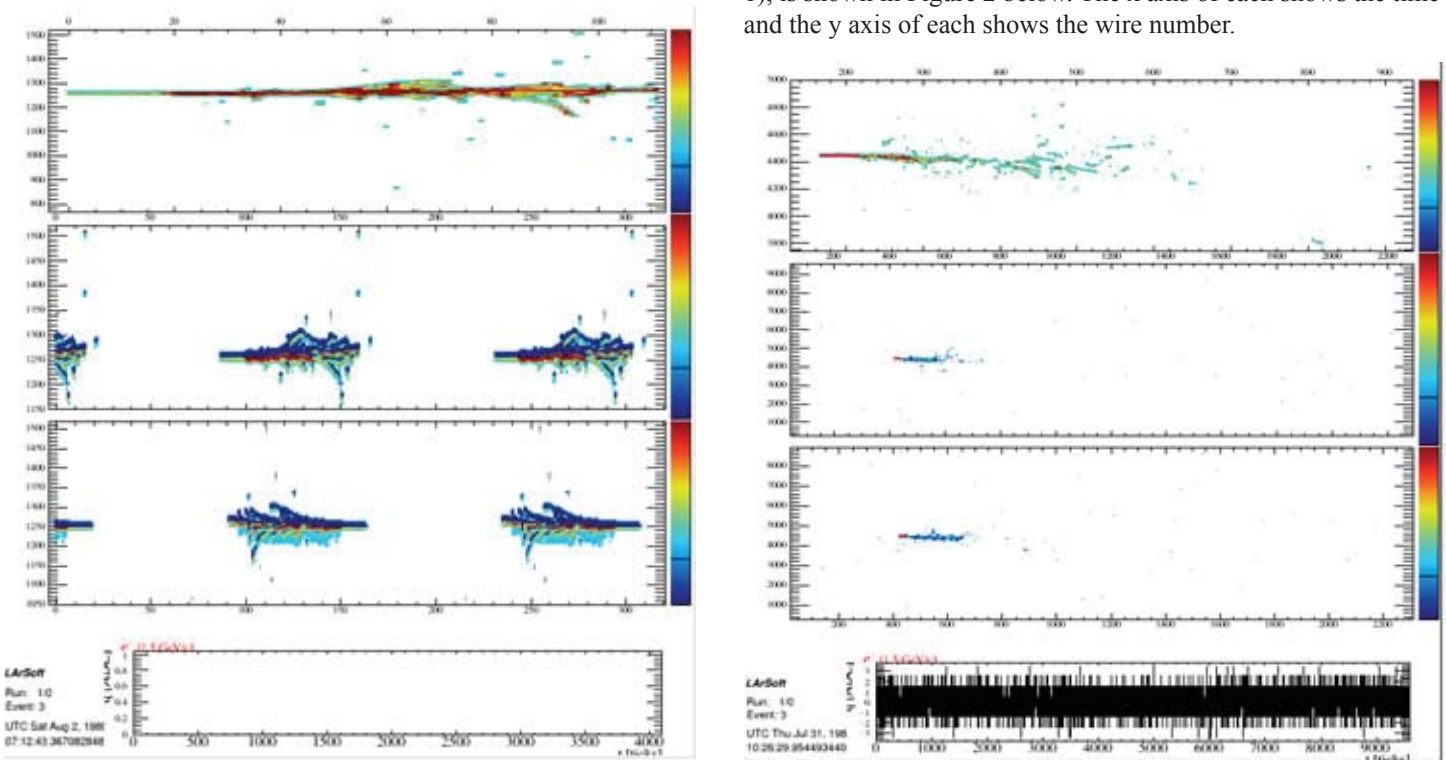

Figure 2 DUNE Electron Simulation (left) and MicroBooNE Electron Simulation (right)

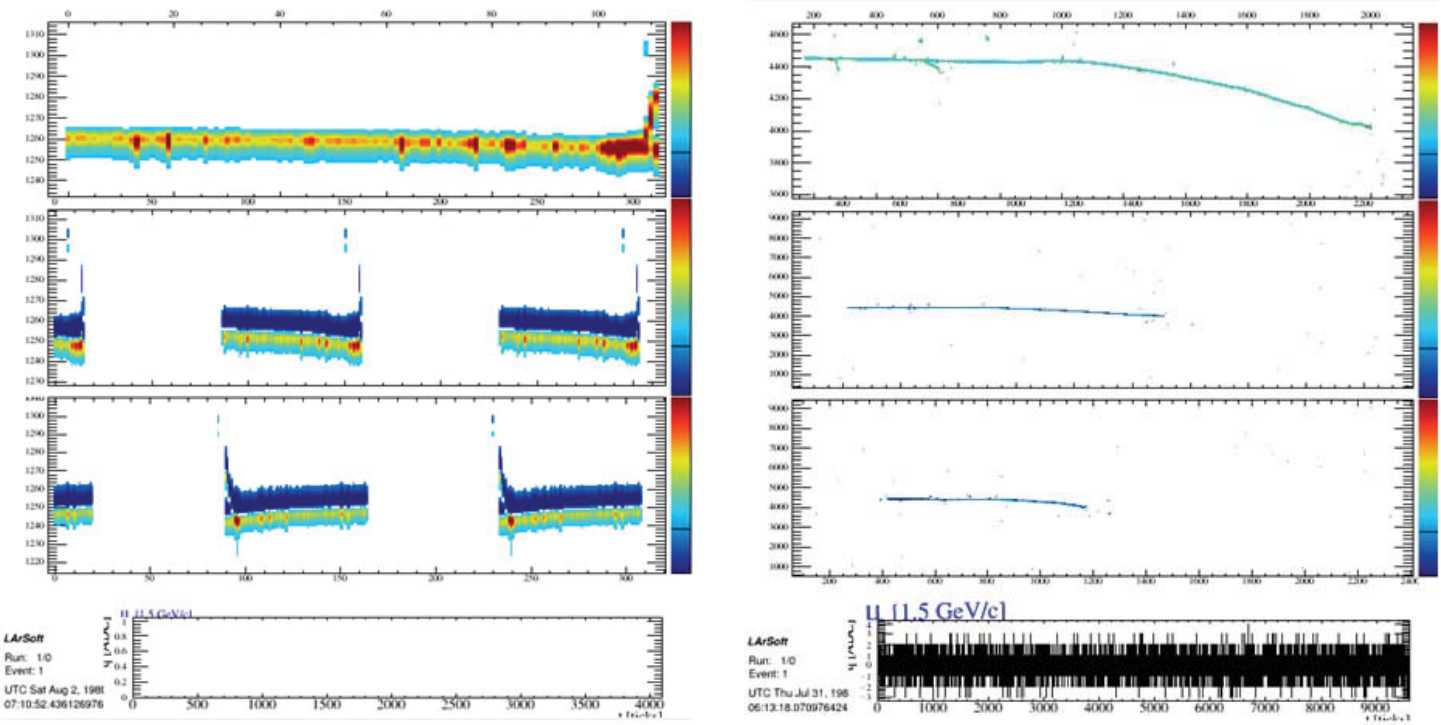

Figure 3 DUNE Muon Simulation (left) and MicroBooNE Muon Simulation (right)

Both of these diagrams demonstrate the electron shower produced from the interactions within the Liquid Argon detector; the DUNE event is slightly more zoomed in, which explains the difference in scale. Another example comparison of a 1.5 GeV muon, in both the detector geometry of DUNE and MicroBooNE, is shown below. Again, the axes show the wire number and the time, and it is shown in the 2D XU, XV, and XY wire plane views.

These events above show a similar straight muon track in both simulations, although the simulation in DUNE is once more zoomed in.

Once we compared the different reactions within the two simulated detectors, and confirmed both simulation softwares functioned well and similarly, we focused on producing neutrino events in the MicroBooNE detector. Two types of neutrino reactions, charged current and neutral current, can occur. In a charged current reaction, a neutrino gives a positive W boson with a nucleon and becomes a lepton (the flavor of which depends on the flavor of the neutrino). In a neutral current reaction, a neutrino gives a neutral Z boson to a nucleon, and scatters off without changing into a lepton. These reactions are shown in Figure 4 below.

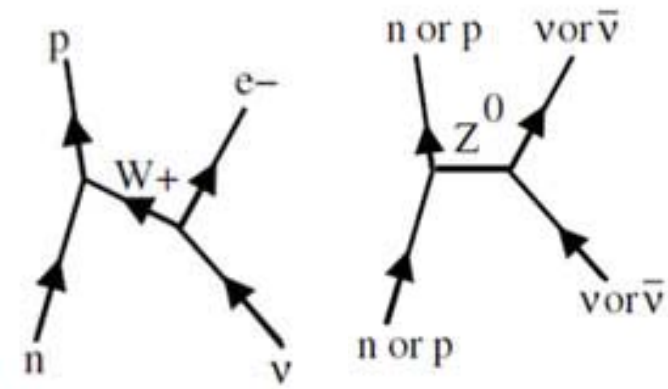

Figure 4 Charged Current Reaction (left) and Neutral Current Reaction (right)

Our study simulated one hundred events each of 3 GeV charged current electron neutrinos, charged current muon neutrinos, and neutral current muon neutrinos. Then, we ran both standard and Wire Cell reconstruction on each event. An example of each sort of event with Wire Cell Reconstruction is shown in Figure 4 below.

Next, we examined specifically 100 neutral current muon neutrino events, and examined their Monte Carlo (MC) truth, which displays the expected track path, the Wire Cell reconstruction, and the standard LArSoft reconstruction. First, we directly compared the Monte Carlo truth to the Wire Cell reconstruction. In doing so, we noted an intrinsic difficulty with the Wire Cell reconstruction, which can be seen in Figure 6 below.

Rather than producing a straight track as displayed in the Monte Carlo truth, many planes of charge were produced. However, when looking at the 2D wire plane views, these planes were not obvious, and the 2D Wire Cell planes matched almost exactly with the 2D Standard viewer. This is demonstrated in Figure 7,

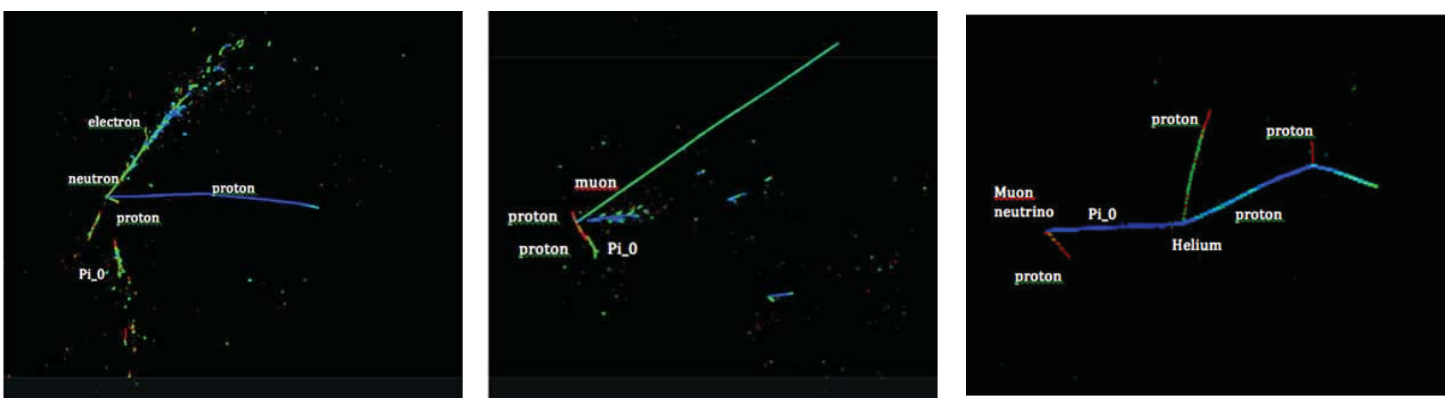

Figure 5 Electron Neutrino (left), Charged Current Muon Neutrino (center), and Neutral Current Muon Neutrino (right)

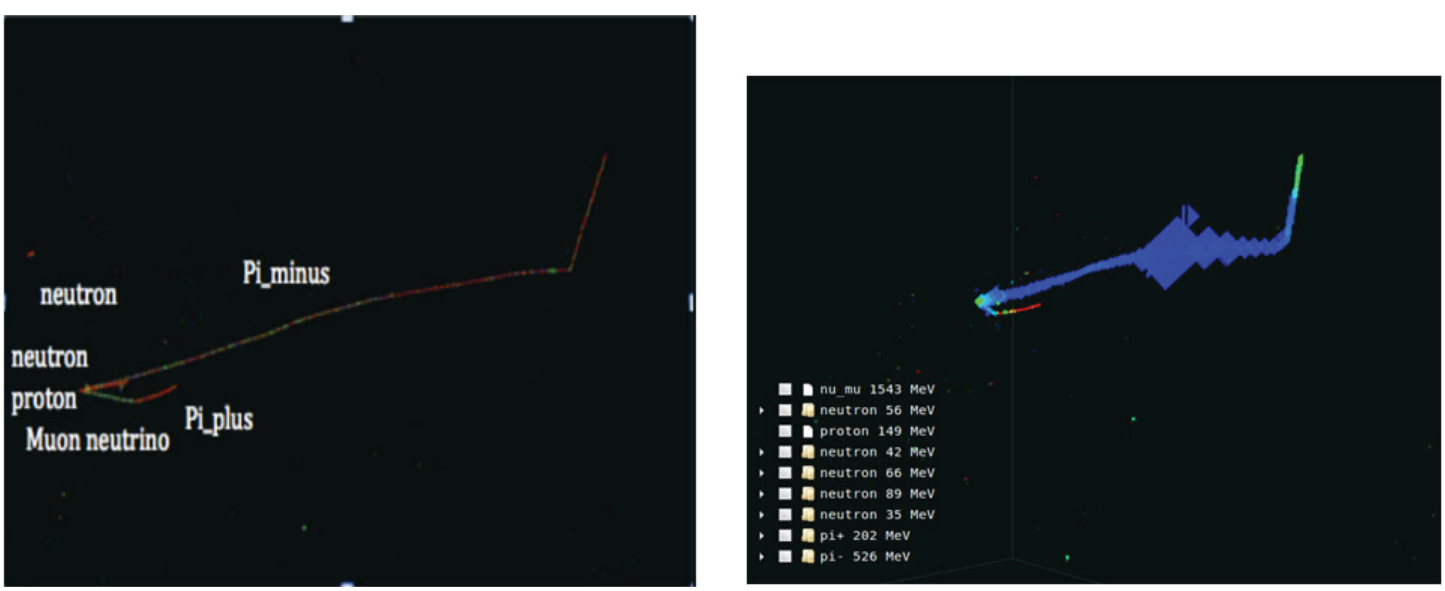

Figure 6 Monte Carlo Truth (left) and Wire Cell Reconstruction (right)

which shows the standard and Wire Cell 2D Wire plane views for the event in Figure 6.

The figure to the left once again displays wire count and time on each of its axes. Although the scales of the images are slightly different, the tracks in both the standard and the wire cell reconstruction appear identical. This proved true for all events that had these planes of charge in the 3D Wire Cell reconstruction. This demonstrates that these planes of charge occurred with tracks that run parallel to the wire planes. Such events are caused by an intrinsic difficulty in recording and understanding the signals from the wire plane. This is due to the configuration of the wire planes; the U, V, and Y wire planes are placed at sixty-degree angles to one another, and charge is recorded at different wire crossings. However, if ionization charge passes through several wire crossings simultaneously, the track can be traced as any of a plane possible wire crossings. Thus, rather than producing a straight charge, a series of planes of charges are produced. This points to the need for algorithms to reduce the number of possible wire crossings; however, in order to do, assumptions about the tracks need to made, which could lead to inaccuracies. However, this analysis points to both the accuracies of the Wire Cell reconstruction, as well as the next steps that researchers need to take.

Next, our study examined the different 3D reconstruction algorithms provided in the LArSoft Standard Reconstruction, and compared them to the Wire Cell Reconstruction. There are three different algorithms that use the method outlined as the standard reconstruction, trackkalmanhit, pandoraNuKHit, and cctrack, and each has different philosophies and methods on how to take the data from the 2D wire plane views and reconstruct them to form a 3D image of the tracks. Our study examined the reconstructions

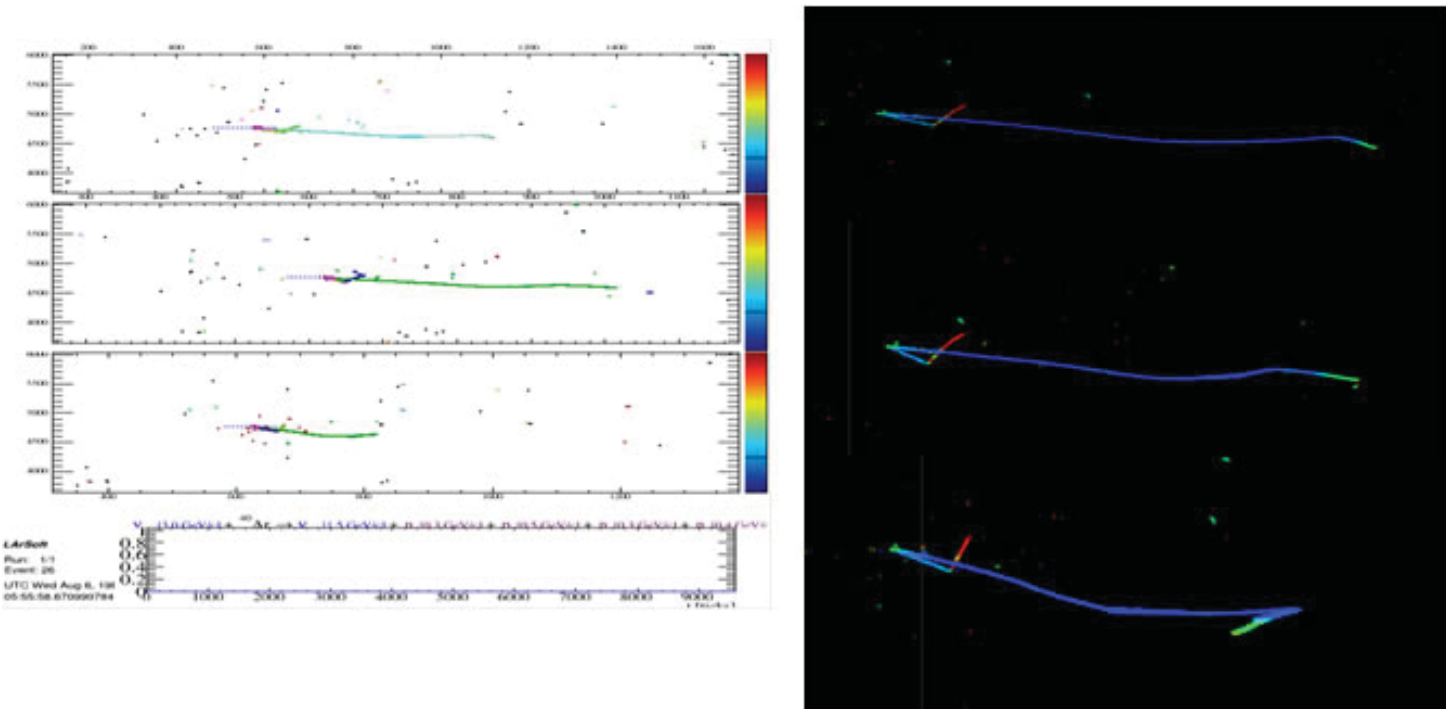

Figure 7 Standard 2D Wire Plane Views (left) and Wire Cell 2D Wire Plane Views (right)

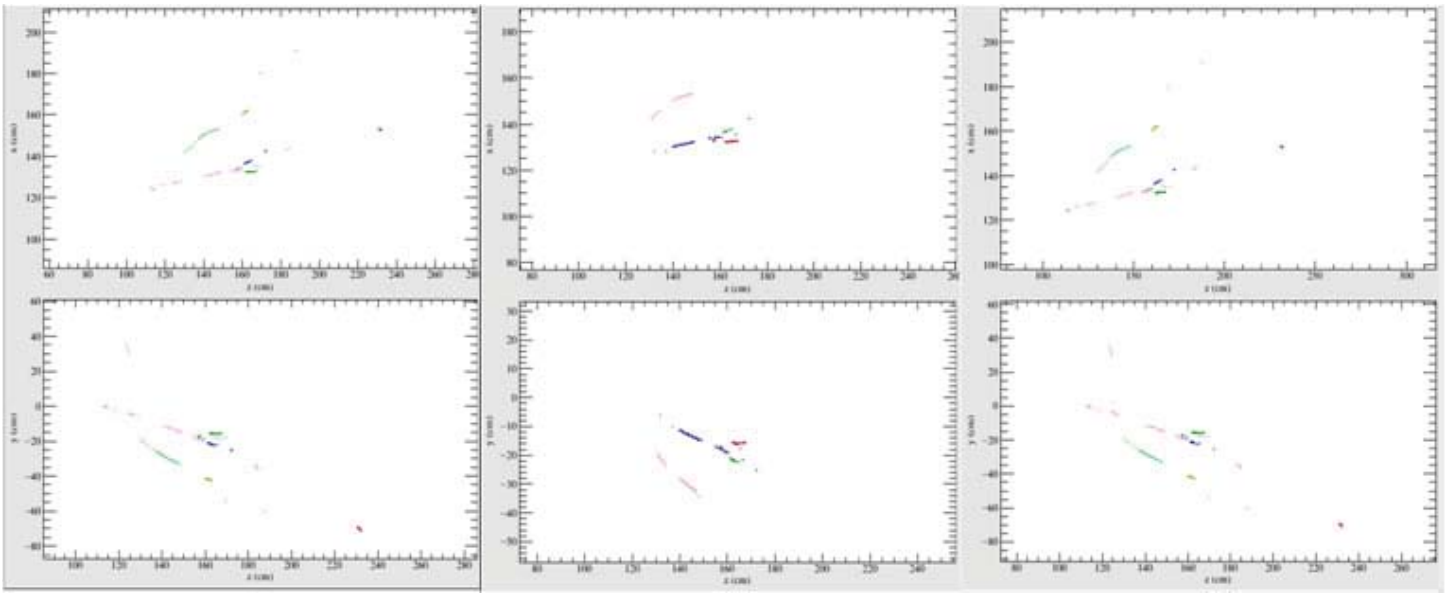

Figure 8 trackkalmanhit (left), pandoraNuKHit (center), and cctrack (right)

that each of these algorithms produced for several events, and compared them to the wire cell reconstruction. Figure 8 shows a sample event of these three reconstruction algorithms, with the reconstruction projected on the XZ and YZ planes.

As demonstrated in these diagrams, radically different reconstructions are produced from the three different algorithms, to the point where they almost appear to not be the same event. Next, our study examined the same event with the Wire Cell Reconstruction and MC Truth to compare the two reconstructions, and the number of tracks they were supposed to record versus the number of tracks they actually recorded. This is displayed in Figure 9 below.

These diagrams demonstrate that the Wire Cell Reconstruction picks up many more tracks than any of the standard algorithms; the standard algorithms miss several tracks, including the vertex of the two proton branches entirely, and have gaps in the middle of several tracks. Upon examining many more events, our study concluded that the Wire Cell reconstruction picked up at least as many tracks as the standard algorithms, and in many cases more tracks more clearly. Therefore, the study concluded that although there are still steps that need to be taken to improve the precision of the Wire Cell Reconstruction, it appears to be the most successful current method of reconstruction for the LArTPC.

III. Conclusion

In conclusion, this study tested and confirmed the efficiency of the simulation software for both DUNE and MicroBooNE. In addition, after examining the different types of reconstruction, it found both methods had their own strengths and weaknesses. However, the Wire Cell reconstruction appeared to be the most effective, with future research and precision necessary to be completely successful in creating three-dimensional reconstructions of the particle interactions within the LArTPCs for both MicroBooNE and DUNE.

IV. Acknowledgements

This project was supported in part by the U.S. Department of Energy, Office of Science, Office of Workforce Development for Teachers and Scientists (WDTS) under the Science Undergraduate Laboratory Internships Program (SULI).

I would like to thank my mentor, Mary Bishai, for her help and guidance throughout this summer. I'd also like to thank Xin Qian for his assistance in understanding different reconstruction methods and many helpful discussions, as well as the Electron Detector Group (EDG) for all their feedback and assistance throughout the summer.

V. Literature Cited

[1]Grosso, Ryan. "The MicroBooNE Experiment." University of Cincinnati, 5 Apr. 2013. Web. 26 July 2015. <http://www.microboone.fnal.gov/talks/APS_April_Grosso.pdf>.

[2]Agostinelli, S. et al. (GEANT4 Collaboration) "GEANT4: A Simulation toolkit", Nucl.Instrum.Meth. A506 (2003) 250-303.

[3]Church, Eric D. "LArSoft: A Software Package for Liquid Argon Time Projection Drift Chambers", arXiv:1311.6774.

[4]"Wire Cell Reconstruction." < http://www.phy.bnl.gov/wire-cell/>

[5]Miceli, Tia. "MicroBooNE." Fermilab, 9 June 2015. 26 July 2015. <http://www-microboone.fnal.gov/public/talks.html>

[6]Brice, Steve. "The Booster Neutrino Experiment." 9 October 2002. 26 July 2015. <http://www.boone.fnal.gov>

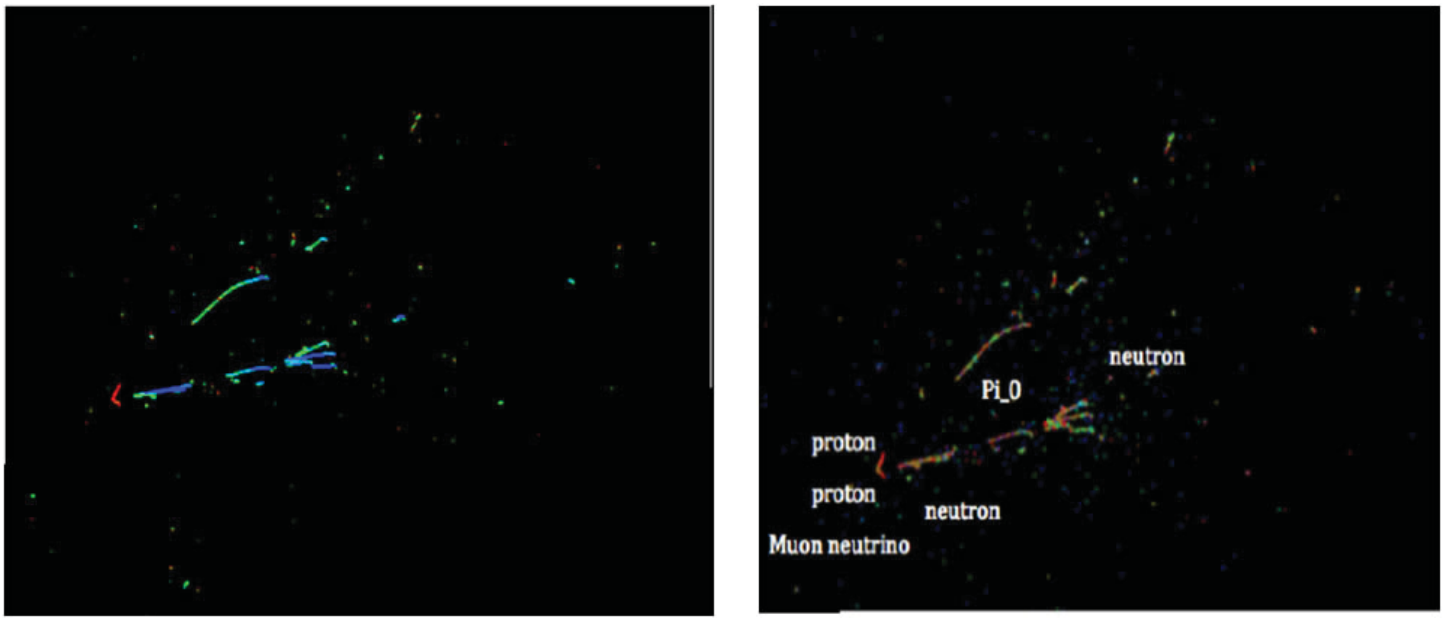

Figure 9 Wire Cell Reconstruction (left) and MC Truth (right)

The efficiency of 4-poster tick management stations on three tick species populations within Brookhaven National Laboratory

Tayelor Gosselin
Department of Wildlife, Fisheries, and Conservation, University of Maine, Orono, ME 04469
Tim Green
Environmental Protection Division, Brookhaven National Laboratory, Upton, New York 11973

Abstract

Increased risk of contracting Lyme Disease and other tick related illnesses has led to many research and management projects being conducted throughout the United States. In 2013, Brookhaven National Laboratory (BNL) set up fourteen 4-poster tick management systems in an effort to control populations of three tick species: blacklegged (deer) tick (Ixodes scapularis), American dog tick (Dermacentor variabilis), and lone star tick (Amblyomma americanum). An increase in the deer population in 2014 resulted in four additional systems being added. In 2015, when the deer population decreased, three systems were removed. Each station, filled with corn to bait deer, has four rollers coated in 10% permethrin which kills ticks attempting to feed on treated deer. Camera traps are present at all stations to determine usage and assist in determining the BNL deer population. Tick populations are determined by flagging, where a 0.46 by 0.76 meter flag is dragged across vegetation 30 times for 1 minute each at every site. Captured ticks were then identified and recorded. Other 4-poster studies show an overall decrease in tick populations, with significant results showing after the third year of treatment. One such study has been carried out on Shelter Island and Fire Island, with results supporting the use of 4-poster devices as a means to control the tick populations. Although this was the third year of the study at BNL, percent control was less than expected, with the highest control at 59% for A. americanum males.

I. Introduction

Lyme disease, a vector-borne illness, is one of the most commonly reported illnesses of its kind within the United States. Between 1992 and 2011, 87,588 cases were reported within New York alone, 12,871 of those cases reported from Suffolk County. New York also holds a spot within the top fourteen states that account for 95% of all Lyme disease cases reported in the United States (CDC 2015). In addition to Lyme disease ticks can carry an array of other diseases, the transmission of which depending on what species is attached and feeding. On Long Island possible illnesses includes Ehrlichiosis, Southern tick-associated rash illness (STARI), Tularemia, Rocky Mountain spotted fever (RMSF), Lyme disease, Anaplasmosis, and Babesiosis. Tick species present on Long Island that transmit these diseases include the blacklegged (deer) tick (Ixodes scapularis), lone star tick (Amblyomma americanum), and the dog tick (Dermacentor variabilis). During the ticks' larval and nymph stage, they attach to birds and small mammals, and can be infected if feeding on a reservoir competent host (animal infected by a parasite that serves as a source of infection for other species) (Stafford 2004; Stafford n.d.). After the larval and nymph stages, non-infected ticks are less likely to be infected as they feed on larger hosts such as the white-tailed deer (Odocoileus virginianus) that are not competent hosts. White-tailed deer not only serve as a meal to ticks, but also assist in tick reproduction and transport into new areas, leading to the relation between the deer population and the abundance and distribution of ticks (Stafford n.d.).

The 4-poster passive acaricide application system was developed and patented in 1994 as a way to apply "acaricide to the head, neck and ears of a deer as they feed", controlling the free-living populations of ticks in the process (Pound et. al 2000; Curtis et. al 2011). Before the 4-poster device was implemented for tick control, the only methods available were not able to control the free-living tick population. These methods included, but were not limited to, biological controls, chemical applications, "pesticide treatment of small mammals", habitat modification, and reduction in available hosts (Pound, Lemeilleur et. al 2000). After its initial development and testing, the 4-poster system was further tested in a variety of tick population control studies, many of which reached the conclusion that these systems have a significant impact on controlling free-living tick populations and reducing the risk of tick-borne diseases (Brei et. al 2009; Carroll et. al 2009; Curtis et. al 2011; Pound et. al 2000; Pound, Lemeilleur et. al 2000). With this in mind, Brookhaven National Laboratory (BNL) began using the 4-poster tick management systems. This paper compares the first year's tick population to that of the third year, where significant results have typically been found.

II. Methods

A. Study Area

BNL covers 5,265 acres within Suffolk County, Long Island, NY. The diverse habitat (lawns, roadside, forests, etc.) result in significant edge habitat where deer tend to thrive. In addition, BNL has historically had no deer management, resulting in a large deer population on site (BNL 2009) that has ranged from 50 – 100 deer/mi2. A variety of other animals besides deer utilize the 4-posters as well, and include wild turkey (Meleagris gallopavo), grey squirrels (Sciurus carolinensis), Canada geese (Branta canadensis), groundhogs (Marmota monax), and raccoons (Procyon lotor).

B. 4-Posters

In 2013, fourteen 4-poster devices were deployed throughout the BNL property. In 2014, due to light use at some sites, three devices were removed and set up as duplicates at sites 3, 4, and 11 where use was heavy in 2013; and four additional devices were added in areas of high deer presence. In 2015, duplicates at sites 4 and 11 were removed after the deer population was reduce, leav-

ing a total of fifteen devices in operation throughout BNL. Each device has a central bait bin filled with corn which dispenses on either side to a feeding trough to attract deer. Each feeding trough has two permethrin-treated paint rollers which coat the deer's head, neck, and ears as they feed (Pound et. al 2000; Pound, Lemeilleur et. al 2000; Curtis et. al 2011). Due to decreased usage, devices were serviced once per week in 2015 instead of on a twice per week schedule as in previous years. Corn was refilled to maintain a 200 lb supply and the amount consumed between each refilling was recorded. The rollers were initially treated with 40mL of permethrin, and subsequently with an additional 1.25mL applied via a hand gun applicator for every 1.5lbs of corn consumed.

Each 4-poster device was monitored for usage by wildlife using a Wildgame Innovations infared digital camera (model W5EGC) or Moultrie model D-333 camera set up adjacent to the device. Memory cards for each camera were replaced every two weeks and sorted into one of five categories: deer, raccoon, turkey, other animals, and no animals. Deer took priority as they were the target species, and any picture with deer, regardless of the presence of other animals, was categorized as deer. After deer the order of importance was as follows: raccoon, turkey, other animals, no animals. Any picture containing a human or vehicle was placed into the 'No Animals' category.

C. Tick Sampling

A 0.46 x 0.76 meter flag was dragged across vegetation and leaf litter to sample the tick population. The flag consisted of a cream-colored corduroy material, allowing for ticks to easily cling to it. In 2014, the flag was reduced to approximately half its original size, resulting in timed samples changing from 30 30-second samples, as was done in 2013, to 30 one-minute samples for comparability. After each one-minute sample, the flag was checked for any ticks. If ticks were present, the species was identified as one of three: A. americanum, I. scapularis, or D. variabilis and recorded. Life stage (larvae, nymph, or adult) and gender, if adult, were also recorded for each collected tick. The ticks were then removed from the flag using a sticky-tape lint roller and disposed of. The vegetation of the one-minute sample was also recorded and consisted of any mix between wooded, grassy, herbaceous, and shrubby vegetation. Tick population sampling was conducted in July of 2013, and June-July in 2014 and 2015.

III. Analysis

The Kruskal-Wallis H test was used to compare differences between A. americanum adult male, adult female, nymph, and I. scapularis nymph populations from July 2013, 2014, and 2015. As the data collected was nonparametric, this test was chosen because comparisons could be made between several years unlike the Mann-Whitney U test which can only compare two years. Percent control was calculated between each focus life stage in 2013-2015 and 2014-2015 using a modification of Henderson's method where: percent control= 100 – [(T / U) x 100], where T and U are mean after treatment and mean before treatment respectively (Schulze et. al 2007). Insignificant numbers of I. scapularis adults and larvae and all life stages of D. variabilis resulted in no statistical analysis being conducted.

IV. Results

A. Tick Sampling

The Kruskal-Wallis H test showed significant results in differences between population means of A. americanum adult males (P=0.0392), adult females (P=0.0202), and nymphs (P<0.0001), but no significant difference in I. scapularis nymphs (P=0.995) throughout the three sampling years. Comparing 2013 to 2015, adult male A. americanum had the highest percent control (59.0%) followed by adult females (55.8%), and nymphs (0.5%) (Table 1). I. scapularis nymphs was the only life stage to have a negative percent control (-7.3%). Five of the eleven sites had 100% control in at least one of the three life stages of A. americanum evaluated, while six sites had at least one negative percent control in one of the four categories (A. americanum adults (male, female) and nymphs and I. scapularis nymph). Between 2014 and 2015, adult female A. americanum had the highest percent control (51.6%), followed by adult males (7.6%) (Table 2). Both A. americanum and I. scapularis nymphs had a negative percent control (-137.0% and -38.6% respectively). Like the 2013-2015 comparison, five of the eleven sites had 100% control in at least one of the three life stages of A. americanum. Unlike the 2013-2015 comparison, eight of the eleven sites in the 2014-2015 comparison had a negative percent control in at least one of the four categories.

V. Discussion

A. Tick Sampling

Of the sampled species and life stages, only the A. americanum adult males, adult females, nymphs, and I. scapularis nymphs showed significant results, and thus were the focus stages of the study. Very little or no data was found for the remaining life stages of the focus species, and thus were not viable to use in population estimates. Larvae were sampled at sites, but are most abundant in August. Due to the high numbers of A. americanum larvae, abundance of larvae captured was estimated, making the data collected unreliable in calculating a true larval population. Although little to no data was found previously, there was an increase in adult male and female D. variabilis at several sites during the July 2015 sampling.

An overall comparison of the three years of conducting the study indicated a significant difference within A. americanum adult male (P=0.0392), adult female (P=0.0202), and nymph (P<0.0001) populations, but no significant difference was found in I. scapularis nymph (P=0.995) populations (Figure 1). The inability to detect a difference within the I. scapularis nymph population may be due to the small number of nymphs actually detected throughout the sites, whereas the A. americanum was numerous and abundant at all sites. One factor that may result in the finding of more A. americanum than I. scapularis is the hosts they feed on. The A. americanum is very aggressive and non-specific when seeking hosts. They can be found on people, small and large mammals (white-footed mice and white-tailed deer), and wild turkeys (Holderman and Kaufman 2013), all of which are found on the BNL site. Unlike A. americanum, I. scapularis are very specific in their selection of hosts, depending on the life cycle stage they are at, and with a low probability of ever finding one due to only crawling short distances, starvation is a major cause of mortality (Patnaude and Mather 2000; Ginsberg and Zhioua 1996) . In addition, I. scapularis is more susceptible to desiccation, and therefore tend to be in areas with higher moisture or humidity.

Several sites saw multiple increases in tick populations in both the 2013-2015 and 2014-2015 percent control comparisons (Tables 1 & 2). This is most likely due to the habitat composition and "microclimatic factors such as temperature and humidity"

(Ginsberg and Zhioua 1996; Burks et. al 1996). Variations in temperature can influence the success rate of ticks finding hosts to feed from. Along with humidity, these two factors influence tick behavior and activity, and may result in an increase or decrease in mortality rates (Ogden et. al 2005). I. scapularis host questing is affected by relative humidity within the area. Schulze (et. al 2001) found I. scapularis questing early in the morning when temperatures were low and humidity was at its peak. This humidity could determine the height the ticks may quest at away from the leaf litter layer, and increase or decrease chances of finding a host (Ogden et. al 2005).

The amount of shade available, or lack thereof, due to canopy cover and other vegetation, may also be a factor in site tick abundance and species variation. Canopy cover, unlike grassy/herbaceous areas, would provide shade and a lower temperature than exposed areas, appealing to species ticks feed upon. Forest type (coniferous/deciduous) also contributes to the distribution of I. scapularis and A. americanum throughout the sites. It is not clear however as to what type of forest I. scapularis prefers. Some studies have stated that greater abundance would be found in coniferous forests rather than deciduous, while others state the opposite. A. americanum however, primarily occupy not only woods of both types, but also the woody edges and grassy habitats too (Ginsberg and Zhioua 1996). At sites where grassy areas had more coverage than forests, A. americanum was more likely to be found, and with potential researcher bias this may have been a cause of error. If during one year of the study, the grassy areas were sampled more than the forests, there may be an increase in A. americanum, while researchers who favor forests may see less.

Although this study has shown an overall decrease in tick numbers, it is not to the extent expected (Table 1; Figure 1). This could be due to numerous factors, including abiotic and unintentional error on the researchers' part. During the winter months, ticks burrow into the soil and leaf litter, a period known as overwintering. High amounts of snow fall during this period will insulate them, decreasing the winter mortality, whereas cold, dry winters would reduce survivability (Hayes et. al 2015; Nearing 2015). This past winter (2014-2015), snowfall for the month of March was absurdly high (23.9 inches), and maintained a 20.6 in. average between the months of January - March (Newsday 2015). The months of January - March of 2013-2014 also had unusual amounts of snowfall (19.7 inches) compared to previous records, and may be the cause of limited percent control of free-living tick species observed during the study. Another area of possible error is the length of 4-poster deployment. In this study, the 4-posters were in use from mid-April to late September or early October. Other studies with longer periods of 4-poster use also had significant results in controlling the tick population (Carroll et. al 2009; Curtis et. al 2011; Pound et. al 2000). This may suggest that the 4-poster devices were pulled too early to have the level of impact that we were expecting.

Regardless of the level of control, it is evident that the 4-poster devices are able to control the free-living A. americanum and I. scapularis populations, and thus decrease the risk of human illness. With BNL efforts to reduce the deer population to below 30 deer/mi. sq., the tick population is expected to decrease, as lower deer densities theoretically decrease the potential of deer as final hosts. Comparing data of high deer densities with 4-posters to that of lower densities with 4-posters may have a significant effect on tick populations. However, due to unforeseen factors such as severity and length of winter months and 4-poster deployment, the efficiency the 4-posters can provide still remains uncertain. Keeping a record of snowfall and tick abundances may assist in determining levels of control following particularly snowy or lengthy winters, and further validate the 4-poster system as a means of tick control.

VI. Acknowledgments

I would like to thank my mentor, Tim Green, for his help and guidance throughout this study. Thanks to Jennifer Higbie and Kathy Schwager as well for giving help when needed. This project was supported in part by the U.S. Department of Energy, Office of Science, Office of Workforce Development for Teachers and Scientists (WDTS) under the Science Undergraduate Laboratory Internships Program (SULI).

VII. Bibliography

BNL. www0.bnl.gov,. 2009. Natural Resource Management, Environmental Protection Division (EPD), Brookhaven National Laboratory, BNL. <http://www0.bnl.gov/esd/wildlife/Deer.asp>.

Brei, B., J. Brownstein, J. George, J. Pound, J. Miller, T. Daniels, R. Falco, K. Stafford, T. Schulze, T. Mather, J. Carroll, and D. Fish. 2009. Evaluation of the United States Department of Agriculture Northeast Area-Wide Tick Control Project by Meta-Analysis. Vector-Borne and Zoonotic Diseases 9:423-430.

Burks, C., R. Stewart, G. Needham, and R. Lee. 1996. The role of direct chilling injury and inoculative freezing in cold tolerance of Amblyomma americanum, Dermacentor variabilis and Ixodes scapularis. Physiological Entomology 21:44-50.

Carroll, J., D. Hill, P. Allen, K. Young, E. Miramontes, M. Kramer, J. Pound, J. Miller, and J. George. 2009. The Impact of 4-Poster Deer Self-Treatment Devices at Three Locations in Maryland. Vector-Borne and Zoonotic Diseases 9:407-416.

CDC. cdc.gov,. 2015. Data and Statistics| Lyme Disease | CDC. <http://www.cdc.gov/lyme/stats/index.html>.

Curtis, P., S. Walker, and D. Gilrein. 2011. Shelter Island and Fire Island 4-Poster Deer and Tick Study.

Ginsberg, H., and E. Zhioua. 1996. Nymphal survival and habitat distribution of Ixodes scapularis and Amblyomma americanum ticks (Acari: Ixodidae) on Fire Island, New York, USA. Exp Appl Acarol 20:533-544.

Hayes, L., J. Scott, and K. Stafford. 2015. Influences of weather on Ixodes scapularis nymphal densities at long-term study sites in Connecticut. Ticks and Tick-borne Diseases 6:258-266.

Holderman, C., and P. Kaufman. 2013. lone star tick - Amblyomma americanum (Linnaeus). Entnemdept.ufl.edu. <http://entnemdept.ufl.edu/creatures/urban/medical/lone_star_tick.htm>.

Nearing, B. 2015. Snow protects infected ticks. Cary Institute of Ecosystem Studies. <http://www.caryinstitute.org/newsroom/snow-protects-infected-ticks>.

Newsday,. 2015. Long Island weather: Snowfall totals since 1947. <http://data.newsday.com/long-island/data/weather/snowfall-history/>.

Ogden, N., M. Bigras-Poulin, C. O'Callaghan, I. Barker, L.

Lindsay, A. Maarouf, K. Smoyer-Tomic, D. Waltner-Toews, and D. Charron. 2005. A dynamic population model to investigate effects of climate on geographic range and seasonality of the tick Ixodes scapularis. International Journal for Parasitology 35:375-389.

Patnaude, M., and T. Mather. 2000. blacklegged tick or deer tick - Ixodes scapularis Say. Entnemdept.ufl.edu. <http://entnemdept.ufl.edu/creatures/urban/medical/deer_tick.htm>.

Pound, J., J. Miller, and J. George. 2000. Efficacy of Amitraz Applied to White-Tailed Deer by the '4-Poster' Topical Treatment Device in Controlling Free-Living Lone Star Ticks (Acari: Ixodidae). Journal of Medical Entomology 37:878-884.

Pound, J., J. Miller, J. George, and C. Lemeilleur. 2000. The '4-Poster' Passive Topical Treatment Device to Apply Acaricide for Controlling Ticks (Acari: Ixodidae) Feeding on White-Tailed Deer. Journal of Medical Entomology 37:588-594.

Stafford, K. 2004. Tick management handbook. Connecticut Agricultural Experiment Station, New Haven, Conn.

Stafford,. n.d. Management of Host Animals. 1st edition. The Connecticut Agricultural Experimentation Station.

Schulze, T., R. Jordan, C. Schulze, S. Healy, M. Jahn, and J. Piesman. 2007. Integrated Use of 4-Poster Passive Topical Treatment Devices for Deer, Targeted Acaricide Applications, and Maxforce TMS Bait Boxes to Rapidly Suppress Populations of Ixodes scapularis (Acari: Ixodidae) in a Residential Landscape. Journal of Medical Entomology 44:830-839.

Schulze, T., R. Jordan, and R. Hung. 2001. Effects of Selected Meteorological Factors on Diurnal Questing of Ixodes scapularis and Amblyomma americanum (Acari: Ixodidae). Journal of Medical Entomology 38:318-324.

VIII. Figures & Tables

Table 1. Percent control between 2013 and 2015 at each 4-poster device between species/life stage. Negative percentages indicate an increase in ticks at the site. Negative signs (-) indicate an unquantifiable increase from zero.

2013-2015				
	A. americanum		I. scapularis	
	Male	Female	Nymph	Nymph
4P-2	75.0%	80.0%	98.3%	68.4%
4P-3	100.0%	100.0%	66.7%	-140.0%
4P-4	-	-200.0%	-152.9%	-
4P-5	75.0%	100.0%	77.3%	85.0%
4P-6	100.0%	100.0%	94.4%	66.7%
4P-7	0.0%	85.7%	-182.6%	0.0%
4P-10	57.1%	40.0%	75.2%	-300.0%
4P-11	80.0%	80.0%	-48.3%	80.0%
4P-12	61.5%	78.6%	-171.6%	-
4P-13	100.0%	50.0%	53.2%	0.0%
4P-14	0.0%	100.0%	96.2%	60.0%
Average	**59.0%**	**55.8%**	**0.5%**	**-7.3%**

Table 2. Percent control between 2014 and 2015 at each 4-poster device between species/life stage. Negative percentages indicate an increase in ticks at the site. Negative signs (-) indicate an unquantifiable increase from zero.

2014-2015				
	A. americanum		I. scapularis	
	Male	Female	Nymph	Nymph
4P-2	0.0%	0.0%	-30.0%	45.5%
4P-3	100.0%	100.0%	35.5%	-50.0%
4P-4	-150.0%	-	-72.0%	-
4P-5	-	100.0%	-55.6%	-50.0%
4P-6	100.0%	100.0%	80.3%	63.2%
4P-7	33.3%	0.0%	-712.0%	-300.0%
4P-10	-200.0%	25.0%	28.6%	-300.0%
4P-11	-	0.0%	-266.7%	66.7%
4P-12	-	57.1%	-550.0%	0.0%
4P-13	100.0%	85.7%	18.2%	100.0%
4P-14	100.0%	100.0%	16.7%	0.0%
Average	**7.6%**	**51.6%**	**-137.0%**	**-38.6%**

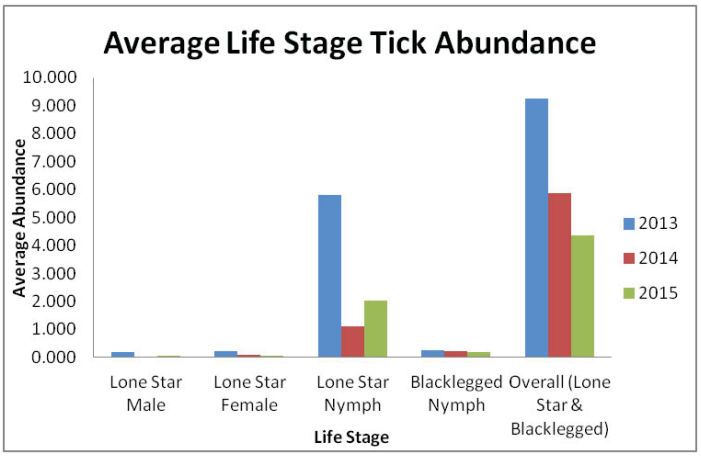

Figure 1. Average abundance of lone star (A. americanum) and blacklegged tick (I. scapularis) life stages throughout the three-year study. Pooled tick abundance is also compared among the three years.

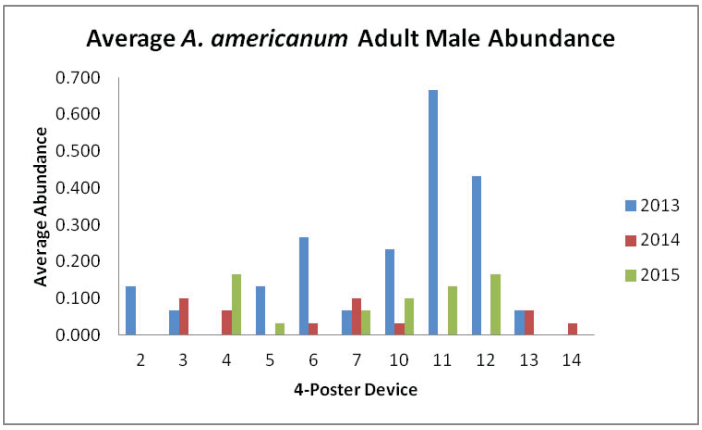

Figure 2. Average A. americanum males captured by flagging at 4-Poster sites from July 201, 2014, and 2015.

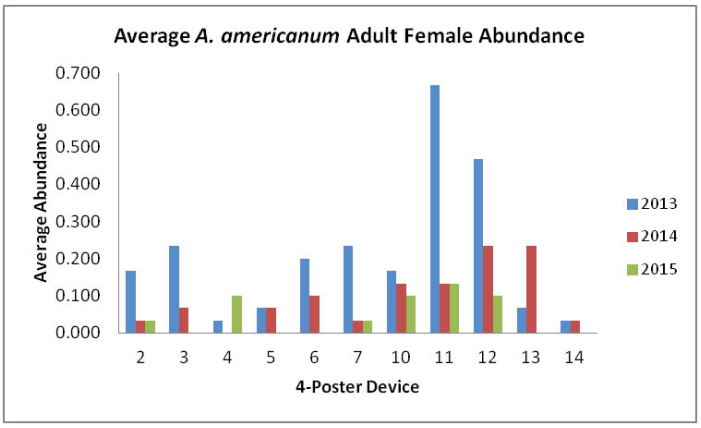

Figure 3. Average A. americanum females captured by flagging at 4-Poster sites from July 201, 2014, and 2015.

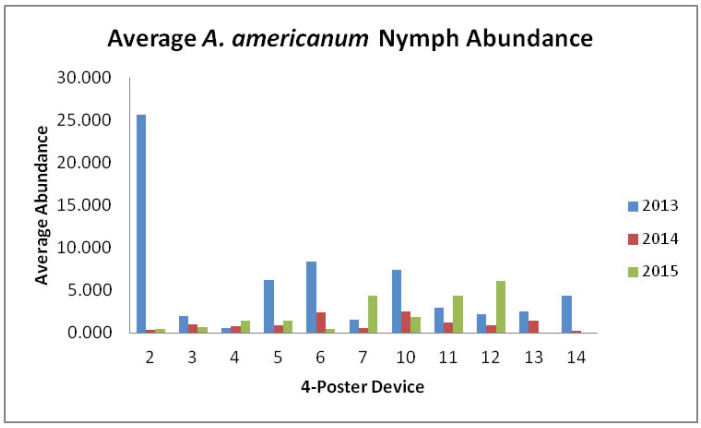

Figure 4. Average A. americanum nymphs captured by flagging at 4-Poster sites from July 201, 2014, and 2015.

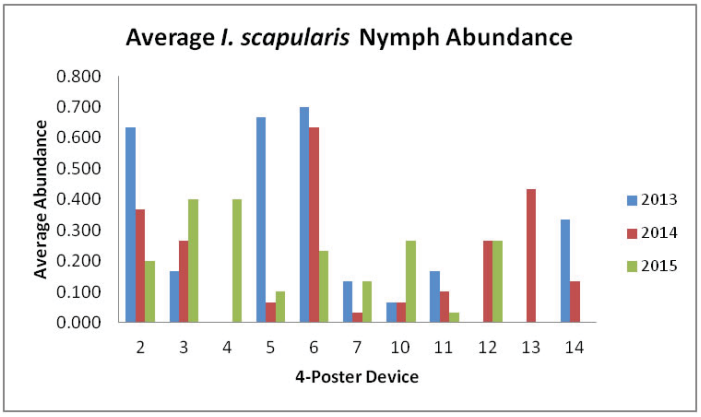

Figure 5. Average I. scapularis nymphs captured by flagging at 4-Poster sites from July 201, 2014, and 2015.

The shallow-to-deep transition in convective clouds during the Green Ocean Amazon 2014/5 campaign

Cari Gostic
Atmospheric Sciences Department, Cornell Univeristy, Ithaca, NY 14853
Michael Jensen
Biological, Environmental and Climate Sciences Department, Brookhaven National Laboratory, Upton, NY 11973

Abstract

The United States Department of Energy created the Atmospheric Radiation Measurement (ARM) Program in 1989 to study cloud formation processes and their influence on radiative transfer. At Brookhaven National Laboratory, our analysis of data from the ARM mobile facility (AMF) in Manacapuru, Brazil, strives to uncover a better understanding of complex tropical cloud life cycles as part of the Green Ocean Amazon (GOAmazon) 2014/5 campaign. This study is unique in that it focuses on an undeveloped tropical area, from which long-term atmospheric data is rarely available. Our project uses measurements obtained from the AMF to determine which atmospheric conditions facilitate a localized transition from shallow to deep convective clouds rather than the persistence of shallow cumulus throughout the day. Observations from the vertically-pointing W-band ARM cloud radar are used to identify convective clouds and their transition. Radiosondes, an eddy correlation flux measurement system, surface meteorological instrumentation, a microwave radiometer profiler and a broadband radiometer provide measurements of temperature, water vapor mixing ratio, atmospheric pressure, sensible/latent heat fluxes and solar radiative fluxes among several other variables which describe the environment in which the clouds form and grow. The obtained results suggest that pre-sunrise moisture level and temperature drive diurnal convective cloud development in the Amazon region, and that the absence of a low-level dry layer in the early hours of the day is necessary for deep convection to develop later on. This analysis of data from the ARM archive has enhanced my abilities in computer programming, specifically in the Python language, and taught me the usefulness of programming in scientific analysis. Additionally, I learned how to formally carry out an observational research project to gain understanding about an unknown scientific phenomenon.

I. Introduction

ARM deploys facilities throughout earth's diverse climate regimes and collects detailed atmospheric data at each site. As part of the GOAmazon campaign[1] in Brazil, the AMF provides measurements integral to our understanding of tropical cloud systems, the primary drivers of global atmospheric circulation. Our study focuses on tropical convection. We specifically explore the transition from shallow-to-deep convective clouds. This transition is not well parameterized by current climate models, contributing to temporal errors in model simulations of the peak and duration of convective precipitation.[2] Studies that utilize a cloud- resolving model assert that the development of deep convection depends on the moisture content of the free troposphere.[2] An observational study centered in the Great Plains (U.S.) emphasizes the role of high relative humidity above the boundary layer, instability, inhomogeneity in boundary layer temperature, and an absence of wind shear in the convective transition events in this climactic regime.[3] Our analysis of data from the AMF in Manacapuru, Brazil, explores these factors among others, with an emphasis on relative humidity, convective inhibition (CIN), potential temperature (θ), equivalent potential temperature (θ_e), and mixing ratio (w). θ and θ_e describe instability of an air parcel by adjusting raw temperatures to the temperature a parcel would gain by compression or expansion at a base pressure, and evaporation or condensation at a base water vapor content, respectively. w is a ratio of the mass of water vapor to the mass of other "dry" gases in an air parcel. This study strives to discover what thermodynamic conditions facilitate a transition from shallow-to-deep convection in the humid, tropical climate of the Amazon Rainforest.

II. Methods and Materials

Cases were selected that showed either a persistence of shallow cumulus throughout the day, or a transition from shallow-to-deep convection. The W-Band ARM Cloud Radar (WACR) provided the images used to sort dates ranging from February 26, 2014 through July 7, 2015, into Non-Transition or Transition categories using the following criteria:

Non-Transition: (Figure 1a)

1. Clouds < 5 km in thickness with some clouds > 2 km in thickness.
2. Clouds persist between sunrise and sunset.
3. No clouds > 5 km in thickness occur within the observation area.

Condition (3) was confirmed using satellite images, and is necessary because of the vertically- pointing nature of the WACR. This check ensures that WACR observations showing a lack of transition to deep convection are representative of the surrounding area.

Transition: (Figure 1b)

1. A transition from shallow clouds < 5 km thick to deep convective clouds > 8 km thick occurs, with cloud base heights within the boundary layer.
2. No clouds > 8 km thick occur after 3 UTC and prior to the transition.
3. The transition occurs before sunset.

Cloud thickness refers to the vertical distance between a cloud's base and its cloud top height. For all cases, clouds with bases above 8 km are disregarded as cirrus clouds. A total of 52 transition cases and 40 non-transition cases were identified using this criteria.

Python programming language was used to composite and

analyze data for each category to create plots that show differences in local thermodynamic conditions between transition and non- transition cases. We compiled data from each type of case and the median of a given measurement at each time and height was calculated. Medians are better descriptors of the data than averages because medians minimize the contribution from outliers. The data is not normalized because the transition time of different dates varies. Surface meteorological instrumentation (MET) provides measurements of surface temperature, pressure, relative humidity, and wind. From these values, θ, w, and θ_e are calculated. The shortwave pyranometers (SKYRAD) and eddy correlation flux stations (ECOR) provide raw measurements of surface downwelling shortwave solar flux, and latent/sensible heat flux respectively. The profiling microwave radiometer (MWRP) provides measurements of vertical profiles of temperature, relative humidity, and water vapor density up to 10 km. Surface plots as well as atmospheric profiles were used to analyze conditions that facilitate a transition from shallow-to- deep convection.

III. Results

On average, at the surface, transition cases exhibit slightly higher pre-sunrise temperature and θ, but lower post-sunrise temperature and θ (figure 2a). Peak post-sunrise θ_e also tends to be higher for transition cases (figure 2b). w tends to be higher for transition cases pre-sunrise, and maintains a higher peak for a longer period post-sunrise (figure 2c).

Transition cases exhibit lower post-sunrise short-wave solar flux (on the order of 400-600 W/m²), and lower latent heat flux and sensible heat flux at the surface (on the order of 60 W/m² and 20 W/m² respectively). Transition cases show higher low-to-mid level relative humidity throughout the day, and experience significant mid-level moistening during post-sunrise hours while non-transition cases show low-level drying during post-sunrise hours (figure 3 a,b). This result is mirrored by the plot of average water vapor density, which shows higher water vapor density at lower levels of the atmosphere (< 3 km) for transition cases. On average, pre-sunrise CIN is more negative for non-transition cases than transition cases, which corresponds to greater inhibition of convective development (figure 4). Though average pressure is consistently higher for transition cases, the difference is on the order of < 1 millibar.

Surface winds and pressure, soil moisture, as well as convective available potential energy (CAPE) are similar enough to discount as major distinguishing factors between transition and non-transition cases.

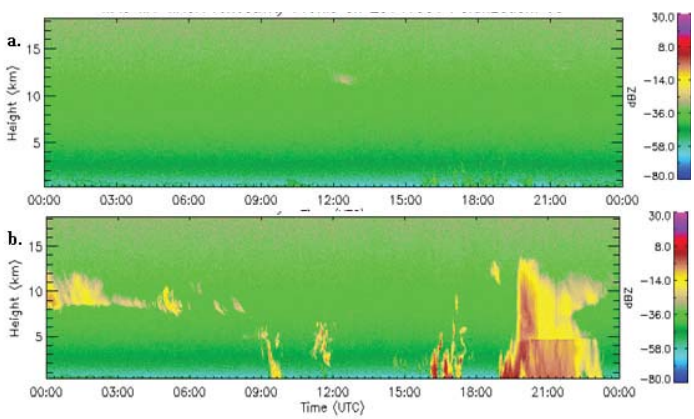

Figure 1: WACR images for typical (a) non-transition and (b) transition cases.

IV. Discussion and Conclusions

The results suggest that pre-sunrise thermodynamic conditions influence the probability that a transition from shallow-to-deep convection will occur during daytime hours. Pre-sunrise conditions dictate the types of clouds that form as thermal lifting occurs after sunrise. This is confirmed by measurements of short-wave solar flux, and latent/sensible heat flux. Non- transition dates, which average lower pre-sunrise temperature, θ, θ_e, and w, experience higher total short-wave flux, latent heat flux and sensible heat flux during daytime hours which is consistent with less complete or thinner cloud cover. In contrast, transition cases average higher pre-sunrise temperature, θ, θ_e, and w and show lower daytime short-wave solar flux, and latent/sensible heat flux. This is because high temperature, θ, θ_e, and w values indicate surface conditions that are favorable for convective development. The greater difference in pre-sunrise θ_e than θ between transition and non-transition cases shows that moisture levels may play a greater role than temperature in facilitating convective development in the tropics, though both are contributors to conditions favorable for a shallow-to-deep transition to occur.

Though pre-sunrise relative humidity at the surface is comparable between transition and non-transition cases, differences in the vertical profile of relative humidity can explain the prevention of a transition from shallow-to-deep convection in non-transition cases. The dry layer above the surface that exists in non-transition cases acts to stabilize the lower atmosphere, and contributes to more negative CIN values. Though high values of CAPE may exist on non- transition days, this energy cannot be realized due to this lower CIN and thermal lifting alone is not strong enough to effectively moisten the dry lower-to-mid levels of the atmosphere once the sun rises. The more humid pre-sunrise atmospheric pro-

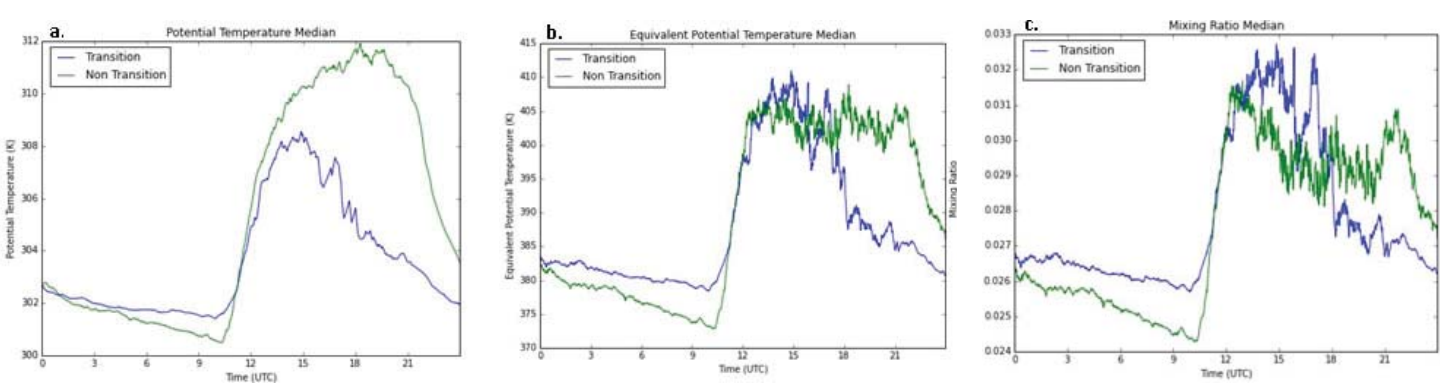

Figure 2. (a) Median potential temperature, (b) equivalent potential temperatuer, and (c) mixing ration for transition vs.non-transition casses. The sun begins to rise at 12 UTC.

file on transition days fosters less negative CIN values, which allows greater access to the CAPE that exists. Therefore, more instability exists before sunrise, so that after sunrise thermal lifting can moisten the lower-to-mid layers of the atmosphere more effectively. This facilitates the transition from shallow-to-deep convection.

The time range of our analysis (February, 2014-July, 2015) is defined by the availability of WACR plots from the AMF in Brazil. Additionally, each instrument has its own unique restrictions within this period. MET, ECOR and SKYRAD measurements are available for most of the date range, however, MWRP data is only available after October, 2014.

This study adds to our knowledge of tropical convection and the conditions that facilitate a transition from shallow-to-deep convection. At the typical transition time (15-18 UTC), non- transition dates exhibit CAPE values comparable to those of transition dates. However, the thermodynamic conditions that exist before sunrise determine if this energy can be realized. These findings can be used to refine parameterizations of the transition from shallow-to-deep transition in climate models to yield more accurate results.

V. Acknowledgments

This project was supported in part by the U.S. Department of Energy, Office of Science, Office of Workforce Development for Teachers and Scientists (WDTS) under the Science Undergraduate Laboratory Internships Program (SULI). I would like to thank Brookhaven National Laboratory, the Office of Educational Programs, Scott Giangrande, Tami Toto, Karen Johnson and my mentor Michael Jensen for the guidance and leadership they provided.

Data were obtained from the Atmospheric Radiation Measurement (ARM) Climate Research Facility, a U.S. Department of Energy Office of Science user facility sponsored by the Office of Biological and Environmental Research.

VI. References

[1] S. Martin, "Observations and Modeling of the Green Ocean Amazon: Year-to-Year Differences," DOE/SC-ARM-13-009, 29pp (2013).

[2] Chiang-Ming Wu, Bjorn Stevens and Akio Arakawa. "What Controls the Transition from Shallow to Deep Convection?" J. Atmos. Sci. 66, 1793-1806 (2009).

[3] Yunyan Zhang and Stephen A. Klein, "Mechanisms Affecting the Transition from Shallow to Deep Convection over Land: Inferences from Observations of the Diurnal Cycle Collected at the ARM Southern Great Plains Site," J. Atmos. Sci. 67, 2943-959 (2010).

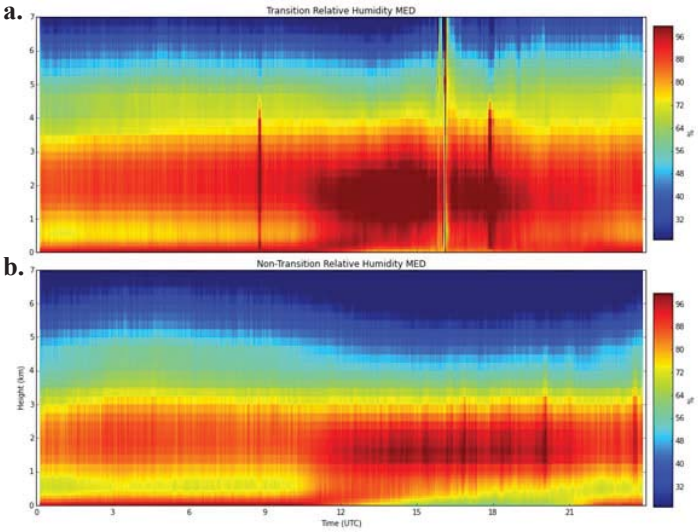

Figure 3: Median relative humidity profiles of (a) non-transition and (b) transition cases.

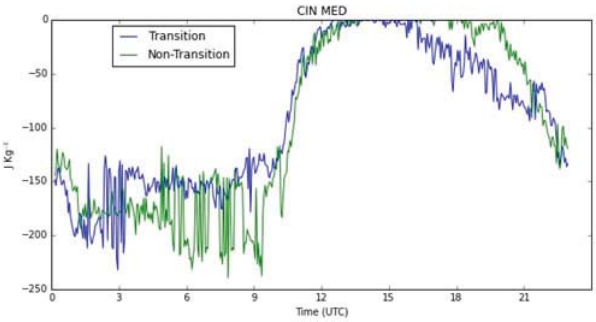

Figure 4: Convective inhibition tends to be more negative (more inhibition) before sunrise for non-transition cases.

Automated testing of nuclear data using zero- power nuclear reactors

Mecheal Greene
Cheyney University, Cheney, PA 19319
David Brown
Brookhaven National Laboratory, Upton, NY 11973

Abstract

The Cross Section Evaluation Working Group (CSEWG) produces the ENDF/B (Evaluated Nuclear Data File/B) nuclear data library for use in reactor simulation, criticality safety, and a variety of other nuclear applications. Although CSEWG strives to be thorough in its format and basic physics checks of the evaluations in the ENDF/B library, testing often was done in an ad- hoc manner and occasionally tests "fall through the cracks." To counter this, the National Nuclear Data Center (NNDC) introduced the ADVANCE continuous integration system which is used to test data as it is committed to the CSEWG data repository. This project is meant to extend ADVANCE by establishing a distributed benchmarking framework. The new framework consists of simulations of critical assemblies, critical assemblies are small, zero-power nuclear reactors the assemblies' small size and simple design mean that they can be modeled completely with very high fidelity. Thus, simulations of the criticality benchmarks are the core of the nuclear data community's data validation efforts. However, there are many benchmarks available, and not all are sensitive to a particular changeset. Therefore a computer program running on the ADVANCE server searches a local database for all simulated assemblies that would be affected by data changes and reruns all relevant simulations on our computing cluster. When the simulations are finished, a process on the cluster would report the simulation results back to the ADVANCE server for regression studies.

I. Introduction

Nuclear reaction data is required for any simulation of any nuclear system including reactors, detectors, nuclear medicine, radiography, and national security. Data testing is also done to determine the observed order of accuracy. The main library in the United States is Evaluated Nuclear Data File (ENDF/B), which is produced by the Cross Section Evaluation Working Group (CSWEG), an informal yet a very long running collaboration of industry, academia and national labs coordinated by BNL.

ENDF/B contains core nuclear reaction data such as cross sections, spectra, angular distributions, fission product yields, thermal neutron scattering, photo-atomic in the adopted format maintained by CSEWG. CSEWG's quality assurance involves a lot of testing, and the testing takes many forms such as simple format checks, simple physics checks, and more serious simulations of integral benchmarks. In preparation for ENDF/B-VII.1 [Chadwick2011], BNL created ADVANCE (Automated Data Verification and Assurance for Nuclear Calculations Enhancement), which is a continuous integration system and deployment concept which originated from industry software. ADVANCE currently handles simple tests and data validation capabilities traditionally part of CSEWG's Phase I testing [Dunford2002]. As part of this project, the ADVANCE system will be expanded to include benchmarking against the critical assemblies described in the ICSBEP Handbook [ICSBEP2014].

Critical assemblies are small, zero-power nuclear reactors, that have been being made since the 1950's. Critical assemblies are simple configurations, so they are easy to model and fast to simulate. There are many different varieties of benchmarks which use different types of fuels, structural materials, and reflectors. Benchmarks are simple but take different amounts of time to run depending on the complexity of the assembly model and spectrum of the generated neutrons. The tests must be run in parallel and if they are not intended to be ran all at the same time, then there can be a plan put in place to come up with a scheme to target the specific jobs or tests you want to run in parallel.

II. Benchmarking

A critical assembly is an assembly containing fissile material intended to sustain a controlled fission chain reaction at a low power level. Witn these criticality assemblies, one can measure the neutron spectrum and the reaction rates as well as perhaps the

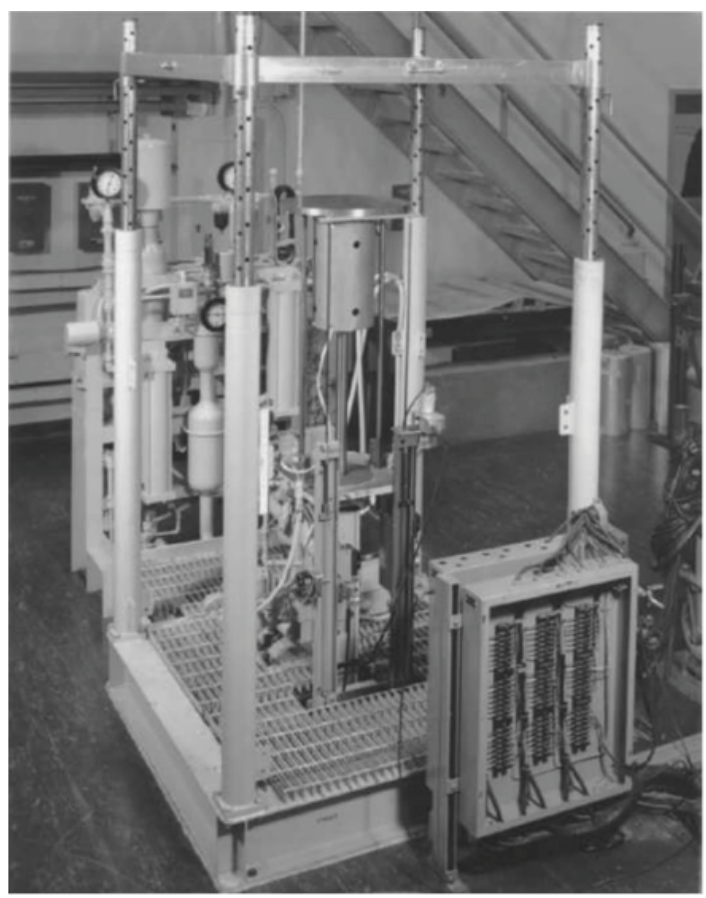

Figure 1: This is a photograph of a vertical assembly machine (HEU-COMP-FAST-002a)

simplest observable, the reactivity coefficient k-effective abbreviated k_{eff}. When $k_{eff} > 1$ the reactor is super critical, meaning that more neutrons are being produced than are being absorbed in the reactor core or can escape from the core. When $k_{eff} < 1$ the reactor core is subcritical, and more neutrons are leaking than are being created. When the $k_{eff} = 1$ the reactor core is exactly critical.

LLNL has developed the neutron trampost code called COG11.1 which is export controlled and licensed for criticality safety applications. COG tracks neutrons, photons, electrons and most recently added the ability to also track alpha particles. Later protons and deutrons will be added as well. COG requires nuclear data and takes the data in various forms. In the fast region ENDF or ACE are used, in the unresolved residance region ACE , and are used in the thermal neutron scattering ACE or ENDF. We were provided LLNL's benchmark suite [Lee2014] which include 145 Plutonium (PU) cases and 359 Highly Enriched Uranium (HEU) cases.

III. How We Intend To Use COG in ADVANCE

ADVANCE pulls ENDF evaluations from the NNDC's GForge source code repository and then performs on demand testing whenever there is a change in the repository. ADVANCE is built off of the Buildbot continuous integration system [Buildbot2015]. Buildbot uses master-slave configuration to manage the builds and the build master is hosted on the ADVANCE server. Currently all build slaves run on the ADVANCE server however ADVANCE is moving to a distributed system arrangement to support this automated benchmarking project.

The first remote build slaves will be hosted on the NNDC cluster to enable faster calculations of the benchmarks. We have adopted LLNL's `cnp_test_suite` [Brown2013] to control the benchmark automation. `cnp_test_suite` contains a database that is used to determine which tests will be affected by a particular change set.

The database is an SQLite3 database, uses dialect of SQL and contains two tables:

1. benchmarks has details from the ICSBEP [ICSBEP2014] with expected k_{eff}
2. decks has results of our runs and what we parsed

To seed the database of benchmark tests, the COG inputs were parsed. In particular, we pulled the assembly material composition from the COG input files if there is a need to adjust the material composition to match what is in the data library. Other information used to populate the initial database were the keff +/- d $k_{eff,}$ name, various metadata, runtime, and whether the deck needs thermal neutron scattering data (also known as Sab data), delayed neutrons or unresolved resonance probability tables. After COG ran in serial mode on the cluster, the results were parsed for every Pu and HEU job. We also parsed the results for the total runtime to see how each individual job took a different amount of time to finish and the results were parsed to see whether the jobs required thermal neutron scattering data to run correctly.

While adapting to the `cnp_test_suite` we encountered issues porting to the BNL cluster and the batch queuing system. This queuing system allows us to run jobs in parallel to speed up time the jobs take to run vastly. As COG is a somewhat old code, it took some work to determine it's optimal run time environment. We were not able to get COG running in parallel using MPI by the completion of this project

IV. Architecture

Here we discuss the architecture of our additions to the ADVANCE system.

The `problem` classes organize and orchestrate the setup and running of the classes. The `problem` classes also are involved in the data collection and the eventual `teardown()` of a test problem. `NewCrash` is a well defined problem class and there is also a `DummyNewCrash` which is simply just for parsing the pre-existing inputs. There is also different ways to run these `problem` classes, for instance they can be ran in either serial mode or MPI mode. The only difference between the two is that MPI uses more nodes then the serial mode which means its lot faster than when its being ran in serial mode.

The `TransportCode` class is what drives an actual transport code and it also manages the code specific to the `setup()` and `teardown()` steps. The `setup()` makes a workspace for the jobs so that each job that is able to run and will be ran

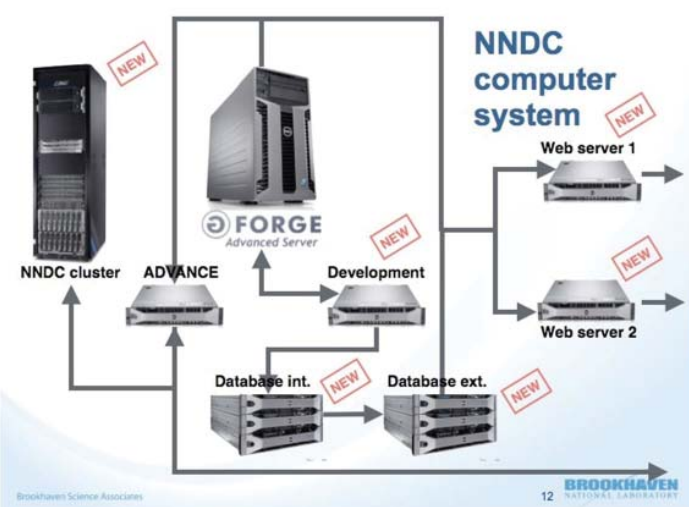

Figure 2: A layout of the NNDC cluster computer system, showing how the cluster is connected to GForge, the ADVANCE server, databases, and web servers [Arcilla2015].

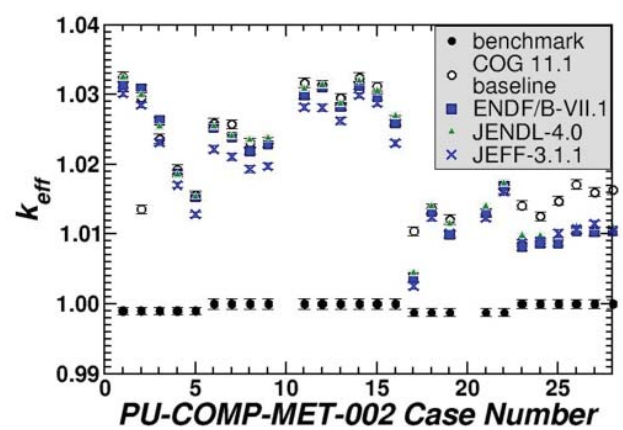

Figure 3: The comparison of typical results for our COG compared to simulations with MCNP from reference [ICSBEP2014] . The benchmarks results are from the handbook [ICSBEP2014]. The agreement between the benchmarks and the simulations are typical for some of the less well studied bases.

in a controlled environment. The `teardown()` function cleans up those temporary work directories that are being made by the setup() function. The `teardown()` cleans those directories because if they are not constantly cleaned, then the disk space will needlessly fill up. This can happen quickly if one runs around 100 jobs every run. This is also why we have a database to store the job results, so that the results stay safe and won't be affected by the `teardown()` code. The `TransportCode` also manages the nuclear data libraries and is associated with the input deck parser class and the output parsing as well.

The pictures below are examples from the code such as `TestSuite`, `TestProblem`, `CodeDummyRun`, `CriticalAssembly`, `DeckTest`, `COG11_1Code`, `COG11_1InputDeck`, `InputDeck`, `code2InputDeck`, `TransportCode`, `NuclearDataLibrary`, `code2Code`, `CodeCrashTest` and `CodeCrashRun`.

V. Conclusion

The objectives left to complete are to finish implementing data for the nuclear library hooks. COG hasn't been able to run with MPI yet, so we have only been running it in serial mode. We would like to simplify the use of the BNL batch queuing system, we are also planning on assigning the code to a build-bot, build-slave and attach it to the ADVANCE build-master.

VI. References

[ICSBEP2014] (1, 2, 3, 4) "International Handbook of Evaluated Criticality Safety Benchmark Experiments", NEA/NSC/DOC(95)03 (2014) [Arcilla2015] R. Arcilla, personal communication (2015)

[Pylint2015] (1, 2) Pylint, https://www.archlinux.org/, Downloaded (2015) [Dunford2002] C. Dunford, "CSEWG Retrospective", BNL-52675 (2002)

[Chadwick2011] M. B. Chadwick, M. Herman, P. Oblozinsky, et al., "ENDF/B-VII.1 nuclear data for science and technology: Cross sections, covariances, fission product yields and decay data", Nuclear Data Sheets, 112(12):2887-2996 (2011)

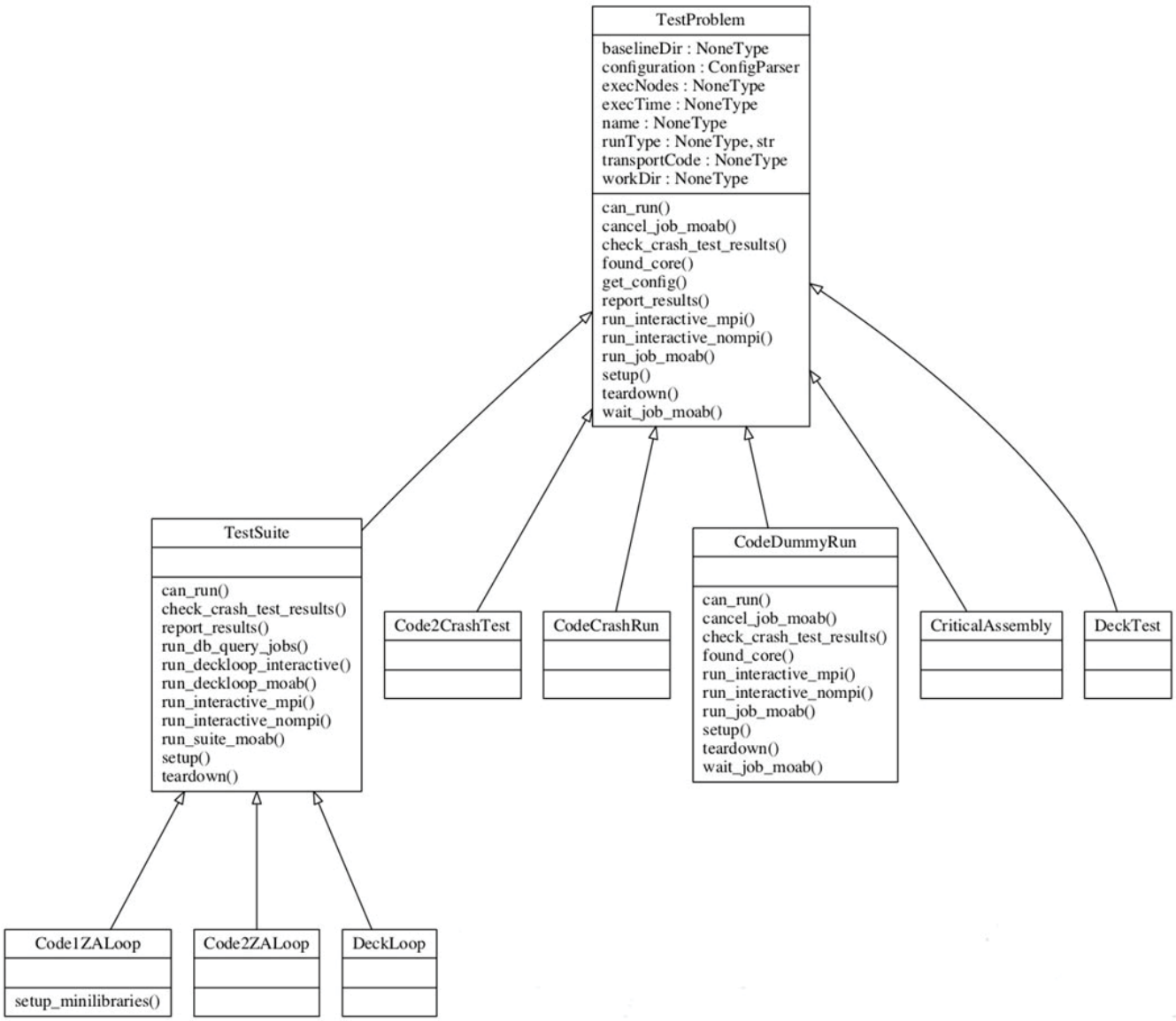

Figure 4: This is a basic layout of the `TestProblem` class and all of the other class that inherit from it. Figure generated using `pylint` [Pylint2015].

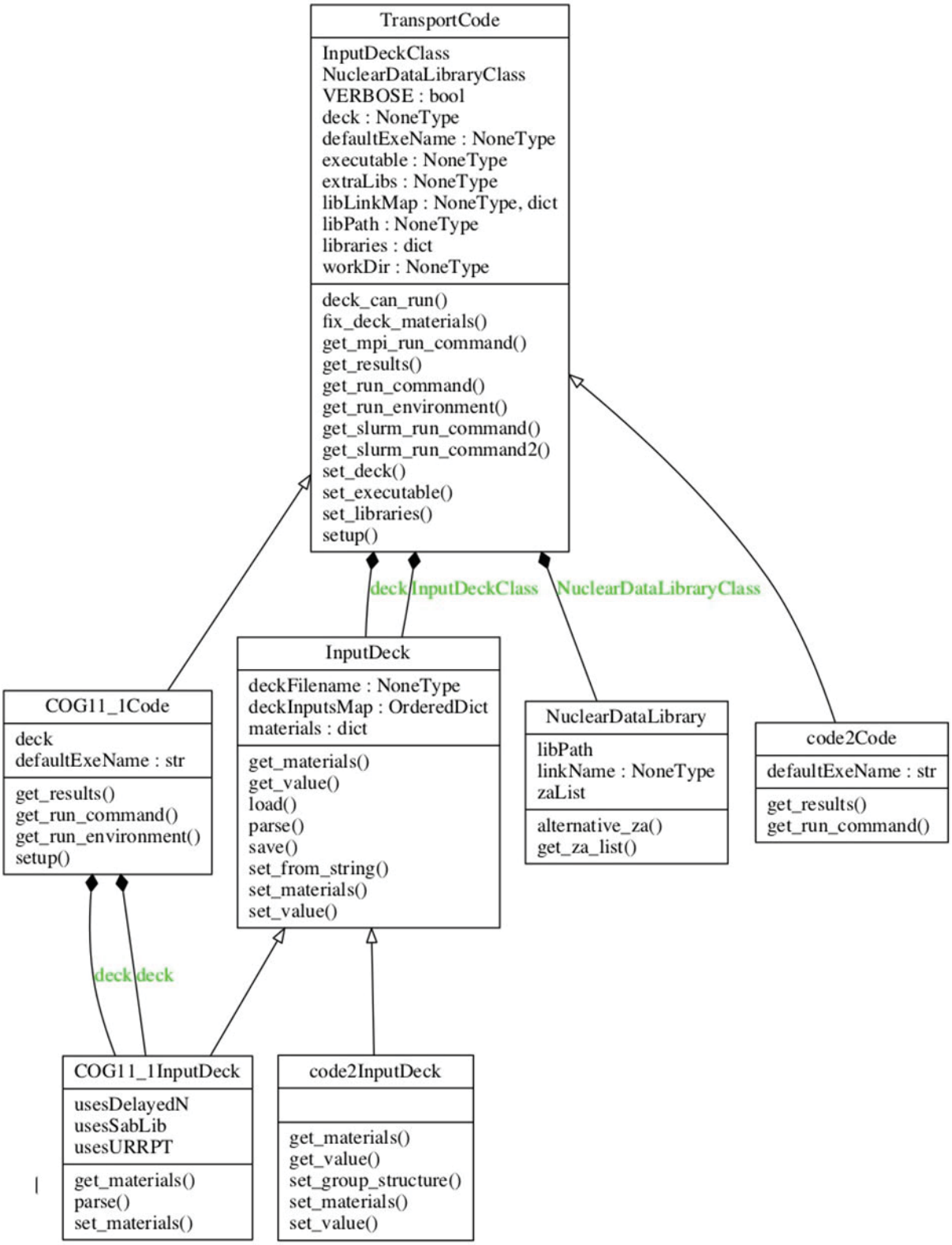

Figure 5: This is a basic layout of the TransportCode class and all of the other classes that inherit from it. We generated the figure using pylint [Pylint2015].

[Lee2014] C. Lee, personal communication (2014)

[Brown2013] D. Brown, M. A. Descalle, P. Vranas cnp_test_suite (2013) [Buildbot2015] Buildbot, http://trac.buildbot.net/wiki/DownloadInstall, (2015)

VII. Acknowledgements

I would like to thank everyone in the National Nuclear Data Center, and especially my mentor David Brown. This project was supported in part by the U.S. Department of Energy, Office of Science, Office of Workforce Development for Teachers and Scientists (WDTS) under the National Science Foundation (NSF).

Optimization of a fast camera with a twenty-nanosecond resolution

Jon Gustafson
Physics Department, Fordham University, Bronx, NY 10458
Andrei Nomerotski
Physics Department, Brookhaven National Lab, Upton, NY 11973

Abstract

A fast camera is an imaging sensor with a time resolution typically on the nanoscale. The main advantage of having a nanosecond resolution camera is the ability to detect multiple events that occur on a nanosecond or greater time scale without having to time-gate the detector. This project's objective was to ascertain how to optimally map light onto the XRI-UNO fast camera detector developed by X-Ray Imatex; more particularly, to determine how to map light emitted from a 40mm phosphor screen onto a 14mm by 14mm XRI-UNO Medipix2/Timepix sensor in such a way that the light is exposed to the entire sensor and that the sensor collects as much light as possible. To do this, we collected magnification and focus data using the Canon 50mm f/1.2 lens, the Canon 50mm f/1.2 speed booster lens, the Canon 85mm f/1.2 lens, and the Navitar 50mm f/0.95 lens in the Fast Imaging Laboratory at Brookhaven National Laboratory's Physics Department. Ultimately with this type of data, we were able to ascertain how to optimally map light onto the sensor. Using Python we plotted demagnification graphs and figured out what distances the lenses would need to be from the screen so that light emitted from the screen would be mapped onto the entire sensor. We also determined how wide the camera mounts would need to be when the lenses were at these different distances by plotting focus graphs. Ultimately, we concluded that the Canon 50mm f/1.2 speed booster lens optimally maps light onto the sensor, as this lens allows the sensor to collect more light than the other lenses while still allowing the light to be mapped onto the entire sensor.

I. Introduction

A. Limitations of Charge-Coupled Devices

The development of fast imaging detectors based on CMOS technology has resulted from the failure of CCDs to effectively image particles during very short time intervals, typically on the nanosecond and microsecond time scale. The main reason why CCDs fail to effectively image particles during small time intervals is because of how a CCD operates. A simple CCD primarily operates by storing charge (generated from incident photons hitting the CCD during an exposure) within pixels and by then transferring that charge between pixels.

The CCD stores charge within the pixels through capacitors. The CCD transfers charge between pixels by switching potentials on a series of gated electrodes positioned on each pixel's surface. In this transfer process, charge is first shifted along the rows of pixels, ultimately placing a charge from the final column of pixels into an output register. The charge is then transferred pixel by pixel along the output register to a charge amplifier that converts the charge to a voltage, which can than be read with external electronics.[1] What makes this principle of operation of a typical CCD limited is the fact that this charge transferring process results in a slow readout process. For example, for particles arriving at a CCD detector over microsecond time periods, the rate at which these particles would arrive at the detector would far exceed the frame rate of a typical CCD.[2] Typical CCDs only have standard frame rates generally on the order of a tens of frames per second.[1]

Fast-framing CCDs that are based on the principle of local charge storage in CCD registers at the pixel level have been developed to address this issue of slow readout times.[3] Each pixel in a fast-framing CCD has a light-sensitive element, as well as memory elements that allow multiple images to be recorded at extremely rapid frame rates before readout.[1] These fast-framing CCD's ultimately are severely limited as well because the number of memory elements in each pixel only allows for approximately tens of frames to be stored.[2] Using a higher numbers of memory elements for each pixel in theory can allow more images to be recorded during an exposure; however this comes at the expense of sensitivity because as the number of memory elements increases, there is less of a photoactive region.

B. Intelligent CMOS Sensors

As stated before, CMOS sensors were developed to address the limitations of CCD sensors. CMOS sensors ultimately addressed these limitations by taking an alternative approach to imaging. This alternative approach was to change the type of pixel used in the detector.

Instead of using the limited CCD pixels that merely acquired and transferred charge, the CMOS detector used active pixels that each had their own photodetector and readout electronics. These CMOS active pixels are oftentimes considered intelligent pixels and this is because of their high density of transistors. Logic functions can be built into each of the CMOS pixels using these transistors ultimately allowing for in-pixel signal processing.[1,3] This in-pixel signal processing is what directly addressed the limitations of typical CCDs. By having in-pixel signal processing, there was a considerable data reduction from the amount of full-frame data that a typical CCD normally would collect,[4] as well as much faster readout times. The in-pixel signal processor allowed for counting at a nanosecond time resolution, thus allowing particles to be imaged during short time intervals. Ultimately, this fast imaging capability of CMOS detectors has opened the door to many new kinds of experiments. This is why optimizing the detector is important. An optimal fast imaging detector produces high quality images and thus is necessary for the success of future experiments.

II. Methods

A. Preparations

In order to determine how to optimally map light emitted from a 40mm phosphor screen onto a 14mm by 14mm Medip-

ix2/Timepix sensor, we decided to collect magnification and focus data with the Canon 50mm f/1.2 lens, the Canon 50mm f/1.2 speed booster lens, the Canon 85mm f/1.2 lens, and the Navitar 50mm f/0.95 lens. However, before collecting this data, we needed to first make some alterations to these lenses. The first alteration we made was adding a 3D printed mount to the back of the Canon 50mm f/1.2 lens, the Canon 50mm f/1.2 speed booster lens, and the Navitar 50mm f/0.95 lens (See Fig. 1. – Fig.4). These camera mounts ultimately allowed the lenses mentioned above to be screwed onto a XYZ stage, thus giving us motional control of the lenses.

The second alteration we made was connecting an Arduino Mega 2560 to the Canon 85mm f/1.2 lens (See Fig. 5.). The primary reason we connected an Arduino to this Canon 85mm f/1.2 lens was to control the focus of the lens. Using a keyboard module with the Arduino, we were able to send signals to this lens and move the focus from infinity to <0.95. We did this by programming the Arduino to map each key press on the keyboard module to a certain time delay between the starting and stopping signals sent to the lens. We then changed the length of the time delay between the starting and stopping signals for different buttons in order to simulate a coarse and fine adjustment for the focus.

With these alterations, we were now ready to start collecting magnification and focus data with our camera lenses.

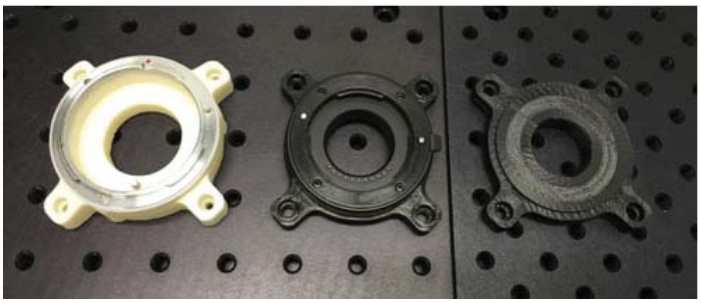

Fig. 1. Image of the 3D printed camera mounts for the Canon 50mm f/1.2 lens, the Canon 50mm f/1.2 speed booster lens, and the Navitar 50mm f/0.95 lens (from left to right).

B. Data Collection

The collection of magnification and focus data with the Canon 50mm f/1.2 lens, the Canon 50mm f/1.2 speed booster lens, the Canon 85mm f/1.2 lens, and the Navitar 50mm f/0.95 lens took place in the Fast Imaging Laboratory at Brookhaven National Laboratory's Physics Department. We utilized a 40mm makeshift screen illuminated with light to simulate the phosphor screen. We then established a reference point (a fixed point) on each of the lenses where distances would be measured (See Fig. 6.).

We then began collecting data by measuring the demagnification factor of the image at different distances between the makeshift screen and the fixed point on the lenses. We collected this demagnification data for all the lenses at both the closest and furthest focus (See Fig. 7. for an illustration of our experimental

Fig. 2. Image of the Canon 50mm f/1.2 lens with the 3D printed camera mount.

Fig. 3. Image of the Canon 50mm f/1.2 speed booster lens with the 3D printed camera mount.

Fig. 4. Image of the Navitar 50mm f/0.95 lens with the 3D printed camera mount.

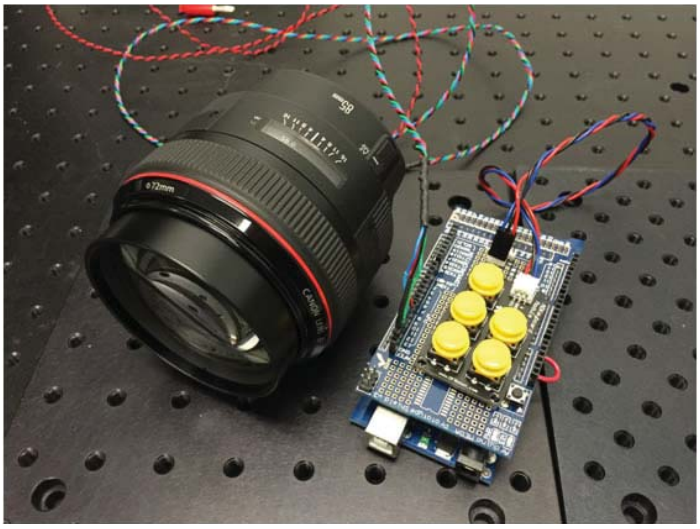

Fig. 5. Image of the Canon 85mm f/1.2 lens with the Arduino Mega 2560 connected. Because of the wires, there was no 3D printed camera mount used.

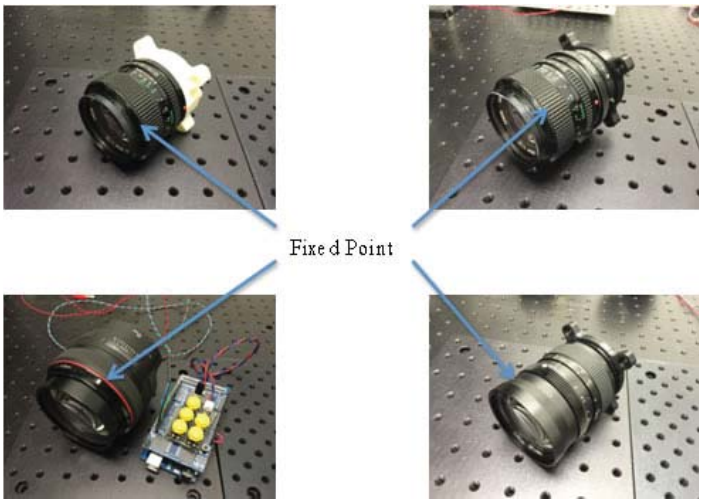

Fig. 6. Image of the fixed point established for each lens. The fixed point serves as a reference point for measured distances.

setup).

After collecting this demagnification data, we then turned our attention towards collecting focus data. To be more specific, we measured the distance between the fixed point on the lenses to the resulting focused image at different distances between the makeshift screen and the fixed point on the lenses. We collected this data again for all the lenses at both the closest and furthest focus (See Fig. 8. for a sketch of the measured distances).

III. Results

A. Demagnification Analysis

After collecting the demagnification data for the Canon 50mm f/1.2 lens, the Canon 50mm f/1.2 speed booster lens, the Canon 85mm f/1.2 lens, and the Navitar 50mm f/0.95 lens, we decided to start our analysis by plotting demagnification factor verses S1 using the Pylab module in Python. We plotted demagnification factor verses S1 graphs for each lens. Since we measured demagnification factor when each lens was at the closest focus and the farthest focus, each graph had two demagnification curves. Ultimately, after analyzing these graphs, we noticed that there was a linear relationship between demagnification factor verses S1, as well as that the closest focus demagnification curve and the farthest focus demagnification curve were just vertical shifts of each other. We then utilized this information to determine how to optimally map light emitted from a 40mm screen onto a 14mm by 14mm sensor. We knew that in order to map a 40mm screen onto a 14mm by 14mm sensor, a demagnification factor of 2.857 was needed. With this understanding, we then found the S1 distance in which the closest focus demagnification curve and the farthest demagnification curve had a value of 2.857 for each lens. We were then able to determine a range of S1 distances for each lens allowing the required 2.857 demagnification factor (See Fig. 9. – Fig. 12.).

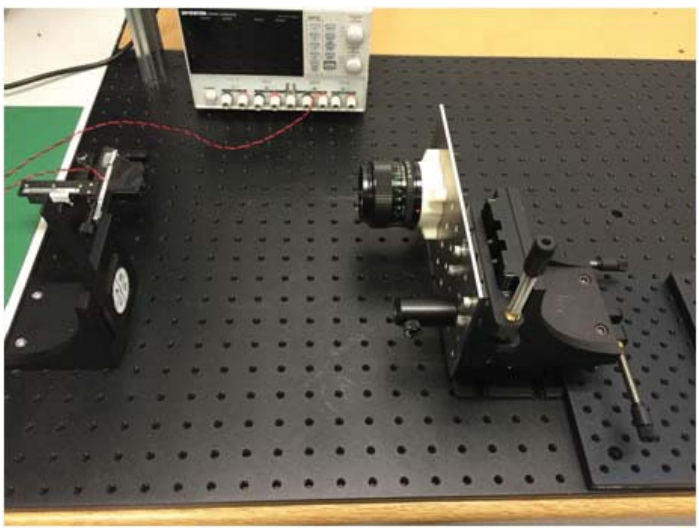

Fig. 7. An illustration of the experimental setup. We used an illuminated makeshift screen as our light source and an XYZ stage to control the movement of the lenses.

Ultimately, from these graphs we were able to conclude that the Canon 50mm f/1.2 speed booster lens optimally maps light onto the sensor. The Canon 50 mm f/1.2 speed booster lens allows for a 2.857 demagnification factor when the distance between the screen and the fixed point on the lens is approximately 10.1cm. The Canon 50mm f/1.2 speed booster lens allows us to collect more light than the other lenses (has smallest S1 distance) while still allowing light to be mapped onto the entire sensor.

B. Focus Analysis

After analyzing the demagnification data, we then turned our attention to the focus data collected with the Canon 50mm f/1.2 lens, the Canon 50mm f/1.2 speed booster lens, the Canon 85mm f/1.2 lens, and the Navitar 50mm f/0.95 lens. To analyze the focus data, we plotted S2 verses S1, using the Pylab module in Python, for each lens. Again, since we measured focus data when each lens was at the closest focus and the farthest focus, each graph had two focus curves. Ultimately, from this data, we were able to determine how wide our camera mounts need to be for each lens in order to map light emitted from the screen onto the entire sensor. From the S1 distances, determined from the demagnification graphs above, that allow for a 2.857 demagnification factor, we found the corresponding S2 distances for each of the lenses (See Fig. 13. – Fig. 16).

Ultimately from these graphs, we were able to conclude that the Canon 50mm f/1.2 speed booster lens requires a mount width dependent on the S2 distance of approximately 8.7cm. This mount

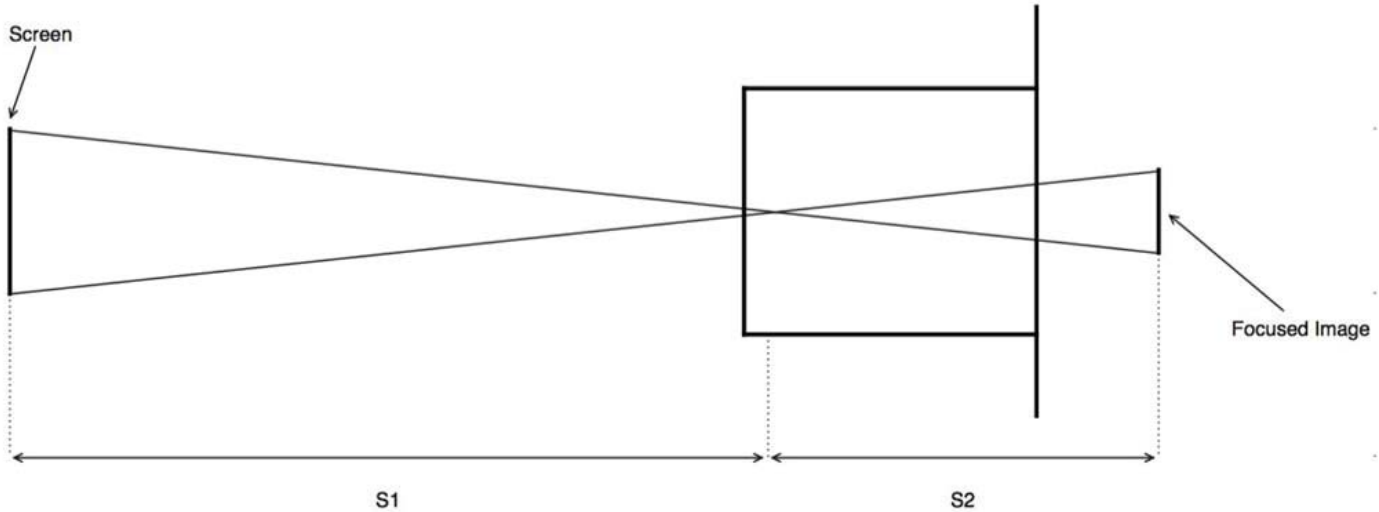

FIG. 8. Sketch illustrating the distances that were measured during data collection. All distances were measured from a fixed point on the lens near the front of the lens.

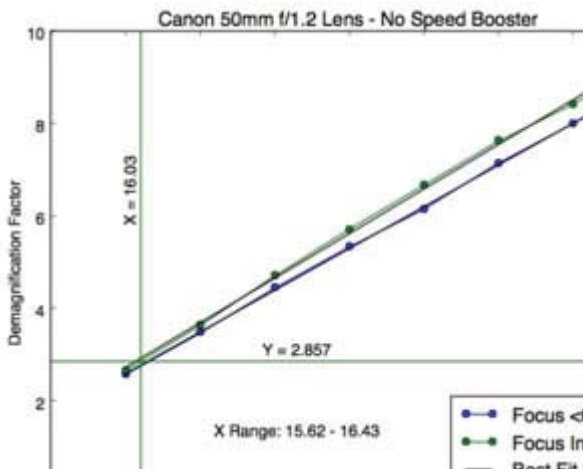

FIG. 9. Plot of demagnification factor verses S1 for the Canon 50mm f/1.2 lens without the speed booster. This plot shows where the fixed point on the lens needs to be in order to map a 40mm screen onto the entire sensor.

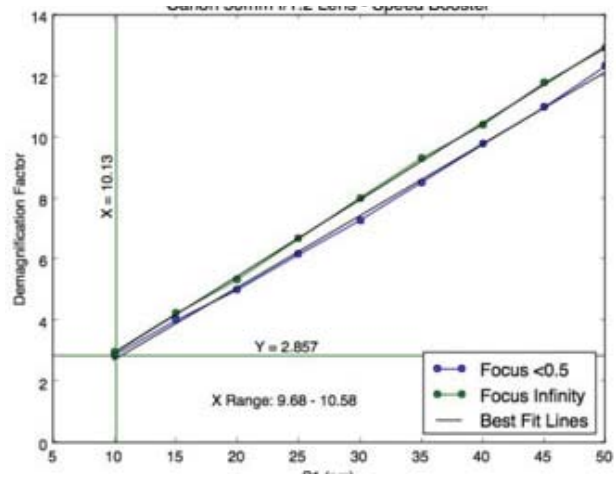

FIG. 10. Plot of demagnification factor verses S1 for the Canon 50mm f/1.2 lens with the speed booster. This plot shows where the fixed point on the lens needs to be in order to map a 40mm screen onto the entire sensor. Note that with the speed booster, the Canon 50mm f/1.2 lens can map light from the 40mm screen onto the entire sensor at a closer S1 distance.

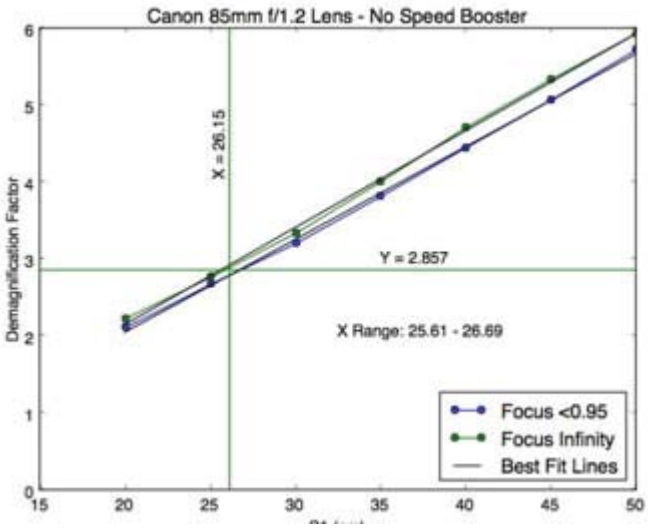

FIG. 11. Plot of demagnification factor verses S1 for the Canon 85mm f/1.2 lens without the speed booster. This plot shows where the fixed point on the lens needs to be in order to map a 40mm screen onto the entire sensor.

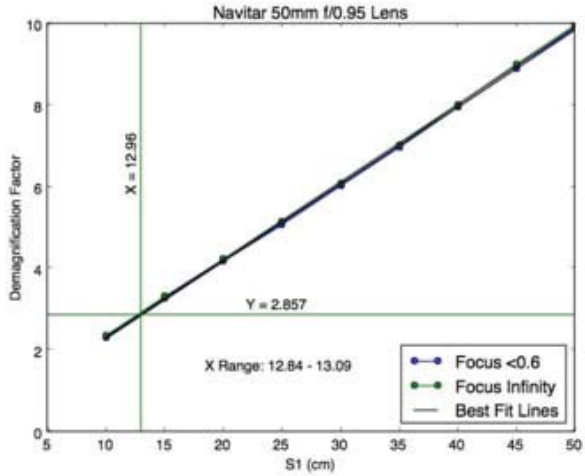

FIG. 12. Plot of demagnification factor verses S1 for the Navitar 50mm f/0.95 lens. This plot shows where the fixed point on the lens needs to be in order to map a 40mm screen onto the entire sensor.

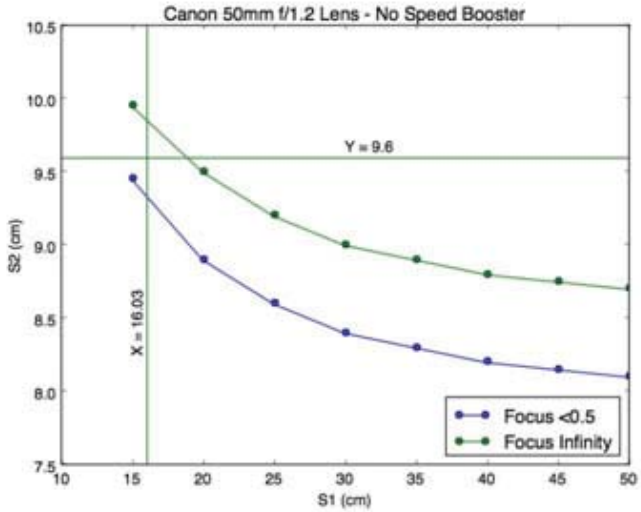

FIG. 13. Plot of S2 verses S1 for the Canon 50mm f/1.2 lens without the speed booster. This shows how far the sensor needs to be from the fixed point on the lens when light from the 40mm screen is mapped onto the entire sensor.

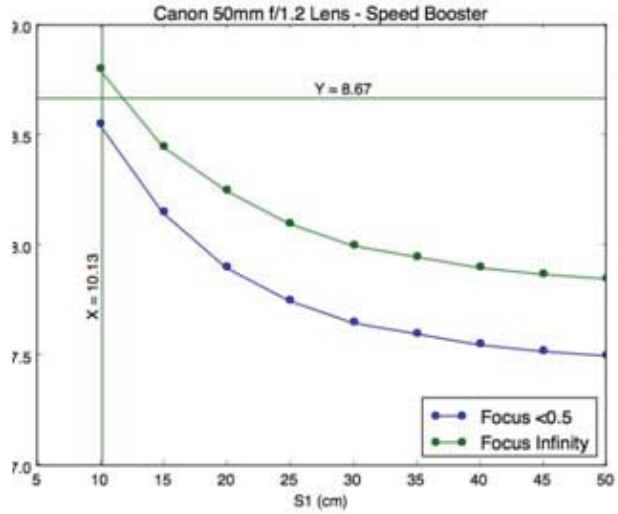

FIG. 14. Plot of S2 verses S1 for the Canon 50mm f/1.2 lens with the speed booster. This shows how far the sensor needs to be from the fixed point on the lens when light from the 40mm screen is mapped onto the entire sensor.

size dependent on the S2 distance results in a focused image when the fixed point of the lens is at 10.1cm away from the screen.

IV. Conclusions

By collecting magnification and focus data with the Canon 50mm f/1.2 lens, the Canon 50mm f/1.2 speed booster lens, the Canon 85mm f/1.2 lens, and the Navitar 50mm f/0.95 lens, we were ultimately able to determine how to optimally map light emitted from a 40mm phosphor screen onto a 14mm by 14mm XRI-UNO Medipix2/Timepix sensor. We concluded that the Canon 50mm f/1.2 speed booster lens maps light emitted from a 40mm screen onto the entire sensor at a S1 distance of approximately 10.1cm, which is closer than the other lenses.

We also concluded that when the Canon 50mm f/1.2 speed booster lens is at this S1 distance, the lens requires a mount width dependent the corresponding S2 distance, 8.7cm.

V. References

[1]Vallance, Claire, Mark Brouard, Alexandra Lauer, Craig S. Slater, Edward Halford, Benjamin Winter, Simon J. King, Jason W. L. Lee, Daniel E. Pooley, Iain Sedgwick, Renato Turchetta, Andrei Nomerotski, Jaya John John, and Laura Hill. "Fast Sensors for Time-of-flight Imaging Applications." Physical Chemistry Chemical Physics 16.2 (2013): 383. Web.

[2]Sedgwick, I; Clark, A; Crooks, J.; Turchetta, R.; Hill, L.; John, J.J.; Nomerotski, A; Pisarczyk, R.; Brouard, M.; Gardiner, S.H.; Halford, E.; Lee, J.; Lipciuc, M.L.; Slater, C.; Vallance, C.; Wilman, E.S.; Winter, B.; Yuen, W. H., "PImMS: A self-triggered, 25ns resolution monolithic CMOS sensor for Time-of-Flight and Imaging Mass Spectrometry," New Circuits and Systems Conference (NEWCAS), 2012 IEEE 10th International , vol., no., pp.497,500, 17-20 June 2012

[3]Nomerotski, A., M. Brouard, E. Campbell, A. Clark, J. Crooks, J. Fopma, J. J. John, A. J. Johnsen, C. Slater, R. Turchetta, C. Vallance, E. Wilman, and W. H. Yuen. "Pixel Imaging Mass Spectrometry with Fast and Intelligent Pixel Detectors." Journal of Instrumentation 5.07 (2010): C07007. Web.

[4]Nomerotski, A., S. Adigun-Boaye, M. Brouard, E. Campbell, A. Clark, J. Crooks, J. J. John, A. J. Johnsen, C. Slater, R. Truchetta, C. Vallance, E. Wilman, and W. H. Yuen. "Pixel Imaging Mass Spectrometry with Fast Silicon Detectors." Nuclear Instruments and Methods in Physics Research Section A: Accelerators, Spectrometers, Detectors and Associated Equipment 633.Supplement 1 (2011): S243-246. Web.

VI. Acknowledgements

This project was supported in part by the U.S. Department of Energy, Office of Science, Office of Workforce Development for Teachers and Scientists (WDTS) under the Science Undergraduate Laboratory Internships Program (SULI).

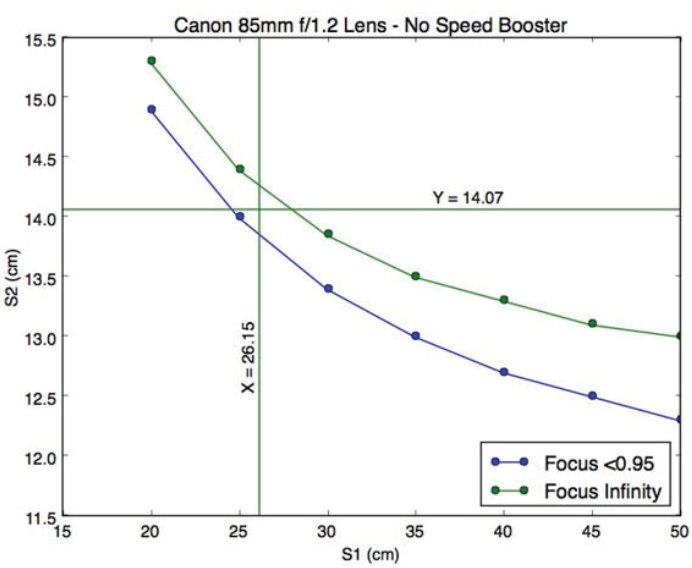

FIG. 15. Plot of S2 verses S1 for the Canon 85mm f/1.2 lens without the speed booster. This shows how far the sensor needs to be from the fixed point on the lens when light from the 40mm screen is mapped onto the entire sensor.

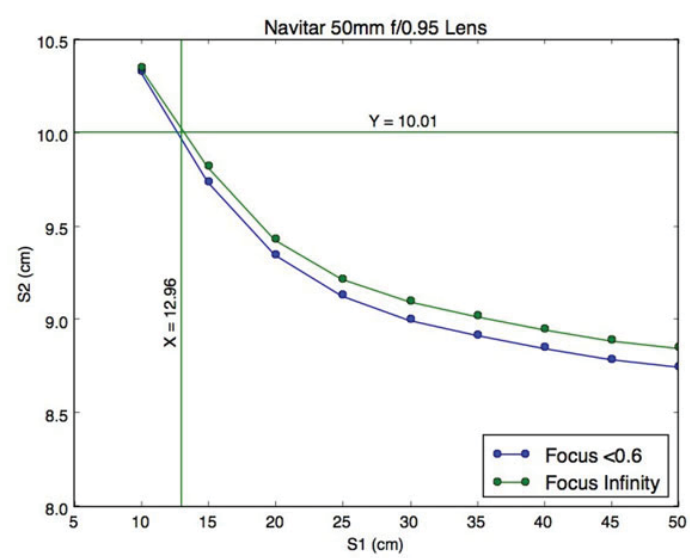

FIG. 16. Plot of S2 verses S1 for the Navitar 50mm f/0.95 lens. This shows how far the sensor needs to be from the fixed point on the lens when light from the 40mm screen is mapped onto the entire sensor.

Drell-Yan studies and simulations at 500 GeV for pp collisions

Samuel George Heppelmann
Physics, Pennsylvania State Univeristy, University Park, PA 16802
Elke Aschenauer
Physics, Brookhaven National Laboratory, Upton, NY 11973

Abstract

Drell-Yan production in the forward region of the STAR experiment will be measured using the implementation of the new Forward PreShower detector, the Forward Meson Spectrometer (FMS), and an additional PostShower detector. Without the additional information of the Pre- and Post Shower, the Drell-Yan signal is indistinguishable from background noise in the FMS region. In order to correctly identify and measure the signal in the forward region, hadron and photon signal contributions to the run 2015 must be suppressed. Signal suppression can be achieved by tagging particle showers from each triggered event and classifying individual particles as hadrons, electrons, or photons. For Drell-Yan, additional cuts must be made using more advance techniques such as Boosted Decision Trees. Drell-Yan can decay into a di-electron or di-muon pair. To test our method, single particle simulations were generated to check the suppression factor and optimize tagging. Additional techniques such as cuts on multiplicity and shower shape will further improve background rejection.

I. Introduction

In pp collisions, the Drell-Yan process occurs when a quark from one proton collides with an anti-quark from the other proton, annihilating into a virtual photon or a Z boson and subsequently decaying into a charged lepton anti-lepton pair. The initial momentum of the quark or anti-quark, at the point of collision, samples the momentum distributions of partons that make up the bound state proton. For high energy, as the relativistic protons pass through one-another, the interaction of the colliding partons with the rest of the proton is small but important.

The Sivers function, which characterizes the impact of initial state interactions between the parton and the protons on the parton distributions associated with transverse spin asymmetries, can be studied for Drell-Yan processes. There is a deep symmetry between the Drell-Yan process, where protons collide to produce lepton pairs and DIS where lepton-proton scattering occurs. However, in the Drell-Yan case, the initial state force interaction force is repulsive while in DIS, the corresponding force is attractive. For this reason, the sign of the spin asymmetry in Drell-Yan is predicted to be the opposite of the corresponding asymmetry in DIS (fig1).

Due to the rarity of Drell-Yan events, the simulation of the both the Drell-Yan process and the large QCD background are crucial to understanding how well we can distinguish the signal from the background. Single particle simulations are first performed with the full STAR detector geometry. Cuts and optimizations using Boosted Decision Trees are performed on the single particle output to separate signal from background. Only DY events above 4 GeV invariant mass are viable signal, under 4 GeV, the background dominates. With a parameterization of the separation, fast simulations are run with 60 million events of the QCD background to classify hadron misidentification and com-

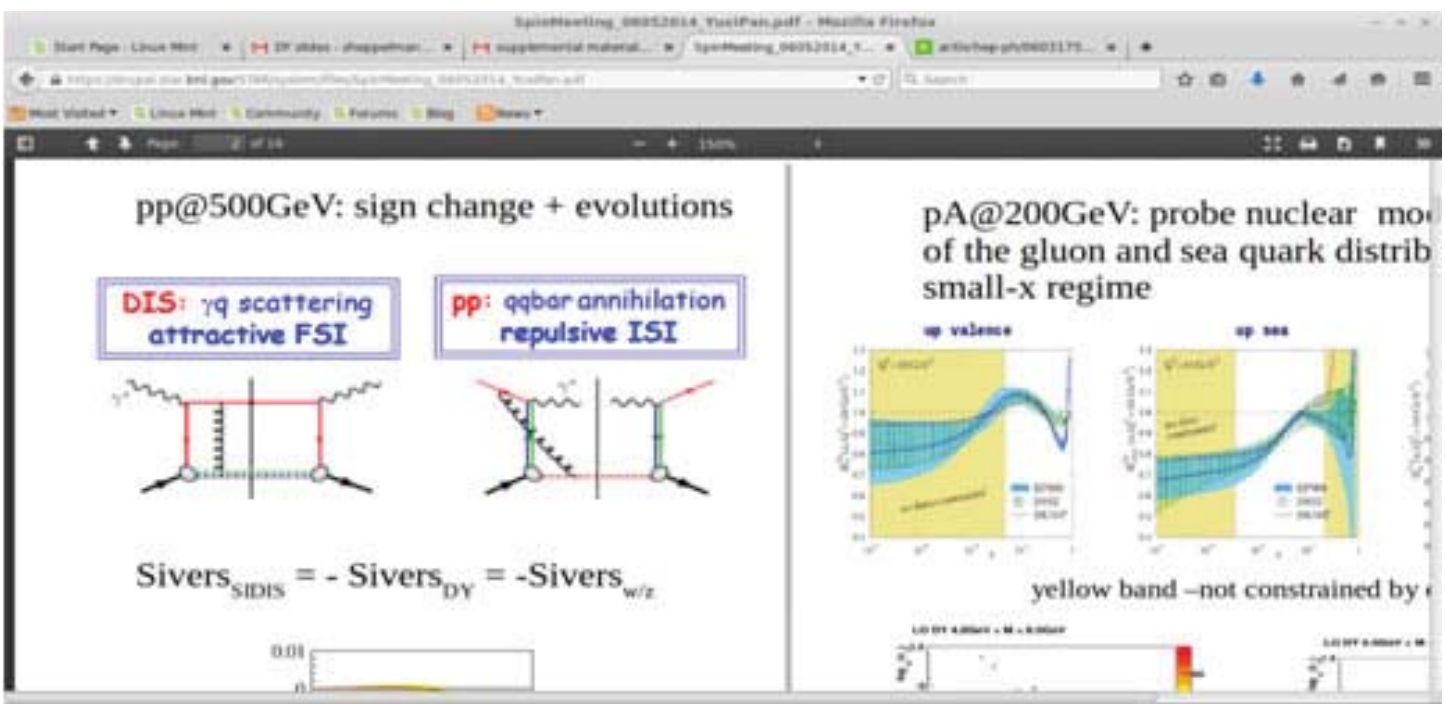

Figure 1.) As seen in the diagram, the Sivers function for DIS has the opposite sign from DY and W/Z creation.

pare with the Drell-Yan Signal.

II. Detectors

The rapidity of interest is $2.5 < \eta < 4.0$. The current STAR detectors in this rapidity are the Forward Meson Spectrometer (fig. 5), pb-glass electromagnetic detector with photomultiplier tubes, and the PreShower(fig. 3), three layers of scintillator with silicon photomultipliers. The FMS is primarily sensitive to electrons and photons while hadrons will leave as minimum ionizing particles. Due to rarity of Drell-Yan events, additional discrimination is required for background separation. A third detector, a scintillator behind the FMS, must be added to detect the Drell-Yan asymmetry. If event energy in the the third detector (postShower) is higher than a set threshold, the event is classified as a hadron. Without additional hadron suppression, the background will dominate the signal. The preShower, which consists of three layers of scintillator, provides photon and charged particle separation. The first two layers provide x and y positioning. A lead converter precedes the third scintillator causing photons to shower in lead and deposit significant energy in the third scintillator. To suppress photons, the signal should have energy deposition in each layer of the preshower. The three detector (preShower, FMS and proposed postShower) setup provides photon/particle separation and electron/hadron discrimination.

III. GEANT4/Single Particle Simulations

Single particle simulations were run in GEANT4 using the STAR geometry framework. The postShower was added to the current STAR geometry. The postShower is a duplicate of the preShower's three scintillator design located behind the FMS. Proposed postShower designs will not included 3 layers, additional layers do not improve hadron discrimination. For the ease of duplicating the design of the preShower the layers were not removed from the simulation.

Five million single particle events were run through the STAR geometry at intervals of 5 GeV ranging from 15 to 60 GeV.

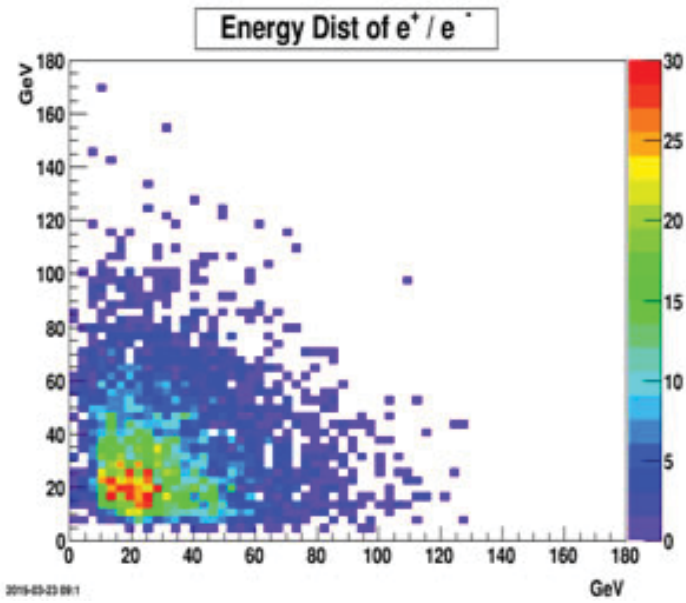

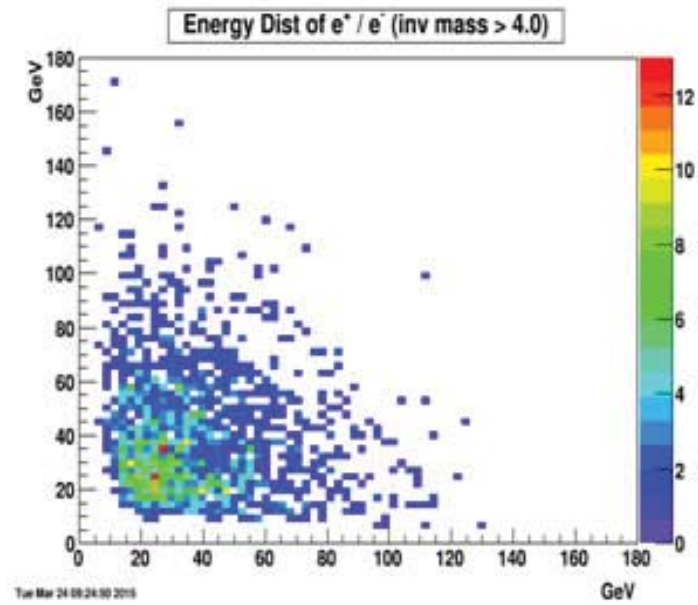

Figure 2 (left) & 3.) Loss of signal from the invariant mass cut can be seen from Pythia simulated energy distribution of the e+ and e-.

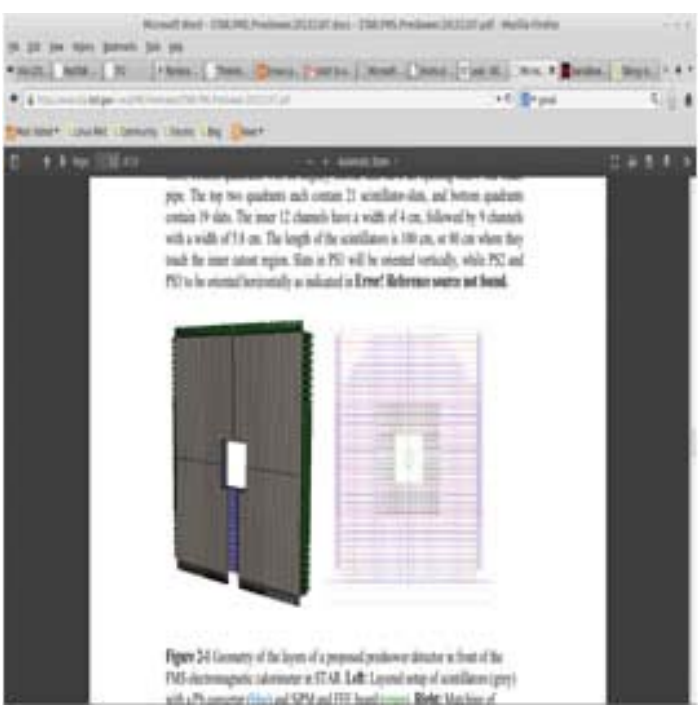

Figure 4 (left) & 5.) Preshower(left) and FMS(right).

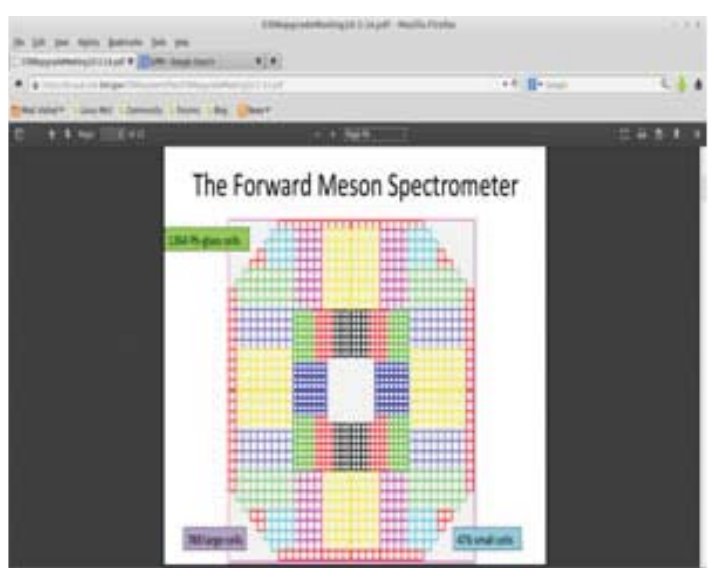

For lower energies, 100,000 provided efficient information to parametrize the rejection of the signal. For higher energies, from 45 to 60 GeV, 1 million events were necessary to parameterize. A parametrized rejection function was established at 90% electron efficiency.

If higher rejection power is required, more single particle events must run at the higher energies (45-60 GeV) which will provide higher rejection while sacrificing electron efficiency. Due to the processing intensive nature of single particle simulations, studies of higher rejections were not conducted.

IV. Boosted Decision Trees

Hard cuts for the background suppression of Drell-Yan is not efficient with the current STAR detectors. To achieve higher suppressions, Boosted Decisions Trees (BDT) were implemented to identify signal from background. A Decision Tree is a sequence of splits which categorize data. Training data is piped through a signal binary split or a node which classify a characteristic of the data. The split groups are then further categorized on additional criteria. This process continues until the final bins are either completely signal or background or the user has set a limit to the depth of the tree.

Boosted Decision Trees are an extension of the decision tree in which several trees are formed from the same training data and systematically assigned weight values to final nodes to improve tree stability. A single decision tree can varying drastically with changes in the a training sample's statistical fluctuations. Boosting will weight final nodes that contain misidentified signal or background and weighting will be used when generating the following tree. The most common weighting technique is adaptive boosting which assigns a common boost weight.

$$a = (1- err)/err$$

For Adaptive Boosting (AdaBoost), the results of a classifier are defined as h(x), x being the tuple of input variables. h(x) is then encoded to be h(x) = +1 and -1 for signal and background respectively. The boosted event classification is then

$$y_{Boost}(x) = \frac{1}{N}\sum_{i}^{N} ln(\alpha_i)\cdot h(x)$$

N is the the total number of classifiers in the collection. Small values of y(x) indicate a background signal while large values signify a signal event.

AdaBoost preforms well on weak classifiers, or decision trees with smaller depth and less discrimination power by themselves. The smaller depth is less prone to over-training data. The process is also improve by slow learning (more trees and smaller boost steps).

For the purposes of Drell-Yan, Boosted Decision Trees (BDT) provide higher discrimination than traditional hard cuts. Prior to creating the BDT, hard cuts were applied to provide additional discrimination. However after comparison, the BDT's performance was not affected by including hard cuts as the cuts are essentially included in the first two nodes of the decision tree.

The BDT process was preformed at 10 different energies from 15 GeV to 60 GeV in increments of 5 GeV. A rejection power, the factor the background can be reduced, was produced at each energy and a fifth order polynomial was fitted to the energies to parameterize the rejection as a function of energy. Rejection is more effective at higher energies where hadrons are less likely misidentified.

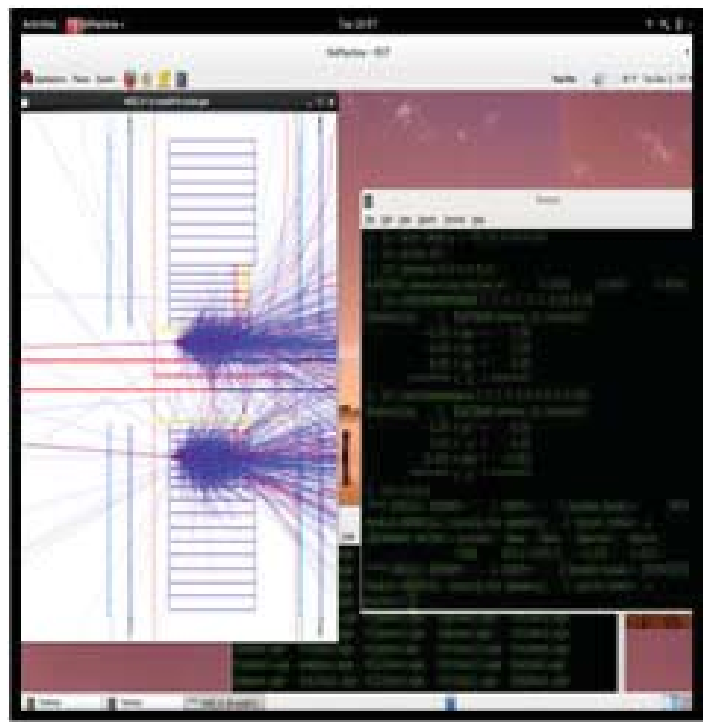

Figure 6.) Tracks from GEANT4 single particle simulation in the STAR geometry. From left to right, the PreShower, FMS and Post-Shower.

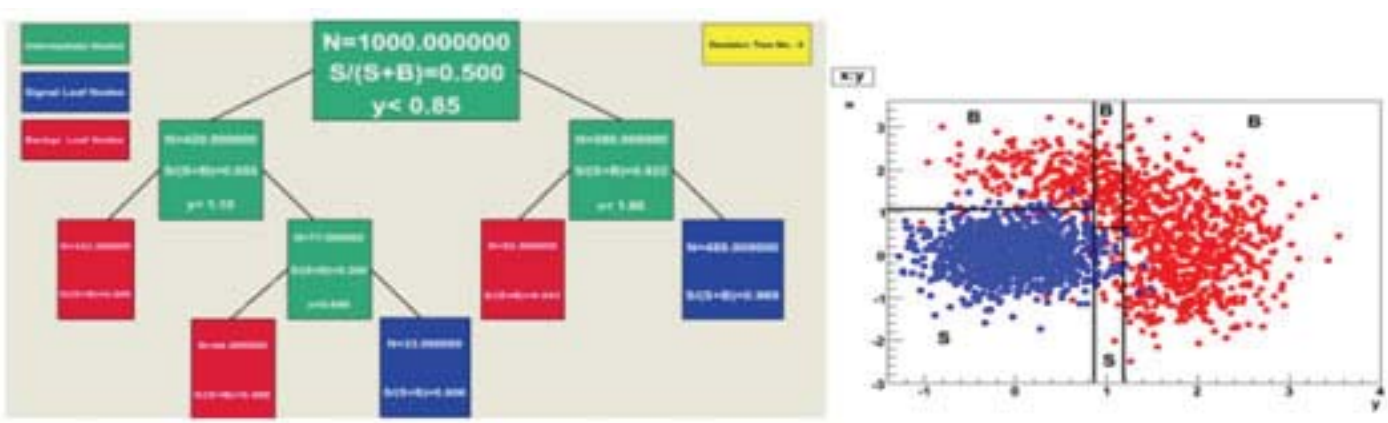

Figure 7&8.) Example of a simple decisions tree making selection cuts on two variables. Second plot (left) shows the improved separation from simple hard cuts.

V. Fast Simulation

Fast Simulation for Drell-Yan consisted of two separate signal and background pythia6.4 simulations. The background simulation included a parametrized e/h discrimination function to label misidentified hadrons. The simulation produced 600 million QCD 2->2 events from $2.7 < \eta < 3.8$. Events were smeared using the simulated detector resolutions of the Forward Meson Spectrometer. The total luminosity summed to 77 ¯pb. Events that were misidentified as hadrons were copied into trees and compared with the Drell-Yan simulation. The pythia6.4 simulation includes:

VI. Included processes

PYTHA SETTING	Process
SetMSUB(11,1)	qq->qq
SetMSUB(12,1)	qqbar->qqbar
SetMSUB(13,1)	qqbar->gg
SetMSUB(28,1)	qg->qg
SetMSUB(53,1)	gg->qqbar
SetMSUB(68,1)	gg->gg

heavy flavour:

PYTHA SETTING	Process
SetMSUB(81,1)	qqbar->QQbar
SetMSUB(82,1)	gg->QQbar
SetMSUB(86,1)	gg->J/psi+g
SetMSUB(87,1)	gg->chi0c+g
SetMSUB(88,1)	gg->chi1c+g
SetMSUB(89,1)	gg->chi2c+g
SetMSUB(106,1)	gg -> J/Psi+p

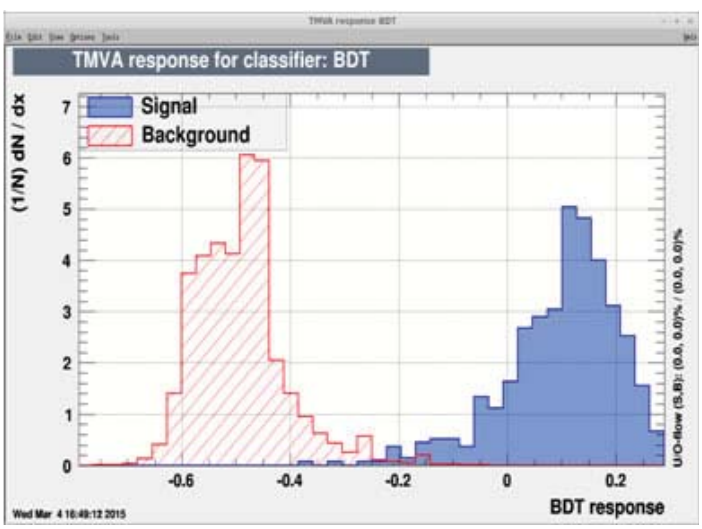

Figure 10.) Signal and background separation from the Boosted Decision Trees, signal in blue and background in red.

Figure 11. UNAVAILABLE) Rejection power as a function of energy with connected error bars. A smooth polynomial was fit to the rejection curve.

After the QCD background was produced, a normalized Drell-Yan signal was generated using the pythia6 settings:

myPythia6->SetMSUB(1,1) //ffbar->gamma*/Z
and all decay channels besides the gamma*->e+e- were turned off.

For both Drell-Yan and QCD simulations, pythia was set to TuneA 500 GeV. For the current results, the QCD 2->2 used ckin3 = 3.0 GeV. Ckin3 is the allowed range of pT values for hard 2->2 QCD processes with pT in the rest frame of the interaction. For further study, 1 million events of QCD backgrounds Ckin3 = 1.0 GeV and Ckin3 = 3.0 GeV were generated to compare the effects of background distribution but differences were negligible.

All fast simulations were run on RCF and stored on GPFS.

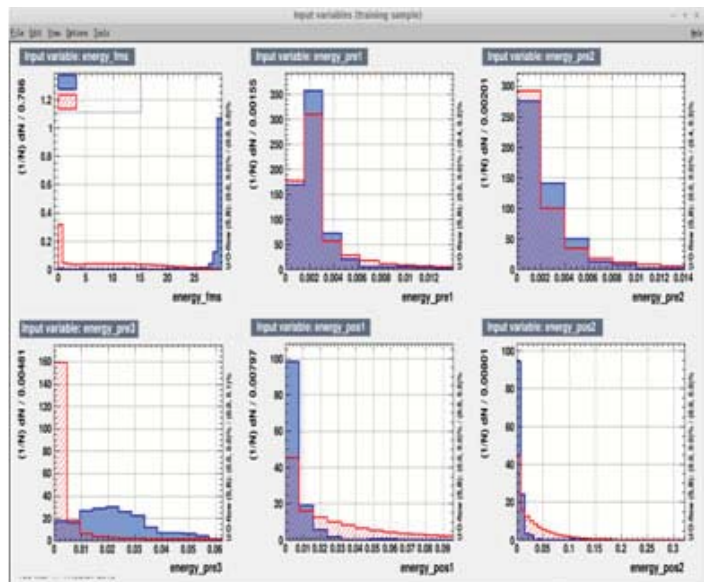

Figure 9.) Energy of Background vs Signal of Drell Yan for each detector. Clockwise from top left, FMS, PreShower Layer 1, PostShower Layer 1, and PreShower Layer 3.

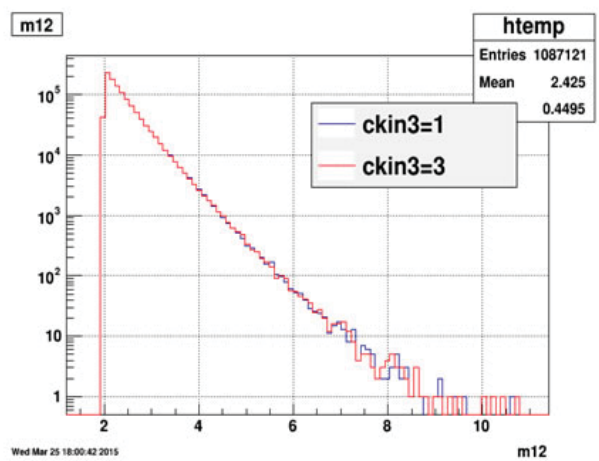

Figure 12.) Invariant mass of background generated from ckin3=1 GeV and ckin3=3 GeV.

VII. Conclusion

The Pythia simulations show the Drell-Yan Signal is measurable at the 500 GeV. The simulation was preformed with 77 ¯pb while plans for 500 GeV pp runs are closer to 400 ¯pb. The installment of the postShower in the 2.5 to 4.0 pseudo-rapidity range is necessary for the background suppression of the QCD 2->2 process.

VIII. References

Yuxi Pan, STAR collaboration, "pp-pA LoI write-up on DY simulations", UCLA, May 16., 2014

IX. Acknowledgements

This project was supported by the U.S. Department of Energy and the Office of Education's SURP program at Brookhaven National Laboratory and the STAR collaborations. A special thanks to Dr. Grant Webb for his contributions and support.

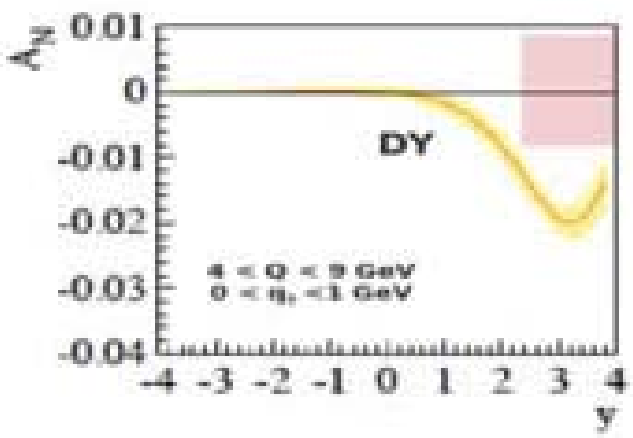

Figure 14.) Error of Drell-Yan measurement for 400 ¯pb luminosity from 2.5 to 4.0 pseudo-rapidity. AN plot from Z. Kang et al. ArXiv:1401.5078. with polarization of 55% and k = 77 ¯pb / 400 ¯pb

$$\delta A_N = \frac{1}{p}\sqrt{\frac{N}{2} * k}$$

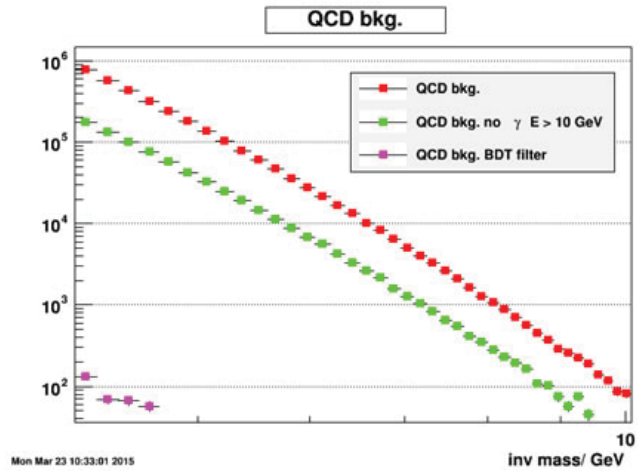

Figure 13.) After the fast simulation of QCD 2->2 and Drell-Yan, the BDT filter can be compared to the original QCD background signal. Full background shown in red, background with energy cut and photon filter shown in green and BDT filter signal in pink.

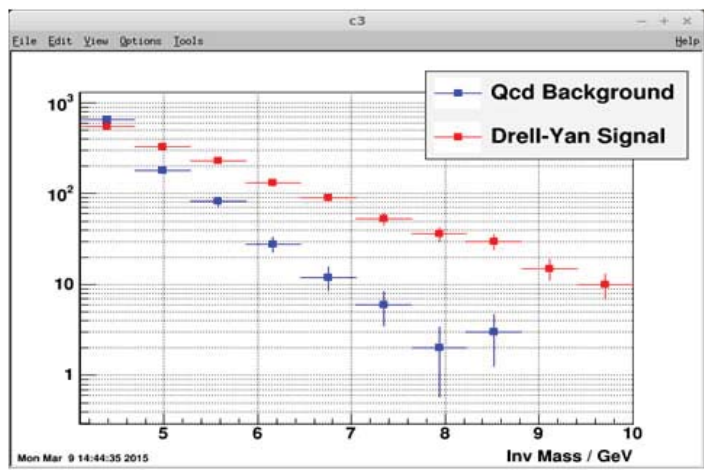

Figure 15.) Plotting the background after BDT rejection (blue) along with a normalized Drell-Yan signal (red).

A study of the performance of non-volatile dual in-line memory

Shawn Hoose
Department of Physics and Astronomy, Stony Brook University, Stony Brook, NY 11794
Antonio Wong and Chris Hollowell
Physics Department, Brookhaven National Laboratory, Upton, NY 11973

Using non-volatile memory has major advantages for data storage and analysis versus standard memory devices since this type of storage prevents data loss in the event of a system crash, and as such is extremely useful for large data analysis, such as for the data that comes from Brookhaven National Laboratory's Relativistic Heavy Ion Collider. I ran two different benchmark suites, iozone and bonnie++, across a single NVMe Solid State Drive under three different file systems, EXT4, EXT3, and XFS. Through these tests, I was able to determine the speed at which a wide array of processes are accomplished, such as randomly reading and writing to memory. By determining which file system is better capable and more suited to analyze and store the data, the time required for experiments to analyze and interpret their data can be significantly diminished, in turn allowing more experiments to be analyzed in a shorter amount of time. I found that while using a single NVMe process, the XFS file system performed the best with block writing, but was comparable to EXT4 with block reading. With 32 NVMe processes running in parallel, I found that EXT4 exceeded the other file systems in block writing, while block reading was uniform across all 3.

We were interested in comparing the speeds of process on different kinds of memory drives. By running the benchmarking suites bonnie++ and iozone across 4 different memory drives and through 3 different file systems on the majority of those drives, we were able to determine which drive and file system combination would be the fastest and most reliable to use for large data analysis; such as that which is present with the Relativistic Heavy Ion Collider. In order to test this, we ran three different tests using the two benchmarching suites across all the machines and file system combinations. The three tests include a single process bonnie++ test, a 32 parallel processes bonnie++ test, and an auto configuration iozone test with a created file size of 150GB. These test allow us to see the performance of the drives and file systems across a large array of processes, including the ones that we were most interested in, block reading and block writing. Graphs for all of the tests that we ran and analyzed are in Appendix A.

Our 4 different drives were a Non-Volatile Memory express (NVMe), a Serial Attached SCSI (SAS), and two Solid State Drives (SSD). A NVMe is an SSD made with an industry standard of attaching SSD's together using a bus. This allows it to be faster than typical SSD's and it eliminates latency and bandwidth limitation imposed by SAS controllers in the middle of Input/Output operations. They are natively supported by the Red Hat Enterprise Linux and Scientific Linux 6.5+ operating systems. SSD's are storage drives that store data using circuits, rather than the moving disk and reading arm of a standard hard drive. This allows for faster reading and writing as well as a longer life time, since there are no moving parts. SSD's also offer the same data retention capabilities that NVMe's offer. SAS's are a protocol for data to be moved on the memory device using the SCSI command set using SCSI attached in series.

On the NVMe and SAS devices we tested three different file systems; EXT4, EXT3, and XFS. When we ran our tests across the SSD devices, however, we only tested the EXT4 file system based on ease and the prior results from the NVMe tests. The difference between the file systems is how the data is stored and referenced hierarchically on the drive; this will affect reading and writing speed depending on where you are referencing the data to and from.

I first began by benchmarking the NVMe and SAS devices on the EXT4 file system. Once that was complete, I would unmount the drives and reinstall a new file system and then run the same exact tests again. For both of the benchmarking suites, we wanted to run a test that would be the most broad and expansive, which turned out to be the default test for both bonnie++ and iozone. In order to run bonnie++ in the way that would be most beneficial and efficient, we ran the command

```
./bonnie++ -d /DRIVE
```

Where "DRIVE" is the mounted directory where the drive is, such as /nvme or /sas. A bash script was written by my mentor to allow for parallel bonnie++ processes to run. This script ran however many parallel process you desired in the desired directory and saved all output to that drive; for our tests we ran 32 parallel processes. For iozone, we wanted to use the automated test, as it would encompass the kind of processes that we wanted to test. In order to get this to run, we ran

```
~/iozone/src/current/iozone -a -g 150G
```

where the first argument is the installed path of iozone; -a tells iozone to run the automated test, while -g 150G tells it that when it creates files to test on, it is to create files of size 150GB. These tests were used across all file system and drive combinations.

Once we had ran all the tests on all the different machine combinations, we had to plot the data and compare. This was easily accomplished via a plotting program that I had written in Python. This program extracts the block read and block write data from the output files and plots them using matplotlib. The graphs are then saved to your current directory under a name that you specify. I was primarily interested in comparing the speeds of the NVMe and the SSD's. This was reinforced when the NVMe was compared against the SAS drive and it was shown that the SAS drive speeds did not come close to the NVMe drive, allowing us to focus on the SSD's and NVMe drives.

When comparing the NVMe to the SAS drives, I was able to compare them across all 3 file systems. It was very clear that the SAS drive had a much poorer performance across all aspects as compared to the NVMe drive. The NVMe drive out performed the SAS drive on all three file systems, whether running a single process or running 32 parallel processes by a large margin, anywhere from 4 times faster (Single processor EXT4 block write speed) to

25 times faster (32 Parallel processes EXT3 block read speed). This allowed me to dismiss the SAS results for future comparisons.

The next task was to compare the two different SSD's in order to see which one performed better, and then compare that one to the NVMe device. We tested two SSD's: One made by Samsung and one made by Crucial. We installed the EXT4 file system on both drives and began running our three standard tests again. By comparing the bonnie++ results again, I found that for a single process the Samsung SSD had a faster block write speed, while the two drives had similar block read speeds. For the 32 parallel processes, however, I found that yet again the Samsung outperformed the Crucial drive but with a faster block read while both of them had similar block write speeds. Now it was time to compare the SSD's to the NVMe device. Across both the single process and the 32 parallel processes it was found that the NVMe device outperformed both SSD's by a decent margin. The NVMe performed twice as well for the single process in block reading and only 150 MB/s faster for block write. For 32 parallel processes, however, the NVMe device performed 4 times faster for block read and two times faster for block write against both SSD devices.

To help with the analysis of the data and to ease the process, I wrote a program to help plot the data. This program is written in Python, uses matplotlib to plot the data, and pyGTK to create a graphical user interface (GUI). This program reads through bonnie++ output files for the block read and block write data values. It then creates the plot with the appropriate user selected Y-axis values (between KB/s or MB/s), user defined plot title, and user defined filename to save as. The output plot is saved as a .png in the current working directory. The plot is also displayed in the current GUI window and may be cleared and different files plotted. You can select a large number of files either from the GUI itself or you can name their path in the command line when initially running the plotting program.

After the analysis of all of our results, it was clear that the NVMe devices perform much better than SSD's and SAS devices. The NVMe device performed roughly 4 times better on average than the SAS devices that are currently in use; meaning that if it is cost efficient, that a single NVMe device can replace 4 SAS drives, which would also allow for 4 times as many drives in the same physical space. The only drawback is that NVMe drives are relatively new and, as such, are costly. The transition from SAS drives to NVMe devices is the proper direction in the near future, with the proper funding.

Understanding the polarization switching exhibited by Moth-Eye Nanostructures

Alexander S. Kaiser
Department of Physics, University of Maryland, Baltimore County, Baltimore, MD 21250
Andreas C. Liapis and Chuck T. Black
Center of Functional Nanomaterials, Brookhaven National Laboratory, Upton, NY 11973
Matthew D. Eisaman
Sustainable Energy Technologies Department, Brookhaven National Laboratory, Upton, NY, 11973

Abstract

Moth-eye nanostructures provide broadband anti-reflection (AR) capabilities that have been shown to create more efficient solar cells, while also having other applications such as military camouflage. These structures are fabricated using block copolymer self-assembly, an AlOx mask, and then selective removal of certain nanoscale regions on a silicon surface through plasma etching, resulting in a series of densely packed cones with sub-wavelength height. While the AR capabilities of these structures are well known, behavioral polarization switching has been observed between orthogonal linear polarizations (s- and p-polarizations) as the height of the moth-eye nanostructures increases. To determine if the structure is changing the polarization of light, we have set up a fully automated experiment that measures the power of reflected light that passes through a rotating quarter-wave plate and a polarization analyzer. We then use this to measure reflection as a function of angle of incidence for a number of different wavelengths, as well as to characterize the polarization state of the reflected beam. This phenomenon has been documented before, but the explanations are complicated and somewhat unclear. We believe that by doing this analysis we will be able to explain this more clearly, and in a simplified manner.

I. Introduction and Objectives

Solar cells are a huge area of research because of their role in the renewable energy industry. Solar cells are made using the following premise: an air – silicon interface has high reflectance because of the large index contrast. To reduce this reflection, solar cells introduce a thin layer of a material that has some intermediate index (e.g. Si3N4) and some set thickness. The downfall of this method is that this thin layer is tuned to reduce reflection for a particular wavelength, and does not work well for a broad range of wavelengths.

Moth-Eye Nanostructures resolve these problems by creating an index gradient that gradually moves from the index of air to the index of silicon. By doing this, the material is broadband, meaning it works for many wavelengths, and it has been shown that it can further reduce reflection over large range of angles. The structures are fabricated through block copolymer self-assembly and plasma etching, which allows precise control over the texture's lateral feature size in the range of 10 – 70 nm, vertical profile and feature density.1 In doing reflection measurements of these structures, we found that at a particular cone height, we find what looks like polarization switching. Because there is currently no explanation for this, we decided to find look into this and see if light reflecting off of these structures causes the polarization of the light to change.

II. Methods

The first order of business was to create a setup, along with LabVIEW code, in order to measure the reflectance versus angle of incidence for these structures. The setup that we made can be seen in figure 1. This setup works with the beam moving through a combination of a half-wave plate and polarizer, which allows us to control the power and polarization of the beam. Following this, we have can put in another combination of a half-wave plate and polarizer to switch to an orthogonal polarization. Lastly, we have the sample mounted on a rotation stage and allow it to rotate between around 5˚ and 85 ˚. We then measure the reflected power as a function of this angle and plot it. After plotting it, we were able to plot it against the TMM theory that was created by using parameters such has cone height and pitch, as well as wavelength.

Later on, we wanted to find a direct way to measure the polar-

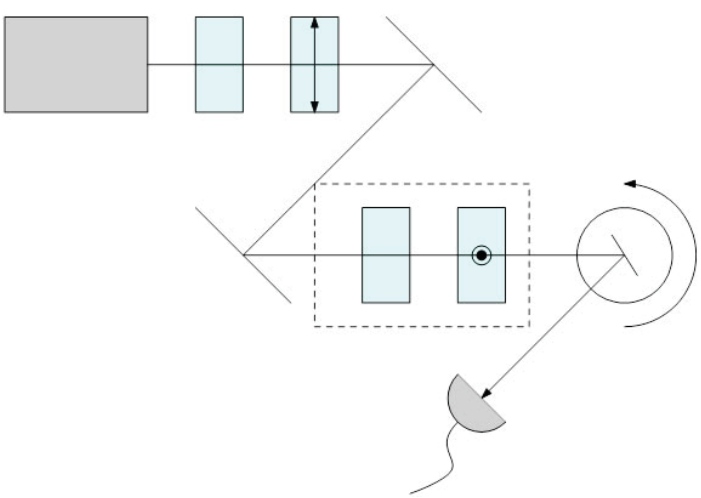

Figure 1. This is the Reflectance measurement setup. Moving from the top left to bottom: laser, half-wave plate, polarizer, two mirrors, another half-wave plate, polarizer, sample mounted on a rotation stage, and lastly a silicon detector.

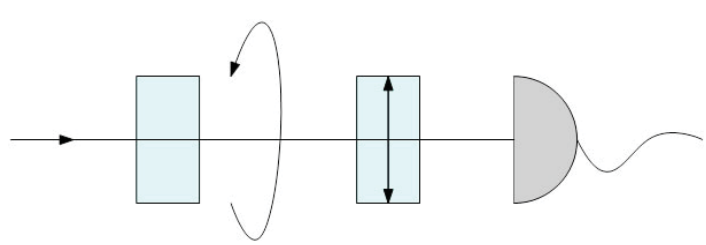

Figure 2. This is the polarimeter that we built. It is a rotating quarter-wave plate followed by a polarizer.

ization of the reflected light and compare it to the polarization of the incident light. To do this, we began with building a polarimeter, which is shown in figure 2. This setup is a quarter-wave plate that rotates from 0˚ to 360˚, followed by a polarizer and then a detector. We then measure the power as a function of quarter-wave plate angle and plot it. In doing this, we find that the function is of the following form:

$$P(\theta) = A + B\,Sin[2(\theta+E)] + C\,Cos[4(\theta+E)] + D\,Sin[4(\theta+E)] \quad (1)$$

Knowing this form of the curve, we can use Fourier series techniques to determine Stokes parameters. Stokes parameters are a set of four numbers that represent the polarization of the reflected light and will allow us to finally determine whether or not the polarization of light changes upon reflection.

Working through the math, we were able to find that the Stokes parameters are:

$$S_0 = A - C$$
$$S_1 = 2C$$
$$S_2 = 2D$$
$$S_3 = B \quad (2)$$

Using all of this information, we should be able to find all of the information that is required to fully understand this phenomenon that we are seeing.

III. Results

The first set of results that we looked at were the reflectance versus angle data. We made these measurements for pure silicon and compared this to Moth-Eye Nanostructure samples that had various etch times (corresponding to nanocone heights) that can be seen in figures four through eight.

The first thing that we can say is that as the nanocone height

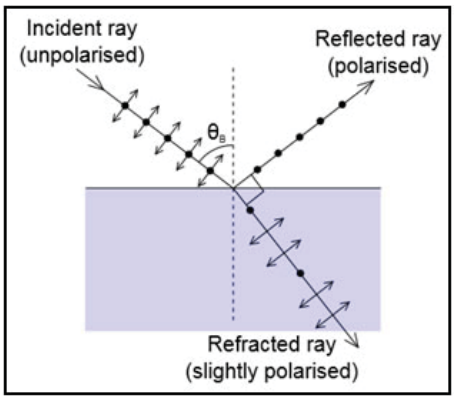

Figure 3. Picture highlighting the concept of Brewster's Angle. Via Wikipedia Commons

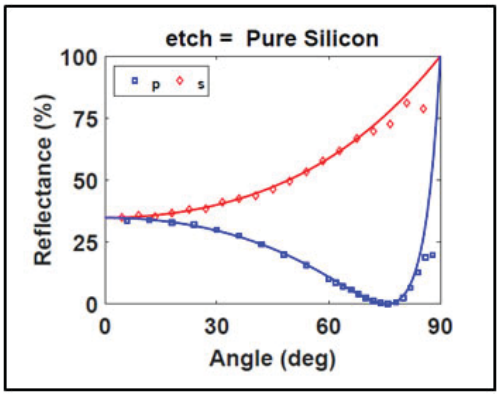

Figure 4. Reflectance data for pure silicon

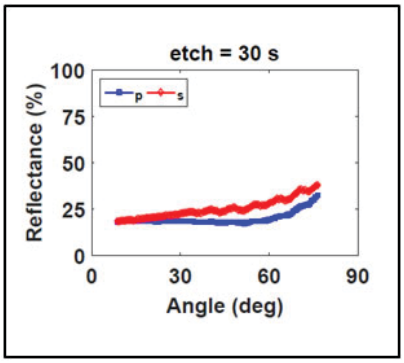

Figure 5. 30s etch time sample, corresponds to about 60 nm tall cones

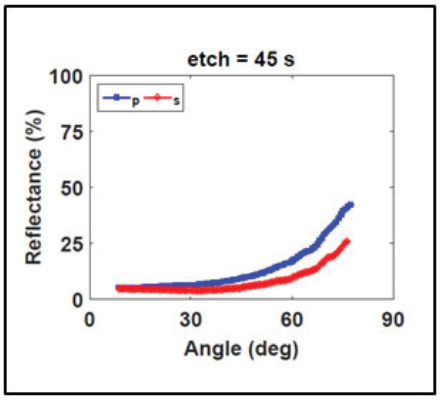

Figure 6. 45s etch time sample, corresponds to about 100 nm tall cones

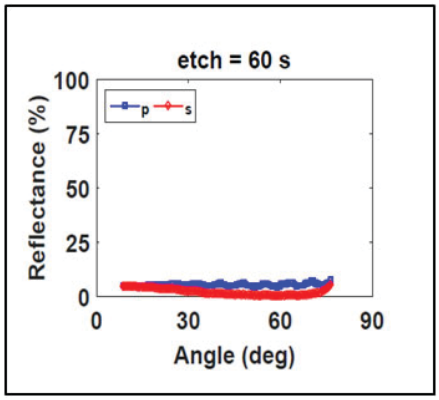

Figure 7. 60s etch time sample, corresponds to about 150 nm tall cones

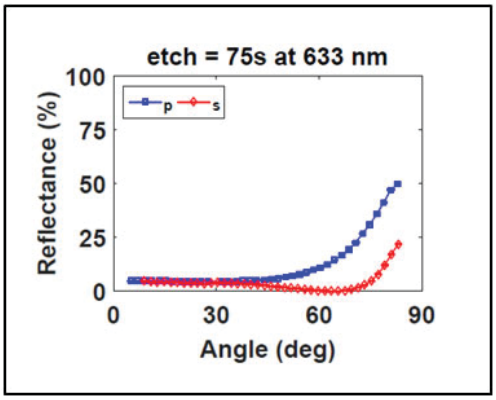

Figure 8. 75s etch time sample, corresponds to about 200 nm tall cones

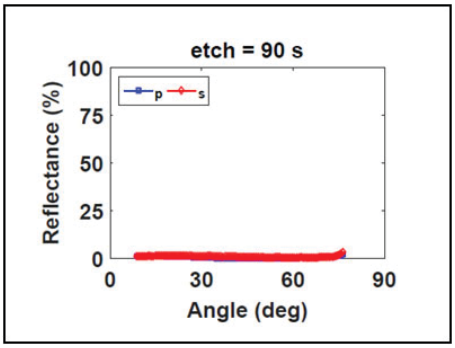

Figure 9. 90s etch time sample, corresponds to about 250 nm tall cones

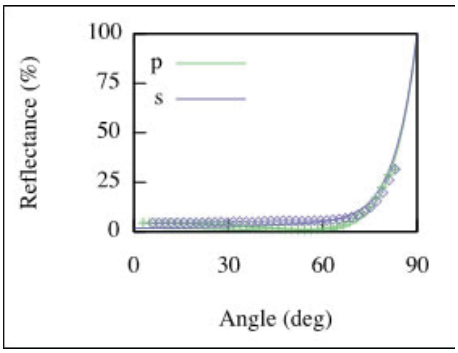

Figure 10. This is reflectance data for sample of 200 nm cone height at 532 nm.

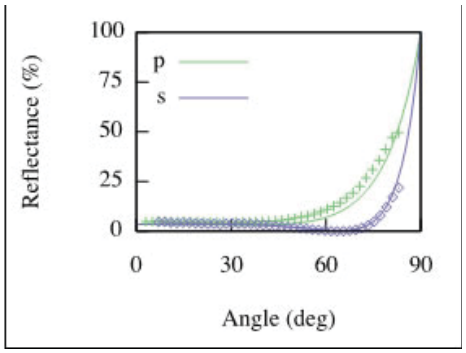

Figure 11. This is reflectance data for sample of 200 nm cone height at 633 nm.

increases, we find that the reflection decreases drastically. We even see for the 250 nm tall sample that it appears to have ~1% reflection for a large range of angles.

Looking back at figure four, we see that there is a point of zero reflection at around 75˚. This angle is called Brewster's angle. This angle is a physical phenomenon that can be explained with the help of figure 3. Using this figure, we can define a couple of different things: plane of incidence, s-polarization and p-polarization. The plane of incidence is the plane that is formed by the incident and reflected beams, s-polarization refers to the polarization of the light that is perpendicular to this plane and p-polarization refers to the polarization of the light that is parallel to this plane. We find that the Brewster angle occurs for the p-polarization at the angle where the polarization is in the same direction as direction of the beam because this is a violation of Maxwell's equations, thus giving us zero reflection.

Now, we want to compare figure 4 and figure 8. In figure 4, as mentioned before, we see a Brewster angle around 75˚ for p-polarization. But, looking at figure 8, we see what looks like a Brewster angle, around 65˚, for s-polarization. And this brings up our primary question: is reflection off of these structures causing the polarization of incident light to change?

Unfortunately, we were not able to come to a certain answer to this question. But, in the meantime, we looked at the same sample for two different wavelengths. This can be seen in figures 10 and 11. In these figures, we can see that for the data at 633 nm that s-polarization seems to have the Brewster angle noted before. But, with the data at 532 nm, we notice that the reflectance for p-polarization is again lower than that of the s-polarization.

So, we believe we see this because of an anisotropy of the material. By that, we mean that as the two different polarizations that interact with the material behave differently as we vary the wavelength. This anisotropy is displayed in figure 12.

Looking at this plot, we see that the s- and p-polarizations have minimum reflectance at different wavelengths. It turns out that s-polarization has a minimum at around 532 nm, while p-polarization has a minimum around 633 nm. And this is what we are really seeing as the "Brewster angle."

While we believe that this is the explanation for exactly what we are seeing, we wouldn't be doing our jobs if we stopped there.

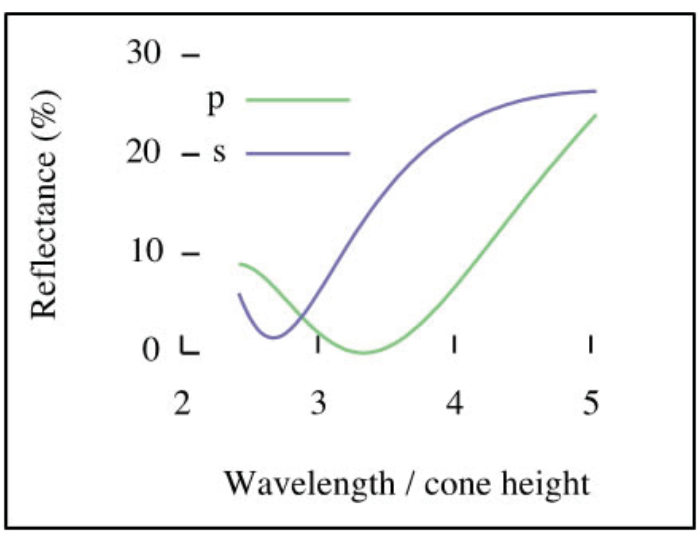

Figure 12. Plot of reflectance as a function of wavelength divided by cone height for s- and p-polarizations

So, we built a polarimeter that is shown previously in figure 2. This will allow us to measure the polarization state of the light and compare it to the incident polarization moving forward.

IV. Conclusion

This research has taught us a lot of different things about Moth-Eye Nanostructures and its optical properties. The first thing that we can conclude about these structures is that they can serve as very good AR coatings. We found that they could replace current AR coatings for a few reasons: these structures are broadband while current AR coatings only work for a single wavelength. In addition, these structures work for a broad range of angles where as the ones being used now do not.

While we were not able to make any definitive conclusions about the polarization switching that was previously observed, we are very close to being able to make a definitive conclusion. Again, we believe that our explanation is one that makes sense and actually can explain this phenomenon in a much simpler way than it has in the past. Because of progress that was made this summer, we believe that we can actually publish a paper on everything that we have seen and collected.

V. Acknowledgements

This research used resources of the Center for Functional Nanomaterials, which is a U.S. DOE Office of Science User Facility, at Brookhaven National Laboratory under Contract No. DE-SC0012704. This work was partially supported by the U.S. Department of Energy, Sustainable Energies Technology Department under Contract No. DE-AC02-98CH10886. This project was partially supported by the U.S. Department of Energy, Office of Science, Office of Workforce Development for Teachers and Scientists (WDTS) under the Science Undergraduate Laboratory Internships Program (SULI).

VI. References

[1]Rahman, A., et al., Nat Comms 6, 5963 (2015).

Thick CCD sensor characterization using interferometry techniques

Alexander Karlis
Physics Department, Manhattan College, New York, NY 10471
Peter Takacs
Instrumentation Division, Brookhaven National Laboratory, Upton, NY 11973

Abstract

The Large Synoptic Survey Telescope (LSST), being built in a remote location deep within Chile, will provide a new way at looking into deep space, probing mysteries like Dark Matter, Dark Energy, and Gravitational Waves. Such sophisticated devices require even more sophisticated technology; hence, the development of the 3200 Megapixel digital camera inside the LSST. Another name for all digital cameras are Charge Coupled Devices (CCD). These CCD's need to be characterized in a fashion that provides the user fruitful information about how well the incoming light is being read by the sensors, also known as the Modulation Transfer Function (MTF). The MTF is used to characterize the process by observing the response of the sensor when a system of fringe-pattern sinusoids with variable spatial frequency is projected onto the pixels of the CCD. The MTF is, in essence, a 'goodness test'. The sinusoidal patterns are produced using a single-mode fiber source in a simple configuration of the Michelson interferometer; tilting one of the mirrors, when the optical path difference between both arms is zero, produces fringes. Pictures were taken of the fringe pattern projected on the CCD sensor and put into a program Fringe Projector, in which, calculates the MTF of the silicon inside the CCD. I used the interferometer to produce these fringes on the CCD sensor, captured pictures of the fringes, and then ran the data through the Fringe Projector program. I have learned a multitude of skills and nuances that goes on in the laboratory here at Brookhaven such as interferometry, signal processing and computer skills. The optical design software Zemax was used to assist in the modeling of the interferometer and Mathematica was used to develop the Fringe Projector code.

I. Background

A. Large Synoptic Survey Telescope

The Large Synoptic Survey Telescope (LSST) is going to be one of the most pivotal pieces of telescopic machinery of all time. Upon its completion, it will be surveying the entire night's sky and beyond, into the furthest reaches of the Universe. Current mysteries like Dark Matter, Dark Energy, and Gravitational Waves are just one of many subjects that will be probed with the advanced capabilities of the LSST's renowned technology. The LSST requires some of the world's most sophisticated cameras and inside those digital cameras, are Charge Coupled Devices, or CCDs. The goal is to measure the resolution of the LSST's Charge Coupled Devices, or CCDs. CCDs are nothing more than just digital cameras. Now, what makes these CCDs special is the fact that they are thick Silicon CCDs, opposed to, a modern camera which have thin Silicon layer. The reasoning behind the thick silicon layer, is a trade-off between different functions that the thick CCD can achieve opposed to its thin counterpart. The thick Silicon CCD allows a more accurate capturing of higher energy photons, and because of the thickness of the Silicon CCDs, charge diffusion becomes relevant. Charge diffusion means that incoming light does not only interact with one pixel, but is spread over a few pixel arrays. And the reason this is happening is because different wavelengths of light has its own penetration depth.

II. Methods

A. Project Overview

This experiment was designed to characterize the pixel sensor by way of the modulation transfer function (MTF). This form of characterization requires that the MTF be measured over a range of spatial frequencies. The way that proved to be suitable and, not too intricate, was the way of an interferometer, in particular, a Michelson Interferometer. In a Michelson interferometer, a fringe pattern is usually produced when one of the arms in the interferometer is displaced; resulting in a change of optical path length, or distance that the light has to travel. In this case, fringes are produced when one of the mirrors is being tilted, as shown in figure (1). A wave from the source, S1, propagates to the beamsplitter, BS. Then the beamsplitter, cuts the propagating wave's amplitude in half, reflecting one half toward the stationary mirror, M2, and the other half to the tilted mirror, M2. Both halves of the wave reflect from their respective mirrors, recombine, and inter-

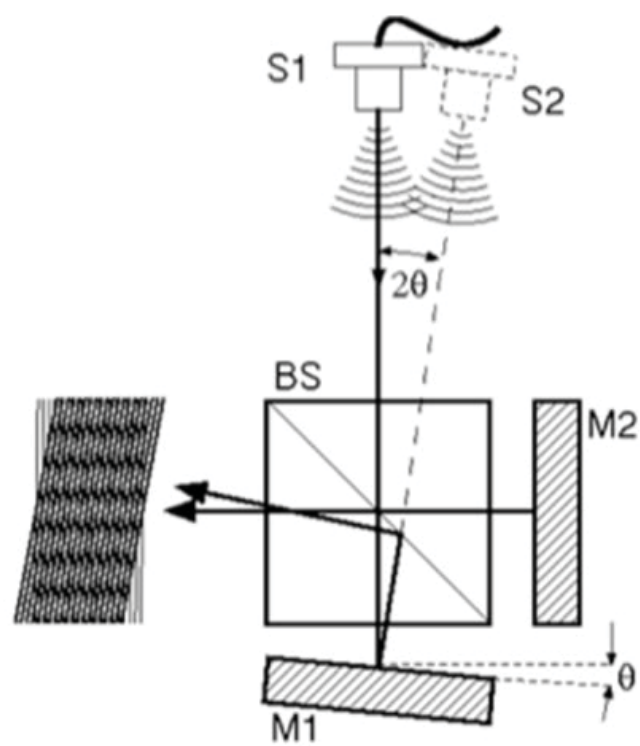

(Figure 1) This diagram of the interferometer portrays the way in which fringes are displayed when mirror 1 (M1) is tilted. [1]

fere with each other; thus producing constructive and destructive interference fringes. The key to producing fringes in this Michelson interferometer was to make sure that the Optical Path Length between both arms of the interferometer was zero. By using the interferometer with diverging single-mode optical fiber of 532nm, a fringe pattern of variable frequency was emitted onto the sensors when a certain amount of tilt was applied to mirror M1.

B. Modeling

In order to accurately gain a fair assessment of the output signal on the CCD sensors, a model was built in an optical design program called Zemax. Zemax provided a real world optical set-up of the experiment, and was able to demonstrate the errors that sometimes become apparent in experimental work. The perfect beamsplitter cube consists of two 45° triangular prisms cemented together on their respective hypotenuse sides. Due to some imperfections in the manufacturing of optical equipment, it was necessary to tweak the angles of the two prisms to be imperfect. This imperfect set-up provided ghost images that proved to be nuisance in data gathering process. Beamsplitter cubes provide back-reflection, reflections due to the reflective nature of glass. These are undesirable because they provide unwanted noise in Power Spectral Density (PSD) plots. PSDs are plots of power versus spatial frequency, and in this case provide a magnitude of the spectral line that appears at the frequency in the interference pattern corresponding to the mirror tilt angle [1]. Nonetheless, the Newport© website provides that the error in a beamsplitter cube could have a reflected and transmitted beam deviance of ±5 arc minutes. The newly modified beamsplitters were then added into the interferometer model. Figure (2) and Figure (3) provide a look at the difference in interference patterns that have two different prisms for the beamsplitters.

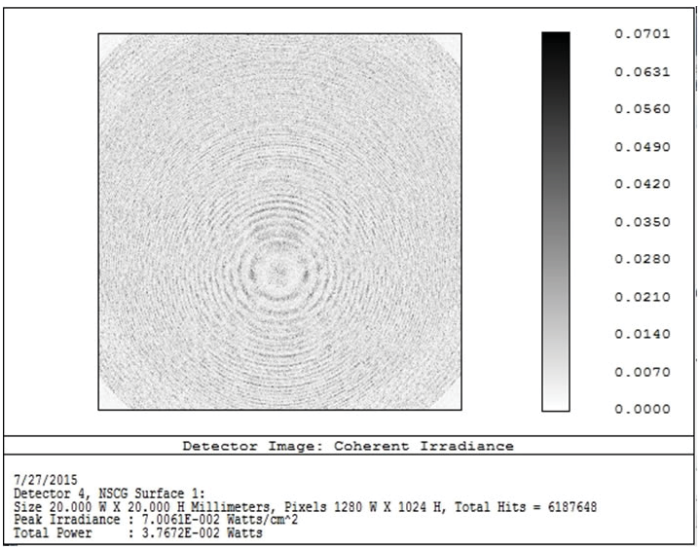

(Figure 2) Fringe pattern of both prisms having the largest angle plus ~5 arc minutes.

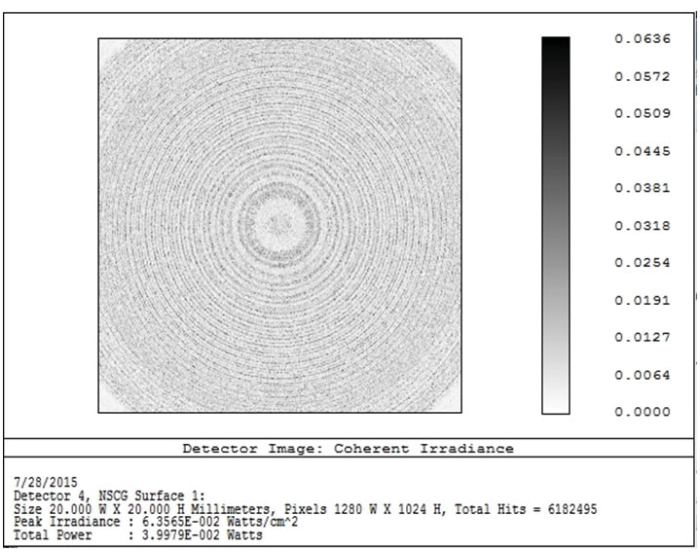

(Figure 3) Fringe pattern with perfect 45-45-90° prisms for beamsplitter.

III. Results

A. Power Spectral Density plots and Nyquist Frequency

Once the modeling was adequate, real-world sensor testing came into play. Figure (4) is a picture of the actual apparatus that was used for the interferometry portion of the experiment.

As previously stated, the key to this experiment was that the tilting mirror had the ability of having variable tilt to account for variable spatial frequency of the fringes. The best way to account for the variable tilt was to install two motor actuators in order to move the mirror very small amounts without human error. The Thorlabs Z812 motor actuator was fixed in the back of the moveable mirror to give it the desired tilt. The trick was, however, to tilt the mirror in increments that would allow for the PSD plots to arrive at the Nyquist Frequency and fold back down. The Nyquist frequency for this sensor is 0.10μm-1 corresponding to the pixel width and sampling period of the sensors is 10μm. In order to get the Modulation Transfer Function (MTF), it is important for the PSD to go beyond the Nyquist Frequency as shown in Figure (5). As spatial frequency increases, the spectral line moves approaches the right most part of the plot. Once the spectral line reaches the Nyquist Frequency, it begins to fold back toward the origin. This is due to aliasing that the signal is experiencing.

B. Modulation Transfer Function

From the Power Spectral Density plots, PSD, it possible to get a Modulation Transfer Function. As previously stated this is a way to describe the response of the CCD to sinusoidal patterns of variable spatial frequency. Essentially, the MTF measures the

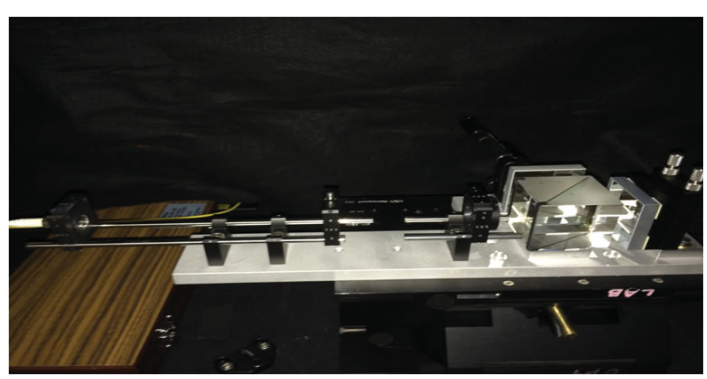

(Figure 4) This is the set-up of the interferometer used inside a dark box.

modulation or contrasts between two subjects; in this case, light and dark fringes. Which is one of the ways to generalize how good the CCD sensor is, and the MTF given by,

$$MTF = \frac{I_{max} - I_{min}}{I_{max} + I_{min}} \quad (1)$$

The equation describes the MTF at a particular spatial frequency by contrast in the image plane, where I-max and I-min are the maximum and minimum values of the observed sinusoidal pattern. And the I-max minus I-min amplitude is proportional to the square root of the PSD value. Figure (6) is the Modulation Transfer Function accumulated for this data set. As fringe spacing decreases (fringe density increases), it becomes increasingly difficult for the CCD sensor to effectively transfer this decrease in contrast. As result, the MTF decreases.

C. The Point Spread Function

The Point Spread Function, PSF, is the CCDs imaging response to a point source, which, internally, is what we are after. Finally, after a plethora of different processes and calculations, we arrive at the point spread function. If anyone is familiar with a Gaussian curve, The PSF is the size of the diffraction-limited image spot produced by the sensor. It is approximately a Gaussian intensity distribution, so its width (diameter) can be described by the sigma value. And that width happens to be 4.12 micrometers.

IV. Conclusion

The LSST is going to be the most sophisticated telescope in history. That being said, the most sophisticated technology is required to make sure that this telescope is running at full capacity. One of the most important factors that play a large role in this telescope, are the CCD sensors. My job, was an important one; characterizing the CCD sensors response to sinusoidal fringe pattern created by a Michelson interferometer. Some projects in the future could include doing this same experiment but with different wavelengths of light and seeing how the point spread function's Gaussian curve width changes. Also, a big project for this would be to look at the edge effects that the emitted light has on the edges of the pixel array.

V. References

[1]P. Z. Takacs ; I. Kotov ; J. Frank ; P. O'Connor ; V. Radeka; D. M. Lawrence; PSF and MTF measurement methods for thick CCD sensor characterization. Proc. SPIE 7742, High Energy, Optical, and Infrared Detectors for Astronomy IV, 774207 (July 02, 2010); doi:10.1117/12.856738.

VI. Acknowledgements

This project was supported in part by the U.S. Department of Energy, Office of Science, Office of Workforce Development for Teachers and Scientists (WDTS) under the Science Undergraduate Laboratory Internships Program (SULI).

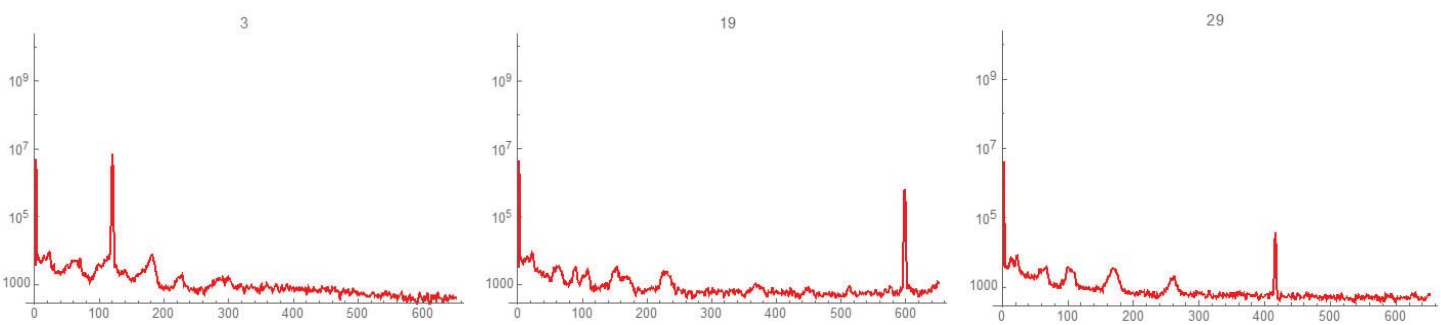

Figure 5- These PSD plots have power on the y-axis and spatial frequency in the x-axis.

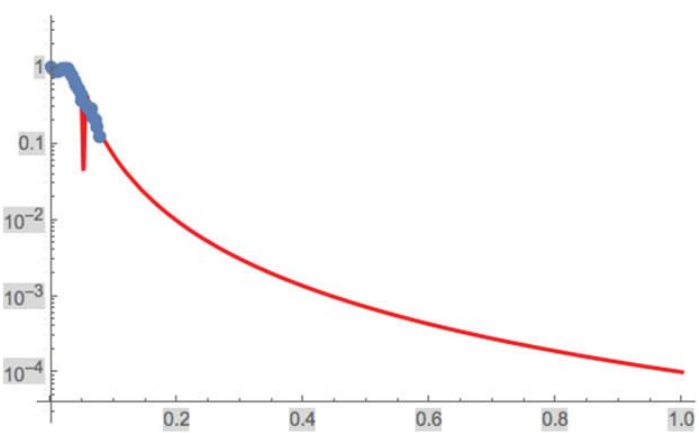

Figure 6

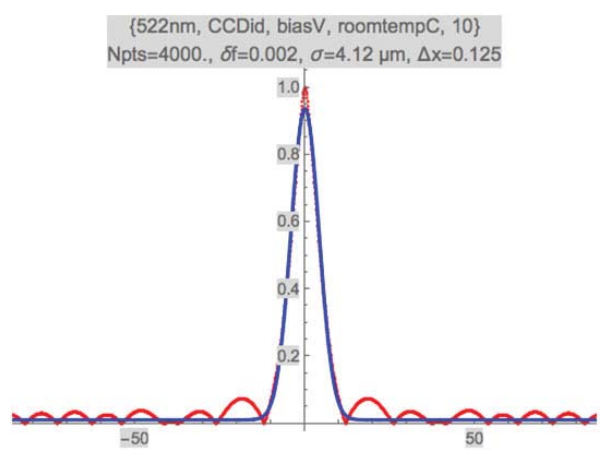

Figure 7- The PSF of 522nm light.

Atomic scale investigations of model TiO_2(110) catalysts

Alexander Kramer
Chemistry, State University of New York at Geneseo, Geneseo NY, 14454
David Grinter, Si Luo, Sanjaya Senanayake, Dario Stacchiola, and Jose Rodriguez
Chemistry Department, Brookhaven National Laboratory, Upton, NY 11973

Abstract

The surface of TiO_2(110), functionalized with potassium and gold, has been studied to understand the nature of the active site in a model catalyst for the carbon dioxide hydrogenation reaction. One aim of this project is to compare our model Au/K/TiO_2(110) system with the proposed structure of a complex active catalyst site involving a single gold atom surrounded by potassium ligands. A scanning tunneling microscope (STM) was used to scan a crystal of TiO_2(110) under UHV conditions to obtain an image of the crystal's surface with atomic resolution. X-ray photoelectron spectroscopy (XPS) was used to understand charge transfer and oxidation state changes of the system. Sputtering with argon (Ar) ions and annealing to 1000 K prepared an atomically flat surface of the sample. Three differently prepared surfaces: TiO_2(110) exposed to oxygen (o-TiO_2 (110)), TiO_2 exposed to H_2O (h-TiO_2 (110)), and reduced TiO_2 (r-TiO_2 (110)), were scanned to observe where the potassium (K) adsorbs, then scanned again after depositing gold nanoparticles (up to 1 nm diameter) to analyze how the gold was dispersed on the surface and to see if it interacts directly with the potassium. After this the Au/K/TiO_2 samples were annealed to 500 K and scanned again to observe whether sintering of the particles occurred. The experiment is still in the initial stages, but despite this a number of preliminary findings have been made. Knowing how the active site of the catalyst is constructed allows a better understanding of the mechanism of catalysis and which element(s) within the catalyst stabilize the active site.

I. Introduction

In today's advanced society heterogeneous catalysts are become increasingly important. The effects of catalysis is greatly felt in industry. Catalysts are used to achieve the greatest reaction rate for industrial reactions. TiO_2 has been shown to be an exceptional catalyst. The catalyst has very high stability along with favorable electronic properties that allow it to be usable in many fields of research and industry.[2]

Recent data reports that Au/K/TiO_2 (110) and Cu/K/TiO2 (110) show high activity for hydrogenation of CO_2 that also gives a high yield of alcohols ($CO_2 + 3H2 \rightarrow CH_2OH + H_2O$). Potassium (K), along with the other alkali metals is well known to increase the activity of Au/oxide catalysts for the water-gas shift reaction (WGS). Understanding the surface of the prepared catalyst and the structure of the active site is important so that we may be able to explain how the reaction occurs at a molecular level.

At the conclusion of this project we will compare our model Au/K/TiO_2(110) system with the proposed structure of a complex active catalyst site involving a single gold atom surrounded by potassium ligands.[1] Our resulting image of the structure of the active site will be different from that which is proposed in the article cited above.

II. Sample Preparation

In order to scan the TiO_2 crystal two processes must be complete first, the crystal must be cleaned and a tip for the STM must be made. In order to make the scanning tip for the STM we prepared a 2M solution of Potassium Hydroxide (KOH). Using some wire we dip the wire in the solution of KOH and attach the wire to the positive end of a power source. The beaker containing the KOH solution is lined with a sheet of copper (Cu) metal. Using the apparatus set up shown in figure 2, we run an electrical current from the wire through the KOH solution to the cooper lining within the beaker. The current usually ranges from 6-9 volts (V), causing a current of 2-10 milliamps (mA). As the current flows the ions in the solution react with the wire causing it to be etched where the wire meets the surface of the solution creating an extremely sharp tip. Once the tip is made it is rinsed with distilled water and ethanol. After this it is placed in the STM and heated to about 500K to make sure there are no impurities on the tip. Before the tip may be used to scan the crystal must first be cleaned to ensure a flat surface with minimal impurities. This is done by sputtering and annealing it, repeating this process multiple times. The process of sputtering is one in which the crystal is bombarded with Argon (Ar) ions which are accelerated to a few keV and collide with the surface. Their kinetic energy is transferred to the atoms at the surface, which are ejected into the vacuum, as depicted in figure 3. The crystal is exposed to the beam of Ar ions for a few minutes after which the surface is rough and requires annealing to order the atoms and form a flat surface suitable for STM imaging. In order to heat the crystal a current is run through a filament a short distance behind the plate that the crystal is mounted on. As

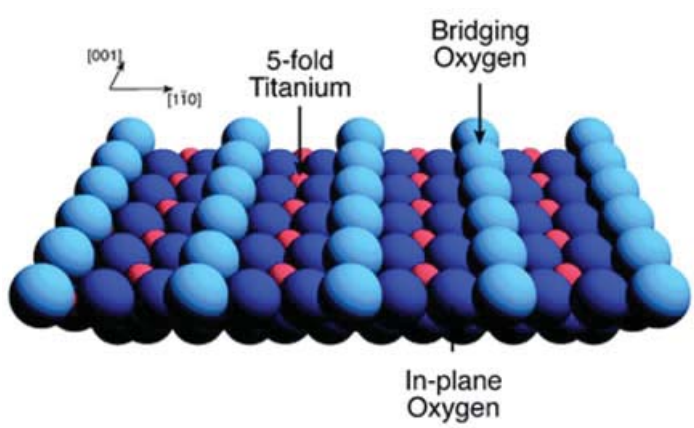

Figure 1. A space filling model of the ideal TiO_2(110) surface. The blue spheres represent oxygen atoms, and the red spheres represent titanium. At the surface of the catalyst not all of the bridging oxygen atoms (light blue) are present, these are called oxygen vacancies (O_b-vac).

the current passes through the filament electrons are ejected due to thermionic emission and are accelerated by applying a 700 V bias to the sample plate. This electron bombardment of the back of the sample plate causes the temperature of the crystal to increase to ~1000K. The crystal is heated for about 5-10 minutes. This sequence of sputtering and annealing is repeated a few times; after which it is moved to the STM stage for imaging once it has cooled to room temperature. It is first scanned to make sure that the crystals surface is flat and clear of any impurities, if the crystal is not clean or flat enough it will go through the sputtering and annealing processes again until it is. The sample preparation and all measurements take place within the UHV chamber shown in Image 1. A close-up of the STM stage can be seen in image 2.

Figure 2. The picture above is of the apparatus used for the tip etching process

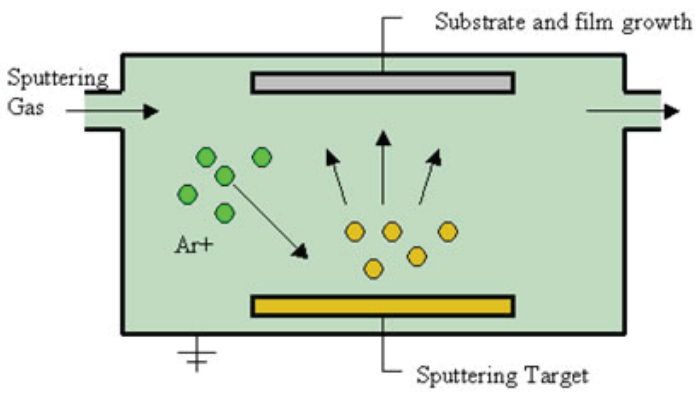

Figure 3- The process of sputtering

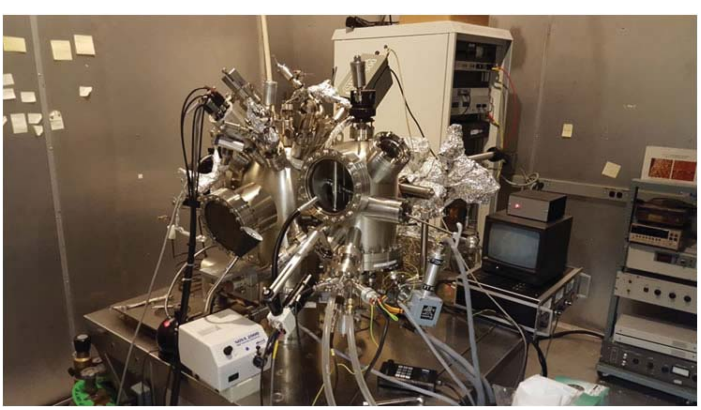

Figure 4 The picture to the left is the UHV system used for this research.

impurities it is scanned to observe the surface. The initial scanning of the clean TiO_2 (110) crystal shows the location of point defects such as oxygen vacancies (Ovac) and hydroxyl groups. Figure 7 shows a typical image of the reduced TiO_2(110) surface, with the bright rows corresponding to the Ti5f rows (see Figure 1). After images of the clean surface are collected the crystal is exposed to very small coverages of potassium at room temperature then scanned again. Once we have collected these images we can compare them to the clean surface images and record where the K atoms land and if there is any correlation between the Ovac¬ ¬and where the K atoms land. Once the scanning of the K exposed crystal is complete the crystal is then exposed to Au at room temperature, which forms clusters up to ~1 nm tall. The location and number of Au clusters in each image are measured including whether they form on a terrace or at the step edges of the surface. The number of Au atoms within the clusters can be estimated by measuring their height and assuming 3-D particles composed of fcc gold.. We repeat the potassium and gold deposition for three surface terminations of TiO_2(110): the reduced surface, r-TiO_2 (110), the oxidized surface, o-TiO_2 (110), and the hydrated surface, h-TiO_2(110). The oxidized surface was formed by exposure to 1 Langmuir of O2 at room temperature (10 seconds of 1×10-7 Torr) h-TiO_2 (110) was exposed to water in both gaseous and solid phases. For the gas-phase water, the surface was exposed to 1 L H_2O (100 seconds of 1×10-8 Torr) at room temperature. In order to form amorphous solid water (ASW) on the TiO_2(110) surface, liquid nitrogen was used to lower the temperature of the crystal to ~100 K (-173 °C) before exposing to 5 L H_2O (100 seconds of 5×10-8 Torr). The crystal must be this cold because under UHV conditions the freezing point of water is decreased dramatically. The sintering behaviour of the gold nanoparticles was also studied by annealing the various Au/K/TiO_2 systems to 550 K for 5 minutes.

Figure 5- the image to the left is a picture of the STM stage used for this research.

IV. Discussion

Based on the images provided by the STM we can observe some aspects about how the K atoms and the Au clusters are affected by the how the crystal is prepared. Figure 8 is an image of Au clusters (1519 MLE) on the surface of 1519 MLE K/TiO_2(110). The Au however does not appear to bind directly next to K sites on o-TiO_2(110) under UHV conditions. The K atoms on o-TiO_2(110) appear to create Ovac at the surface however they also are very mobile on the o-TiO_2(110) surface, therefore the STM is unable to accurately determine their exact position. The results from the h-TiO_2(110) do show some evidence of Au bound next to K sites.

V. Conclusions

The aim of this work was to examine how potassium interacted with a model catalyst system, that of Au/TiO_2(110). Based off of the research done so far we can tell that there is a relationship between the K and Au on the surface of the catalysts allowing them to form nanoparticles. More research is required; mainly involving understanding the electronics and oxidation states of the surface of the catalysts; which will be further studied using XPS.

VI. References

[1]Yang, M., S. Li, Y. Wang, J. A. Herron, Y. Xu, L. F. Allard, S. Lee, J. Huang, M. Mavrikakis, and M. Flytzani-Stephanopoulos. "Catalytically Active Au-O(OH) x- Species Stabilized by Alkali Ions on Zeolites and Mesoporous Oxides." Science 346.6216 (2014): 1498-501.Bagheri, Samira, Nurhidayatullaili Muhd Julkapli, and Sharifah Bee Abd Hamid. "Titanium Dioxide as a Catalyst Support in Heterogeneous Catalysis." The Scientific World Journal 2014 (2014): 1-21. Web.

2

VII. Acknowledgements

This project was supported by the U.S. Department of Energy. All research was performed at Brookhaven National Laboratory under the Science Undergraduate Laboratory Internships Program (SULI).

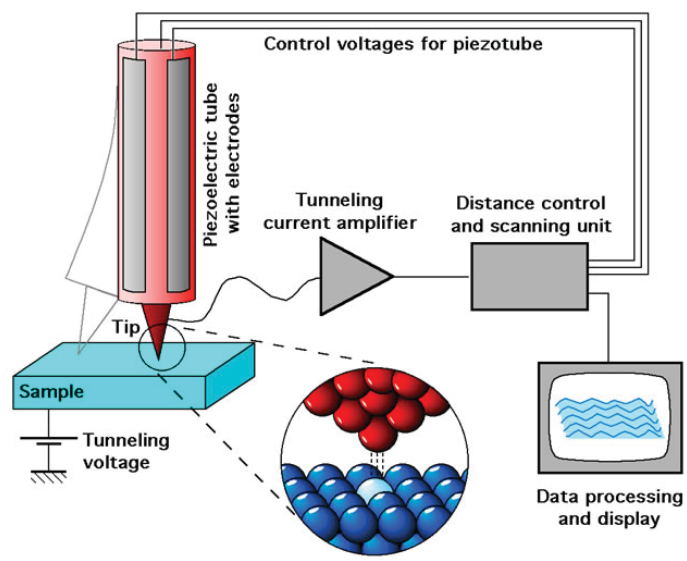

Figure 6- STM schematic the image to the left depicts how the STM scans the crystal

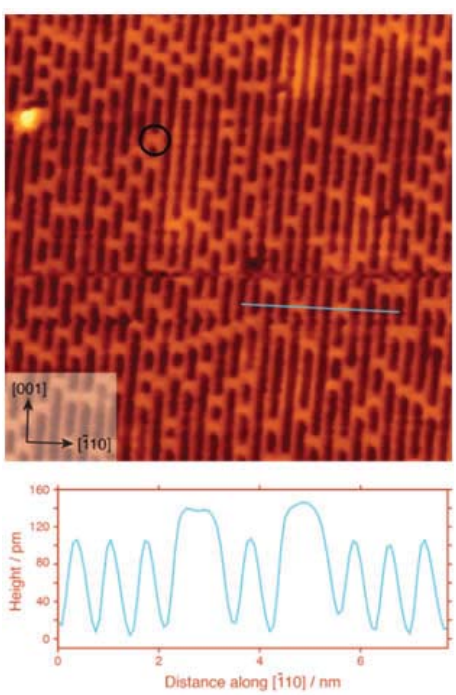

Figure 7- A 20x20 nm^2 STM image of the surface of r-TiO_2(110). The line profile below depicts the height at certain points on the surface across the blue line. The bright features between the rows are oxygen vacancies (an example is marked with a black circle)

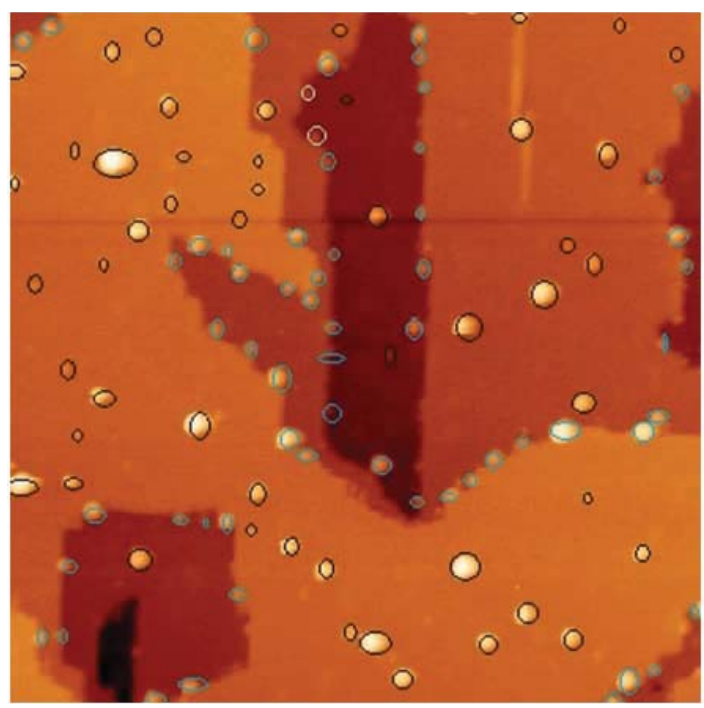

Figure 8- The image above is a 100 x 100 nm^2 shows gold clusters on the surface of the crystal. Those circled in blue are located on the step edges and those circled in black are located on the terraces.

Developing and optimizing the assembly process to manufacture an electromagnetic caloriometer module for sPHENIX

Spencer Laddy-Locks
Mechanical Engineering, Stony Brook University, Stony Brook 11790
Donald Lynch
Physics, Brookhaven National Laboratory, Upton, NY 11973

Abstract

The electromagnetic calorimeter (EmCal) is going to be one type of calorimeter in the proposed sPHENIX detector at Brookhaven National Laboratory. Scheduled to be started in 2017, the sPHENIX project would be the newest upgrade to the Relativistic Heavy Ion Collider (RHIC). The EmCal will allow scientists and physicists to analyze the electromagnetic particles that are emitted by quarks and gluons after a collision. The detector will do this by using approximately 25,000 double projective tungsten towers that have 750 scintillating fibers at a 10% taper. My research/engineering focus was to design, test, and optimize two different molds which would each create a single module. The first of two methods utilized six stainless steel screens which have 750 holes in them, each screen's holes get progressively closer together which creates the double taper. The second method for manufacturing a module employs wireframes, these wireframes allow the 750 fibers to be threaded with no taper until they are separated and placed at compound angles. I used Autodesk Inventor to design and 3D print prototypes of the molds. These printed molds were then used to create the first prototype modules. The results of these modules were very promising and suggested that with some small changes to both of the molds and methods we would be able to efficiently create around 25,000 of these units. The results of the first module helped us find flaws in the design which were then later addressed in newer revisions. The 3D printer allowed for quick changes in design, which is important in engineering where designs evolve very frequently. Optimizing both processes would be significantly more difficult without those tools. While working with scientists and engineers at BNL, I have increased my understanding of engineering and more importantly collaboration. I am now more familiar with tolerances, composite properties, optimization, and manufacturing limitations. Additionally while working on the sPHENIX project at BNL I have gained experience and invaluable connections.

I. Background

Figure: 1

The electromagnetic calorimeter converts electromagnetic particles into photons.These photons can then be read by a sensor which converts the light into an electronic signal. This is used to calculate the energy of the particle. To do all of this in sPHENIX, the proposed EmCal will use approximately 25,000 tungsten epoxy composite towers. These towers are made by pouring tungsten powder into a mold, and then infusing it with epoxy. This process is straight forward, yet must be optimized in order to use the least amount of resources possible. During these ten weeks I worked on iterating the design and optimizing the mold for manufacturing.

There are two proposed methods to create the tungsten modules. Each has its pro's and con's. The first method provided great registration for the fibers, this however makes it harder to thread all 750 of them. The second method provides faster threading of the fibers, though the registration could be a problem. In order to find out which method would produce the best results, both methods/molds were designed and 3D printed.

II. Methods, Tests & Calculations

A. Method I

The first method for creating these bricks is to use seven tapered screens. These screens have 750 holes that progressively get closer to one another. Figure 2 shows how the tapered hole pattern looks with all of the screens overlaid. The screens are what hold the fibers in place during the tungsten pour. The fibers in this method are registered sufficiently, however because the fibers must be filled at a taper, it is more difficult to fill the screens.

i. To help speed up the threading process a funnel was designed to help align the fibers at the right angle (figure 3). This funnel sped up the process immensely. Before the funnel was introduced threading took 27-30 min. This makes manufacturing 25,000 of these bricks unreasonable. Though when the fibers were guided by the funnel that time was reduced to eight minutes.
ii. To further optimize the filling process, shim spacers were used to space the screens apart while filling. The optimal shim spacing was found to be 900 microns. This spacing allows for the fibers to fall through at an angle of 82°.

B. Method II

The second method for creating these bricks is to use wireframes. The wireframes register the fibers in two ways. The "Blue" wireframes register the fibers vertically, and the "Red" wireframes register the fibers horizontally. The wireframes are held at compound angles to create the taper. The wireframes are placed in an alternating pattern. This makes the fibers register horizontally then vertically throughout the mold. The challenging part about the wireframes is that even with this alternating pattern, the fibers still seem to have trouble staying registered.

i. This method allows all 750 fibers to be filled in around five minutes which is quick, however the mold cannot be machined. Disposable molds would only be implemented if in the end, it is cost effective.
ii. To help register the fibers even further a "bowtie" mold was created (figure 6). This "bowtie" allows the fibers to taper

from 100% to 90% and then back to 100%. This creates two bricks in the end that need to be cut and machined. This "bowtie" helps register the fibers because the pattern starts and ends with a 100% screen.

iii. This method has a lot of merit, though while designing and making changes to this mold it has become apparent that it might become too complicated to manufacture. Design for manufacturing is one of the most important things to consider when designing the mold.

C. Test Blocks

An important parameter that must be accounted for with the tungsten bricks is the radiation length. The radiation length of the brick determines how well the detector absorbs particles. With the constrained size of the bricks the only way the radiation lengths of the bricks can be increased to 18, what the goal is, is to increase the overall density. The overall density to get 18 radiation lengths is approximately 10 g/cm^3. The first brick's density was measured to be 8.88 g/cm^3, this is too low for the experiment. The second brick, having around the same 8.88 g/cm^3 result, suggests that the method of filling the mold is not adequate to get the 10 g/cm^3 that is required. This issue called for some experimenting to try and get the right density before continuing with the bricks.

i. Three blocks, each the same size, were created utilizing very similar techniques that were used to create the bricks. These blocks should give the "best case scenario" density with the process currently in use. The results of the blocks (figure 7) suggested that the maximum pure tungsten and epoxy density that is possible using this procedure is 11.7 g/cm^3.

ii. The volume of the fibers inside of the bricks needed to be taken into account before comparing the 8.88 g/cm^3 to the

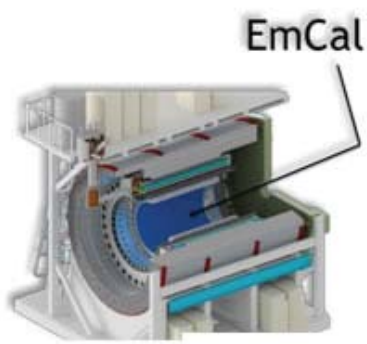

Figure: 1

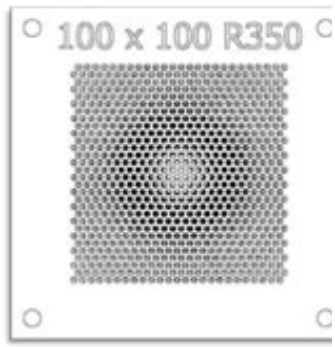

Figure: 2

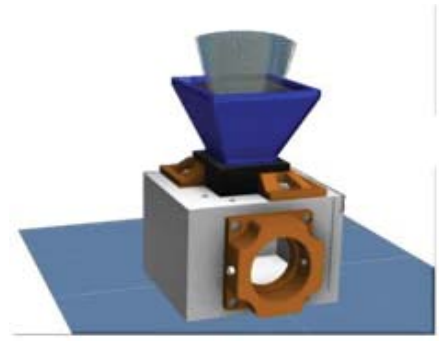

Figure: 3

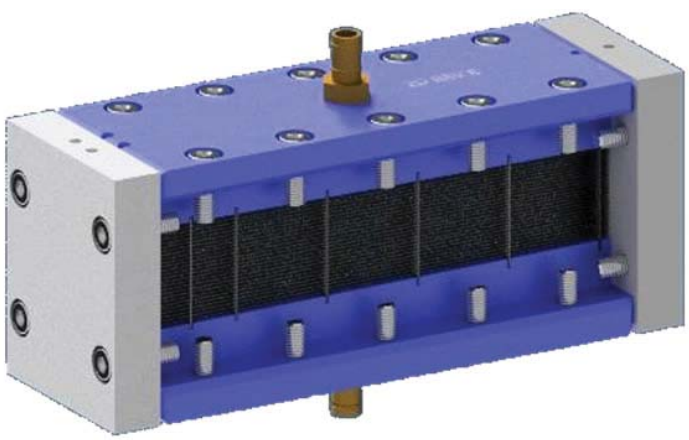

Figure: 4 First method mold

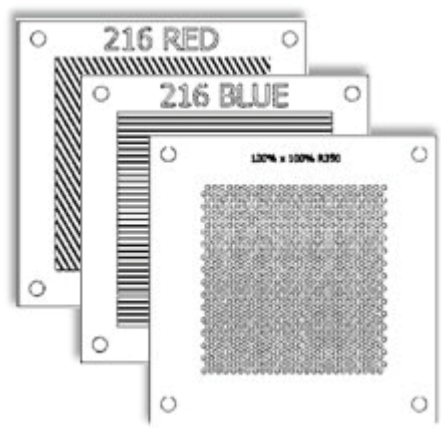

Figure: 5

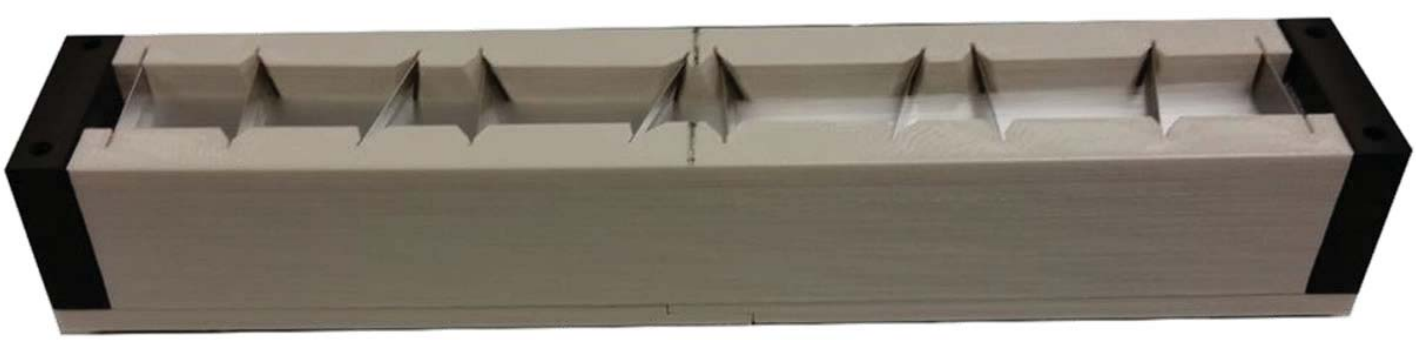

Figure: 6

block densities. The 750 fibers accounted for 21.6% of the bricks total volume. This along with the mass of the fibers were then subtracted from the bricks overall measurements

The following calculations in figure 8 show that the pure tungsten and epoxy density (with fibers and screens taken out of the equation) is 11.11 g/cm^3. This is very similar to what the block densities were.

iii. With all of the information from both the bricks and the blocks, a ratio was calculated. In figure 9, this ratio was used to calculate what the pure tungsten and epoxy density needed to be in order to get the desired overall density of the brick. When the overall density is set to 10 g/cm^3, the pure tungsten and epoxy density needs to be 12.5 g/cm^3. From the block tests it is known that this 12.5 g/cm^3 is not feasible with the process currently in use.

III. Data and Results

A. Data

The current data suggests that the density of the double projective bricks is at its maximum for this process. If density needs to increase, further research must go into compacting the tungsten in the mold. The threading of the fibers is now optimized enough to move on and think about the tungsten fill process and subsequent manufacturing constraints.

B. Results

The results of the research and development show that it is possible to manufacture a double projective EmCal brick. The process used so far has shown consistent improvements as expected after each iteration of the molds. The process of threading the fibers is becoming less of an obstacle and it is now time to consider manufacturability of both methods. The first method can be manufactured quite easily, the second less so. The second method needs to go through some more rigorous detailing and inspection to try and enhance the mold for production.

IV. Recommendations

While working on both molds for the past 10 weeks I have found that the first method seems more promising for manufacturability. The second method is much more complex and runs the risk of becoming too expensive to mass produce. Through before drawing any more conclusions I would like to see how the second method turns out. If the fibers stay straight and are satisfactory, then I believe the next step would be to take manufacturability into account. Until we have the second method brick create it is hard to tell which method is more practical/reasonable. In the end both methods will be compared to each other and a board will determine which method has more benefits.

Test Blocks Calculations						
	Tungsten Pour			Final Densities		
Block	Tungsten No Vibration Density (g/cm^3)	Tungsten Vibration Density (g/cm^3)	Percent Change in Density Due to Vibration & Top Off (g/cm^3)	Tungsten Epoxy Mass (g)	Tungsten Epoxy Volume (cm^3)	Tungsten Epoxy Density (g/cm^3)
I	10.12	10.19	+ 0.69%	93.6	7.97	11.7
II	9.91	10.31	+ 4.04%	98.2	8.47	11.6
III	9.51	10.58	+ 11.25%	90.4	7.66	11.8
					Average:	11.7

Figure: 7

EmCal Calculations							
Method I Tungsten Brick Density							
Brick	Total Mass (g)	Fiber & Screen Mass (g)	Tungsten Epoxy Mass (g)	Total Volume (cm^3)	Fiber & Screen Volume (cm^3)	Tungsten Epoxy Volume (cm^3)	Tungsten Epoxy Density (g/cm^3)
I	706.4	23.49	682.91	79.52	17.83	61.68	11.07
II	747	25.01	721.99	84.08	19.27	64.82	11.14
Note: Approximated Screen Mass						Average:	11.11

Figure: 8

EmCal Calculations		
Estimated Densities		
Overall Density Goal	Overall Density to Pure Density Ratio	Pure Density Required
10.000	1.250	12.500
8.884	1.250	11.105
Note: 8.885 is current overall density		

Figure: 9

Simulating electron showers in the Deep Underground Neutrino Experiment far detector

Jacob Larkin
Physics and Astronomy, University of Rochester, Rochester, NY 14627
Elizabeth Worcester
Physics, Brookhaven National Laboratory, Upton, NY 11973

The Deep Underground Neutrino Experiment is a long baseline neutrino experiment which will look for neutrino oscillations, i.e. a change in flavor (e, μ, τ). The detector will be a liquid argon time projection chamber (LArTPC) which is able to the detect the final products of neutrino interactions. Simulations can be used to test many of the signals expected in the actual detector. The primary particle in these simulations is an electron since in long baseline neutrino oscillations, the primary physics signal is the appearance of electron neutrinos which will always result in an electron in the final state. The simulations are used to find the expected energy resolution of electron showers and the effect of various reconstruction corrections on that resolution. These Monte Carlo simulations and the reconstructions following them were run using the LArSoft framework for LArTPCs. The ROOT data analysis framework was then used to analyze the results of these simulations and reconstructions. The energy resolution was found to be $\frac{6\%}{\sqrt{E(\mathrm{GeV})}} \oplus 2\%$

I. Introduction

A. Neutrinos

The Deep Underground Neutrino Experiment (DUNE) will be a long baseline neutrino experiment travelling ~1300 km from the Fermi National Accelerator Laboratory (Fermilab) outside Chicago to the Sanford Underground Research Facility (SURF) in South Dakota. The experiment is intended to study neutrino oscillations, which in turn may give insight into the matter antimatter asymmetry in the Universe, as well as providing a better understanding of the physics in the Standard Model. These oscillations can be described by the equation[1]

$$|\nu_i\rangle = \sum_\alpha U_{ai} |\nu_\alpha\rangle, \text{ where}$$

$$U = \begin{pmatrix} 1 & 0 & 0 \\ 0 & \cos\theta_{23} & \sin\theta_{23} \\ 0 & -\sin\theta_{23} & \cos\theta_{23} \end{pmatrix} \begin{pmatrix} \cos\theta_{13} & 0 & e^{i\delta_{CP}}\sin\theta_{13} \\ 0 & 1 & 0 \\ -e^{i\delta_{CP}}\sin\theta_{13} & 0 & c\cos\theta_{13} \end{pmatrix} \begin{pmatrix} \cos\theta_{12} & \sin\theta_{12} & 0 \\ -\sin\theta_{12} & \cos\theta_{12} & 0 \\ 0 & 0 & 1 \end{pmatrix}$$

Previous experiments have found that $\theta_{12}\approx 35°$, $\theta_{13}\approx 10°$ and $\theta_{23}\approx 45°$.1 The value of δ_{CP} is still unknown, however, so this will be a major priority for DUNE. DUNE will be sensitive to the discovery of CP violation for many possible values of δ_{CP}.

Another goal of DUNE will be to determine which mass hierarchy is correct, normal or inverted. The neutrino mass differences, Δm_{21}^2 and Δm_{32}^2, are known, however, the sign of Δm_{32}^2 is still unknown. As a result, there are two possible hierarchies of these masses, m_1, m_2, m_3 in order from least to greatest, or m_3, m_1, m_2. These are referred to as the normal and inverted hierarchies, respectively.[1]

B. DUNE

DUNE will consist of three major components, the beamline, the near detector and the far detector. The beamline will be located at Fermilab and will consist of a beam of protons which will hit a target, producing pions. These pions will be filtered using a magnetic field so that only charged pions are left. Nearly 100% of the time these pions will then decay into muons and muon neutrinos and the muons will be filtered out so that primarily muon neutrinos remain. The neutrinos will pass through the near detector, which will measure the content of the neutrino beam. It will measure what proportion of the beam is of each type of neutrino. This will allow the results at the far detector to be calibrated so only oscillations are considered.

The far detector will be a liquid argon time projection chamber (LArTPC) located 1300 km away at SURF. Four large volumes of liquid argon will be placed about a mile underground, to shield from cosmic rays, where the neutrinos will interact with the argon. Once the interaction occurs several possible situations can result, however, all of them create signals in the detector which can be measured. These signals are in the form of ionization electrons and photons which result from a charged particle moving through the liquid argon. An electric field will be created within the detector so that these ionization electrons will drift in a known direction. Several wire planes will be placed in the detector where these electrons will be collected.

Once the signal is measured, a reconstruction will be done using this data so that the path of the original charged particle, the final product of the neutrino interaction, can be found. This information will show what the final products of the neutrino interactions were and once the final products are known, the flavor of the neutrino will be known. Once the flavor is known, the results can be compared to those at the near detector so any oscillations can be found.

An important step in this process is the ability of the detector, and the reconstructions which follow, to determine the various properties of the particles which move through the detector. One measure of this is the energy resolution. Looking at the energy resolution of the far detector will allow us to better understand how the current design compares to other experiments and identify any further work that needs to be done to improve the design of the detector or the reconstruction algorithms.

II. Methods

A. Simulations/Reconstructions

In order to run the reconstructions, simulated data was first needed. Monte Carlo simulations were run using the LArSoft framework for LArTPCs. The simulations were run in version 4.11 of LArSoft on a Fermilab unix computer. Many test simulations were run directly on this computer, but the simulations used for the analysis were run on FermiGrid, a cluster of many

processors, so many different simulations could be run in parallel.

The primary particle in these simulations was an electron since the primary physics signal at DUNE will be the appearance of electron neutrinos. The simulations were run first in the 35 ton prototype geometry and then in the final far detector geometry. Ten sets of data were generated, each with a fixed initial electron energy ranging from 0.5 GeV to 5 GeV at 0.5 GeV intervals. Each set consisted of 500 simulations of 100 events each. Each of these simulations had a different set of initial starting positions and angles for the initial electron. These initial conditions were generated using a random number generator and were spread uniformly throughout the detector. The same set of 500 initial positions and angles was used at every energy. A test run of 5000 simulations was run as well, but we determined that the statistics from the runs of 500 simulations were sufficient.

These data were then reconstructed using LArSoft. We used the hitcheat module to find hits in the reconstruction. A reconstructed hit is a cluster of wires containing charge that the reconstruction algorithm has associated with the same primary particle in the detector and grouped together.

III. Analysis

The reconstructed data was then run through a LArSoft analysis module I wrote which summed the ADC counts from the Monte Carlo data and got the charge for the hits in the reconstructed data. These were output to a ROOT TTree with the names Raw

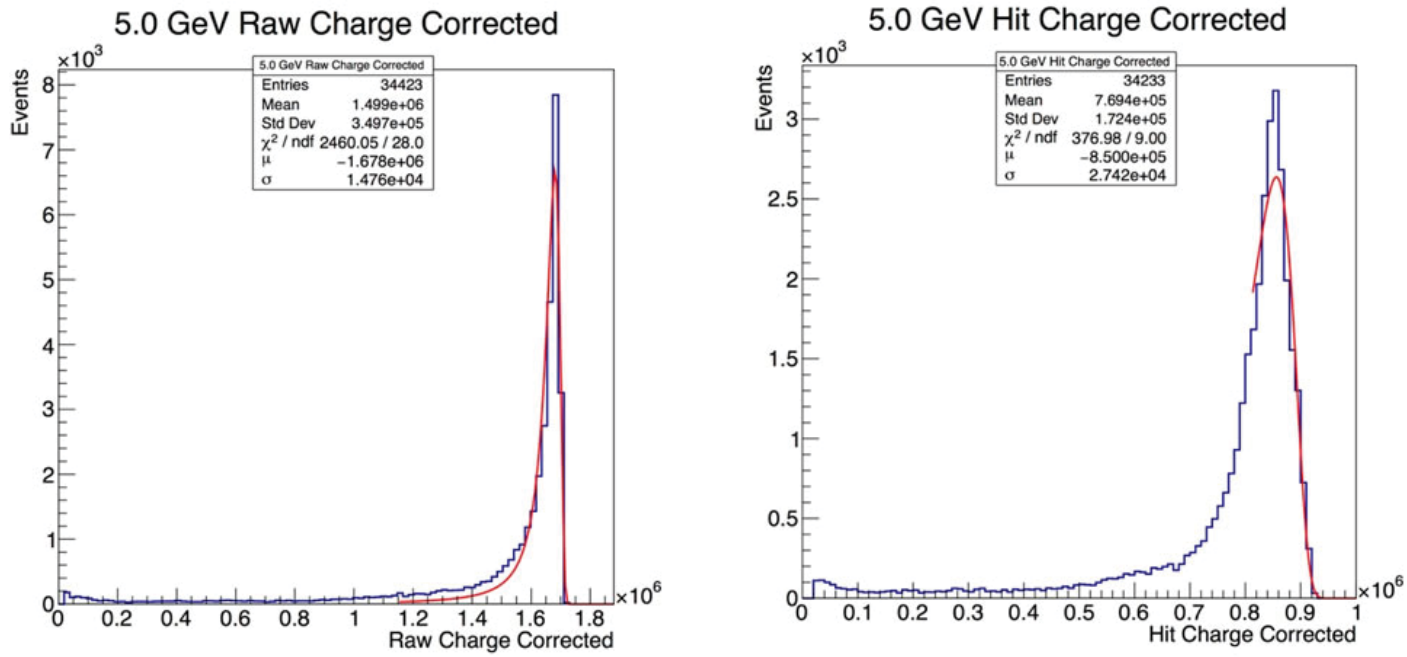

Figure 1: Raw Charge Corrected and Hit Charge Corrected histograms for a 5 GeV initial electron energy. These were fit with a landau function.

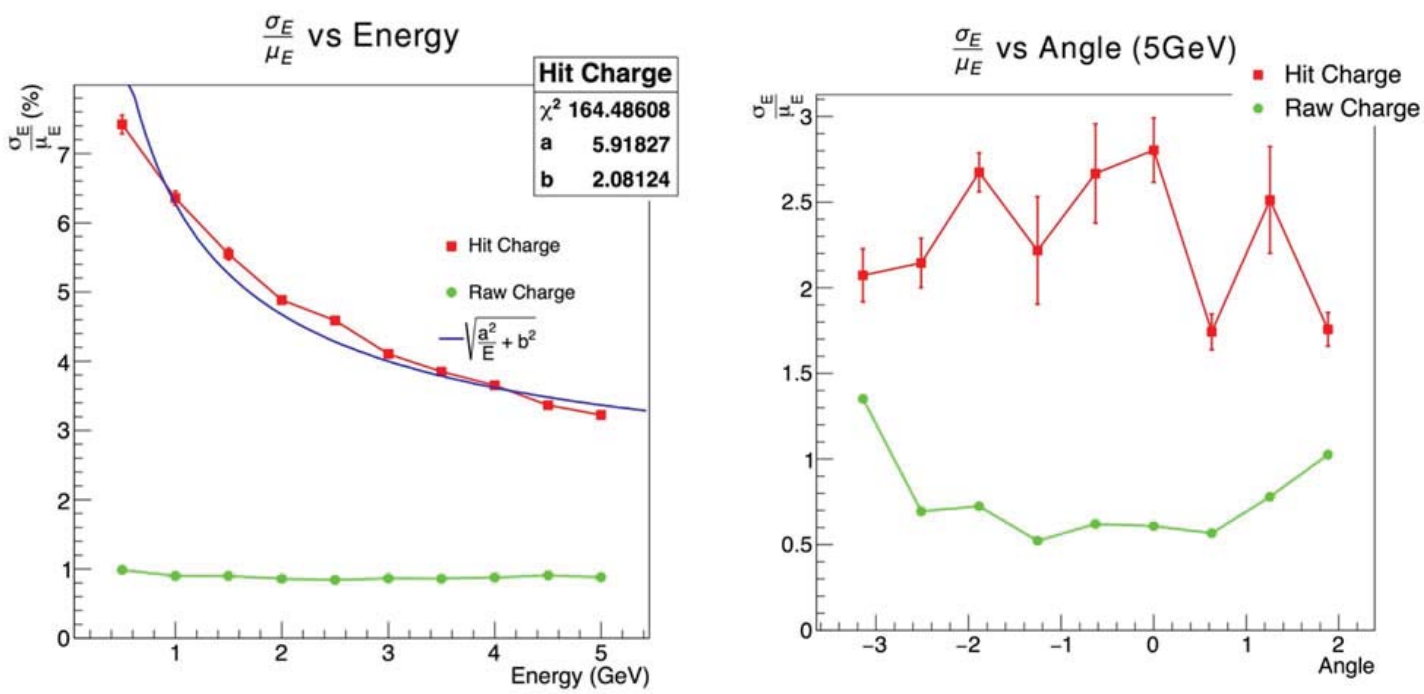

Figure 2: σ_E/E as a function of initial electron energy and angle with respect to the wire plane.

Charge and Hit Charge respectively. The module also applied a correction based on the ionization electron time of flight, and this data was output as Raw and Hit Charge Corrected. The TTrees from each simulation were then combined using the ROOT utility *hadd* such that all events with the same initial electron energy were in a single TTree for a total of 10 TTrees.

The corrected Raw and Hit Charges were then plotted as histograms for each energy using ROOT (see fig. 1). Cuts were made to the data to eliminate any events which resulted in 0 charge or where the end of the initial electron track was outside of the detector. These histograms were fit with a landau function whose range was optimized in order to fit the peak of the distribution as well as possible.

IV. Results

All the charge histograms have a low energy tail below the peak. We believe that this tail is the result of events which occur near the edge of the detector. Scatter plots of distance to the edge vs hit charge corrected and distance to edge vs raw charge corrected are included in the appendix (fig. 3). From these scatter plots it is clear that there is a general trend that low charge events are close to the edges, however some events in the peak are also near the edges. These events require further study.

The width, σ, and most probable value, μ, of these fits were then plotted as σ_E/μ_E vs. the initial electron energy and σ_E/μ_E vs. the angle of the initial electron with respect to the wire plane. The data for hit charge corrected in the energy plot was fit using the function $\sqrt{\frac{a^2}{E(\mathrm{GeV})}+b^2}$. The results of this fit are the energy resolution for hit charge corrected. This equation comes from the larger equation $\frac{\sigma_E}{E}=\frac{a}{\sqrt{E}}\oplus\frac{b}{E}\oplus c$. However, in this case we can ignore the middle term. This is because that term represents the electronic noise from the detector, and this version of LArSoft does not yet simulate electronic noise. The first term represents the quantum fluctuations which are inherent in the process we are interested in, and the third term represents the shower leakage from the detector.[2]

From fig. 2 it is clear that σ_E/μ_E for the raw charge corrected does not vary with energy or angle. This is expected since the raw charge is simply the summed ADC count. Hit charge also does not vary with angle, but does with energy and the fit results in an energy resolution of $\frac{6\%}{\sqrt{E(\mathrm{GeV})}}\oplus 2\%$. We can conclude from the flat graphs in the angle plot that the angle of the electrons with respect to the wire plane does not matter and so we do not have to correct for this.

V. Conclusions

Another LArTPC experiment, ICARUS, reported an energy resolution of $\frac{3\%}{\sqrt{E(\mathrm{GeV})}}\oplus 1\%$.[3] This tells us that further corrections in reconstruction can improve the energy resolution. A low resolution is important since it leads to better accuracy when determining the path of a particle in the liquid argon. This is especially important given the number of events expected in the final experiment. Although 50,000 events were simulated at 10 different energies for this analysis, the final detector is expected to measure 1,000 events over a period of 7 years. Because of this, it is important that every event is as accurate as possible. Refining this energy resolution will be an important step towards improving the future results of DUNE.

VI. References

[1]LBNE Collaboration, " The Long-Baseline Neutrino Experiment: Exploring Fundamental Symmetries of the Universe," (2013), arXiv:1307.7335v3 [hep-ex].

[2]H. Schultz-Coulon and J. Stachel, "Calorimetry II", (2011).

[3]ICARUS Collaboration, "Energy reconstruction of electromagnetic showers from π^0 decays with the ICARUS T600 Liquid Argon TPC," Acta Physics Polonica B (2010), arXiv: 0812.2373v1 [hep-ex].

VII. Acknowledgements

This project was supported in part by the U.S. Department of Energy, Office of Science, Office of Workforce Development for Teachers and Scientists (WDTS) under the Science Undergraduate Laboratory Internships Program (SULI).

VIII. Appendix: Scatter Plots

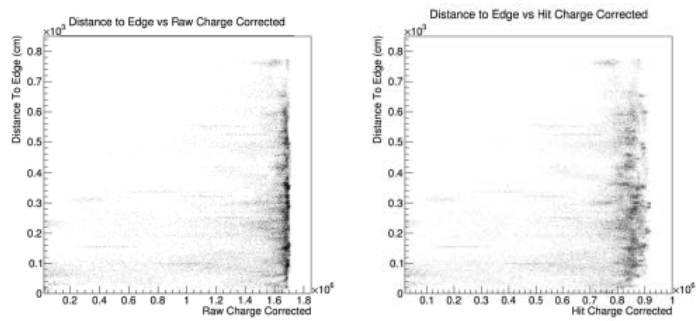

Figure 3: Distance to edge of the detector vs Raw and Hit Charge Corrected.

It is clear from these scatter plots that all events which have low raw or hit charge occur close to the edges (<3m). There is some ambiguity, however, since there are some events close to the edges which are in the peak. This means simply cutting all events near the edges is not the correct solution.

Effects of laser exposure on the niobium tin surface

Zachary Lebens-Higgins
Binghamton University, Binghamton, NY 13905
Triveni Rao
Instrumentation Division, Brookhaven National Lab, Upton, NY 11973

Abstract

Niobium is widely used for superconducting radiofrequency cavities (SRFCs) yet requires a very low operating temperature around 2K. Recently, niobium tin has been shown to be a promising replacement material with a higher operating temperature around 4K that can reduce costs. Typically, chemical polishing or manual polishing are used to obtain a smooth niobium surface. Laser polishing has demonstrated a similar reduction in the surface roughness of niobium which could reduce the cost and the polishing time and is a greener alternative without involving hazardous chemicals. The development of a laser cleaning methodology for niobium tin would further propel the application of the material for SRFCs. We examined the effects of laser shots on the surface of niobium tin samples and compared the surface morphology of the untreated and treated surfaces. For single shot areas, the energy density was varied from 0.3 J/cm^2 – 1.2 J/cm^2 at 45° and 60° with 16 shots on the single spot. We examined the resulting surface morphology with scanning electron microscopy (SEM) and compared the untreated surface with each of the treated areas. Initial results indicate a reduction in the surface roughness for the treated spots with the highest reduction in surface roughness around 0.6 J/cm^2. With further refinement, laser polishing can become a viable technique to obtain a smooth surface finish for niobium tin cavities

I. Introduction

Superconducting radiofrequency cavities (SRFCs) are designed to operate at high accelerating field gradients in particle accelerators. Typically, niobium is used for SRFCs but require a low operating temperature around 2K to obtain high enough accelerating fields. [1] Recent work with niobium tin has demonstrated desirable accelerating fields are obtainable with a higher operating temperature around 4K. Although there has been limited detailed study of niobium tin for SRFCs, it has the potential to replace niobium as it can significantly reduce operating cost. [2]

In order to obtain high accelerating a gradient a relatively smooth surface finish is required. [1] For niobium, chemical or manual polishing are typically used to obtain a desirable surface finish but require significant polishing time or involve hazardous chemicals. [3] Laser treatment has recently been used to obtain a similar reduction in the surface roughness as these other methodologies. [3] Laser polishing has a number of benefits including reduced processing time, process automation, and is a greener alternative without involving hazardous chemicals. [3, 4] Multiple studies have examined the effect of various laser treated area parameters, including energy density, number of shots, and shot overlap, and identified quantities that lead to the highest reduction in surface roughness.[3,5] As niobium tin is an attractive replacement material for SRFCs, a procedure for obtaining a superior surface finish is desirable. We focused on laser exposure in order to identify if a similar reduction in surface roughness could be obtainable as well as what parameters led to the highest reduction in surface roughness. A development of a finishing process for ni-

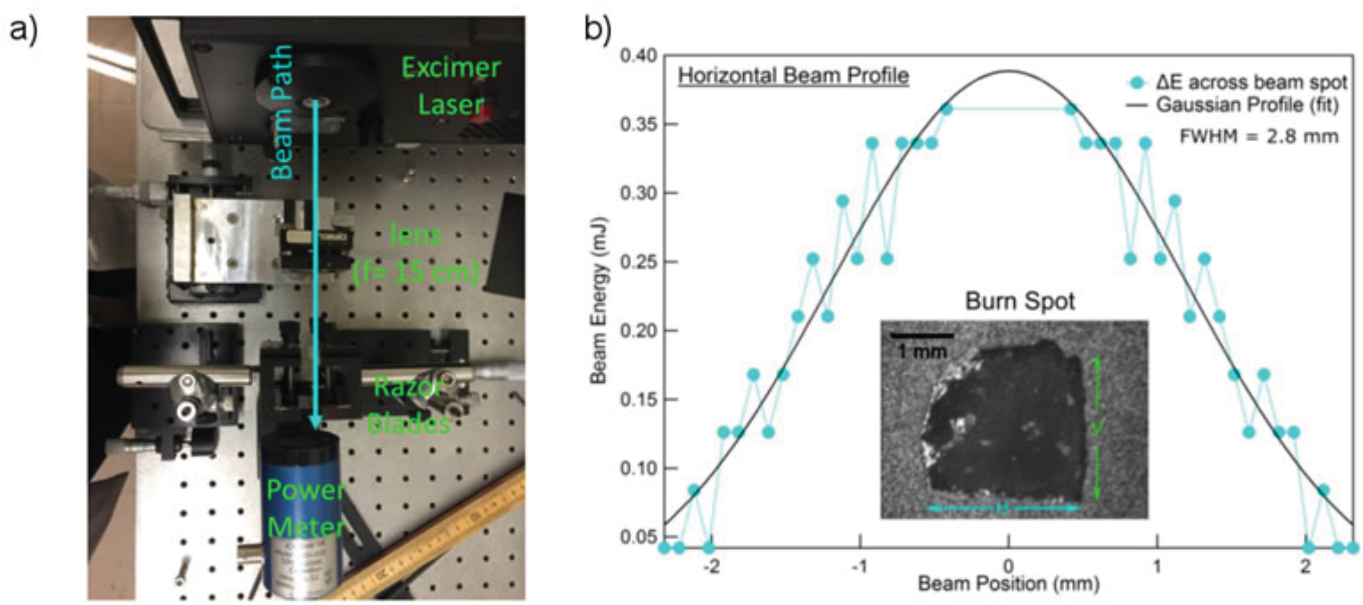

Figure 1a) Experimental Setup for the measurement of the beam profile. The razor blades were moved in increments to measure the energy within small sections of the beam. Measurements were taken with and without the lens. b) Energy distribution of the beam along the horizontal axis compared with a Gaussian profile.

obium tin could further increase the development of this material system for SRFCs.

II. Experimental

The beam was examined in order to determine the initial energy of the beam, the profile of the beam, and the spot size of the beam. The energy of the beam is around 10.6 mJ directly after a gas fill and decreases by around 3% with an hour of continuous measurement. The decrease in the beam energy was monitored to follow the change in energy density at different positions of the laser over time. The beam profile was measured with the experimental setup for the horizontal axis as shown in figure 1a. Two razor blades were used to cut across the beam, select small sections, and measure the section energy. Measurements were taken with and without a lens with a 15 cm focal length. The horizontal beam profile without the lens is shown in figure 1b as well as a Gaussian fit. The FWHM from the calculation was used to approximate the laser spot size at different points behind the lens. A similar experimental setup was used to measure the beam along the vertical axis with two Gaussians required to fit the resulting distribution.

The lens was utilized to focus the beam to smaller spot sizes to obtain higher beam energy densities. The beam spot size at different distances behind the lens were measured with burn paper as shown in the inset of figure 2. This method led to similar spot sizes as determined form the FWHM indicating it was a viable method to estimate the beam spot size. Primarily, positions farther than 8 cm from the lens were used so as to obtain energy densities from 0.2 J/cm^2 to 2 J/cm^2 with the measured spot size for each of these positions shown in figure 2.

The full experimental setup with the position of the laser, the position of the lens, and the position of the cube is shown in figure 3. The lens was placed on two translational stages with around 5 cm of movement for control of the spot size on the sample. The angle of the sample holder was varied from 45° to close to 90° with respect to the beam to examine the effects of different angles of incidence. The cube was pumped down with a scroll pump to a pressure of 1e-3 Torr in order to minimize number of particles in the chamber that might react with the surface during the laser treatment.

The cube was positioned on a motorized x-y translational stage which allows for automation of the laser treatment process. The scan area, number of shots and shot overlap are controlled with a high level of precision with the automated raster scan. An example of a 3x3 scan on burn paper and the direction of the movement is shown in figure 4. The raster scan stops at every point and triggers the laser with a preset delay between each of the points. Overall, the raster scan allows for a great control of the laser process and almost full automation allowing for simpler treatment process.

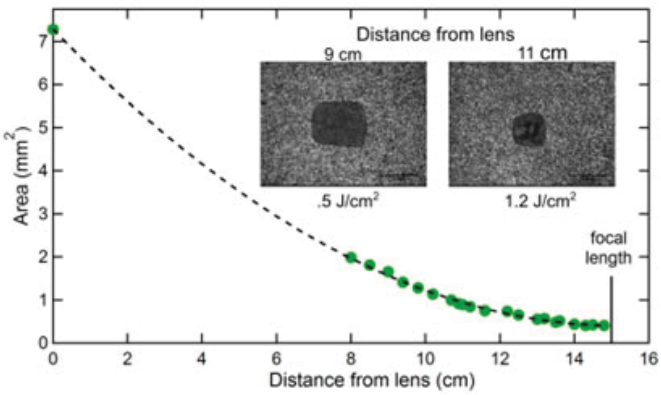

Figure 2) Area of the beam spot based on the distance from the lens. The beam spot for 9 cm and 11 cm is shown for comparison.

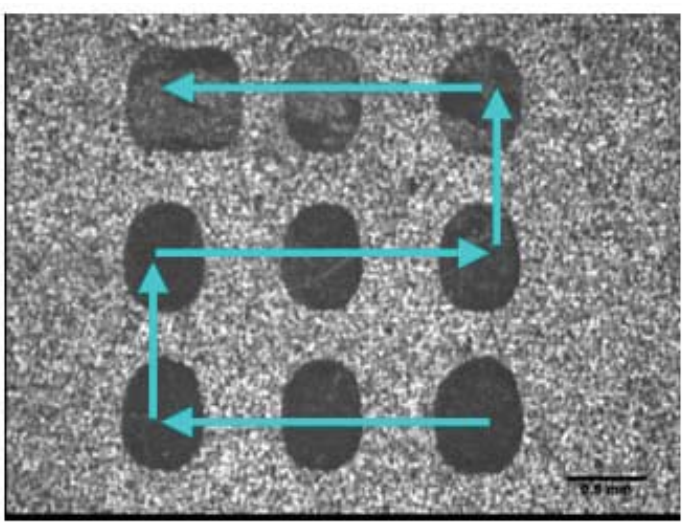

Figure 4) Test of the raster scan with a 3x3 scan on a 4 mm2 area showing the direction of the raster scan movement

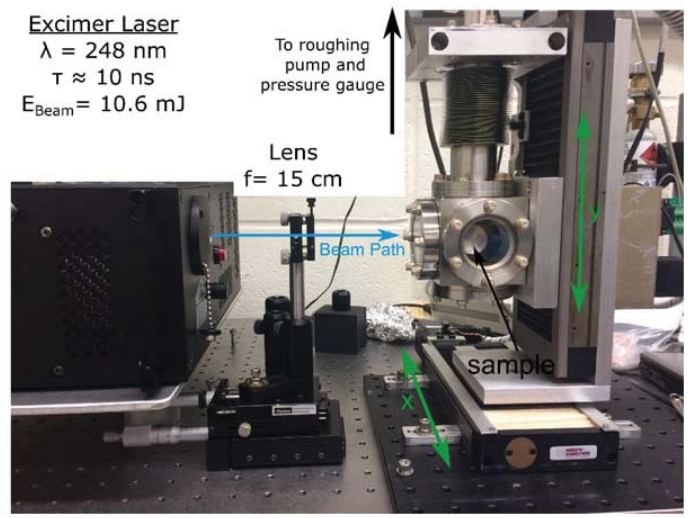

Figure 3) Experimental setup with the position of the lens positioned in front of the cube and the position of the sample within the cube that is on a motorized x-y translational stage.

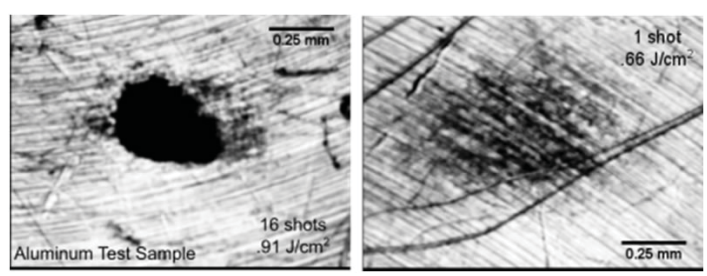

Figure 5) Comparison of the effect of .91 J/cm2 and .66 J/cm2 energy density on the surface of aluminum. The 16 shots led to a large black spot that potentially indicates over-melting while even for 1 shot an effect is observed for .66 J/cm2.

III. Results

A. Aluminum test samples

Aluminum discs were used as preliminary samples to test multiple parameters of the laser treatment process. The primary parameters examined for single shot areas were energy density, delay between points, number of points and angle of incidence. For a few energy densities, larger raster scans were done at a few energy densities to test different levels of overlap between shots and examine the treating of a larger treated area. Throughout all experiments the cube pressure was monitored to determine if there was an increase in the pressure during the treatment related to ablation.

The effects of laser treatment were examined at 45°, 60°, and grazing for a wide range of energy densities. For each angle, there was a threshold energy density that led to an increase in the surface roughness and the emergence of a periodic structure that is expected with surface over-melting. At each angle of incidence a similar threshold energy was observed with the primary difference being an elongation of the spot along the horizontal. Below this energy density, there was a noticeable difference in the sample with potentially some smoothing of the surface even though the machine lines were still somewhat visible in these areas. A comparison of the two regions is shown in figure 5. From these results, we determined only a few shots were needed to treat the surface as even one laser shot led to a noticeable change in the surface morphology. Additionally, there was minimal change in the pressure during the cleaning with a change only observed at the highest energy densities with the lowest delay between laser shots. These results indicate that a relatively short amount of time is required to treat a surface with respect to other surface finishing methodologies.

Larger raster scan areas were tested in order to monitor the laser spot overlap on the sample. A 7x7 raster scan is shown in figure 6 in which each of the laser tracks are distinguishable along the horizontal axis but overlap along the vertical. Along the horizontal axis there is non-uniformity that is possibly related to a different number of shots within an area or related to the Gaussian beam profile. This experiment indicates that more overlap is needed to increase the uniformity of the larger treated area.

B. Laser treatment of the niobium tin surface

Single shot areas on the niobium tin surface were exposed to the laser to determine the effect of different energy densities on the surface topography. Six different laser energies densities of

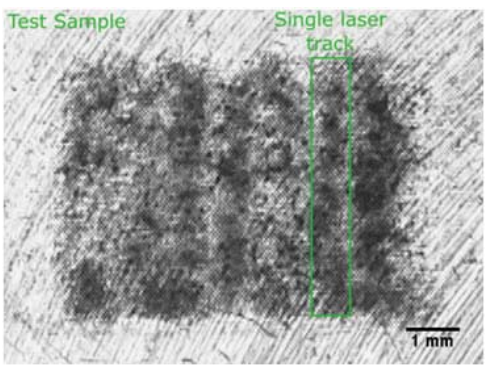

Figure 6) 7x7 Raster scan for a treated area around 2.5 mm2. There is a desired overlap along the vertical axis but more overlap is needed along the horizontal axis as the laser tracks are still distinguishable

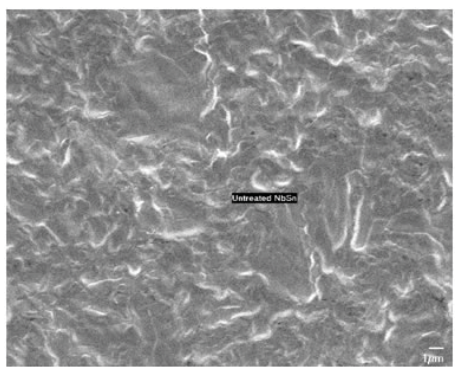

Figure 7) SEM image of untreated niobium tin surface that is dominated by a small features of a few microns in size.

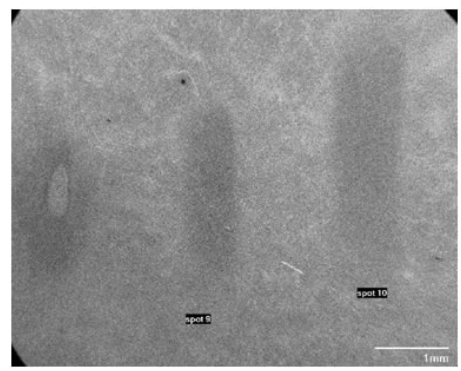

Figure 8) SEM image showing three of the treated spots of .8 J/cm2, .6 J/cm2, and .4 J/cm2 from left to right.

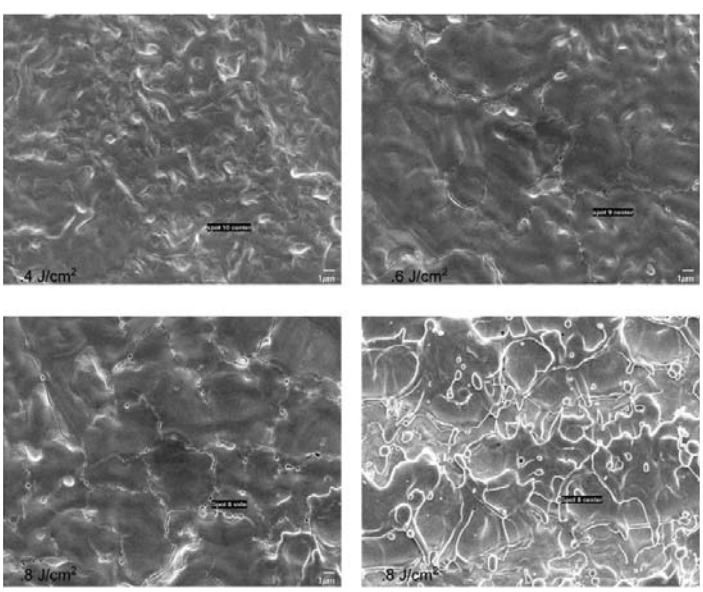

Figure 9) Comparison of .4 J/cm2 and .6 J/cm2 near the center and .8 J/cm2 at the edge and at the center. There are significant changes in the morphology within this small change in energy density.

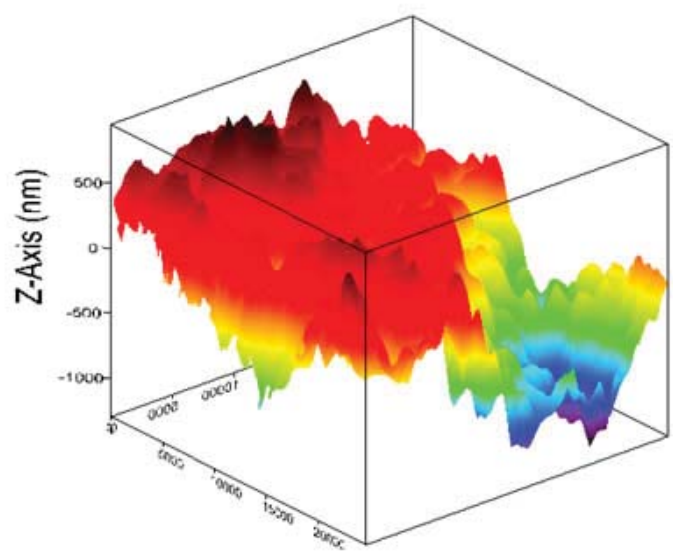

Figure 10: A 25 µm x 25 µm AFM measurement of the untreated area with a surface roughness of 420 nm.

0.3, 0.4, 0.6, 0.8, and 1 J/cm2 at 45° and five different laser energy densities of 0.3, 0.4, 0.6, 0.8, 1 J/cm^2, and 1.2 J/cm^2 at 60° were selected for a total of 11 single laser area treated spots. Sixteen shots were triggered on each of these areas by moving the raster scan by only 1 µm between each shot.

Each treated surface was examined with scanning electron microscopy (SEM) and compared with the untreated surface. Examination of the untreated surface, shown in figure 7, indicates the presence of a large number of small features on the order of a few microns.

Three of the treated spots are shown in figure 8 of 0.4, 0.6 and 0.8 J/cm^2 taken at an angle of incidence of 60°. The spots are distinguishable from the untreated area and decrease in spot size with increasing energy density. Additionally, both the 0.4 J/cm^2 and 0.6 J/cm^2 are roughly homogeneous while the 0.8 J/cm^2 spot displays an intense center with a darker edge region. Higher magnification images of each spot as well as a magnification of the center and edge region of the 0.8 J/cm^2 spot are shown in figure 9. For 0.4 J/cm^2, there are still a significant number of small features indicating only some melting of the surface as it is very similar to the untreated surface. At 0.6 J/cm^2, there is significant uniformity across the spot and all features come in to focus indicating a small change in the height across the region. The edge of the 0.8 J/cm^2 spot is very similar to the 0.6 J/cm^2 related to the Gaussian beam profile with a higher energy density at the center and a smaller energy density at the edge of the beam. For the center of the spot, there are more wavelike features and some smaller features present related to the resolidification process that is possibly due to surface over-melting.

In order to further examine the effects of the laser exposure, the spots were examined with atomic force microscopy (AFM) to compare the variation in surface roughness before and after treatment. A 25 µm x 25 µm AFM measurement of the untreated surface is shown in figure 10. There is a significant number of small sharp peaks as well as larger peaks and valleys. There was significant variation in the surface roughness of the untreated area with an average RMS surface roughness around 450 nm.

For each angle of incidence there was a decrease in the surface roughness observed for an energy density of 0.6 J/cm^2 and for the edge region of the 1 J/cm^2 measurement. The center regions of the spots exposed to the highest energy densities showed an increase in the surface roughness compared to the untreated surface. The 3d topography of the 0.6 J/cm^2 and the center of 1 J/cm^2 are shown in figure 11. At 0.6 J/cm^2 there is still a large number of sharp peaks though they are smaller in size. Additionally, there are no large scale peaks and valleys present. At 1 J/cm2, a periodic wavelike pattern emerges with significantly high peaks and valleys. This is an indication over melting in this region leading to a periodic structure and tall features within the re-solidification process. These results match well with the SEM measurements although the exact location of the AFM measurements is difficult due to the small measurement area of the AFM measurements. The RMS surface roughness was 245 nm and 1290 nm for the 0.6 J/cm^2 and the center spot of the 1 J/cm^2 respectively. Therefore the surface roughness can be reduced with laser exposure with the preliminary results leading to a 45% reduction.

IV. Conclusions

We have developed a method for the exposure of the niobium tin surface to an excimer laser. Within our initial setup, we were able to demonstrate the potential benefits of laser polishing including a limited treatment time due to only a small number of shots required to effect the surface and the automation of the treatment process with easy selection of the desired treatment area and number of shots within that area. Preliminary results examined the effect of exposing the niobium tin surface to a wide range of energy densities. There was a reduction in the surface roughness for some of the exposed spots with the smallest surface roughness observed for 0.6 J/cm^2.

In order to further determine the viability of laser polishing as a finishing technique, further work is needed to optimize the treatment process as well as determine if the treatment is effecting the surface structure and composition in any way. Our next step is treatment in a higher vacuum with the inclusion of a turbo pump in the system or in an inert atmosphere such as argon. This will identify whether there are any surface reactions during the treatment process with the particles in the cube or if there is a reaction due to the surface melting and solidification that causes the final

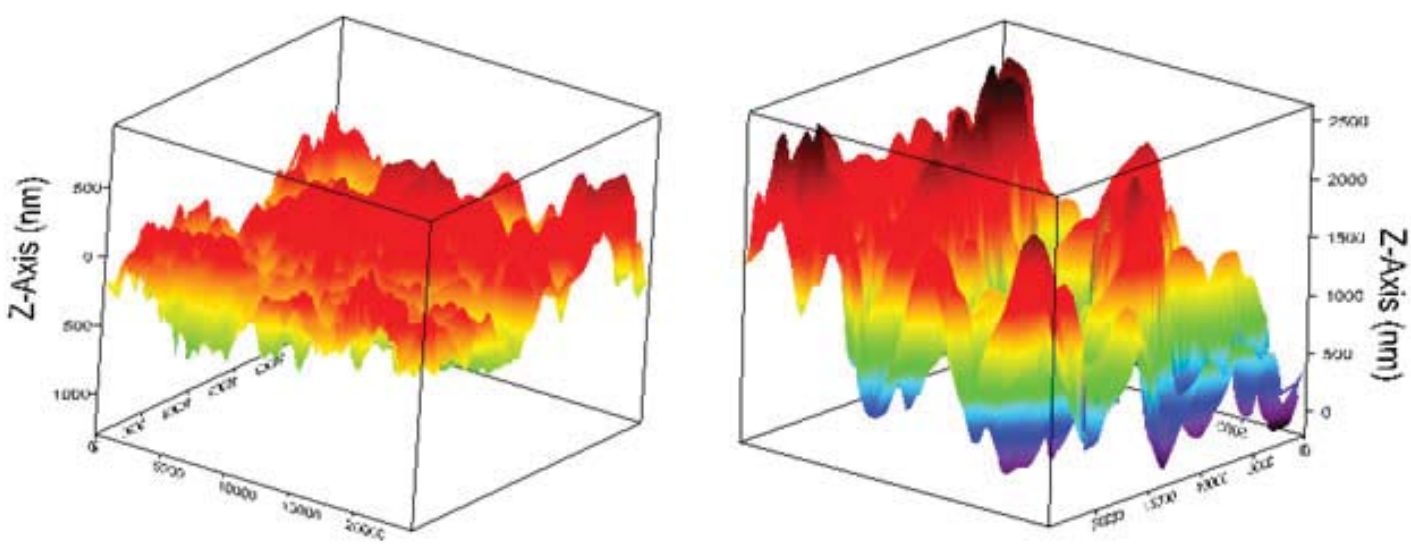

Figure 11: (Left) A 25 µm x 25µm AFM measurement of the .6 J/cm2 treated spot. (Right) A 25 µm x 25µm AFM measurement of the center region of a 1 J/cm2 treated spot.

surface to differ from the ideal niobium tin structure and composition. Additionally further work is needed to further pinpoint the energy density and number of shots within an area before focusing on the treatment of larger areas. Further development of a surface finishing treatment will propel the application of niobium tin for superconducting radiofrequency cavities.

V. References

[1]Reece, C. and G. Ciovati. "Superconducting Radio-Frequency Technology R&D for Future Accelerator Applications" Reviews of Accelerator Science and Technology, 5, 285, 2012

[2]Posen, S., M. Liepe, and D. L. Hall. "Proof-of-principle demonstration of Nb3Sn superconducting radiofrequency cavities for high Q 0 applications" Appl. Phys. Letts. 106, 082601, 2015

[3]Zhao, L., K. J. Michael, C. E Reece, and M. J Kelley. "Laser polishing of niobium for superconducting radio-frequency accelerator applications." Phys. Rev. ST Accel. 17, 083502 Aug 20144

[4]Bordatchev, E. V., A. M. K. Hafiz, and O. R. Tutunea-Fatan. "Performance of laser polishing in finishing of metallic surfaces." Int J Adv Manuf Technol 73, 35 Apr. 2014

[5]Singaravelu, S., K. J. Michael, C. Xu, G. Chen, and M. J. Kelley. "Laser polishing of niobium for application to superconducting radio frequency cavities." Journal of Vacuum Science & Technology B. 30, 051806, 2012

VI. Acknowledgements

This project was supported in part by the U.S. Department of Energy, Office of Science, Office of Workforce Development for Teachers and Scientists (WDTS) under the Science Undergraduate Laboratory Internships Program (SULI).

Raft optimization and readout test stand design of the raft electronics board for the Large Synoptic Survey Telescope

Jessica Li
Department of Mechanical Engineering and Department of Physics and Astronomy,
Stony Brook University, Stony Brook, NY 11790
Justine Haupt
Instrumentation Department, Brookhaven National Laboratory, Upton NY 11973

Abstract

The Large Synoptic Survey Telescope's (LSST) camera consists of an assembly of 21 Raft Tower Modules (RTMs) which contain electronics and Charged Couple Device (CCD) sensors. The design and construction of the LSST at Brookhaven National Laboratory requires extensive testing of the Raft Electronics Boards (REBs) in the RTM assembly. These experiments were conducted in a vacuum cryostat which houses a test stand that supports these boards. A structurally robust support system that allows for movement due to thermal expansion and contraction was developed for the boards. The support and thermal designs of the test stand will be made of copper and designed in Autodesk Inventor and thermally simulated in ANSYS. Designs will allow for cooling of the FPGA chip and other REB components. The main support of the boards consists of aluminum flexible helical couplings which will provide rigidity but also allow for flexure due to thermal expansion and contraction of the system as electronic cadences are performed. The conduction heat equation was used to calculate all the dimensions of copper and length of copper braids used as well as the contact area needed in between elements for dissipation of heat through conduction for sufficient cooling. The design must provide for a 20K temperature drop between the board cold bars and the cold plate and a 16K temperature drop between the raft base plate and the electronics cage walls. This test system will aid in the development and testing of REBs which are responsible for processing LSST's incoming sky data from the CCD sensors. The design process involves multiple iterations to ensure that the best possible design is developed and through these iterations, I learn from the flaws of past mistakes and improve upon the design until it works sufficiently and comply with thermal cooling specifications for the test stand.

I. Background

The Large Synoptic Survey Telescope's (LSST's) camera is made up of 21identical modules called Raft Tower Modules (RTMs).

Each RTM (Figure 2) is an integration of the mechanical and electrical assembly of the Raft Electronics Cage (REC) and the Raft Sensor Assembly (RSA). The REC houses the electronic boards and video processing which interfaces to the data acquisition system. It also contains copper bars which serve as the thermal path for cooling the electronics and CCDs. The RSA is a 3x3 mosaic of CCD sensors mounted on a baseplate made of low expansion material. The baseplate holds ceramic heaters, flexible copper straps for thermal conduction, and flexible electrical cables for the CCDs.

The mechanical requirements of the RTM includes thermal management of the CCDs and electronics, in order to test quantum efficiency, noise, uniformity, and charge transfer efficiency of the third design iteration of the Raft Electronics Boards (REB3s). In order to test the REB3s, an altered RTM was designed to fit in the Raft Optimization And Readout (ROAR) test stand cryostat chamber. Two main tests will be conducted: 1) Using a single REB3 connected to 3 CCDs in a vertical array on the raft, and 2) using three REB3s connected to the whole array of 9 CCDs on a single raft.

An RTM tailored to fit the REB3 boards will be placed in cryogenic vacuum environment inside the ROAR cryostat:

II. Methods

A. CAD 3D Modeling and Design for ROAR REB3 test stand

Using Creo 3.0, a CAD program, support brackets and a coupling system for the Cryotiger were 3D modeled as shown in Figures 5-6. In order to minimize heat transfer between the RTM and vacuum chamber walls, the support brackets were designed to be thin and have a long thermal path for an insulating effect. The chosen material is stainless steel 304 for the support brackets with Garolite washers which act as insulators between the RTM and support brackets. These materials have low thermal conductivity.

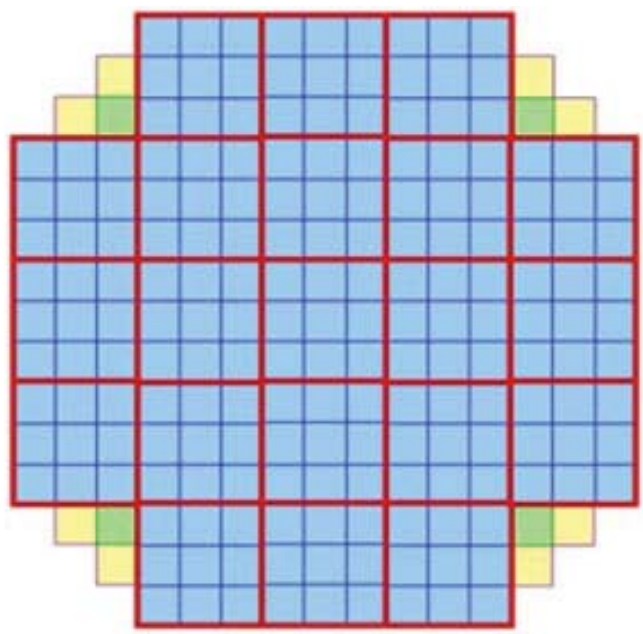

Figure 1. Organization of focal plane: CCD sensors (blue), guide sensors (yellow), wavefront sensors (green), raft boundaries (red)

B. Materials for ROAR test stand

The following list of materials is being used for the test stand:

1. Cu (OFHC): REC walls, Cryotiger, support plate, couplings support plate, thermal straps
2. AlN: ceramic heaters
3. Stainless Steel 304: structural support system
4. G10: spacers and washers in contact with supports to thermally insulate them from the REC walls
5. CE7: raft baseplate

C. Thermal System Calculations

There are two main thermal systems concerned with the cooling of the RTM. The first is the cold plate which cools the REBs and the second is the cryoplate which cools the RSA through the REC walls. Heat is produced from the running of electronics on the REB3 boards and the CCDs. The RTM is set to a cryogenic temperature of 145K where it has the material properties in this table (figure 7).

Heaters are applied to the RSA in order to heat up the RTM gradually as needed when bringing the test stand back to room temperature, or heat the RTM as needed if it is below the specified temperatures. CCDs may delaminate from cooler than specified temperatures and electronics may not work optimally, therefore it is imperative to keep the RTM at the constant specified temperatures as shown in Figure 6. Tabular data was used for thermal conductivities of each material in order to calculate heat transfer between RTM components.

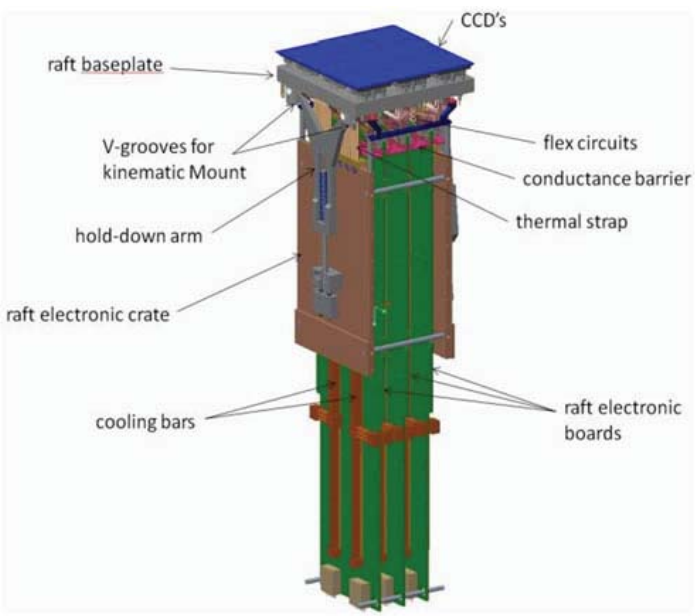

Figure 2. RTM

Figure 4 CAD models of thermal and structural systems.

D. Testing of the REB3s in the ROAR cryostat

The mechanical test stand will be assembled in the lab in the Instrumentation Department in order to electronics testing while connected to the CCD sensors. The data collected will yield information regarding quantum efficiency, noise, uniformity, charge transfer efficiency, and crosstalk between the REB3s while they are in operation.

III. Conclusions and Recommendations

After the CD3 review, I was able to speak to some of the physicists and engineers from around the world and from University of Pennsylvania and Harvard University in order to receive feedback for my test stand prototype. There was concern about slippage of the raft baseplate from the tooling balls due to the attenuated tension applied on the RTM while installed in the ROAR cryostat as opposed to in Test Stand 7 (TS7) which involves Cryostat Integration of the full RTM into a cryogenic vacuum system. In TS7, the RTM would have twice the tension to hold down the baseplate onto the tooling balls while in the ROAR test stand, there would only be half of the tension. There was a debate as to whether the ROAR test stand should accommodate for mechanical systems in conjunction with the testing of the REB3 since the lead time for adding the mechanics would be greater than simply creating an appropriate environment for electronics testing. There

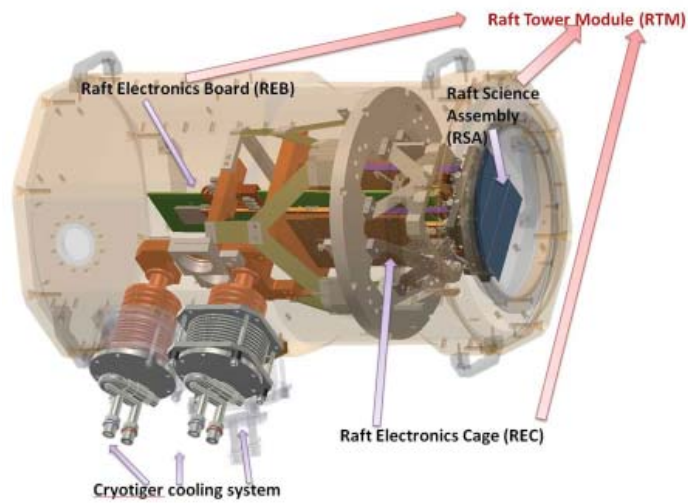

Figure 3. CAD model of the ROAR cryostat with the RTM in place.

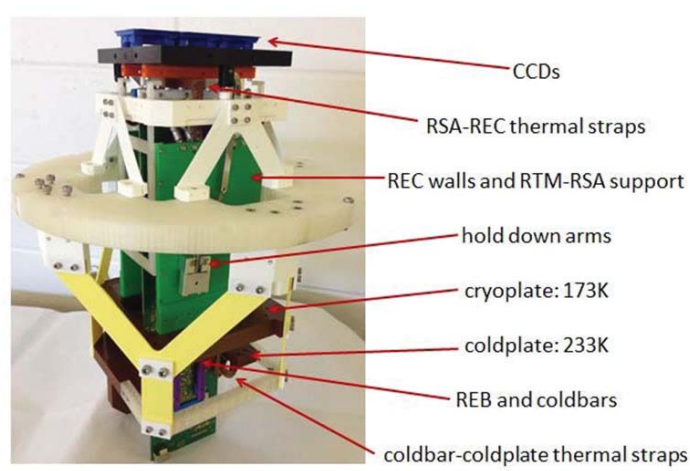

Figure 5 Assembled prototype with thermal and structural support systems

was also a concern of shorting of electronics on the electronics board using the flexible copper thermal braids for cooling of the REB3. In order to ease these concerns, I suggested that we apply Kapton tape to the areas of concern to create a boundary between the electronics and the copper braids. Furthermore, it would be difficult to line up the REC walls to the cryoplate due to the limited room in the cryostat for assembly. A solution would be to design alignment pins that would be removed once the RTM is installed flush to the cryoplate.

IV. Acknowledgements

I would like to thank my mentors Justine Haupt and Steven Bellavia, along with Jason Farrell for their unfaltering patience and for generously devoting so much of their own time to guide and teach me in this project. Furthermore, I would extend my gratitude to Bill Wahl for the encouragement and support they have given me throughout my time here. This project was supported by the U.S. Department of Energy and Office of Science under the Science Undergraduate Laboratory Internships Program (SULI).

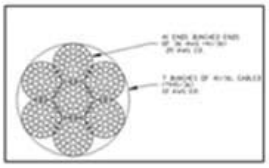

$$k_{Cu} = 400\frac{W}{mK}$$

$$q_{cond}[W] = \frac{-kA(T_1 - T_0)}{L} \qquad n_{braids} = \frac{qL}{kA(T_0 - T_1)}$$

braid gage	wire Gage	# wires/braid	braids/ strap	Indiv. wire Dia	K	Cp	Density	Total A	L	Total Volume	Total Gi	Total Ri	Total Mass	Total M*Cp
	-		-	m	(W/m-K)	(J/Kg-K)	Kg/m^3	m^2	m	m^3	W/K	K/W	Kg	J/K
11	40	1050	7	7.9868E-05	400	342	8960	3.68E-05	0.0679	2.50E-06	0.22	4.610	2.24E-02	7.66E+00
7	40	2156	1	7.9868E-05	400	342	8960	1.08E-05	0.0679	7.33E-07	0.06	15.715	6.57E-03	2.25E+00
8	44	4655	4	0.0000508	400	342	8960	3.77E-05	0.0679	2.56E-06	0.22	4.498	2.30E-02	7.85E+00

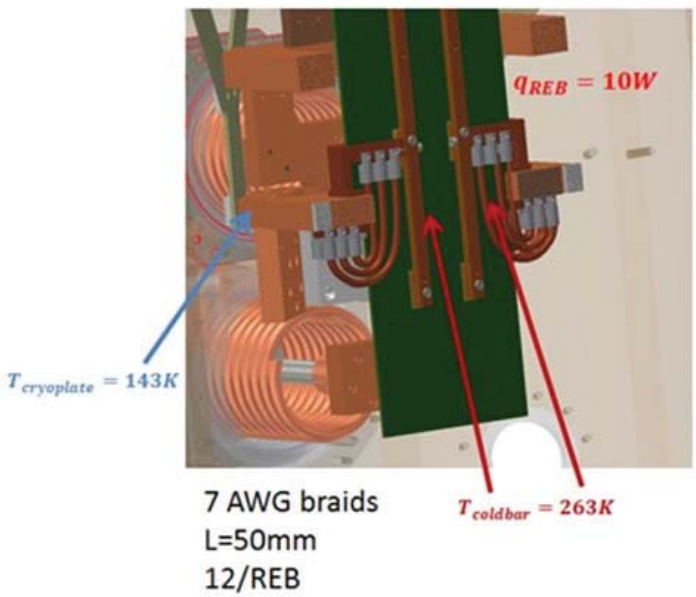

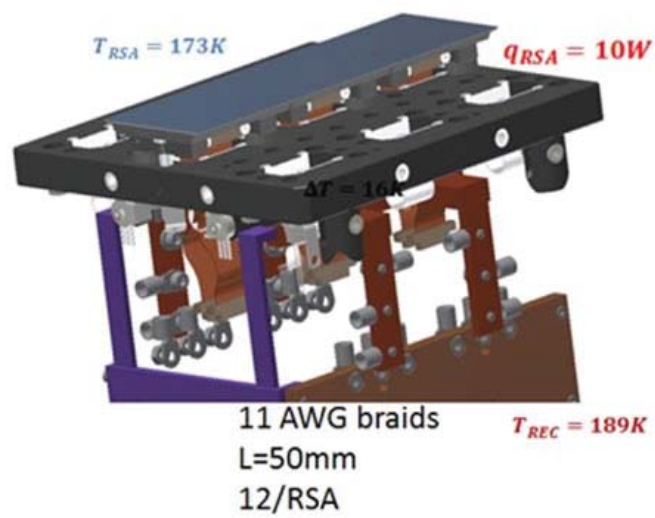

Figure 6 Excel calculations for choosing gauge and length of thermal braids.

The following material properties were used for cryogenic conditions.

Material	Density (kg/m^3)	Young's Modulus (GPa)	Poisson's Ratio
SS 304	7750	193.0	0.31
G10	1910	32.3	0.12
Cu (OFHC) braided wire	8940	1.0	0.01
Cu (OFHC)	8915	115.0	0.31

Figure 7 Table of material properties used for static structural test simulation

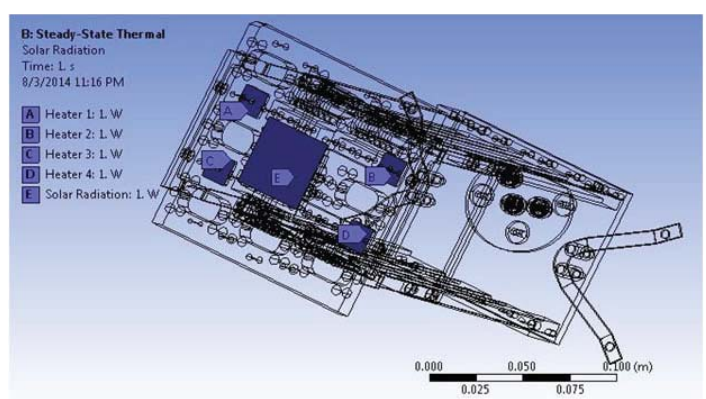

Figure 8 Location of applied heat flows on RSA raft baseplate shown in wireframe view in ANSYS.

Adding diagnostics to the Relativistic Heavy Ion Collider's main magnet power supply phase-loop lock and silicon controlled rectifier-firing board

Raul Martinez
Electrical & Computer Engineering and Computer Science, Syracuse University, Syracuse, NY 13210
Carl Schultheiss
Collider-Accelerator Department: Collider Electric Power Supply Group,
Brookhaven National Laboratory, Upton, NY 11973

Abstract

One of Brookhaven National Laboratory's (BNL) highly used research facilities is the Relativistic Heavy Ion Collider (RHIC). The RHIC's main magnet power supply controls the current that steers its beams around its rings and at the heart of this power system is the Phase-Locked Loop (PLL) and Silicon Control Rectifier (SCR) Firing Board. This board uses a PLL to track the frequencies of the incoming power line that is then used as clock signals to the SCR digital firing section of the board that controls which SCR pairs to fire; the SCR's power the main magnet. Being active for almost two decades the RHIC's hardware has been used extensively and could be experiencing issues that may cause the magnets to fail and without the board functioning correctly the RHIC will not operate properly. Due to these potential problems a diagnostics system was deemed necessary to be added to the board in order to provide internal real time data. This diagnostic system needed to be designed so that it could read and write data from several different PLL and Murray Filter components every time a new set of data was available. That meant that the diagnostics needed to be fast enough to read all of the data from the desired components and write them into a memory block. The system is composed of three modules: a 5:1 Multiplexer where the data was read, a State Machine that selected what component to be read in and a Memory Bank where the data was written to. The system was designed using the Very High-Level Design Language Verilog and the Altera Quartus II programmable logic device (PLD) design software. Once implemented the diagnostic system will be able to assist in finding out if the SCR firing cards are firing the correct SCR pairs or if the PLL is reading the correct phase frequency.

I. Introduction

A. Understanding the system

As mentioned above the overall goal for this specific project was straightforward and concise: a diagnostic system needed to be designed, created and implemented into the RHIC's Phase-Locked Loop (PLL) and Silicon Control Rectifier (SCR) Firing Board to check if it's still hardware is still operating correctly. Before designing and planning for the diagnostics system, the current magnet power supply system and its importance needed to be explored and understood. The main reason why this PLL and SCR firing board is a very important piece of hardware is because the RHIC's main magnet power-supply system uses a 12-Pulse Phase Controller Power Converter.

A 12-Pulse Phase Controller Power Supply's output voltage depends on the SCR pairs that are going to be fired; a total of 12 pairs are fired per cycle hence the 12-pulses. Before the SCR pair can be fired the 3-phase power lines frequency goes through the PLL, the reason the frequency is so important is because the frequency runs the firing system.

The phase locked loop uses a feedback control system that takes the incoming 3-Phase power line signal's frequency and uses it as a reference to its counter. The phase lock loop locks on to the incoming power lines frequency by using a counter that counts up to match the power lines frequency. The PLL is able to tracks the changes in the frequency by adjusting it's "inner counter" to match the those changes. If the frequency doesn't change then the PLL will remain counting up to the same value and resetting, making it a clock. The phase lock loops then uses the counter as the firing boards master clock signal, which times the entire card. If the master clock timing is off, the SCR pairs will not fire or the wrong pair could be fired because of an overlap in signals.

B. Understanding the task

Now that the RHIC's main magnet power supply and the task of the project was understood and depicted, it was time to understand what parts of the system needed to be observed and diagnosed. The main part of this system is the PLL because, not only does it generate a master clock for the system but it also uses the incoming power lines frequency to generate a reference and command counters that are used in the SCR selection and firing process of the board, which is related to the incoming power line. That meant that the diagnostics system's focus was to find out if the PLL itself was working correctly for this specific design.

The PLL 's control system is composed of modules that include a low-pass Murray filter, a numerical controlled oscillator (NCO), a phase detector (PD), and a phase accumulator (PA). Since these where the PLL main components the system needed to be designed to focus on those specific parts. In order to check the PLL's functionality, data had to be acquired from the different parts of the PLL control system so that is could be analyzed. The diagnostics system needed to be designed in a way that all the data could would be readable and the data corresponding to the part of the system we where analyzing and not another section. Not only that but it had to make sure all the data was valid.

II. Diagnostic System Design Planning

The first step in creating any kind of system was planning. So the first step in this project was planning out what the diagnostic system needed to have component wise so that it ran efficiently and did everyone of it's required functions like reading and writing data for example. Before the design plan could be started a few things had to be noted. The system was going to be programmed using the Very-High Level Description Language-Verilog and the Altera Quartus II programmable logic device (PLD) design soft-

ware in order to program the Altera Cyclone III FPGA board.

A few of the basics as discussed above where that the system needed to have valid data when writing it to memory, that meant that the system needed to meet a hold and set time that would allow the system to cycle through the data, read and write it somewhere before a new set of data was generated. If the systems hold and set times where not set correctly the data being taken could be skewed and would mess up the analysis. Since we want accurate data that also meant that the system clock speed needed to be faster than the PLL's clock, which is around 44.8289kHz but the PLL frequency would serve as the system enable because the data would be valid every cycle. The Cyclone III FPGA has an internal clock that runs at 150MHz but that was going to be too fast for this system, so the signal needed to go through a clock divider to be slowed down to a reasonable speed.

All the data that was going to be taken from the system needed to be stored somewhere. Since the system sample rate was going to be the frequency of the firing card, which was around 44.8289kHz, the memory needed to be big enough to take enough samples every second from the different parts of the system. The data samples that where going to be taken where roughly 32-bit words in size or where going to be made that size to keep uniformity. That meant the memory block was going to be around 44829x32 because memory needed to be big enough to fit 1-second worth of data and the samples were ready at a rate of 44829kHz which is the same as 44829 cycles/second or 44829

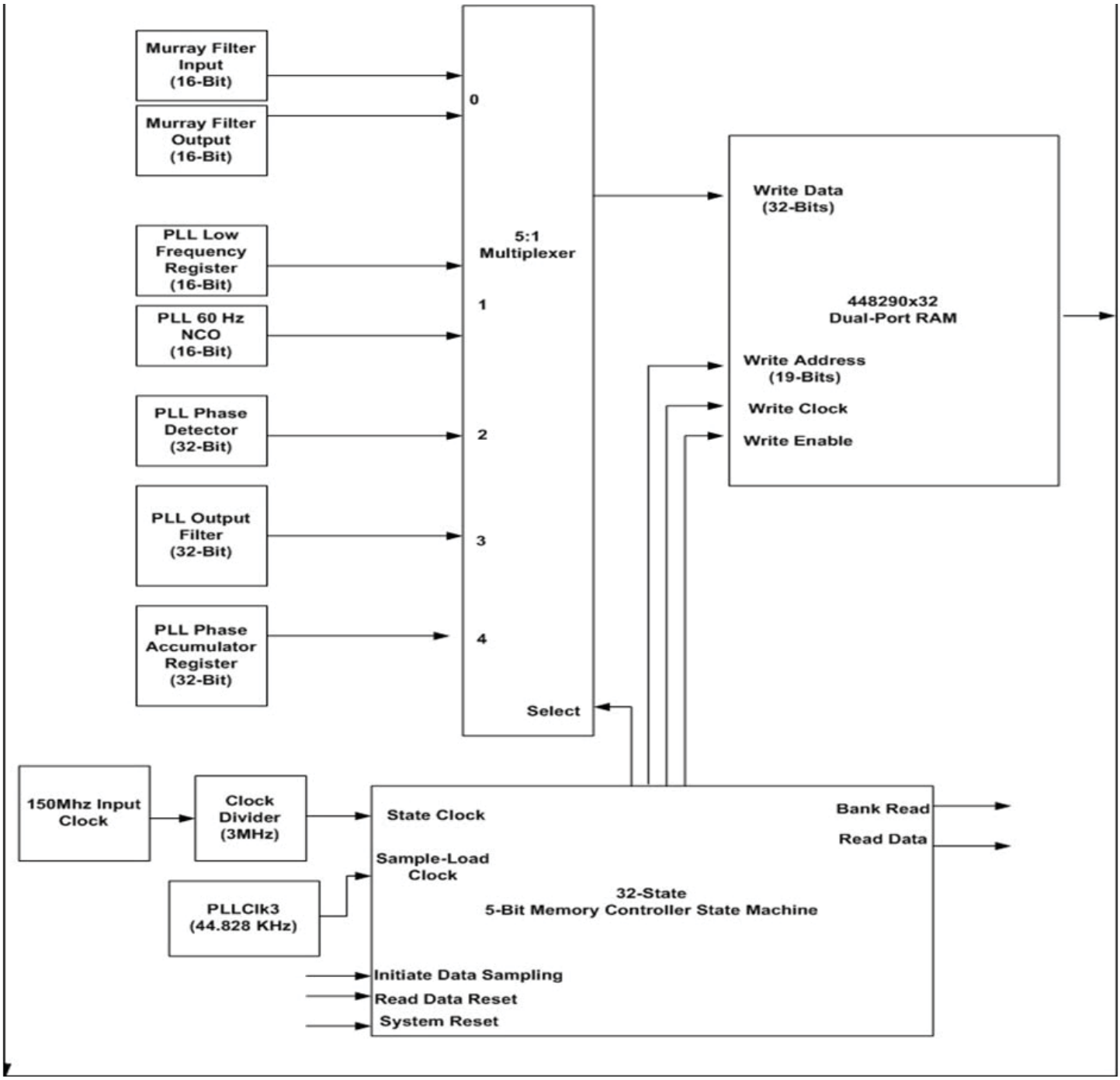

Figure 1: The diagram above shows the basic parts of the planned diagnostics system design. The reason for the bit sizes for the different components as well as the inputs and outputs will be discussed in the next section.

samples every second. Since we want to be able to read from and write to memory, the system needed to have Dual-Port RAM as its memory component. Dual-Port RAM allows the system to write into the memory blocks and allows the user to read from memory.

The next component that needed to be part of the diagnostic system was a very important one. Since the system was gathering data from multiple parts of the firing board, that data needed to be properly handled and not mixed with other data being read from the different PLL components. Since this is a big system there are multiple data paths that use a lot of the same signals so having a way to decide what data was going to be used was needed. That meant that a multiplexer needed to be used as a way to separate what data was going through the system first. This system's focus was the PLL and its control system so we wanted data from the Murray filter, NCO, phase detector, and a phase accumulator so the multiplexer needed to be big enough to fit those components.

The multiplexer would handle the data being written to memory so the next piece of the system needed to help the multiplexer select which piece of data was to be written and when it would be written. In order to be able to select what data to pass from the multiplexer a finite state machine needed to be implemented into the system. The finite state machine would handle selecting which piece of data to be inputted by the data. The finite state machine was probably the most important part of the diagnostic system because not only was it the selector for the multiplexer but it would also serve as the Dual-Port RAM's write enable and write clock signals. The state machine would also generate a write address that would be sent to memory so the RAM knew where to store the data the multiplexer passed to it. This was practical to do since the state machine would be deciding what data to pass, it would make sense for it to also serve as the RAM's writing controller.

In the end the main components that were going to be in the diagnostic system where going to be the multiplexer, the finite state machine and the Dual-Port RAM. Figure 1 below shows a block diagram containing the different system components discussed and planned connection scheme. The design will be discussed further in the next section of the report.

III. Designing the Diagnostic System

The Diagnostic System design is mainly composed of three modules; a multiplexer, memory bank and state machine as discussed in the previous section.

A. The Multiplexer

The first component is a 5:1 Multiplexer, which was outputting the data that was going to be read into memory. There where seven signals that were very important and vital for the system. The problem was that they were not all the same size. The signals that where of interest where the Murray Filter input and output, the PLL NCO and it's Lo-Frequency register, the Phase Detector, the Phase Accumulator and the PLL's output filter which helps with checking the error in the PLL control system. The reason why a 5:1 Multiplexer was used rather than a 7:1 was due to the variety of sizes of the signals.

The Murray Filter input and output where both 16-bit pieces of data. The PLL's NCO and Lo-Frequency register where 16-bit piece of data. The PLL's phase detector was a 32-bit signal. The PLL's phase accumulator and output filter where both 40-bit signals. In order to optimize the system, the Murray Filter's input and output where concatenated together to create a 32-bit word. The PLL NCO and Lo-Frequency signals where also concatenated. The PLL output filter and phase accumulator's 8-least significant bits where dropped in order to make both signals 32-bit words. Now rather than having 7 different signals, there were only 5 signal inputs for the multiplexer. Each one of the 5 signals was assigned one of the multiplexer's inputs. The state machine would select which one of the 5 would be allowed to pass through the multiplexer.

B. The Finite-State Machine

The next module in the system is the Finite-State Machine. This part of the system was the most complex of the three because the different functions and tasks this state machine needed to carry out. That meant the state machine needed to have enough states so it could carry out every function correctly. The first thing the state machine needed to be able to do was generate a select signal for the multiplexer. Since there are 5 possible signals to choose from the select signal needed to be big enough to cycle through the 5 possibilities, which is why a 3-bit was going to be used. By making it 3-bits the signal was able to cycle from 0-7, giving it ample room to select the one of the 5 signals wanted. The remaining 3 "selectors" where not used in the system so that meant the state machine needed a minimum of 5 states so each signal could pass the multiplexer. The state machine was also going send a few signals to the Dual-Port RAM.

The state machine was cycling through the data that was being passed through the multiplexer because of its select signal, once the data passed the multiplexer it would be written to the Dual-Port RAM. The Dual-Port RAM was going to have at least 44829 different locations that data could be stored in so a counter was added into the state machine to address the different addresses. Since the state machine was going to be going through its different states to send the select signal to the multiplexer, it had the ability to keep count of how many times a signal was passing. Each time a signal passed the address counter would be incremented. The address was going to be a 16-bit signal so it could address up to 65536 different words, a 15-bit address wouldn't be enough to address the targeted 44829. Since the address counter would increment when the select signal changed the state machine still only needed 5 states.

So far the state machine was responsible for selecting what input to pass through the multiplexer and sending an address to the Dual-Port RAM to let it know where to write the data. The Dual-Port RAM however still needed a write clock and an enable signal and since the state machine was sending the address signal to memory it made sense for the state machine to also send two pulses to the RAM, one for the clock and one for the enable. Each time the address was send to the memory a write enable was also sent to the RAM to let it know that the multiplexer and state machine were about to send it data. The following state the state machine would send a pulse that would be that write clock so that when it went high the memory would allow the data from the multiplexer be stored in the address sent from the state machine. In the next state both the write clock and enable would be set to low.

The state machine now had 15 states, 3 states for each of the 5 inputs going through the multiplexer. Two states where added at the end of that last state for safety. As mentioned earlier, the systems clock was faster than the sampling clock so it could be a possibility that the state machine could finish before new samples where generated, and since the PLL clock was the system enabled

the PLL clock signal could still be high when the state machine finishes its task. The state machine would then assume new data is present because the enable is high and it would continue to write the same data, which would skew the system. In order to prevent this from happening, a state was added so that the state machine would wait until the PLL clock signal went low. Once it was low it would go to the next state where it would remain until the PLL clock went high again and new samples where available. Two safe states were added at the beginning of the already present 17. The first safe state was the initial state. This state was only obtainable if the system went through a hard reset, meaning the system-reset input was high. This state reset all of the signals in the state machine, even the address. The next safe state was used as a "system safe state" meaning the state machine finished one cycle; it went through the next 17 states. Once it finished going through the 17 states that meant all the data except the write address was going to be new. The purpose of the safe state was so that none of the signals kept the data from its previous run, the reason why the address wasn't reset was because it incremented continuously until memory was full. When memory was filled, a signal was sent to from the state machine itself that was returned as an input, which told the state machine to reset the write address; this will be discussed in the next section.

In the end, the state machine had 19 states that were used; a system reset, a restart cycle state, a PLL clock low waiting state, a PLL clock high waiting state, each of the 5 multiplexer input had 3 states each where one was enabling memory, selecting what data to pass and where to send it to in memory the other set the write clock and the third reset the clock and enable signals. Since there are 19 states being used that meant that a 5-bit signal was needed to cycle through the states. A 5-bit signal produces 32 possible states even though the system only uses 19; the remaining 11 states where not used but if for some reason the system managed to slip into one of those unused states the state machine would automatically send it to the restart cycle safe state.

C. Dual-Port RAM

The memory bank used for the system was a Dual-Port RAM because the user would have the ability to write to memory as well as read from it. The focal point of this project is having the power to write to memory and extract that has been written in memory to analyze the data. Originally, as mentioned in the previous sections, the memory was set up to fit up to 524,288 different 32-bit data points because we wanted the system to fit 44828 samples for each of the 5 different input signals which turns out to 225,000 samples. But it turned out that the FPGA board being used for this system didn't have enough memory to fit that much data because of all of that data and modules already programmed onto the board.

To fix this problem a new timing scheme was needed. Originally the PLL clock, which ran at 44.282kHz was the system-sampling rate reference because it was the systems goal to obtain 44828 samples a second. It turned that if the PLL clock signal went through a counter and only enabled the system every 90 counts that it was possible to gather almost 500 samples a second. Although it wasn't near the planned 44828, it was enough to reconstruct the data using sampling theory. This new sampling scheme was effective because the state machine was already generating 16-bit signals, now all it needed was 10-bits. Since the system is no longer using all 65,000 possible addresses, the addresses needed to reset even soon.

To acknowledge this potential issue two signals where added to the state machine, Bank Read and Data Read. Memory was now going to use 1024 possible space instead of the 65,000, so when the address reached around 500, the Bank Read signal would go high alerting the system that the fist half of the memory was filled and telling memory to switch to the second half of the memory bank. When the address reached around 997 the Data Read signal would go high. When both signals where high the VME would send a high signal to the initiate data read input of the state machine so the address counter would reset as well as the Bank and Data read signals. Due to this it didn't matter that the address was

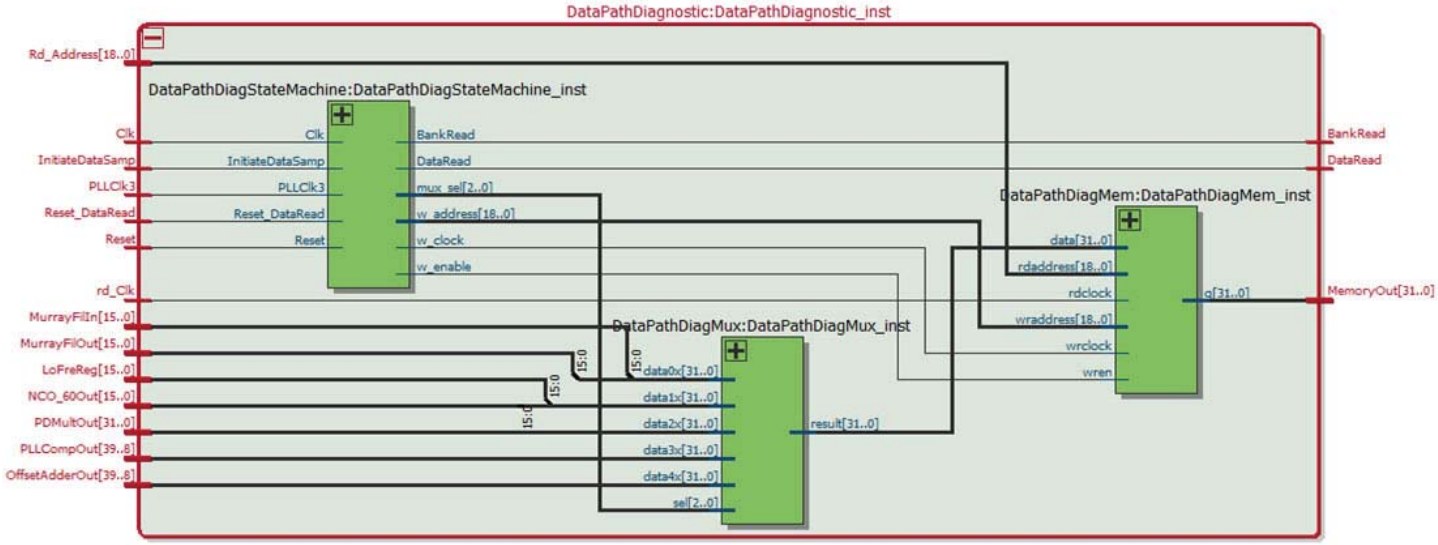

Figure 2: The diagram above shows the system RTL box diagram. You can see the connections being made from inside the combined module that were described in section D. The outer connections are inputs and outputs that are coming from outside of the system. Everything in the light green box is generated from the 3 modules.

a 16-bit signal, only the 10 most significant bits where used in the system. Once the data was written in memory the Dual Port RAM would then output an address to let the VME know that there was data ready to be read out of memory. The VME was used to read data from memory from either one of the two banks. When the VME wanted to read from the memory it would send a read address and a read clock signal to memory.

D. System Instantiation

Now that each part of the system was designed it was time to combine all three of the system's components into one module. The multiplexer's select input needed to be connected to the state machine's mux select output which was the signal generated by the state machine to address what data to pass through the multiplexer. The multiplexer's result output needed to be connected with the Dual-Port RAM's data input, which was the data that was going to be written into memory. The state machines write address, clock and enable signals needed to connect to the memory write inputs. Lastly the signals coming from outside the system like the PLL and Murray filter data needed to be connected from outside of the module. Figure 2 below shows the different modules being instantiated into one block that were just described.

IV. Results and Conclusion

Once the three modules were successfully coded, instantiated and compiled, it was time to instantiate the newly designed system to the PLL and SCR Firing Board hardware code. By adding it to the existing hardware and compiling it into one whole system it was possible to test the system and trouble shoot it if it required.

After successfully combining the created diagnostic system with the firing board it was time to load the board into the computer backplane, which had the full test system. The full test system included part of the RHIC Main Magnet Power Supply system, which powered a test magnet. This test system allows the user to test new boards that are designed before they are implemented into the over RHIC Power Supply System.

It turned out that when loaded onto the hardware it was able to execute its function. The system was able to load the data it wanted from the different PLL components, pass it into the multiplexer and successfully write it onto the memory bank. The state machine state transition timing was good and the multiplexer hold and set times where properly met so the data didn't get lost at the bus. The addresses generated by the state machine where properly incrementing and reset as soon as the memory banks were filled and ready to be outputted.

The image below shows a screenshot of a logic analyzer that shows the system properly functioning. We can see the states properly incrementing and transitioning at the rising edge of the clock. You can see that the write address only changes every 3 states as planned as well as the state outputs that correspond the active state like the write enable and multiplexer select. You can see the PLL clock signal counting up to 90 and sending a pulse once the count is met. We can also see the proper data being loaded into the multiplexer and then outputted into memory. In the end it is safe to say from the image below that the system properly worked and executed its main functions. The system application will allow the user to gather data and use it to analyze and determine if the card is properly operating.

V. Acknowledgements

I'd like to thank the Collider-Accelerator Department, especially my mentor, Carl Schultheiss, for his advice and support throughout my project. I'd also like to thank the Office of Educational Programs, especially Noel Blackburn, Mike Stegman, Sal Gonzalez, and Cindi Biancarosa, for their support throughout our project.

This project was supported in part by the U.S. Department of Energy, Office of Science, and Office of Workforce Development for Teachers and Scientists (WDTS) under the Science Undergraduate Laboratory Internships Program (SULI).

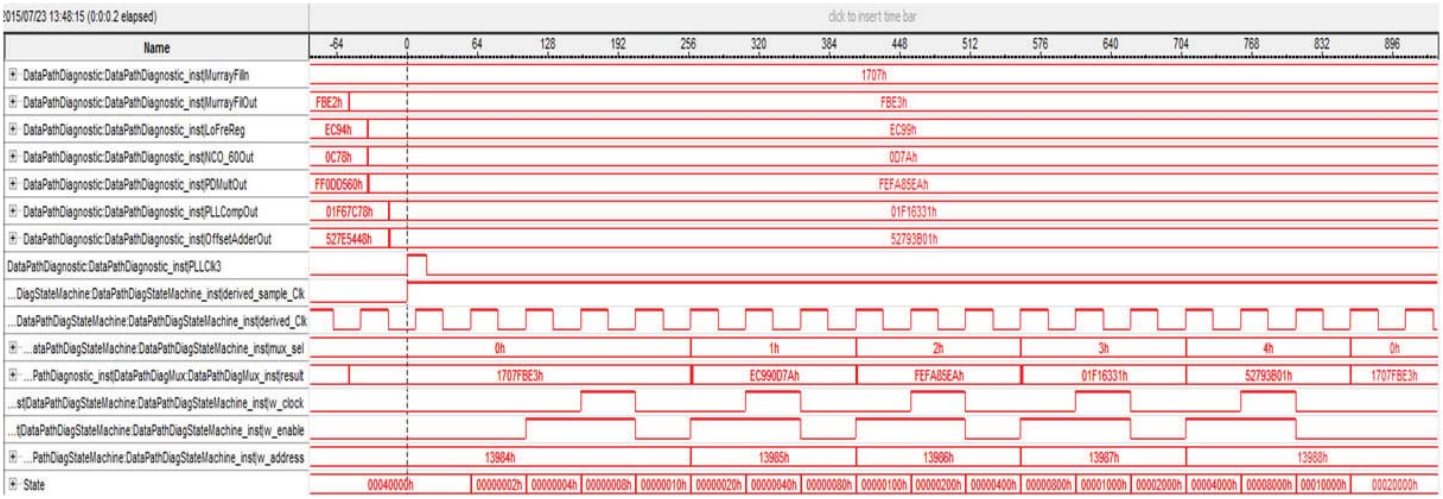

Figure 3: The figure above shows the Diagnostic System and its internal signals. From the image it is safe to conclude that the system works properly and executes all of the required commands.

Development and commissioning of tools for measurements and online calculation of electron beam lifetime in the National Synchrotron Light Source - II storage ring

Jessica Mele
Applied Mathematics and Statistics, Stony Brook University, Stony Brook, NY 11794
Guimei Wang, Boris Podobedov, and Timur Shaftan
Photon Sciences, Brookhaven National Laboratory, Upton, NY 11973

Abstract

The National Synchrotron Light Source – II (NSLS-II), a 792 meter-long storage ring designed to run 500 mA of a 3-GeV beam, currently serves high-brightness X-rays to seven beamlines (60-70 in its final build out). High X-ray brightness requires beams with high current and small size leading to a high charge density of the electrons in the circulating bunches. The powerful high-density electron beam decays in intensity over time due to particle loss caused by the intrabeam scattering of electrons. The Touschek effect, which describes particle loss due to momentum transfers in collisions, dominates the beam's lifetime, a figure of merit of the beam performance that is critical for the whole facility. Short lifetime leads to shorter periods of beam availability between subsequent refills and a lower efficiency of operations that usually indicates problems with the machine set-up. This project is focused on the development of methods for online lifetime measurements and calculations. The expected Touschek lifetime can be calculated using analytic functions and a complex integral that depend on a set of beam parameters. I developed a Python graphical user interface (GUI) that reads Process Variables (PVs) from the NSLS-II control system and uses them to compute the necessary derived quantities and the parameter of interest for the Touschek integral calculations. The computation of the expected lifetime in my program includes two separate equations to provide a cross-check and ensure reliable results. The program takes readings from beam position monitors and direct current-current transformers to determine the actual lifetime of the beam by creating a plot of beam current versus time. The GUI displays PVs, derived quantities, a current plot, and the discrepancy between the measured and expected lifetimes to machine personnel.

I. Introduction

The National Synchrotron Light Source – II (NSLS-II) is the 792 meter long storage ring that holds a beam with an energy of 3-GeV. The electrons enter the storage ring vacuum at 3-GeV. As these bunches circulate, they emit high energy photons that are released from the storage ring and distributed to beamlines. NSLS-II currently serves high-brightness X-rays to 7 beamlines and will expand to approximately 60-70 in its final build. From here, beamline scientists use the X-rays to conduct groundbreaking research.

The powerful high-density electron beam decays in intensity in time due to particle loss caused by the intrabeam scattering of electrons. The continuous loss of particles results in a finite beam lifetime.[1] The beam's intensity decay rate is proportional to the number of particles in each circulating bunch of electrons and is therefore modeled by exponential decay. The formula for the decay in current over time is given by:

$$I(t) = I_0 * exp\left(\frac{-t}{\tau}\right) \tag{1.1}$$

Where I_0 represents the initial current, t is the time of the measurement and τ is the lifetime of the storage ring. Considering this equation at the specific instance where $t = \tau$ (lifetime):

$$I(\tau) = I_0 * exp(-1) = \frac{I_0}{e} \Rightarrow I(\tau) = \frac{I_0}{e} \tag{1.2}$$

Indicates that the intensity at a specific time $t = \tau$ (lifetime) is reduced from the initial intensity by a factor of e.

Looking at a rough sketch of a graph of current versus time (see Figure 1) for a general injection of electrons until an intensity I_0,where the initial intensity I_0 and the calculated intensity of $\frac{I_0}{e}$ are labeled as the start and finish points respectively, lifetime is described as the time it takes to decay from start to finish.

Lifetime is not a constant value, but a function of time. As the current of the storage ring decreases, the lifetime increases (see Figure 2). When the electrons are first injected into the storage ring and the intensity is high, there is a high level of gas desorption on the surface of the vacuum chamber that leads to a reduction in the vacuum pressure. As the beam begins to experience particle loss, the vacuum improves thus improving the lifetime as well. [1]

The dominating factor for the beam lifetime at NSLS-II is particle loss due to the Touschek effect. The Touschek effect describes particle loss due to momentum transfers in collisions between electrons and other residual gas atoms in the storage ring. Specifically, this occurs when the large momentum of the transverse oscillations of particles transfer into large longitudinal momentum. When the transferred momentum exceeds the rf-momentum acceptance of the storage ring, particles are lost.[2]

Short lifetime leads to more frequent refills and lower efficiency of operations that is usually caused by problems with the machine set-up. Beamline scientists favor long lifetimes due to longer periods of beam availability between the subsequent refills. Currently there is a program that frequently updates and displays the current, daily amp hours, and actual lifetime of the electron storage ring (see Figure 3). In order to determine whether or not the facility is performing well there exists a desire to compare these measured values with expected values.

This project is focused on development of methods for online lifetime measurements and calculations and will reliably display the measure of facility performance, with regards to the beam's lifetime, to all NSLS-II accelerator and beamline scientists.

II. Methods

Calculating the Measured Lifetime of the Beam

There are Beam Position Monitors (BPMs) and Direct-Current Current Transformers (DCCTs) located at various positions around the storage ring. As seen in (Figure 4), BPMs are connected to the storage ring in four places. As electrons pass through the sections of the storage ring where these devices are located, an induced current is created and read in through the appropriate devices. These devices can then tell us the total current of the beam.

The current values read in from these devices are then plotted with respect to time. If we take the time interval to be extremely minute, we can form a linear fit to the data points and calculate the measured lifetime.

$$I(t) = I_0 * exp\left(\frac{-t}{\tau}\right)$$

$$t \ll \tau$$

$$I(t) = I_0(1 - \frac{-t}{\tau})$$

$$I(t) = kt + c$$

$$k = \frac{-I_0}{\tau}, c = I_0$$

$$\tau = \frac{-c}{k}$$

The measured lifetime needs to be compared to an expected lifetime so that machine personnel can monitor the facility's performance while it is running. Without an expected value to use for comparison, beam users do not have a way of determining how well the beam is running or if improvements can be made to lengthen the lifetime.

A. Calculating the expected lifetime of the beam

The expected Touschek lifetime can be calculated using analytic functions and a complex integral that depend on a set of beam parameters. There are two equations that can calculate the expected Touschek lifetime of the electron storage ring:

(3,1)

$$\tau TS(x) = \frac{8 * \pi * \gamma^3 * \sigma zn * xa * \sigma xp * ya * x^2}{N0 * r0^2 * c * f\left[\left(\frac{x}{\gamma * \sigma xp}\right)^2\right]} * \frac{1}{3600}$$

Where the function ***f*** is:

(3.2)

$$f(\varepsilon) = 0.5 * \int_0^1 \left(\frac{2}{u} - ln\left(\frac{1}{u}\right) - 2\right) * exp\left(\frac{-\varepsilon}{u}\right) du$$

(4,1)

$$\tau TB(x) = \frac{\sigma xp * \gamma^3 * x^2 * 8 * \pi^{1.5} * \sigma zn * xa * ya}{\sqrt{\pi} * N0 * r0^2 * c * CW\left[\left(\frac{x}{\gamma * \sigma xp}\right)^2\right]} * \frac{1}{3600}$$

Where the function *CW* is:

$$CW(\varepsilon) = \frac{-3}{2} * \exp(-\varepsilon) + \frac{\varepsilon}{2} * \int_\varepsilon^\infty \frac{\ln(u)}{u * \exp(u)} du + \frac{(3 * \varepsilon - \varepsilon * \ln(\varepsilon) + 2)}{2} * \int_\varepsilon^\infty \frac{1}{u * \exp(u)} du$$

σxp = beam divergence
γ = relativistic energy (Lorentz factor)
xa = average width of Gaussian distribution
ya = average height of Gaussian distribution
N0 = number of electrons per bunch
r0 = electron radius, m
σzn = bunch length, m
x = εRFn = energy accpetance

The filling pattern monitor PV (Figure 5) reads in a list of values from buckets around the storage ring. The storage ring is comprised of 1320 buckets, each uniquely filled with varying values in current. Therefore, the value of the total current of the ring can be defined as the sum of the individual currents found along these buckets multiplied by the revolution frequency. As you can see from Figure 5, the values read in from the various buckets around the storage ring are extremely inconsistent with one another. My program is complex enough to take this inconsistency into consideration to accurately calculate the expected lifetime of the electron beam.

The equations for calculating lifetime are calculated with the parameter of interest of the integrals being:

$$Parameter\ of\ interest(\varepsilon): \left(\frac{x}{\gamma * \sigma xp}\right)^2$$

with x = εRFn

If we set the number of bunches and the single bunch current to be 1 mA, then the values *τTS(x)* and *τTB(x)* can be considered as τ^* where the total lifetime of the storage ring is defined as:

$$\frac{1}{\tau} = \frac{\sum X_i^2 * I_{tot}}{\tau^*}$$

$$X_i = \frac{I_i}{I_{tot}}$$

Where each I_i is the value of the current at the ith bucket from the filling pattern monitor PV.

III. Results

The GUI (see Figure 6) displays imported PVs (on the left) and necessary derived quantities (on the right). The center of the window displays two graphs: current versus time and lifetime versus time. Directly underneath the graphs are the expected lifetimes from each of the two formulas for the Touschek lifetime predictions, the measured lifetime and difference between the two values.

The entire program is written in the Python programming language. The window itself, as well as all of the widgets, were created using PyQt4. I chose to disable the imported PVs from the control system so that users cannot accidentally change these values. The coupling value is the only PV that I left enabled. This is due to the fact that the coupling value comes from X-ray diagnostics, which are currently not running for NSLS-II.

The plots in the center of the window were created using matplotlib. The program reads in the total current of the beam and the lifetime of the beam from the control system. Plots are then created to show their dependencies. The graphs are embedded using a FigureCanvas method of matplotlib so that it can update the graphs by drawing in new values as more values get imported into the program.

The program has one calculate button. If there is no coupling value entered into the appropriate text field, then an error message will pop-up to remind the user that a coupling value is needed. If there is a number in the text field, then the program will run and

display all appropriate values. The button is also connected to a timer so that once it is pressed, it will continue to update itself. It is currently set to run every minute.

The difference between the expected and measured lifetimes is given by the measured value subtracted from the expected value. Therefore, if the number is extremely positive, then there are improvements to be made to the facility to further lengthen the beam's lifetime.

IV. Future Work

As mentioned above, the coupling value text field is currently designed to receive user input. Once the X-ray diagnostics are running for the beam, the program will be updated. It will then read in the coupling value from the diagnostics and give users an option as to whether they would like to keep that value, or return to using a user input value.

In addition, I would like to explore new interpolation methods for calculating the average Gaussian widths and heights of the beam. When comparing my results to those in a Mathcad file, all of the derived quantities were accurate to at least three decimal places, except for the average Gaussian widths and heights. As a result, the values of my expected Touschek lifetimes were smaller in comparison. I believe that with the further exploration of different interpolation methods, I can increase the accuracy of my program to a much higher degree.

Unfortunately, due to a few weeks of beam unavailability, I was unable to fully test and debug my program. In the future, I would like to debug my program so that I can run it for longer periods of time without interruptions. From there I can continue to fix any problems and investigate any discrepancies that arise.

With more testing and in time, this program will be able to accurately and reliably display all values of interest to machine personnel. This program will contribute to monitoring the facility's performance and help to improve the overall lifetime of the beam.

V. Acknowledgments

This project was supported in part by the U.S. Department of Energy, Office of Science, and Office of Workforce Development for Teachers and Scientists (WDTS) under the Science Undergraduate Laboratory Internships Program (SULI).

I would also like to thank my mentor, Timur Shaftan, for his never ending support and dedication to the project throughout the entire summer program. In addition to his help, I would like to thank Guimei Wang for her persistent contributions to the testing of the Python program.

VI. References

[1]Wille, Klaus. The Physics of Particle Accelerators: An Introduction. Oxford: Oxford University Press, 2000.

[2]Wiedemann, Helmut. Particle Accelerator Physics. Berlin: Spring-Verlag Berlin Heidelberg, 1993.

[3]Bruck, Henri. Circular Particle Accelerators. Paris: PUF, 1966.

[4]Walker, R.P. "Calculation of the Touschek Lifetime in Electron Storage Rings." Particle Accelerator Conference (1987): 491-493.

[5]Sands, Matthew. The Physics of Electron Storage Rings. Santa Cruz: SLAC, 1970.

VII. Figures

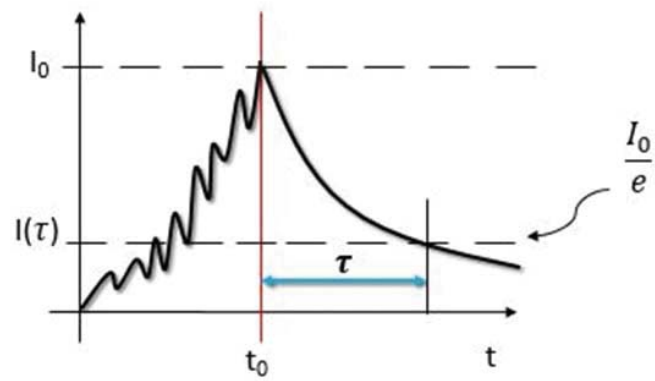

Figure 1: Rough sketch of a graph that shows current versus time and highlights the initial current and final current at t = lifetime.

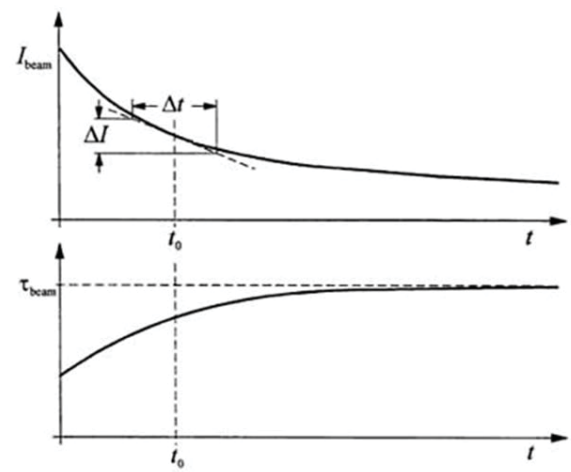

Figure 2: Time dependencies of beam current and lifetime. From *The Physics of Particle Accelerators*, Klaus Wille[1]

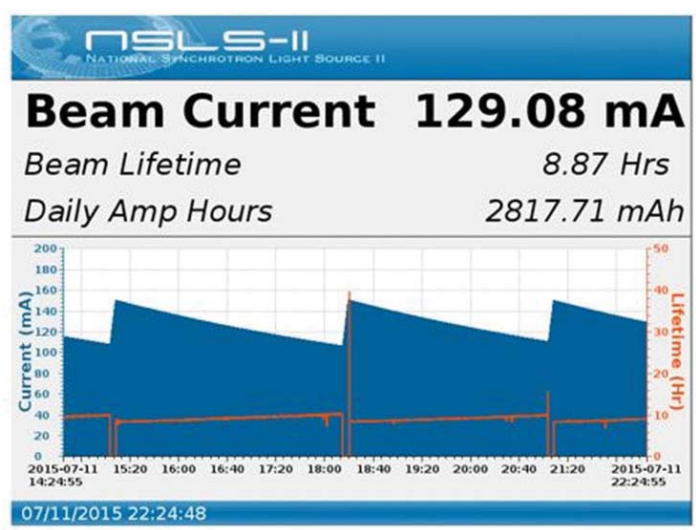

Figure 3: Status page of the NSLS-II shows time dependencies of lifetime and current from real-time data collection. From status.nsls2.bnl.gov

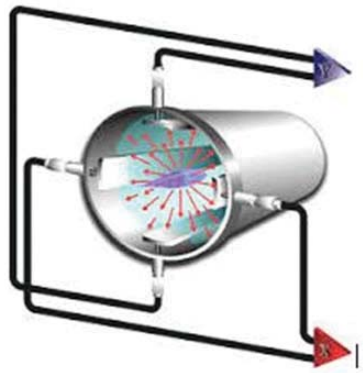

BPM

From http://durpdg.dur.ac.uk/vvc/accelerators/bpm.html

Figure 4 (right): Beam position monitor: device used to measure the current of the electron beam.

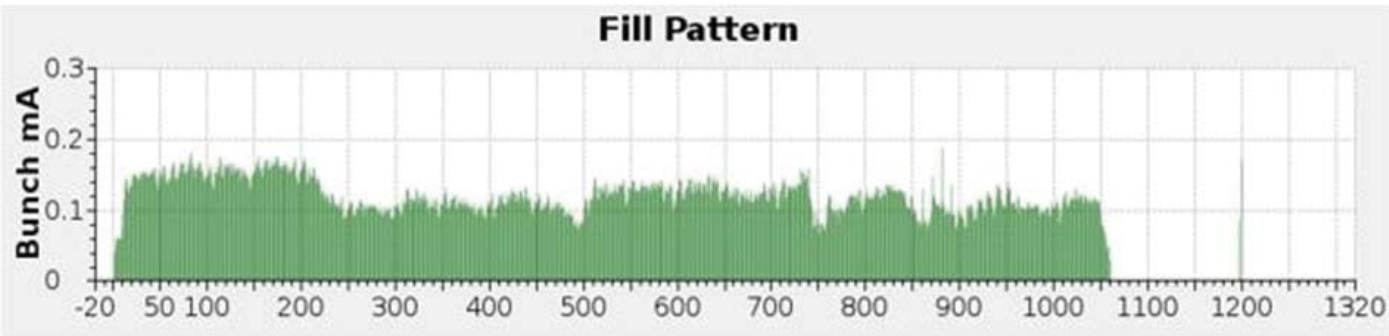

https://twitter.com/nsls2ops

Figure 5: Filling pattern monitor data of the 1320 buckets around the storage ring.

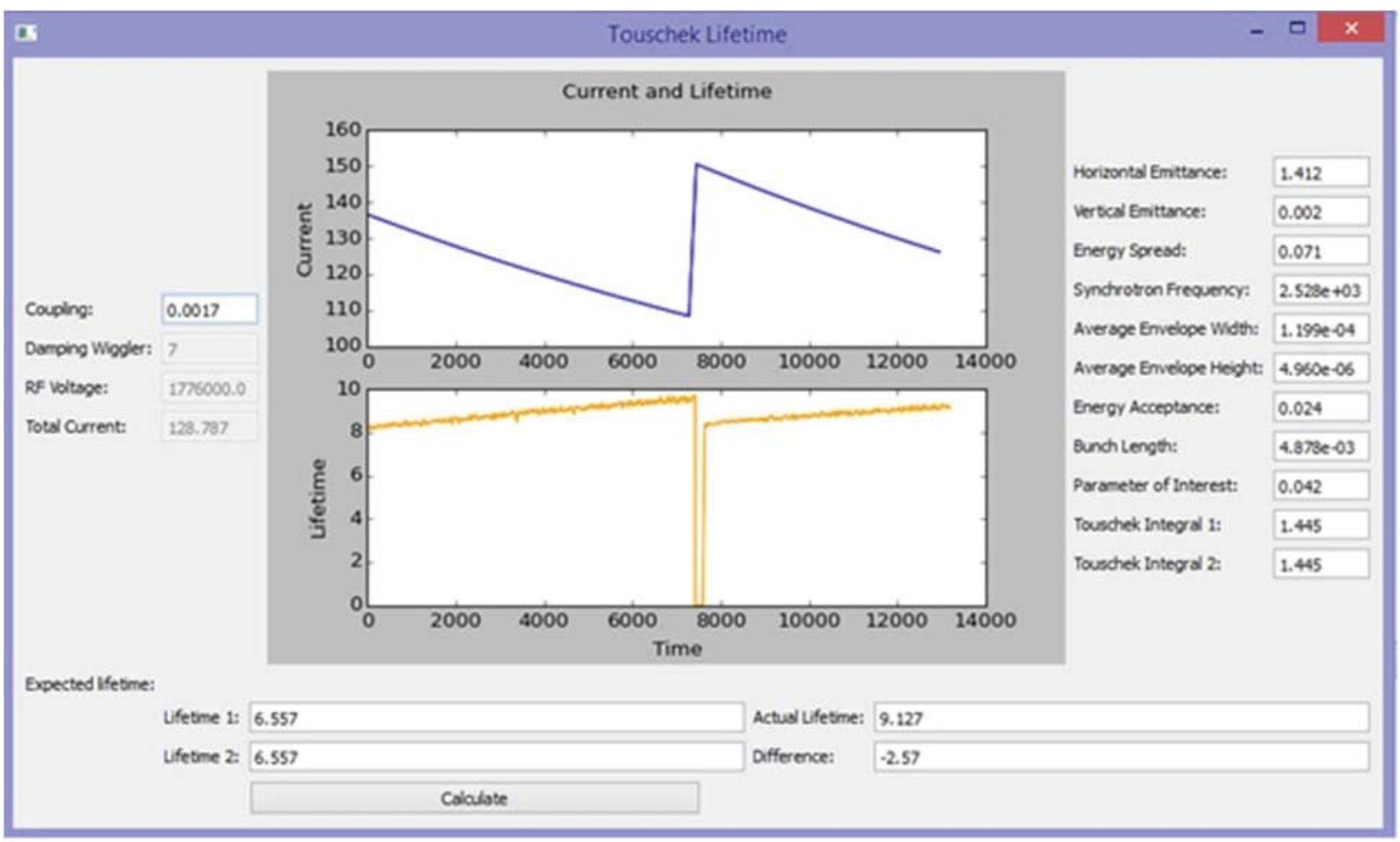

Figure 6: GUI Window: Process variables, dependencies of current and lifetime with time, derived quantities, expected lifetimes, measured lifetime and the difference between the expected and measured lifetimes.

Identification and location of mutated Arabidopsis genes through map-based cloning

Kristina Michta
Department of Chemistry, University of Massachusetts at Lowell, Lowell, MA 01854
Changcheng Xu and Jilian Fan
Biosciences Department, Brookhaven National Laboratory, Upton, NY 11973

Abstract

The purpose of my research this summer was to determine where specific mutated genes in the Arabidopsis plant are located through the use of map-based cloning. In the future, this research could play a key role in identifying gene mutations useful for augmenting oil biosynthesis to be used for greener biofuels. Map-based cloning is a technique which starts with the known sequence of a genome and uses genetic linkages between molecular markers, whose location within the genome is known, and the mutated gene to locate the mutation. After DNA from Arabidopsis plants was extracted, the polymerase chain reaction (PCR) technique was used to amplify specific fragments of DNA so that the concentration of these fragments was enough for gel electrophoresis (GE) which was used to visually see if a particular plant sample contained a heterozygous or homozygous expression of the DNA fragment. If the marker is close enough in proximity to the mutant, recombination occurs and is expressed as a heterozygous double band. When the marker is very close to the mutant, the heterozygous expression will disappear as the alleles of the gene and marker are now close enough to overlap and appear a single band. The goal was to use increasingly more markers until the change of heterozygous to homozygous expression was observed and the area of the mutated gene was located. Thus far, the location of the mutation has been narrowed down to the second chromosome in the region between markers AthBIO2b and 2b-777.

I. Background

A. Biofuels

Biofuels are energy sources derived from biological materials such as plant sugars and starches which are used as gasoline alternatives or plant oils which are used as diesel alternatives[1]. Biofuels can be blended together with traditional fuel sources to generate cleaner fuels or they can be used completely on their own as a fuel source. When compared to traditional gasoline and diesel fuels, biofuels are much cleaner due to the fact that they generally release much fewer emissions which are harmful to the environment.

Specifically looking at diesel fuels compared to biodiesel fuels, Figures 1 and 2 above show that when biodiesels are blended with traditional diesels in a 20% biodiesel: 80% diesel ratio, major emissions such as hydrocarbons, carbon monoxide (CO), particulate matter (PM), and carbon dioxide (CO2) are reduced by 20%, 12%, 12%, and 15% respectively. When 100% biodiesel is used instead of traditional diesel fuels, these major emissions are cut even further by 67%, 48%, 47%, and 78% respectively. These emissions, among others which are also shown to be reduced by biodiesels, all contribute greatly to the negative effects of climate change. As a result it would be greatly beneficial to further research how to extract larger quantities of plant oils more efficiently and cost effectively to be used for future biodiesel production.

B. Arabidopsis Plant

The Arabidopsis plant is a small plant which is a member of the Brassicaceae or mustard family and it is commonly used in genetic, biochemical, and physiological studies. The Arabidopsis plant is used largely for several different reasons including the fact that it has a fast life cycle and it requires little more than water, air, light, and a few minerals to grow[4]. The fact that it has a relatively small and tractable genome that is easily manipulated and whose genome sequence is now completely mapped makes it a very desirable plant to work with[5]. In addition, it is typically very easy to observe mutations in the Arabidopsis plant through obvious changes in phenotypes.

Figure 3 shows the difference between a normal Arabidopsis plant on the left and a M1-7xler F2 Arabidopsis plant on the right. It can easily be seen that the mutated species is significantly shorter than the non-mutated plant

C. Map-based Cloning

Map-Based cloning is a technique which starts with the known sequence of a genome. It then uses genetic linkages between molecular markers, whose location within the genome is known, and the mutated gene to locate the mutation[6]. If the marker is in proximity to the mutation, recombination between the marker and mutated gene occurs and expresses a heterozygous characteristic. When the marker is very close to the mutant, the heterozygous expression will disappear as the alleles of the gene and the marker are now close enough to overlap exhibiting a homozygous characteristic. The goal of using map-based cloning is to use increasingly more markers until the change of heterozygous expression to homozygous expression is observed and the location of the mutation is found.

D. Polymerase Chain Reaction (PCR)

Polymerase chain reaction (PCR) is a technique used to amplify specific fragments of DNA so that they will be at high enough concentration to be seen using gel electrophoresis. Figure 4 illustrates how the PCR process works step by step.

First, a DNA duplex is heated in order to separate its two strands. Then DNA primers are specially selected and added as short single-strands complementary to the sequences on either side of the desired region to be amplified. The primers hybridize to the DNA strands and begin to start synthesis of complementary DNA strands. At the end of the first cycle, two DNA duplexes are present, including the region to be amplified and then serve as templates for the next round of synthesis. In this way, the amount of the selected DNA region doubles over and over with each cycle[7].

E. Gel Electrophoresis (GE)

Gel electrophoresis (GE) is a technique which uses an electric current running through an agarose gel to separate DNA fragments based on their size. Because of the negatively charged phosphates in the DNA fragments, the DNA is repulsed from the negative cathode and travels toward the positive anode[8]. Differences in molecular weight of DNA fragments allow for separation to occur because smaller DNA molecules are lighter and are able to move more rapidly. On the other hand larger DNA fragments are heavier and therefore move more slowly. As a result, the DNA fragments that are larger are closer to the top of the gel while, smaller fragments are near the bottom. In order to visually observe the bands of DNA, the fragments are stained with a fluorescent dye so that the gel can be examined under ultraviolet light.

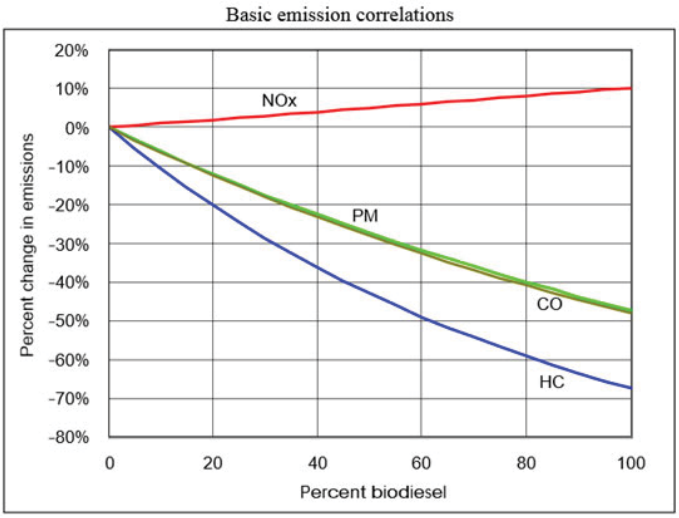

Figure 1: Basic emission correlations for percent biodiesel in fuel sources[2]

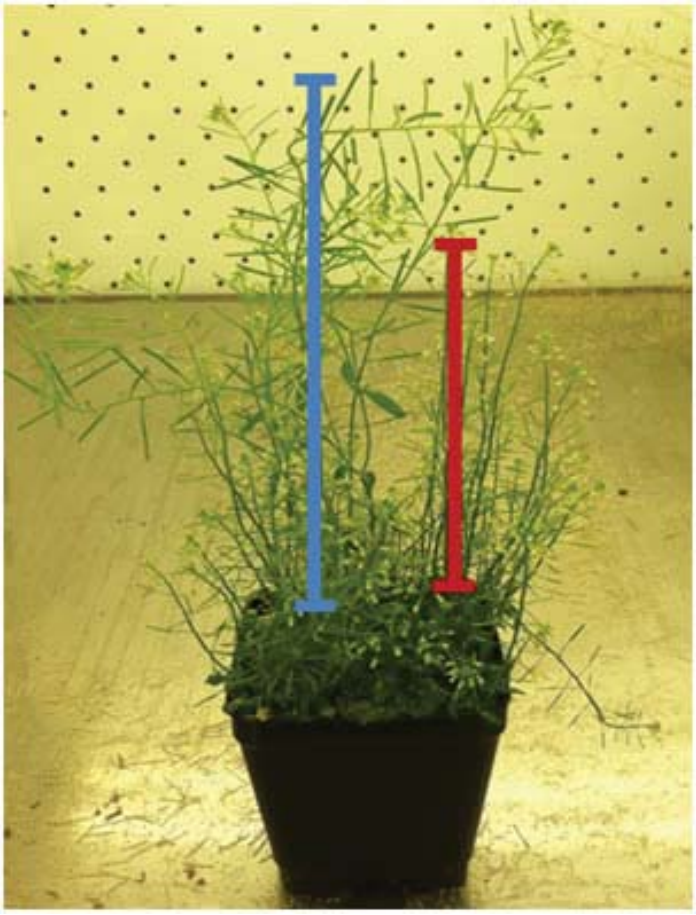

Figure 3: Pot of M1-7xler F2 *Arabidopsis* plants. Plant on the left shows a normal phenotype while the plant on the right shows a mutated phenotype

II. Methods

A. Growing Arabidopsis Plants from Seed

During the research conducted this summer the opportunity to study the Arabidopsis plant and locate where specific mutations were within the genome presented itself. In order to do so, mutated Arabidopsis plants needed to be planted from seed and grown. First second generation M1-7xler F2 Arabidopsis seeds were obtained. These seeds were already previously mutated from normal

Average Biodiesel Emissions Compared to Conventional Diesel *

Emission Type	B-100	B-20
Regulated		
Total Unburned Hydrocarbons	-67%	-20%
Carbon Monoxide	-48%	-12%
Particulate Matter (PM)	-47%	-12%
NOX	10%	-2% - 2%
Non-Regulated		
Sulfates	-100%	-20%
Polycyclic Aromatic Hydrocarbons	-80%	-13%
Nitrated PAHs	-90%	-50%
Ozone Potential	-50%	-10%
Carbon Dioxide Emissions	-78%	-15%
CARB:	-90% (from RVO)	

** Source: EPA, NREL*

Figure 2: Percent reduction in emissions for 100% biodiesel and 20% biodiesel blends[3]

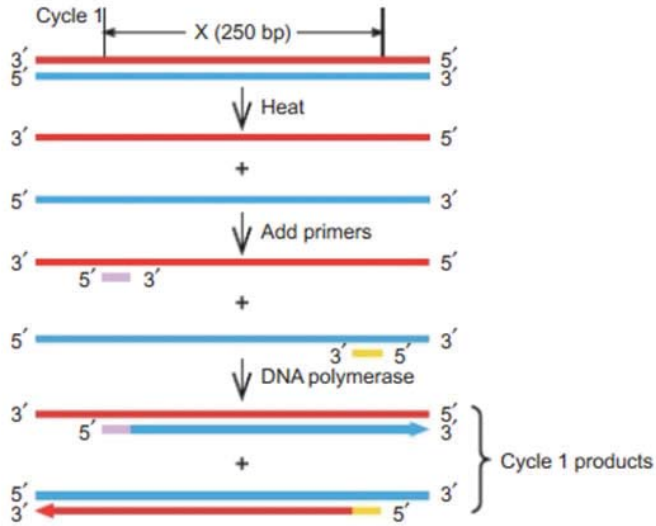

Figure 4: Step by step PCR process[7]

Arabidopsis seeds of the Columbia ecotype by using the mutagen ethyl methanesulfonate and then crossed with the Landsberg ecotype. The seeds were then sterilized and planted individually in rows in petri-dishes filled with nutrient-rich agar gel mediums. The seeds were placed into a 22°C Percival plant growth chamber and allowed to grow for about two weeks. Once the seeds had grown enough in the petri-dishes, the seedlings were transplanted into small soil pots in four rows of five each. When transplanting the seedlings, it was attempted to only transplant those which exhibited mutated phenotypes. Mutated seedlings could be distinguished by their smaller leaves which tended to be curled while non-mutated seedlings were larger and uncurled. The pots were transferred to the greenhouse where they received fertilizer occasionally to provide extra nutrients and were regularly watered. Once in the greenhouse, the seedlings were allowed to grow for at least another week before the extraction of the DNA was performed.

B. Extraction of DNA

After about three weeks of growth from seed, the small Arabidopsis plants were ready to have their DNA extracted in order to use later for PCR and GE analysis. For each small plant, a micro-test tube was prepared with 200µL of previously prepared sterilized DNA extraction buffer. A small sample of a young leaf tissue was then removed from each plant and placed into the corresponding test tube. Next, the leaf tissue was ground using a small pestle and 400µL of 100% ethanol was added to each test tube. The test tubes were then shaken to mix the solution and then centrifuged at 1300rpm for a total of five minutes. Each test tube was then emptied of its contents ensuring that all ethanol was dried before adding 200µL of 1xTE buffer to the remaining DNA precipitate. Finally the test tubes were vortexed in order to suspend all DNA precipitate and then stored in a 40°C refrigerator.

C. PCR

Using the previously prepared DNA extractions, PCR was performed on these samples in order to be amplified enough to use for GE. For each DNA sample a small test tube was prepared on ice with a 24µL solution of comprising of 5x TAG DNA buffer, MgCl2, dNTP, forward primer, reverse primer, distilled water, and TAG enzyme. 1µL of DNA sample was then added to each test tube bringing the solution to 25µL. The samples were then placed into a BIO-RAD PCR machine where the PCR was run at the proper temperatures and conditions determined by the specific primer being used. The primer chosen for each PCR was determined by first going through all the chromosome I primers. The primers for chromosomes II, III, IV, and V would also be systematically chosen based on results from the GE.

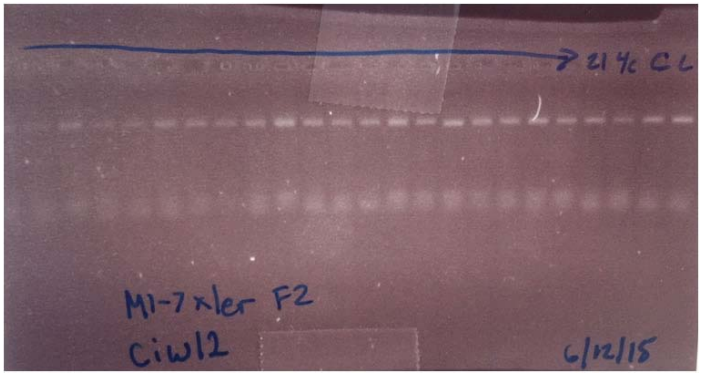

Figure 5: GE banding for PCR DNA samples #1-21 with heterozygous, Columbia, and Landsberg controls for the chromosome I primer ciw12

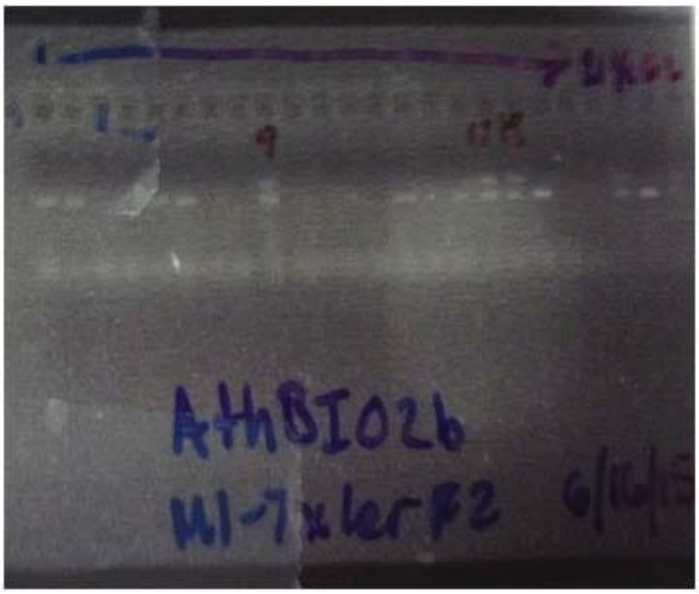

Figure 7: GE banding for PCR DNA samples #1-21 with heterozygous, Columbia, and Landsberg controls for the chromosome II primer AthBIO2b

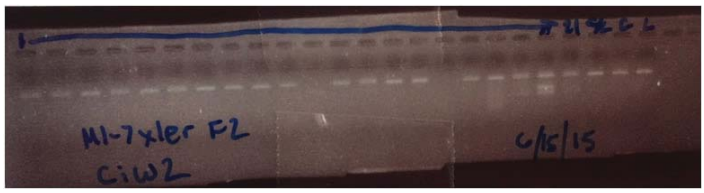

Figure 6: GE banding for PCR DNA samples #1-21 with heterozygous, Columbia, and Landsberg controls for the chromosome II primer ciw2

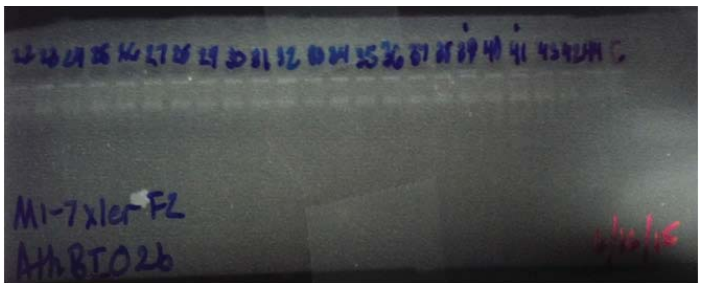

Figure 8: GE banding for PCR DNA samples #22-44 with heterozygous, Columbia, and Landsberg controls for the chromosome II primer AthBIO2b

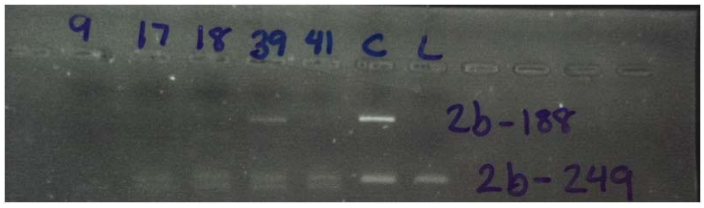

Figure 9: GE banding for PCR DNA samples #9, 17, 18, 39, and 41 with Columbia and Landsberg controls for the chromosome II primers 2b-188 and 2b-249

Once PCR was run on the DNA samples, gel electrophoresis was used to visually look for recombination of DNA fragments. Using a 3.7-3.8% agar gel, about 10µL of each PCR sample was loaded into the loading wells. GE was typically run for 15 minutes at 110V and then for additional increments of 10 minutes at 100V if the gel needed to be run longer to achieve better separation. After each GE run, the gels were placed under ultraviolet light to examine the banding of the DNA fragments. Results of GE helped to determine which primers to use in the next batch of PCR.

III. Results

A. Identifying the Chromosome

Figure 5 shows the gel electrophoresis for the PCR DNA samples #1-21 with a heterozygous, Columbia, and Landsberg DNA as controls. These PCR samples were run with the chromosome I primer ciw12. It can be seen that there are several Landsberg single bands that appear slightly lower and many Columbia single bands that appear slightly higher. The Columbia bands are comprised of 128 base pair while the Landsberg bands have 115 base pair. It can also be seen that there are no heterozygous double bands present.

When all the chromosome I primers were run with the first twenty-one samples of PCR DNA and the three controls and no recombination was observed, primers from chromosome II were then run. Figure 6 shows the gel electrophoresis for the PCR DNA samples #1-21 with a heterozygous, Columbia, and Landsberg DNA as controls. These PCR samples were run with the chromosome II primer ciw2. It can be seen that there are several Landsberg single bands that appear slightly lower and many Columbia single bands that appear slightly higher. The Columbia bands are comprised of 105 base pair while the Landsberg bands have 90 base pair. It can also be seen that there may be a few heterozygous double bands present.

Figure 7 shows the gel electrophoresis for the PCR DNA samples #1-21 with a heterozygous, Columbia, and Landsberg DNA as controls. These PCR samples were run with the chromosome II primer AthBIO2b. It can be seen that there are no Landsberg single bands that appear slightly higher and many Columbia single bands that appear slightly lower. The Columbia bands are comprised of 141 base pair while the Landsberg bands have 209 base pair. It can also be seen that there three distinct heterozygous double bands present. Figure 8 shows the gel electrophoresis for the PCR DNA samples #22-44 with a Columbia DNA as a control. These PCR samples were also run with the chromosome II primer AthBIO2b. It can be seen that there are no Landsberg single bands that appear slightly higher and many Columbia single bands that appear slightly lower. The Columbia bands are comprised of 141 base pair while the Landsberg bands have 209 base pair. It can also be seen that there two distinct heterozygous double bands present.

B. To the Right of AthBIO2b

Further testing of primers on chromosome II to the right of the AthBIO2b primer was conducted. Figure 9 shows gel electrophoresis for the five heterozygous samples #9, 17, 18, 39, and 41 with pure Columbia and Landsberg samples as controls using the Chromosome II markers 2b-188 and 2b-249. The 2b-188 and 2b-249 markers do not show any heterozygous bands overlapping to become single Columbia bands.

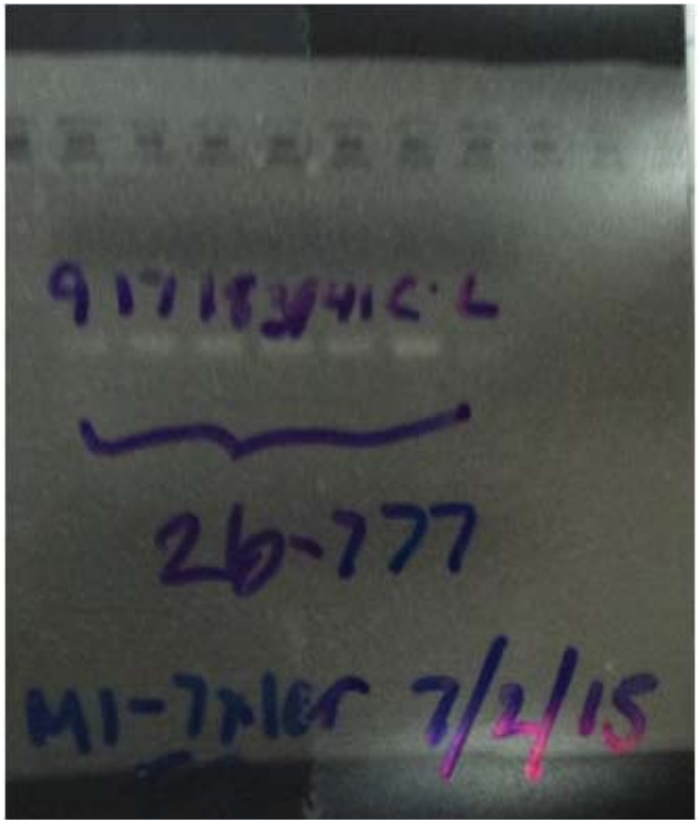

Figure 10: GE banding for PCR DNA samples #9, 18, 17, 39, and 41 with Columbia and Landsberg controls for the chromosome II primer 2b-777

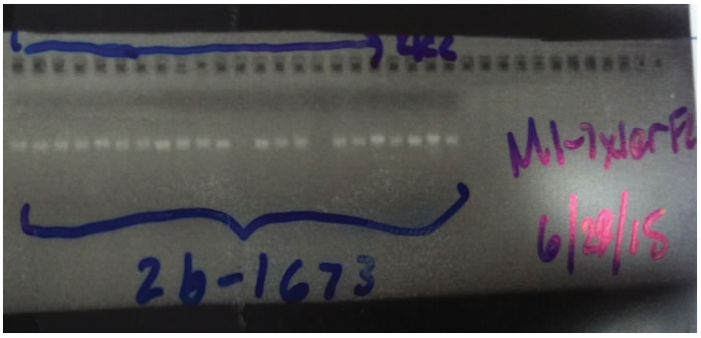

Figure 11: GE banding for PCR DNA samples #1-21 with Columbia and Landsberg controls for the chromosome II primer 2b-1673

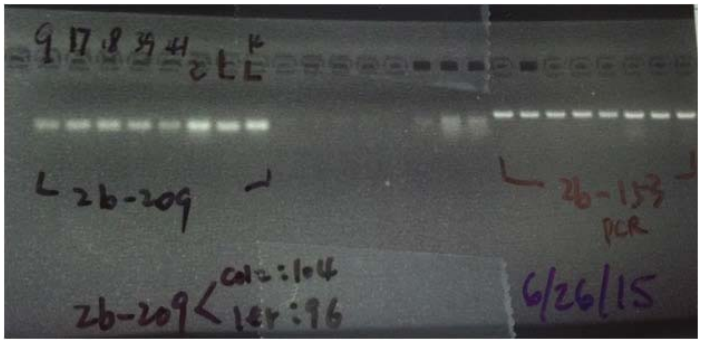

Figure 12: GE banding for PCR DNA samples #9, 18, 17, 39, and 41 with Columbia and Landsberg controls for the chromosome II primers 2b-209 and 2b-153

C. To the Left of AthBIO2b

Further testing of primers on chromosome II to the left of the AthBIO2b primer was conducted. Figure 10 shows gel electrophoresis for the five heterozygous samples #9, 17, 18, 39, and 41 with pure Columbia and Landsberg samples as controls using the Chromosome II marker 2b-777. The 2b-777 marker shows all heterozygous bands overlapping to become single Columbia bands. The Columbia bands are comprised of 157 base pair while the Landsberg bands have 137 base pair.

Figure 11 shows the gel electrophoresis for samples #1-21 with pure Columbia and Landsberg samples as controls using the Chromosome II marker 2b-1673. This marker does not show any heterozygous bands in addition to showing the presence of single Landsberg bands. The Columbia bands are comprised of 143 base pair while the Landsberg bands have 129 base pair.

Figure 12 shows gel electrophoresis for the five heterozygous samples #9, 17, 18, 39, and 41 with pure Columbia and Landsberg samples as controls using the Chromosome II markers 2b-209 and 2b-153. Both markers show all heterozygous bands overlapping to become single Columbia bands.

IV. Discussion:

The research performed this summer provided an opportunity to gain a great deal of information on how map-based cloning and different techniques are used to locate where mutated genes are within a genome. When looking at the GE results for the first twenty-one PCR DNA samples using the primers from chromosome I, the presence of only Colombia or Landsberg single bands and no heterozygous double banding indicated that the mutation was not located on chromosome I. If the mutation had been located on the first chromosome, recombination of alleles between the genetic markers and the mutated gene would have occurred and been expressed as the heterozygous double bands. The same results were seen for all of the chromosome II primers until the last primer, AthBIO2b, was tested. With this primer, there were no Landsberg single bands, many Columbia single bands, and three distinct heterozygous double bands in the first twenty-one samples. These results seemed to indicate that the mutation was on chromosome II. Further testing of the remaining 110 PCR DNA samples showed that there were two more distinct heterozygous bands. The presence of only heterozygous and Columbia bands among 131 DNA samples confirmed that the mutation was on chromosome II and was relatively close to the AthBIO2b marker due to the low count of heterozygous double bands. Since the chromosome on which the mutation was on was located, it was the hope to start looking for the mutation on the right side of the AthBIO2b marker and to be able to use it as a left flanking marker. Two primers, 2b-188 and 2b-249, were used to test the right side of the AthBIO2b primer. These primers were 188 kilo-base pairs and 249 kilo-base pairs away respectively. Analysis of the GE's for each primer showed that none of the five already determined heterozygous DNA samples were overlapping to become single Columbia bands. These results indicated that these primers were moving further away from the mutation and the mutated gene was therefore located to the left of the AthBIO2b primer.

In the hopes of using the AthBIO2b primer as a right flanking marker, primers to the left were then tested on the five know heterozygous DNA samples. One of the several primers tested was the 2b-777 primer located 777 kilo-base pairs away from the original primer. The GE results from this primer showed that all the heterozygous double bands became single banded Columbia bands. This would suggest that the mutation was very close to this marker made apparent by the complete overlapping between the marker and the mutation. Next, the primer, 2b-1673 located 1673 kilo-base pairs away, was tested and showed no heterozygous double bands but the presence of both Columbia and Landsberg single bands. This suggested that once again the mutation was located somewhere closer to the 2b-777 primer. Testing of the primers 2b-209 and 2b-153, located between the 2b-777 and AthBIO2b primers was conducted with the same five heterozygous DNA samples. These GE results showed that as with the 2b-777 marker, all the heterozygous double bands were converted to Columbia single bands. It would be expected that from all of these GE results using different primers located on chromosome II that the mutation is located somewhere within the region of the 2b-777 primer and the AthBIO2b primer.

Being able to locate where specific mutated genes related to oil synthesis in the Arabidopsis plant will help scientists to better understand the characteristics and properties of the mutated genes. This better understanding can then help scientists to develop more efficient and cost effective biodiesels and biofuels in the future. The research conducted this summer was only part of an ongoing project. There are still many more DNA samples to be added to the sample pool of the M1-7xler F2 Arabidopsis plant mutation which will be helpful in making any results gathered more accurate. Additionally, it is the hope to be able to narrow down more closely the location of the mutated gene on the second chromosome between primers 2b-777 and AthBIO2b. Once the gene is located, it would be useful to further study its properties and the effects it has on plant oil synthesis.

V. References

[1]BioFuels and the Environment. http://www.epa.gov/ncea/biofuels/basicinfo.htm#whatis. 2015. (accessed July 26, 2015)

[2]A Comprehensive Analysis of Biodiesel Impacts on Exhaust Emissions. http://www.epa.gov/otaq/models/analysis/biodsl/p02001.pdf. (accessed July 26, 2015)

[3]How Beneficial is Biodiesel?. http://www.springboardbiodiesel.com/Small-scale-biodiesel-production. (accessed July 26, 2015)

[4]Arabidopsis: The Model Plant. http://www.nsf.gov/pubs/2002/bio0202/model.htm. (accessed July 26, 2015)

[5]Jander, G.; et al. Arabidopsis map-based cloning in the post-genome era. Plant Physiol., 2002, 129.

[6]Weaver, R. F. Molecular Biology. Fifth Edition. McGraw Hill: New York, 2012; pp 62.

[7]Weaver, R. F. Molecular Biology. Fifth Edition. McGraw Hill: New York, 2012; pp 78.

[8]Lukowitz, W.; Gillmor, C.S.; Scheible, W. Positional cloning in Arabidopsis. Why it feels good to have a genome initiative working for you. Plant Physiol., 2000, 123.

VI. Acknowledgements

This project was supported in part by the U.S. Department of Energy, Office of Science, Office of Workforce Development for Teachers and Scientists (WDTS) under the Science Undergraduate Laboratory Internships Program (SULI).

Construction and analysis of reduced graphene oxide/ ruthenium oxide supercapacitors electrodes using electrophoretic deposition

Dakoda W. Mullinax and Z. Amir
Department of Chemistry, Physics and Geology, Winthrop University, Rock Hill, SC 29733
Viet Pham, Dmytro Nykypanchuk, and James Dickerson
Center For Functional Nanomaterials, Brookhaven National Laboratory, Upton, NY 11973

Abstract

Novel, low cost, environmentally friendly, and high-performance energy storage systems have been increasingly in demand as a result of the needs of modern society its and emerging ecological concerns. Supercapacitors, or electrochemical capacitors, are a promising candidate for alternative energy storage because of their high power density and their potential to reach relatively high energy densities. Also with their long life cycle and short charge and discharge time, supercapacitors may replace the use of batteries and provide environmentally friendly energy. In this work, we used electrophoretic deposition (EPD) to develop a high performance capacitors based on reduced graphene oxide and ruthenium oxide (rGO/RuO2) composite electrodes. The morphology of fabricated rGO/RuO2 was analyzed using scanning electron microscopy (SEM), and the structure of the electrodes was analyzed using x-ray diffraction. Electrochemical capacitive properties of rGO/RuO2 are characterized using a two-electrode cell configuration in a H2SO4 electrolyte solution. The ultimate objective of our research is to fabricate supercapacitors with an improved performance than the ones already existing using EPD as the fabrication method, further impact the electrical storage device market, and potentially change how electronics are made.

I. Introduction

The energy demands of modern society and the growing concerns for the ecosystem has resulted in a push for low cost, environmentally friendly, and high-performance energy storage systems. Among storage systems, supercapacitors, or electrochemical capacitors, possess a high power density, a long life cycle, a small stature, and while there energy density is low now, less than 10 W h kg-1, they have the potential to reach relatively high energy densities.[1,2] The production of supercapacitors could replace the use of batteries all together, and provide an inexpensive, environmentally friendly energy with multiple applications such as powering portable electronics and electrical vehicles[3].

Graphene is a one-atom-thick single layer of sp2-bonded carbon that looks like a crystal lattice.[4,5] It has become of interest to researchers because of its high electrical and thermal conductivity, high surface area6 (2675 m^2/g), and its high chemical tolerance[2,7,8], which makes it an ideal material for high performance supercapacitors. Unfortunately, Van der Waals interactions between sheets of graphene cause it to stack and this in turn causes the graphene to lose much of its surface area. Also, as many other electrical double layer capacitors electrode (EDLCs) materials, it suffers from low energy density that significantly and that limits their practical applications.[5, 7,9] To prevent this phenomenon from happening, Chen et al mentioned incorporating nanoparticles into graphene oxide.[7,10] Ruthenium oxide (RuO_2) is recognized for its stability in an electrochemical environment[4] and not only acts as a spacer to allow the formation of a porous electrode structure[5] so that an electrolyte can penetrate both sides of the electrodes, but also adds pseudo-capacitance, improving the total capacitance via fast Faradic reactions.[11] RuO_2, however suffers from low power density and instability during cycling.

In order to achieve high power density and energy density, as well as good cycling stability of supercapacitors, we combine RuO_2 with graphene creating a hybrid structure. Few methods have been used to prepare RuO_2/graphene electrodes; some of which include: aerogels[12], magnetron sputtering[13], and one-pot hydrothermal routes[14]. The capacitances reported from previous studies are 400 F/g at current density of 1.0 A/g for sample made by Sol-gel and annealed at 150 °C for 2 hours2, and 570 F/g by the

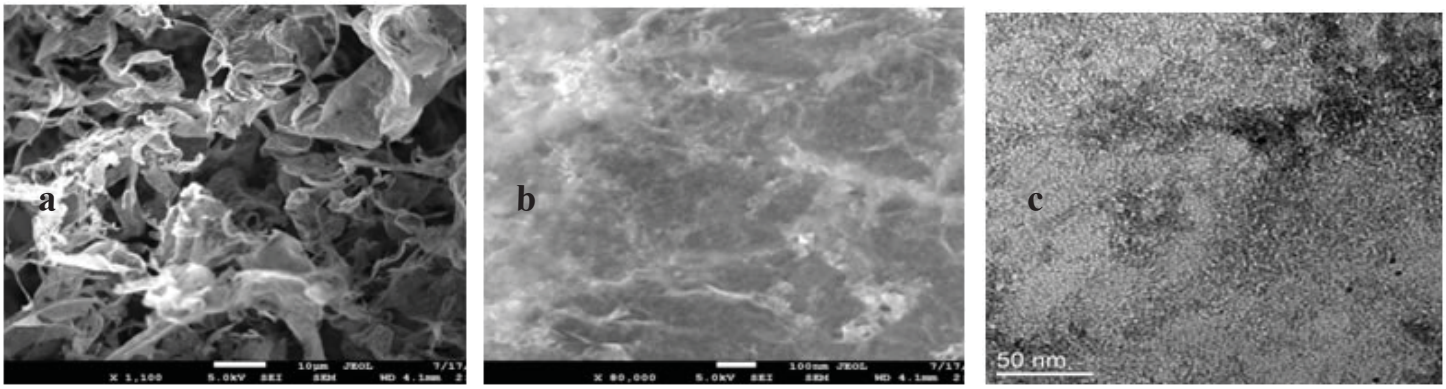

Fig. 1: (a-b) SEM images of rGO /RuO2 electrodes. (c) TEM image of rGO/RuO2 electrodes.

same method[9]. Other reports have used the hydrothermal method, and the samples were annealed at 150 °C for 2 hours leading to capacitances of 471 F/g and 551 F/g respectively.[7,15]

In the current study, electrophoretic deposition (EPD) was used to fabricate reduced graphene oxide-ruthenium oxide (RGO-RuO_2) electrodes. EPD is a two-step process where particles in a colloidal suspension move toward an electrode and form a deposit on the electrode. Sintering occurs afterwards to form a dense, compact layer.[16] Not only does EPD not require relatively high temperatures so a basic chemical oven is all that is needed to seal the deposited layer, but also EPD does not require a binder[17] and is an easy way to control the thickness and porosity of the structure.

II. Experimental

A. Preparation of GO: GO was synthesized from expanded graphite by the modified Hummers method, described elsewhere.[18]

B. Preparation of RGO-RuO_2: The as-prepared GO was diluted to a concentration of 0.5 mg/ml and sonicated for 10 minutes to obtain a homogenous solution, 20 ml of H_2O_2 was then added and the solution was heated at 95 °C. Ruthenium tri-chloride hydrate (RuCl3.xH_2O), was then added into 200 mL of GO solution (0.5 mg/mL) under mixing. Then, the suspension was neutralized with 1M NaOH to a pH ~7 and stirred for 12 hours at room temperature to obtain GO-RuO_2. Subsequently, the pH of the GO-RuO_2 suspension was adjusted by adding 1M NaOH to 12, and the suspension was aged at 90 °C for 12 hours to deoxygenation of GO.

Details of the synthesis are given elsewhere.[19] The synthesized sample is called HRGO-RuO_2.

C. Electrode preparation: In a homemade cell, stainless steel, Nickel foam and gold coated PET were placed as working and counter electrodes. DC voltage between 2-7V was applied for 100-600s between the working (positive) and counter (negative) electrodes (Keithley 2400 source meter). The HRGO-RuO_2 samples were dried at room temperature for 2 hours, and then in the oven at 150 °C for 2 hours. The samples on stainless steel and PET were soaked in H_2SO_4 electrolyte solution while the Nickel foam was soaked in KOH.

D. Characterization: The surface morphology of fabricated rGO/RuO_2 electrodes were analyzed using the 7600F High Resolution Analytical Scanning Electron Microscope (SEM) and a JOEL 2100F field emission Transmission Electron Microscope (TEM). The structure of the deposited layer needs to be amorphous to improve the pseudo-capacitance effect, so the structure of the electrodes was analyzed using a Rigaku Ultima III x-ray diffractometer at the Center of Functional Nanomaterials (CFN) at Brookhaven National Laboratory. The electrochemical capacitive properties, or cyclic voltammetry (CV) measurements of the rGO/RuO_2 electrodes made by EPD were performed on the PARSTAT 2273 –Princeton Applied Research workstation, using a two-electrode cell configuration in H2SO4 electrolyte solution while the charge-discharge characteristics were performed using the galvanostatic charge-discharge (GCD) tests on the Arbin battery tester BT 2000 at the CFN.

III. Results

Fig. 1. (a, b) shows SEM images of rGO-RuO_2 with a three dimensional porous structure. The RuO_2 nanoparticles were densely anchored across the graphene sheets. The microstructure of the rGO-RuO_2 was further characterized by TEM. The low magnification of the TEM micrograph in Fig. 1(c) shows the ultra-small RuO_2 nanoparticles densely decorating the rGO sheets. The results reported here are for the rGO-RuO_2 on PET coated with gold. The deposition on both stainless steel and Nickel foam were difficult since the layers peeled off after being dried at room temperature. The electrochemical capacitive behavior of the rGO-RuO_2 electrodes fabricated by EPD on a flexible substrate was evaluated by CV and GVD techniques.

Fig. 2. (a) shows the CV curves in 0.5 M H2SO4 electrolyte for different scan rates, the curves were nearly rectangular indicating an ideal capacitive behavior. The GCD curves in Fig.2. (b) were symmetrically triangular, which is another indication of a perfect capacitive behavior.

The specific capacitance of the fabricated supercapacitor by EPD calculated from the discharge curves was 400F/g and 368 F/g and at current densities of 1.0 and 20.A/g.

IV. Conclusions

We report a facile method to fabricate rGO/RuO_2 supercapacitor electrodes by electrophoretic deposition on a flexible substrate. The fabricated supercapacitor performed well both in normal and stressed conditions. The capacitance obtained was around 370 F/g. The supercapacitors have a very good cycling stability, with capacitance retention of 93% after 5000 cycles. Research is still being done to improve the energy density of the electrodes.

V. Acknowledgements

This work was supported in part by the U.S. Department of Energy, Office of Science, and Office of Workforce Development for Teachers and Scientists (WDTS) under the Visiting Faculty Program (VFP). The research used resources of the Center for Functional Nanomaterials, which is a U.S. DOE Office of Science Facility, at Brookhaven National Laboratory under Contract No. DE-SC0012704. I would also like to thank Fatima Amir, Viet Pham, and Dmytro Nykypanchuk for mentoring me throughout our research. I also would like to thank Dr. J. Dickerson for allowing us to use the electrophoretic deposition facility for the samples' prepraration.

VI. References

[1]G. Wang, L. Zhang, J. Zhang, Chem. Soc. Rev., 2012, 41, 797.
[2]J. Zhang et al. , Energy Environ. Sci., 2011, 4, 4009.
[3]A. K. Mishra and S. Ramaprabhu, J. Phys. Chem. C, 2011, 115, 14006.
[4]R. B. Rakhi, W. Chen, D. Cha and H. N. Alshareef, J. Mater. Chem., 2011, 21, 16197
[5]J. Y. Kim, K.-H. Kim, S.-B. Yoon, H.-K. Kim, S.-H. Park and K.-B. Kim, Nanoscale, 2013, 5, 6804.

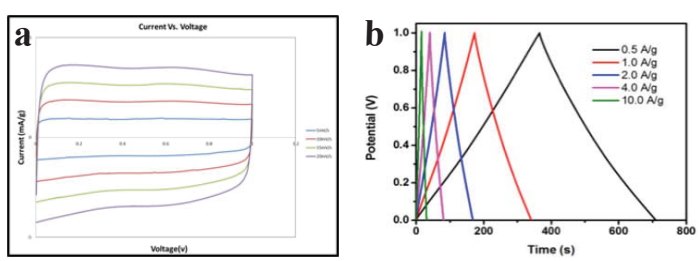

Fig. 2: (a, b) CV and charge-discharge curves of RGO-RuO_2 in H2SO4 electrolytes

[6]J. L. Xia , F. Chen , J. H. Li , N. J. Tao , Nat. Nanotechnol. 2009, 4 , 505
[7]Y. Chen, X. Zhang, D. Zhang and Y. Ma, J. Alloy. Compd., 2012, 511, 251.
[8]Y. Huang, J. Liang, and Y. Chen, Small, 2012, 8, 1805.
[9]Z. S. Wu et al., Adv. Funct. Mater., 2010, 20, 3595.
[10]J. Yan et al. Carbon, 2010, 48, 1731
[11]N. Soin, S. S. Roy, S. K. Mitra, T. Thundat and J. A. McLaughlin, J. Mater. Chem., 2012, 22, 14944.
[12]D.J. Suh, T.-J. Park, W.-I. Kim, I.-K. Hong, J. Power Sources, 2003, 1, 117.
[13]G. Battaglin, V. Rigato, S. Zandolin, A. Benedetti, S. Ferro, L. Nanni, A.D. Battisti, Chem. Mater. 2004, 16, 946.
[14]J. Shen, T. Li, W. Huang, Y. Long, N. Li, M. Ye, Electrochimica Acta, 2013, 95, 155.
[15]N. Lin, J. Tian, Z. Shan, K. Chen, W. Liao, Electrochimica Acta, 2013, 99, 219.
[16]O.O. Van der Biest and L.J. Vanderperre, Annu. Rev. Mater. Sci., 1999, 29, 327
[17]J.H. Jang et al., J. Electrochem. Soc., 2006, 153, (2) A321
[18]V. H. Pham, T. Gebre and J. H. Dickerson, Nanoscale, 2015, 7, 5947.
[19]F. Z. Amir, V. H. Pham, J. H. Dickerson, RSC advances accepted

Targeting lipid abundant mutants of *Arabidopsis thaliana*

Kimberly Okoli
Biological Sciences Department, Cornell University, Ithaca, NY 14853
Jilian Fan
Biosciences Department, Brookhaven National Laboratory, Upton, NY 11973

Abstract

The field of engineering green biomass for the production of plant oils for biofuel is expanding. Deriving biofuels from sustainable bioresources is environmentally friendly, has low energy intensive operations, and optimally utilizes our environment. Plant oils, such as lipids, provide more energy per unit of mass than starches though starches are produced much more in plants. In this study at Brookhaven National Laboratory, I tried to determine which genetic marker is linked to the mutation responsible for the production of lipids in the plant, Arabidopsis thaliana, and thus where in the genome it is located. The methods utilized in this study were DNA extraction followed by polymerase chain reaction (PCR) and gel electrophoresis.

Mapbased genetic cloning identifies the gene responsible for a mutation. Several thinlayer chromatography (TLC) tests were also used to ascertain if certain samples contained polar lipids, which can be found in the mutation of interest. Though the experiment has not reached an end, some tentative results can be reached, namely that the mutation seems to be linked to several marker on chromosome 5. Throughout the course of the project, I learned both basic and advanced lab techniques, namely the use of an autoclave for sterilization purposes, PCR arrays, and TLC tests. Along with this, I also gained a comprehensive understanding of lipid production pathways in plants.

I. Background

Arabidopsis thalania is a small, flowering mustard green native to Eurasia. Though technically a weed, it is edible and used in salads, comparable to dandelioins. A. thalania has a short life cycle and a relatively small genome of only 5 chromosome. This makes it a model plant species and a perfect candidate for both molecular and genetic experimentation,as several generations can be cultivated in a relatively short amount of time.

In recent years, there has been much concern about the state of the planet, the rate at which nonrenewable resources are being consumed and our dependency on them. To combat this, there has been an increased interest in finding more sustainable forms of energy such as plant oils. Plant oils are an energyrich source of renewable fuel, most of which occurs in the form of triacylglycerol (TAG). Not only does the mutant of interest in this study produce lipids past germination, a behavior not typical of plants, the lipids produced are polar. TAGs consist of glycerol and three fatty acid chains, and are considered neutral lipids. The mutant of interest in this study accumulates a different type lipid in its leaves: trigalacttosyldiaglycerol (TGDG).

TGDG contains two fatty acid chains and one other group, making it a polar lipid. Polar lipids can be identified in leaves using thin layer chromatography (TLC).

Once plants containing the mutant of interest are identified, it is possible to determine where in the genome this mutation is located with mapbased cloning and polymerase chain reaction

(PCR). In this case the mutation will not lead to genetic recombination between two known ecotypes, meaning the PCR product of a marker near the mutation will have few if any heterozygous ladders. Plants containing the mutant of interest can be identified genotypically, by checking lipid content, or phenotypically. Wild type A. thalania are noticeably larger than the mutants.

II. METHODS

A. ThinLayer Chromatography

1. At least 60 mg of leaves from young plants were measured out and placed in individual centrifuge tubes.
2. A 1:7 ratio of the fresh weight of the leaves in milligrams to extraction buffer in microliters was added and the tubes were all placed on a vortex on a low setting for 15 minutes or until all the chlorophyll in the leaf samples were gone.
3. Half the volume of extraction buffer was calculated and that much KCl buffer was added
4. The tubes were placed in a centrifuge for 1 minute at 13,000 rpm. This separated the liquid so the total lipid collected at the bottom of the tube.
5. A pencil line was drawn about half an inch from the bottom of the TLC plate and 60 µL of lipid from each sample was placed on the plate above the line.
6. When the samples dried, the plate was placed in a tank with developing solvent until the solvent traveled almost all the way up the plate.

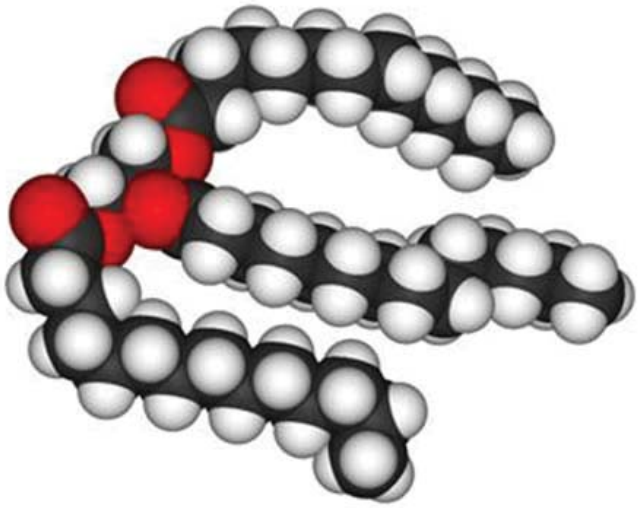

Figure 1: triacylglycerol molecule

For rough mapping, simple sequence length polymorphism (SSLP) markers were used when performing PCR and gel electrophoresis.

B. PolymeraseChain Reaction

1. Individual leaves from separate young plants were placed in different centrifuge tubes and 200 µL of DNA extraction buffer was added.
2. Blue pestles were used to ground up the leaves and 400 µL of 100% ethanol was added in order to make the DNA precipitate.
3. The centrifuge tubes were shaken in order to mix completely and then placed in the centrifuge for 5 minutes at 13,000 rpm
4. After the tubes were removed from the centrifuge, the supernatant was discarded and the tubes were left upside down in order to remove all of the liquid.
5. Once all the ethanol was removed from the centrifuge tubes, 200 µL of TE buffer was added, the tubes were vortexed and pipetted into PCR tubes along with DNA polymerase, primers, an enzyme and dNTP. Each PCR had a different set of primers from markers on

chromosome I (nga63, nga280, nga111, ciw12), chromosome II (ciw2, nga1126, AthBio2b, nga126), chromosome III (ciw11, nga6), chromosome (nga8, ciw7, nga1107), and chromosome V (nga151, nga139, nga76, MBK51). The PCR tubes were placed in the PCR machine.

6. 9 µL of PCR product for each sample was loaded into the agarose gel for electrophoresis.
7. The gel was examined with a gel imager and bands were determined to be either columbia, lensberg, or heterozygous.

III. RESULTS

A linkage was found with several markers on Chromosome V.

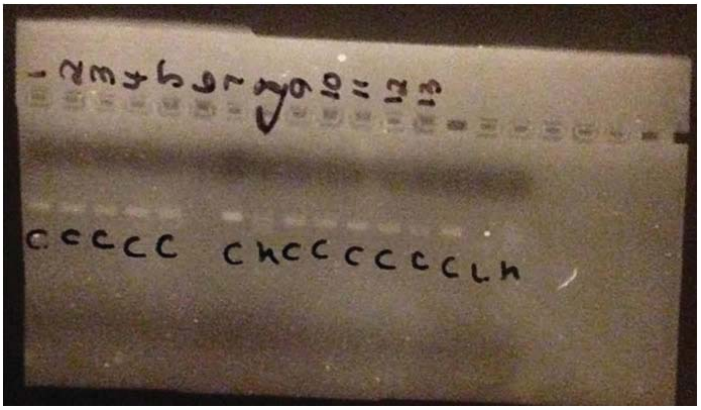

The above is 13 samples of the mutant strain M114 j12 xler f2 with the marker nga139. this is the most promising PCR result, as only one of the 13 tested samples showed heterozygous bands. Samples 5 and 6 have no bands, most likely due to an error in the DNA extraction process.

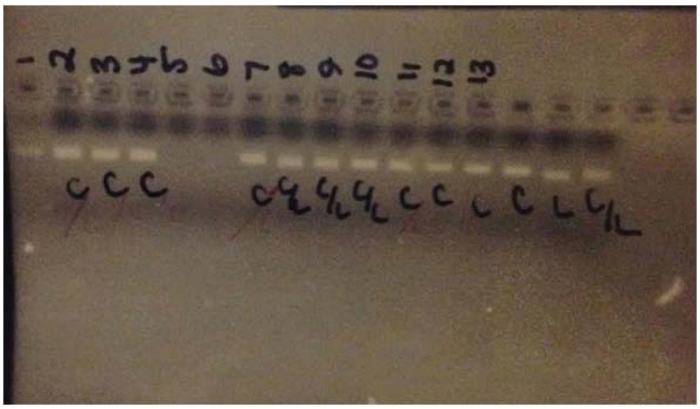

The above is 13 samples of the mutant strain M114 j12 xler f2 with the marker nga151 This is another promising PCR result, as only three of the 13 tested samples showed heterozygous bands.

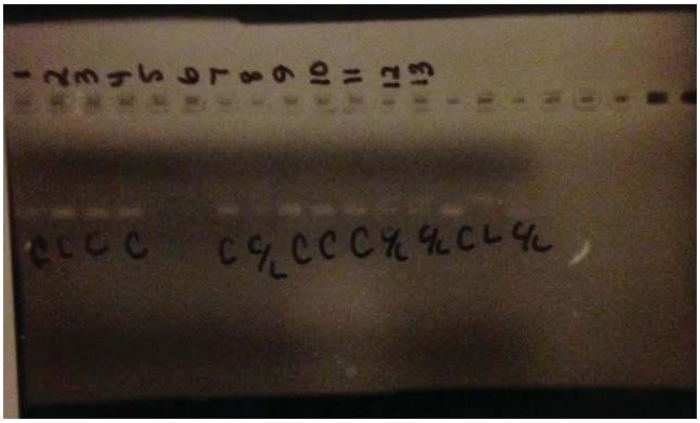

The above is 13 samples of the mutant strain M114 j12 xler f2 with the marker nga76. This is another promising PCR result, as only three of the 13 tested samples showed heterozygous bands.

In contrast, markers with no linkage showed results similar to this marker on Chromosome V:

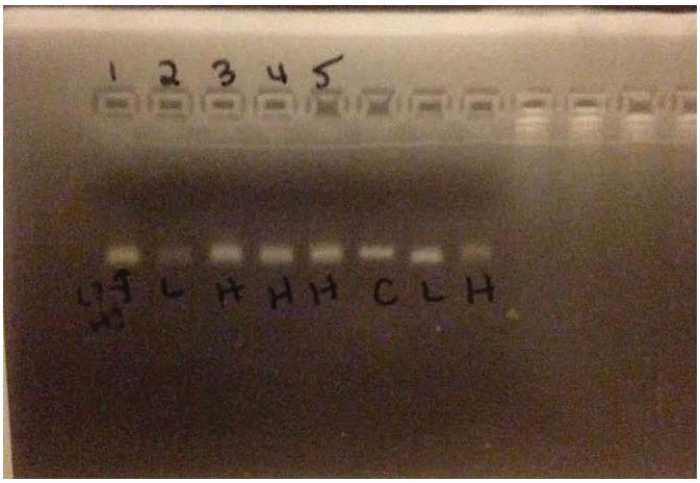

The above is 13 samples of the mutant strain M114 j12 xler f2 with the marker MBK51. This is not a promising PCR result, as all of the tested samples showed heterozygous bands.

IV. DISCUSSION

This experiment is a continuation of my research from last summer, in which I initially identified lipid abundant mutants from F1 generations. in that experiment I used many of the same methods, including thin layer chromatography, polymerase chain reactions and DNA extraction.

The main focus of my experiment was using polymerase chain reactions to identify heterozygous recombination The mutant of interest inhibited recombination, thus if a marker showed recombination, it must not have been affected by the mutation of interest and thus must not be near it. On every PCR test, there were 3 controls: one from each ecotype and a heterozygous sample. An ecotype is a geographic subspecies that is genetically distinct due to environmental adaptational needs. The two ecotypes of interest are Columbia (C) and Lensberg (L). A preexisting knowledge of the ecotype to which the mutation is linked was necessary in order to accurately identify the PCR results to be expected in the region around the mutation. After performing multiple PCRs, I found three markers showing promising linkages (Figure 2).

The next step is to further narrow down the location. This is done by ordering nearby markers on either side of the markers previously identified on the chromosome and performing more PCR tests. One of these markers should show an even closer linkage to the mutation, hopefully eventually defining a pair of markers flanking the mutation less nm than 40,000 base pairs apart. Once those markers are found, the entire region will be sequenced to find to mutation. An effective way to do this would be to design PCR primers for overlapping 500 base pair segments along the entire region. Each segment would then be sequenced and compared to wildtype until the mutation is identified.

Thus far in this experiment, several mutants around Nga139 were ordered. We focused on markers around nga139 as it showed the least amount of heterozygous bands of all the markers and thus had the least recombination. the mutation is most likely around this marker. we know it is not especially close to that marker, however, as when 80 additional DNA samples of the same strain were tested, only 49 showed columbia bands. this result does not necessarily indicate a lack of linkage between the mutant and nga139. however, it does mean that the marker must be a little further away.

Visualization of the RHIC Computing Facility

Do Om
Engineering, Suffolk County Community College, Selden NY 11784
Antonio Wong
Physics Department, Brookhaven National Laboratory, Upton NY 11973

Abstract

The RACF (RHIC-ATLAS Computing Facility) provides the computer processing, storage, and analysis resources for the RHIC experiments conducted at the Brookhaven National Laboratory, as well supporting the computer needs of US collaborators of the ATLAS experiment at the LHC for CERN. Its data center consists of a vast unit processing farm, a distributed and centralized disk storage farm, robotic tape silos, and its own high-speed internal network. The specifications of each hardware component inside of the data center is entered into an inventory manager called GLPI. My project was to create an interactive web application that would model the layout of the data center using information from the GLPI database and would also retrieve and display information in an easily readable and accessible fashion. Currently, there is no organized way that computers stored in the data center are kept track of. To find a specific computer, one must look through scattered excel charts, if they exist, or to physically look through the rows of racks and find it that way. And while there are commercially available products that would take care of this problem, they are either prohibitively expensive or part of larger software suites that must be integrated into the RACF's current setup.

I. Introduction

This project was created using HTML, CSS, JavaScript, PHP, and MySQL. Most of the visuals were implemented using a JavaScript library called D3.js, which is used primarily to make charts and graphs but it was useful here because it allows the binding of data onto specific elements of the page and for the creation of many scalable vector graphic objects that can transform with a given dataset. The dataset used here is not only the location data of the racks but also the height, width, and depth dimensions. The individual racks, represented on the web site as vector graphics objects, will position itself with its proper dimensions using only the information from the database. The only thing that is hardcoded is the map dimensions.

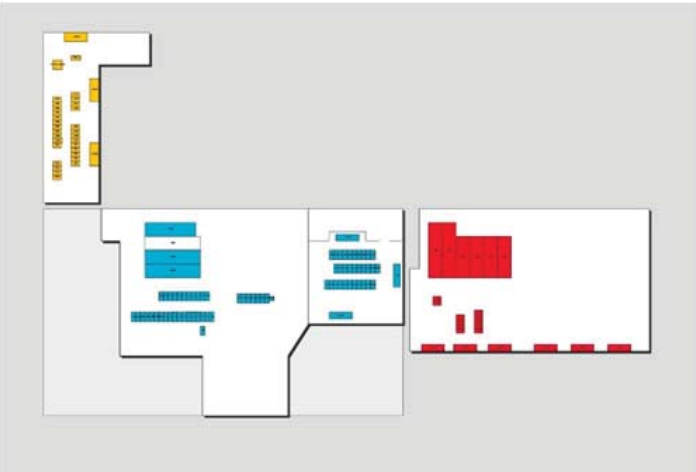

II. Progress

Creating a graphical interface poses a design and usability problem more so than a technical one, consequently allowing for many different ways to approach the problem. Following these general design guidelines helped me through the process.

First, input must be simple. Since location and dimension information needs to be manually inputted into GLPI for each rack, this process should be made as simple and easy as possible. To that end, all the rooms of the data center are displayed on a single page, while the location of each rack is positioned by x-y coordinates, making input as simple as entering the proper room name and two numbers.

Second, the site must be fast. The aim of the site is to increase efficiency by making information readily available. To best achieve this, the site should be fast. That means reducing visual clutter and redundant information and abstracting away unnecessary details of the rooms. The ability to zoom in and out of the map allows for quick navigation. Mouse over popup labels help readability when zoomed out. And since all objects on the page are vector graphic objects, there is no image quality loss when zooming. AJAX calls are used to update the page without having to refresh. A search bar is available to filter racks by name, room, OS, and model.

All racks and information boxes are color coded to help give an intuitive sense of location. Info boxes display the hostname, computer model, technician in charge, and the operating system. Info boxes all display the same information in the same order, maintaining consistency of use, and they also are collapsible, increasing usable space.

III. Conclusion

I also experimented with alternative ways to present the interface. One idea was a collapsible dendrogram. Click one node and branches connected to that node will reveal themselves. Ultimately though, a dendrogram will take up too much screen real estate to be truly useful. It can be useful if used with a different set of data. Another method is a 3D render. Since the width, height, and depth are known dimensions for a rack, a full 3D render of the data center in browser is another viable option. This can be done using Three.js and WebGL and without the need for any external plugins. 3D adds the benefits of scale and greater interactability to the model.

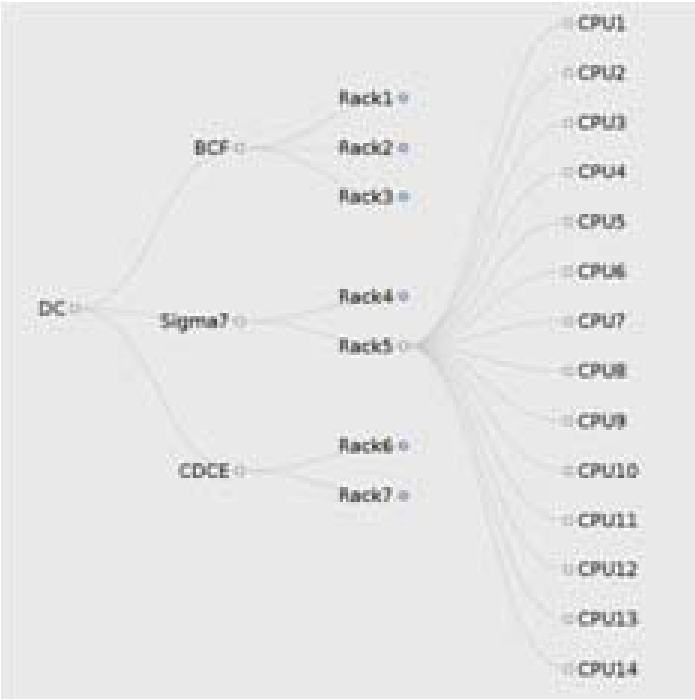

IV. Acknowledgements

This project was supported in part by the U.S. Department of Energy, Office of Science, Office of Workforce Development for Teachers and Scientists (WDTS) under the Community College Internships Program (CCI).

Development of scientific control and computing capabilities at the Inelastic X-ray Scattering beamline, National Synchrotron Light Source II

John Oto
Chemical Engineering, University of Illinois Urbana-Champaign, Urbana, IL 61801
Kazimierz Gofron and Yong Cai
National Synchrotron Light Source II, Brookhaven National Laboratory, Upton, NY 11973

Abstract

Because of the experimental capabilities at the National Synchrotron Light Source II (NSLS-II), scientists from around the world come to utilize the unique technology. NSLS-II produces high brightness X-ray light which is then captured for utilization on what are known as beamlines. Often between 25 m to 100 m long and with multiple hutches filled with complex instrumentation driven by motors and other mechanisms, beamlines need to be controlled through developed operator interfaces (OPI). It is important to ensure that these OPIs are, not only effective, but easy to use and understand. In order to create these OPIs, a program called Control System Studio (CS-Studio) was used because of its rich graphical programming tools. In this session, the primary focus has been creating various OPIs that allow the user to effectively, and accurately monitor and control the Inelastic X-ray Scattering (IXS) beamline. While some screens are more complex than others, the overall intuitive nature of the OPIs allow all users to come and use the beamline, and as a result achieving the goal of making IXS the most user friendly system available. The system allows users to obtain a better understanding of the unique technology used on the IXS beamline such as the Spectrometer Arm, the Beam Positioning Monitors, Slits, and the Tagma Detector. In turn, the efficiency of experiments in terms of time and control can be improved.

I. Introduction

A. Background

National Synchrotron Light Source II is a high end facility which produces x-ray light that can be captured and used for experimentation on one of 60 possible beamlines. Each beamline is constructed with a goal in mind and houses unique and complex instrumentation. Because of the amount of users, and the growing amount of technology, it is important that controls for the beamlines are developed and refined. Here at NSLS-II, the beamline motors are controlled through an EPICS system, a database which monitors and updates based on current activity. However, it is necessary to be able to control the system in an easier way; this is achieved by the development of different operating interfaces, or OPIs. The development of OPIs creates a simple environment in which the user will be able to communicate directly with the components necessary and receive immediate results. These OPIs can range from simple one line screens, to screens that display the changes of multiple motors. Thus, it is important that the OPIs created are of high quality. In order to develop these OPIs, a graphic rich program known as Control System Studios (often referred to as CS-Studio or CSS) was used. CS-Studio uses a combination of java and python scripts to simplify the controls of the beamline.

B. IXS Beamline and Mission

In this session, the primary focus was to develop screens for The Inelastic X-Ray Scattering (IXS) beamline here at NSLS-II. IXS is a beamline that specializes in collisions created between x-rays and a sample of matter. By studying this, specific properties of the material can be determined. The scientific application of the beamline is to study the mesoscopic dynamics in liquids, soft matter, and biological systems, as well as to study phonons in single crystals, surfaces, interfaces and systems under extreme conditions. The ultimate scientific goal of IXS is to have the world leading .1 meV beam, and thus explore the dynamics of materials at levels no one has been able to study before.[1]

The beamline itself is complex and unique. It runs more than 60 meters, and has four visible hutches as well as a CRL behind the shield. Each hutch is specialized from FOE to the endstation. There are unique components such as the 4B HRM, the Spectrometer Arm, the pseudo 2D Tagma detector, and two x-ray Beam Positioning Monitors (BPM).

Because of the complexity of the different components on the beamline itself, the goal, from a control standpoint, is to create OPIs that are easy to understand. While CS-Studio is used at all the beamlines here at NSLS-II, IXS hopes to create the most user friendly screens available. The way that this will be done is to create more intuitive screens as well as visual displays that monitor the changes that occur during activity. In order to achieve this, screens needed to be created, translated, and updated. The developmental focus of this session was creating the endstation screen, translating the tagma detector screens, mimicking motion on screen, as well as updating and refining screens that monitor the conditions of the beamline.

II. Materials and Methods

A. Overall

In order to implement user interfaces to the beamline control, OPI screens were developed and translated into the graphic rich environment known as CS-Studio. CS-Studio creates fields that utilize buttons and graphics to control and navigate through the many components. Screens vary in complexity and usage as well. They can also be developed for one specific purpose, or as a GUI usable for many different beamlines. In order to fulfill the goal of being more user friendly, screens were designed to be more intuitive and to seemingly mimic the different interactions that occur. In addition to this, screens are translated from an older system known as MEDM into CS-Studio.

B. Endstation

The D-Hutch of the IXS beamline is also referred to as the

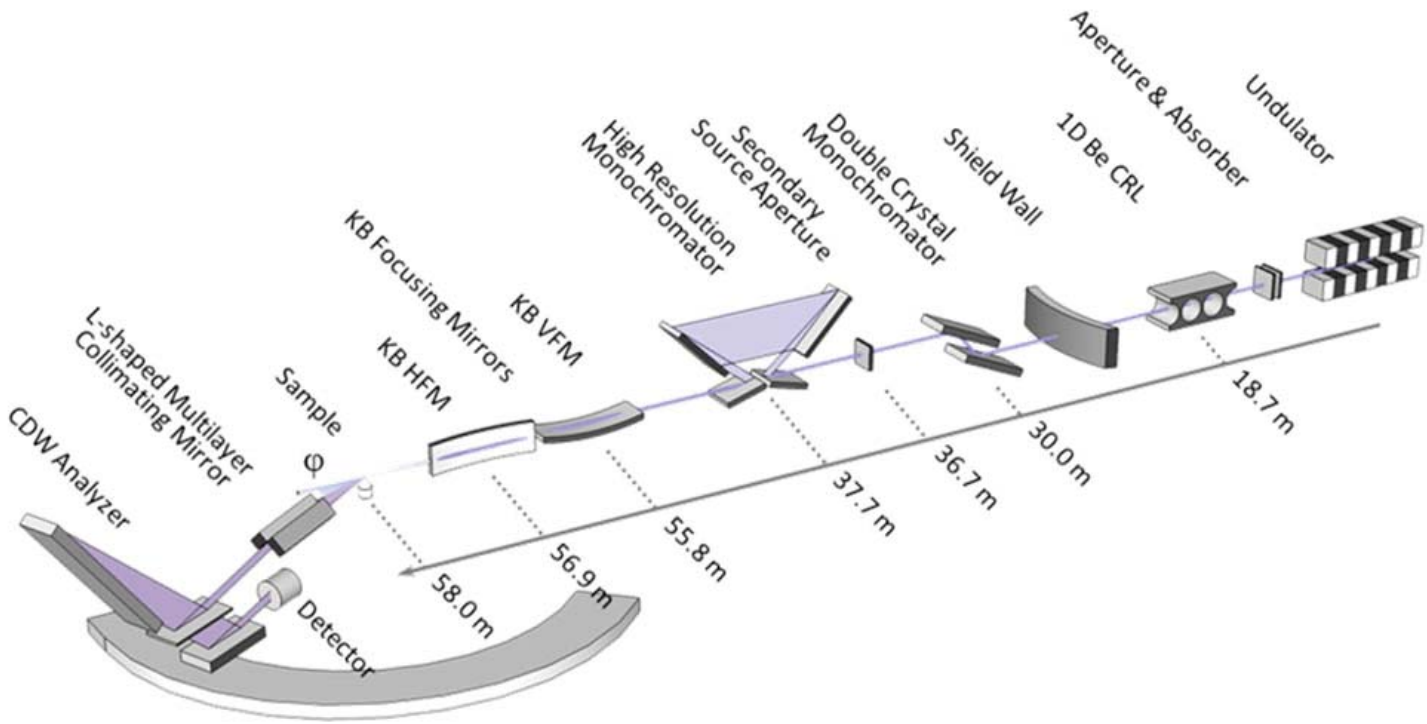

endstation. The screen that is necessary for the endstation involves simplifying the many complex components present. In order to do this, 7 pictures of the hutch were obtained. Each image displayed the analyzer at a different angle range. The pictures were set up with a rule that the picture would change in order to display the correct picture with the corresponding angle. In addition to this, buttons were placed along the beamline in order to represent their actual location. Ideally, the analyzer will eventually be driven using the momentum as well as the angle. Because of this the coefficients of the momentum were calculated and an input for the value was added to the screen. The screen also has drop down menus to link to all the components of the hutch in one location, and a readback gauge was added to display the value for 2θ.

C. Tagma Detector

The Tagma detector is one of the components that can be found in the endstation of the beamline. To create the screens for this, existing screens in the MEDM system were translated to CS-Studio. The old screens were studied in order to determine which parts could be excluded from the translation. CS-Studio allows a much larger screen window than MEDM so the multiple screens that were used for MEDM were condensed down to just one. The graphs were also split into multiple graphs as well so that it would be easier to analyze a single threshold group in addition to seeing them all at the same time. The screen utilizes a scale bar to change the values as well as standard input fields.

D. BPM and SmarAct

These two screens were designed with the goal of mimicking motion. The screen for the beam positioning monitor was designed to display the actual movement of the component in relation to the process variable for the motors controlling the component. By using the position on the screen in relation to the set locations of the BPM, a "crawling" motion could be calculated. The relationship between pixel modification and position is linear, so it was solved using a system of equations. The screen also has one line for the motors actual movement, and then buttons that will move the BPM to the desired position.

The screen for the SmarAct utilized an in environment XY plot to display the changes of the three slit sets upstream of the endstation. Three arrays were created using the variables of each side of the slit. This created a rectangle that will "open and close" when the slits are varied. It also has the motor information for each of the sides of the slits and links to unique screens for each of the slit sets. The plot on which the arrays were placed has a window of -5 to 5 as that is the limits of the slit openings.

III. Results

A. Endstation

Pictured below in Figure 1 is the screen for the endstation of the beamline taken on 7/31/15 during the finishing stages of its development. The seven pictures of the beamline are overlaid, and it changes with the correct angle value. The buttons are placed along the hutch in the actual location of each component. Per design request, the button along the moving part of the picture also move along with the picture to give a more accurate interpretation of the motion. There is a gauge for the angle value in the top right. In the top left, there are drop down menus for all the components in the hutch as well as the cameras and the motion controllers associated with it.

B. Tagma Detector Screen

The screens in Figure 2 are the screens for the tagma detector used on the IXS beamline. The left screen is the original MEDM screen and the screen to the right is the designed CS-Studio screen. The goal was to take the 7 sub screens of the MEDM system and condense it onto one screen. The different graphs are used to monitor the different counts that the detector recognizes. The buttons that are on the screens are direct translations of the old system. The old system used python and C to control specific

things while the CS-Studio screen simplifies that command into a simple button. The graphs on the screen are also copies of the ones found in the MEDM screens, but they scale to the correct window of count so it is easier to determine if there is an issue or an outlier in the data.

C. BPM and SmarAct

The screens in Figure 3 are the screens for the BPM screen and the SmarAct screens. The left screen is the screen designed for the BPM. The same design was used for both BPMs on the beamline, but two different screens were called to account for the movement equations. The Rectangle shape represents a real interpretation of the BPM. A rule was added to have it move in correspondence to the movement of the actual BPM. The red square is a representation of the beam itself. There are buttons on the left that allow the user to go to the position of the correct section. There is also the motor line that gives the user information on the movement of the component.

The SmarAct screen shown to the right has the array for slits at the top. It then has buttons which link the user to the specific screens for each set of slits as well. It then displays the different motor lines that can control the slits. Colors are used to distinguish each set of slits from one another. The screen is a single location for all of the SmarAct slits on the beamline.

IV. Discussion

The development of user screens to control the beamlines will continue to be a necessary task even after the end of this session. The impetus behind controls is the complexity of the components available here at NSLS-II. Because of the emergence of new technology and different ways to use the technology, controls will always be an important and developing field. In addition to the creation of these major screens, a lot of work was put into the refinement of current screens and the development of using screens for specific purposes. While not shown, screens were modified and updated to be more effective on a long term scale. The screens that were the focus of the internship were critical in the developmental stages of the beamline production. In order to produce these screens, CS-Studio was used with the intentions that these screens would make the beamline interfaces more user friendly.

The Endstation screen was the primary focus of the internship controls development. There are four hutches on the IXS beamline, but most of the focus will be directed towards the endstation as that is where the sample is located. The beam will enter the endstation and will then encounter KB mirrors (one vertical and then the second horizontal). The Beam will then encounter a Beam Conditioning Unit before colliding with the sample inelastically. The scattered photons will then go through another mirror and slits before going through a "dragonfly" analyzer. The beamlets from the analyzer will then be analyzed by the Tagma detector. The complexity of this process and the components involved make it necessary for the screen to be intuitive in nature. In addition to this, it is important to consider how the material behaves when analyzed at different angles and momentums which is why the analyzer will be driven by the angle and the momentum. As it is the screen that most users will need to use, a lot of time and effort went into to developing the screen and the screens related to its components.

The Tagma detector is the pseudo 2D strip detector that resides in the endstation of the IXS beamline. Attached to the "dragonfly" analyzer, the tagma detector captures the beamlets on its strips. Each strip houses 32 channels that count the number of photon pulses that are present. Counting detectors are used to analyze the pulse statistics more effectively as they eliminate almost all background noise present.[2] This allows users to accurately determine how many photons are present in a specific range. If there are too little or too much they can be ignored. This is important as the photons scatter after collision allowing users to get a better analysis of the information. The screen was translated from the MEDM system in order to maintain a consistency for the beamline interfaces. In addition to that, the screens created allow the user to analyze more than the screens did. This is because the separation of windows on the graph give a more specific read to what is occurring. In addition to that, since the screen is now condensed into one screen, the user will not have an overly populated work station needed to analyze the data incoming.

The BPM is a five part system that utilizes different materials to cut the beam. It is divided into a Diode section, an empty

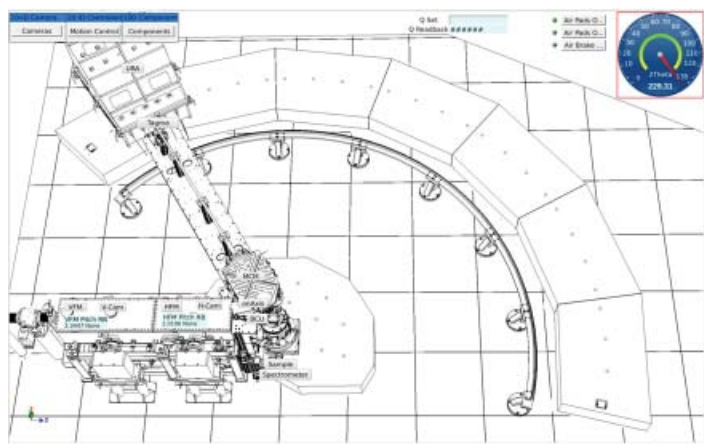

Figure 1: Endstation

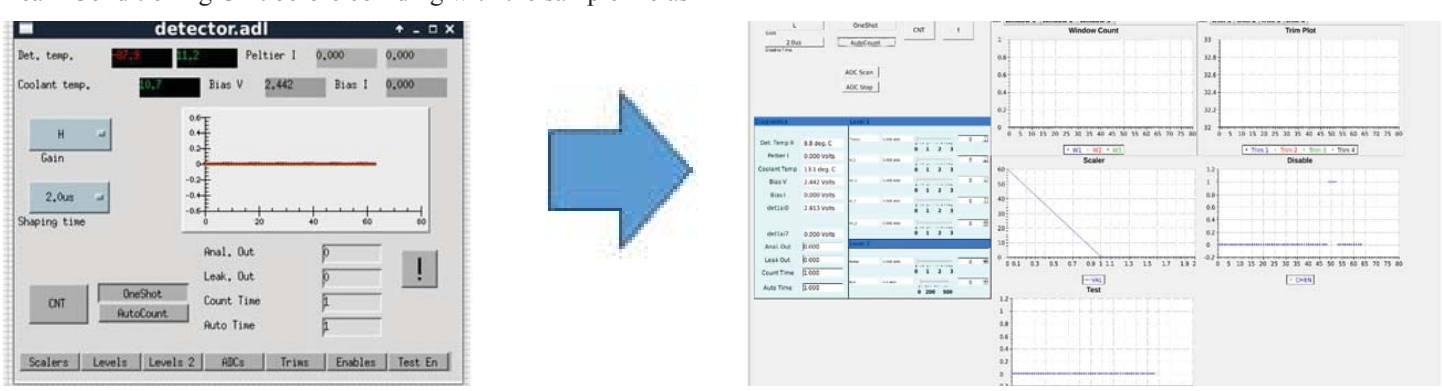

Figure 2: Tagma Detector Screens

section, a Nickel foil section, a titanium foil section, and a YAG crystal section. The user will need to move the BPM to the desired location depending on what they are testing. Because it is moving in such a way, it is necessary for the user to see how it is moving. By creating a dynamic image on the screen, users will be able to determine if the BPM stops moving between foils or if the behavior at another spot is the desired one. The buttons that were placed with the set locations built in alleviate the necessity to know the exact position of each section as it will be provided. The buttons could have been implemented into the picture of the BPM, however this was seen as something that could cause issues and it was thus avoided.

The SmarAct system is a unique system that controls many of the slits on the IXS beamline. Because of this, all the motors run in a similar fashion. Thus, it was determined that creating one screen for this would be beneficial as it would simplify the screens on the main screen. The slits commonly have four panels (a top, a bottom, an inner, and an outer). The slits often need to be modified in a certain direction, whether it is by opening in one way and closing in another, or simply centering it, it is a dynamic component on the beamline. Because of this, it was believed that the rectangular arrays created would be beneficial for the users. To visually see which direction the slits would be opened in as well as their openings in relation to the other slits on the beamline is beneficial information.

As stated, many more screens were developed or refined in order to enhance the user capabilities of the beamline. Screens that monitored changes in temperature and pressure were implemented to help the understanding of the system. All of these changes were made with the intention to make the beamline more intuitive and user friendly. However, these steps were only the first steps taken in a long term goal.

V. Conclusion

The screens that were developed in this session can all be considered a success as they all work and do their desired function. However, the development and refinement of user screens is a process that will not end until the screens are no longer usable due to the development of new technology. While the screens were completed and functioning, there is always work that could be done on them. The endstation screen was produced during this session, but there are still new components being added to the hutch every day. With each new component, a new screen will need to be developed and then added to the user screen. Eventually, the template used for the creation of the endstation screen will be used for the other hutches of the beamline. This will bring IXS that much closer to being one of the most user friendly/ intuitive beamlines available. Refinements can be made to the tagma screen when more information about the system/usability is known. Some screens were developed specifically for the components of the IXS beamline. Those screens could eventually be converted into a macro system in order to extend their use to other beamlines as well. If more time was available, I would've liked to create and refine more screens for the beamline. With each screen that is developed, a more intuitive user interface is obtained. While there are still many obstacles to go through before achieving a completely intuitive interface, the developmental success found during this session brings IXS one step closer to that point.

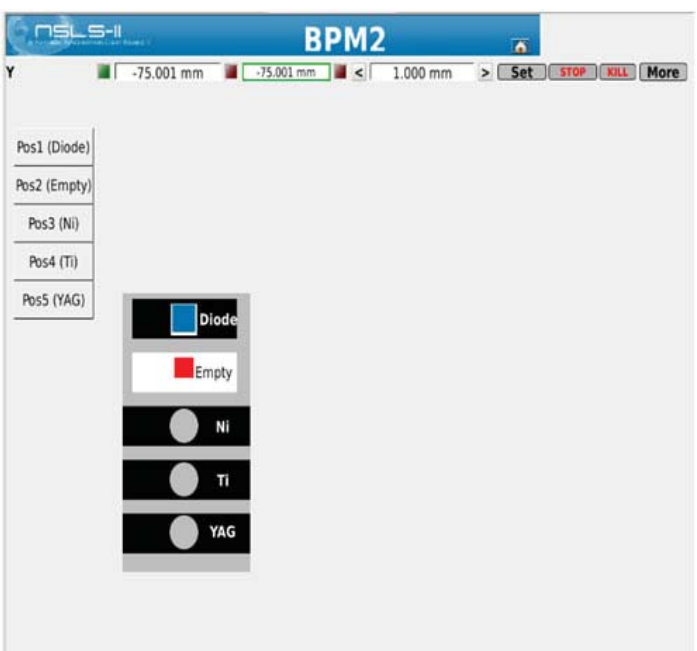

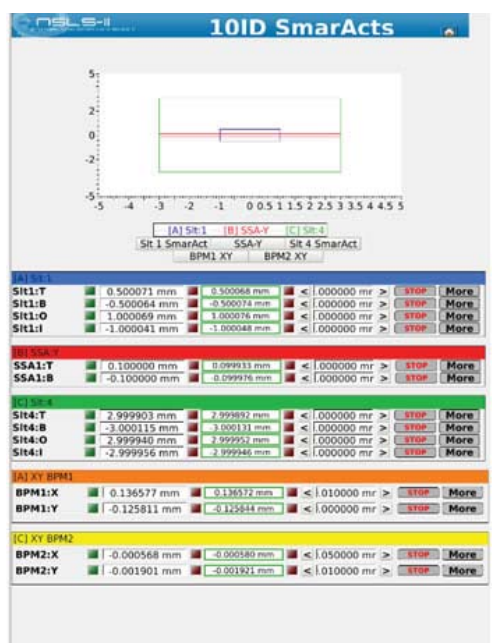

Figure 3: BPM and SmarAct Screens

VI. Acknowledgements

The development of the User Screens could not be completed without the assistance of my Mentor Yong Cai, Controls Engineer Kazimierz Gofron, Beamline Engineer Scott Coburn, CS-Studio developer Kunal Schroff, and the rest of the IXS beamline staff.

This project was supported in part by the U.S. Department of Energy, Office of Science, Office of Workforce Development for Teachers and Scientists (WDTS) under the Science Undergraduate Laboratory Internships Program (SULI).

VII. References

[1]Cai, Yong et al. "The Ultrahigh Resolution Inelastic X-ray Scattering Beamline at NSLS-II: 'First Results'". Powerpoint Presentation.

[2]Keister, J. et al. "Compact pseudo-2D strip detector system for sub meV IXS" Journal of Physics 493rd ser. (2014): n. pag.

Creation of high charge state lithium and calcium ion beams using laser ablation

Kevin Palm
Department of Physics, Cornell University, Ithaca, NY 14853
Masahiro Okamura
Collider-Accelerator Department, Brookhaven National Laboratory, Upton, NY 11973

ABSTRACT

Calcium and lithium ion beams are required by the NASA Space Radiation Laboratory (NSRL) at Brookhaven National Laboratory (BNL) to simulate the effects of cosmic radiation in space. Earth's atmosphere blocks this heavy ion radiation, but it would have significant biological effects on the surface of a planet, such as Mars, with a thin atmosphere. In our experiment, we extracted the ions from a plasma plume created by laser ablation on lithium and calcium targets with a 6ns Nd:YAG laser operating at a wavelength of 1064nm. Laser ablation has an advantage over other similar processes because the laser requires no warm-up time and is, therefore, quicker and more cost effective. We found significant oxygen contamination in both the Ca and Li high charge state beams due to the rapid oxidation of the surfaces. A large spot size, low power laser was then used to analyze the low charge state beams. The low charge state Ca beam did not have any apparent oxygen contamination, showing the potential to clean the target entirely with a low power beam once in the chamber. The Li target was clearly still oxidizing in the chamber after each low power shot. To measure the rate of oxidation, we shot the low power laser at the target repeatedly at 10sec, 30sec, 60sec, and 120sec interval lengths, showing a linear relation between the interval time and the amount of oxygen in the beam. Our results show the possibility of using a double shot technique to create a cleaner beam, with one low powered defocused laser to clean the surface at a set interval and a second focused laser to create a high charge Li state beam.

I. INTRODUCTION

A laser ion source (LIS) is an effective and simple method for creating a variety of high charge state ions. A plasma plume is created by a pulsed power laser focused on the target surface. Ions are extracted from the expanded plasma and subsequently are collimated into a beam. By replacing target materials, ion species can be easily changed. LIS has not yet been extensively tested on Li and Ca targets due to their high reactivity. These beams would be useful to simulate the effects of cosmic radiation in space, where heavy metal ions form a small percentage of the total composition of the radiation.[1] Although small in percentage, the heavy ions could have a significant effect on one's biology because of their high penetrating quality. NSRL requires high charge state Ca and Li ion beams to properly study these effects. Li ion beams also have a potential use for neutron beam creation.[2] LIS has an advantage over other current neutron sources because it can create a pulsed neutron beam as opposed to a continuous beam. Neutron beams have many current uses, such as Neutron Capture Therapy for treating cancer. High charge state beams are also more useful for accelerator experiments because the higher the charge state to mass ratio is, the easier the ions are to accelerate. Thus, in this paper we studied using LIS on Li and Ca targets to create high charge state ion beams.

II. EXPERIMENTAL SETUP

Figure 1 shows the experimental setup. The targets were irradiated with a neodymium-doped yttrium aluminum garnet (Nd:YAG) laser operating at a wavelength of 1064 nm and 6 ns of pulse length. The laser was focused on the target with a plano-convex lens with a focal length of 100 mm. The distance of the lens from the target was adjustable from outside of the target chamber, allowing for the beam to be focused and defocused without venting the vacuum. The incident angle between the laser path and the beam line was 20°. The target chamber and subsequent beamline were held below 1.8 x 10-4 Pa for the duration of the experiment.

Both Li and Ca oxidize rapidly when exposed to the oxygen in the atmosphere. To limit the exposure of the targets, special precautions were taken in the making of the targets. The metals were polished, rolled to the proper thickness using a rolling mill, and immediately stored in a portable vacuum chamber. The targets were released from vacuum in an artificial atmospheric chamber purged with argon gas and attached to the target mount while inside the chamber. The mount was then taken from the artificial atmospheric chamber and quickly attached to the XY stage in the target chamber. The chamber was immediately pumped down to vacuum.

Figure 2 is a sketch of the Li target holder. The Li target requires a specialized holder because of its softness to stabilize the metal without cutting through it. The Ca target did not require a specialized holder because of its rigidity and a planar rectangular aluminum frame was used. Each target had a thickness of 1 mm.

A Faraday Cup (FC) with φ = 10 mm aperture was placed at 2.4 m away from the targets to measure the beam current. The suppressor voltage of FC was set to −3.5 kV. The plasma was an-

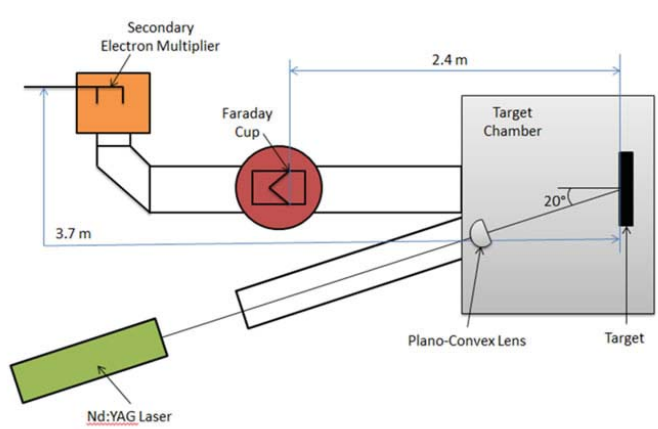

Figure 1: LIS Experimental Setup

alyzed by an electrostatic ion analyzer (EIA) with an entrance slit of 200 µm for low power density experiments and 40 µm for high power density experiments. The selected ions were detected by a secondary electron multiplier (SEM). The total distance between the detector and target was 3.7 m. Ion species and charge states were determined by time of flight information in the SEM signal and the applied voltage to the EIA.

III. RESULTS AND DISCUSSION

It was clear from the initial tests that an appreciable amount of oxide formed on the surfaces of the targets, despite the careful mounting procedure. The analysis showed significant amounts of both the ^{7}Li and ^{6}Li isotopes in the Li experiments, while only ^{40}Ca was observed in the Ca experiments with no other notable isotopes.

We assumed that the SEM has a constant sensitivity for different materials, charge states, and particle velocities. All beam current data was normalized to a 1 m distance from the source and a beam area of 1 cm^2 by summing all of the individual curves in the SEM ion analysis, scaling the peak of this curve to the peak of the real beam current measured by the FC, and finally scaling the current to the proper distance and beam area using the relation

$I \alpha L^{-3} * S$

where I, L, and S are the current, distance from target, and beam area respectively.

A. High Charge State

A focused beam with power density on the order of 1012 W/cm^2 was used to create high charge state Li and Ca beams. For the Li beam, the analysis showed oxygen charge states ranging from O^{1+} to O^{8+} as well as $^{7}Li^{3+}$, $^{7}Li^{2+}$, $^{7}Li^{1+}$, and $^{6}Li^{3+}$. From the data, it is very difficult to conclude the exact amount of each ion species in the beam because the ratio of charge state to mass was very similar for many of the ion species, making their peaks indistinguishable from one another. Examples of such ion species are $^{7}Li^{3+}$ and O^{7+} as well as $^{6}Li^{3+}$ and O^{8+}. Since it was clear that both Li and O were present in appreciable amounts in the beam, we could not make any safe assumptions of the composition of the beam, but it was clear that the LIS was capable of creating Li^{3+}, which is the highest possible charge state of Li. The beam composition data can be seen in Figure 3.

Similar oxygen contamination was found in the Ca high charge state beam. Ca ions ranging from charge state Ca^{2+} to Ca^{19+} were present in the beam as well as O^{4+} through O^{8+}. Many O and Ca peaks were indistinguishable due to similar charge state to mass ratios, causing difficulty in properly quantifying the amount of each element in the beam. The histogram showing the abundance of the ions (Figure 4) shows a double peak in the Ca ion data, with one peak at Ca^{3+} and a second peak at Ca^{14+}. A double peak is very unusual, and could have been the result of poor surface roughness causing inconsistencies in the data. Surface roughness data was recorded after the chamber had been opened and it was found that the surface had a variation of ±0.25 mm, which is

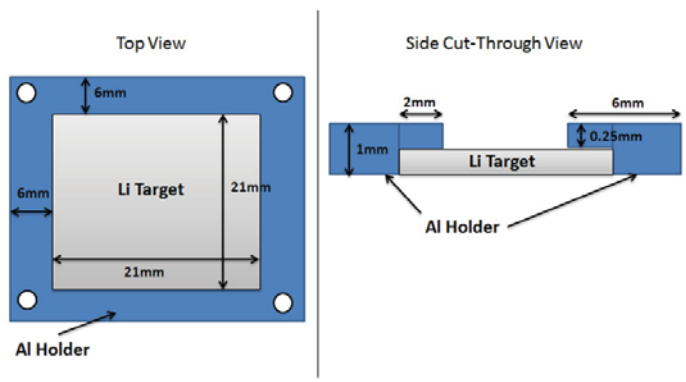

Figure 2: Sketch of Li Target holder

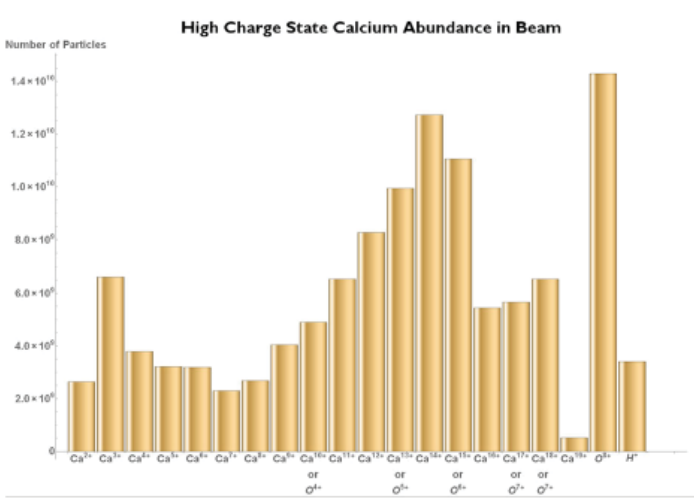

Figure 4: Total current created from Ca target broken down by individual ion

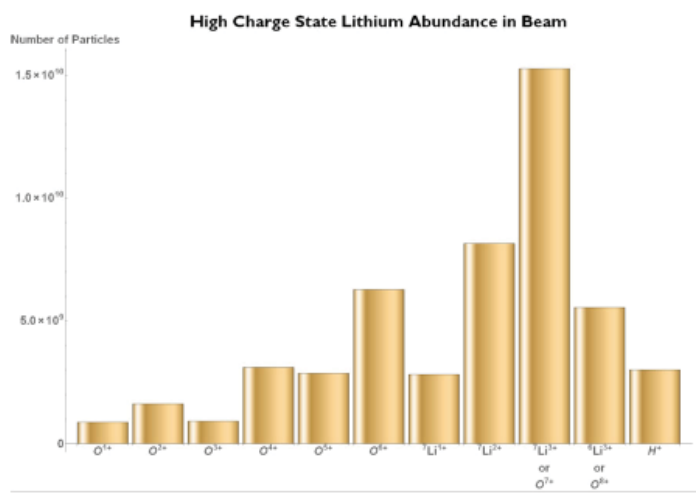

Figure 3: Total current created from Li target broken down by individual ion

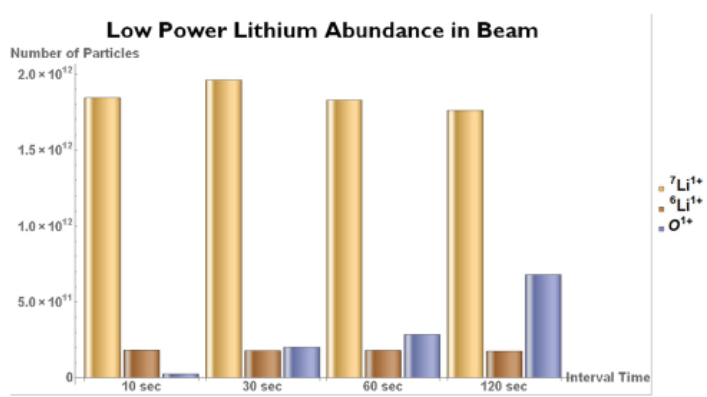

Figure 5: Total current of ions found in beam by interval time

outside of our tolerance of ±0.1 mm. The surface roughness measurement was not recorded before the experiment to limit oxygen exposure of the target. Although the data were inconsistent, it repeatedly showed the creation of Ca^{19+}, which is the second highest charge state possible of Ca, showing the ability of LIS to create a high charge state Ca beam.

B. Low Power Interval Shots

An experiment was run to test if a low powered laser with a large spot size could clean the surface of the Li target while under vacuum inside the target chamber. A power density of 5.0 x 108 W/cm^2 was used with a 0.28 cm^2 spot size. At this power density, the only ions to appear were $^7Li^{1+}$, $^6Li^{1+}$, and O^{1+}. Initial qualitative experiments were run to test if the amount of O^{1+} could be lowered in the beam. It was found that repeatedly firing the laser at a single spot did reduce the height of the O^{1+} peak measured by the SEM, however if the target was allowed to sit without being fired upon for longer than 5 seconds and then fired upon again, the oxygen peak would increase. This implies that even under a vacuum of 10^{-4} Pa, the Li target was still being oxidized. At this pressure, there are still approximately 8.9 x 1014 collisions per second of O2 molecules with the spot being irradiated by the laser.

An experiment was run to determine how much oxygen is present in the beam at constant interval irradiation of the target. Data were taken for interval lengths of 10 sec, 30 sec, 60 sec, and 120 sec. Before the data were recorded, the laser was shot at the interval length being tested until the ion output stabilized. Approximately 50 laser shots were required to stabilize the beam for each experiment. The results can be seen in Figure 5. The amount of ^6Li compared to ^7Li was found to be approximately 9% for each interval length, which is fairly consistent with its reported natural abundance of 7.5% .3 The amount of O^{1+} in the beam was plotted versus the interval time, showing a clear linear relationship with an R^2 value of 0.982, seen in Figure 6.

C. Low Charge State Calcium

A low power experiment was run on the Ca target with a power density of 1.7 x 108 W/cm2 and spot size 0.52 cm2. With these conditions, only Ca1+ and Ca2+ were observed with no oxygen ions (Figure 7). This result shows that after the initial oxide is cleaned off of the surface, no subsequent oxide is formed on the target surface while it is under vacuum.

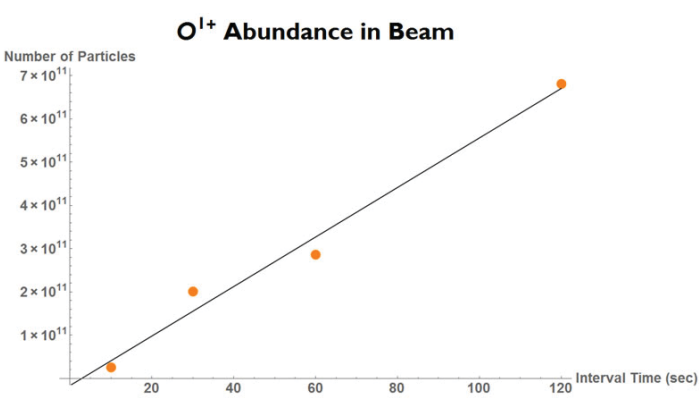

Figure 6: Total beam current of O1$^+$ created plotted vs. interval shot time

IV. CONCLUSION

Using LIS can create high charge state Li and Ca ions, showing the ability to completely strip Li atoms of electrons and strip Ca of all but one electron. There was an apparent oxygen contamination in both beams. We found that the Ca target did not oxidize any further in the chamber, implying that a clean high charge state beam can potentially be created by using a low power, large spot size beam to clean the surface of the target while under vacuum in the target chamber and then focusing the laser to create the high charge state beam. The Li target was clearly oxidizing in the vacuum chamber held below 1.8 x 10^{-4} Pa. A linear relationship between oxygen amount and interval shot time for a low power density, large spot size laser on the Li target shows the potential to regulate the amount of oxide on the surface while the target is inside the chamber. This result shows that a double shot setup, with one low power, large spot size laser shot at interval times to clean the target and a second focused high powered laser to create the high charge state beam, could potentially be used to create a high charge state Li beam with significantly less oxygen contamination.

V. REFERENCES

[1]S. Eidelman et al., Physics Letters B592, 1 (2004)

[2]E. Norbeck, Jr. and C. S. Littlejohn, Physical Review 108, 3 (1957)

[3]"Lithium: Isotope Data." Lithium»isotope Data [WebElements Periodic Table]. N.p., n.d. Web. 25 July 2015.

VI. ACKNOWLEDGEMENTS

I would like to thank my mentor Dr. Masahiro Okamura for his guidance on this project, as well as Dr. Takeshi Kanesue and Dr. Dannie Steski from BNL. This project was supported in part by the U.S. Department of Energy, Office of Science, Office of Workforce Development for Teachers and Scientists (WDTS) under the Science Undergraduate Laboratory Internships Program (SULI).

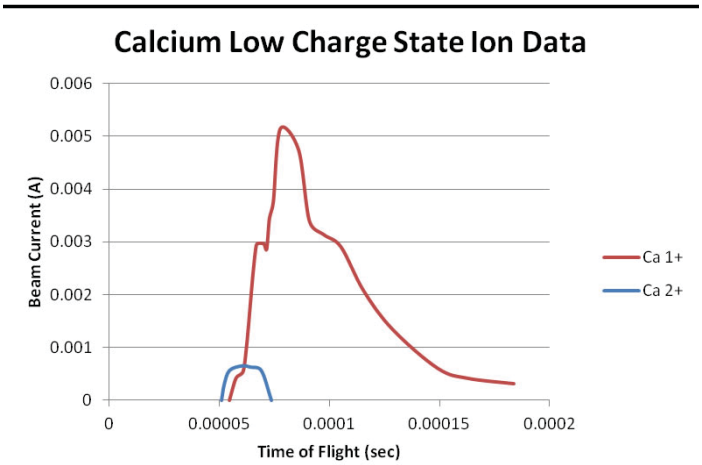

Figure 7: Normalized ion data of low charge state Ca experiment

An analysis of understory plant diversity in the Long Island Central Pine Barrens

Ari Rice
Department of Biology, Lawrence University, Appleton, Wisconsin, 54911
Kathy Schwager, Jennifer Higbie, and Tim Green
Environmental Protection Division, Brookhaven National Laboratory, Upton, NY 11973

Abstract

The Central Pine Barrens of Long Island are a remnant of a once-extensive ecosystem that stretched from Cape Cod to southern New Jersey. They are characterized by sandy, acidic soil, a low shrub layer, and a mixture of oaks (*Quercus* spp.) and pitch pine (*Pinus rigida*) as the dominant trees. They host a wide variety of plants and animals that are rare or uncommon elsewhere, but because of fire suppression, urban expansion, and invasive species, much of the original Pine Barrens habitat has since been destroyed or heavily degraded. Thus, it is critical that we take measures to study, evaluate, and protect what remains of this unique ecosystem. In this study, I analyzed understory vegetation from nineteen forested plots at Brookhaven National Laboratory (BNL). All plants within each plot were identified at the species level and transect surveys were conducted in order to determine their relative abundance. Factors that were thought to influence plant diversity included the presence of certain trees within plots, habitat type, canopy cover, and the occurrence of fire within the past five years. Results showed the dominant understory species to be black huckleberry (*Gaylussacia baccata*), Pennsylvania Sedge (*Carex pensylvanica*), and two species of blueberry (*Vaccinium* spp.). The prevalence of these four dominant plants showed no significant relationship with pine cover, and only the early lowbush blueberry (*Vaccinium pallidum*) showed a significant correlation with oak canopy cover. However, other tests revealed the relative abundances of these species to be anything but random. This suggests that other factors such as soil composition, nutrient availability, and interspecific competition may play a larger role in determining which dominant understory plants occur in a given area.

I. Background

A pine-dominated plant community, a high frequency of wildfires, and a prevalence of sandy soils are the major defining features of a pine barrens ecosystem. Indeed, these three features often act as limiting factors where plant growth is concerned. The sandy, course-grained soils of pine barrens regions hold little water or nutrients and preclude all but the hardiest plants from colonizing most areas. Fires are a common occurrence, and under conditions where most trees would perish, fire-resistant pine trees thrive—forming shrublands, savannahs, and open woodlands within this otherwise harsh environment (Jordan, 2003; Kurkczewski and Boyle, 2000; Reiners, 1965).

The Central Pine Barrens of Long Island are located almost entirely in Suffolk County, New York, but are part of the Atlantic Coastal Pine Barrens ecoregion (Figure 1). The climate within this region is temperate, with the ocean moderating temperature extremes and giving rise to consistently high humidity. Precipitation is consistent throughout the year, but the quick-draining soil prevents moisture from accumulating in all but the most low-lying areas (Reiners, 1965). The soil is also acidic, and for most of Long Island's Central Pine Barrens, habitat types and succession are determined by the frequency of fire (Reiners, 1965). In areas where fires are frequent and intense, pitch pines colonize the exposed sand and form an early-successional shrubland. Scrub oak (*Quercus ilicifolia*) is a common feature of these shrublands, and as fire becomes less frequent, these pines grow taller, create a closed canopy, and allow the soil to retain more moisture and nutrients (Kurczewski and Boyle, 2000). Tree oaks grow under these conditions, and as they become more prominent, scrub oak is gradually replaced by a shrub layer of blueberry and huckleberry. Pitch pines are eventually phased out, hardwoods take over, and in the absence of fire or disturbance, and the plant community becomes oak-hickory forest (Figure 2). That said, pine barrens habitats are generally divided into the categories of dwarf pine plains, pine-scrub oak heathland, pine forest, pine-oak forest, oak-pine forest, and coastal oak forest (Kurczewski and Boyle, 2000; Jordan et. al, 2003; Foundation for Ecological Research in the Northeast, 2007).

None of these plant communities are static, however. Before European settlement, the forests of central Long Island were thought to be a mosaic of oak-pine forests and successional areas recently affected by fire. The clearing of these forests led to a dramatic increase in early successional habitats, but with fire sup-

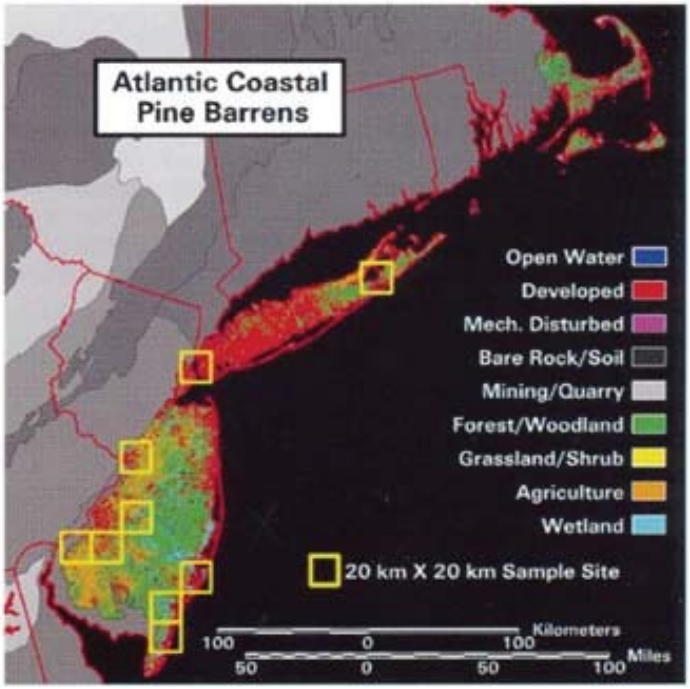

Figure 1- A map of the Atlantic Coastal Pine Barrens from Sohl, 2003. Colored areas represent the ecoregion as a whole, with the Long Island Pine Barrens located in the small green area near the center.

pression in the 20th century, this habitat has reverted back to oak-pine forest in some areas (Kurczewski and Boyle, 2000; Oswald et. Al, 2010; Foster and Motzkin, 2003). And while a significant portion of Long Island's Central Pine Barrens are currently under some form of protection, this unique ecosystem remains threatened by habitat fragmentation, invasive species, and continued fire suppression. Indeed, some areas may require active management if they are to provide for globally rare species such as the sickle-leafed golden-aster (*Pityopsis falcata*), the bushy rockrose (*Helianthemum dumosum*), and the sand-plain gerardia (*Agalinis acuta*)(Clemants et. al, 2006). For this reason, it is crucial that we understand the ecology of understory plant communities in the pine barrens. What are the most dominant species of plants and why? Does the presence of certain trees influence understory composition? Does fire increase understory plant diversity? These are questions that this paper intends to answer.

II. Study Site

In this study, I surveyed understory plant communities from nineteen forested plots located within Brookhaven National Laboratory. The property belonging to Brookhaven National Labo-

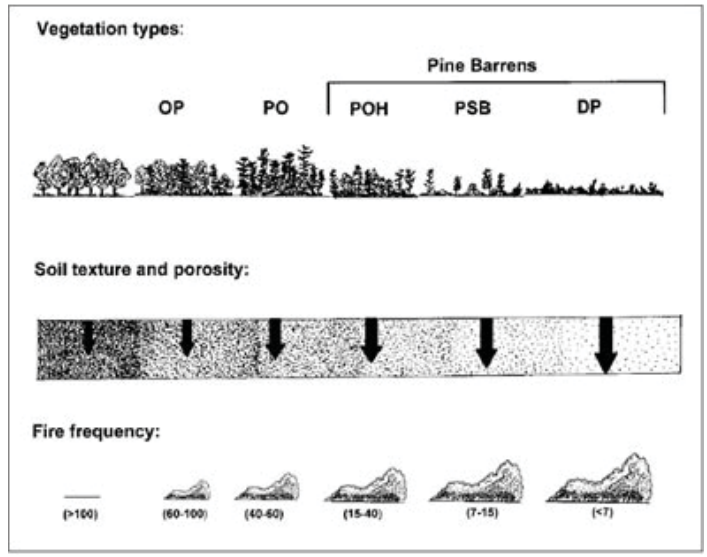

Figure 2- A chart displaying the trends associated with successional growth in the Pine Barrens, from Kurczewski and Boyle, 2000.

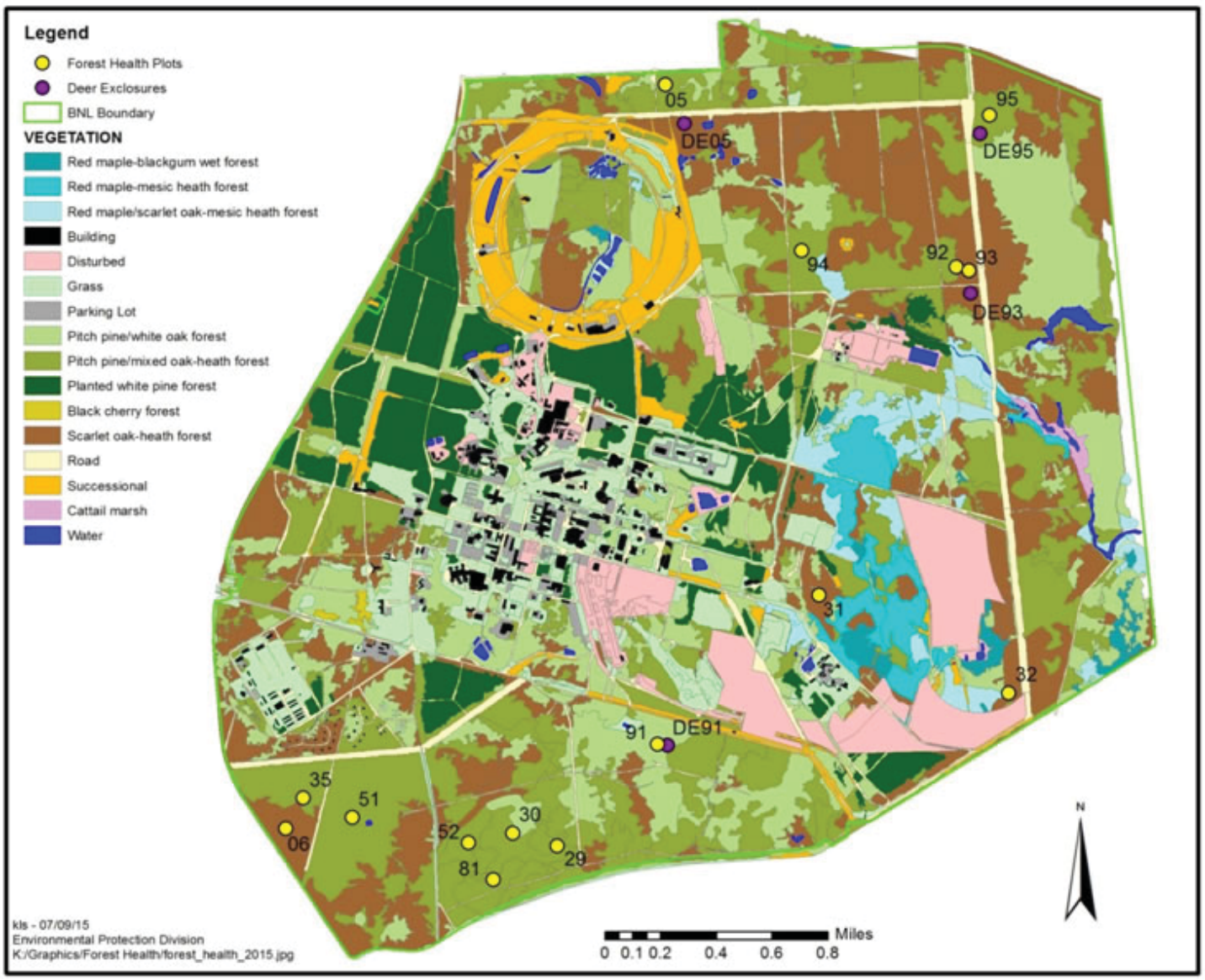

Figure 3- A map depicting the locations of each plot at BNL. Plots included within deer exclosures are marked in purple, while all other plots are marked in yellow

ratory consists of 5,265 acres within central Suffolk County and contains extensive pine barrens habitat. Dwarf pine plains and scrub- oak heathland are largely absent at this site, while coastal oak, oak-pine, and pine-oak forest exist as the predominant habitat type. Several large tracts of eastern white pines (*Pinus strobus*) were established at this site in the 1930's, and the richer, moisture-retaining soil from the southeastern portions of the property supports hardwoods such as red maple (*Acer rubrum*), black tupelo (*Nyssa sylvatica*), and shagbark hickory (*Carya ovata*). The understory within the latter contains a wide variety of ferns, shrubs, and sedges, but because the plant communities in these areas differ greatly from that of the surrounding pine barrens, these white pine plantations and mesic hardwood forests were not included on surveys.

Within the plots that were surveyed, the dominant understory plants were black huckleberry (*Gaylussacia baccata*), early lowbush Blueberry (*Vaccinium pallidum*), and late lowbush blueberry (*Vaccinium angustifolium*). At BNL, these three species of woody, low-growing shrubs form a distinctive community that Reiners refers to as a "heath-shrub synusia" (1965). Large swaths of forest floor are blanketed with some combination of them, and the shrubs themselves are remarkably similar in terms of appearance and ecology. All three reproduce primarily through rhizomes, prefer well-drained soil, grow best in areas with scattered shade, and have the tendency to re-sprout after fire (Reiners, 1965; Matlack, 1997; Brayton and Woodwell, 1966). And while the pine barrens habitat within BNL contains other understory plants such as *Carex pensylvanica, Pteridium aquilinum*, and *Cypripedium acaule*, none of these occur at the same level of abundance as the aforementioned shrubs.

III. Materials and Methods

Nineteen forested plots were surveyed according to protocols established by the Foundation for Ecological Research in the Northeast (FERN)(Figure 3). Two of these plots were established within the duration of this study (See protocol for details on plot establishment), while the remaining seventeen were created in previous years. Transect tape was used to measure out each 25 x 16-meter plot, and floral and faunal inventories were taken within each plot throughout the survey process. Four plots were located within deer exclosures, and the habitat type for each plot was determined through a combination of ArcGIS data and pine vs. hardwood cover.

Canopy, subcanopy, shrub, and herbaceous plant cover were estimated as percentages within plots, and the relative abundances of understory plants were determined through line transect surveys. Ten line transects along the 25-meter axis were conducted within each plot, and vegetation was recorded at 1-meter intervals along each transect by vertically dropping a 2-meter pole at certain points and recording the vegetation that touched it. Each

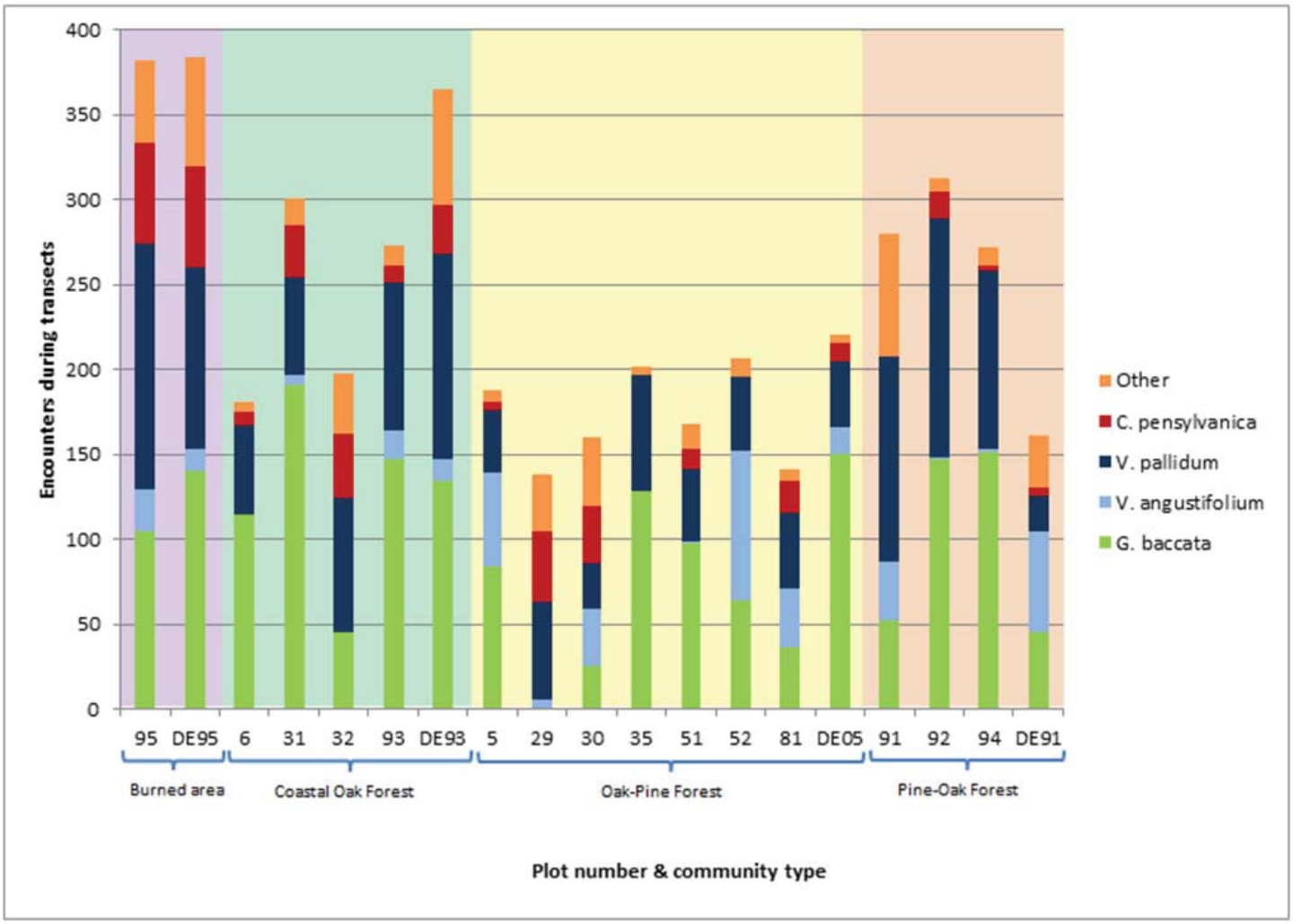

Figure 4-Overall vegetation cover based on encounters along transects. Numbers prefaced by "DE" refer to plots within deer exclosures.

line transect consisted of twenty data points (adding up to two hundred points per plot), and the starting point for each transect was randomly determined, but never more than 3 meters from the edge of the plot. Transects were spaced apart from each other at 1.5-meter intervals, and great care was taken not to destroy or trample vegetation growing along transects.

These same line transects were also used to gather information on canopy cover. The presence or absence of a pitch pine and/or hardwood canopy was noted at each point along transects with the help of a densitometer.

Data collected from plots was entered into Microsoft Access and further processed with Microsoft Excel. Bar graphs were created to display the relative abundances of certain plants per plot and overall species richness within different habitat types. The "dominant" species of plants across plots were determined by two criteria: The plant must occur in thirteen or more plots and have an average encounter rate of more than 10% within all plots. These dominant plants were further analyzed in terms of linear regression analyses (which measured their abundance as functions of pine and hardwood canopy cover), an Anderson Darling test (which tested for normality), and two Kruskal-Wallis tests (when the data was found to have a non-parametric distribution).

IV. Results

Data collected on transects indicated that *Gaylussacia baccata* was the most dominant species of plant within plots, followed by *Vaccinium pallidum, V. angustifolium,* and *Carex pensylvanica* (otherwise known as Pennsylvania Sedge). Other species that occurred in significant numbers along transects included *Pteridium aquilinum, Gaultheria procumbens, Vaccinium corymbosum, Quercus ilicifolia*, and small specimens of *Q. alba* and *Q. coccinea* (See Appendix- Table 1). However, none of these were numerous enough to be considered dominant, and are thus grouped together in the visual representation of the transect data within Figure 4.

According to Figure 4, the overall amount of vegetation encountered on transects was highest in the two recently-burned plots, lowest in oak-pine forest, and moderately high in pine-oak and coastal oak forest. *C. pensyvlanica* was most abundant in the burned plots and least common in pine-oak forest.

G. baccata was abundant in every habitat type (with the exception of plot 29), and *V. pallidum* appeared to be least common in oak-pine forest.

Among *G. baccata, C. pensylvanica*, and the two species of *Vaccinium*, none were significantly correlated with the presence

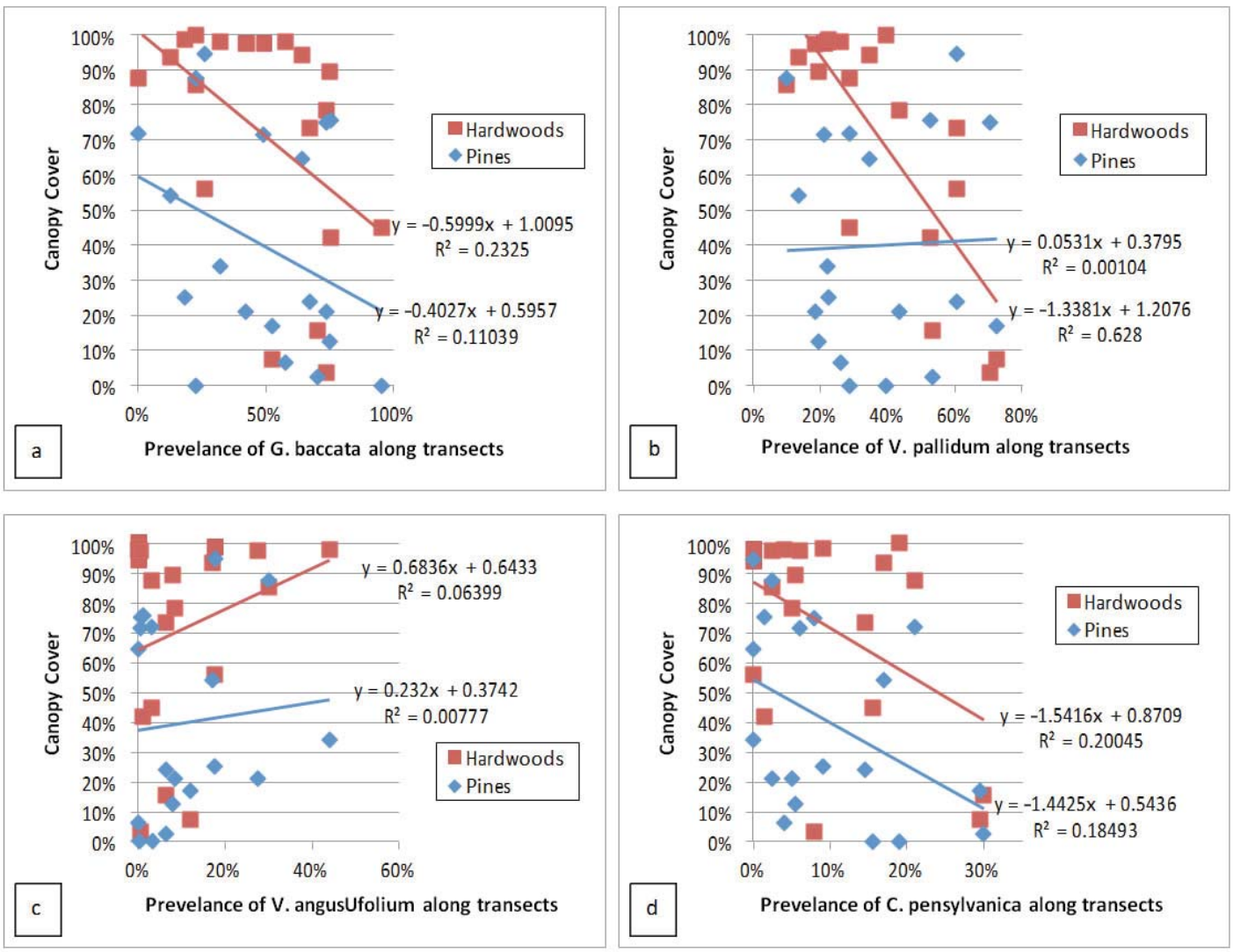

Figure 5- Linear regression analyses featuring the abundance of dominant vegetation as functions of pine and hardwood canopy cover.

of pitch pines overhead, and only *V. pallidum* showed a significant correlation with hardwood canopy cover (Figures 5a-5d). As shown in 5b, this was a negative correlation, with *V. pallidum* becoming less numerous as hardwood cover increased.

The Anderson-Darling test showed a non-parametric distribution of dominant plants within transect data (See Appendix Figure 2), and a Kruskal-Wallis test showed insignificant results when plant counts were measured against plots (P=0.921)(Appendix Table 2a). However, another Kruskal-Wallis showed highly significant results when plant counts were measured against the species of plants that comprised them (P>0.001)(Appendix Table 2b).

Species richness showed the highest values in coastal oak forest (with an average of 17.2 species per plot) but also showed considerable deviation from the mean (Figure 6). Pine-oak forest displayed the second-highest values for species richness and the lowest amount of deviation. Oak-pine forest experienced slightly lower species richness, and the burned areas that had previously been pine-oak or oak pine forest showed the lowest species richness (with an average of 9.5 species per plot).

V. Discussion

The dominance of *G. baccata, V. pallidum,* and *V. angustifolium* at BNL is consistent with previous studies from this area as well as those from other parts of the Atlantic Coastal Pine Barrens (Brayton and Woodwell, 1966; Stalter and Lamont, 2014; Jordan, 2003; Matlack et. al, 1993). The relative abundances of these shrubs (With *G. baccata* being the most abundant and *V. angustifolium* being the least) is furthermore consistent with studies conducted at Brookhaven in the past (Reiners, 1965; Whittaker and Woodwell, 1969). Although none of these studies mention Carex pensylvanica as a dominant understory plant, this widespread sedge is regularly associated with *Vaccinium* and *Gaylussacia* in pine barrens habitats (Abrams and Dickmann, 1981). As an early successional species, its abundance is thought to positively correlate with fire frequency and negatively correlate with increased litter depth and canopy cover (Matlack and Good, 1989). And while canopy cover data from Figure 5 did not show a significant correlation with *C. pensylvanica*, the sedge's overall abundance in burned vs. unburned plots support the hypothesis that it benefits from fires.

This study did not find significant correlations between most of the dominant plant species and canopy cover. Nevertheless, *G. baccata* became less numerous as overall canopy cover increased. *V. angustifolium* increased with canopy cover, though this may simply reflect on it being crowded out by taller, faster-growing shrubs in areas that receive more sunlight. *V. pallidum* showed a unique trend: It showed no correlation whatsoever to pine cover, but significantly decreased in response to oak cover (R^2= 0.628). And while some of these patterns contradict information from previous studies, others are supported within the literature. Oaks tend to produce denser canopies than pine trees, and despite being a late successional plant associated with the oak-pine forest (Whittaker and Woodwell, 1969), *G. baccata* is thought to thrive under less canopy cover and take advantage of the sunny conditions produced by canopy gaps (Reiners, 1967; Buell and Cantlon, 1950; Matlack, 1997). Indeed, previous studies at Brookhaven have shown the total shrub biomass to increase in areas with less shade and a more open canopy (Reiners, 1967).

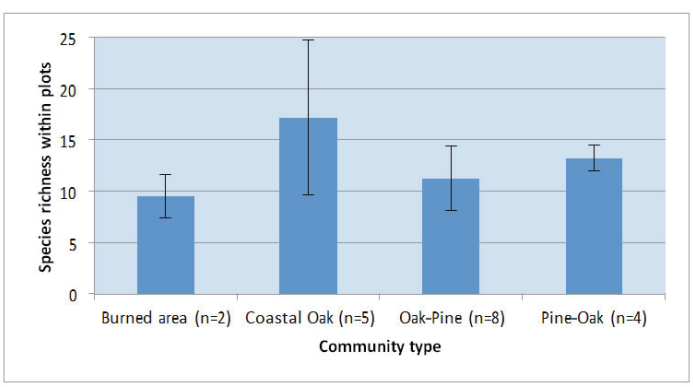

Figure 6-Average numbers of plant species occurring across different habitat types.

Nevertheless, a considerable amount of the literature on canopy-shrub relationships seems to present contradictory evidence. In Reiners' study from 1967, *V. pallidum* did not show a positive response to decreased oak cover and "seemed limited to a lesser degree in oak-dominated stands." In another study from New Jersey, *V. pallidum* was more abundant in pine-dominated forests (Buell and Cantlon, 1950). According to Collins and Good, neither *G. baccata* nor *V. pallidum* showed any significant relationship with canopy cover or type (1987).

In this study, the lack of significant data from all but one linear regression suggests that canopy cover plays a relatively minor role in determining which dominant plants are most numerous in a given area. Still, some plants were consistently more plentiful than others, and the results of the plant count- vs-species Kruskall-Wallis test (p>0.001) implied that their relative abundance is non-random and most likely due to some other series of factors.

One of the most likely growth-limiting factors for *G. baccata, V. angustifolium,* and *V. pallidum* is interspecific competition. Indeed, all three plants occupy similar niches, vie for similar habitats, and share very similar life histories. They primarily reproduce through rhizomes, prefer sandy upland soil, and are capable of springing back from their rootstocks after a fire (Jordan 2003; Reiners 1965).

However, each species is thought to vary in terms of regenerative abilities and tolerance to various kinds of disturbance. *G. baccata*, for instance, possesses shallower roots than *V. pallidum* and sends up fewer stems in response to a burn (Collins and Good, 1987). So in this respect, *G. baccata* is more limited in its ability to recover from severe wildfire and has actually been shown to drop out of areas where fires occur more than once every ten years (Jordan, 2003; Buell and Cantlon 1953; Reiners, 1965).

G. baccata also tends to grow taller than *V. pallidum*, and consistently overtops *V. angustifolium*. This puts it at a competitive edge against both species in areas that do not see regular fires. However, *G. baccata* is slow to colonize new areas (Matlack, 1997) and is less shade-tolerant, so *Vaccinium* may dominate under both extremes in terms of shade and fire-related disturbance.

Some of the factors that influence the presence of these dominant plants (such as climate, weather, and photoperiod) cannot be studied within a single site and become more apparent when one considers their ranges. *V. angustifolium* occurs as far north as subarctic Canada and overlaps with the more southerly V. *pallidum* along a narrow strip that includes southern New York and Long Island. Long Island is near the southern limit of *V. angustifolium*'s range, and according to Reiners, the range of this cold-tolerant plant has been shifting north since the Pleistocene (1965).

At BNL, it is significantly less common than *V. pallidum*, and whether this becomes even more pronounced with climate change remains yet to be seen.

Dominant plants aside, burned areas yielded the highest understory plant cover and the lowest species richness. Coastal oak forest showed incredible variability in terms of cover and species richness, but experienced especially high levels of the latter. Pine-oak forest occupied somewhat of a middle ground, and oak-pine forest seemed to show little in terms of overall plant diversity. If the coastal oak forest from this study is considered a climax community, these results would appear to contradict the common notion that light disturbance maintains the high diversity in woodland ecosystems. However, some bias may have been unintentionally introduced into this study because two plots within coastal oak communities (31 and 32) were located very close to mesic areas. The proximity to these mesic areas may have produced a "spillover effect" in terms of species that occurred in these two plots and accounted for why some plants that normally do not grow in dry pine barrens habitats (such as *Cornus florida* and *Nyssa sylvatica*) were found here.

For future studies that pertain to BNL's dominant understory plants, a closer look at interspecific interactions may be needed. More precise measurements on plant density and canopy cover may reveal trends that this particular study was unable to ascertain. Perhaps a wider sampling of vegetation communities with a narrower focus on specific plants (such as *G. baccata* or *V. pallidum*) will provide more conclusive information on these species and their requirements. Finally, future studies could examine other factors such as soil pH, presence of deer, and leaf litter depth as factors that influence plant growth.

This study nonetheless carries important implications for managing pine barrens plant communities. Interspecific competition, light penetration, and fire appear to play major roles in determining the understory composition within BNL's wooded areas, and without regular fires or tree-falls to create open canopy space, a forest may not be able to provide the habitat complexity that certain plants and animals require. And while the dominant plants at BNL can easily re-sprout from rhizomes, the fact that they rarely reproduce by seed makes them particularly vulnerable to certain types of human disturbance. Earth-moving operations can take them out of an area for decades, and according to Jordan, it may take over a century for this type of shrub understory to fully recover (2003). Hence, the protection of remaining pine barrens habitat is especially crucial, and the plants that comprise these unique ecosystem are by all means worthy of further protection and research.

VI. Acknowledgments

I would like to thank Kathy Schwager, Jennifer Higbie, Fred Rispoli, and Tim Green for their wonderful mentorship and assistance with this project. I would also like to thank Lauren Gazerwitz, Taylor Ruhle, and anyone else who helped collect data for this project. Finally, I extend my grattitude to the Brookhaven National Laboratory, the National Science Foundation, Department of Energy, and the SULI program for without whom this project would not have been possible.

VII. Works Cited

Abrams, M. D., & Dickmann, D. I. (1982). Early revegetation of clear-cut and burned jack pine sites in northern lower Michigan. Canadian Journal of Botany, 60(6), 946-954.

Brayton, R. D., & Woodwell, G. M. (1966). Effects of ionizing radiation and fire on *Gaylussacia baccata* and *Vaccinium vacillans*. American Journal of Botany, 816-820.

Buell, M. F., & Cantlon, J. E. (1950). A study of two communities of the New Jersey Pine Barrens and a comparison of methods. Ecology, 567-586.

Buell, M. F., & Cantlon, J. E. (1953). Effects of prescribed burning on ground cover in the New Jersey pine region. Ecology, 520-528.

Clemants, S., Clemants, S. E., & Gracie, C. (2006). Wildflowers in the field and forest: a field guide to the northeastern United States. Oxford University Press.

Collins, S. L., & Good, R. E. (1987). Canopy-ground layer relationships of oak-pine forests in the New Jersey Pine Barrens. American Midland Naturalist, 280-288.

Foster, D. R., & Motzkin, G. (2003). Interpreting and conserving the openland habitats of coastal New England: insights from landscape history. Forest Ecology and Management, 185(1), 127-150.

Foundation for Ecological Research in the Northeast. 2007. Forest health monitoring protocols for the Long Island Central Pine Barrens. Foundation for Ecological Research in the Northeast, Upton, NY, USA.

Jordan, M. J., Patterson, W. A., & Windisch, A. G. (2003). Conceptual ecological models for the Long Island pitch pine barrens: implications for managing rare plant communities. Forest Ecology and Management, 185(1), 151-168.

Kurczewski, F. E., & Boyle, H. F. (2000). Historical changes in the pine barrens of central Suffolk County, New York. Northeastern Naturalist, 7(2), 95-112.

Matlack, G. R. (1997). Resource allocation among clonal shoots of the fire-tolerant shrub Gaylussacia baccata. Oikos, 509-518.

Matlack, G. R., Gibson, D. J., & Good, R. E. (1993). Regeneration of the shrub *Gaylussacia baccata* and associated species after low-intensity fire in an Atlantic coastal plain forest. American Journal of Botany, 119-126.

Matlack, G. R., & Good, R. E. (1989). Plant-scale pattern among herbs and shrubs of a fire-dominated coastal plain forest. Vegetatio, 82(2), 95-103.

Oswald, W. W., Foster, D. R., Doughty, E. D., & Macdonald, D. (2010). A record of Holocene environmental and ecological changes from Wildwood Lake, Long Island, New York. Journal of Quaternary Science, 25(6), 967-974.

Reiners, W. A. (1965). Ecology of a heath-shrub synusia in the pine barrens of Long Island, New York. Bulletin of the Torrey Botanical Club, 448-464.

Reiners, W. A. (1967). Relationships between vegetational strata in the pine barrens of central Long Island, New York. Bulletin of the Torrey Botanical Club, 87-99.

Sohl, T. L. (2003). Atlantic coastal pine barrens. United States Geological Survey Fact Sheet FS-092-03.

Stalter, R., & Lamont, E. E. (2014). Vascular Flora of

Brookhaven National Laboratory, Long Island, New York. Northeastern Naturalist, 21(2), 285-302.
Whittaker, R. H., & Woodwell, G. (1969). Structure, production and diversity of the oak-pine forest at Brookhaven, New York. The Journal of Ecology, 155-174.

VIII. Appendix

Appendix Figure 1- Photographs of dominant vegetation at BNL. Pictured LEFT TO RIGHT: *Carex pensylvanica, Vaccinium angustifolium, Gaylussacia baccata,* and *Vaccinium pallidum.*

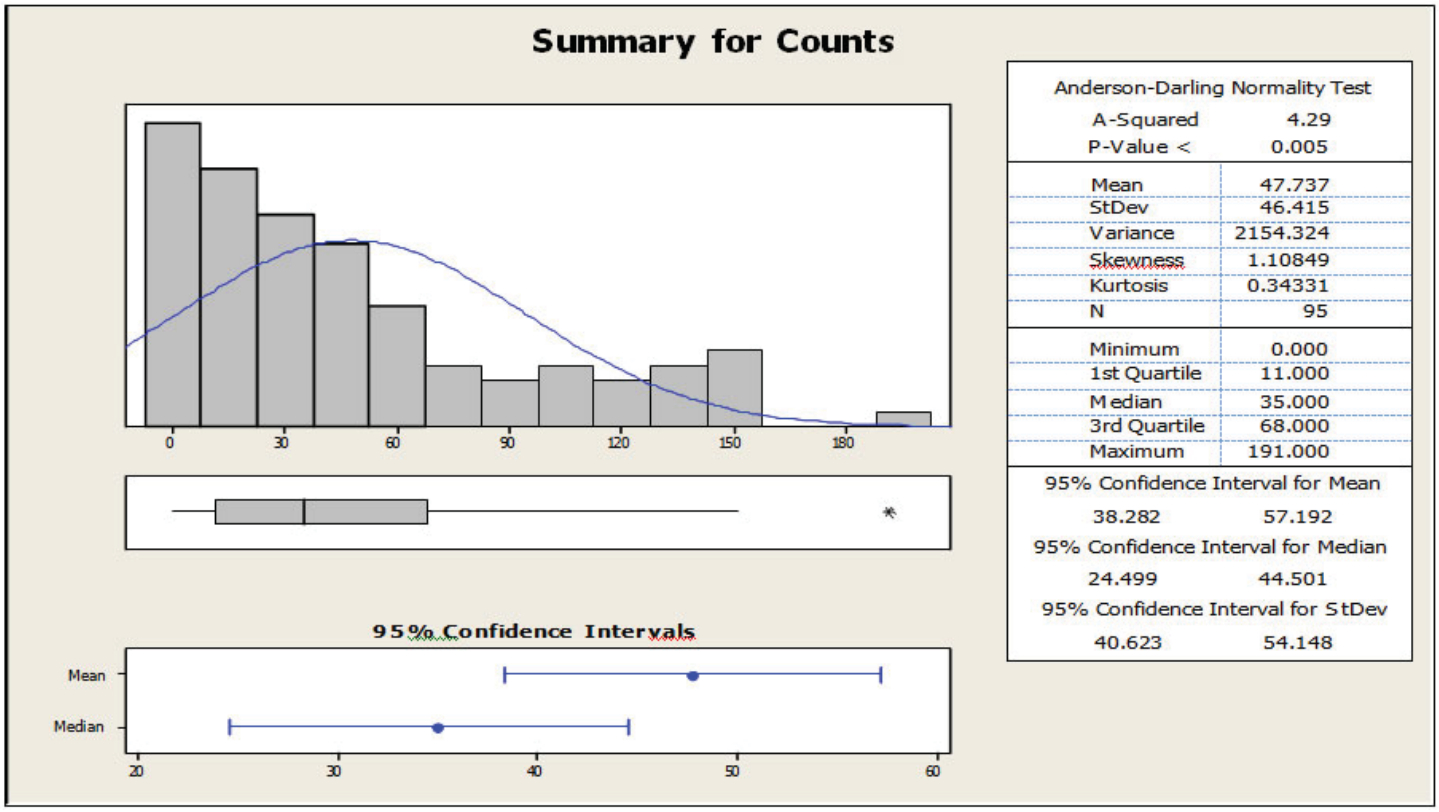

Appendix Figure 2- Distribution of data as shown by an Anderson-Darling Normality Test

Appendix Table 1- A complete list of plants found within plots.

Species	Common Name	# of plots in which present
Acer rubrum	Red Maple	4
Amalanchier canadensis	Shadblow Serviceberry	12
Carex pensylvanica	Pennsylvania Sedge	17
Carya ovata	Shagbark Hickory	1
Chimaphila maculata	Spotted Wintergreen	6
Comptonia peregrine	Sweetfern	2
Cornus florida	Flowering Dogwood	1
Cypripedium acuale	Pink Lady's Slipper	5
Dennstaedtia punctilobula	Hay-Scented Fern	2
Dichanthelium spp.	Rosette-grass spp.	3
Gaultheria procumbens	Wintergreen	2
Gaylussacia baccata	Black Huckleberry	18
Juncus tenuis	Path Rush	1
Lyonia ligustrina	Maleberry	3
Lyonia mariana	Staggerbush	4
Maianthemum canadense	Canada Mayflower	1
Melampyrum lineare	Cow-Wheat	7
Monotropa uniflora	Indian Pipe	2
Nyssa sylvatica	Black Tupelo	2
Parthenocissus quinquefolia	Virginia Creeper	1
Pinus rigida	Pitch Pine	18
Prunus serotina	Black Cherry	6
Pteridium aquilinum	Bracken Fern	15
Quercus alba	White Oak	18
Quercus coccinea	Scarlet Oak	15
Quercus ilicifolia	Scrub Oak	14
Quercus prinus	Chestnut Oak	3
Quercus stellata	Post Oak	1
Rubus flagellaris	Bristly Dewberry	6
Sassafras albidum	Sassafras	4
Shizachyrium scoparium	Little Bluestem	1
Smilax spp.	Greenbriar spp.	11
Toxicodendron radicans	Poison Ivy	2
Vaccinium angustifolium	Late Lowbush Blueberry	15
Vaccinium corymbosum	Highbush Blueberry	2
Vaccinium pallidum	Early Lowbush Blueberry	19
Viburnum dentatum	Arrowwood Viburnum	2
Vitus spp.	Grape spp.	1

Appendix Table 2a- Kruskal-Wallis test for count vs. species

Species	N	Median	Ave Rank	Z
C. pensylvanica	19	12	30.9	-3.01
G. baccata	19	105	73.1	4.43
Other	19	15	37.6	-1.85
V. angustifolium	19	13	31	-3.01
V. pallidum	19	57	67.4	3.44
Overall	95		48	

H = 42.37 DF = 4 P=0.000

Appendix Table 2b- Kruskal-Wallis test for count vs. location

Location	N	Median	Ave Rank	Z
1	5	59	67.3	1.61
2	5	64	67.7	1.64
3	5	8	37.6	-0.87
4	5	31	50.6	0.22
5	5	38	47.9	-0.01
6	5	17	50.8	0.23
7	5	68	62.8	1.23
8	5	37	44.8	-0.27
9	5	33	37.2	-0.9
10	5	34	44.8	-0.27
11	5	5	36.1	-0.99
12	5	15	40.3	-0.64
13	5	44	46.9	-0.09
14	5	35	42.3	-0.48
15	5	16	43.5	-0.38
16	5	52	54.5	0.54
17	5	16	48.7	0.06
18	5	11	44.1	-0.32
19	5	31	44.1	-0.32
Overall	95		48	

H = 10.31 DF = 18 P = 0.921

Investigating vortex dynamics in trilayer structures of ferromagnetic materials separated by a nonmagnetic spacer layer

Angelika Rothberg
Chemical and Biological Engineering, Rensselaer Polytechnic Institute, Troy, NY 12180
Joe Garlow
Material Science and Engineering, Stony Brook University, Stony Brook, NY 11794
Yimei Zhu
Condensed Matter Physics and Material Sciences, Brookhaven National Laboratory, Upton, NY 11973

Abstract

Trilayer heterostructures of two ferromagnetic layers separated by a conductive, nonmagnetic spacer layer exhibit the giant magnetoresistance (GMR) effect, a phenomenon driven by the so-called RKKY coupling, a type of indirect exchange coupling where spin interaction oscillates between ferromagnetic and antiferromagnetic depending on the thickness of the spacer layer. While the discovery of GMR was recognized by the Nobel Prize in 2007, today's semiconductor industry is moving toward its novel applications with a new technology called spintronics, which uses electrons to control spins that allow electronic devices to run faster, cheaper, and consume less energy. Here, we investigate magnetic trilayer heterostructures in the strong dipolar coupling regime by sandwiching an insulating spacer of varying thickness between two ferromagnetic layers to understand electron-spin interaction. Square magnetic elements composed of Py(15nm)/SiO2(5 and 15nm)/Py(25nm) trilayers were synthesized on top of silicon nitride windows through the processes of electron beam lithography, electron beam evaporation and liftoff. The spin behavior of the magnetic vortices under various applied magnetic fields was directly observed with Lorentz Transmission Electron Microscopy to determine the impact dipolar coupling strength has on coupled vortex dynamics, particularly vortex annihilation. In trilayers with the 15 nm spacer layer, we observed that the two vortex cores move adjacent to one another as the magnetic field increased. In trilayers with the 5 nm spacer layer, which exhibit a much stronger dipolar coupling, the vortex cores move on top of one another and behave almost as a single vortex. These experimental observations agree well with our micromagnetic simulations and shed light on spin coupling mechanisms in ferromagnetic heterostructures.

I. Background

The giant magnetoresistance (GMR) effect is a phenomenon in which the resistance of a material exhibits a large change when exposed to an external magnetic field. This concept was developed from a series of discoveries, the first from Lord Kelvin about 150 years ago. The British physicist found that iron and nickel exhibit a small increase in electrical resistance along the direction of an applied magnetic field and a similar decrease in resistance in the transverse direction. This effect was named anisotropic magnetoresistance (AMR), and led to the production of the first hard drives in the 1990s, which didn't show much improvement in strength from Lord Kelvin's initial discoveries. This was partially due to the fact that technologists in the 1980s hypothesized that there couldn't be significant improvements in magnetoresistive sensing. Despite this dismissal, Albert Fert and Peter Grünberg continued to study AMR and discovered two key properties that led to their discovery of GMR: spin-dependent scattering and exchange coupling.

According to quantum mechanics, electrons act as if they are spinning, meaning they possess intrinsic angular momentum. In spin-dependent scattering, the way an electron interacts with a ferromagnetic material depends on the relative orientation of the electron's spin and the magnetic field inside the ferromagnet. Inside a ferromagnet, the velocities of the electrons point in all different directions, but the average electron velocity points in the direction of the current. If an electron is scattered, it will change direction, so the effect of scattering is to reduce the current, which in turn increases the material's electrical resistance. The probability of scattering depends on the number of available quantum states for the electron to scatter into, which depends on the rela-

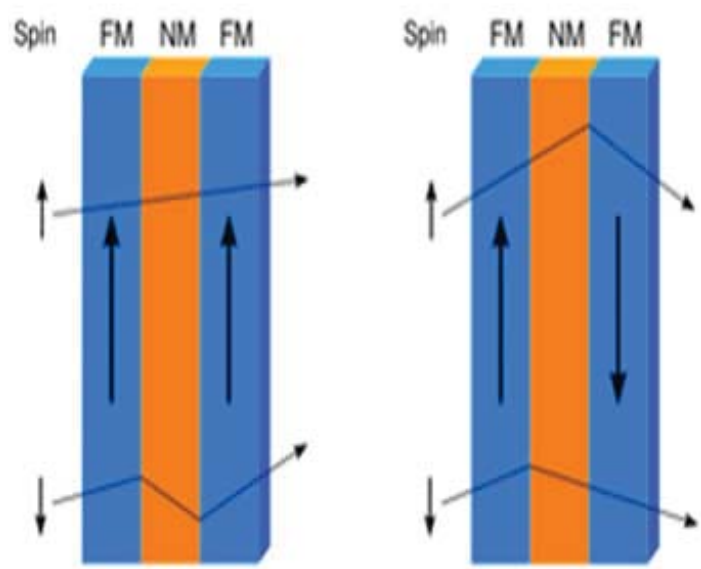

Figure 1: This figure depicts two spin valves composed of two ferromagnetic (FM) layers separated by a nonmagnetic layer. Shown on the left side, when the magnetic fields in the two FM layers are aligned, half the electrons experience relatively little scattering, leading to a significant reduction in resistance. Shown on the right side, the magnetic fields in the two layers point in opposite directions, and because half the electrons are spin-up and half are spin-down, each interacts with a parallel and antiparallel field and the spin-up and spin-down electrons scatter in the same way.

tive direction of the electron's spin and the magnetic field within the ferromagnet. As the number of available quantum states increases, the probability of scattering and the electrical resistance increase as well. If the spin and magnetic field are aligned anti-parallel to one another, more states are available for electron scattering, so the electrical resistance is greater than if the spin and magnetic field are aligned parallel to one another (Figure 1).

The other key advance was the discovery of interlayer exchange coupling, done by Grünberg. Both he and Fert worked with very two thin ferromagnetic layers separated with a thin nonmagnetic spacer layer. Grünberg observed that with no applied magnetic field, the magnetic fields in the two layers were opposite, but when he applied an external magnetic field, the magnetic fields in the two layers aligned, demonstrating that the application of an external field can control the relative directions of the internal magnetic field (Figure 2).

Fert and Grünberg combined their two discoveries, spin-dependent scattering and interlayer exchange coupling, to produce giant magnetoresistance, an electrical resistance heavily dependent on the applied magnetic field. GMR is driven by RKKY coupling, a type of indirect exchange coupling in which spin interaction oscillates between ferromagnetic and antiferromagnetic depending on the thickness of the spacer layer (Figure 3). A magnetic ion induces a spin polarization in the conduction electrons in the surrounding area, which is felt by the moments of the other magnetic ions within range, leading to an indirect coupling. This is most prevalent in rare-earth metals, whose magnetic electrons in the 4f shell are shielded by 5s and 5p electrons. Here, direct exchange is rather weak, and indirect exchange via the conduction electrons gives rise to magnetic order in these materials.

Leading up to the discovery of GMR, Fert had been investigating magnetoresistance in multiple layers of Fe and Cr, up to 60 layers of each. He conducted his experiments at liquid helium temperatures, about four degrees above absolute zero. Here, he observed a 50% change in resistance as he switched the magnetic fields from alternating to pointing in the same direction. Grünberg, on the other hand, studied trilayer structures of Fe/Cr/Fe at room temperature, and found about a 1.5% change in resistance. This helped him recognize the technological implications of his discovery and obtained patents for GMR-based read heads.

Around the same time, IBM also recognized the possibilities, and began their own investigation into GMR-based read heads. A group, led by Stuart Parkin, produced films by sputtering, dislodging atoms from a target with a powerful atomic beam and depositing these atoms on a substrate. These films were less uniform than those of Fert and Grünberg, but were much easier to synthesize, and produced a large enough effect at room temperature to make a much improved read head. GMR read heads scan the hard drive and sense the magnetic field made by an array of tiny magnetic domains arranged in a circular pattern. The domains have one of two possible orientations, which correspond to a zero or one and produce a unique pattern of current in the read head. Because the GMR effect is so much stronger than AMR, the domains can be much smaller and much more information can be stored on the disk. Once GMR was discovered, IBM moved fast, and was able to bring GMR-based read heads to market within 9 years and produce the first multigigabyte hard drive (Figure 4).

This is so important because the semiconductor industry is consistently looking to improve upon itself, which gives rise to the investigation of dipolar coupling in magnetic trilayer heterostructures. The main difference between this type of coupling and RKKY coupling, the type exhibited in GMR, is the presence of an insulating spacer layer instead of a nonmagnetic spacer layer. Dipolar coupling hasn't been studied nearly as much as RKKY so the technological implications of investigating this are not quite as well known, but there is definite potential for improvements in the field of spintronics, which uses electrons to control spins that allow electronic devices to run faster, cheaper, and consume less energy.

II. Methods and Materials

In this experiment, trilayer structures heterostructures of two ferromagnetic layers separated by an insulating layer of varying thicknesses were synthesized using electron beam lithography, electron beam evaporation, and liftoff. Electron Beam Lithography (EBL) is one of the most important techniques in nanofabrication because of its ability to form two dimensional patterns on a nanometer scale. It involves the exposure by a highly focused electron beam to modify the solubility of a resist material during a subsequent development step (Figure 5). The main objective in

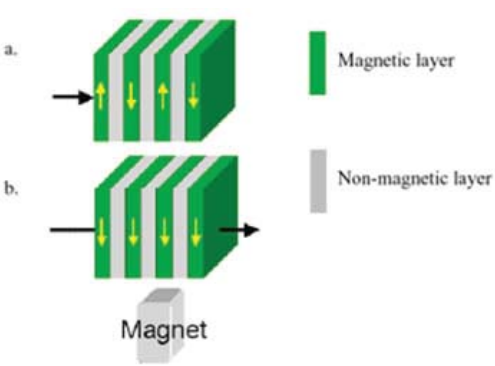

Figure 2: a. The interlayer exchange coupling aligns the magnetization of the ferromagnetic layers in opposing directions in the absence of an applied magnetic field b. An external field overcomes the exchange coupling and aligns the magnetizations in the two layers

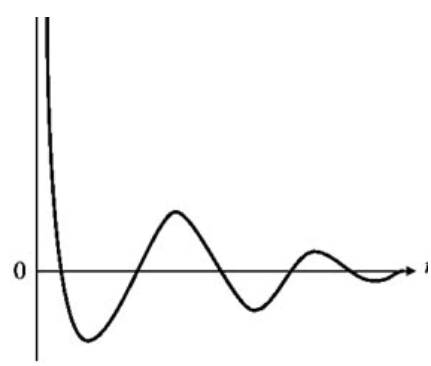

Figure 3: This graph represents the oscillatory nature of the RKKY exchange coefficient j. Depending on the separation between a pair of ions, their magnetic coupling will be either ferromagnetic or antiferromagnetic.

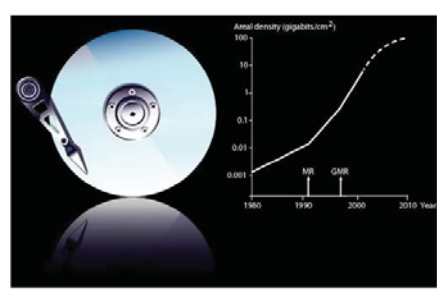

Figure 4: The image on the left is a GMR-based hard drive, and the graph depicts an exponential increase in hard disk storage density.

EBL writing is to etch patterns in the resist with high resolution, high density, high sensitivity, and high reliability, which are determined by a few key factors: ability to create a finely focused spot, choice of resist, substrate and developer, and process conditions (electron beam energy and dose, and development time and temperature).

The inelastic collisions of electrons with the resist result in ionization and are accompanied by physio-chemical changes in the resist, which makes the choice of resist so essential in undergoing successful EBL. EBL can be done with two types of resist. Positive tone resists undergo a conversion from low to high solubility upon exposure to electrons, while negative tone resists are converted from high to low solubility by the electrons. The most common example of positive tone resist is poly-methyl methacrylate (PMMA), which was the resist used in this experiment. PMMA is a long chain polymer that is broken into smaller, more soluble fragments by the electron beam. Because the chain is so long, it takes many scission events before the resulting fragments become significantly soluble, which makes the distribution of fragment sizes so important in understanding the relationship between exposure dose and development behavior. Figure 6 shows that as dose increases, the average fragment size decreases and solubility in the developer increases.

After exposure, the resist is immersed in a liquid developer to dissolve the fragments. Here, temperature and duration are key factors as the development becomes hotter and longer. For example, when developed in cold temperatures, PMMA freezes out the development of all but the very smallest fragments, resulting in very high resolution as much of the scattered electrons cause insufficient exposure to reach this threshold. During development, the solvent penetrates into the polymer matrix and starts to surround the fragments. As the molecules start to interact, a gel, whose thickness depends on amount of fragmentation and strength of solvent, begins to form. Once completely surrounded by the solvent, the fragments detach from the matrix and diffuse into the solvent. After the EBL process was completed on top of silicon nitride windows, the samples were synthesized in an electron beam evaporator.

Electron beam evaporation is a type of physical vapor deposition in which a target anode is bombarded by a beam of electrons given off by a heated filament in a high vacuum system. The electron beam causes atoms from the target to evaporate and then precipitate into solid form, coating everything within line of sight with the anode material. Electron beam evaporation requires the chamber to be at a very low pressure, which is achieved through a series of three pumps: roughing, turbomolecular, and ion. The roughing pump is able to bring the pressure from atmosphere down to 10^{-3} Torr, followed by the turbomolecular pump, which brings the pressure down further to ~$10^{-6}/10^{-7}$ Torr, and finished with the ion pump, which can bring the pressure all the way down to 10^{-10} Torr if the vacuum is of very good quality. This vacuum is so essential because it creates an environment in which contamination is limited. The evaporator also contains two electron guns which have three sources on each side and a device that measures thickness based on the oscillations of the electrons. Another key factor of electron beam evaporation is the water cooling, which is important in order to keep the crucibles from melting.

In this experiment, we created three different types of trilay-

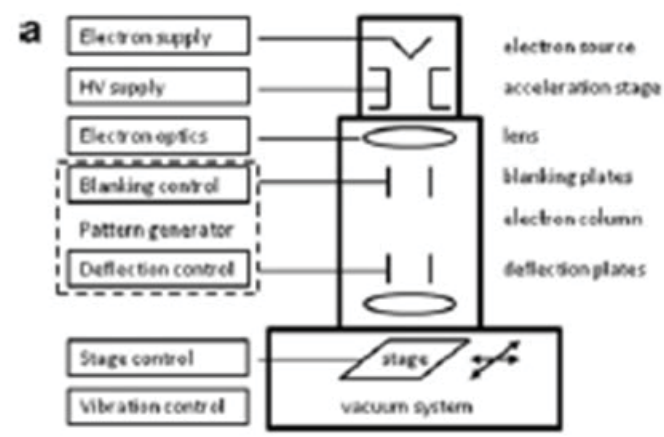

Figure 5: Schematic diagram of an EBL system.

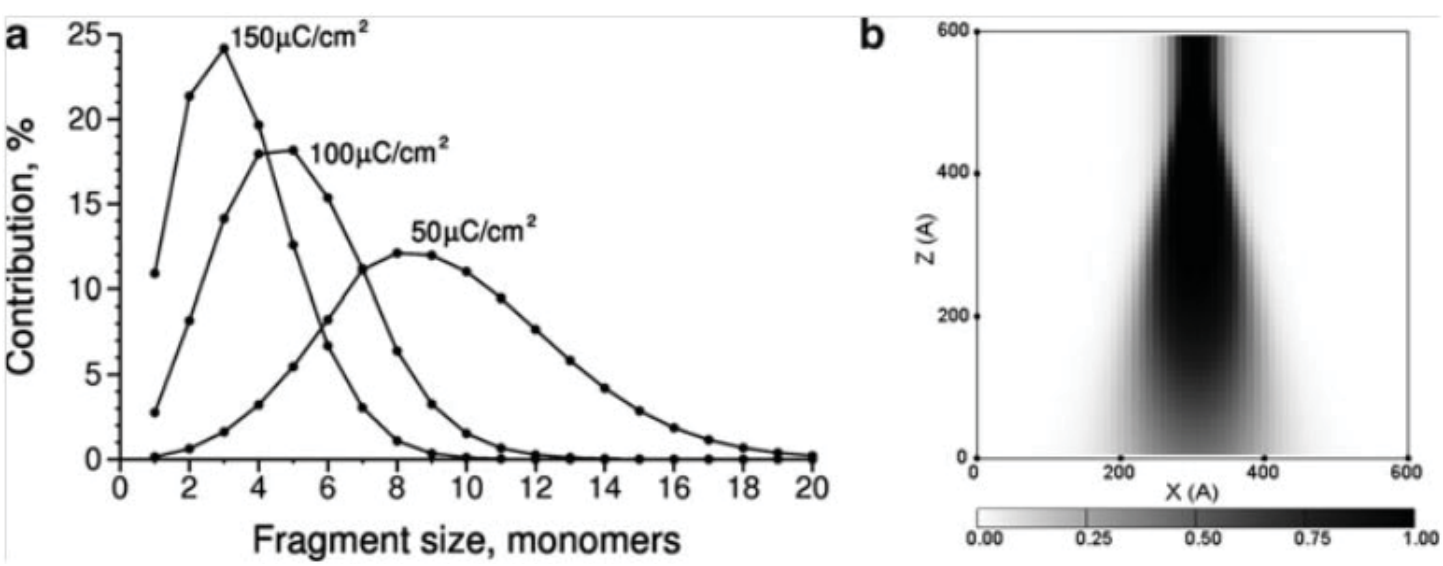

Figure 6: a. Distribution of PMMA fragment sizes and exposure dose at 10 keV b. Spatial distribution of the volume fraction of small fragments within the resist due to exposure at a single point

er structures. Each consisted of a bottom layer of 15 nm permalloy (a combination of 20% Fe and 80% Ni) and top layer of 25 nm permalloy, separated by a layer of silicon dioxide (SiO_2) of three different thicknesses: 1 nm, 5 nm, and 15 nm. To begin the process, the substrate was inserted into the load lock chamber, followed by the closing of V1. In order to transfer the substrate into the main chamber, the roughing and turbomolecular pump had to be turned on. When the pressure dipped to around 10^{-6}, V2 was closed and V1 was opened, allowing the arm to enter the chamber. The opening and closing of the valves was very important to be mindful of, as the pressure differs throughout the various chambers, meaning they can't be exposed to one another. After the substrate was transferred from the arm to the substrate holder, the substrate shutter was closed to prevent unwanted contamination from collecting on the substrate, V2 was opened and V1 was closed. Next, the gun and position were chosen and the water was turned on. After making sure the electron gun was open, the beam sweep and electron gun (along with HV and filament) were turned on. In order to begin depositing, the current was raised slowly until the material reached a constant deposition rate of about .3 Å/s. At this point, the electron gun was blocked and the substrate shutter was reopened. Here, it was important to remember to check that the thickness monitor was on the correct setting for the material and press 'start' in order to begin measuring the thickness of the material deposited. The electron gun was opened and the material began to deposit. When the thickness began to approach the desired amount, the current was decreased in order to decrease the rate of deposition to about .1 Å/s in order to make the sample's thickness as precise as possible. After reaching the desired thickness, the electron gun was blocked, the shutter was closed, and the current was decreased to 0. The filament and HV were turned off before switching the source, and once done, this process was repeated until the trilayers were complete. After deposition was complete, the trilayers were taken out of the chamber by opening the substrate shutter, closing V2 and opening V1, and using the arm to transfer the substrate holder from the chamber to the load lock. After this, V1 was closed and the turbomolecular and roughing pumps were closed, and the gas was turned on in order for the load lock to open. Once the load lock opened, the gas was turned off and the sample could be removed.

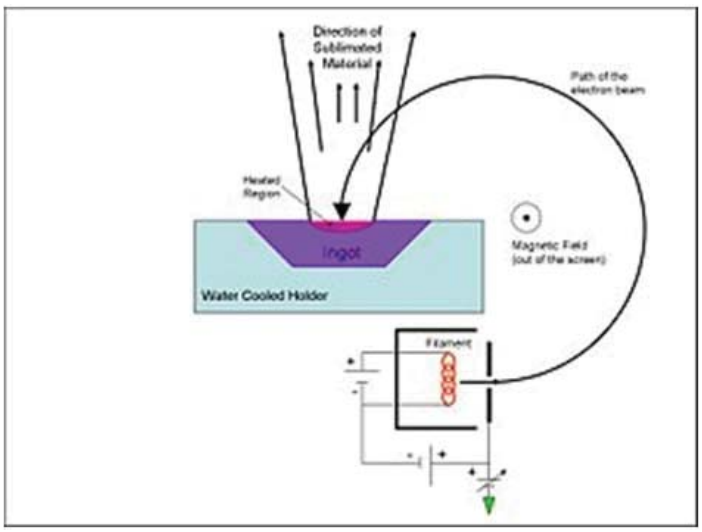

Figure 7: A schematic of electron beam evaporation.

After deposition was complete and the sample was removed, the process of liftoff followed (Figure 8). This process is the final step in electron beam lithography, where the resist applied during EBL is washed out with parts of the target material covering it, leaving only the material in the "holes" that had direct contact with the substrate in place. One major problem with liftoff, however, is the potential for retention, where the unwanted parts of the metal layer remain on the substrate. This can occur for a number of different reasons, including the scenario in which parts that should have been lifted off don't dissolve properly, or that the metal has adhered so well to the parts that should remain that it prevents lift-off. Although this can be a drawback, the EBL/liftoff procedures are advantageous when direct etching of a material would have negative effects on the layer below.

When the samples were finally completed, they were analyzed using Lorentz Transmission Electron Microscopy (TEM) in a JEOL 3000F high resolution transmission electron microscope (Figure 9). Transmission Electron Microscopy is an important tool in correlating structural and magnetic properties and getting information on the chemistry of samples. In TEM, a continuous beam of highly accelerated electrons is transmitted through a very thin sample, interacting with the sample as it passes through, which create the TEM images. At small magnifications, image contrast

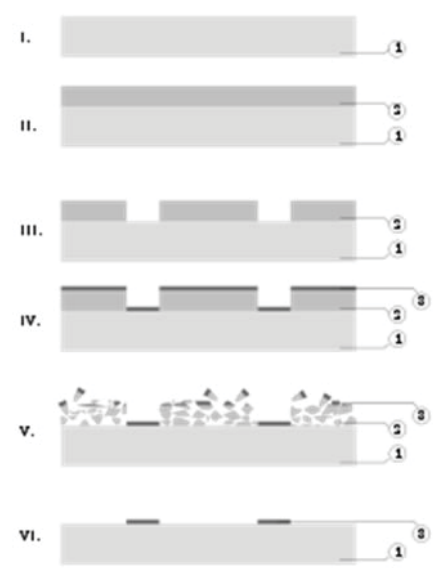

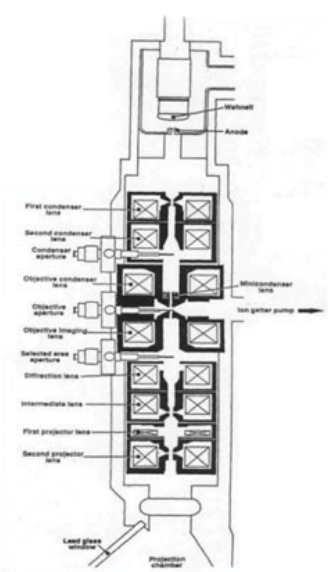

Figure 8 (left): Schematic depicting the steps of liftoff. I. Preparation of the substrate II. Deposition of the sacrificial stencil layer III. Patterning the sacrificial layer (etching) IV. Deposition of the target material V. Washing out of the sacrificial layer with the target material on its surface VI. Final pattern layers (1. Substrate 2. Sacrificial layer 3. Target material)

Figure 9 (right): Schematic of a TEM column, consisting of an electron gun, condenser system, objective lenses, diffraction/intermediate lenses, projective lenses, image observation, and vacuum system.

is caused by absorption of electrons in the material, which is determined by specimen thickness and elemental composition. TEM images are magnified and focused on an imaging device, such as a fluorescent screen or digital imaging device.

Lorentz microscopy is a specialized method of TEM that allows for magnetic samples to be examined, which is necessary due to the fact that magnetic samples cause the electron beam in a conventional TEM to be severely disturbed, making imaging impossible. The magnetic field that stems from the specimen will deviate the electron beam as it passes through and those electrons won't be in line with the optic axis, and not be included in the image. This is why it is so important that the magnetic sample doesn't get lost inside the microscope, as it will attach to the objective lens. In order to combat this and the other problem of interference of the objective lens field and the internal magnetic field of the sample, the field strength of the objective lens has to be decreased significantly or be switched completely off.

In this experiment, we analyzed the hysteresis curves of each sample by beginning with an in focus view at 0 degrees, and tilting up to 10 degrees. At this point, we increased the field of the objective lens in order to saturate the sample, and then began tilting downwards to -7 degrees. The images taken in these steps represent a full hysteresis loop, which is a representation of magnetization of the sample as a function of magnetic field strength H, a measure of the externally applied field which drives the magnetization. Hysteresis, a measure of the field required to drive a ferromagnetic material back to zero magnetization, is an important property to analyze because understanding the loops different materials make is one of the keys to magnetic recording.

III. Data and Results

See Figure 10.

IV. Discussion

The three step process of electron beam lithography, electron beam evaporation, and liftoff resulted in two trilayer structures, each with a top and bottom layer of 15 and 25 nm Permalloy, respectively, separated by a layer of silicon dioxide with two different thicknesses: 5 and 15 nm. These two samples were imaged using Lorentz Transmission Electron Microscopy in order to help understand the movement of magnetic vortices due to varied dipolar coupling strength. Because of the 10 nm difference in the thickness of the SiO2 spacer layer, the dipolar coupling is stronger in the trilayer with the 5 nm spacer than the coupling in the trilayer with the 15 nm spacer. In Figure 10A, the sample with a 5 nm thick spacer layer is shown. Initially there is no vortex present. To begin the analysis, the sample is tilted up, therefore increasing the magnetic field. After the magnetic field is increased, a vortex forms in the layer depicted by the underfocused image and then appears in the layer depicted by the overfocused image, suggesting different chiralities of the layers. The vortex moves in the direction of the magnetic field and then disappears as the field is still increasing. When tilting downwards, or decreasing the magnetic field, the vortex renucleates and appears in only the underfocused layer and again moves in the direction of the magnetic field.

In Figure 10B, the sample with a 15 nm spacer layer is shown. Initially, there is no vortex present. As the sample is tilted upwards, the magnetic field strength increases and the vortex appears in the underfocused layer. It doesn't appear in the overfocused layer, however, until it is tilted downwards and magnetic field strength is decreased. In each case, the vortex is only viewable in one of the layers, and renucleates with only one vortex. In Figure 10C, the spacer layer is also 15 nm, but initially there are vortex cores present. Because of the weakened dipolar coupling strength, we don't expect the cores to move as closely as the vortices in the trilayers with the 5 nm spacer layer, and we found that the cores moved adjacent to one another as magnetic field was increased and then annihilated. This was also unique in that upon renucleation, only one vortex core was present.

Because there are some similarities between the images, we are able to make comparisons between the samples. First, we compare 10B and 10C, both of which have 15 nm spacer layers. The main difference between the two trilayers is that 10B has two vortices while 10C has one. In 10B, the cores move towards one another in the direction of the magnetic field, and the single core in 10C moves in the direction of the magnetic field also. They also annihilate at similar magnetic field strengths, pointing to consistency in the trilayers. Another interesting comparison to make is between 10A and 10C. Both trilayers have one vortex whose core moves in the direction of the field, but annihilation occurs at 64 Oe in 4A, while it occurs in 10C at 171 Oe. This shows that magnetic field strength at annihilation is much higher in the sample where coupling is weaker. In addition, both trilayers exhibit a "flip," where the chirality of the vortex switches just before annihilation.

V. Conclusions and Recommendations

This experiment was driven by the interest in learning more about the importance of dipolar strength coupling, a type of coupling that could be essential when taking the next steps in data storage. Through a three step process of electron beam lithography, electron beam evaporation, and liftoff, we were able to analyze two trilayer structures that had different spacer layers using Lorentz Transmission Electron Microscopy. We found that in trilayer with the 15 nm separation layer, the two vortex cores moved adjacent to one another as the magnetic field increased, while in trilayers with the 5 nm spacer layer, which exhibit stronger dipolar coupling, the vortex cores move on top of one another and behave almost as a single vortex. Understanding this may be the key to new discoveries in the field of spintronics, as improvements can always be made. The next step in this research could be the investigation of Colossal Magnetoresistance, which has the same effect of GMR, but to an even higher degree.

VI. References

[1] Pollard, S. (2015). *Understanding Ordering and Dynamics of Topological Magnetism With Transmission Electron Microscopy*. Stony Brook University.

[2] Poulopoulos, P., & Baberschke, K. (1999). Magnetism in thin films. *Journal of Physics: Condensed Matter*, 11(48), 9495–9515.

[3] Stiles, M. D. (1999). Interlayer exchange coupling. *Journal of Magnetism and Magnetic Materials*, 200(1-3), 322–337.

[4] Tsymbal, E. Y., & Pettifor, D. G. (2001). Perspectives of giant magnetoresistance. *Solid State Physics - Advances in Research and Applications*, 56(C), 113–237.

[5] Mattox, D. M. (2010). *Handbook of Physical Vapor Deposition (PVD) Processing. Handbook of Physical Vapor Deposition (PVD) Processing*.

[6] Daughton, J. M. (1999). GMR applications. *Journal of*

Experimental Results

Magnetic vortex dynamics as a function of applied field

A. 5 nm spacer layer

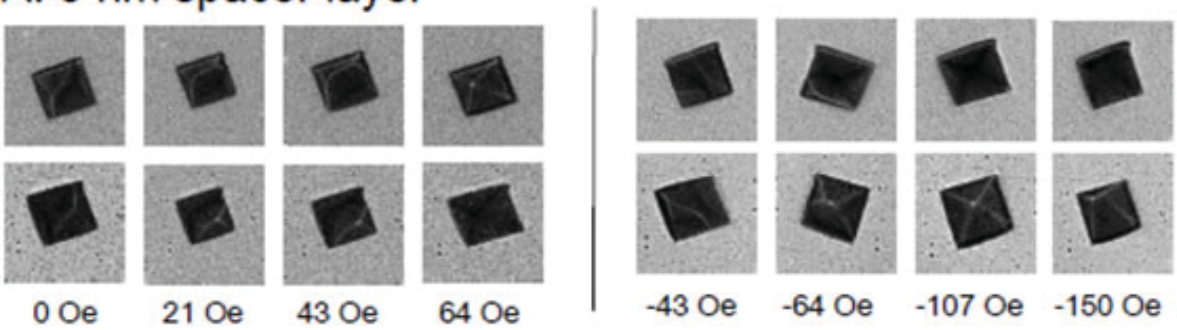

B. 15 nm spacer layer

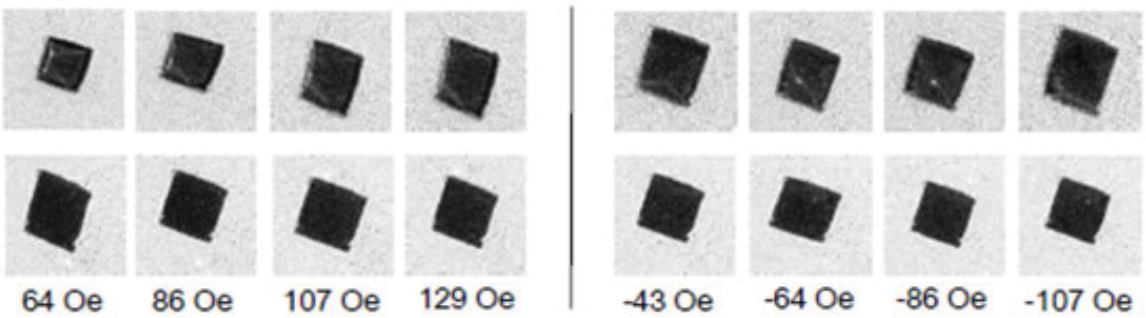

C. 15 nm spacer layer

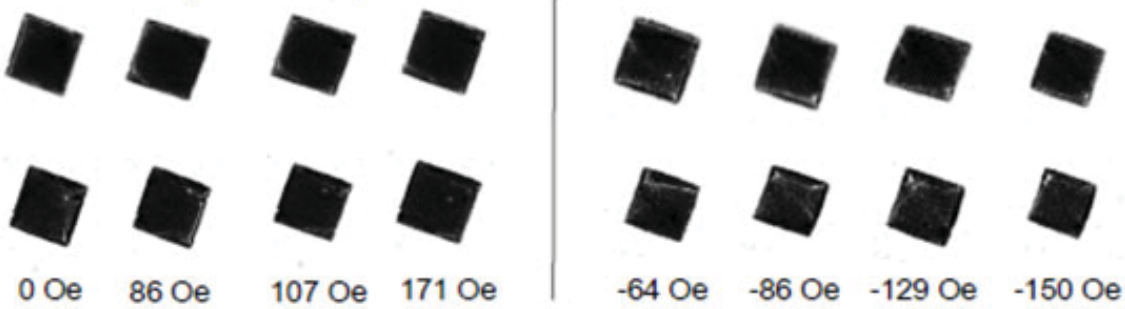

Simulation Results

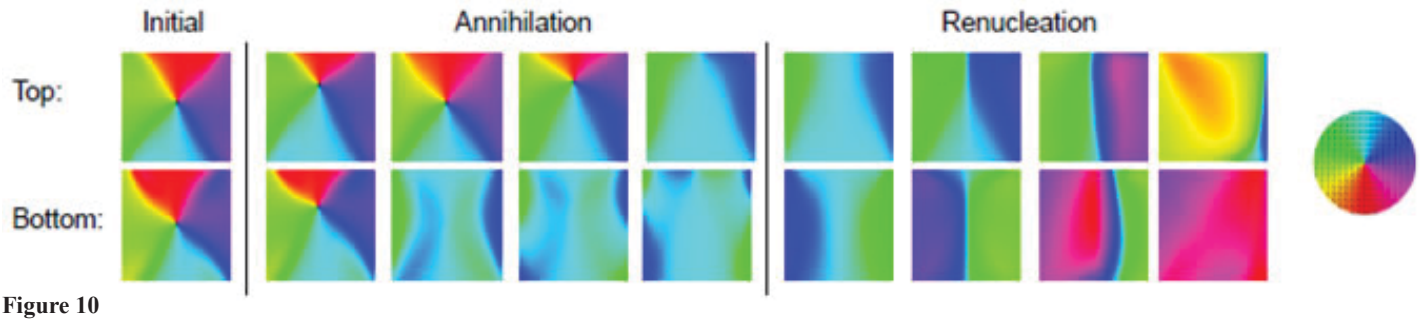

Figure 10

Magnetism and Magnetic Materials, 192(2), 334–342.
[7] Chou, K. W., Puzic, A., Stoll, H., Schütz, G., Van Waeyenberge, B., Tyliszczak, T., … Back, C. H. (2006). Vortex dynamics in coupled ferromagnetic multilayer structures. *Journal of Applied Physics*, 99(8), 08F305.
[8] Power, S., & Ferreira, M. (2013). Indirect Exchange and Ruderman–Kittel–Kasuya–Yosida (RKKY) Interactions in Magnetically-Doped Graphene. *Crystals*, 3(1), 49–78.
[19] Zweck, J. (2012). *Lorentz Microscopy. In-Situ Electron Microscopy: Applications in Physics, Chemistry and Materials Science*, 347–369.

The use of EMPIRE to simulate the neutron induced reactions on ^{86}Kr

Elizabeth Rubino
Physics Department, Florida Atlantic University, Boca Raton, FL 33431
David Brown
Nuclear Science and Technology Department, Brookhaven National Laboratory, Upton, NY 11973

Krypton is used as a diagnostic of the neutron flux in inertial confinement fusion systems such as Lawrence Livermore National Laboratory's National Ignition Facility or Sandia National Labo ratory's Z-machine. It is uniquely suited to this role because it is a non-reactive gas and may be mixed directly into the fuel (either deuterium-tritium or deuterium-deuterium). The ^{86}Kr(n, γ)^{87}Kr reaction is used as a diagnostic at energies below roughly 5 MeV while ^{86}Kr(n, 2n)^{85m}Kr is used as a diagnostic above about 5 MeV. Recently Triangle Universities National Laboratory measured ^{86}Kr(n, 2n)^{85m}Kr at 9 energies ranging from 10.86 MeV to 14.8 MeV and ^{86}Kr(n, γ)^{87}Kr at 11 energies ranging from 370 keV to 14.8 MeV. Also, recently Los Alamos National Laboratory measured ^{86}Kr(n, nl)^{86}Kr at Los Alamos' Neutron Science Center. All three data sets have been added to the Experimental Nuclear Reaction Data database. The ^{86}Kr(n, nl')^{86}Kr and ^{86}Kr(n, 2n)^{85}mKr data sheds new light on the structure of ^{86}Kr necessitating a re-evaluation of ^{86}Kr in the fast region. In this project, we re-evaluated all neutron induced reactions on ^{86}Kr, taking into account thelatest cross section measurements and gamma-ray transition systematics in the N=50 region and using EMPIRE, a nuclear reaction modeling code from Brookhaven National Laboratory.

I. INTRODUCTION

^{86}Kr is used as a Inertial Confinement Fusion (ICF) radiochemical tracer as krypton is a nonreactive noble gas and can be mixed directly into deuterium-tritium or deuterium-deuterium fuel. The ^{86}Kr(n,2n)^{85m}Kr and ^{86}Kr(n,γ)^{87}7Kr reactions are particularly important for National Ignition Facility at Lawrence Livermore National Laboratory and the Z-Machine at Sandia National Laboratory because both reactions result in nuclei that decay with half lives convenient for activation measurements. The half life of ^{85m}Kr is 4.480 hours and the half life of ^{87}Kr is 76.3 minutes. Additionally these reactions also have astrophysical importance as ^{85}Kr is a branching point for the slow neutron-capture process (s-process) for asymptotic giant branch (AGB) stars. This is important because AGB stars are believed to be the source of about half of the elements with Z>26. The last reaction, ^{86}Kr(n,nγ')^{86}Kr, is important because partial gamma cross section have never been integrated into an evaluation before despite the fact that they provide valuable insight into the structure of ^{86}Kr.

As a result of this application-oriented and basic science interest on reactions on ^{86}Kr, three new measurements were undertaken. Bhike et al. [1] at Triangle Universities Nuclear Laboratory (TUNL) measured ^{86}Kr(n, 2n)^{85}mKr at 9 energies ranging from 10.86 MeV to 14.8 MeV and ^{86}Kr(n, γ)87Kr at 11 energies ranging from 370 keV to 14.8 MeV. The ^{86}Kr(n, 2n)^{85}mKr corroborates the earlier Kondaiah measurement [2]. Also, Fotiades at al. [3] at Los Alamos National Laboratory (LANL) measured ^{86}Kr(n, nl)^{86}Kr using the Germanium Array for Neutron-Induced Excitations (GEANIE) at Los Alamos' Neutron Science Center (LANCSE). All three data sets have been added to the Experimental Nuclear Reaction Data (EXFOR) database.

In this paper, we describe the beginnings of a new evaluation of all neutron induced reactions on ^{86}Kr, fusing results from the EMPIRE nuclear reaction code [4] with previously evaluated resonances in the Atlas of Neutron Resonances [5] and the experiments mentioned above. For reactions with neutrons below 20 MeV, all of the channels listed in Table I are shown. The difficulties in modeling the detailed nuclear structure of ^{86}Kr prevented us from completing this evaluation in the limited time available for this project.

The organization of this paper is as follows. We begin with a short introduction to Hauser-Feshbach reaction theory and the EMPIRE code. Next, we describe our choice of optical model potential and the excellent agreement we achieve with previously obtained ^{86}Kr(n, tot) and ^{86}Kr(n, el)^{86}Kr data as found in the EXFOR database [7]. Following this, we delve into the cross section evaluation process for each of the newly measured cross sections. Along the way, we describe our evaluation of electromagnetic reduced matrix elements B(XL) for ^{86}Kr and ^{85}Kr.

II. INTRODUCTION TO HAUSER-FESHBACH THEORY

The Hauser-Feshbach theory is used to model nuclear reactions in the EMPIRE code. The theory performs well for medium to heavy nuclei such as ^{86}Kr. The theory contains many moving parts that can be altered so the models fit the data more appropriately. The basic equations for the Hauser-Feshbach theory are:

$$\sigma_{a,b}(E) = \sigma_{a,b}^{dir}(E) + \sum_{J\pi\pi} \sigma_a^{CN}(E,J) P_b(E,J) \qquad (1)$$

$$P_b(E,J) = \frac{\alpha_b \Gamma_b(E,J)}{\sum_c \alpha_c \Gamma_c(E,J)} \qquad (2)$$

$$\Gamma_b(E,J) = \sum_{I\pi\ell j} \int_0^{E-B_p} dE' \rho(E', I\pi) T_{p,\ell j}^J (E - B_p - E') \qquad (3)$$

incoming channel is a, outgoing is b (composed of the outgoing particle p and the residual nucleus) $\sigma_{a,b}^{dir}(E)$ is the direct part of the cross section, computed with the coupled channels codes ECIS or OPTMAN or with distorted wave Born approximation (DWBA) in EMPIRE $\tau_a^{CN}(E, J\pi)$ is the formation cross section for the compound nucleus with quantum numbers commensurate with incoming channel a where J is total angular momentum, I is the spin, f is the orbital angular momentum, j is angular momen-

tum, α is the rescaling factor, P is the decay probability of the compound nucleus, Γ is the total width, E is the excitation energy, ρ is the level density, and T is the transmission coefficient.

III. ^{86}Kr(n, tot) AND ^{86}Kr(n, el)^{86}Kr

The total cross section and elastic cross section plots required no revisions, the model from running EMPIRE in default mode was sufficient. The optical model is the parameter in the Hauser-Feshbach theory that affects the shape of the total and elastic cross section plots. The isotope ^{86}Kr is a nearly spherical mid-shell nucleus with a relatively small deformation. As a result the Koning-Delaroche spherical optical model [9] works great and EMPIRE (or any other code that is based on the Hauser-Feshbach theory) does not have to be altered. The elastic cross section plot could not be tweaked due to the fact that there is no available experimental data for this reaction and thus nothing to compare the model to for accuracy.

IV. ^{86}Kr(n, nl)^{86}Kr AND ^{86}Kr(n, n_{inel})^{86}Kr

The ^{86}Kr(n,nγ')^{86}Kr experiment was conducted at the LANSCE Weapons Neutron Research facility using GEANIE (GEANIE consists of 10 Compton-suppressed planar Germanium detectors and 10 Compton-suppressed coaxial Germanium detectors, but the results of the experiment only come from the 4 of the latter detectors chosen for optimal time and energy resolution). The neutron flux was measured using a fission chamber containing ^{238}U and ^{235}U foils. There were ten new transitions discovered that had not previously been observed for this reaction and overall, they measured partial cross sections for 22 transitions at neutron Energies between 1 MeV and 20 MeV. The neutron beam was pulsed and the experimenters used the time-of-flight method to determine the incident energy of the neutrons on target. The experimenters used natural iron foils on either side of krypton cell, perpendicular to the beam, so the known cross sections in the krypton experiment. The experimenters also accounted for the efficiency of the detectors, target thickness, and "dead-time" of the neutron beam. More experimental details can be found in Ref. [3].

Products	Q-Value (keV)	Threshhold (keV)
^{87}Kr + γ	0.0	0.0
^{86}Kr + n	0.0	0.0
^{83}Se + α	-2278.7	2305.46
^{86}Br + p	-6851.06	6931.52
^{82}Se + n + α	-8096.65	8191.74
^{85}Br + d	-9754.6	9869.16
^{85}Kr + 2n	-9856.65	9972.4
^{79}Ge + 2α	-10517.6	10641.1
^{85}Br + n +p	-11979.16	12119.84
^{84}Br + t	-12361.1	12506.2
^{84}Se + ^{3}He	-14177.85	14344.35
^{82}As + p + α	-14805.14	14979.01
^{78}Ge + n + 2α	-16253.44	16444.31
^{84}Kr + 3n	-16969.0	17168.2
^{85}Se + 2p	-17358.65	17562.51
^{81}Se + 2n + α	-17372.89	17576.91
^{81}As + d + α	-18221.67	18435.66
^{84}Br + n + d	-18618.3	18836.9
^{83}Br + n + t	-19202.07	19427.57
^{84}Se + p + d	-19671.32	19902.33

TABLE I. Q-Values and threshold energies for all 86Kr(n,*) up to 20 MeV (table adapted from ref. [6]).

Now inelastic scattering data is rare and partial gamma data such as ^{86}Kr(n,nγ')^{86}Kr have until now not been fully integrated into and evaluation. The reason is simple: reaction codes such as EMPIRE only simulate the population and then depopulation of levels known at the time of compilation of the Reference Input Parameter Library (RIPL) [10]. The level and gamma data in RIPL are often incomplete when compared against the newest measurements such as that in [3]. Even worse, to properly simulate the depopulation of a level scheme, one must understand the population of all levels above a given level that can feed that given level.

In the case of ^{86}Kr, Fotiades et al. [3] observed ten new gamma-ray transitions and placed a new level. These data have been integrated into the recent ENSDF evaluation [11], but these have not been propagated into RIPL. We added these new data to our local copy of the RIPL library.

In Fig. 4, we show the total inelastic cross section as computed by EMPIRE. In Fig. 5, we also show the 1565 keV gamma from the first excited state. In this first gamma excitation function, we show the default EMPIRE calculation in red, including the gammas and new level from [3] and [11]. We note that the agreement is not very satisfactory.

In an effort to do a better job reproducing the partial gamma cross section, we first tried using EMPIRE's built in distorted wave Born approximation solver for the direct portion of the cross section (shown in green). This was also not satisfactory. Finally, we turned on the full coupled-channels calculation for inelastic levels in EMPIRE (shown in purple). This brought the simulation closer to data, but not close enough.

We had to provide branching ratios, and γ-rays for levels that otherwise EMPIRE would assume to go straight to the ground state as they had no available decay data. In order to solve the latter issue, it was necessary to determine the possible γ-rays, multipolarities, half-lives, spins, parities, and branching ratios for each energy level with unspecified decay data in ^{86}Kr using selection rules and systematics. In Fig. 6, it is clear which transitions were added (in red) and which transitions are known (in

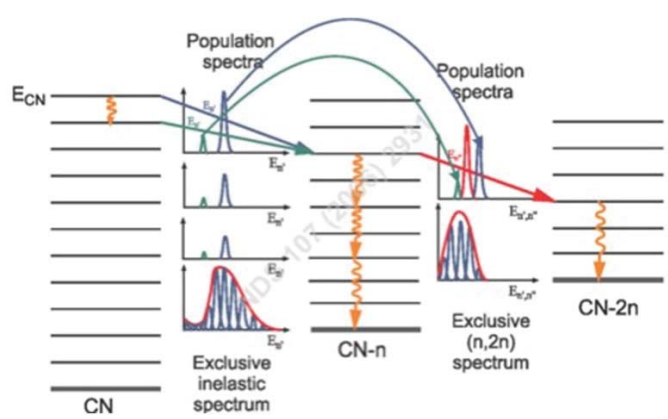

FIG. 1. Illustrates the compound nuclear reaction decay (figure from reference [8])

black). It should be noted that the 4400.8 keV level with a transition of 4400.7 keV on ENSDF from Ref. [12] was replaced with our predictions. This was accomplished by calculating the average B(E1), B(E2), and B(M1) values after deleting major outliers (found on the NNDC website for isotones with N=50, [13]). The mean value of B(E1) is 6.823 ±1.450, the mean value of B(E2) is $9.398\times10^{-7}\pm2.534\times10^{-4}$, and the mean value of B(M1) is 0.2046 ±0.1442. A code was then made to determine the possible allowable γ-rays and subsequent multipolarities using single-particle estimates that can be found in Ref. [14]. Then, the half-lives were calculated for all three B(XL) values as we were unsure which was correct. We then had to make an informed decision regarding which transitions were possible and used this information to calculate the branching ratios of the allowable γ-rays. This approximated information had to be put into the RIPL file and EMPIRE was rerun to ensure that the models more accurately matched the experimental data. It is clear from Fig. 5 and Fig. 7 that the additional transitions made the feedings into these levels better and thus the models fit the data better.

As for the ^{86}Kr(n,n'$_{inel}$)^{86}Kr reaction, it was not necessary to alter the model as there is no available data for this reaction and thus nothing to compare the model to for accuracy. Keeping in mind that the partial-γ models generally have the correct shape and incorrect feedings where some models overshoot the data and other undershoot the data, we believe that the shape for the total inelastic cross section plot is correct, and the values for the cross section are approximately correct as the overpredictions and underpredictions seem to balance each other out.

V. ^{86}Kr(n, γ)^{86}Kr

The experimental data for the ^{86}Kr(n,γ)^{87}Kr reaction was collected at TUNL. The experiment involved an ^{86}Kr stainless steel cell surrounded by ^{115}In or ^{197}Au foils for neutron flux determination. There were three monitor reactions: ^{115}In(n,γ)^{116m1}In with a half-life of 54.29 minutes for neutron energies 0.37 MeV and 0.86 MeV, ^{197}Au(n,2n)^{196}Au with a half-life of 6.1669 days for the 14.8MeV neutron energy, ^{115}In(n,n')^{115m}In with a half-life of 4.486 hours for all other neutron energies. There were also three reactions used to produce neutrons: ^{3}H(p,n)^{3}He for neutron energies below 4 MeV, ^{2}H(d,n)^{3}He for neutron energies between 4

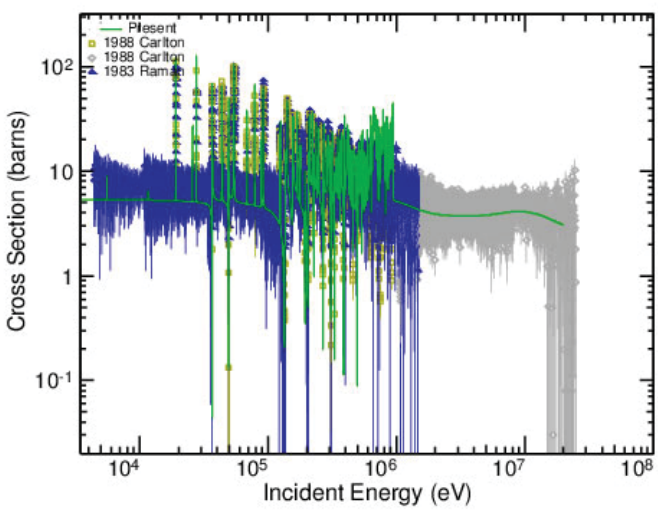

FIG. 2. Total cross section plot

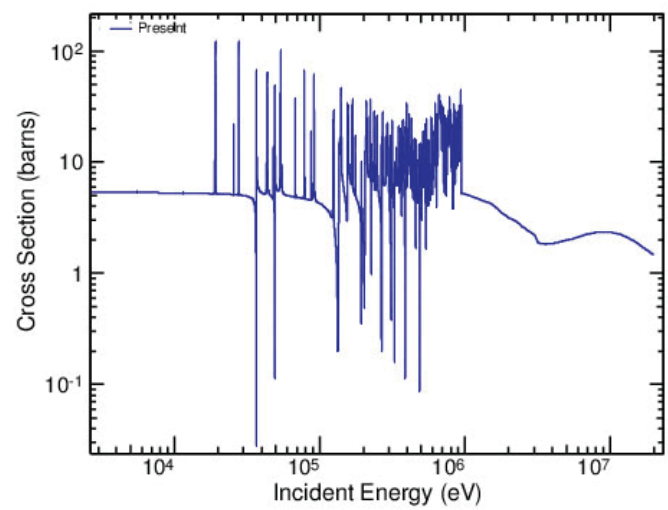

FIG. 3. Elastic cross section plot

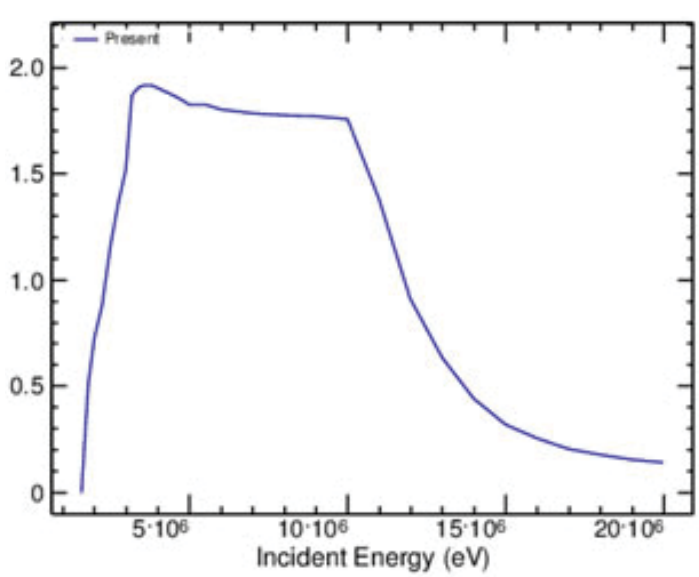

FIG. 4. Total inelastic cross section plot

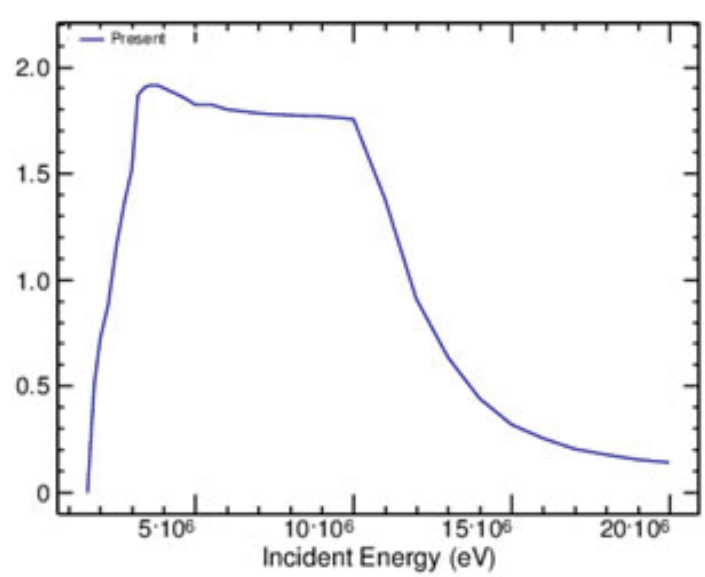

FIG. 5. 1565 keV level, 1564.8 keV gamma inelastic cross section plot

MeV and 14.5 MeV, and $^{3}H(d,n)^{4}He$ at 14.8 MeV. The experiment accounted for the efficiency of the high-purity germanium detectors and for gas-out or untritiated target contributions (for certain neutron producing reactions). More experimental details can be found in Ref. [1].

In order to fit the neutron-capture cross section, we experimented with alternate γ-ray strength function parameterizations (shown in Fig. 10). EMPIRE automatically rescales the γ-ray strength function in order to reproduce the thermal neutron capture cross section. Neither of these were sufficient to fit the data. The shape of the new capture data does not look like the capture cross section for neighboring elements. We scrutinized the experimental procedures to seek out any possible sources of error and determined that the cross sections used for the monitor foils may not have been correct. We rescaled the cross sections using updated monitor data from the International Reactor Dosimetry and Fusion File (IRDFF). This also did not help improve agreement between our calculations and the experimental results.

VI. $^{86}Kr(n, 2n)^{85}mKr$, $^{86}Kr(n, 2n)^{85}g$ Kr, and $^{86}6Kr(n, 2n)^{85}Kr$

The $^{86}Kr(n,2n)^{85}mKr$ experiment at TUNL was performed using the same cell, monitor reactions, and neutron reactions as $^{86}Kr(n,\gamma)^{87}Kr$. And thus the monitor foil cross sections were also rescaled based on the IRDFF data. More experimental details can be found in Ref. [1]. The Kondaiah experiment was conducted using a quinol-clathrate of krypton as opposed to a cell of krypton gas such as the ones used in the TUNL experiments and the GEANIE experiment. The Georgia 200 kV accelerator provided neutrons as a result of the $^{3}H(d,n)4He$ reaction to irradiate the sample and the measurements were taken with Ge(Li) detectors. The neutron flux was determined by detecting alpha particles in a silicon detector perpendicular to the beam. The experimenters accounted for the deterioration of the titanium-tritium target in the neutron flux determination. Monitor powders of either silicon, aluminum, or iron were used the reactions being $^{28}Si(n,p)28Al$ with a half-life of 2.238 minutes, $^{27}Al(n,p)^{27}Mg$ with a half-life of 9.46 minutes, $^{56}Fe(n,p)^{56}Mn$ with a half-life of 2.58 hours, and $^{27}Al(n,\alpha)^{24}Na$ with a half-life of 14.96 hours. More experimental details can be found in Ref. [2].

In order to produce the isomeric cross sections, the steps were similar to those used to get the inelastic cross section plots. We had to check the RIPL level file against ENSDF energy levels and γ-energies. Again, we had to provide branching ratios and γ-rays for levels that were assumed to go straight to the ground state as they had no available decay data. It was necessary to determine

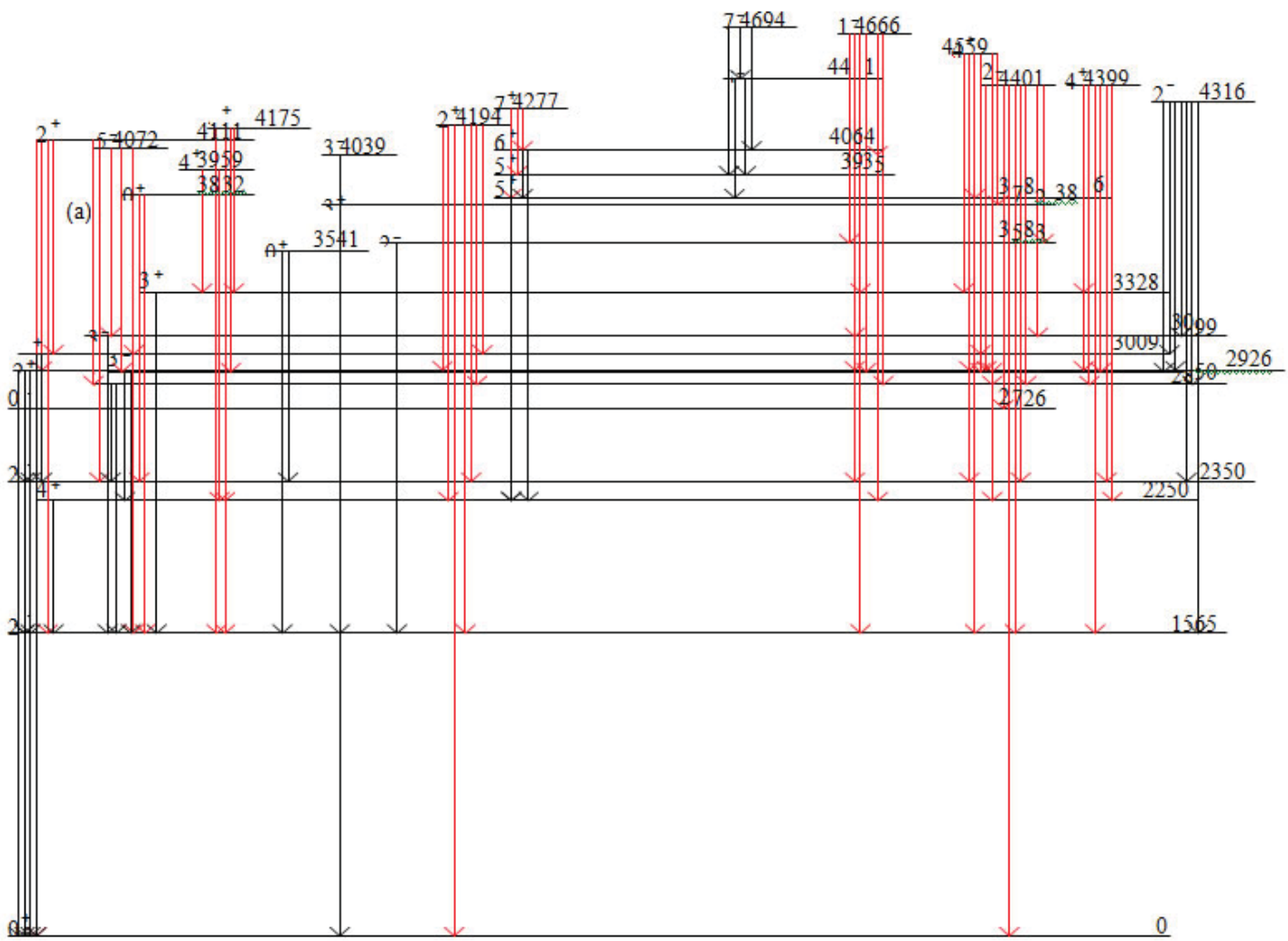

FIG. 6. ^{86}Kr level scheme plot, the red lines represent the transitions that came from systematics and the black lines represent transitions that are known and are listed on ENSDF

the possible γ-rays, multipolarities, half-lives, and branching ratios for each energy level with unspecified decay data in ^{85}Kr. In Fig. 12, it is clear which transitions were added (in red) and which transitions are known (in black).This was accomplished by calculating the average B(E1), B(E2), and B(M1) values after deleting major outliers (found on the NNDC website for isotones with N=50). The same code was used for this reaction as the neutron-capture reaction to determine the possible allowable γ-rays and subsequent multipolarities. Then, the half-lives were calculated and used to calculate the branching ratios of the allowable γ-rays. This approximated information had to be put into the RIPL file and EMPIRE was rerun to ensure that the models accurately matched the experimental data.

The ^{86}Kr(n,2n)^{85}g Kr and ^{86}Kr(n,2n)^{85}Kr reaction cross section plots could not be altered as we do not have experimental data to date to compare them to for accuracy. It should also be noted that the TALYS evaluation from Ref. [16] is in fair agreement with the data and the empire MODELS in Fig. 11.

VII. CONCLUSIONS

Overall, the ^{86}Kr neutron-induced evaluation still requires a bit of work, particularly the inelastic partial gamma cross section plots and the neutron-capture cross section plot. The inelastic partial-γ cross section plots require further investigation into the nuclear structure of ^{86}Kr which could include working backwards from the experimental data to determine further level scheme information that would help fit the data. The neutron-capture cross section plot requires investigation into both the workings of EMPIRE for this reaction and into the details of the experiment for any possible sources of error as the shape of the experimental data differs from neutron-capture data of nearby nuclei. The ^{86}Kr(n,2n)^{85m}Kr came out in significant agreement with the data from TUNL although it did overshoot a little bit which may be further investigated in the future.

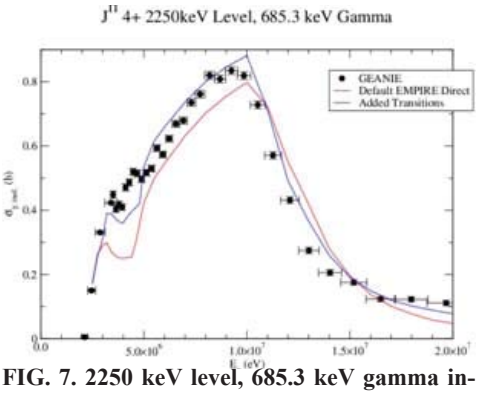

FIG. 7. 2250 keV level, 685.3 keV gamma inelastic cross sec- tion plot

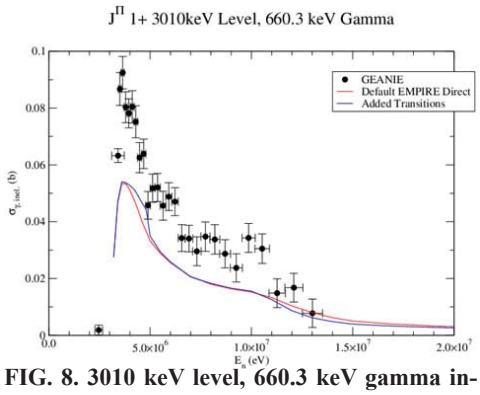

FIG. 8. 3010 keV level, 660.3 keV gamma inelastic cross sec- tion plot

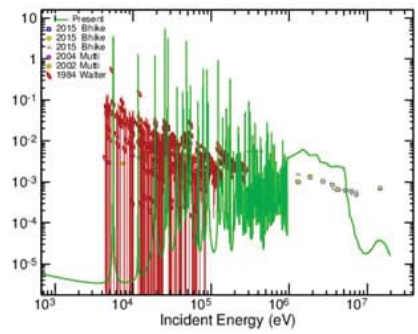

FIG. 9. Neutron capture cross section plot comparing original monitor foil cross sections and rescaled to IRDFF monitor foil cross sections

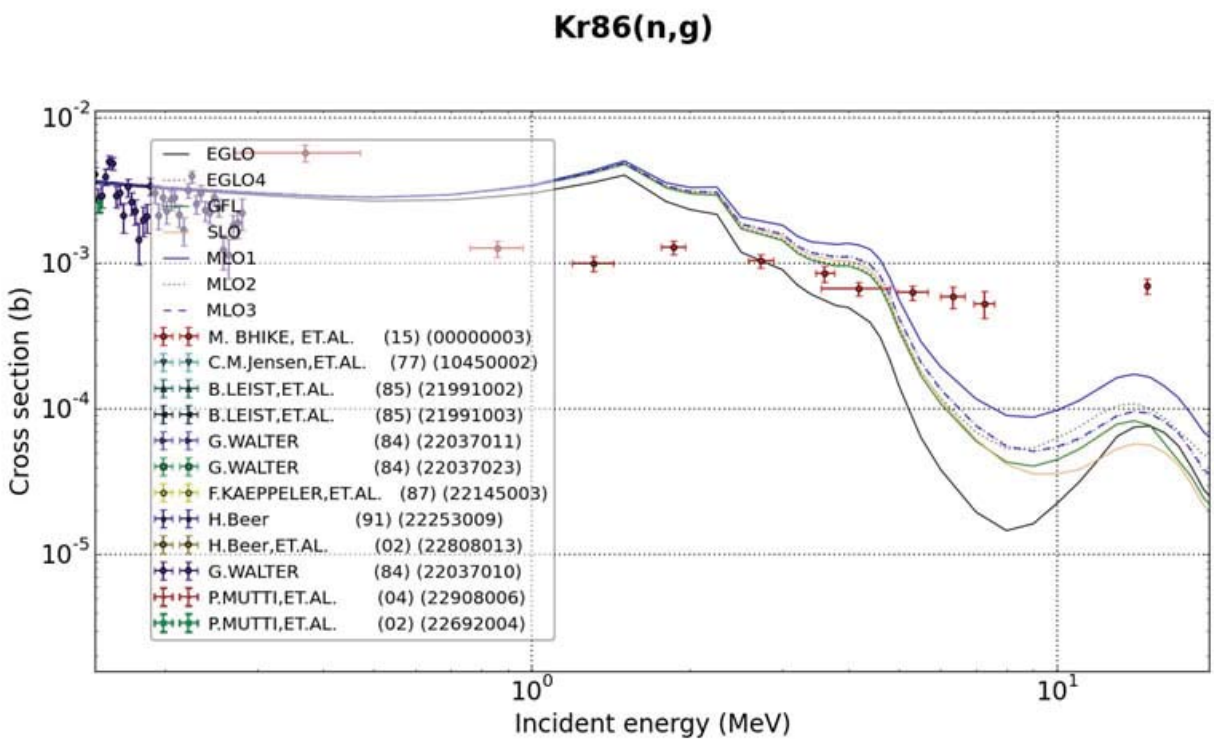

FIG. 10. Neutron capture cross section plot comparing the gamma ray strength function options.

VIII. ACKNOWLEDGEMENTS

I would like to thank my mentor, David Brown, for all of his help with this project. I would also like to thank Michal Herman and Gustavo Nobre for their assistance in completing this project. This project was supported in part by the U.S. Department of Energy, Office of Science, Office of Workforce Development for Teachers and Scientists (WDTS) under the Science Undergraduate Laboratory Internships Program (SULI).

IX. REFERNCES

[1] Bhike, M., E. Rubino, and M. Gooden, et. al. "Measurements of the ^{86}Kr(n, γ)^{87}Kr and ^{86}Kr(n, 2n)^{85}Krm Reaction Cross Sections below En=15 MeV."Phys. Rev. C. 27 July 2015. Web. 28 July 2015.

[2] E. Kondaiah, N. Ranakumar, R.W. Fink, "Neutron activation cross sections at 14.4 MeV for Kr and Xe isotopes", Nuclear Physics A, Volume 120, Issue 2, 1968, Pages 337-341, ISSN 0375-9474, http://dx.doi.org/10.1016/0375-9474(68)90770-7.

[3] Fotiades, N., M. Devlin, R. O. Nelson, and T. Granier. "Low-spin States in 86 Kr from the (n, nl) Reaction."Phys. Rev. C 87.4 (2013): n. pag. Web.

[4] M. Herman, R. Capote, B.V. Carlson, et. al., "EMPIRE: Nuclear Reaction Model Code System for Data Evaluation", Nuclear Data Sheets, Volume 108, Issue 12, December 2007, Pages 2655-2715, ISSN 0090-3752, http://dx.doi.org/10.1016/j.nds.2007.11.003.

[5] S. F. Mughabghab, " Atlas of Neutron Resonances: Resonance Parameters and Thermal Cross Sections Z=1-100", Amsterdam: Elseview, 2006. Print.

[6] G. Audi, M. Wang, A. H. Wapstra, et. al.," The 2012 Atomic Mass Evaluation and the Mass Tables, Nuclear Data Sheets, Nuclear Data Sheets, Volume 120, June 2014, Pages 1-5, ISSN 0090-3752, http://dx.doi.org/10.1016/j.nds.2014.06.126.

[7] N. Otuka, E. Dupont, V. Semkova, et. al.," Towards a More Complete and Accurate Experimental Nuclear Reaction Data Library (EXFOR): International Collaboration Between Nuclear Reaction Data Centres (NRDC)", Nuclear Data Sheets, Volume 120, June 2014, Pages 272-276, ISSN 0090-3752, http://dx.doi.org/10.1016/j.nds.2014.07.065.

[8] M.B. Chadwick, P. Oblo˘zinsky´, M. Herman, et. al., "ENDF/B-VII.0: Next Generation Evaluated Nuclear Data Library for Nuclear Science and Technology", Nuclear Data Sheets, Volume 107, Issue 12, December 2006, Pages 2931-3060, ISSN 0090-3752, http://dx.doi.org/ 10.1016/j.nds.2006.11.001.

[9] A. J. Koning, J. P. Delaroche, NUCL. Phys. A 713, 231 (2003).

[10] R. Capote, M. Herman, P. Oblo˘zinsky´, et. al., "RIPL: Reference Input Parameter Library for Calculation of Nuclear Reactions and Nuclear Data Evaluations", Nuclear Data Sheets, Volume 110, Issue 12, December 2009, Pages 3107-3214, ISSN 0090-3752, http://dx.doi.org/ 10.1016/j.nds.2009.10.004.

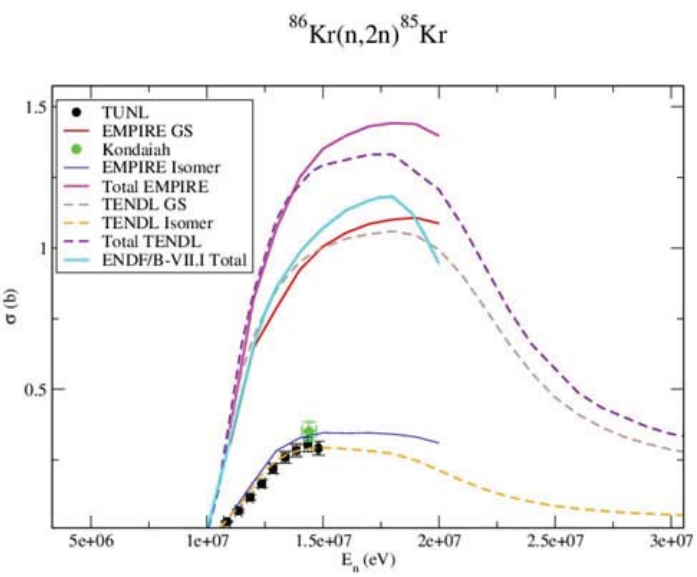

FIG. 11. ^{86}Kr(n,2n) cross section plot

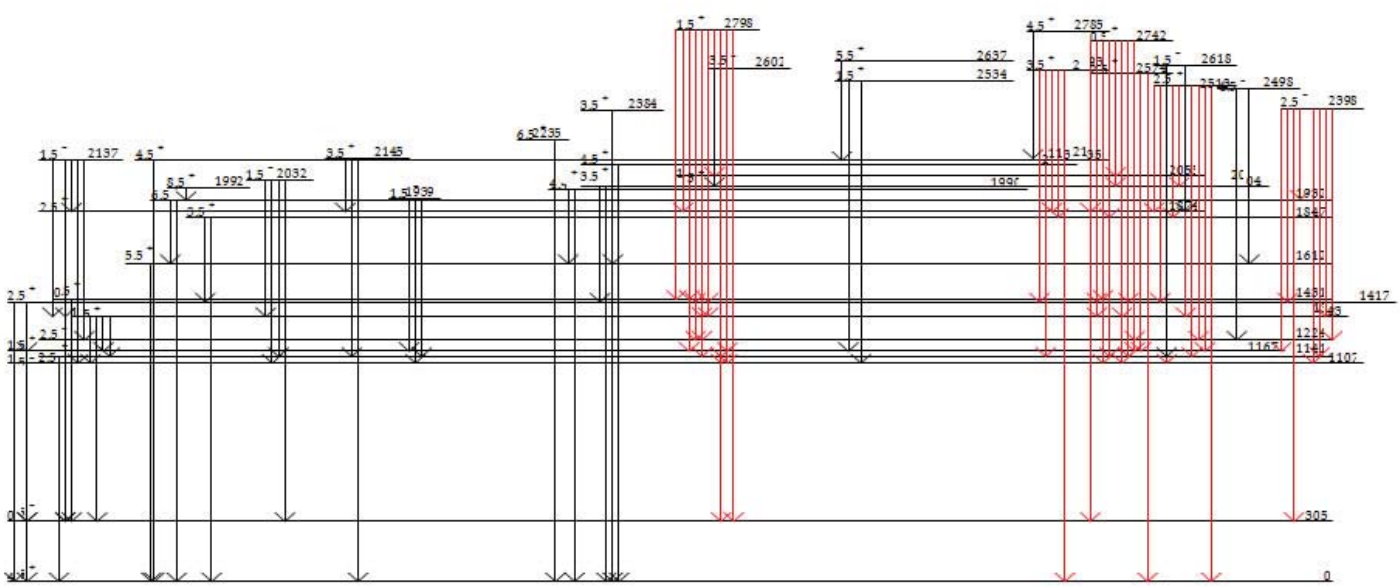

FIG. 12. ^{85}Kr level scheme plot, the red lines represent the transitions that came from systematics and the black lines represent transitions that are known and are listed on ENSDF

[11] Evaluated Nuclear Structure Data File a computer file of evaluated experimental nuclear structure data maintained by the National Nuclear Data Center, Brookhaven National Laboratory.
[12] Schwengner, R., R. Massarczyk, G. Rusev, et. al. "Pygmy Dipole Strength in 86 Kr and Systematics of N = 50 Isotones." Phys. Rev. C 87.2 (2013): n. pag. Web.
[13] National Nuclear Data Center, information extracted from the NuDat 2 database, http://www.nndc.bnl.gov/ nudat2/
[14] Martin, M. J. (September 27, 1982) "Reduced Gamma-Ray Matrix Elements, Transition Probabilities, and Single-Particle Estimates" [Memorandum]. Oak Ridge National Laboratory.
[15] A.J. Koning and D. Rochman, "Modern Nuclear Data Evaluation With The TALYS Code System", Nuclear Data Sheets 113 (2012) 2841
[16] R. Capote, K. Zolotarev, V. Pronyaev, and A. Trkov. "Updating and Extending the IRDF-2002 Dosimetry Library." Reactor Dosimetry: 14th International Symposium(2012): 197-209. Web.

Impacts of white-tailed deer on forest health in the Pine Barrens on Long Island

Taylor Ruhle
Fisheries and Wildlife Science, Paul Smith's College, Paul Smiths, New York 12970
Lauren Gazerwitz
Natural Resources, University of New Hampshire, Durham, New Hampshire, 03824
Kathy Schwager
Environmental Health and Protection, Brookhaven National Laboratory, Upton, New York 11973

Abstract

Excessive browsing due to the overpopulation of white-tailed deer (Odocoileus virginianus) has had impacts to forest health throughout the eastern United States, including the Long Island Pine Barrens Region. Pine Barrens are a unique ecological system characterized by dry, nutrient poor soils and the presence of pitch pines (*Pinus rigida*), oaks (*Quercus sp.*), scrub oak (*Quercus ilicifolia*), blueberries (*Vaccinium sp.*), and huckleberries (*Gaylussacia sp.)*. In this ecosystem, white-tailed deer have impacted the size and abundance of tree seedlings and saplings, as well as the abundance of understory species. For this project, we collected data from pre-established forest health monitoring plots and deer exclosures as a continuation of a long-term assessment of pine barrens health within Brookhaven National Laboratory (BNL). Throughout our project, we assessed four deer exclosures and their associated forest health plots, where we looked at canopy closure, understory plants and their abundances, tree seedlings, and saplings within the plot. In doing this we found that short shrub and sapling abundances within plots differed inside and outside deer exclosures. These results suggest that different plants may react differently to the effects of deer browse. These differences may have also occurred due to varying environmental conditions other than deer, such as light or soils. Over time, BNL will be able to use our data to look farther into how, how long, or if a forest can be naturally restored to its historic composition after the exclusion of deer. This experience has allowed us to become acquainted with new field techniques and equipment, as well as to work in a habitat that we haven't had the chance to work in before.

I. Introduction

White-tailed deer (*Odocoileus virginianus*) are often selective browsers, but as resources become scarce they will eat anything available to them (Halls 1984). In recent decades, Long Island, New York has been plagued by an overpopulation of deer (U.S. Department of Energy 2013). As local populations increase past carrying capacities, forest health is negatively affected by over-browsing of low shrubs, trees, and herbaceous plant species, which can prevent regeneration (Boulanger et. al. 2015; Tanentzap et al. 2009). Throughout the United States, these populations are managed through the implementation of birth control, hunting regulations, culling, and the creation of deer exclosures (Alverson et al. 1988). On Long Island, specifically at Brookhaven National Laboratory (BNL), the deer population is managed by culling and by monitoring deer exclosures to track forest health (Timothy Green, Brookhaven National Laboratory, personal communication; U.S. Department of Energy 2013). However, management at the lab has only begun within the past year, and effects may not become apparent for several years.

For our project, we focused on changes in plant community in 4 pre-established deer exclosures compared with their paired plots throughout BNL from June to August 2015. Deer exclosures were established in the summers of 2011 and 2012, three of the paired plots were established in 2005 and 2006, and the remaining paired plot was established in 2015. Our objective was to compare vegetation diversity, growth, and abundance between deer-excluded and non-excluded areas in the Long Island Pine Barrens. The data collected will serve as part of a long-term study monitoring how long, or even if forest recovery will take place after the exclusion of white-tailed deer.

II. Methods

A. Study Site

BNL is a national research laboratory that sits on 5,265 acres of land in Upton, NY in Suffolk County, Long Island. In 1917, the land was cleared for the creation of Camp Upton, a United States Army base that served to house troops during both World Wars (Brookhaven National Lab). In the time between the World Wars it remained untouched as Upton National Forest. In 1947, Camp Upton became Brookhaven National Lab, dedicated to research on atomic energy (Brookhaven National Laboratory).

Currently, BNL is part of the 102,500 acres of protected pine barrens forest in Long Island. BNL forms the center of the Central Pine Barrens, one of only three pine barrens systems in the world. Its forests are characterized by pitch pine (*Pinus rigida*), oak species (*Quercus spp*.), and an understory consisting of scrub oak (*Quercus ilicifolia*) and various heath species such as blueberries (*Vaccinium spp*.) and huckleberries (*Gaylussacia spp*.). (Natural Resource Management Plan for Brookhaven National Laboratory Citation)

Four deer exclosures and their associated paired forest health plots were monitored to compare vegetation communities both affected by and excluded from white-tailed deer (Figure 1). Plots surveyed were located in oak-pine, pitch pine, and coastal oak forest types. Dominant plants found throughout plots included pitch pine, white oak (*Quercus alba*), scarlet oak (*Quercus coccinea*), scrub oak, black huckleberry (*Gaylussacia baccata*), late lowbush blueberry (*Vaccinium pallidum*), and early lowbush blueberry (*Vaccinium angustifolium*).

B. Forest Health Monitoring Protocols

To establish plots within BNL, coordinates were chosen randomly using ArcGIS. Within each 16 x 25 meter plot, all flora and fauna species were recorded, photographs were taken, strata cover and height were recorded, and ten transects were run along the 16

meter edge (Foundation for Ecological Research in the Northeast, 2007). Starting points on each transect were randomly chosen, and from there, a 2 meter tent pole was used to record all adjacent plant species at each additional meter along transects. Litter and duff samples were taken at four locations along transects, and canopy cover type (pitch pine and/or hardwood) was also noted. After the borders of the plot had been marked and established, a large, live, and healthy tree in the immediate area surrounding the plot was spray painted and marked as a witness tree. Four belt transects were constructed within each plot to collect data on seedling and sapling growth. Live trees, dead trees, and downed logs greater than 10-centimeters DBH were also identified and measured for each plot.

C. Statistical Analyses

Unpaired t-tests were performed to test the significance between sapling abundance and heath species abundance within deer exclosures and their paired plots (GraphPad 2015).

III. Results

We recorded vegetative data in four deer exclosures and their associated forest health plots throughout BNL. Species richness for each plot was recorded and was found to be insignificant between deer exclosures and paired plots (p-value = 0.7522, t = 0.3169). Differences in abundances between *G. baccata, V. pallidum, V. angustifolium,* and saplings in the deer exclosures and paired plots were also compared. Within these plots, we found that *G. baccata* abundance in deer exclosures (11.4 ± 4.58 stems per transect, mean ± SD) versus paired plots (8.95 ± 4.7 stems transect, mean ± SD) was significant (p-value = 0.0206, t = 2.36) (Figure 2). We found that of all plots surveyed, 56% of *G. baccata* was located within deer exclosures. Of the *V. pallidum* found within monitored plots, only 39% was located within deer exclosures. These results were also significant (p-value = 0.0029, t = 3.07), showing that *V. pallidum* was less abundant in deer exclosures (5.53 ± 4.12 stems per transect, mean ± SD) than in paired plots (8.95 ± 4.7 stems per transect, mean ± SD) (Figure 3). *V. angustifolium* did not have any significant differences (p-value = 0.3004, t = 1.0425) in abundance between deer exclosures (2.48 + 2.7 stems per transect, mean + SD) and paired plots (3.08 + 2.44 stems per transect, mean + SD) (Figure 3).

Sapling abundances between deer exclosures and paired plots were also compared. Based on our statistical analyses, we found that deer exclosures (4.25 ± 3.7 stems per belt transect, mean ± SD) had significantly more saplings than paired plots (1.44 ± 2.68 stems per belt transect, mean ± SD) (p-value = 0.0197, t = 2.46) (Figure 5).

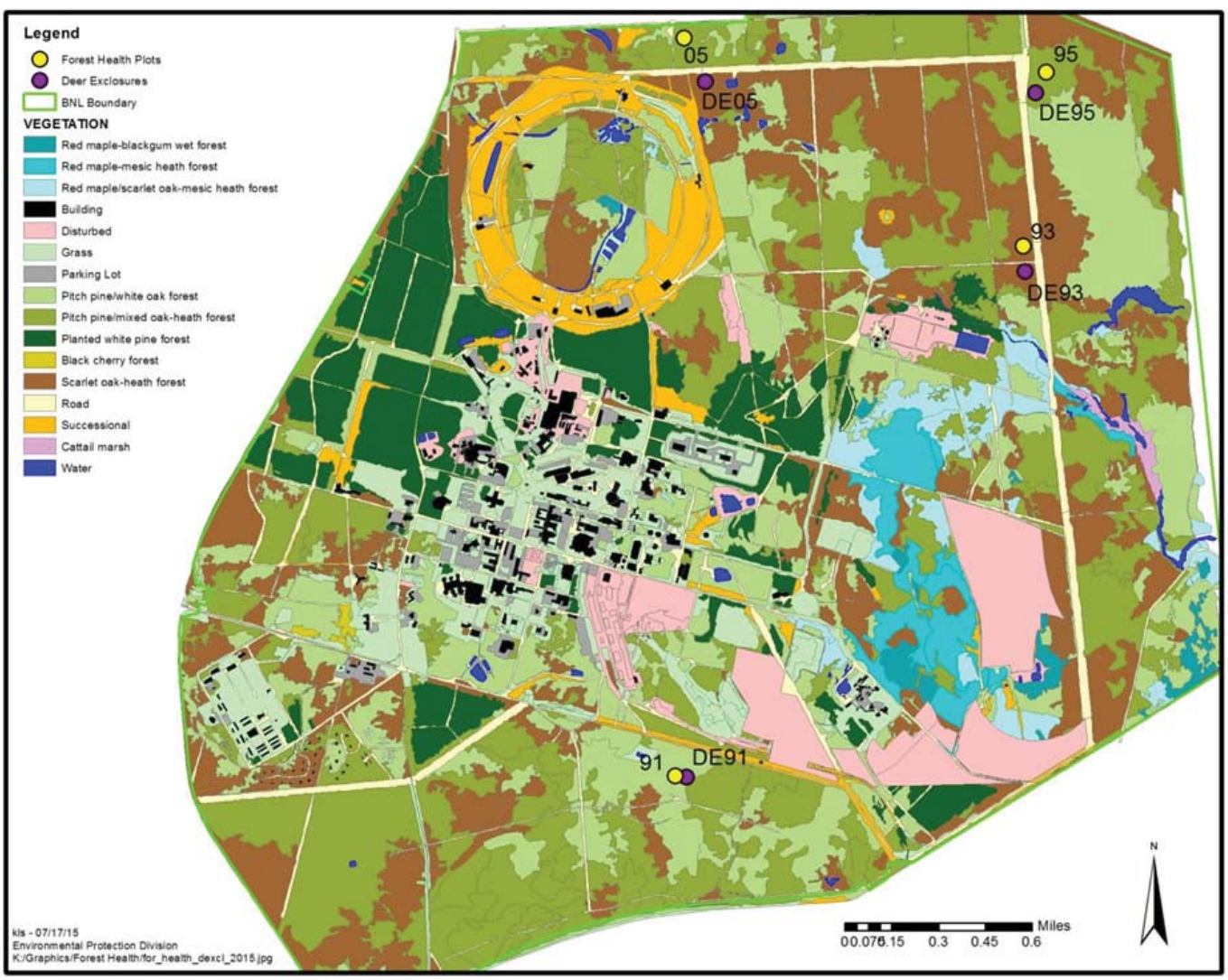

Figure 1: Deer exclosures and their associated forest health plots, monitored June-July 2015 at Brookhaven National Laboratory

IV. Discussion

There were no notable differences in species richness between deer exclosures and their paired plots. This finding can be backed by Pekin et al. (2015), who found that grazing by ungulates effects plant dominance within an area, but not necessarily the diversity within that area. Within our plots, plant species richness differed by four species at most between deer exclosures and paired plots. While white-tailed deer can affect species composition through selective feeding (Boulanger et al. 2015), the large population of deer present at BNL forces individuals to be less selective in their food choices and to consume a broader range of vegetation found throughout the site. While species richness remained similar throughout plots, differences in plant species abundance did arise between them; most notably *G. baccata* and *V. pallidum*. BNL has had problems with overpopulations of deer over 20 year, and unfortunately a lot of damage may have already been done. However, there is no record of baseline forest health data from before the explosion of the white-tailed deer population, and thus we do not know the full extent of the impacts they have had on the forest. Deer may reduce local seed sources, diminishing the seedbank needed for the future regeneration of palatable plants (Tanentzap et al. 2009). Species richness within plots may not have been significant because exclosures have only been up for three years. Three years may not been enough time to allow for adequate regeneration of plants heavily affected by deer. However, deer browse of new growth may have exhausted the seedbank prior to the construction of exclosures, resulting in an insignificant difference in species richness.

Based on our results, *G. baccata* showed the greatest abundance in paired plots versus deer exclosures. This information is supported by the findings of Rawinski (2008) which state that forest floors are typically composed of unpalatable food sources for white-tailed deer, such as *G. baccata*. A study by Reiners (1967) states that *Gaylussacia sp*. is generally more abundant than *Vaccinium sp*. in the Pine Barrens on Long Island. However, when it came to the deer exclosures, *V. pallidum* was much more prevalent than *G. baccata*. Strained resources due to high population sizes at the Lab could cause deer to feed on G. baccata. *G. baccata* generally grows taller than Vaccinium sp., and could shade out the *Vaccinium*. If deer are browsing G. baccata outside of the deer exclosures, they may be lessening competition between these species, resulting in an increased abundance of *Vaccinium sp.* outside of the exclosures (Reiners, 1967). In 2009, Mudrak and colleagues found that 36% of plant species in their

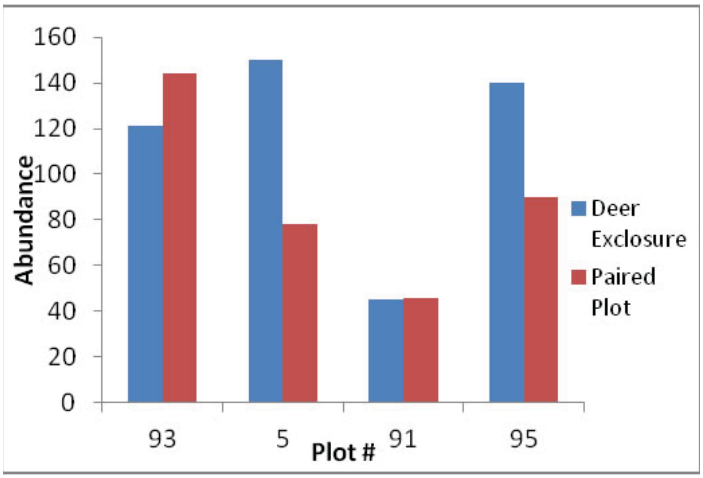

Figure 2: Black huckleberry (Gaylussacia baccata) abundance in deer exclosures versus paired plots at Brookhaven National Laboratory, NY. Data collected June-July 2015.

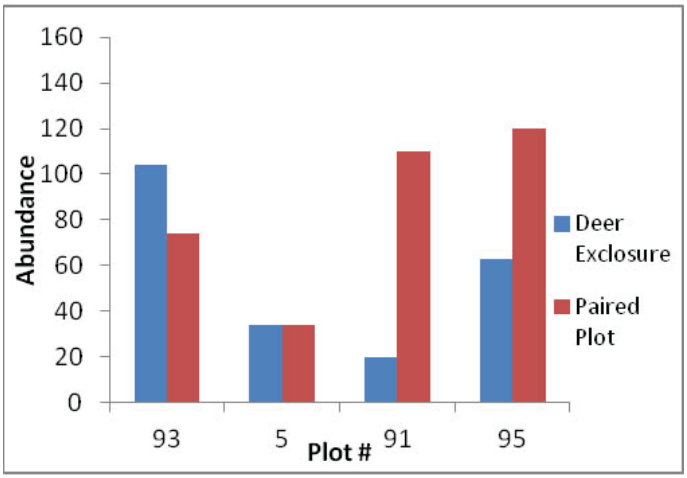

Figure 3: Late lowbush blueberry (Vaccinium pallidum) abundance in deer exclosures versus paired plots at Brookhaven National Laboratory, NY. Data collected June-July 2015.

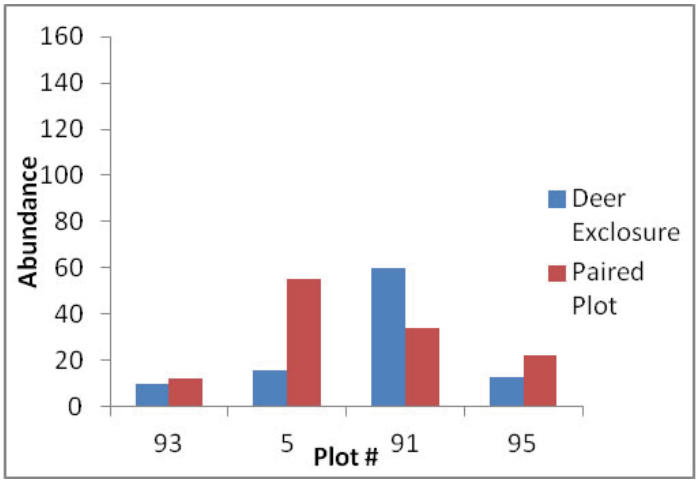

Figure 4: Early lowbush blueberry (Vaccinium angustifolium) abundance in deer exclosures versus paired plots at Brookhaven National Laboratory, NY. Data collected June-July 2015.

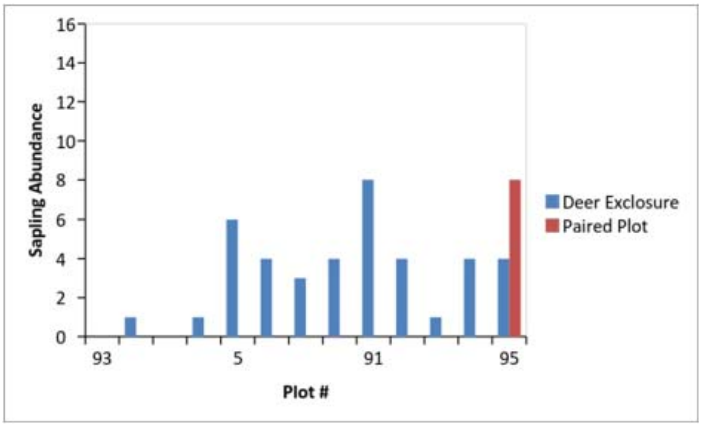

Figure 5: Sapling abundances per belt transect in deer exclosures versus paired plots at Brookhaven National Lab, NY. Data collected June-July 2015.

study showed inconsistent change between deer exclosures and paired plots. This information suggests that different species have different responses to the presence of deer (Mudrak, 2009). This information could also suggest factors such as light or soils could be influencing plant abundances (Reiners, 1967). *V. angustifolium* showed no significant changes in abundance between the deer exclosures or the paired plots. *V. angustifolium* had the lowest mean stems present in both deer exclosures and paired plots as compared to *V. pallidum* and *G. baccata*. This information is also supported by Reiners (1967), who claimed *V. angustifolium* had the lowest biomass out of the three heath species in the previously mentioned study.

When it came to sapling abundance, deer exclosures had significantly higher abundances than paired plots. Similarly, in a study done by Tanentzap et al. (2009), exclosures contained greater sapling densities than control plots, even after four decades of deer management. In a study done by McGarvey et al. (2013), sapling abundance was reduced outside the deer exclosures due to deer browse; a fact further supporting our results. Long-term deer browse can reduce woody plant regeneration and a plant's ability to grow above the browse line (2 meters). If deer browsing on saplings continues at similar rates in the future, saplings will not be able to grow past the browse line and the forest will have a greater chance of diminishing as the overstory trees senesce (Gubanyi et al., 2008; Griggs et al., 2006). In the future, browse-tolerant species may be the only ones that can successfully regenerate (Griggs et al., 2006).

V. Literature Cited

Alverson, W.S., D.M. Waller, and S.L. Solheim. 1988. oFrests too deer: edge effects in Northern Wisconsin. Conservation Biology 2(4):348-358.

Boulanger, V., B. Baltzinger, S. Said, P. Ballon, J.F. Picard, and J.L. Dupouey. 2015. Decreasing deer browsing pressure influenced understory vegetation dynamics over 30 years. Annals of Forest Science 72(3):367-378.

Brookhaven National Laboratory [BNL]. About Brookhaven: Camp Upton. < https://www.bnl.gov/about/history/campupton.php>. Accessed 9 July 2015.

Brookhaven National Laboratory. 2011. Natural Resource Management Plan for Brookhaven National Laboratory. Brookhaven Science Associates, Upton, NY, USA.

Foundation for Ecological Research in the Northeast. 2007. Forest health monitoring protocols for the Long Island Central Pine Barrens. Foundation for Ecological Research in the Northeast, Upton, NY, USA.

GraphPad. 2015. QuickCalcs t-test calculator. <http://www.graphpad.com/quickcalcs/ttest2/ >. Accessed 22 July 2015.

Griggs, J.A., J.H. Rock, C.R. Webster, M.A. Jenkins. 2006. Vegetative legacy of a protected deer herd in Cades Cove, Great Smoky Mountains National Park. Natural Areas Journal 26(2):126-136.

Gubanyi, J.A., J.A. Savidge, S.E. Hygnstrom, K.C. VerCauteren, G.W. Garabrandt, and S.P. Korte. 2008. Deer impact on vegetation on natural areas in Southeastern Nebraska. Natural Areas Journal 28(2):121-129.

Halls, L.K. 1984. White-tailed Deer: Ecology and Management. Stackpole, Harrisburg, Pennsylvania, USA.

McGarvey, J.C., N.A. Bourg, J.R. Thompson, W.J. McShea, and X. Shen. 2013. Effects of twenty years of deer exclusion on woody vegetation at three life-history stages in a mid-Atlantic temperate deciduous forest. Northeastern Naturalist 20(3):451-468.

Mudrak, E.L., S.E. Johnson, and D.M. Waller. 2009. Forty-seven year changes in vegetation at the Apostle Islands: effects of deer on the forest understory. Natural Areas Journal 29(2):167-176.

Pekin, B.K., B.A. Endress, M.J. Wisdom, B.J. Naylor, and C.G. Parks. 2015. Impact of ungulate exclusion on understorey succession in relation to forest management in the Intermountain Western United States. Applied Vegetation Science 18(2):252-260.

Rawinski, T.J. 2008. Impacts of white-tailed deer overabundance in forest ecosystems: An overview. U.S. Forest Service, U.S. Department of Agriculture, Newton Square, Pennsylvania, USA.

Reiners, W.A. 1967. Relationships between vegetational strata in the pine barrens of central Long Island, New York. Bulletin of the Torrey Botanical Garden 94(2):87-99.

Tanentzap, A.J., L.E. Burrows, W.G. Lee, G. Nugent, J.M. Maxwell, and D.A. Coomes. 2009. Landscape-level vegetation recovery from herbivory: progress after four decades of invasive red deer control. Journal of Applied Ecology 46:1064-1072.

U.S. Department of Energy. 2013. Environmental assessment for the management of the white-tailed deer (Odocoileus virginanus) population at Brookhaven National Laboratory Upton, NY. U.S. Department of Energy, New York, USA.

Determining meteorological system accuracy using a root sum of squares analysis

Megan Safranek
Environmental Engineering, University of Delaware, Newark, DE 19716
John Heiser
Biological, Environmental, and Climate Sciences, Brookhaven National Laboratory, Upton, NY 11973

Abstract

Meteorological Services at Brookhaven National Laboratory (BNL) is required to assess the accuracy of on-site meteorological systems. The analysis of system accuracy was performed according to the American National Standard, as published by the American Nuclear Society. In order to determine if data quality from a system is sufficient, calculations should encompass all components impacting the overall accuracy. Significant sources of error may include the sensor, installation, operation, data processing, and calibration error. The known accuracy of a complete system provides insight into the reliability of collected data. While calibrations are performed in accordance to the National Institute for Standards and Technology, the Department of Energy's Meteorological Coordinating Council suggests using the root sum of squares method as well in order to remove any uncertainty in the instruments or data. The objective of this project was to use the root sum of the squares (RSS) analysis method to calculate the total system error of meteorological instruments at BNL. Other parameters involved in the RSS analysis include studying the functioning and components of each system, gathering accuracy information published in manufacturer manuals, converting analog readings into corresponding meteorological units, and analyzing calibration data. The result of this study indicated whether the meteorological data collected through the various systems meet the accuracy criteria established by the American National Standard. With this analysis, the department can identify error producing elements within systems and thereby design improvements to the sensor network. From this project, I have gained valuable experience in analyzing systems, identifying sources of error, and calculating system accuracy.

I. Introduction

A root sum of squares (RSS) analysis has been performed for the meteorological sensor network on site at Brookhaven National Laboratory (BNL) in order to confirm the accuracy of meteorological data collected. The specific instrument systems evaluated were barometric pressure, air temperature, relative humidity, wind speed, wind direction, solar radiation, and precipitation. The RSS analysis considers all components of error within a system in order to calculate the overall system accuracy, as seen in Equation (1) below. The total system accuracy value is then assessed in comparison to the ANSI/ANS-3.11-2005 American National Standard to determine if the accuracy is sufficient.[1] This system analysis was performed as advised by the Department of Energy's Meteorological Coordinating Council (DMCC) in order to remove any doubts in the system ability. While the DMCC recognizes the calibrations of instrument at BNL are performed in accordance to the National Institute for Standards and Technology (NIST), the RSS removes any uncertainty about the system and its data. Furthermore, the analysis will help easily identify components contributing significant error that need to be replaced/upgraded.

Eq. 1 $$RSS = \sqrt{(r_1)^2 + (r_2)^2 + \ldots + (r_x)^2}$$

r_n = error of a system component

For meteorological system analysis, some of the standard error components considered are the sensor, installation, operation, data processing, and calibration error. The main component errors common to all of the meteorological equipment at BNL are sensor measurement error, installation error, and the data logger error. It is important to note that throughout all RSS calculations, the upper bounds of measurement error were used. This was done in order to estimate the upper bound on system accuracy to insure that the meteorological systems will meet or be better than the desired accuracy standards specified in ANSI/ANS-3.11-2005 American National Standard.

For the measurement error, the values were based on the manufacturer's value, which includes the error from all associated cables for the system. Alternatively, if an instrument was calibrated by NIST standards, the calibration data would be used to calculate the sensor accuracy because the data is more precise than the manufacturer's original claim.

The component of installation error was another important consideration for all equipment. It was found that, other than gross mis-installation or misplacement of the sensors, installation error does not significantly affect the functioning of most of the meteorological sensors evaluated and therefore contributes little to the RSS error. The exception to this is the wind direction, which may have an offset error due if not properly aligned. This will be explained in more detail in the wind direction section.

Finally, error due to the data logger affects all of the systems because each system is connected to a Campbell CR1000 data logger which contributes an error of 0.06% of the reading received from the sensor.[2] The highest potential error comes from the maximum analog output of each system, which was then used to calculate the error in volts. Next, this value was converted to the appropriate meteorological units to be used in the RSS equation.

II. Barometric Pressure

The R.M. Young 61302V Barometric Pressure sensors are mounted at the 2 meter location of the 10-meter met tower. The system consists of a R.M. Young 61002 Gill Pressure port in order to decrease dynamic pressure error due to wind, a R.M. Young 61302V Barometric Pressure sensor, the Campbell CR1000 data logger, and all necessary cables. Installation error was not considered to contribute any error for this system. The published error for the Gill Pressure Port and barometric pressure sensor were ± 0.5mb and ±0.3mb respectively,[3,4] which include any error due to voltage loss in the cables. To calculate the error due to the data

logger, the maximum analog reading of 5.0 V was multiplied by the .06 % error in reading from the data logger to get .003V.2 Using this information, the potential range of 500 to 1100 mb was used to calculate that the sensor produces 120 mb/V. Finally, to convert the error value to millibars, the 120mb/V was multiplied by the .003V to get an accuracy of ±0.36 mb or hPa. The RSS equation calculated the total system accuracy to be ±0.69 mb or hPa. The acceptable error for barometric pressure systems according to the American National Standard published by ANSI/ANS is ± 3 mb or hPa. With this information, it was concluded that the barometric pressure system met and exceed the accuracy expectations set by the ANSI/ANS 3.11 standards.

III. Air Temperature

Air temperature sensors are present at the 2, 10, 50, and 85 meter heights on the met towers. The R.M. Young Model 41342VC Temperature probes are used at the 10-, 50- and 85-meter locations. The systems at the 10, 50 and 85 m locations all consist of the same components. The temperature probes are calibrated to achieve an accuracy of at least ±0.1 °C,[5] which includes the error caused by cables. The system also includes a R.M. Young 41003 Multi-plate Radiation Shield to prevent air temperature readings from being significantly altered due to solar radiation. The naturally aspirated radiation shield has an error of ±0.4 °C for wind speeds at 3 m/s, ±0.7 °C at 2 m/s, and ±1.5 °C at 1 m/s.[6] The general trend seen is that as wind speed decreases, error increases. This change in error is because, at lower wind speeds, the shield and air inside heat up significantly from lack of ventilation. This heating alters the air temperature readings of the sensor. Additionally, the air temperature systems use a data logger which, at the maximum 1V reading, can cause up to a .0006 V error.[2] The next step is to consider that the 100 °C range which shows the sensor reads 100 °C per Volt. After multiplying this by the 0.0006 V error, the result is an error of ±0.06 °C due to the data logger. Finally, the system has no error due to installation.

The resulting RSS calculation has three different results due to the difference in error related to variance in wind speed. The system accuracy is ±0.42 °C at 3 m/s wind speed, ±0.71°C at 2 m/s, and ±1.5°C at 1m/s. The required accuracy to meet the ANSI/ANS standard is ± 0.5°C.2 The error in the Multi-plate Radiation Shield is lower at speeds above 3 m/s. From this result, it can be concluded that when wind speed is 3 m/s or greater, the accuracy of the system is acceptable. However, when wind speed drops below 3 m/s, there is more error in the system than the limit in the standard. This finding has indicated to the Meteorological Services department that the use of the multi-plate aspirator is a concern that must be addressed in order to always fall within the desired accuracy.

The temperature system located at 2 meters is different from the other locations as it uses the Campbell/Rotronic HC2-S3 Relative Humidity and Temperature combination probe. This sensor has a calibrated accuracy of ±0.1 °C and is enclosed in an R.M. Young 43502 Aspirated Radiation Shield.[5] This shield is power aspirated at a constant rate, which results in only having a potential ±0.2 °C error.[7] The data logger error is the same as in the previously mentioned air temperature system. The RSS calculation for total system error was ±0.23 °C at the 2 meter location and met the requirements of having at least a ±0.5 °C accuracy. This system is significantly more accurate than the systems using naturally aspirated shields.

Relative Humidity

Relative humidity is measured at the 2 meter location of the 10-meter met tower and the sensors are Campbell/Rotronic HC2-S3 Relative Humidity and Temperature combination probes. Manufacturers stated overall RH accuracy of the sensor and its cables is ±0.8 % at 23°C increasing to ~2.3 % at -10°C to -30°C.8 Additionally, the installation of the system does not contribute any error. The system also includes a R.M. Young 43502 Aspirated Radiation Shield (powered) which is stated to produce a ±0.2 °C error.[7] As published in a manual by Campbell (see RH accuracy graph), a change of only 0.2 °C has little effect on the sensor

Barometric Pressure (2m)	
Component:	**Error (hPa):**
Gill Pressure Port	0.5
Bar. Pressure Sensor	0.3
Instsallation	0
Data Logger	0.36
Wire	(included)
RSS	0.69

Air Temperature (85/50/10 m)			
Component:	**Error: (°C)**		
Platinum Temp. Probe	0.1		
Installation	0		
multiplate	0.4	0.7	1.5
Data Logger	0.06		
Wire	(included)		
	(@3m/s)	(@2m/s)	(@1m/s)
RSS	0.42	0.71	1.50

Air Temperature (2m)	
Component:	**Error: (°C)**
Relative Temp Probe	0.1
Installation	0
Power Aspirator	0.2
Data Logger	0.06
Wire	(included)
RSS	0.23

Humidity (2m)	
Component:	**Error (%):**
Relative Humidity Probe	2.3
Installation	0
Power Aspirator	Negligible
Data Logger	0.06
Wire	(included)
RSS	2.30

Wind Speed (85/50/10m)	
Component:	**Error (m/s):**
Sensor	0.05
Installation	0
Data Logger	Negligible
Amplification Board	Negligible
Wire	(included)
RSS	0.05

Wind Direction (85/50/10m)	
Component:	**Error: (°)**
Sensor	3
Installation	1
Data Logger	0.213
Wire	(included)
RSS	3.17

error. Therefore the highest potential error within the expected temperature range seen by the sensor occurs at very low temperatures and is approximately ±2.3%. For the final component, data logger error, we took the maximum 1V sensor output and multiplied by the 0.0006 error in data logger readings.[2] Then the value of 100% humidity per volt is multiplied by the 0.0006 V to get ±0.06%. The RSS method calculates the total relative humidity sensor accuracy to be ±2.44%. This is better than the ANSI/ANS requirement of ±5.0%. Therefore, the data collected from the relative humidity sensor system is accurate and acceptable.

IV. Wind Speed and Direction

R.M Young 05106 Marine Wind Monitors are located at 10, 50, and 85 meters on the met towers to collect wind speed and direction data. The system includes the wind sensor, the data logger, and the accompanying cables. The wind direction sensor functions as a potentiometer that associates the resistance when facing a given location to a specified direction in degrees. The manufacturer's published error for the direction sensor is ±3°.[9] When calculating error due to the data logger, the 5 ° blind spot in the potentiometer from 355°-0° needs to be considered and the maximum analog reading is 1 V. This means that there are 355 °/V which can then be multiplied by the ±0.0006 V reading error of the data logger to get an error of ±0.213° due to the data logger.2 Additionally, the sensor must be installed to align with 0° north reading. This installation component results in a ±1° error. With all of these component errors considered, the overall accuracy was calculated to be ±3.17 °. This accuracy of the wind direction sensor exceeds the accuracy expectations of ±5.0 ° set by the ANSI/ANS 3.11 standards.

The data for wind speed is collected from the same sensor used for wind direction. This system consists of the wind sensor, data logger, and amplification board and accompanying cables. There is no installation error for this system. Wind speed is calculated by counting the number of pulses given off in a certain time period. There are 3 pulses per revolution. The frequency and pulse count is then used to calculate the RPM and speed in m/s. The amplification board was developed at BNL and amplifies the TTL signal given off by the pulses. This increases the ability of the device to be able to read wind speeds much lower than the unmodified sensor. Since this device simply amplifies signals that would otherwise be lost, it contributes negligible or no error to the system.

All wind sensors are calibrated to NIST standards which allows increased accuracy over the standard calibration. For the error component of the sensor itself, the NIST calibration data, consisting of 14 data points over the range of the sensor, was used to determine the accuracy. The adjusted wind speed was compared to the actual wind speed and the resultant standard error was calculated according to Equation 2 below. This was done for all sensors and the worst case error is used as the component error in order to be sure the overall error is acceptable in even the least accurate sensor. An example of this procedure is provided in Appendix B.

$$\text{Eq.(2)} \quad Standard\ Error = \sqrt{\frac{\sum_1^n \left(\left(actual\ speed - calculated\ speed \right)^2 \right)}{n-2}}$$

The resultant component error for the wind speed sensor was ±0.05 m/s. The data logger error was considered by looking at the functioning of the pulse counter. The data logger pulse count error is stated to be ±3ppm + 1 count. The wind sensor maximum is 100 m/s or 60,000 pulses per minutes. The 3ppm is low enough, compared to the +1 count to be negligible and therefore the +1 count dominates the error. This results in the error being greatest at the low wind speeds. Taking the stall speed of 0.3 m/s for the best sensor in the group (range is 0.3 to 0.4 m/s) would yield 184 pulse per minute and a resulting error of 1/184 * 0.3 m/s or 0.0016 m/s due to pulse count errors in the data logger.

Altogether, the RSS analysis of the components showed the wind speed system has an overall accuracy of ±0.05 m/s, which is better than the ±0.2 m/s accuracy required.

V. Solar Radiation

Solar radiation is recorded by pyranometers located at the solar base station on the roof of building 490D at BNL. The solar base station typically uses the Kipp & Zonen CMP 22 research grade pyranometer. The solar radiation measuring system consists of the pyranometer, the Campbell CR1000 data logger, a CVF3 Ventilator, and all necessary cables. According to the manufacturer, the total instrument uncertainty includes; the expanded uncertainty due to random effects and errors during calibration and given by the World Radiation Center in Davos as 0.67%, a direction error of 0.5% and transfer procedure from calibration by comparison of 0.5%. 10 These include all components except the data logger which has an error of 0.06% in voltage measurement. The RSS is then given by (0.67^2 + 0.5^2 + 0.5^2 + 0.06^2)^0.5 = 1.0%

The use of the CMP 22 pyranometer is preferred by BNL. However, the Kipp & Zonen CMP 21 pyranometer is also used at times when the CMP 22 is out for calibration. The system components are the same as the CMP 22 system. According to the manufacturer, the total instrument uncertainty includes; the expanded uncertainty due to random effects and errors during calibration and given by the World Radiation Center in Davos as 1.31%, a

Solar Radiation (CMP-22)	
Component	**Error: (%)**
Sensor	1
Installation	(included)
Data logger	0.06
Cable	(included)
CVF3 Ventilator	(Included)
RSS	1.00

Solar Radiation (CMP-21)	
Component	**Error:(%)**
Sensor	1.5
Installation	(included)
Data logger	0.06
Cable	(included)
CVF3 Ventilator	(Included)
RSS	1.50

Precipitation:	
Component:	**Error: (%)**
Sensor	3
Installation	0
Data Logger	Negligible
Wire	(included)
RSS	3.00

direction error of 0.5% and transfer procedure from calibration by comparison of 0.5%.[10] These include all components except the data logger which has an error of 0.06% in voltage measurement. The RSS is then given by (1.31^2 + 0.5^2 + 0.5^2 + 0.06^2)^0.5 = 1.5%

VI. Precipitation

Precipitation is tracked at the solar base station on the roof of 490D at BNL using a tipping bucket rain gauge system with a wind shield. The precipitation measuring system consists of the NovaLynx 260-2500E-12 Rain Gauge, the Campbell CR1000 data logger, and all necessary cables. The rain gauge works by using a tipping bucket system with 0.01 inches per tip and a magnet operated reed switch. The NovaLynx 260-2500E-12 rain gauge has a published accuracy of ±3.0 % of the volume of the measured precipitation.[11] This value includes the error due to all associated wires. There is no installation error for the precipitation system. Additionally, the data logger for the rain gauge uses a switch closure pulse counter. There is de-bounce circuitry, which eliminates error due to bounce and the switch closure time versus the data logger scan rate is sufficiently long as to make missed pulses negligible. The RSS method calculated the overall accuracy of the precipitation measuring system to be ±3.0% of volume, which is better than the ANSI/ANS 3.11 standard of ±10.0%.

VII. Conclusions

The RSS error analysis of the meteorological systems at BNL has confirmed that most all instruments exceed the accuracy requirements set by the ANSI/ANS 3.11 standards. This can be seen in Appendix A. The only systems with deficiencies were the air temperature sensors with a naturally aspirated radiation shield and then only at low wind speeds. As discussed earlier, if the wind speed is 2 m/s or less the air temperature reading has significantly more error, causing the system accuracy to fall below the requirement. This discovery has led to researching a potential solution, such as replacing the current shields with the more accurate power aspirated shields. Electric power availability and cost are critical factors in deciding on the best solution to get the air temperature system to meet the accuracy requirement.

VIII. References

1 American Nuclear Society. (2005) ANSI/ANS-3.11-2005 American National Standard for Determining Meteorological Information and Nuclear Facilities. La Grange Park, IL.

2 Campbell Scientific Inc. (2015). CR1000 measurement and Control System Manual. Logan, UT.

3 R.M. Young Company. (2000). Gill Pressure Port Model 61002 Manual. Traverse City, MI.

4 R.M. Young Company. (2012). Barometric Pressure Sensor Model 61302V Manual. Traverse City, MI.

5 Heiser, John. (2013). Instrument Calibration Plan and Procedures. Upton, NY: Brookhaven National Laboratory Meteorological Services.

6 R.M. Young Company. (2014). Multi-Plate Radiation Shield Model 41003 Manual. Traverse City, MI.

7 R.M. Young Company. (2014). Compact Aspirated Radiation Shield Model 43502 Manual. Traverse City, MI.

8 Campbell Scientific Inc. (2015). HC2S3 Temperature and Relative Humidity Probe Manual. Logan, UT.

9 R.M. Young Company. (2015). Wind Monitor-MA Model 05106 Manual. Traverse City, MI.

10 Kipp & Zonen. (2013). CMP Series Pyranometers Manual. Delft, Netherlands.

11 NovaLynx. (2000). Tipping Bucket Rain Gauge Model 260-2500E-12 Manual. Auburn, CA.

IX. Acknowledgements

I would like to thank my mentor, John Heiser, for his guidance during this project and Terrence Sullivan for his assistance.

This project was supported in part by the U.S. Department of Energy, Office of Science, Office of Workforce Development for Teachers and Scientists (WDTS) under the Science Undergraduate Laboratory Internships Program (SULI).

X. Appendices

A. Final Analysis Results

Measurement	Units	Accuracy (±)	Calculated RSS Accuracy (±)
Barometric Pressure	Millibars or hetopascals	3	0.69 mb
Air Temperature (2m)	Degrees Celsius	0.5	0.23 °C
Air Temperature (10/50/85m) @3 m/s	Degrees Celsius	0.5	0.42 °C
Air Temperature (10/50/85m) @2 m/s	Degrees Celsius	0.5	0.71 °C
Air Temperature (10/50/85m) @1m/s	Degrees Celsius	0.5	1.50 °C
Relative Humidity	Percent	4	2.30 %
Wind Speed	Meters per second	0.2 or 5% of reading	0.05 m/s
Wind Direction	Degrees	5	3.17 °
Solar Radiation CMP22	Watts/meter^2	5% of observed	1.00 %
Solar Radiation CMP21	Watts/meter^3	5% of observed	1.50 %
Precipictation	Millimeters	10% of volume	3.00 %

B. Example Wind Speed Sensor Error Calculation

Serial #95881				
Actual Speed (m/s)	**RPM**	**Adjusted Speed (m/s)**	**Difference**	**Difference^2**
29.40	5966.00	29.39	0.01	4.36E-05
24.50	4966.00	24.49	0.01	4.36E-05
19.50	3959.00	19.56	-0.06	3.49E-03
15.60	3157.00	15.63	-0.03	8.58E-04
13.70	2757.00	13.67	0.03	9.42E-04
11.70	2357.00	11.71	-0.01	8.65E-05
9.80	1960.00	9.76	0.04	1.30E-03
7.80	1560.00	7.80	0.00	1.60E-05
5.90	1166.00	5.87	0.03	7.08E-04
4.90	966.00	4.89	0.01	4.36E-05
3.90	771.00	3.94	-0.04	1.44E-03
3.00	575.00	2.98	0.02	5.06E-04
2.00	377.00	2.01	-0.01	5.33E-05
1.10	176.00	1.02	0.08	6.02E-03
			Sum	**0.02**
			Standard Error	**0.04**

Designing the booster to Alternating Gradient Synchrotron injection lines for the electric dipole moment experiment

Michael Severance
Stony Brook University, Stony Brook, NY 11790
N.Tsoupas
Brookhaven National Laboratory, Upton, NY 11973

Abstract

For the Electric Dipole Moment (EDM) experiment, it is necessary to have two injection lines from the booster ring to the Alternating Gradient Synchrotron (AGS). The injection lines will feed into the AGS in such a way so that the two lines will travel in opposite directions with one travelling clockwise and the other travelling counterclockwise. It is my job to design these two lines. To do this, I have utilized Methodical Accelerator Design (MAD) code have set up all the elements of these lines and then have simulated the beam passing through these elements to ensure that certain conditions are met. I have also left a lot of flexibility in my designs. That is, I have designed multiple lines with a varying amount of quadrupoles and have also designed two types of injection schemes. The first scheme, vertical injection, would involve raising both the lines, since the AGS is about a meter higher than the booster ring, and then bending the lines as needed. The second scheme, horizontal injection, seems to be a much simpler and more novel configuration since we would raise both lines together and then bend the lines individually.

I. Background

The desire for the very sensitive storage ring electric dipole moment (EDM) measurements started over a decade ago, after the precise measurement of the magnetic moment of the muon. These EDM measurements are particularly intriguing to physicists because of how they violate the symmetries of both time reversal and of parity as compared to the magnetic dipole moments which do not have these violations. It is true that there are other interesting factors associated to these EDM measurements, but it is truly interesting to see how nature breaks its symmetries. It must also be stated that these measurements are to be very difficult to perform, which is why a lot of planning is needed to endure that these measurements are done properly.

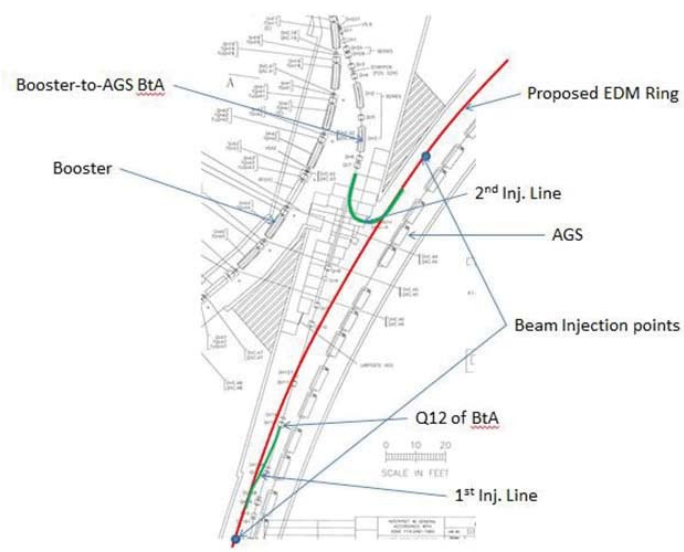

Fig 1: Basic schematic for the vertical injection scheme.

II. The injection

For the EDM project, we will need to injection lines from the booster ring into the Alternating Gradient Synchrotron (AGS). These lines will move in opposite directions around the AGS, with one moving clockwise and the other moving counter-clockwise. Something to take into account is that the AGS is elevated by about 1 meter above the booster ring. This would mean that we would have to elevate the beam line and also bend it so that we can send these lines around the AGS. Another thing to note is that the beams that are entering the AGS should be " the same" as the beam already there (i.e. same beta function, etc.).

There are two possible ways to do this, one would be a horizontal injection scheme and the other would be a vertical injection scheme. Essentially the horizontal injection scheme would involve raising the two lines separately while the horizontal injection scheme would involve raising the two lines separately and the bending each line. More information on these two schemes can be seen later on in the paper.

III. Vertical injection

For the vertical injection scheme, we will have to raise both of the lines separately. Also, we will have to bend one of the lines since these two lines will be travelling in opposite directions. This can be seen in the figure below.

The basic arrangement that we will need for both lines would be a dipole followed by some number of quadrupoles (which is greater than 1) and then another dipole. It should be noted that since we are bending the beam in one direction and then in the opposite direction, it is impossible to only use on quadrupole. But, I digress. This will allow us to bend the beam up be the needed

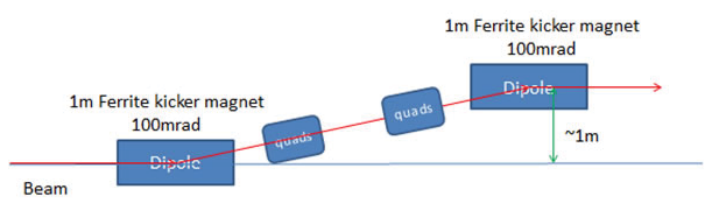

Fig 2. Here we can see the aforementioned way of raising the beam.

distance of about 1 meter. A picture of this can be seen below.

Next we can see that various arrangements of optical elements that were used (varying the quadrupoles) to allow for more flexibility in the design. We can notice from the figures below that we can achieve an achromatic beam using these varying amount of quadrupoles. We can also see how the beta functions upon entry match the beta functions upon exit. We can also see that our values for η are zero at both the entry and the exit of the cell.

IV. Horizontal injection scheme

For this scheme we will raise both lines together and then bend them separately. We can see the overview in the figure below.

Now let us zoom in on the actual injection line. We can see this below. You will notice that we will use our designs from the vertical injection scheme for the first part of the line since we still need to raise both lines. Also, in the figure below, we have shown that initial part with three quadrupoles, but again we can use any number of quads greater than one.

Now let us examine the actual bending portion of the beam after they have been raised. Note that we only show one line but the other line would be exactly like this but inverted.

This scheme seems a bit better since we only have to perform a raise once instead of twice since we raising the beam once together. But that will be a decision that will be made we they are actually building it.

V. Conclusion

It would appear there is now a lot of flexibility when designing these beam lines. When it ultimately comes time to build these beam lines, those in charge will be able to use varying designs so that the process of actually assembling these may be more cost efficient, easier to build, or have some other benefit from a design standpoint.

VI. Acknowledgements

This project was supported in part by the U.S. Department of Energy, Office of Science, Office of Workforce Development for Teachers and Scientists (WDTS) under the Science Undergraduate Laboratory Internships Program (SULI). With that being said, I would really like to thank the DOE for having programs like this available and for funding this research.

I would also like to thank BNL and all of the employees that I have come into contact with as they have shown a great deal of

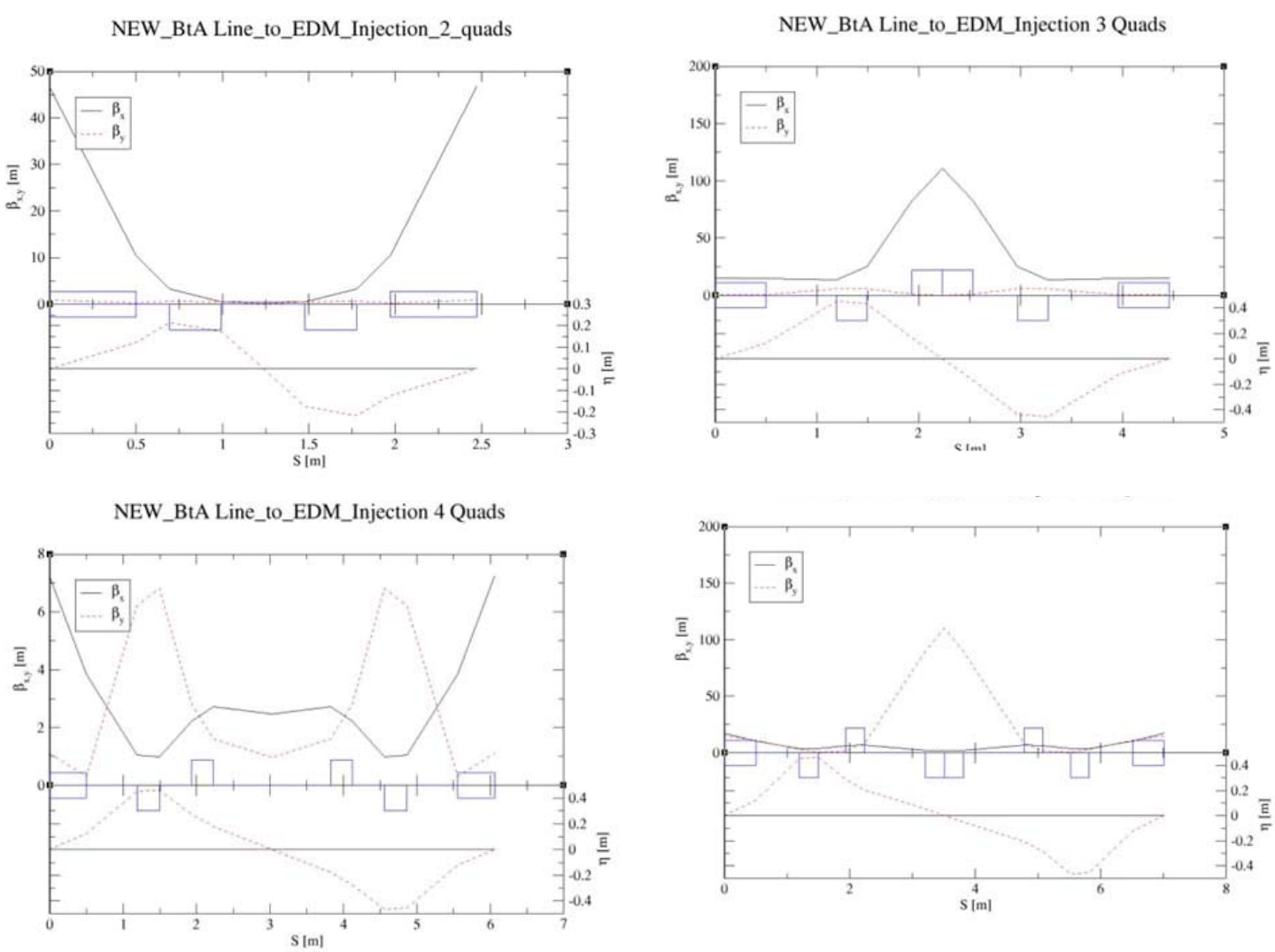

Fig 3: Here we can see the lines that contain 2 quadrupoles (top left), 3 quadrupoles (top right), 4 quadrupoles (bottom left), and 5 quadrupoles (bottom right)

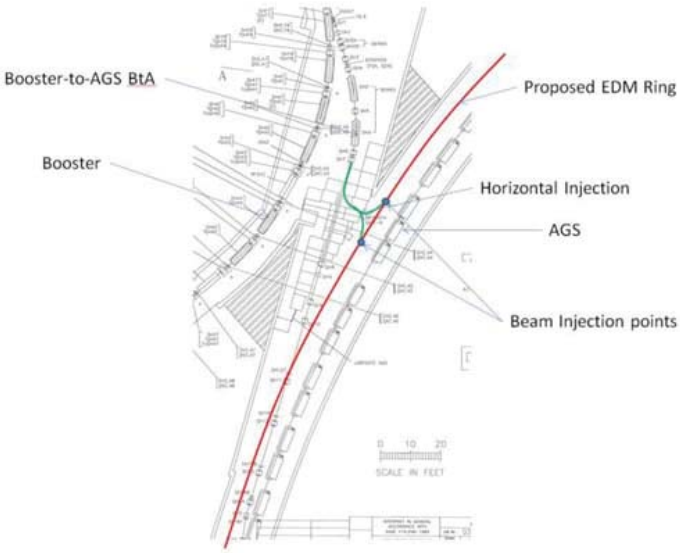

Fig 4: An overview of what the horizontal injection scheme would look like

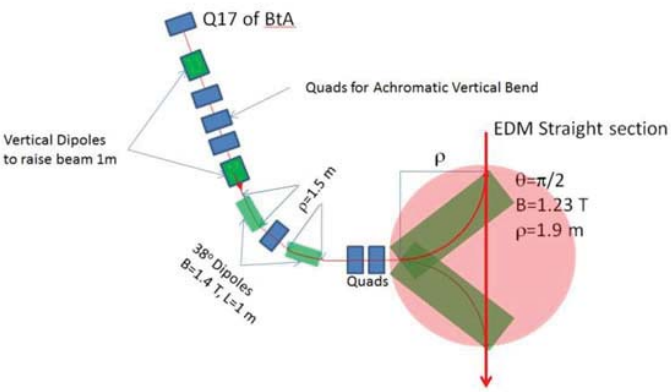

Fig 5: A closer look at the horizontal injection scheme.

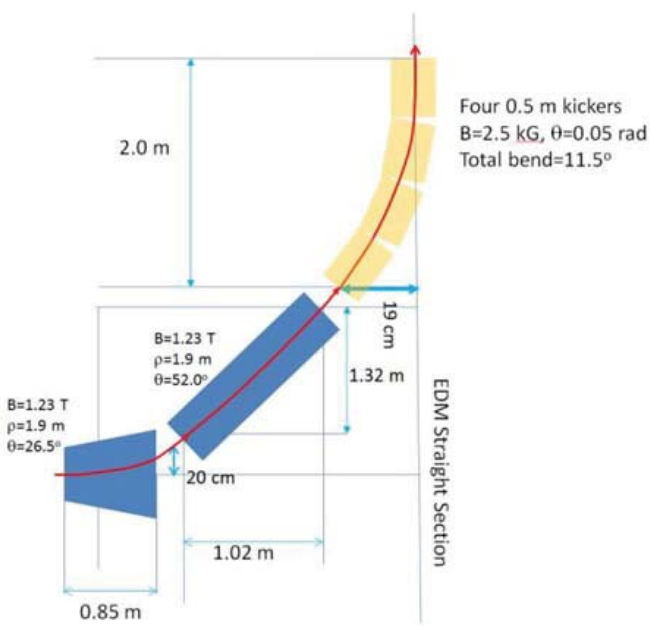

Fig 6: Here is yet another zoom in of the last bend that would be needed for the horizontal injection scheme.

hospitality and really have made this place feel like home. This especially includes my officemates Nick Bonura, Tom DeMartino, and Dennis Donaldson.

Finally, I like to especially thank my mentor through the SULI program, Nicholaos Tsoupas, for his constant encouragement and for his insight on all of the troubles that I ran into. Without his trust and expertise, this project would not have been possible. I am very lucky to have such a great man as someone who I can look up to.

What does the future hold for the Nuclear Nonproliferation Treaty?

Laura Shanklin
State University of New York at Geneseo
Katherine Bachner and Susan Pepper
Nonproliferation and National Security Department, Brookhaven National Laboratory, Upton, NY 11973

DISCLAIMER

This report was prepared as an account of work sponsored by an agency of the United States Government. Neither the United States Government nor any agency thereof, nor any of their employees, nor any of their contractors, subcontractors, or their employees, makes any warranty, express or implied, or assumes any legal liability or responsibility for the accuracy, completeness, or any third party's use or the results of such use of any information, apparatus, product, or process disclosed, or represents that its use would not infringe privately owned rights. Reference herein to any specific commercial product, process, or service by trade name, trademark, manufacturer, or otherwise, does not necessarily constitute or imply its endorsement, recommendation, or favoring by the United States Government or any agency thereof or its contractors or subcontractors. The views and opinions of authors expressed herein do not necessarily state or reflect those of the United States Government or any agency thereof.

Abstract

The Nuclear Nonproliferation Treaty (NPT) has a wide-ranging impact including to the Nonproliferation and National Security Department at Brookhaven National Laboratory. As a group within this department, the Safeguards and Nonproliferation Policy Group is concerned with supporting the International Atomic Energy Agency's safeguards through various strategies, including project management and training. The department also provides direct support to DOE/NNSA in its efforts to support the U.S. government's delegations to the NPT Preparatory Committees and Review Conferences by providing policy analysis and advice on the Treaty. The NPT is often viewed as the cornerstone of the Nonproliferation Regime. Understanding the challenges the future holds for the NPT will help the Department of Energy achieve its mission. Every five years the NPT undergoes a Review Conference, with the latest conference being held in April-May 2015. With varying media coverage, it can be difficult to accurately pinpoint an objective assessment of the proceedings, and to find a comprehensive and unbiased report of the challenges that ultimately led to the failure of an agreed upon final document. This internship project involved compiling a study of the history of the NPT along with a detailed outline of events from the 2015 Review Conference. This work will provide valuable reference materials in making predictions for future conferences, conferences which have a large affect on the success of the nonproliferation regime at large. My study of various documents has led to the conclusion that the ongoing modernization of nuclear weapons and arguable failure of disarmament outlined through the 2010 NPT RevCon Action Plan caused Non-Nuclear Weapon States(NNWS) to question whether Nuclear-Weapon States (NWS) have sufficiently fulfilled requirements outlined in article VI of the NPT - the article that deals with disarmament. The seventieth anniversary of the bombings of Hiroshima and Nagasaki allowed states with a pro-disarmament objective to bring a humanitarian aspect to the table. The discussion on a MEWMDFZ proved to be the cause of the inability of the RevCon to achieve a final document - a process requiring consensus among all gathered parties, and without which the RevCon cannot be considered a success. A study of what happened at this recent RevCon lead to bigger discoveries evaluating the success of the NPT and the implementation of its three pillars. This project and the required research have led to a valuable knowledge gain about the nuclear nonproliferation regime and NPT, as well as skills in analyzing documents and compiling data.

I. Introduction

The Nuclear Nonproliferation Treaty (NPT) is the cornerstone of the nuclear nonproliferation regime. The Treaty was designed to support the regime through three mutually reinforcing pillars: nonproliferation, nuclear disarmament, and the peaceful use of nuclear energy. The NPT entered into force in 1970, with a Review Conference held every 5 years as outlined in Article VIII, paragraph 3 in order to allow States to gather to ensure continuous work toward goals outlined in the treaty.[3] Nonproliferation experts and analysts had high hopes for a successful conclusion of the RevCon in the lead-up to the 2015 RC, but faced major disappointment when the Conference collapsed without a final agreed upon document and little media attention. According to the Dunn Theorem, back-to-back successes are a rarity in the NPT RevCon world, as agreement on a final document is usually seen every other year.[9] In order to understand what happened at the 2015 RevCon it is important to study the context driving the various States involved. The ongoing modernization of nuclear weapons and failure to meet disarmament objectives outlined through the 2010 Action plan caused NNWS to question whether NWS are sufficiently fulfilling requirements of article VI.[3] The 70th anniversary of the bombings of Hiroshima and Nagasaki allowed NNWS with a disarmament agenda to bring a humanitarian aspect to the table, but many among the NWS considered that it did not hold any real traction, because it was dismissed by the P5 as making no new discoveries, because the harsh effects of nuclear weapons are known and understood by most. The most anticipated topic leading up to the 2015 RevCon was the Middle East Weapons of Mass Destruction Free Zone (MEWMDFZ) as agreed to in the landmark 1995 NPT Review and Extension Conference; while this was a promise that led to the indefinite extension of the Treaty in 1995, it nonetheless proved to be a major cause of disagreement in 2015. Debate over the conditions necessary for a MEWMDFZ would eventually contribute to the collapse of the RevCon. A study of what happened at this recent conference will hopefully lead to further insights evaluating the success of the NPT and the implementation of its three pillars. Furthermore, it is worth asking the question, does the NPT, and more specifically the disarmament pillar, serve the individual interests of the NWS by serving the interest of International Community. In regard to these conflicts of interests, a study of Game Theory may provide an explanation of the perceived lack of enthusiasm for disarmament by NWS.

II. History of the NPT

The major push for a treaty preventing nuclear proliferation started in the 1960s. The United States proposed the creation of a multilateral nuclear force through NATO, which triggered Soviet criticism of so-called "nuclear sharing."[1] Soviet fear stemmed from the perceived national security threat Germany presented. Both sides during the Cold War had an economic incentive to adopt a treaty resembling the NPT, because the development and deployment of nuclear weapons proved to be expensive.[2] The Irish Resolution adopted in December 1961 called for NWS to secure conclusion of an international agreement that relinquished control of nuclear weapons and refrained from transmitting information for manufacture of these weapons to NNWS. It also called for NNWS not to manufacture or otherwise control nuclear weapons. This resolution led to the creation of the Eighteen-Nation Disarmament Conference, and eventually the conclusion of the Limited Test Ban Treaty in 1963, the latter dealing with the prevention of nuclear testing. Negotiations of the NPT began in 1965 in France, and widened the scope in comparison to the Irish Resolution to include disarmament and nuclear weapon free zones in discussions. The Treaty entered into force March 5th, 1970. All but four states have gradually joined as members to the Treaty. States outside the Treaty include Israel, India, Pakistan, and DPRK.[1] The DPRK however represents a special case, in which the state joined the Treaty and later withdrew. The Treaty was given a 25-year time limit and was to be revisited every five years.[2] This means that a Review conference is held every 5 years in order to ensure the NPT is upholding the pillars outlined in the document.

The NPT consists of three pillars, which are each uniquely essential to the overall nonproliferation regime. The first pillar involves nonproliferation. The NPT defines a nuclear-weapon state as a state which had manufactured and exploded a nuclear weapon or other nuclear explosive device prior to January 1st, 1967.[1] This means that upon its entry into force, five nations were codified as NWS: the United States, Soviet Union, United Kingdom, France, and China. No provision exists to add a nuclear-weapon state that undertook manufacture and detonation after 1967. Article I states that nuclear-weapon states will not transfer nuclear weapons to non-nuclear weapon states. Non-nuclear weapon states agree to a corollary commitment in Article II. Article III of the NPT addresses nonproliferation by requiring non-nuclear weapon states to agree to accept "comprehensive safeguards" to all nuclear materials and facilities.

The second pillar of the NPT addresses disarmament, which proved to be a topic of major debate in 2015, as non-nuclear weapon States see efforts to fulfill disarmament obligations by NWS as reluctant at best. Article VI calls for disarmament in general terms. It calls for states "to pursue negotiations in good faith on effective measures relating to cessation of the nuclear arms race at an early date and to nuclear disarmament, and on a Treaty on general and complete disarmament under strict and effective international control." It is important to note the vague language in relation to disarmament outlined in Article VI, because it calls for an objective with no timeline or outline for events to meet this goal. The vagueness of the language allows for NWS to claim they are fufilling Article VI requirements by slowly reducing nuclear stockpiles, while modernizing weapons which undermines any real progress towards the ultimate goal of complete disarmament. The third and final pillar deals with peaceful uses. Article IV declares that all states have an equal right to pursue peaceful nuclear development in conformity with Articles I and II. Some examples of peaceful uses might include cancer treatment and developing "hearty" rice that improves nutrition among the poor.[1] Considering the overwhelming widespread support for the NPT, the three pillars outlined above have defined the goals of the international community when dealing with nuclear issues.

As stated by Jayantha Dhanapala, acclaimed scientist on the Board of Sponsers for the Bulletin of Atomic Scientists, "The road ahead for the Treaty will be greatly influenced by the road behind" [4]. This means that a study of previous Review Conferences will uncover the major themes of debate, and hopefully help explain behavior at the most recent conference. It is important to note how these agreed upon provisions affect parties to the Treaty. If language in the final document drafted at the RevCon is regarded as a "subsequent agreement" or "subsequent practice in application," the document is legally binding to all parties. [4] The implications of Review Conferences have an impact on policy objectives in addition to the legal influence. Perhaps most importantly, RevCons are often seen as a litmus test for the viability of the Nuclear Nonproliferation Regime. [1] Examining failures helps detect weaknesses in the regime. The five year revisitation process allows governments and various nongovernmental stakeholders to study the status of the regime. The RevCons also offer a mechanism for discussion by permitting a guarenteed and organized discussion every five years, which gives the states an opportunity to come together and discuss issues of noncompliance. Looking at previous conferences offers a way to study the evolution of the NPT and possibly the nonproliferation regime as a whole.

III. Nuclear Disarmament: Haves versus have-nots

A key aspect of the NPT and cause of disagreement is the perceived failure of NWS to disarm their weapons. NWS argue that their gradually lowering stockpile numbers prove their continued effort towards complete disarmament as outlined in Article VI. NNWS retaliate by pointing out increased modernization of a smaller stockpile with increased capability undermines disarmament efforts. A basic understanding of game theory leads one to wonder whether NWS will ever fully disarm, although they have agreed to under the NPT. How long will the NWS be able to drag on the disarmament process before NNWS frustration causes the collapse of the NPT? This question uncovers a larger theme of disagreement, because some see the NPT as a discriminatory treaty creating nuclear haves and have nots. This question is of great importance to the future of the NPT and the overall Nonproliferation regime.

Perhaps the biggest proponent for complete disarmament comes from the Non-Aligned Movement (NAM). This movement started as an effort to create an alternative to states emerging from colonization and joining the Western or Eastern political blocs during the Cold War era.[6] The NAM is grounded on the idea that such military blocs aggravate international tensions, and states should be able to pursue self-interest free from these blocs. One of the NAM's main objectives calls for "general and complete disarmament." [6] At the 2015 Review Conference the NAM gave an official statement emphasizing the importance of the NPT to the nonproliferation regime, while stressing the ongoing importance of implementing all three pillars equally for international peace and security. [7] The statement criticized states codified as NWS for modernizing their nuclear weapons and even in some cases researching and developing new delivery systems. These actions

arguably thwart the disarmament pillar of the NPT. Specifically, the statement argues that modernization "undermines the unilateral and bilateral reductions made thus far." [7] The NAM points out that the use of nuclear weapons would be a crime against humanity, and violate humanitarian law.

Countries refute the claim that they are not fulfilling their disarmament objectives by citing the sharp decline of stockpiles.[14] Perhaps the best example is the United States. The number of nuclear warheads the United States is armed with has decreased dramatically since the Cold War era - a number that reflects the geopolitical atmosphere. However, Putin's recent announcement of a plan to add 40 interconinetal ballistic missles Russia's nuclear arsenal reflects rising tensions.[12] In 1967, the United States nuclear arsenal peaked with 31,255 weapons.[13] After signing the New Strategic Arms Reduction Treaty with Russia, the United States promised to deploy no more than 1,550 weapons by 2010. In 2013, President Obama took this one step further when he announced his intention to lower this number to 1,000 warheads. [5] Some argue that this reduction reflects the changing geopolitical atmosphere, rather than the more optimistic view that the world has become more enlightened regarding the potentially disastrous effects of nuclear weapons use. In regards to the political atmosphere, the collapse of the Soviet Union brought an end to the Cold War, and left the United States as virtually the only superpower in this time. The United States' foreign policy turned to focus on other enemies, such as Iraq, whom did not hold nuclear capabilities, thus making nuclear weapons not a central part of policy. Viewing disarmament through this international relations theory approach predicts that conflict will arise as China overtakes the United States as the world hegemon. A transition like this is likely to produce conflict, according to game theorists, who might conclude that China's status as a NWS would suggest that the United States will put a greater emphasis on nuclear weapons in the future. [5] Concerns of a second nuclear age are enforced by the increased nuclear weapon modernization and the capabilities of Iran, Pakistan, India, and North Korea.[5]

Although the US holds an obligation to disarm, experts speculate on how few weapons the state can hold on to while meeting foreign policy objectives. If Yale University political scientist Paul Bracken is correct in his theory that we are dawning on a "second nuclear age"- how many weapons does the United States need to maintain for deterrence against a nuclear attack?5 Experts largely agree that the United States needs enough weapons to be able to absorb a nuclear attack, and strike back. Other experts see a greater importance in nuclear capability in relation to our geopolitical advantage. Foreign Policy writer Matthew Kroenig conducted a study on all nuclear armed countries from 1945-2001 which held outside variables constant. He concluded that the nuclear armed country with more warheads than its opponent was 1/3 as likely to be challenged militarily by other countries, and more than 10 times likely to prevail in a crisis. [5] He defined "prevailing" as achieving political goals. It may seem like nuclear war is so devastating that greater differences in capability do not make a huge difference, but as a conflict escalates, these differences do have an effect on political leaders' cost-benefit analysis, and ultimately the geopolitical outcome.[5] This analysis may be considered compelling, because it suggests that the size of an arsenal is important in relation to not only deterrence, but to achieving a particular international political agenda. This view offers yet another explanation of the modernization of nuclear weapons.

Are NWS ever going to fufill their disarmament obligations under Article VI? A basic study of game theory explains that complete disarmament may be an idealist vision, although NWS have commited to working towards this vision under Article VI of the NPT. Game theory suggests that the best possible outcome isn't achievable because of the uncertainty of your opponent's move. It would be best for every state to give up nuclear weapons, but it is unlikely that all states will completely disarm, because of the chance that the opposing state will hold onto some weapons. This explains the current dilemma of slow disarmament with no end in sight. However, this is not an argument that should weaken the NPT, but rather the opposite. The existence of a treaty that calls for this seemingly out of reach goal is a positive sign in the midst of a grim looking situation.

Although game theory concludes that disarmament is not in the best interest for most states, history shows us that some states disarm for national gain rather than altruistic reasons. South Africa offers an example of a state who disarmed out of self-interest. South Africa orignially launched a weapons program in 1978 out of fear of a Soviet backed invasion of Namibia. In 1989 it was able to abandon this program following Namibia's independence and the dissolution of the Soviet Union, as detterunce was no longer necessary.[15] However, the decision to disarm was not alturistic, but rather an attempt to asimilate into the global economy. Ukraine, Belarous, and Kazakhstan represent a different story of disarmament. Following the dissolution of the Soviet Union, these three states inherited more than 3,000 strategic nuclear weapons.16 These states agreed to forswear the nuclear weapons and join the NPT as NNWS under the Lisbon Protocol.16 International pressure caused these states to disarm, while Ukraine was also offered security and economic guarentees.[17] These cases show a more realistic story of disarmament.

Analysis of the debate on disarmament reveals a broader problem with the NPT. The NPT is inherently a discriminatory treaty, as it defines nuclear weapon states, and non-nuclear weapon states, and does not allow for new NWS. This distinction assigns different rules to different members, which has unsurprisingly led to tension. In order to relieve these tensions, it is necessary for NWS to put a greater emphasis on disarmament, and to create a more open discussion on plans to reduce the number of weapons worldwide. Although there are arguments on why disarmament is not in the best interest of the "haves," these countries have a legally binding obligation to do so. Although the treaty is discriminatory by nature, its ultimate goal is to ensure a world without nuclear weapons, which means that no states codified as NWS would exist. Most argue that the treaty is the only institutional way to achieve this goal.

IV. Failure in 2015: Middle East Weapons of Mass Destruction Free Zone to blame and a larger trend

Discussion on the Middle East Weapons of Mass Destruction Free Zone (MEWMDFZ) is the major reason for the collapse of the 2015 RevCon, because the US, UK, and Canada rejected the draft provisions on this topic. This does not mean the document was perfect otherwise, and some argue this failure based on the MEWMDFZ issue might have come to the relief of delegations who no longer faced the need of explaining to their bosses why they approved a text that lacked the disarmament language they had hoped for. The final blow in 2015 stemmed from the 2010 Review Conference final document's call for a conference on

a MEWMDFZ by 2012.[8] This conference was never held, and therefore became a foreseen cause of dispute five years later. The issue reportedly remained a mystery until the last day of the conference when Egypt revealed a paper full of demands: The "Arab Paper" called for the United Nations Security General (UNSG) to call the conference within 180 days of this RevCon, cutting out multilateral negotiations on the agenda and outcome. These "eyebrow raising demands"[9] caused experts to question whether Egypt's proposal was serious, or if the Egyptian delegation simply wanted to make noise about Israel. [9] In the end the RevCon President's final text proposed a conference convened by the UNSG after all States in the region agree upon an agenda and outcome, including Israel. All decisions made in the preparatory consultations for the MEWMDFZ needed to be made by consensus. But the conference could not be postponed for any reason, including a lack of consensus[9]. The United States did not accept the draft and the Review Conference ended without an agreed upon final document.

Although the MEWMDFZ seemed to be the ultimate cause for the absence of a final document, a separate theory suggests a pattern of failure larger than individual RC failures or successes. The Dunn Theorem argues that back-to-back successes are a rarity in reference to NPT Review Conferences.[9] This theory seems to hold truth. Historically, each alternating RevCon can be viewed as a "flop." Is this a coincidence, or is this grounded on an understandable pattern of events? It's hard to tell for sure, but these seeming coincidences could reflect the importance the NPT holds for member states: Back-to-back failures may seem too risky for the only existing treaty preventing the spread of nuclear weapons and material. If negotiators are of this mindset, they would increase effort to agree on a document following a failed conference. This theory is one possible way to explain historic outcomes of the NPT RevCons, although it is impossible to know for certain why this trend exists. Some argue that an agreed upon document doesn't necessarily reflect a "successful" conference, which questions whether a trend is even evident.

V. Future Challenges and Recommendations

The outcome of the 2015 RevCon makes it evident that there are clear challenges to the NPT and the nonproliferation regime at large. One future recommendation is to continue to support the treaty to the fullest extent possible. Because of some evident flaws in the treaty, such as required unanimous consensus on the final document at RevCons and its discriminatory nature, there is often some question as to whether the creation of a new treaty would be more effective, but this option, especially from the current U.S. perspective, is not pragmatic and is viewed by many as potentially undermining the NPT. There is some agreement among experts that creating a new document (for example, a Nuclear Weapons Convention), will be highly difficult, as it will not command broad support and will be viewed as undermining the NPT. This seems to be of consensus in the expert community, at least in NWS, as creating a document with this broad support for such goals seems near impossible. However, understanding the flaws in the NPT and its review conferences is essential for the international community to work towards adapting processes that utilize the document to its full potential, and ultimately work towards the goal of a world free of nuclear weapons.

The importance of the NPT must not be understated when looking ahead. President John F. Kennedy predicted in his famous 1963 speech that 15 to 25 nations could possess nuclear weapons in a decade. [11] This seems far-fetched to us today, as only three states have attained nuclear weapons since the NPT entered into force in 1970, making a total of nine states with nuclear weapons. There are multiple reasons some experts could argue that the NPT is failing. The failure of NWS to fufill article VI obligations is a cause for concern. The lack of a formal response to noncompliance, as seen in the case of North Korea is another area where the NPT is weak. Experts also point out that nonstate actors such as terrorist groups can not join the NPT. Some argue that all states want to obtain a nuclear weapon, but are incapable of this. Experts often find this logic to be flawed, claiming that 44 states are capable of developing a weapon, but make a conscious political choice not to.[11] One explanation for this seems to be that the NPT has provided political deterrence for developing nuclear weapons programs. A general rule for international law asserts that the longer this treaty is in place, the stronger it becomes. A strong international treaty heightens the cost of developing a nuclear weapons program, as states want to avoid being the outsider in relation to the international community, and wish to abide by nuclear norms. If we look at the realistic capabilities of NWS it is clear the enormous role the NPT has played in deterring proliferation. Although it is imperfect, it is essential in moving towards a more peaceful world free of nuclear weapons. As Obama stated in his 2009 Prague speech: "I'm not naive. This goal will not be reached quickly –- perhaps not in my lifetime. It will take patience and persistence. But now we, too, must ignore the voices who tell us that the world cannot change. We have to insist, 'Yes, we can.'"[18] With the help of the NPT, we can make this seemingly idealist vision a future reality.

VI. References

[1]Deterring Nuclear Proliferation: The Importance of IAEA Safeguards- Michael D. Rosenthal

[2]https://history.state.gov/milestones/1961-1968/npt

[3]http://www.un.org/disarmament/WMD/Nuclear/NPT.shtml

[4]http://cns.miis.edu/npr/pdfs/103stoi.pdf

[5]http://foreignpolicy.com/2013/09/03/think-again-american-nuclear-disarmament/

[6]http://cns.miis.edu/nam/about.html

[7]http://www.reachingcriticalwill.org/images/documents/Disarmament-fora/npt/revcon2015/statements/27April_NAM.pdf

[8]http://www.inss.org.il/index.aspx?id=4538&articleid=7766

[9]ttp://armscontrolwonk.com/

[10]http://www.un.org/disarmament/HomePage/HR/docs/2002/2002July14_France.pdf

[11]http://www.internationalpolicydigest.org/2014/11/29/non-proliferation-treaty-irrelevant/

[12]http://www.independent.co.uk/news/world/europe/vladimir-putin-announces-russia-will-add-40-new-ballistic-missiles-to-nuclear-arsenal-in-2015-10323304.html

[13]http://www.defense.gov/npr/docs/10-05-03_Fact_Sheet_US_Nuclear_Transparency__FINAL_w_Date.pdf

[14]http://www.nti.org/analysis/articles/united-states-nuclear-disarmament/

[15]http://www.nti.org/analysis/articles/south-africa-nuclear-disarmament/

[16]http://www.nti.org/analysis/articles/south-africa-nuclear-disarmament/

[17]http://adst.org/2014/04/making-the-world-a-safer-place-nuclear-arsenals-and-the-fall-of-the-ussr/

[18]https://www.whitehouse.gov/the-press-office/remarks-president-barack-obama-prague-delivered

VII. Acknowledgements

This project was supported in part by the U.S. Department of Energy, Office of Science, Office of Workforce Development for Teachers and Scientists (WDTS) under the Science Undergraduate Laboratory Internships Program (SULI). I would like to thank my mentor Susan Pepper for her guidance on this paper. I would also like to thank Katherine Bacher for her guidance and assistance.

Preliminary tasks for charge coupled device quantum efficiency measurements

Thomas Smith
Mathematics Department, Saint Joseph's College, Patchogue, NY, 11772
Ivan Kotov
Instrumentation Division, Brookhaven National Laboratory, Upton NY, 11973

The purpose of this research is to gather information that will be used to calculate the quantum efficiency of the charge coupled devices (CCDs) used in the Large Synoptic Survey Telescope (LSST). Quantum efficiency (QE) is simply the ratio of the number of photons hitting the sensor, to the number of charge carriers (electrons) produced. This measurement is given in electrons per photon, or amps per watt. Although the formula QE = (# of photons / # of electrons) is simple, we don't know how many photons are hitting the sensor, so this number must be calculated another way. The formula that we actually use is:

$$QE_{ccd} = \frac{Ne_{ccd}}{Np_{ccd}} = \frac{Ne_{ccd}}{\frac{Q_{pd}}{Q_e}} * R_{pd} * QE_{pd} * \frac{A_{pd}}{A_{ccd}}$$

Where Ne is number of electrons, Np is number of photons, Q is charge, R is the ratio of photodiodes and A is area. Most of these quantities are either already known (Area, QEpd, Qe) or will be measured at run time (NEccd, Qpd), however, the ratio of the photodiodes must be measured and calculated in advance. Most of my work this summer was focused on measuring and calculating the ratio for all wavelengths of visible light, near ultraviolet light, and near infrared light (about 300-1100 nm wavelengths).

The QE analysis code, written in C++, is used to take input from a monitoring photodiode and a CCD in order to determine the quantum efficiency of the CCD. The code in its current iteration can also take input from 2 photodiodes. This feature is useful because various analysis and calibration tasks must be performed with the photodiodes before we can begin the QE analysis on the CCDs.

The first of which was monochromator calibration. The code was used to plot the signal coming from the monitoring and calibrated photodiode, and by comparing relative magnitudes at different wavelengths to their relative magnitudes in the NIST spectral database, we were able to correct the offset to properly calibrate the monochromator. There is a full report available on this calibration.

Another use for this code that was implemented this summer, was finding the ratio of the monitoring to the calibrated photodiode with respect to wavelength. This ratio will be used in the quantum efficiency tests. This uses a baseline subtraction and integration method to obtain both values, then dividing these values to find the ratio. The baseline subtraction and integral will be discussed in detail.

I. Finding the baseline

Finding the baseline of the photodiode readings is critical in getting useful information out of these readings. The baseline often has a significant magnitude that must be accounted for, and for very small signals the difference between the baseline and zero is actually larger than the difference between the signal and the baseline. For this reason, we need an accurate, fairly robust way to find the baseline.

In all iterations of the code the way the baseline is found is similar. A range is calculated around the neighborhood of the baseline, and then a histogram is made with the bounds of the histogram being these found values. When this is plotted it should contain nearly all of the points of the baseline, which when experiencing a normal amount of noise should resemble a Gaussian. The histogram is then fitted with the Gaussian, and the mean of the Gaussian is the baseline.

One thing that is different with the original version of the code compared to all future iterations is the way the bounds for the histogram are found. The original way was not sensitive to small signals and was more vulnerable to small noise spikes. The following code details how the bounds for the histogram were found in this way:

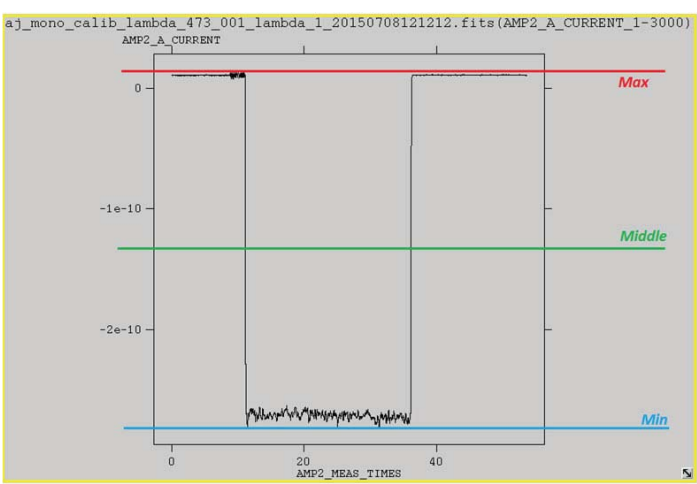

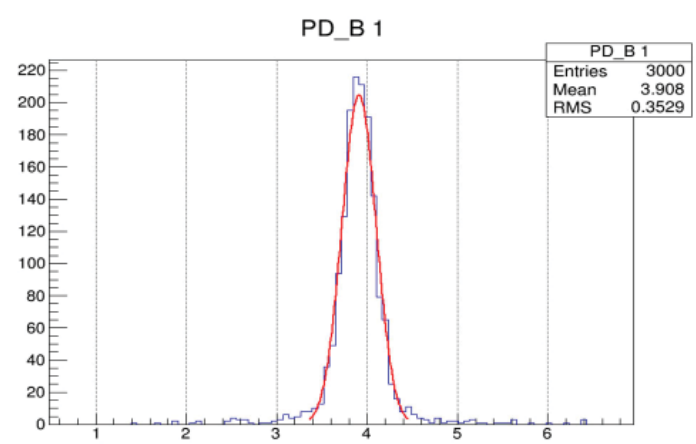

```
double max = *std::max_element(FileF::TabData[1].
begin(),FileF::TabData[1].end());
double min = *std::min_element(FileF::TabData[1].
begin(),FileF::TabData[1].end());
double maxa = (max<0)?-max:max;
double maxw = 4.*sqrt(maxa);
double maxR = ( (min+1.) < (max-maxw) )?max-max-
w:min+1;
PDhisB[nf] = new TH1D(title, title, 100, maxR,
max + 2.);
```

It is important to note that since the signal is negative the baseline will be near the max value.

A problem that arose with this is that when the signal was small, the signal level was so close to the baseline that it would be included in this interval, and thus would cause the Gaussian to be fitted improperly.

Another method which proved to be much more robust was created to deal with this problem. This new method found the baseline in the following way: The max and min values were found, and then an average was found to determine the middle value. Assuming a relatively uniform level of noise (or even some small noise spikes) for the signal and the baseline, the middle value would be pretty close to what it should be. Everything above this middle line was assumed to be baseline values, and everything below this line was assumed to be signal values (because signal is negative).

The average of all the baseline values was calculated, which served as a midpoint of our baseline range. The difference between this value and the max is then calculated and called dB (not to be confused with dB as in decibels). The range of values for the histogram is established as being from the average minus dB to the average plus dB (the max). Since the average is the center point of the range, the baseline values will be centered in the histogram and the range is restricted to the minimum size to include the all of the baseline values. This has the added benefit that more bins of the histogram are being used and a more accurate Gaussian fit is possible. The code for this is as follows:

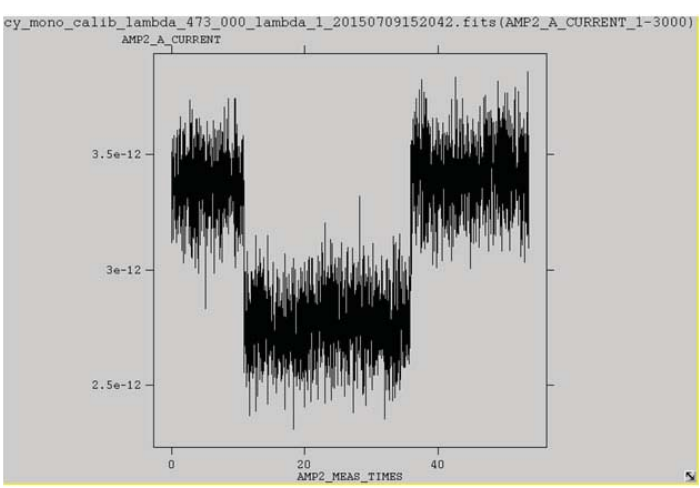


```
double max = *std::max_element(FileF::TabData[1].
begin(),FileF::TabData[1].end());
double min = *std::min_element(FileF::TabData[1].
begin(),FileF::TabData[1].end());
double middle = (max + min) /2;
double numB = 0., AvB = 0.;
for(int i = 0; i < FileF::nrows; i++){
if(FileF::TabData[1][i] >= middle){
      AvB += FileF::TabData[1][i]; numB++;
}
}
if(numB > 0) {AvB /= numB;}
else {AvB = 0.;}
double dB = max – AvB;
double rangeB = AvB - .95*dB;
PDhisB = new TH1D(title, title, 100, rangeB, max);
```

Although it is more computationally expensive because of the for loop, the benefit is a more robust and accurate baseline calculation (the impact on actual run time is negligible).

The following image is the baseline histogram for a large signal with a fitted Gaussian.

The code is now also able to handle very small signals where noise can be a problem. Here is an example of a reading with a very small signal. We can see that the lowest points of the baseline are actually lower than the highest points of the signal level. When this is the case, we want the baseline range to be as restricted as possible, so there is not too much overlap to alter the Gaussian fit.

In the following histogram, we see that to the left there is a little bit of overlap with the signal; however the Gaussian fit is not affected.

II. Finding the integral

Now that we have the baseline, we are able to perform our integral calculations. These integral calculations are important because the picoammeters give us the current with respect to time. The value that we are interested in for quantum efficiency is the charge. Charge is found by integrating current with respect to time.

In order to get the best results, several different methods of integration were used and compared to find the best one. All methods use a rectangular integral approximation where the signal value minus the baseline is multiplied by the time of the respective value. Time is calculated by taking the time of the next value minus the time of the previous value, divided by 2.

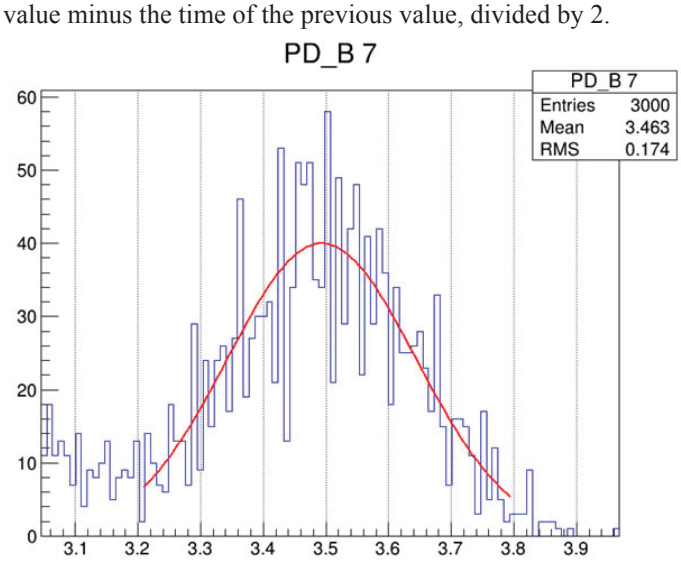

A. First method of integration:

The first method picks a point somewhere in the center of the signal and uses pointers to move from that point to the right, while totaling up the areas of the rectangles, until it reaches a value higher than the baseline. Then, it returns to the original point and moves left, while totaling up the areas of the rectangles, until it reaches a value higher than the baseline. The sum of these two total areas should make up the total area of the signal (the signal integral). This method works pretty well in most cases, but there are at least 2 cases in which this method would give a false area.

1- If there is a small signal, the noise within the signal area will often go above the baseline, causing the pointer incrementing/decrementing loops to stop early yielding an area that is too small. The following reading may experience this issue in at least one place.

2- Even with a good large signal, huge noise spikes could also cause the integration loops to end early for the same reason as above.

This is the integration function:

```
double   PhDi::Integral(vector<double>::iterator first,
            vector<double>::iterator last,
            vector<double>::iterator point,
            const double base,
            const double b_rms,
            double & readings,
            vector<double> & Time,
            double & iTime )
{
  int indx;
  double ti;
  double Int = base - *point;
  double InT = Int/60.; // should be: *nplc/60.;
  double limit = 4.*abs(b_rms);
  if (abs(b_rms) < 0.0001 ) limit = 0.1*(base - *point);

  if (first == last) return Int;

  indx = std::distance(first,point) - 1;
 if (point==first)  {ti = Time[indx+1] - Time[indx];}
   else  if  (point==last)  {ti  =  Time[indx]   - Time[indx-1] ;}
 else     {ti =(Time[indx+1] - Time[indx-1])/2.;}
  InT = Int*ti;

  vector<double>::iterator stop, start;
  stop = start = point;
  for (; stop != last; ++stop) {
    double val = base - *stop;
    if ( val < limit) break;
    Int += val;
    indx = std::distance(first,stop) - 1;
      if  (stop==first)     {ti  =  Time[indx+1]  - Time[indx]  ;}
     else  if  (stop==last)  {ti  =  Time[indx]   - Time[indx-1] ;}
  else     {ti =(Time[indx+1] - Time[indx-1])/2.;}
    InT += val*ti;
  }
  for (; start != first; --start) {
    double val = base - *start;
    if (val < limit) break;
```

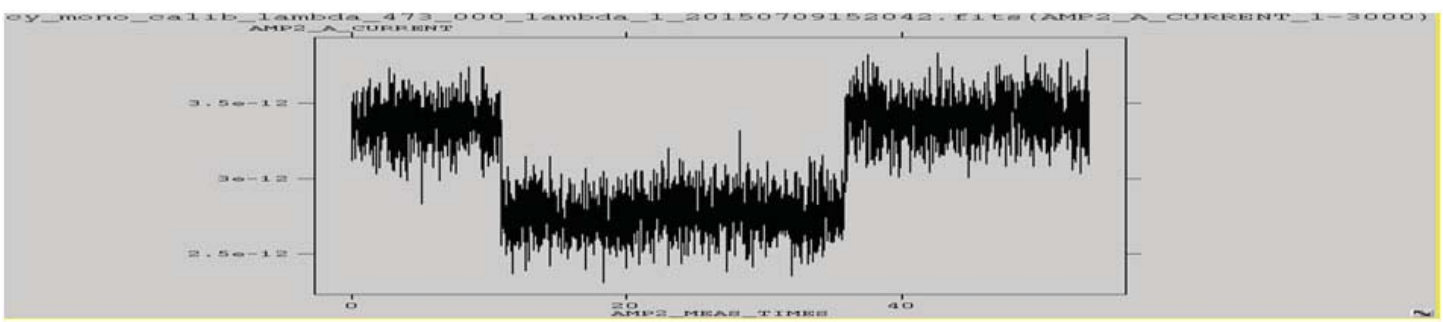

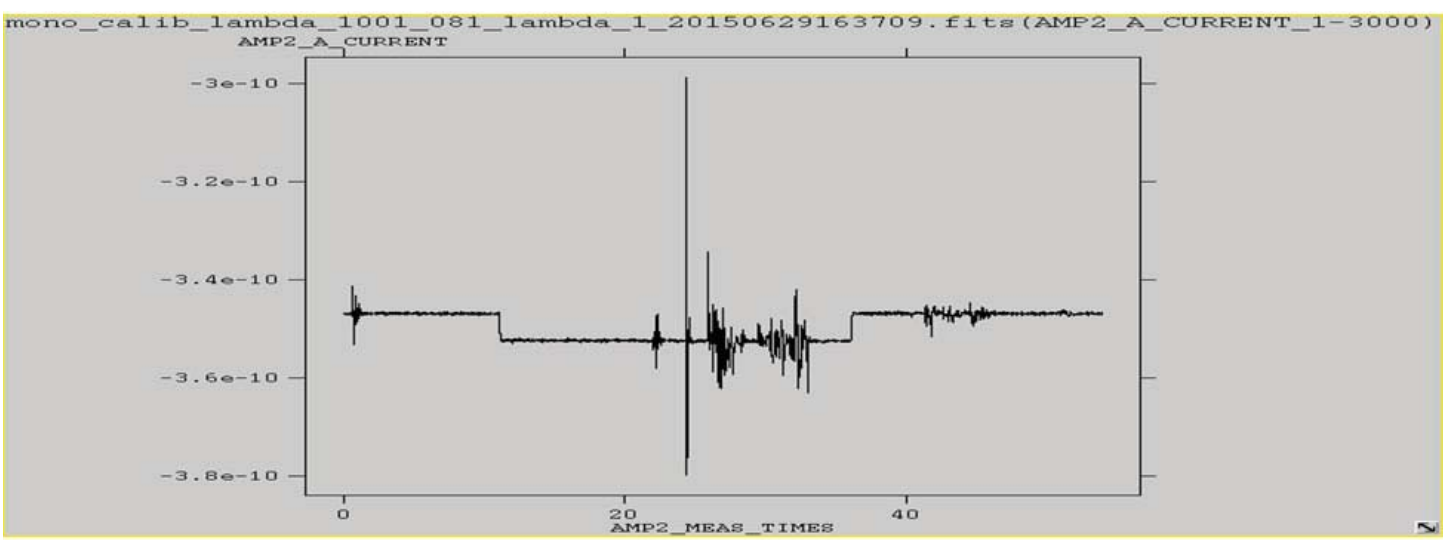

```
    Int += val;
    indx = std::distance(first,start) - 1;
      if (start==first)    {ti = Time[indx+1] -
Time[indx]  ;}
     else if (start==last) {ti = Time[indx]  -
Time[indx-1] ;}
  else     {ti =(Time[indx+1] - Time[indx-1])/2.;}
    InT += val*ti;
  }
  readings = std::distance(start, stop);

  int ind_strt = std::distance(first,start) - 1;
  int ind_stop = std::distance(first,stop) - 1;
  iTime = Time[ind_stop] - Time[ind_strt];

  return InT;
}
```

B. Improving the integral:

In order to make integration as robust as possible, we wanted to eliminate the code having to make decisions. We created a function that just integrated the entire set of values from start to finish with respect to the calculated baseline. The baseline values do fluctuate by small amounts, but because the calculated baseline is the center of the Gaussian of these values, the integral of the entire reading should cause the baseline values to cancel themselves almost completely out. This means that in the end the calculated integral should be just of the signal. This method has at least 3 distinct advantages over its predecessor.

1- The code does not make decisions, so there is less that can go wrong and all calculations are more consistent, predictable, and easy to debug if something does go wrong.
2- Small signals can be integrated with good accuracy
3- This code is generally resistant to most noise spikes. This is because most noise spikes are symmetrical and cancel themselves out, even large ones.

One issue that is an area of continued interest is developing analysis code that is robust to asymmetric noise spikes as they don't cancel themselves out when integrated.

This is the code for the new integral function called IntegralTotal:

```
double PhDi::IntegralTotal(vector<double>::iterator first,
          vector<double>::iterator last,
          const double base,
          vector<double> & Time,
          double & iTime )
{
  int indx = 0;
  double ti;
      double InT = 0.0;
```

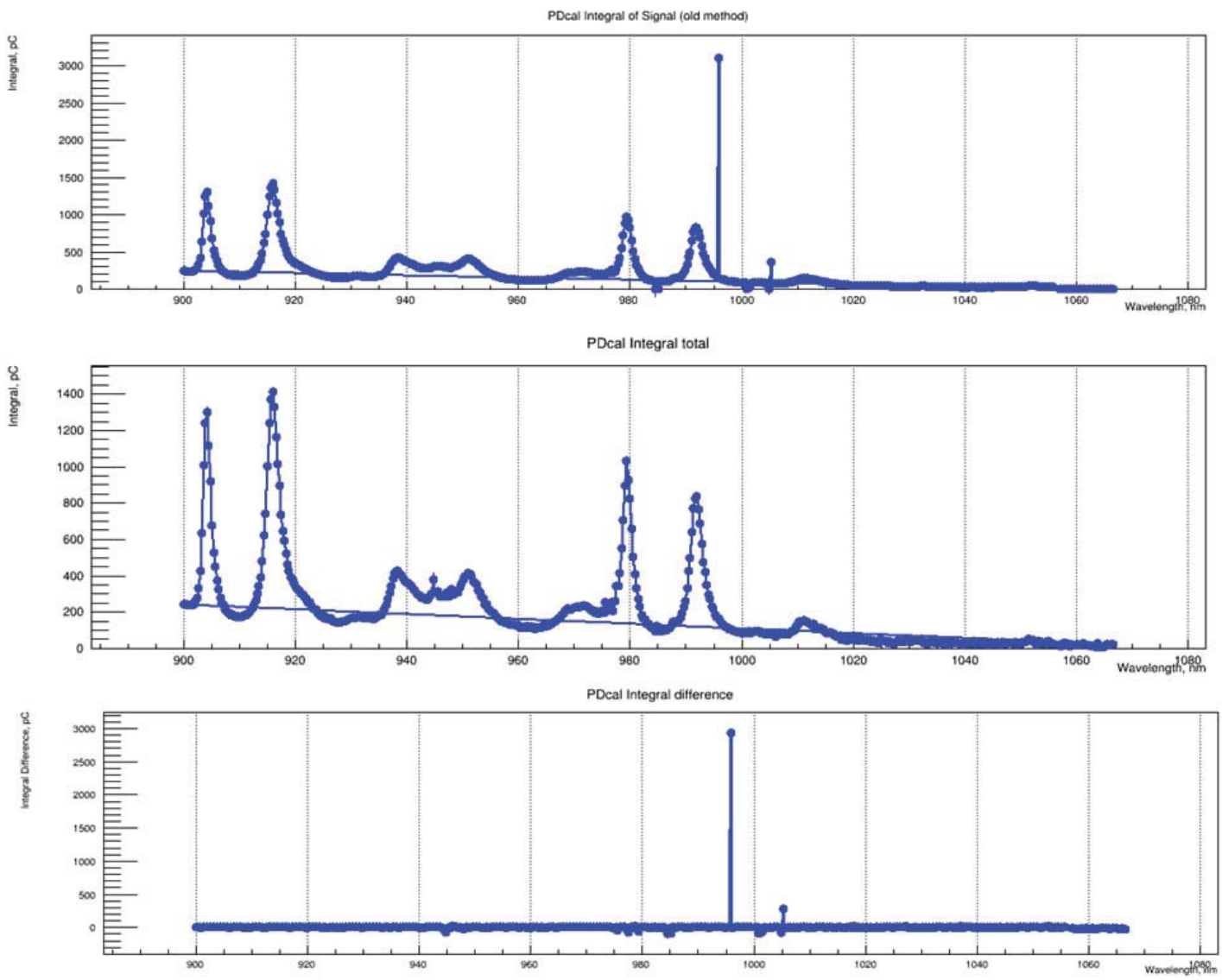

```
      vector<double>::iterator stop, start;
  stop = start = first;

      double val = base - *stop;
      ti = Time[indx+1] - Time[indx];
      InT += val*ti;
      indx++;

  for (; stop != last; ++stop) {
             val = base - *stop;
   if (stop==last) {ti = Time[indx]  - Time[indx-1]
;}
  else     {ti =(Time[indx+1] - Time[indx-1])/2.;}
    InT += val*ti;
             indx++;
  }

  int ind_strt = std::distance(first,start) - 1;
  int ind_stop = std::distance(first,stop) - 1;
  iTime = Time[ind_stop] - Time[ind_strt];

  return InT;
}
```

III. Comparison of integration results

In order to compare the performance of the different integration methods, a plot was added to the analysis code that will display 3 graphs: Integral with old method, integral with new method, and the difference between the two (old minus new). This is the plot of the integrated signal from the calibrated photodiode plotted against wavelength during a scan from 900 to 1066nm:

We can see that the total integral was able to successfully integrate readings that gave the original method difficulty (due to high noise) while preserving the accuracy the old method had when integrating good readings. The average difference between the two methods for good readings were plus or minus <10pC.

This project was supported in part by the U.S. Department of Energy, Office of Science, Office of Workforce Development for Teachers and Scientists (WDTS) under the Science Undergraduate Laboratory Internships Program (SULI).

Replacement of the Nd:YAG Chiller

Derek Squires
Engineering Science, Suffolk Community College, Selden NY 11784
John Biemer and Ariel Nunez
Facilities and Operations, Brookhaven National Laboratory, Upton NY 11973

ABSTRACT

Supply of cool, clean air is a primary concern for many work spaces at Brookhaven National Laboratory. Not only is it important to provide comfortable cooling in general office spaces, but it is even more important to provide the proper environment in many laboratory and experimental areas. A chiller is responsible for removing the heat absorbed by a refrigerant from the return air of a space and returning it to a lower temperature. The chiller then supplies the colder refrigerant to the air handler for further cooling of the space's air. At the Accelerator Test Facility in building 820 there are specific temperature and humidity ranges that must be met to operate the YAG laser. On April 29, 2015 the existing chiller failed and a temporary chiller was immediately connected to continue operation of the laser. In the meantime, a nearly identical chiller was located at the Fire Protection Division that will replace the failed chiller. The challenge to overcome with the new chiller was two-fold. First, the replacement chiller has a lower voltage requirement than the failed chiller (208 volts versus 460 volts). Second, the condenser coil of the replacement chiller is located in a different part of the chiller and, therefore, the outlet and inlet piping are in different locations than the failed chiller. My main responsibility for this project was to assist the Facility Complex Engineer, Ariel Nunez, with designing the piping requirements to adapt the new chiller to the existing piping of the failed chiller. I generated AutoCAD drawings to assist the plumbers in completing this task. From this project, I have gained valuable experience in the AutoCAD drafting program and learned about the various code requirements for electrical and mechanical engineering projects.

I. INTRODUCTION

The YAG laser room is a Class 1,000 clean room that requires strict humidity and temperature conditions. If the temperature fluctuates outside of the targeted range of 72-72.2 degree Fahrenheit or the 40-50% humidity range then the experimental results of the room's users could be compromised. To prevent this situation, the room has a dedicated air conditioning system. This system is comprised of many components that contribute to the successful operation and monitoring of these conditions. On April 29, 2015 the existing chiller for the clean room failed. Initially, the AC mechanics were receiving alerts that the compressors within the unit were tripping out. After concluding that one of the compressors failed, a rental chiller was ordered and installed on May 1, 2015. The failed unit was inspected and a condenser coil leak was discovered. This leak caused a pressure drop in the refrigerant piping of approximately 200 psi. Additionally, when refrigerant leaks from a coil there is also a loss of oil from the system. This particular unit has hermetically sealed compressors that require a very specific amount of oil circulating through its loop for proper lubrication. In the event of poor lubrication there can be damage to various parts of the compressor. When a hermetically sealed compressor has internal damage it needs to be completely replaced because there is no access to the various components inside the compressor.

While the rental unit was operating, the Facility Project Manager, John Biemer, and the Facility Complex Engineer, Ariel Nunez, consulted the laser room's users to evaluate possible permanent solutions to this problem. The first possible solution was to completely replace the unit by purchasing a brand new unit from a manufacturer. Purchasing a new unit can be costly and the estimated investment in this project was at least $30,000 for the unit and the associated labor. The second possible solution was to utilize a unit from the Fire Protection Division that had been used briefly but had since been replaced. It had already been purchased and, therefore, would be free to use for this project. The only costs involved would be the labor involved by various trades. The estimated cost for this option was $20,000.

Conveniently, this unit provides 20 tons of cooling, the same amount of cooling that the failed unit provided. It did, however, have different electrical and plumbing requirements and labor costs would apply to this project as well. The failed unit operated under 480 volts while this newer unit only required 208 volts. Also, the newer unit's evaporator had vertically aligned inlet and outlet connections to the glycol/water piping while the failed unit had horizontally aligned piping connections. My summer project was to assist Ariel Nunez with the resolution of this two pronged problem and successfully adapt the new chiller to the existing piping and electrical configuration.

II. PROGRESS

The initial task to this project was to choose a location for the new unit. The failed unit was located on a concrete pad to the south of the building. There was plenty of existing space for the new unit and it provided flexibility in terms of location. Originally, Mr. Nunez and I wanted to locate the unit near the center of the pad, close to where the failed unit had been. This location would allow us to minimize the piping modifications necessary and, therefore, lower the costs of new piping and fittings. The final decision, however, was to locate the unit as far south as possible. This location allowed for the inclusion of an in-line strainer near the inlet of the unit, braided vibration eliminators, and new pressure and temperature gauges. If the unit had been placed further north it would have limited the space for these new components and would compromise the quality of the unit's operation.

Once this location was chosen, we worked to design the optimal piping configuration. Reducing the friction of fluids within the piping is an important consideration while designing HVAC systems. In order to reduce the fluid friction within the new pip-

ing, we used 45 degree elbow fittings to direct the new piping towards the inlet and outlet connections. This configuration would have been ideal but it would limit the space available for future maintenance of the chiller's compressors. Upon installation the plumber's maximized the space for this maintenance by using 90 degree elbows. These fittings kept the new piping closer to the existing piping. If a compressor ever needed replacement, the mechanics would now have ample room to work safely and efficiently.

To assist in the proper installation of the piping, I created an AutoCAD representation of the design Mr. Nunez and I had created. This drawing helped the plumbers understand which components to include and where they belonged in the new piping arrangement. Additionally, there was a lot of discussion regarding where to locate the new electrical disconnect for the new unit and where it would be in relation to the new step-down transformer. These types of plans are integral to the successful planning and execution of engineering projects in the workplace. Without detailed plans it would be very difficult to estimate materials and minimize the number of modifications needed during project completion. Due to the technical nature of many engineering projects, a significant amount of time and effort are invested in planning and coordination to reduce the likelihood of errors.

After the completion of the project, I took the final measurements for all of the new equipment and the existing equipment and constructed a 3D model of the area. This image shows that model and is labeled to provide clarification to the various components in the model. The model was created using Google's SketchUp program. I consider the experience I acquired with both AutoCAD and SketchUp to be invaluable and an enormous addition to my skillset.

III. FUTURE WORK

Since the installation of the new unit, experimental operations have continued and there have not been any significant issues with the conditions of the YAG laser room. The system will continue to be monitored and there will be normal, routine scheduled maintenance on the components of the system. Because of the new plumbing work, insulation work is needed and will be scheduled once all of the parties involved agree to move forward with finalizing the project.

IV. IMPACT

The YAG laser provides significant contributions to the missions of both the Department of Energy and Brookhaven National Laboratory. There is a lot of research that takes place at this facility and users travel from across the world to run their experiments with the YAG laser. This project, therefore, is instrumental in maintaining the opportunities for these users to continue their research. If this cooling system were to cease permanently, so would the operations of the room. The bulk of the funding for this project falls under what is called "chargeback" work. Because the facility requires cooling 24 hours a day and 7 days a week for scientific and experimental reasons, the Facilities and Operations department is not responsible for most of the costs. Learning about the various funding methods was a great experience and certainly new for me.

Figure 1 shows the horizontal arrangement of the former chilled water piping

V. CONCLUSION

Overall, this project provided experiences with many different aspects of both engineering and project management. It was exciting to witness the planning aspects and the design aspects of a project with such significance to Brookhaven National Laboratory and the Department of Energy. The workplace skills I acquired during this project were also invaluable and are skills I will take with me wherever my engineering career takes me.

VI. APPENDIX

A. Participants:

Name	Institution	Role
John Biemer	Brookhaven National Laboratory	Mr. Biemer was my project mentor. He provided access to facilities, answers to project related questions, and insight into the project management career path. He also helped me understand the planning and coordination aspects of this project.
Ariel Nunez	Brookhaven National Laboratory	Mr. Nunez was the project engineer that guided me through the intricate details of the engineering process. He provided practical insights into what works and what doesn't work and for what reasons.

B. Scientific Facilities:

For this project I spent the majority of my time at building 820 (the Accelerator Test Facility) and building 728M, where my office was located.

C. Notable Outcomes:

As shown in the report, I generated drawings and schematics for the completion of this project.

Figure 2 shows the vertical arrangement of the chilled water piping

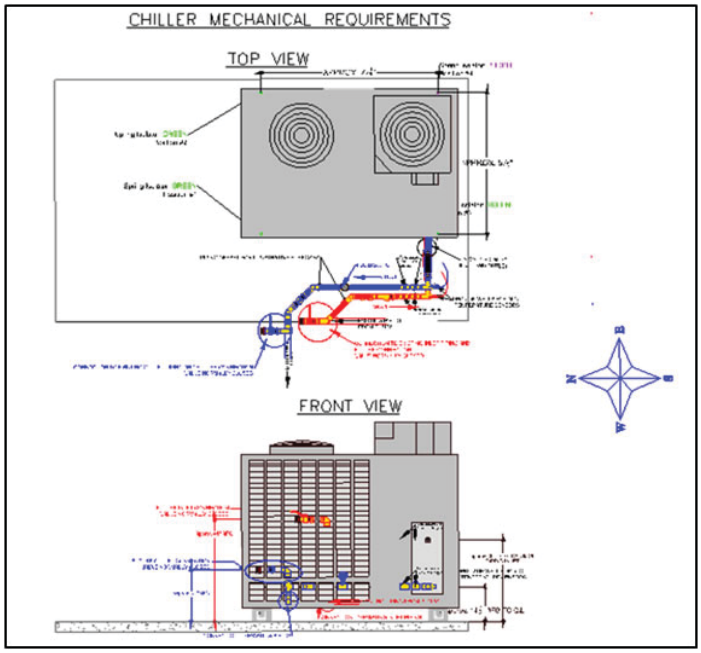

Figure 3 displays the AutoCAD drawings that assisted the trades in installing the unit

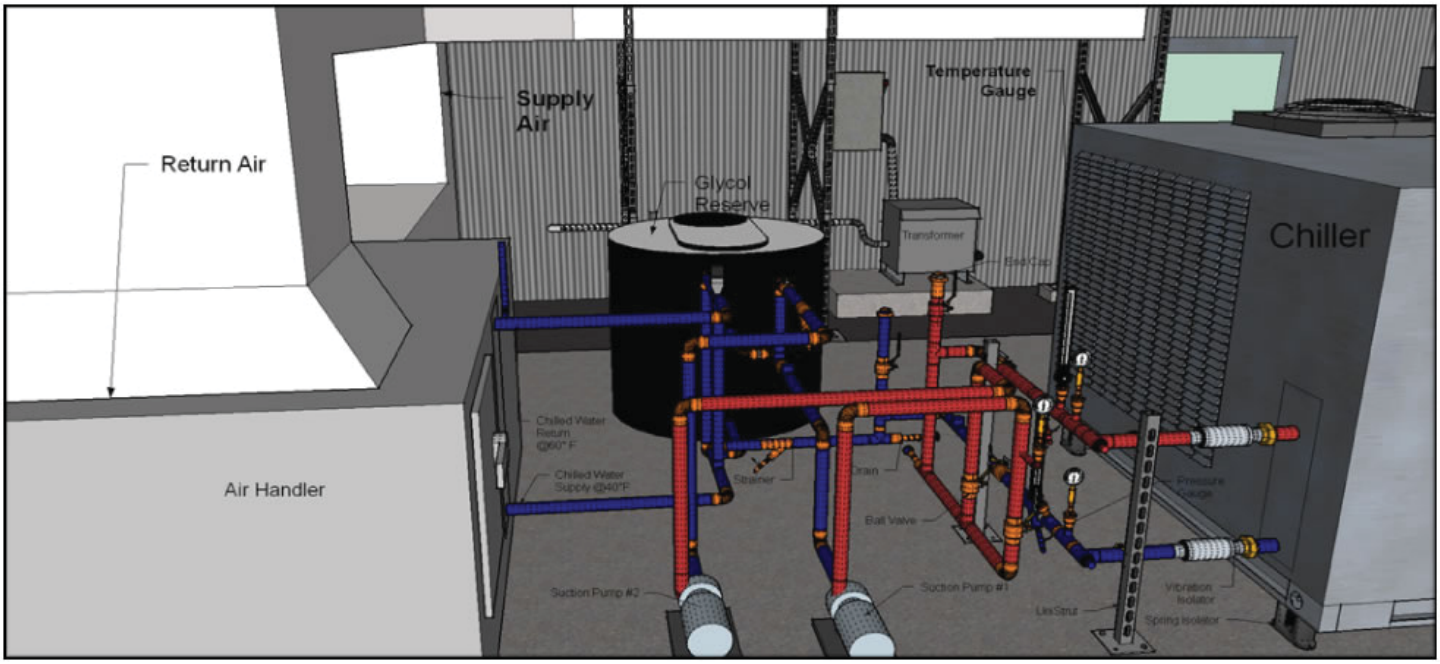

Figure 4 shows the 3D model of the final installation

Proton beam production using titanium hydride by means of a laser ion source

Cayla Stifler
Engineering Physics Systems Department, Providence College, Providence, Rhode Island, 02918
Masahiro Okamura
Collider Accelerator Department, Brookhaven National Laboratory, Upton, New York, 11973

Abstract

Laser ion sources can produce a variety of ions through the laser ablation of a solid target. Such sources provide low charge state ions to the Electron Beam Ion Source (EBIS) to create high charge state ion beams, which are used in collaborations like the Relativistic Heavy Ion Collider and NASA Space Radiation Laboratory. Since proton beams have not been successfully produced at EBIS via a laser ion source, finding a method to create proton beams can improve the versatility of the laser ion source at EBIS. Previous studies suggest the capability of producing proton beams from titanium hydride using a neodymium doped yttrium aluminum garnet (Nd: YAG) laser with a nanosecond laser pulse. We considered the capability of titanium hydride targets for proton production using a 170 ps laser pulse. The results showed the titanium hydride target could produce protons. We also increased the proton peak current by 51.5% using a solenoid with a magnetic flux density of 6 G. The results indicate the possibility of using a sub nanosecond pulsed laser with a titanium hydride target in a laser ion source with further investigation.

I. Introduction

Laser ion sources produce ion beams by irradiating a solid target via laser ablation to produce plasma. Previous studies show using a laser power density over 108 W/cm^2 is necessary to create plasma.[1] Currently, Brookhaven National Laboratory (BNL) uses a laser ion source, LION, as an external source of primary ions for the Electron Beam Ion Source (EBIS). EBIS is a heavy ion pre-injector that provides ions for the Relativistic Heavy Ion Collider and NASA Space Radiation Laboratory. The main advantage of using a laser ion source as a source of primary ions is to make more ion species available for fast switching. By switching the laser irradiation position to different solid targets, different species of ions are produced in a short amount of time. Another advantage of LION is that it does not require the use of discharge gas resulting in a cleaner vacuum and a higher intensity ion beam. LION also produces higher current beams, which can be trapped by EBIS in a short period of time resulting in high efficiency and a narrow charge state distribution.[2]

A solid target sufficient for use in LION to produce proton beams has not yet been developed. Previous studies have found it difficult to produce proton beams from frozen hydrogen targets due to the sublimation temperature of hydrogen being close to the lower limit of the cryo-cooler head.[3] Other studies have shown the creation of proton beams from metallic hydrides using a nanosecond pulsed laser including magnesium, zirconium, and titanium hydride.[3,4] This study tested the production of proton beams using a sub-nanosecond laser on a titanium hydride target. Using a sub nanosecond laser pulse has the potential to reduce target consumption.

II. Materials and Methods

Figure 1 shows the experimental setup. The titanium hydride target in the vacuum chamber was irradiated with a Nd: YAG laser of wavelength 1064 nm with a pulse width of 170 ps. The incident angle between the laser path and beam line was 20 degrees. The vacuum pressure in the chamber was below 2.5x10-4 Pa.

A Faraday cup (FC) with a 10 mm aperture located 2.4 m away from the target was used to measure the beam current. The suppressor voltage of the FC was set to -3.5 kV. We analyzed the plasma with an electrostatic ion analyzer (EIA) with selected ions detected using a secondary electron multiplier (SEM). The total distance between the detector and the target was 3.7 m. The ion species and charge state were determined from the SEM time of flight information and the voltage applied to the EIA.

An aluminum shell was used to hold the titanium hydride powder with the dimensions shown in Figure 2. The powder was pressed for 30 minutes with 10,000 lbs. of pressure. After 30 minutes, the pressure was increased back to 10,000 lbs. and pressed

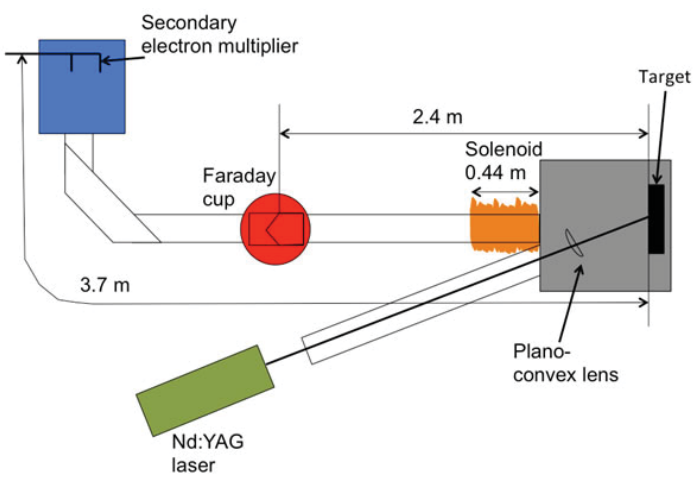

Figure 1 Laser ion source experimental setup

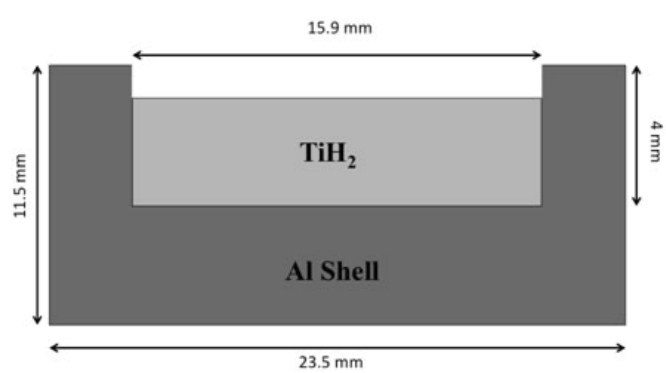

Figure 2 Cross section of titanium hydride powder in aluminum shell

for an additional 15 minutes. We used titanium hydride powder labeled at 99% purity.

III. Results

A 250 mm focal length lens was first used to focus the laser, producing a spot size with diameter of 8.7 mm and power density of $1x10^9$ W/cm^2. Figure 3 shows the total ion current from the TiH_2 target measured by the FC. Figure 4 shows the charge state distribution of the analyzed plasma based on the EIA and SEM data. Based on these data, the faster peak in Figure 3 can be identified as hydrogen.

To increase the hydrogen signal, we changed the lens to one with a focal length of 120 mm, producing a spot size with diameter of 2.9 mm and power density of $4x10^{10}$ W/cm^2. Figure 5 shows the total ion current from the TiH_2 target at the higher power density measured by the FC. Figure 6 shows the charge state distribution of the analyzed plasma based on the EIA and SEM data.

The analysis assumes the SEM sensitivity is proportional to charge state. All currents are normalized to a distance of 1 m from the target and a cross sectional area of 1 cm^2 according to the scaling laws of expanding plasma, $t \propto L$ and $I \propto L^{-3} * S$, where t, L, I, and S are time, length, current, and cross sectional area respectively. Since there was not much overlap between the proton and the titanium peaks, the sum of the SEM data was scaled to the hydrogen peak in the FC signal.

We used a solenoid to further increase the peak current of hydrogen ions. To see the effect of the solenoid, we chose to only look at the FC signal because the SEM data reveal that there is minimal overlap between hydrogen ions and other species. The maximum amplification of the hydrogen peak occurred at a magnetic flux density of 6 G, with the peak hydrogen current increasing by 51.5%. The maximum amplification of the main peak occurred at a magnetic flux density of 30 G. Figure 7 shows the comparisons of the FC signal for magnetic flux densities 0 G, 6 G, and 30 G.

IV. Summary

We observed a proton beam from a titanium hydride target using a sub nanosecond laser pulse. The current for titanium ions was higher than the current for protons in all experimental conditions. Increasing the power density of the laser by an order of magnitude and adding an external magnetic field using a solenoid

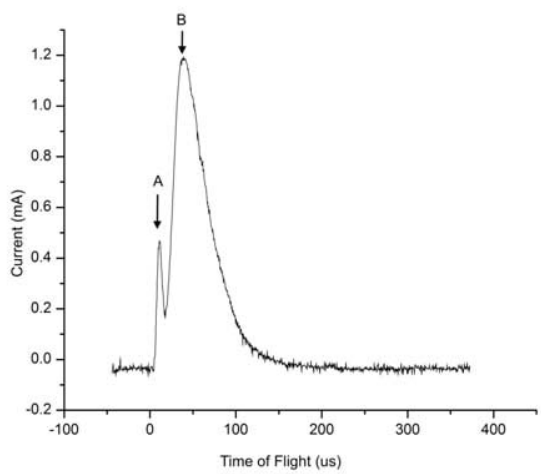

Figure 3 Ion current of TiH_2 target measured by FC for power density of 1x109 W/cm^2. Peak A shows H^+ and peak B shows ionized Ti.

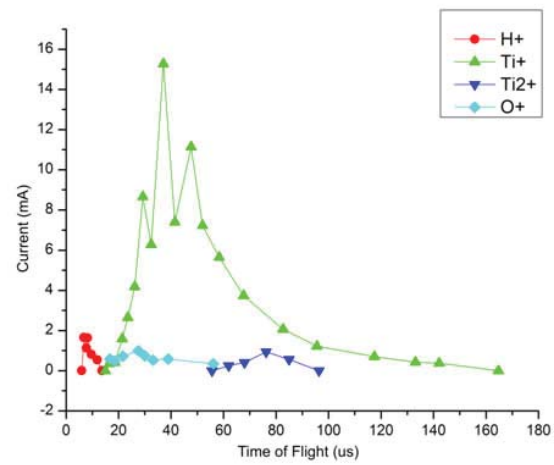

Figure 4 Analyzed laser plasma of TiH_2 target for power density of 1x109 W/cm^2.

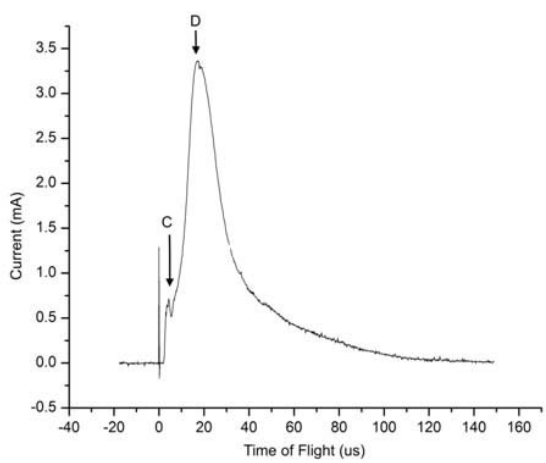

Figure 5 Ion current of TiH^2 target measured by FC for power density of $4x10^{10}$ W/cm^2. Peak C shows H^+ and peak D shows ionized Ti.

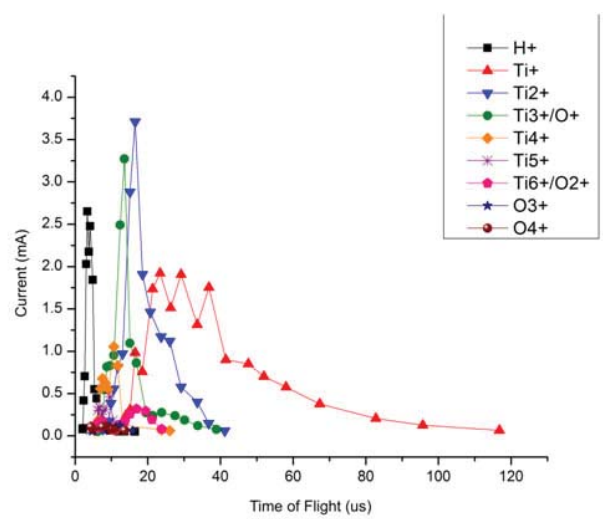

Figure 6 Analyzed laser plasma of TiH_2 target for power density of $4x10^{10}$ W/cm^2.

increases the proton peak current as detected by the FC, but does not suppress the titanium ions. In order for titanium hydride targets to be used in LION as a source of protons, the proton current will need to be selectively increased over titanium ions, a topic for future investigation.

V. References

[1]K. Kondo, T. Yamamoto, M. Sekine, and M. Okamura, Rev. Sci. Instrum. 83. 02B319 (2012).

[2]T. Kansue et. al., Proceedings of International Particle Accelerator Conference 14, WEOAB01, (2014).

[3]M. Sekine, K. Kondo, M. Okamura, and N. Hayashizaki, Rev. Sci. Instrum. 83. 02B318 (2012).

[4]L. Torrisi, AAPP| Physical, Mathematical, and Natural Sciences. 89, no. 2 (2011).

VI. Acknowledgements

I would like to thank Dr. Dannie Steski and Dr. Takeshi Kansue of BNL for their contributions to this project.

This project was supported in part by the U.S. Department of Energy, Office of Science, Office of Workforce Development for Teachers and Scientists (WDTS) under the Science Undergraduate Laboratory Internships Program (SULI).

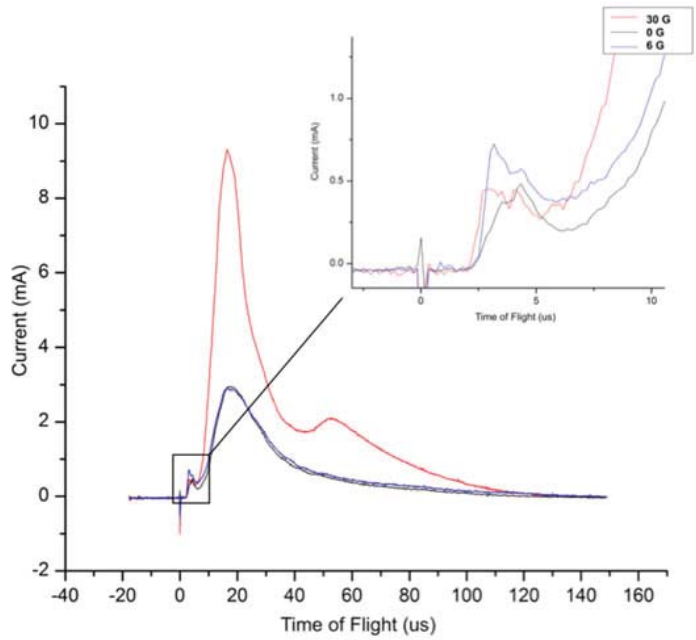

Figure 7 Ion current measured by FC for different magnetic flux densities

Investigating the feasibility of instrument comparison as a means for analyzing data on aerosol concentrations.

Ariel Stolz
Mechanical Engineering, Brown University, Providence, RI 02912
Scott Smith
Biological, Environmental and Climate Sciences Department, Brookhaven National Laboratory, Upton, NY 11973

Abstract

Scientists are still lacking an understanding of aerosols and how to represent them accurately in climate models. This project investigates the viability of using instrument comparison to analyze aerosol concentration data, and also use the data to make a conjecture on the size distribution and type of aerosols that may be the cause for concentration increases. Data were collected from the DOE/ARM funded Aerosol Observing System (AOS) on atmospheric aerosol concentrations from specific locations in May 2015. Using MATLAB and IgorPro, the project compares data from two instruments, the Condensation Particle Counter 3772 (CPC) and the Ultra High Sensitivity Aerosol Spectrometer (UHSAS). The UHSAS measures the size distribution and number of particles within a 0.055 - 1 µm particle diameter and the CPC 3772 range overlaps but also measures particles down to 10nm diameter. The CPC usually measures some oscillation around an average concentration. However, numerous times the concentration increases drastically within a short timespan. The objective is to pinpoint when spikes in the CPC data correlate with the UHSAS data. To measure this we used different statistical techniques, such as calculating the correlation coefficient and generating contour plots. Speculations can be made on the types of aerosols causing the increased concentration based on whether they are within the specific size range. It was difficult to find consistent correlation due to a large amount of sub 55nm particles outside the UHSAS range. Comparing solar irradiance graphs and CPC and UHSAS aerosol concentrations showed that solar radiation might influence new particle formation and growth of aerosols because there was higher correlation a few hours after high solar irradiance indicating particle growth to a size within the UHSAS range. The results of this study are useful in better understanding atmospheric aerosol concentration changes in the area based on an instrument comparison.

I. Introduction/Background

Data were collected from the ground-based DOE/Atmospheric Radiation Measurement Climate Research Facility (ARM) funded Aerosol Observing System (AOS). The AOS pulls air through the sample inlet and then vacuum pumps air through the multiple instruments; each measuring specific parameters of the aerosol content. The mission of ARM is to create remote access stations to measure atmospheric data, including data on aerosols, to better understand climate change and improve upon the climate prediction models [Mission and Vision Statements. ARM U.S. Department of Energy]. In climate models there are two main uncertainties: the first is how clouds affect global radiation; and the second is the distribution and transference of radiation vertically within the atmosphere [Atmospheric System Research (ASR) Science and Program Plan. 2010]. Both these uncertainties are related to aerosol research. Understanding aerosols will enable us to better understand the climate changes we face today and to better predict the future based on increased anthropogenic aerosol production.

Instrument comparison can be extremely useful in making inferences on the data collected. Because aerosols can be extremely variable based on the day, season, or certain global or local events, it is important to verify the data. Instrument comparison is a practical method of assuring accurate data because if two instruments measure the same anomaly it is highly likely that it actually occurred. In 2008 Cai et al, a UHSAS, CPC and other instruments were used to measure aerosols remotely at a site in the Wyoming mountain-tops. Using multiple instruments to compare data they were able to draw conclusions regarding which instruments were better able to measure certain particles of interest and were able to use this to further their research.

II. Methods & Materials

This project compared the data of two instruments which employ different techniques of measuring aerosols. The instruments chosen were the CPC 3772 and the UHSAS. Below are description of how each of these instruments operate.

A. Condensation Particle Counter 3772 (CPC 3772):

Before air enters this instrument it is pulled through a filter to remove aerosols that are too large. This instrument uses live-time coincidence counting to detect any particle with a diameter range of 10 nm – 1 micron at a flow rate of 1.0 L/min. The CPC 3772 can measure particle concentrations within a range of 0 to 10^4 particles/cc. This instrument uses Butanol as the pressurized working fluid. Measurements are recorded every second. ["Condensation Particle Counter Model 3772 Manual." TSI Incorporated. 2015].

B. Ultra high sensitivity aerosol spectrometer (UHSAS):

The UHSAS is an optical spectrometer that can measure particles with a range of 0.06-1 microns. It uses an infrared laser with wavelength 1.054 µm with 1kW of power to detect the volume of the sample by measured radiation scattering. The data can be presented as a histogram showing the count of aerosols within each size distribution. Measurements are averaged over 10 seconds. ["Ultra-High Sensitivity Aerosol Spectrometer Manual (UHSAS)." Droplet Measurement Technologies, 2014]

MATLAB, Igor Pro and Excel were programs used to ana-

lyze the data by creating graphs and running statistical correlations tests. I used MATLAB was used to search data for missing or repeated data points. Occasionally the data can have errors: this can be in the form of missing or repeated timestamps. This erroneous data creates difficulties in running averages and creating graphs. Adjustments by adding empty rows or deleting duplicates were made. The data were averaged so that the instrument's different time units could be accurately compared and to reduce the impact of outliers. The integral of the UHSAS data was taken by totaling each of the histogram bin counts. The units were corrected so that it also measured particles per cm^3.

$$Concentration = \frac{\text{Äconcentration}}{flow\,rate * measurement\,time}\ particles\ per\ cm^3$$

$$= \frac{\text{Äc}}{50cm^3/min * 10\sec * 1min/60\,sec} = \frac{\text{Äc}}{8.\overline{66}}\ particles\ per\ cm^3$$

III. Data and Results

Data were gathered from the CPC 3772 and UHSAS from the location Brookhaven National Laboratory for one week on the days May 25th to May 31st, 2015 Greenwich Mean Time (GMT) [May 24th 20:00 – May 31st 20:00 local time EST].

Multiple methods were used in order to analyze the data. The integral of the USHAS data or a total particle count was compared to the CPC concentration measurement. The data were plotted for the entire week (Figure 1) and also for one day, May 31st (Figure 2). Visually the CPC and UHSAS seem to be following a similar trend however there are many points in which the CPC experiences spikes in concentration but the UHSAS does not. On May 31 there is a large growth event for the CPC measurements that is followed a few hours later by a growth event of the UHSAS.

A correlation test was used in order to find the deviations in the CPC data from the UHSAS data. Because the CPC measured a larger range of diameter sizes, if the machines are operating correctly the CPC particle per cm^3 count should always be either larger than or equal to the UHSAS total sum in particle per cm3. Fluctuations in aerosol concentration of a particle sizes lower than 55nm would cause a drastic difference between the CPC and integral of UHSAS data, however changes above 55 nm would be recorded by both instruments and so the data would fluctuate simultaneously and the difference would remain similar. To obtain information about the correlation coefficient the two data sets were plotted against each other to show linear regression (Figure 3). The UHSAS data are along the x-axis and the CPC data are along the y-axis. The correlation coefficient or R^2 value measures the deviation of the data from the line of best fit, a correlation of

UHSAS and CPC 3772 concentration data for one week with 10 sec average

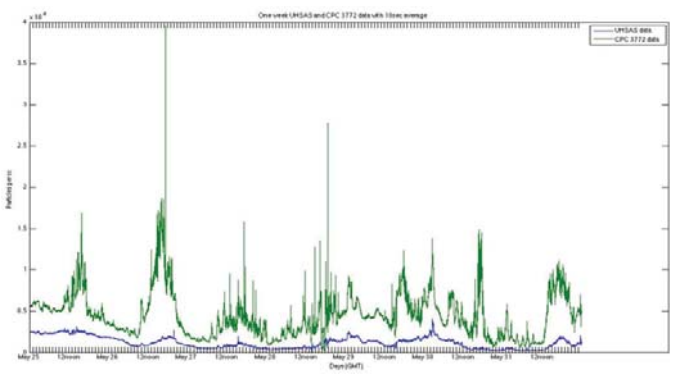

Figure 1: This graph displays the CPC count in particles per cm3 over a 10 second average in green and integrated UHSAS data also over 10 second in blue. The graph covers May 25- May 31st GMT. The CPC count is expected to be above or equal to the UHSAS because it can count particles below 55nm.

May 31 UHSAS and CPC 3772 concentration data for one week with 10 sec average

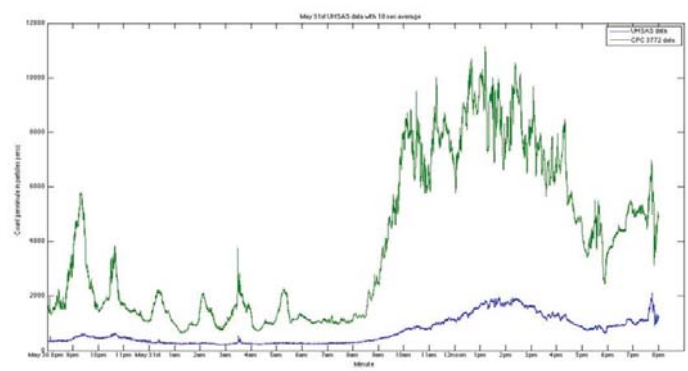

Figure 2: This graph displays the CPC count in particles per cm3 over a 10 second average in green and integrated UHSAS data also over 10 second in blue. The data is from May 30 8pm – May 31st 8pm EST. Visually there seems to be a slight correlation between the two data sets, especially during the hours from 7am - 8pm.

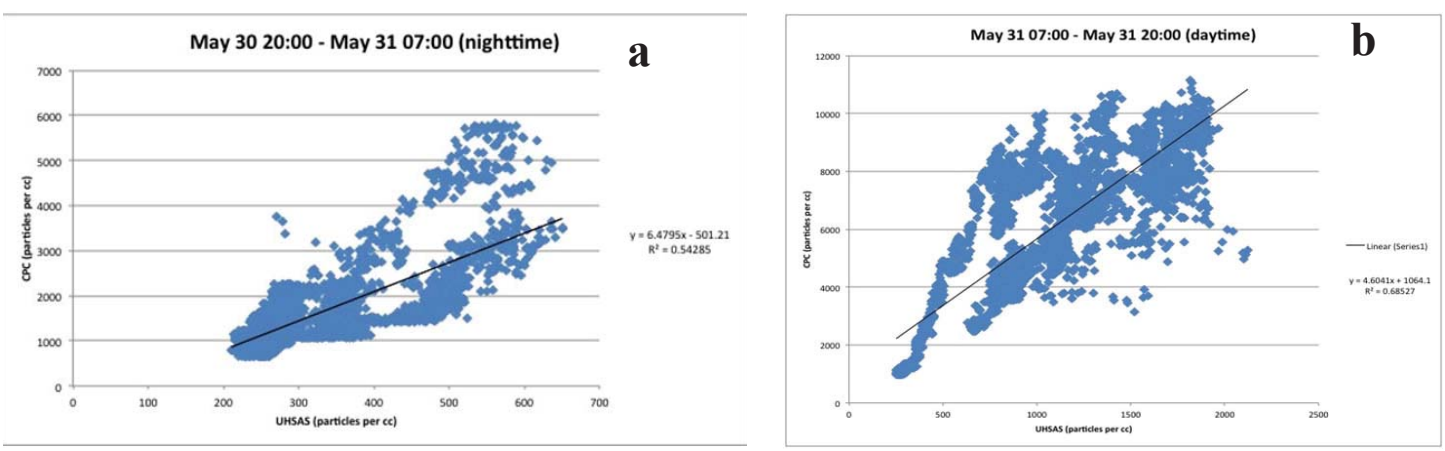

Figure 3: These graphs show the correlation between the UHSAS and CPC data sets for May 30th (a) nighttime and May 31st (b) daytime. The y-axis is CPC data and the x-axis is UHSAS data. The correlation coefficient or R^2 value is 0.5485 for the nighttime and 0.68527 for the daytime. One hypothesis is that energy from solar radiation could be a factor in creating new particle formation events.

1 means that the data is perfectly correlated while 0 means there is no correlation. The correlation was variable ranging from a low correlation of 0.15886 and a high correlation of 0.82717. Correlation tests were also taken for the day and nighttime separately (Table 2) to see if factors such as solar radiation had any effect on aerosols and the correlation between the instruments.

Table 1: Correlation coefficient for each day GMT

Date	Linear Regression (R^2 value)
May 25th	R = 0.40072
May 26th	R = 0.15886
May 27th	R = 0.54886
May 28th	R = 0.71591
May 29th	R = 0.31093
May 30th	R = 0.38063
May 31st	R = 0.82717

Table 2: Correlation coefficients separated by daylight and nighttime.

Date	Linear Regression (R^2 value) NIGHTTIME	R^2 value DAYTIME
May 24th	R = 0.0424	
May 25th	R = 0.0326	R = 0.63305
May 26th	R = 0.13767	R = 0.3313
May 27th	R = 0.52275	R = 0.50988
May 28th	R = 0.81031	R = 0.33593
May 29th	R = 0.60779	R = 0.2058
May 30th	R = 0.5485	R = 0.10203
May 31st		R = 0.68527
Average	**R = 0.386**	**R = 0.40048**

UHSAS data were plotted as a contour plot in order to gain insight into possible causes of increases of aerosols in the area, whether this be new particle formation events or primary anthropogenic aerosol sources. Considering the contour plot below (Figure 4) which shows data for May 31st GMT, there seems to be an outburst of sub 100nm aerosols around 16:00 GMT (12:00 EST). In Figure 2 this increase in particles corresponds to a spike in the integral of the UHSAS data. Also the CPC concentration increases about 2 hour after sunrise, which was recorded at 4:23 EST. Since the UHSAS only measures down to 55 nm the formation of this aerosol cloud may have occurred minutes to hours earlier because as time passes the diameter of the aerosols will increase as they grow by either condensation or coagulation.

The CPC can either be a higher concentration or an equal concentration to the UHSAS because it has a more inclusive range that includes the smaller particles below 55 nm down to 10nm. By measuring the difference between the CPC and UHSAS information could be gathered on how many sub 55 nm particles were present. In Figure 5 there are two peaks on the histogram; one peak is located approximately at a difference of 2000 particles and the other at 4000 particles. So there are usually 2000 or 4000 sub 55 nm particles present at BNL.

IV. Analysis

Using the data collected over one week a few hypotheses could be formed which can be tested further in the future by including more instruments to compare and continuing to collect and gather data over larger time-spans and different times of year. The analysis is split into three sections.

A. Aerosol type based on sizing

Spikes in CPC could indicate there was an aerosol cloud passing from a primary anthropogenic source such as an idle truck or cigarette smoke or a secondary aerosol source from new particle formation. Because the UHSAS only measured particles above 55nm inferences could be made based on the different between the total concentrations measured by each instrument. According to Figure 5 there are often events in which 2000 or 4000 sub

UHSAS contour color map [May 31 2015]
Concentration of Particles Log Scale

Particle Diameter Log Scale

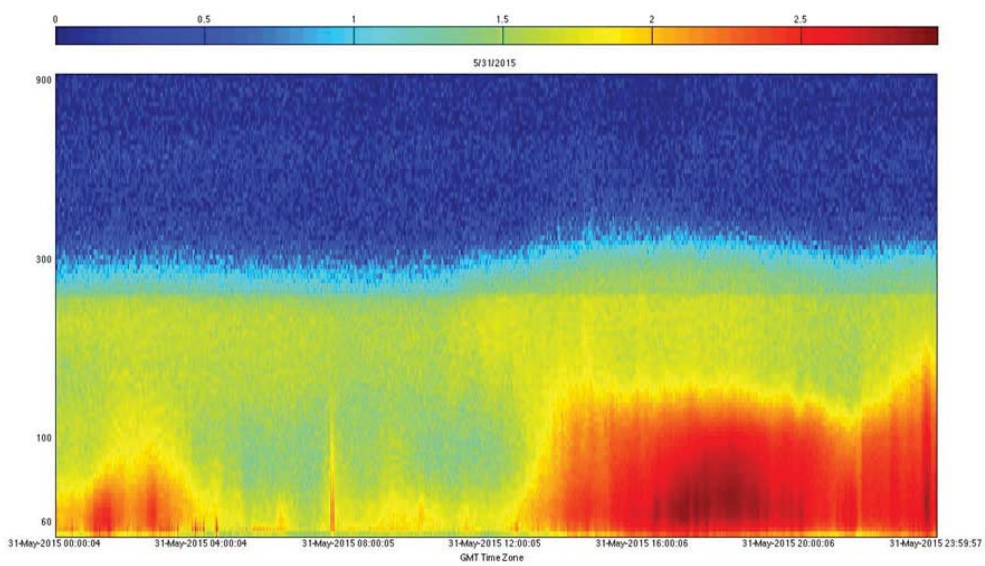

GMT Time Zone

55nm particles are created. There are also multiple instances with a large influx of small particles up to 37,000 small particles. With only the UHSAS as a comparison it is difficult to find correlation because of the large amount of small diameter particles present at BNL.

B. Aerosol Growth over time

Aerosols grow over time by either condensation or coagulation. Usually condensation is the main factor for aerosol growth. Coagulation is more likely to occur when there is a large concentration of aerosols because it involves the aerosols colliding and combining into a single particle with a larger diameter. On May 31 the data appear to replicate a new particle formation event because around 7:00 EST the CPC shows a sharp increase in the particle concentration and 5 hours later at around 12:00 EST the UHSAS also begins to show an increase. The growth of particles over time could explain this phenomenon if the origin of the aerosol cloud occurred at particle diameters smaller than the UHSAS can measure. Over time the diameter became measurable by the UHSAS; explaining the increases in the UHSAS integral. When the new particles have grown to above 55 nm, which would occur later in the day, the correlation coefficient should increase because both instruments are measuring more of the same particles. Using information on the correlation the growth rate can be estimated based on when the CPC first encounters the particles at 10 nm and when the UHSAS first encounters them at 55 cm. The correlation coefficient was the highest at 0.80826 during the time from 13:07:30 EST until 20:00:00 EST. If we estimate that the CPC started seeing particles grow to 10nm at 7:00:00 and by 13:07:30 the particles had reached 55 nm the growth rate is $\frac{45nm}{6.125hours} = 7.35nm/hour$ ··

C. Nighttime vs. Daytime

New particle formation and growth can be caused by incoming solar radiation as an energy source for chemical reactions. At BNL there is a large presence of small sub 3nm diameter particles as a result of new particle formation using solar energy as a catalyst for gaseous chemical reactions [Yu, H., et al. 2014].

This would cause higher correlation later in the day because the particles grow to 55nm and both instruments can measure the same concentration of particles. To test this solar irradiance plots were gathered for the days and compared to the CPC and UHSAS data to look for trends. During the daytime of May 31st, 2015 it was believed that there was a new particle formation event that may have been prompted by the solar radiation. On May 31st the sunrise occurred at 4:23 and daylight began approximately an hour later. Referencing Figure 6, a solar irradiance plot for May 31st, it appears to be a cloudy day due to the non-smoothness of the plot. Also at some points the solar irradiance is higher than the peak irradiance from the sun. This is due to channeling reflected light from the high albedo clouds tops to the surface.

V. Conclusion

By conducting an instrument comparison of the CPC 3772 and UHSAS we were able to make some inferences on aerosols at BNL. We found that there is a large portion of aerosol particles in the sub 55nm diameter range which can only been recorded by the CPC. This made it very difficult to find correlation between the UHSAS and CPC data. New particle formation is a possible origin of large amounts of small particles below 55nm. These particles appear to grow as time passes over the course of a few hours causing higher correlation a few hours after the formation event first hits 10nm. Solar irradiance may have an influence on the formation of new particles because the particles concentration increases similarly to solar radiation increases.

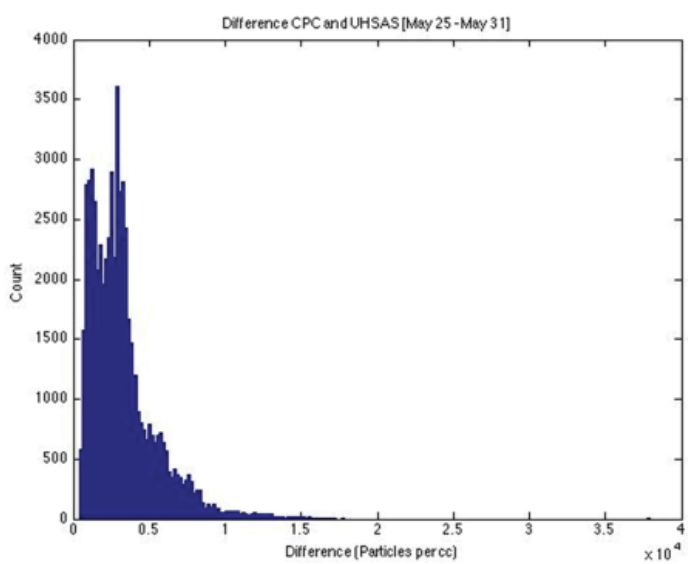

Figure 5: The integral of the UHSAS data was subtracted from the CPC concentration count to find the amount of particles with a diameter below the range of the UHSAS, 55 nm.

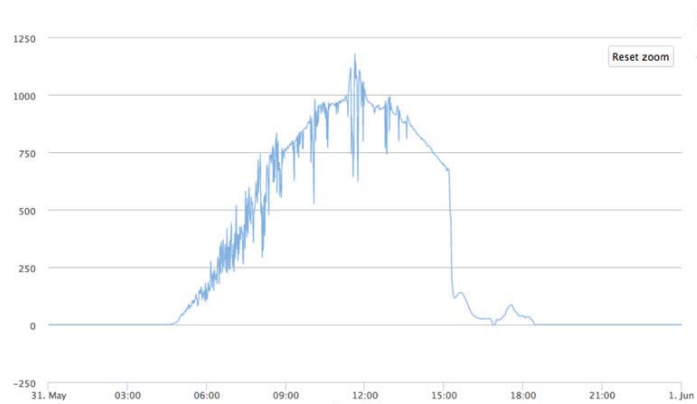

Figure 6: Solar Irradiance plot for May 31st. 2015. The y axis is the solar irradiance and has units of W/m².

VI. References

A. Instrument Manuals

"Condensation Particle Counter Model 3772 Manual." TSI Incorporated. 2015.

"Ultra-High Sensitivity Aerosol Spectrometer Manual (UHSAS)." Droplet Measurement Technologies, 2014. Web 27 July 2015. <http://www.dropletmeasurement.com/ultra-high-sensitivity-aerosol-spectrometer-uhsas.>

B. ARM & DOE Information

DOE Office of Science. "Atmospheric System Research (ASR) Science and Program Plan." ASR (2010). Web. 27 July 2015.

"Mission and Vision Statements." ARM. US Department of Energy. Web. 27 July 2015. <http//www.arm.gov/about/mission>.

C. Scientific Papers

Cai, Y., Montague, D.C, et al. (2008). Performance characteristics of the ultra high sensitivity aerosol spectrometer for particles between 55 and 800 nm: Laboratory and field studies. Aerosol Science. Vol 39, pp 759-769.

Podzimekj, J., Carstens, C., Yue, P.C. (1982). Comparison of several Aitken nuclei counters. Atmospheric Environment. Vol 16, pp 1-11.

Saha, A., O'Neill, N.T., et al. (2012). Analysis of sub-micron parameters derived from multi-altitude and multi-spectral AOD measurements acquired during the 2009 PAM-ARCMIP airborne campaign. Atmospheric Environment. Vol 52, pp 67-81.

Twohy, C.H., Anderson, J.R., et al. (2013) Impacts of aerosol particles on the microphysical and radiative properties of stratocumulus clouds over the southeast Pacific Ocean. Atmospheric Chemistry and Physics. Vol 13, pp 2541 – 2562.

Yu, H., et al. (2014), Sub-3 nm particles observed at the coastal and continental sites in the United States, J. Geophys. Res. Atmos., 119, 860–879,

VII. Acknowledgements

I would like to acknowledge the support of the Department of Energy (DOE) and the Science Undergraduates Laboratory Internships (SULI) Program. I would also like to thank Brookhaven National Laboratory and my mentor Scott Smith for hosting my summer research internship experience.

Reduction of photon scattering on the X-ray Powder Diffraction beamline's detector through radiation simulation

Dennis Tao
Physics, Stony Brook University, Stony Brook, New York 11794
Zheng Hua Xia
Photon Sciences, Brookhaven National Laboratory, Upton, NY 11973

Abstract

At the National Synchrotron Light Source-II (NSLS-II), we are constantly testing different currents to determine if beamline shielding is effective and if there are ways to improve the experimental setups. As radiation is invisible to humans and almost undetectable without use of technology, it is important to make sure there is no leakage. Therefore, it is important to constantly perform tests and simulations to make sure that researchers at the NSLS-II are exposed to as little as possible. Using the computer program FLUKA, I spent the summer at the NSLS-II estimating radiation scattering with different parameters for beamline 28-ID. The scientists wanted the least amount of scattering possible on the detector. This way their sample having the clearest picture on the detector when it is placed in the path of the beam. Other than learning how to operate the program through its manual, I also had to learn how to adjust the program to plot results for different points of view in order to have the clearest picture of the scattering. When completed with my first set of parameters, I created a PowerPoint presentation for the beam line scientists to discuss my results and plans for possible improvements to the beamline's setup. Major concerns throughout the discussion were possible ways to reduce scattering by the time the beam reaches the detector through inclusion or exclusion of materials.

I. Introduction

As photons leave the booster and enter the beamline, they are exposed to new environments. While the majority of the photons will remain in the beam's path, quite a few will deviate and scatter due to the surrounding materials. Such is the case at the XPD beamline, where the scientists there are attempting to reduce scattering at the end of the beamline, where a detector is set up to catch and record the fringe patterns created by the sample. The less scattering caused by the beamline onto the detector, the clearer the fringe pattern will be. Because there are many variables affecting how the photons are scattered, it is impractical to do real world trial and error to see what setup would be the most effective.

Throughout the summer, my project was focused on the reduction of scattering observed on the detector and to discover cheapest and most efficient method to do so. To do this, I used the program FLUKA to run simulations and presented the results to the scientists to discuss possible changes to the setup on the experimental floor in order to improve results. The program was able to generate various graphical representations, such as the one shown below, of nearly any setup I desired. Although there were a few bugs along the way, the program proved to be very effective and allowed me to better understand the scattering patterns.

II. Methods and Materials

After learning the program FLUKA, I placed the parameters that were being used in the beamline into the program and ran it. The initial set up is shown in the FLUKA diagram Figure 1, going from the right to the left. The beam passes through scattering slits then into a lead shield covered by a kapton film. The lead shield blocks a large portion of the scattering generated by the air and the scattering slits. The beam then enters a copper tube, where the air is taken out and the tube is sealed by kapton film. After exiting the tube, the beam passes through the anti-scattering slits, which are placed to prevent scattering from the tube to reach the detector placed at the end. Afterwards, the beam strikes a beam stopper, which is placed to prevent the high intensity of the beam from hitting the detector.

Figure 1 depicts the FLUKA results for the initial setup of the beamline, with the beam coming in from the right side and moving to the left. The closer the colors are to the red side of the visible light spectrum, the larger the concentration of photons (dose rate). Looking at the pattern, we can clearly see that the shield placed before the tube is highly effective in blocking a very large portion of the scattering caused by the scattering slits and air before it.

After some trial and error, I was able to collect consistent results and learn how to manipulate the program to also calculate the same setup with slightly changed parameters. I placed all of my results into a power point presentation and displayed it to my mentor, the head beamline scientist, and beamline engineer. My initial changes to the setup mostly involved altering the thickness of the lead shielding or copper tube. While this is important as less of a material means money saved, I found that the changes generally had little to no effect on the result on the detector. They suggested adding and removing some of the materials, to see a much greater effect that it would have on the results. My mentor

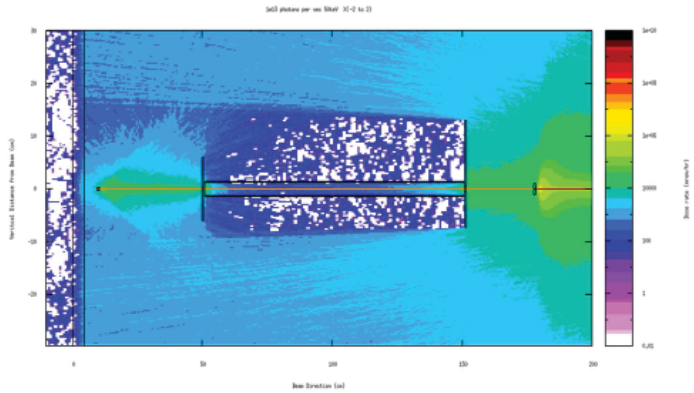

Figure 1: Initial setup of beamline. Tube is sealed with kapton and vacuum is inside.

also suggested changing the axis that I viewed the results on, as a view of the z axis would be more beneficial to compare with actual results on the detector.

Following their suggestions, I fixed up the setup and arranged it into three scenarios: removed tube and kapton windows, kapton windows sealing the tube, and the inclusion of a new lead tube at the end of the setup. I observed the difference in scattering on the detector in these three situations and found that the inclusion of the lead shield had the greatest effect on the experimental setup. The FLUKA results are shown below.

After sorting these results into another presentation, we had another discussion on what direction we should run the simulations in. Clearly, the inclusion of the lead tube was the most effective in reducing scattering out of the three. Therefore, the head scientist wanted to look at a more cost effective approach to the experimental setup. The last process I observed was about the necessity of air in the copper tube. This resulted in another three situations: one with kapton and air, one with kapton and vacuum, and one without kapton but with air. Again the results are shown below.

III. Results

From the results computed by FLUKA, it was clear that the extra lead tube proved to be very effective in blocking scattering. This makes sense, as the extra shielding would contain the photons and force them to exit through a much smaller opening. Seeing the success of this inclusion, the head engineer suggested putting a tube that they had on hand and seeing if it would have a similar result. The head scientist also suggested investigating the effects of the vacuum in the copper tube. Unfortunately, there was a bug in the program that made it unable to process the input file if I had both iron and kapton in it. I wasn't able to figure out why this was happening, so I changed the material of the stainless steel tube to lead and kept the dimensions the same. Doing so, I noticed

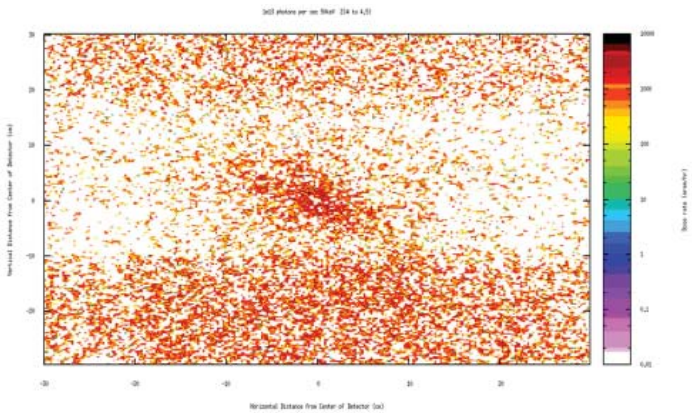

Figure 2: No copper tube or kapton windows

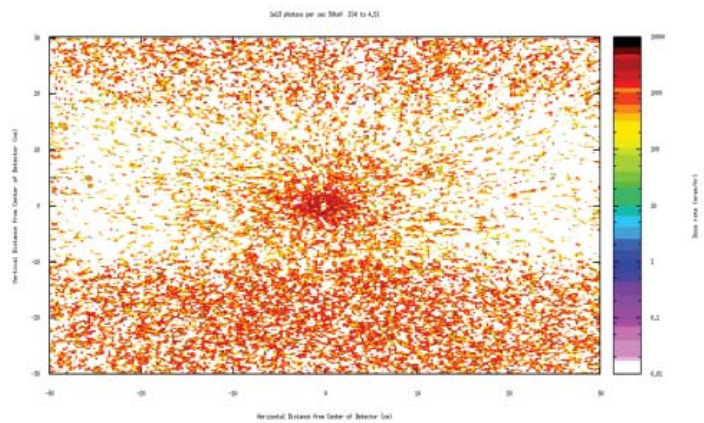

Figure 3: Initial double kapton with vacuum setup.

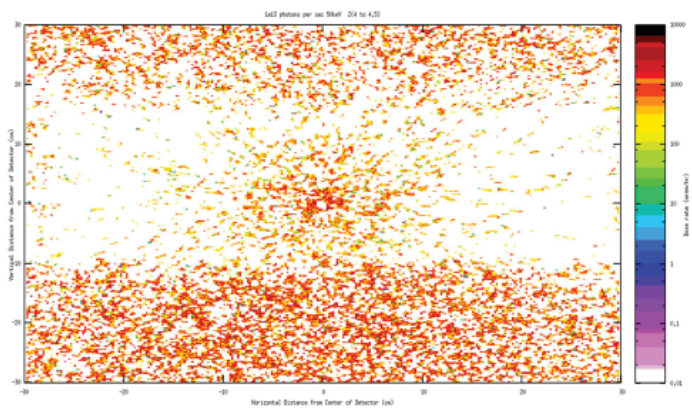

Figure 4: Inclusion of lead tube at the end of the experimental setup.

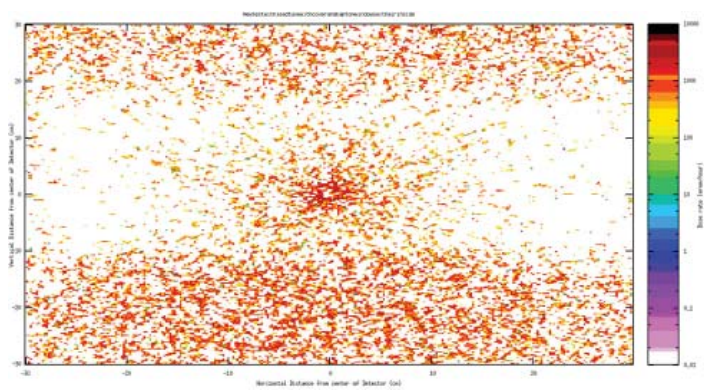

Figure 5: Kapton windows with air inside and lead tube

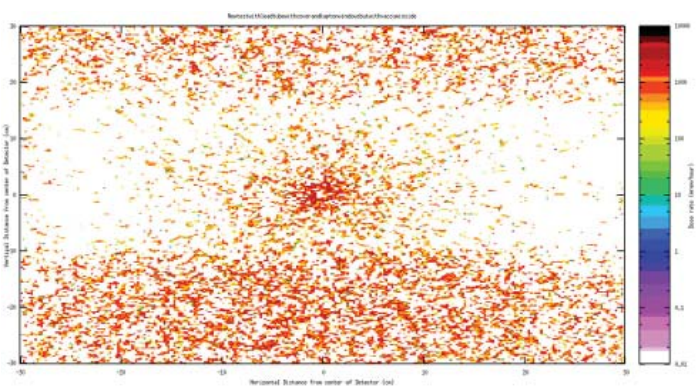

Figure 6: Kapton windows with vacuum and lead tube

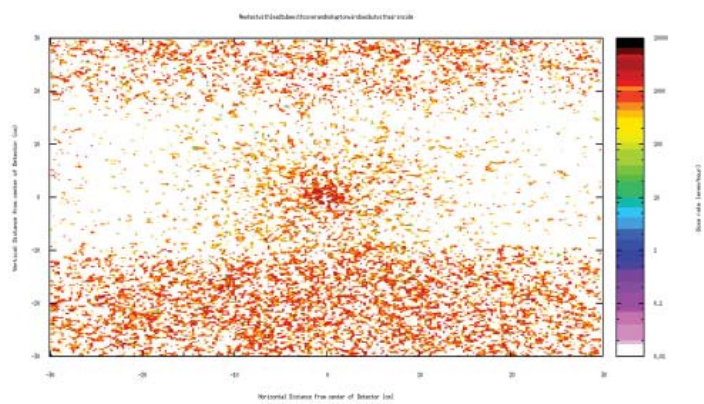

Figure 7: No Kapton windows with air inside and lead tube

that the new parameters worked effectively, though not as well as the initial lead tube that I had made up. If we compare figure 4 and figure 6, we can see that while slight, the figure 6 actually has more scattering. This is of course due to the changed parameters, as I made the parameters similar to the tube that was described to me. Regardless, it is clear that despite the changed parameters, the lead tube is highly effective.

Comparing the three figures from my third run (figures 5, 6, and 7), we notice that the figures 5 and 6 look very similar, regardless of whether or not there is air or vacuum in the tube. Removing the kapton all together, we see that the effects actually lessen the effects of scattering. This reason for this is very hard to determine, but looking at its FLUKA results cut from the x axis, we can see that there is more scattering in the case with kapton compared to the case without.

Looking at the x cut of the two situations, we can see slightly more color on the left side of figure 8 on and after the detector. As the only difference between the two setups is the inclusion of kapton, I hypothesize that the exclusion of the kapton allows more of the photons to scatter further from the center of the beam, and the scattered photons hit the anti-scattering slits, preventing them from reaching the lead tube and therefore the detector. While there is more scattering on the beamline because of this, less of the scattering will actually hit the detector as a result.

IV. Conclusion/Discussion

From the simulations conducted, I conclude that the most effective way to reduce scattering on the detector is to include the lead tube. As a follow up, I conducted FLUKA measurements with the condition of the tube (shown in figures 5, 6, and 7) and find that kapton windows were not in fact necessary. Not only is the kapton windows with vacuum situation more difficult to create, it also has more scattering than the situation with no kapton windows. Therefore, it is more cost effective to simply remove the film and allow air to be in the tube. Unfortunately, I wasn't able to get beam time in order to compare FLUKA results to actual experimental results on the detector. The only picture I was able to compare my results to is shown below.

Unfortunately, they didn't have any images of the detector without the same in front of it, which causes the fringe patterns seen on the picture. This situation represents the double kapton with air setup. The scattering caused by everything but the sample can be best seen in the very center of the pattern. The dark blue represents the dark red in the FLUKA double kapton setup. Looking at Figure 10 and my images, my simulations with FLUKA were on the right track, but with no picture of a scenario without the sample, it is difficult to say how accurate my results were.

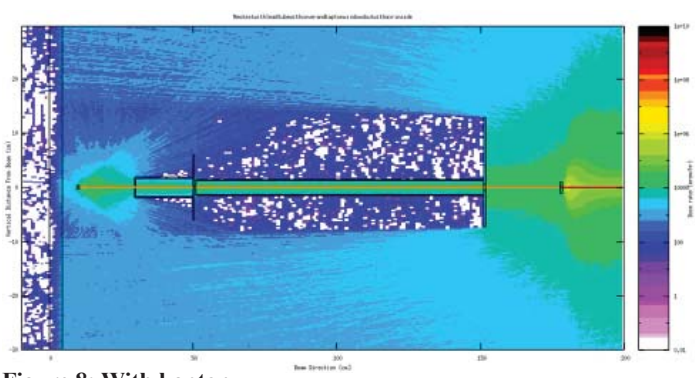

Figure 8: With kapton

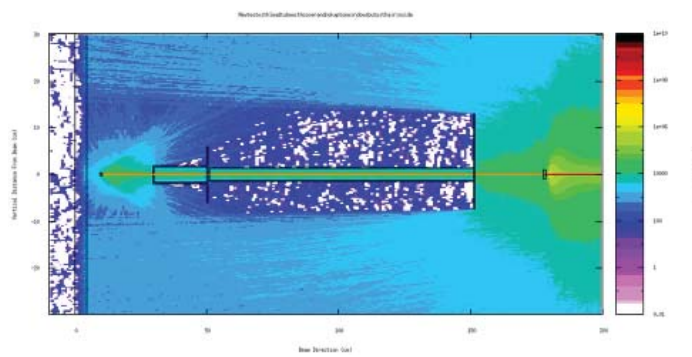

Figure 9: Without kapton

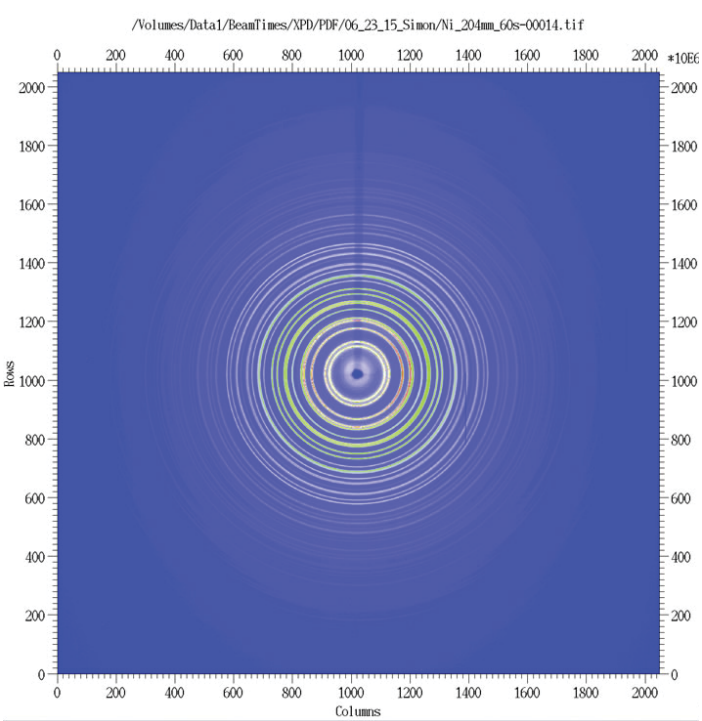

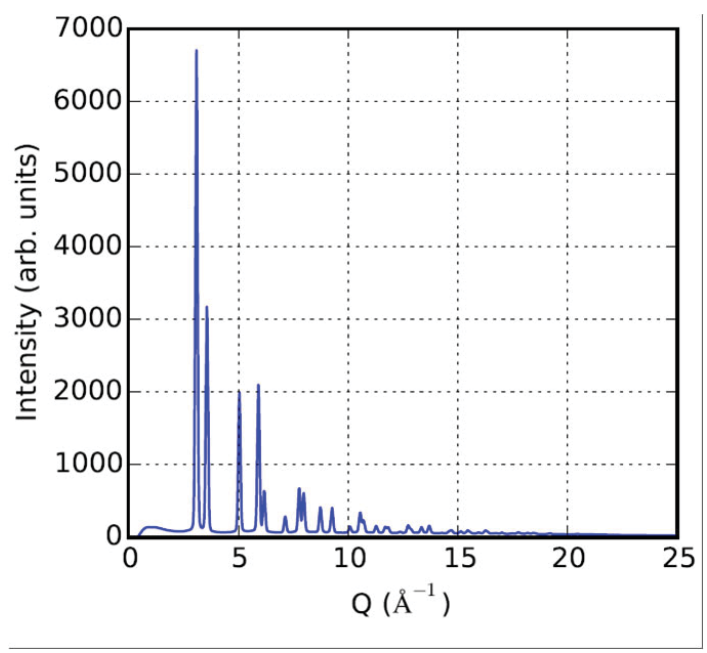

Figure 10 (left): Real data from beamline
Figure 11 (above): 1-D analysis of figure 10

Effects of deer overabundance on bird populations in the Long Island Central Pine Barrens

Raffaele Vesia
Department of Earth and Marine Sciences, Dowling College, Oakdale, NY 11769
Fred Rispoli
Department of Mathematics and Computer Science, Dowling College, Oakdale, NY 11769
Timothy Green and Jennifer Higby
Department of Environmental Health and Safety, Brookhaven National Laboratory, Upton, NY 11973

Abstract

An increase in the white-tailed deer population recorded over the last thirty years and its effects on the population of birds is being investigated at Brookhaven National Laboratory. In particular, browsing by an overabundance of deer has led to a loss of plant density on the ground floor and lower canopy of the Long Island Central Pine Barrens and, perhaps, changing the composition of the bird population[1] (Rooney and Waller 2003). Deer overabundance may be related to impacts on the population of birds. To study this hypothesis, counts of birds and counts of deer recorded at Brookhaven National Laboratory from the years 2000 to 2014 have been obtained. From our research, we have found that there is no significant impact of deer overabundance on the counts of birds at Brookhaven National Laboratory. By using hypothesis tests in Minitab, we found that differences between the counts of birds on years when there are less than 800 counts of deer and on years when there are greater than 800 counts of deer are not statistically significant. Bird counts were also analyzed on the basis of their nesting types which were divided into four categories: Canopy, ground, cavity, and treetop nesters. The counts of each nesting type were analyzed on a Microsoft Excel spreadsheet and on Minitab. We found that the four nesting types of birds are not being significantly impacted by deer overabundance. The relevance of this investigation to the Department of Energy's mission is to assist Brookhaven National Laboratory's stewardship of the land it uses for various activities such as deer culls. Conducting tests in Microsoft Excel such as regression and correlation tests and in Minitab such as paired t-tests, two-tailed t-tests, and Mann-Whitney tests has aided my research.

I. Introduction

There are four parts to the research conducted: The overabundance of white-tailed deer, solar farm construction, a wildfire that occurred in 2012, and changes in the bird populations in New York State, eastern Long Island, and Brookhaven National Laboratory. All four parts pertain to their hypothesized effects on birds.

A. White-tailed Deer Overabundance

Deer overabundance has been recently recognized as a problem affecting a large portion of the northeastern United States[2] (United States Department of Agriculture 2014). Deer populations at the time of European settlement ranged from 8 to 20 per square mile[3] (Research Review 2012). The deer populations in northeastern United States forests were kept at these levels into the late 1800s and early 1900s. Subsequently, the deer population has increased dramatically, especially in New York State since 1985. The United States Department of Agriculture has identified a target density of 20 deer per square mile and The Office of Environmental Protection at Brookhaven National Laboratory has a target density range of between 10 and 30 deer per square mile. However, counts of deer recorded at Brookhaven National Laboratory and in New York State have exceeded the target deer density range. In New York State, one possible consequence of deer overabundance is a decline in bird populations (figure 1). The incidence of deer overabundance at Brookhaven National Laboratory may be related to impacts on the population of birds there as well.

B. Solar Farm Construction at Brookhaven National Laboratory

The construction of the solar farms at Brookhaven National Laboratory between the years 2010 and 2011 may have affected the population of birds. There is a two hundred acre solar farm surrounded by fencing that excludes deer from the area. The exclusion of deer may help mitigate losses of plant life by deer browsing, which allows for more bird species to flourish. However, the clearing of trees in the Biology Fields to create space for solar farm construction may have adversely affected the canopy nesting bird populations. Additionally, ground nesting birds may have proliferated due to the increased availability of treeless land and vegetation that could be used for inhabitation. The counts of birds by nesting types in the years before and after the solar farms were constructed and examined.

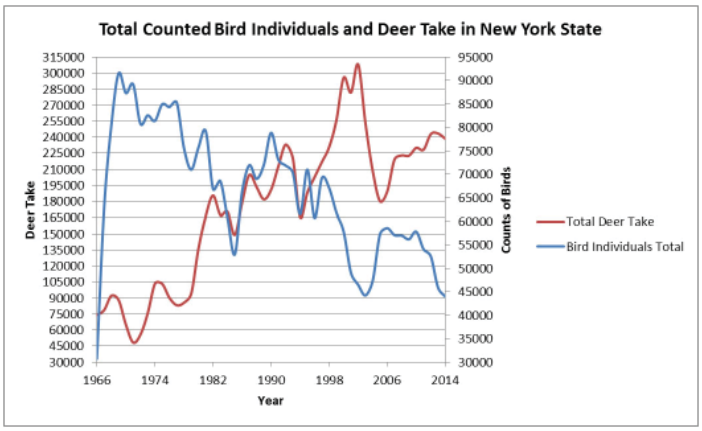

Figure 1. Line graph of total counts of birds and deer take in New York State. Bird counts were recorded from the years 1966 to 20146 (North American Breeding Bird Survey 2015). Deer counts were recorded from the year 1954 to the year 20147 (New York State Department of Environmental Conservation 2015). Deer counts from the year 1966 to 2014 were only included since the bird counts from the North American Breeding Bird Bird Survey date back only as far as 1966.

C. Wildfire at Brookhaven National Laboratory

In early April 2012, there was a wildfire in the first North Transect and first, second, and third parts of the Z-Path at Brookhaven National Laboratory. The wildfire had burned away vegetation on the ground floor of the forests and burned down trees, leaving behind stands of dead trees after the fire had dissipated. The resulted losses of plant life by the wildfire probably had prevented any deer from entering the affected areas since there were no plants available to be eaten as a food resource. Instead, the wildfire may have impacted the populations of birds at the affected areas. The counts of birds in the years before and after the wildfire had occurred were examined.

D. Changes in Bird Counts in New York State, Eastern Long Island, and Brookhaven National Laboratory

Changes in the counts of birds by all four nesting types were examined for a fifteen year interval between the years 2000 and 2014 in New York State, Eastern Long Island, and Brookhaven National Laboratory. It was hypothesized that the counts in nesting birds have changed over time. The overabundance of deer may help contribute to significant changes in nesting birds due to the overconsumption of plants. The overconsumption of plants removes potential nesting materials and locations for birds.

II. Materials and Methods

A. Data Collection and Organization

Data containing counts of deer and birds were obtained from the Waste Management Division at Brookhaven National Laboratory[4,5] (Green and Higby, unpublished data 2014). Both sets of data were collected from the years 2000 to 2014. Other counts of deer and birds in New York State were obtained from the New York State Department of Environmental Conservation and from the North American Breeding Bird Survey, respectively. Bird counts for Eastern Long Island were also collected as well. Bird counts were recorded from the years 1966 to 20146 (North American Breeding Bird Survey 2015). Deer counts were recorded from the year 1954 to the year 20147 (New York State Department of Environmental Conservation 2015).

Datasets containing counts of birds and deer were organized on a Microsoft Excel spreadsheet. Bird counts were organized by using pivot tables and filters to sort the bird counts in alphabetical order by name, transect, and by nesting type, which were classified by using the North American Breeding Bird Survey and the Cornell Lab of Ornithology websites. The nesting types were classified as ground, canopy, cavity, and treetop nesting birds. Counts of birds were summed by total number of birds, bird species, and by each nesting type in every recorded year. Counts of deer collected at Brookhaven National Laboratory had already been classified by the season they were recorded at for each year. Deer counts for each season were summed together to represent the total counts of deer for the entire year.

B. Data Analysis

Datasets containing counts of birds and deer was analyzed on Microsoft Excel by generating graphs. Both datasets were also analyzed in Minitab to test for significant differences between changes in the counts of birds and deer at Brookhaven National Laboratory, changes in the counts of birds by nesting type in the years 2007, 2008, 2009, and 2014 before the solar farms were constructed and in the years 2011, 2012, 2013, and 2014 after the solar farms were constructed, and changes in the averages of the counts of birds by nesting type and by the averages of all bird in the years 2010 and 2011 before the wildfire and the in the years 2013 and 2014 after the wildfire. The year 2012 was excluded from the analysis since that was the year the wildfire had occurred.

Counts of birds in New York State, Eastern Long Island, and Brookhaven National Laboratory were analyzed for fifteen year intervals between the years 2000 and 2014. This analysis was done by ranking the top 20% of all bird species by count and by nesting type. The top 20% of all bird species were analyzed this way instead of all recorded bird species because the top 20% of all bird species constitute 80% of the total population of birds[8] (Rispoli, Zeng, Green, and Higbie 2014). A chi square test for association was done on Minitab to determine if the counts of birds by nesting type have changed over time.

C. Statistical Testing

The analysis of bird and deer data was conducted by using parametric and nonparametric tests in Minitab. Prior to any formal statistical testing, normality tests were done for all datasets to determine if they follow a normal distribution of data. In particular, Anderson-Darling testing was applied to the testing of normality. In the Anderson-Darling test, a p-value of 0.05 or greater indicates a normal distribution of data, while a p-value of less than 0.05 indicates a non-normal distribution of data. Normally distributed data allows for parametric tests to be conducted. All

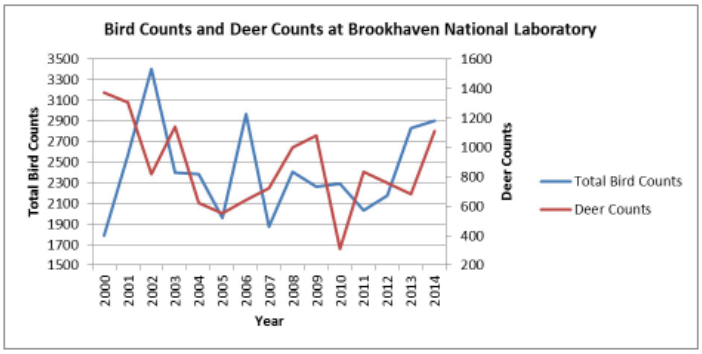

Figure 2. Chart with counts of birds and deer recorded at Brookhaven National Laboratory.

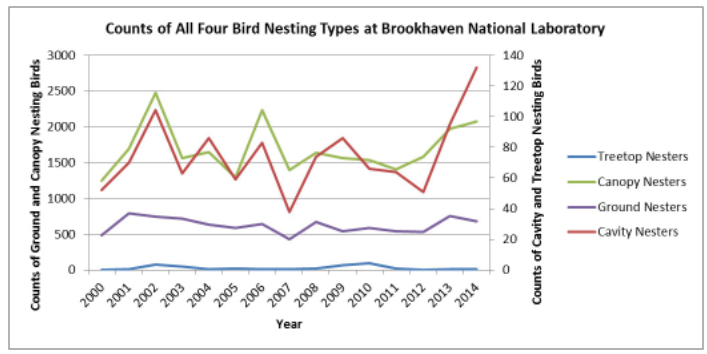

Figure 3. Chart with counts of birds of all four nesting types recorded at Brookhaven National Laboratory. The four nesting types are ground nesting birds, canopy nesting birds, cavity nesting birds, and treetop nesting birds.

deer datasets and most of the bird datasets were found to have followed a normal distribution of data, except for treetop nesting bird counts, which were found to be a non-normal distribution. In that case, corresponding nonparametric tests were applied to the dataset.

III. Results and Discussion

A. Differences between Changes in Birds Counts based on Years of Higher and Lower Deer Counts at Brookhaven National Laboratory

Figure 2 shows the counts of birds and white-tailed deer at Brookhaven National Laboratory and Figure 3 shows the counts of birds by all four nesting types at Brookhaven National Laboratory, from the years 2000 to 2014, by both nesting types and by total counts, and counts of white-tailed deer at Brookhaven National Laboratory from the years 2000 to 2014.

Two-tailed t-tests were conducted to consider if a relatively larger deer population affects birds. This analysis was based on periods when there are less than 800 counts of deer and on periods when there are greater than 800 counts of deer. Figure 4 shows that there is no significant difference between the counts of birds and when there are less than 800 counts of deer and when there are greater than 800 counts of deer. Similar results were seen in figures 5, 6, 7, and 8 (in appendix). Table 1 shows that there is no considerable effect of a larger deer population on birds. Similar results are seen in tables 4, 5, 6, and 7 (in appendix).

The results of the two-tailed t-test indicate that there is no significant difference between the counts of ground nesting birds on years when there are less than 800 counts of deer and on years when there are greater than 800 counts of deer. This may suggest that ground nesting birds are not being affected by higher or lower counts of deer.

Table 1. Correlation test of ground nesting birds and counts of deer.

	% change GN	% change DC
% change GN	1	
% change DC	-0.86729825	1

There is no considerable effect of a relatively larger deer population between on ground nesting birds.

B. Differences between Counts of Birds by Nesting Type at the Biology Fields before and after its Construction

There was no significant difference between the changes in the counts of all nesting birds before and after the solar farms were constructed. Even without the presence of deer due to fencing, the lack of browsing activity by deer in the solar farms apparently did not induce a significant change in the counts of all nesting birds. The paired t-test for the total counts of all nesting birds returned a p-value of 0.889. The paired t-test for the counts of ground, canopy, and cavity nesting birds returned p-values of 0.394, 0.649, and 0.696, respectively. Figures 9, 10, 11, and 12 (in appendix) presents the charts from the paired t-test for total nesting birds, ground, canopy, and cavity nesting birds, respectively. For treetop nesting bird counts, the result from the Mann-Whitney test was a p-value of 0.6650. All p-values from each test greatly exceed 0.05, which indicates that the construction of the solar farms did not significantly impact nesting birds at the Biology Fields at Brookhaven National Laboratory.

C. Differences between the Counts of Birds by Nesting Type and Total Bird Counts at the areas affected by the 2012 Wildfire at Brookhaven National Laboratory

There is a significant difference between the average counts of all bird species before and after the wildfire at Brookhaven National Laboratory. Figure 13 presents that the average counts of bird species after the fire are significantly greater than the average counts of species birds before the fire had occurred at North Transect 1 and at Z-Paths 1, 2, and 3. The number of all bird species is less after the fire than before the fire. It might be possible that losses of plants by the wildfire may have disallowed some bird species to nest.

Although the average counts of ground nesting birds had increased after the wildfire in 2012, there is no significant difference between the average counts of ground nesting birds before and after the wildfire at Brookhaven National Laboratory. Figure 14 presents this lack of significant difference.

The average counts of ground nesting bird species before the wildfire were significantly greater before the wildfire than after the wildfire. Figure 15 presents this significant difference. This might indicate that the areas affected by the wildfire have become less biodiverse. The loss of ground nesting bird biodiversity may be attributed to losses in the plant composition on the forest floor by the wildfire. In other words, there are less plant species that ground nesting bird species could use for nest building.

Figures 16 and 17 presents that the average counts of canopy nesting birds and canopy nesting bird species are significantly greater before the wildfire than after the wildfire. This may indicate that they were adversely affected by the wildfire because of loss of trees. As a result, there are fewer trees available for canopy nesting birds to inhabit. The loss of vegetation by the wildfire may have eliminated deer in the short term since there are not enough plant resources available for the deer to consume as food. This may have prevented any further impact on the birds by deer browsing.

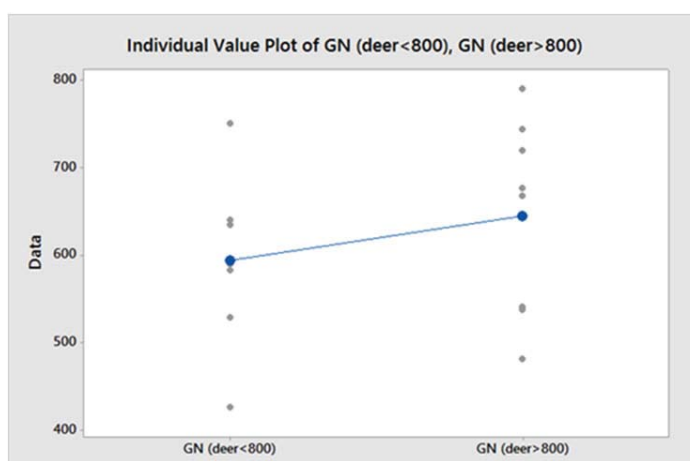

Figure 4. Not a statistically significant test (p-value= 0.368).

D. Changes in the Counts of Birds by Nesting Type in New York State, Eastern Long Island, and Brookhaven National Laboratory

Prior to performing chi-square test of association on the New York State and Eastern Long Island bird counts, a data adjustment on the counts of the four nesting types was conducted. The data adjustment was done because the collection methods of the North American Breeding Bird Survey were not consistent in the years 2000 and 2014. In fact, the number of routes of in Eastern Long Island were not the same in both years. For example, in the year 2000 at Eastern Long Island, bird counts were collected on two routes, while in the year 2014, bird counts were collected at three routes. Similarly, bird surveying was done on seventy four routes in New York State in the year 2000 and done on sixty five routes in the year 2014.

To adjust the datasets, the sum of the bird counts of all four nesting types in 2000 and 2014 was calculated. Then, the totals were examined. The lower total was divided by the higher total to obtain a ratio between the two values. Next, the ratio was multiplied by the bird counts of each of the four nesting types in the year when the total bird counts were higher than the other year. Finally, the sum of the bird counts was done to obtain a total value that is equal to the lower total bird counts. A chi-square test of association of adjustment was performed on these adjusted datasets. Tables 2 and 3 show the adjusted data.

Table 2. Adjusted counts of birds by nesting type of New York State.

Year	CN	GN	CVN	TN	Total
2000	24690	13172	7622	1108	46592
2014	18758	12408	3632	763	35561
2000 (adjusted)	18844	10053	5817	846	35561

Table 3. Adjusted counts of birds by nesting types of Eastern Long Island.

Year	CN	GN	CVN	TN	Total
2000	655	280	241	0	1176
2014	613	413	236	0	1262
2014 (adjusted)	571	385	220	0	1176

There were significant changes in the counts of birds by nesting type in New York State and on Eastern Long Island between the years 2000 and 2014. Both p-values from the chi-square test of association are 0.00. This indicates that there was a significant difference in the change of the bird counts by nesting type in New York State and Eastern Long Island. In New York State, the counts of ground nesting, canopy nesting, cavity nesting, and treetop nesting birds have decreased since the year 2000. In Eastern Long Island, the counts of canopy and cavity nesting birds have decreased, while counts of ground nesting birds have increased since the year 2000. Treetop nesting birds had zero counts since they were not among the top 20% of all bird species recorded at Eastern Long Island and Brookhaven National Laboratory.

Brookhaven National Laboratory did not have any significant changes in the counts of birds by nesting type for over a fifteen year interval. The p-value from the chi-square test of association is 0.332. Although there was a recorded increase in ground, canopy, and cavity nesting birds, there is no significant difference in the counts of birds by nesting types between the years 2000 and 2014. The lack of significant change may be due to Brookhaven National Laboratory being a natural preserve for wildlife. In other words, preserved areas such as forests, meadows, and wetlands may provide habitat for a variety of bird species. The abundance of preserved lands and its management may be mitigating some of the impacts of deer overabundance on the bird population at Brookhaven National Laboratory. Yet, in rest of New York State and Eastern Long Island, there are less preserved areas and more development of unprotected land, which reduces the amount of habitat for birds. Deer overabundance throughout New York State and Eastern Long Island may be significantly impacting bird habitat as well through the browsing of plants since there are more areas that are less preserved and undermanaged. These factors may account for the significant decreases in the counts of birds in New York State and on Eastern Long Island.

IV. Conclusion

The overabundance of deer at Brookhaven National Laboratory is not having a significant impact on birds, regardless of nesting type. More research must be done to determine what other environmental variables are inducing changes in the bird population at Brookhaven National Laboratory. Meanwhile, the construction of the solar farms at the Biology Fields did not have any significant impact on birds. However, the wildfire that had occurred in 2012 did significantly impact the number of bird species at the affected areas. The fencing at the solar farms and the wildfire that had burned down plant life helped exclude deer from these areas. Finally, the number of birds in New York State and Eastern Long Island have significantly changed over time, although they did not at Brookhaven National Laboratory.

V. Acknowledgements

This project was supported in part by the U.S. Department of Energy, Office of Science, Office of Workforce Development for Teachers and Scientists (WDTS) under the Visiting Faculty Program (VFP).

VI. References

[1]Rooney, Thomas P., Waller, Donald M., Direct and Indirect Effects of White-tailed Deer in Forest Ecosystems. (August 2003). 165-176. Forest Ecology and Management, 181 (3). ISSN 0378-1127, http://dx.doi.org/10.1016/S0378-1127(03)00130-0 http://www.sciencedirect.com/science/article/pii/S0378112703001300

[2]United States Department of Agriculture, Long Island White-tailed Deer Damage Management Demonstration Project Report. (August 2014). 1-21. Animal and Plant Health Inspection Service, Wildlife Services.

[3]Research Review, US Forest Service Northern Research Station, No. 16, 2012

[4]Green, Timothy and Higby, Jennifer, Flyover Population Analysis. (2014). [unpublished data]. Waste Management Division, Department of Environmental Health and Safety, Brookhaven National Laboratory, Upton, NY 11973

[5]Green, Timothy, Bird BNL 2014. (2014). [unpublished data]. Waste Management Division, Department of

Environmental Health and Safety, Brookhaven National Laboratory, Upton, NY 11973

[6]Pardieck, K.L., D.J. Ziolkowski Jr., M.-A.R. Hudson., North American Breeding Bird Survey Dataset 1966 - 2014, version 2014.0. (2015). U.S. Geological Survey, Patuxent Wildlife Research Center. www.pwrc.usgs.gov/BBS/RawData/

[7]New York State Department of Environmental Conservation, Deer and Bear Harvests: White- tailed Deer. (2015). Outdoor Activities. http://www.dec.ny.gov/outdoor/42232.html

[8]Rispoli, Fred, Zeng, Suhua, Green, Timothy, Higbie, Jennifer, Even Birds follow Pareto's 80-20 Rule. (February 2014). 41-42. The Royal Statistical Society, Significance.

VII. Figures

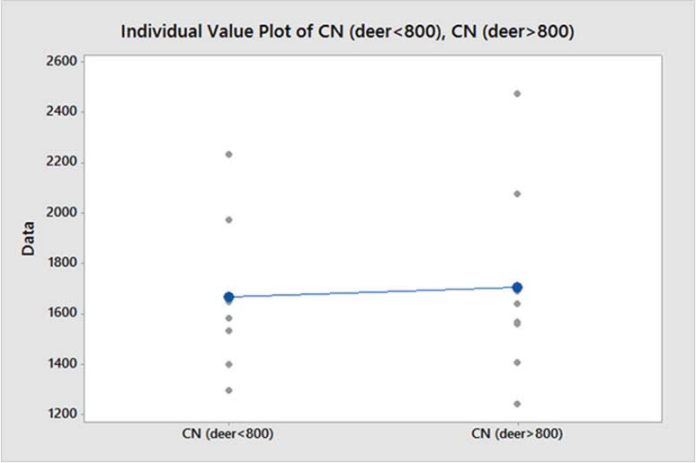

Figure 5. Not a statistically significant test (p-value= 0.832).

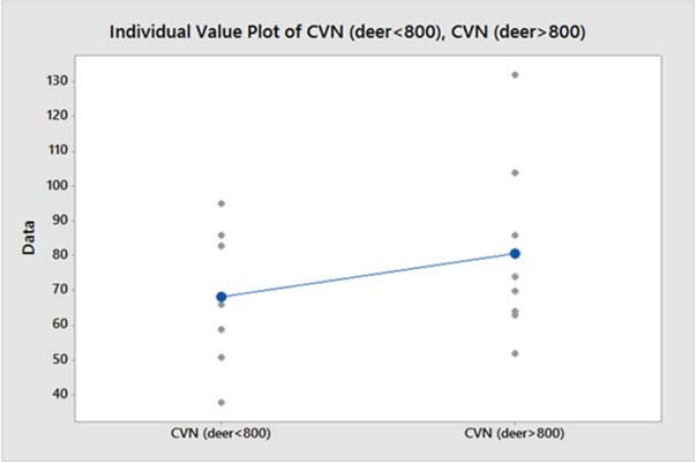

Figure 6. Not a statistically significant test (p-value= 0.327).

Table 4. Correlation test of canopy nesting birds and counts of deer.

	% change CN	% change DC
% change CN	1	
% change DC	-0.198162367	1

There is no considerable effect of a relatively larger deer population on canopy nesting birds.

Table 5. Correlation test of cavity nesting birds and counts of deer.

	% change CN	% change DC
% change CN	1	
% change DC	-0.022098933	1

There is no considerable effect of a relatively larger deer population on cavity nesting birds.

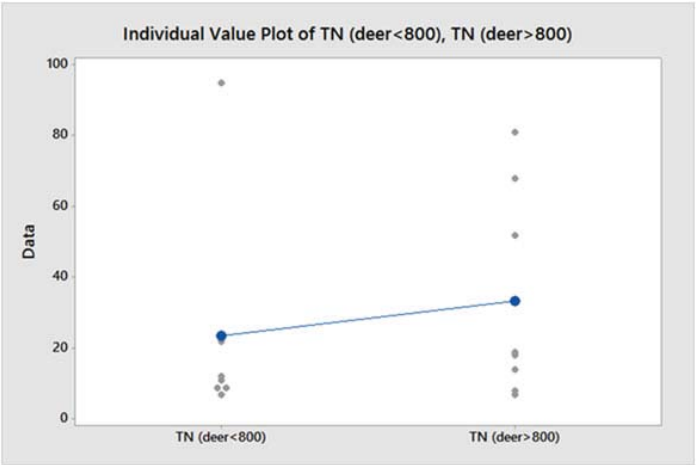

Figure 7. Not a statistically significant test (p-value= 0.548).

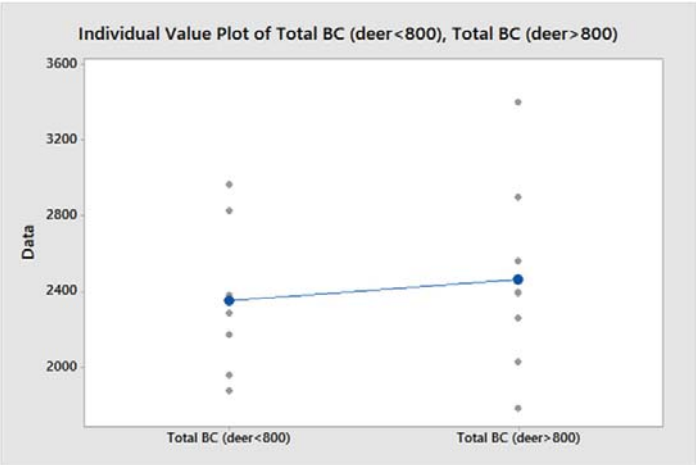

Figure 8. Not a statistically significant test (p-value= 0.640).

Table 6. Correlation test of treetop nesting birds and deer counts.

	% change CN	% change DC
% change CN	1	
% change DC	-0.29013871	1

There is no considerable effect of a relatively larger deer population on treetop nesting birds.

Table 7. Correlation test of the total counts of birds and counts of deer.

	% change CN	% change DC
% change CN	1	
% change DC	-0.209928465	1

There is no considerable effect of a relatively larger deer population on the total number of birds.

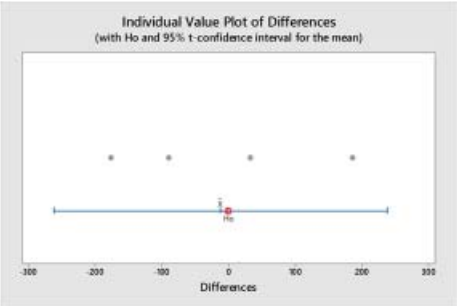

Figure 9. H0= Xbefore solar farms not= Xafter solar farms Not a statistically significant test.

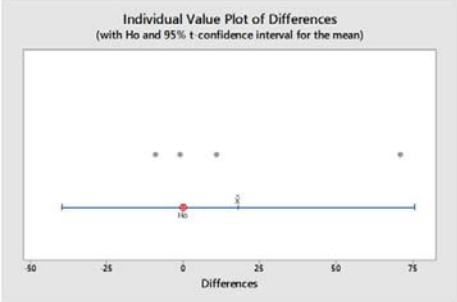

Figure 10. H0= Xground nesters before not= Xground nesters after Not a statistically significant test.

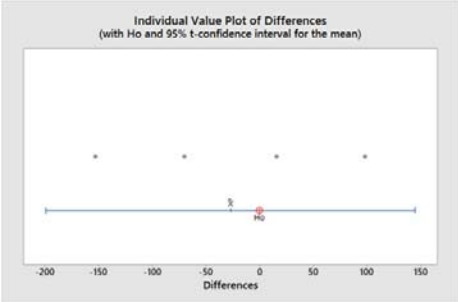

Figure 11. H0= Xcanopy nesters before not= Xcanopy nesters after Not a statistically significant test.

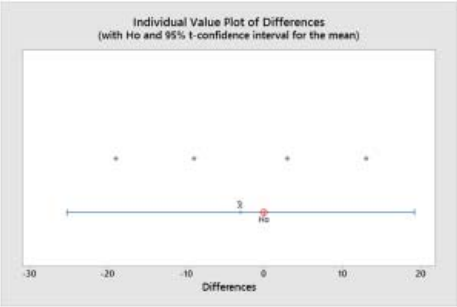

Figure 12. H0= Xcavity nesters before not= Xcavity nesters after Not a statistically significant test.

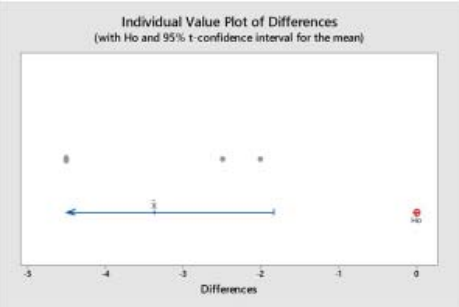

Figure 13. Counts of bird species before and after fire (p-value= 0.007).

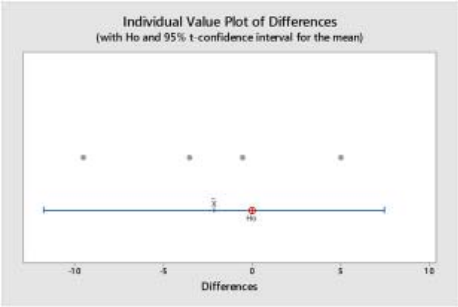

Figure 14. Counts of ground nesting birds before and after fire (p-value= 0.533).

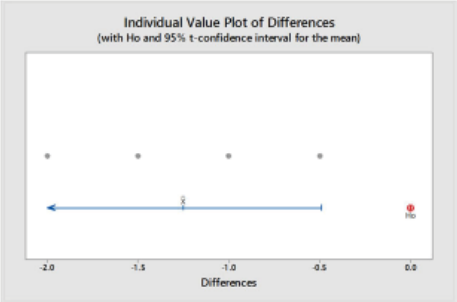

Figure 15. Counts of ground nesting bird species before and after fire (p-value= 0.015).

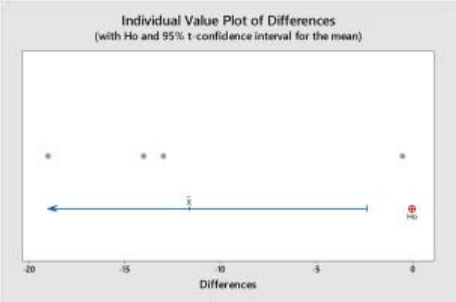

Figure 16. Counts of canopy nesting birds before and after fire (p-value= 0.030).

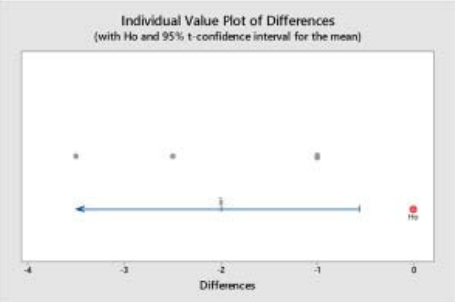

Figure 17. Counts of canopy nesting bird species before and after fire (p-value= 0.023).

Self-assembly of magnetite block copolymer nanocomposites

Adam Vianna
Department of Chemistry, Case Western Reserve University, Cleveland, OH, 44106
Kevin Yager
Center for Functional Nanomaterials, Brookhaven National Laboratory, Upton, NY, 11973
Mikhail Zhernenkov
National Synchrotron Light Source II, Brookhaven National Laboratory, Upton, NY, 11973

Abstract

In this study, we investigate the self-assembly of Iron (II, III) oxide (magnetite) nanoparticles within a block copolymer matrix. First, commercially available 5 nm magnetite nanoparticles were coated with low molecular weight polystyrene ligands. Then, the variety of poly(styrene-b-methyl methacrylate) films ~75 nm- and 125 nm-thick were spin coated on the Si wafers. The nanoparticles were incorporated into the polymer matrix to determine how they arrange within the layers. Atomic force microscopy was used to check the surface morphology of the films while spectroscopic ellipsometry was used for the initial assessment of the film thickness. X-ray reflectometry was used to determine the transverse structure of the multilayer samples. We have determined the spin coating parameters for films without nanoparticles and well-oriented lamellar structure was obtained for both 75 nm- and 125 nm-thick samples. The same parameters have yielded thicker films with nanoparticles so additional experiments must be done. Further x-ray measurements will allow us to determine the spacing of nanoparticles once those films have been successfully spun.

I. Introduction

Nanoparticles have garnered a large amount of attention from the scientific community in recent years. This is primarily because they exhibit electronic, magnetic, optical, catalytic, and other properties that are vastly different from those of the corresponding bulk materials.[1,2] Simultaneously, their small size makes them difficult to work with so self-assembly has become an important tool in this field.

In our project, we are examining the self-assembly of iron (II, III) oxide (magnetite) nanoparticles in a polystyrene (PS) and poly methyl methacrylate (PMMA) block copolymer matrix. Magnetite nanoparticles are of great interest because of their large magnetic moments. Recently, this property has led to possible applications such as magnetic hyperthermia.[3] The PS/PMMA block copolymer has already been shown to efficiently form thin films of regular alternating layers so it is a good base for our studies.[4,5] We will determine how exactly these nanoparticles arrange within block copolymer films and hopefully open the door to more efficient magnetic data storage or nanocomposite circuit boards.

We have targeted a horizontal lamellar structure of block copolymer as the starting point for our studies. Horizontal lamellae are present when there are alternating layers of the polymer chains (PS or PMMA) parallel to the substrate surface1, silicon in our case:

The diagram above shows the theoretical arrangement of layers in a 75nm lamellar structure. We can encourage the formation of this structure by subjecting the silicon substrate to UV light, which causes the surface to become relatively hydrophilic and attract the PMMA chains, which are more polar than the PS chains. This causes the surface of the first copolymer layer to be polystyrene, which then attracts the PS chains in the next polymer layer, resulting in an alternating structure of PS and PMMA.

Since the purpose of this study is to examine the self-assembly of the nanoparticles within the film, the magnetite needs to be given some affinity for one of the layers. We achieved this by mixing the nanoparticles with short amine-functionalized polystyrene chains. The amine functionalization, with its localized electron density, acts as a ligand on the nanoparticle. The polystyrene chains themselves will mix much better with the PS than the PMMA in the block copolymer so they should be localized within the PS layer once the lamellar structure is formed. The addition of polystyrene to the magnetite increases the particle size so the success of this reaction can be checked using dynamic light scattering.

Our analysis has primarily consisted of atomic force microscopy to check the surface morphology of the samples. This is useful as it helps us analyze which spin coating parameters provide a clean lamellar structure as well as to give us an initial value for surface roughness to fit our x-ray data to. We have also used spectroscopic ellipsometry, which analyzes the polarization of light as it reflects off the layers in the film. This gives us a quick thickness measurement. However, the most important technique has been x-ray reflectometry.

Reflectometry involves analyzing the intensity of directly reflected x-rays at small angles to the film surface, above the critical angle of the sample material.[6] Reflectivity is normally presented

Figure 1: diagram of a 75nm 53000:54000 poly(styrene-b-methyl methacrylate) film with a lamellar structure. The layers at the substrate and surface are ~125 nm while the internal layers are ~250nm.

on an arbitrary units log scale normalized to 1 which represents the total reflection. The data is plotted as a function of momentum transfer q, which takes into account both the angle of incidence and the wavelength of the radiation used:

$$q = \frac{4\pi}{\lambda}\sin(\theta) \qquad (1)$$

Where θ is an incident angle in radians and λ is a wavelength in angstroms (Å), such that q is in units of reciprocal angstroms. Past the critical angle, the reflectivity decays roughly proportionally to q^{-4} with oscillations from the interference of the interfaces between layers. A rough value for the total film thickness can be obtained from the average q separation of oscillation peaks:

$$d = \frac{2\pi}{\Delta q} \qquad (2)$$

Where d, the sample's total thickness, is in units of angstroms and Δq is in units of reciprocal angstroms. However, the actual data can be systematically fitted to the known number of layers in the sample to determine the thickness, scattering length density, and roughness at each interface and the sample surface. Since the nanoparticles should form layers within the polystyrene chains of the lamellar structure, this fitting can allow us to determine how they arrange vertically within the film.

II. Materials and Methods

A 5 nm Iron (II, III) oxide magnetic nanoparticles solution in toluene (Sigma Aldrich), anhydrous toluene (Fluka), 5000 mw amine-terminated polystyrene (Sigma Aldrich), and 53000:54000 mw poly (styrene-b-methyl methacrylate) (Polymer Source) were procured commercially and used without further purification. Dynamic light scattering measurements were obtained using a Malvern Zetasizer Nano ZS. Atomic force measurements were taken on an Asylum MFP3D atomic force microscope. Spectroscopic ellipsometry was done on a J.A. Woollam M-2000 ellipsometer using WVASE software. X-ray measurements were obtained using a Rigaku Ultima III x-ray diffractometer equipped with a Cu κα x-ray source. X-ray analysis was done using MOTOFIT software using complex SLD fitting.[7]

The magnetite nanoparticles were coated with polystyrene by ligand exchange in a modified literature procedure.[8] To a 50mL beaker equipped with a stir bar was added 4.2 mL of the magnetite nanoparticle solution. This solution was diluted from 5.0 mg/mL to 3.5 mg/mL by the addition of 1.8 mL of toluene. The beaker was covered with parafilm while 0.717g (0.143 mmol) of amine-terminated polystyrene was weighed out and added to the nanoparticle solution. The beaker was re-covered and the mixture was stirred vigorously for 30 minutes, yielding a black liquid. The product was analyzed by DLS to check for an increase in size over the original nanoparticles.

Polymer films were prepared by dissolving a weighed amount of the PS/PMMA block copolymer in the nanoparticle solution and neat toluene as needed. The silicon substrates were cut into squares and prepared by a toluene rinse and 10 minute UV-ozone treatment. The films were spun at specific speeds to target the desired thickness. They were then annealed in a 205 °C vacuum oven.

AFM and ellipsometric scans were taken both before and after annealing to verify the surface morphology and thickness of the samples respectively. X-ray reflectometry was done overnight (15 hours) on the annealed samples to probe the individual layers as well as overall thickness.

III. Results and Discussion

A. Nanoparticle synthesis:

A change in size between the original nanoparticle solution and the synthesized product was noted by dynamic light scattering. The original solution had particles of an average 6.137 nm size with a standard deviation of 1.700 nm. The particles after the synthesis had an average size of 8.614 nm with a standard deviation of 2.168 nm. Although these ranges overlap, it should be noted that the original nanoparticles did not have a uniform core size so this shift indicates that the polystyrene ligands did attach to most of the particles.

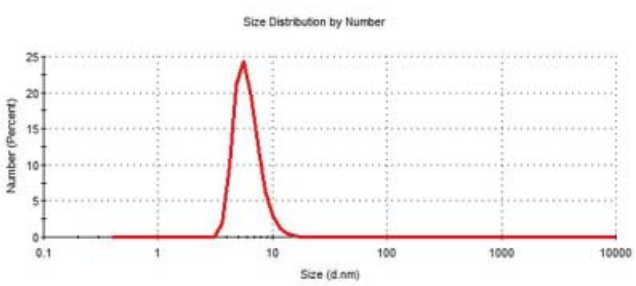

Figure 2: DLS size distribution of nanoparticles in the stock solution

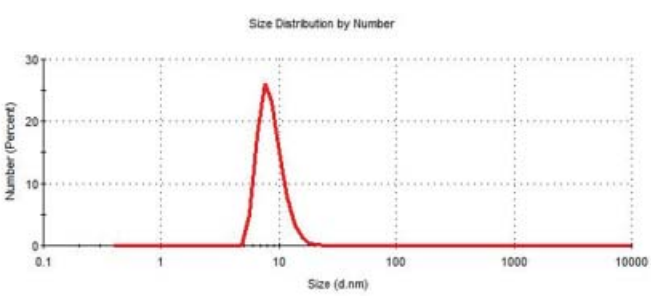

Figure 3: DLS size distribution of nanoparticles with polystyrene ligands

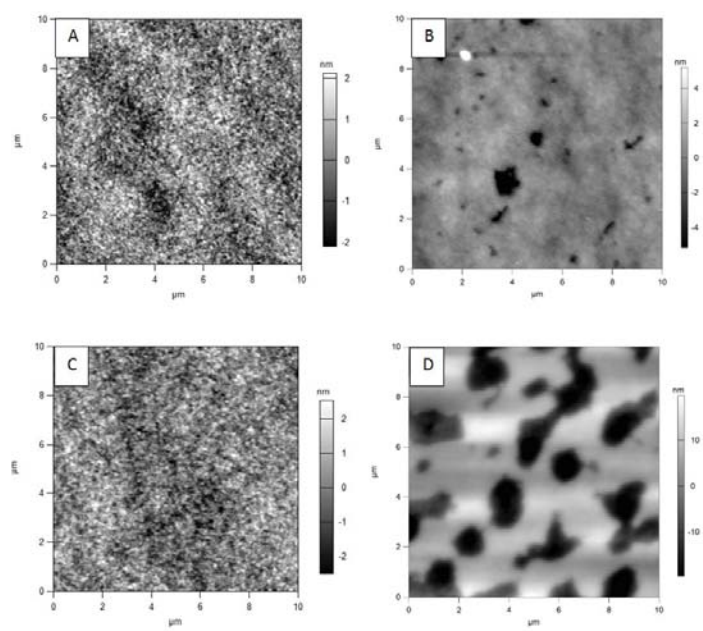

Figure 3: AFM height images of the first films. A) 75 nm prior to annealing B) 75 nm after 5 hours annealing C) 125 nm before annealing D) 125 nm after 16 hours annealing

B. Thin Films

There were two major components of the work with thin films. The first was to determine the exact spin coating parameters to make films of the desired thickness and without islands or holes. The spin coating solutions were made in toluene to a specific mass percentage of solid—block copolymer plus nanoparticles (if present). The target mass percentages were 1.5% and 3.0% for the 75 nm and 125 nm films respectively. The initial spin speed targets were 1200RPM for 75 nm and 2500RPM for 125 nm, yielding the following surfaces:

The 125 nm film had much more surface area covered by depressions than the 75 nm film. We also see an interesting property in the phase images of the annealed samples. The depressions show a fingerprint pattern indicative of a vertical lamellar structure (alternating polymer chains both present on the surface):

This property, while not germane to the project, is an interesting find nonetheless. From these images, we determined that the 75 nm film was sufficiently smooth for x-ray measurements, though the 125 nm film was not. The spin speed was gradually decreased for the 125 nm solution until finding that 1900RPM was the desired speed for those films.

As we can see, 1900RPM provides a very uniform structure for the 125 nm thick film. The next step was to analyze the ellipsometric data from these films to verify that they were at the correct thickness:

The next steps were to generate the spin coat films with 1% volume nanoparticles and obtain x-ray reflectometry data. Once the films were spun, the first check was AFM to check the surface morphology. This was both to verify that no islands or holes formed with the addition of nanoparticles and to possibly observe surface nanoparticles.

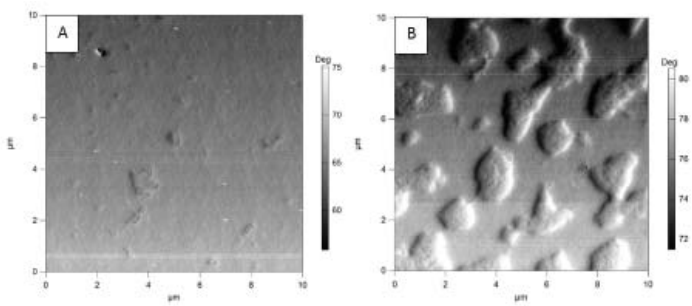

Figure 4: AFM phase images of the first films. a) 75 nm after 5 hours annealing b) 125 nm after 16 hours annealing

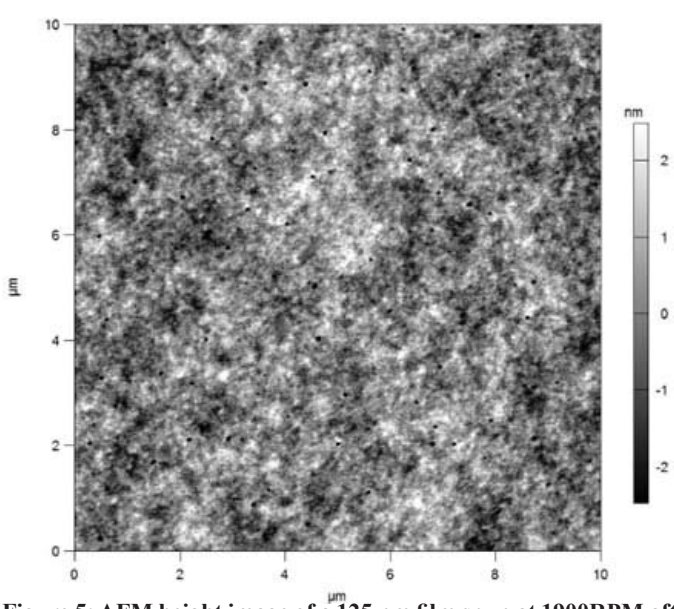

Figure 5: AFM height image of a 125 nm film spun at 1900RPM after annealing 16 hours

Both of the films had a uniform surface after annealing. The phase image of the 75 nm film showed some shadows which could have been nanoparticles. However, they were not visible on height images, indicating that they could be surface distortions from nanoparticles within the film.

Finally, we obtained x-ray reflectometry measurements on the films. Both of the films without nanoparticles had reflectometry that could be fitted layer by layer. However, the reflectometry resolution was not good enough to resovlve thickness oscillations for films with nanoparticles, which indicated that they were much thicker than targeted and made it impossible to analyze the individual layers. The 75 nm film could still be analyzed for overall thickness based off of equation (2), but the 125 nm film thickness couldn't be determined.

Layer	Thickness (Å)	SLD (10^{-6}/Å^2)	Roughness (Å)
1 (PS)	110.46	8.3033	11.083
2 (PMMA)	242.65	10.805	29.602
3 (PS)	237.07	9.5573	21.788
4 (PMMA)	119.91	10.033	10.062
Si backing	INF	20.07	5.7977

Table 1: Fitted data for the 75 nm film without nanoparticles

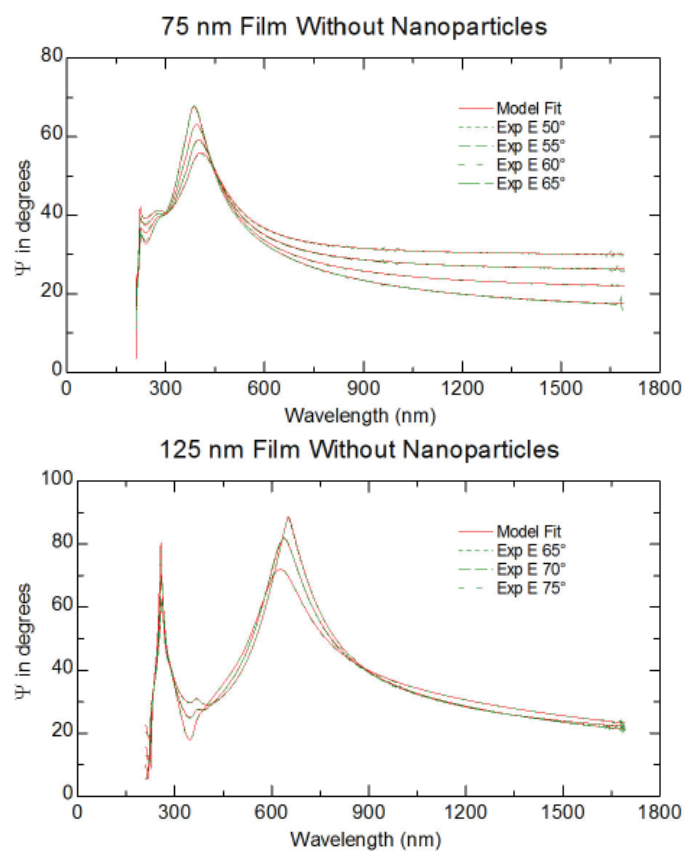

Figure 6 (above): Spectroscopic ellipsometry of the films without nanoparticles. A) 75 nm film with a model fitted thickness of 71.8±0.2 nm B) 125 nm film with a model fitted thickness of 131.0±0.5 nm

Layer	Thickness (Å)	SLD (10^{-6}/Å^2)	Roughness (Å)
1 (PS)	95.64	4.6321	7.0848
2 (PMMA)	277.31	10.684	39.893
3 (PS)	264.4	9.5733	24.17
4 (PMMA)	267.59	10.828	25.337
5 (PS)	259.8	9.5893	17.922
6 (PMMA)	123.12	9.8031	9.3328
Si backing	INF	20.07	5.2369

Table 2: Fitted data for the 125 nm film without nanoparticles

As we can see from the fitted data, the PMMA layers are generally slightly thicker than the PS layers. Furthermore, the fact that the films with nanoparticles were much thicker that expected indicates that there was something affecting the solutions' spin coating properties. There could be some viscosity effects, but the solutions weren't noted to be much thicker when handled. Alternatively, there could have been some intermolecular interactions causing the solutions to stick more to the silicon substrate. Also, the rapid decay in the intensity of the oscillations suggests that we don't have the resolution to properly analyze our samples. This isn't surprising since this type of analysis on thin films would normally be done with synchrotron radiation, though that wasn't readily available.

IV. Conclusion

We have successfully synthesized magnetite nanoparticles coated in polystyrene. Furthermore, we have been able to make polymer films of the desired thickness, though only without nanoparticles. There may be some viscosity effects or intermolecular forces causing the films with nanoparticles to spin much thicker than expected. Once we narrow down the correct parameters, we will be able to probe the nanoparticle distribution through x-ray measurements.

In all, we have laid the framework for the rest of this project. Once we have determined how to generate all samples at the right thickness and with uniform annealing times, we will be able to use reflectometry to properly examine the self assembly of the nanoparticles in the polymer. We should also look into using a synchrotron for this study. This was included in the original project proposal, but it specified the X9 beamline at the National Synchrotron Light Source, which has since closed. The Soft Matter Interfaces beamline at the National Synchrotron Light Source II would have the required capabilities, though it will not be operational until 2017 (scheduled), so another synchrotron should be used. Further studies could be applied to other types of nanoparticles, such as gold.

V. References

[1]F.Einar Kruis, Heinz Fissan, and Aaron Peled, "Synthesis of nanoparticles in the gas phase for electronic, optical and magnetic applications—a review," J. Aerosol Sci. 29, 511-535 (1998)

[2]Y. Li and W. Shen, "Tuning the morphology of metal oxides for catalytic applications," in Nanocatalysis: Synthesis and Applications, first ed. edited by Vivek Polshettiwar and Tewodros Asefa (John Wiley and Sons, Hoboken, NJ, 2013), pp. 333-403

[3]Xianqiao Liu, Valentyn Novosad, Elena A. Rozhkova, Haitao Chen, Volodymyr Yefremenko, John Pearson, Michael Torno, Sam D. Bader, and Axel J. Rosengart, "Surface Functionalized Biocompatible Magnetic Nanospheres for Cancer Hyperthermia," IEEE Transactions on Magnetics. 43, 2462-2464 (2007)

[4]Michael J. Fasolka and Anne M. Mayes, "Block Copolymer Thin Films: Physics and Applications," Annu. Rev. Mater. Res. 31, 323-355 (2001)

[5]Kevin G. Yager, Brian C. Berry, Kirt Page, Derek Patton, Alamgir Karim, and Eric J. Amis, "Disordered nanoparticle interfaces for directed self-assembly," Soft

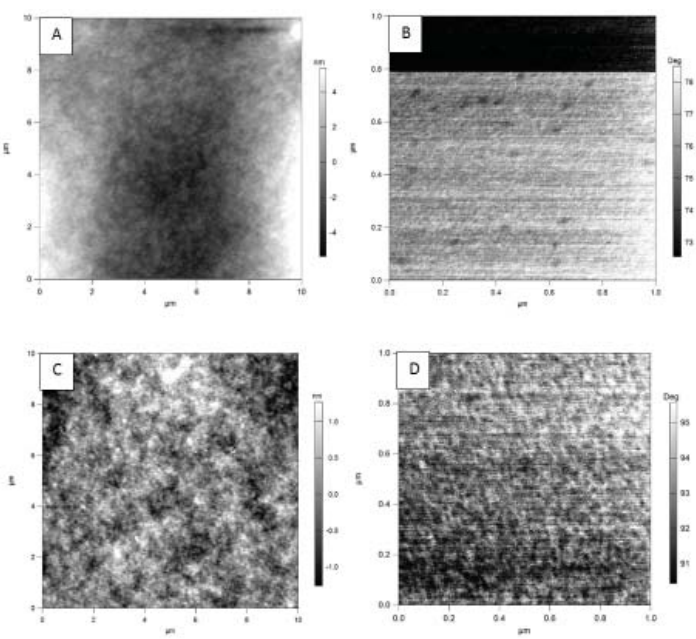

Figure 7: AFM images of annealed films with 1% nanoparticles. A) 75 nm height image after 5 hours annealing B) 75 nm phase image after 5 hours annealing C) 125 nm height image after 16 hours annealing D) 125 nm phase image after 16 hours annealing

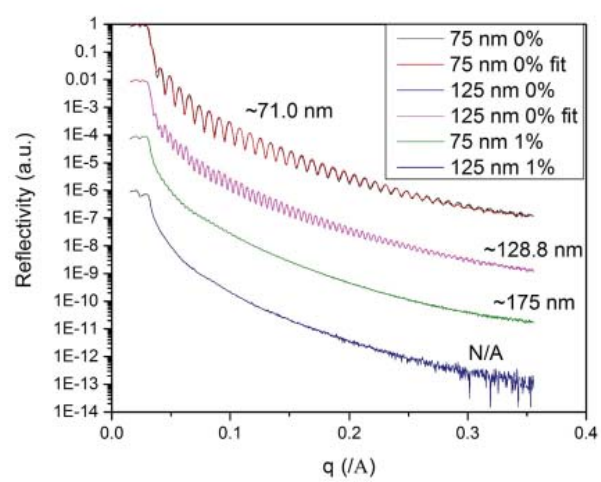

Figure 8: Reflectometry of all initial samples. Thickness values for films without nanoparticles were obtained by complex fitting. The thickness of the 125 nm film with nanoparticles could not be obtained.

Matter. 5, 622-628 (2009)
[6]Metin Tolan, X-ray Scattering from Soft-Matter Thin Films: Materials Science and Basic Research (Springer-Verlag Berlin Heidelberg, New York, NY, 1999), pp. 5-26
[7]Andrew Nelson, "Co-refinement of multiple-contrast neutron/X-ray reflectivity data using MOTOFIT," J. Appl. Crystallogr. 39, pp. 273-276 (2006)
[8]V. Cabuil, N. Hochart, R. Parzynski, and P.J. Lutz, "Synthesis of cyclohexane magnetic fluids through adsorption of end-functionalized polymers on magnetic particles," Progr. Colloid. Polym. Sci. 97, pp. 71-74 (1994)

VI. Acknowledgements

This project was supported in part by the U.S. Department of Energy, Office of Science, Office of Workforce Development for Teachers and Scientists (WDTS) under the Science Undergraduate Laboratory Internships Program (SULI).

I would like to thank Kevin Yager and my mentor Mikhail Zhernenkov for their guidance during this project. I would also like to thank Fang Lu, Charles Black, and Dmytro Nykypanchuk for their assistance with laboratory space and instrumentation.

Single bunch emittance measurements via edge radiation

Linnea Zavala
Department of Physics, Whitworth University, Spokane, WA 99251
Christina Swinson and Mikhail Fedurin
Accelerator Test Facility, Brookhaven National Laboratory, Upton, NY 11973

Abstract

Traditional electron beam emittance measurements destroy the beam and require multiple measurements. At the Accelerator Test Facility (ATF) at Brookhaven National Laboratory (BNL), we tested an alternate measurement method that is minimally invasive and addresses the emittance of a single electron bunch. For an electron beam energy of 64 MeV, the beam was passed through two dipole bending magnets. The edge radiation from the magnets' edges was directed through a 532 nm filter and the interference pattern captured by a camera. When compared to emittance measurements from a more typical method based on beam geometry, a linear relationship between the intensity of the interference pattern and emittance was found. The edge radiation method for measuring emittance can provide information about a specific electron bunch in a beam with minimal destruction.

I. Introduction

The Accelerator Test Facility (ATF) at Brookhaven National Laboratory (BNL) is an Office of Science User Facility with a strong accelerator stewardship mission. The two active beamlines at the ATF receive electron beam from a linear accelerator. This high-brightness beam has energy up to 80 MeV with electron bunches down to sub-picoseconds. Electron beam experiments at the ATF can be paired with the facility's high-power, infrared, CO2 laser.[1]

As a user facility, a variety of beam diagnostics at the ATF help users achieve their experimental goals. One important physical property of the electron beam is emittance, a measure of beam quality. A measurement of normalized emittance is proportional to the average area of the beam in phase space (position versus momentum) and is always conserved.[2] Traditional measurement methods of transverse emittance require knowledge of transverse beam size, which destroys the electron beam. Moreover, the measurements must be spread along the beam and so give the average beam emittance, not the emittance of a single electron bunch. Our experiment provides an alternative to the destructive emittance measurements currently employed at the ATF and the results increase the versatility of ATF diagnostics.

In this paper, the experimental background and setup, subsequent data collection, and analysis are described. The goal of the experiment was to find a way to glean information about single electron bunch emittance from the edge radiation diffraction pattern in a reliable, minimally invasive way.

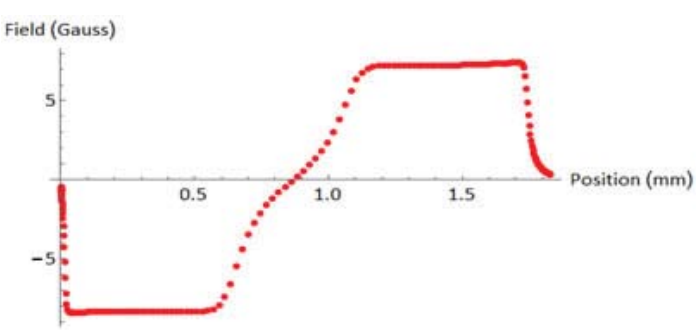

Figure 1. Plot of field vs position of a charge travelling through a 15°, 0.85 T, dipole bending magnet.

II. Methods

A. Dipole Bending Magnets

To minimize electron beam interference, we looked at the edge radiation. Like synchrotron radiation, edge radiation is the wide spectrum of radiation emitted from an accelerated charge; however, edge radiation is specifically when the charge passes the "edge" between two materials.[3] For the case of a dipole bending magnet, edge radiation is from acceleration/deceleration occurring when the charge passes from space into the magnet.[4] When edge radiation from two locations interfere to create a diffraction pattern, the pattern intensity is directly proportional to emittance.

A simulation was performed with Synchrotron Radiation Workshop (SRW) to optimize the parameters for the experiment.5 Based on simulation results, two 15 degree, 0.85 Tesla dipole bending magnets were selected for the experiment in consideration of an achievable beam energy (64 MeV) and the best wavelength for the CCD camera (532 nm). To measure the field and estimate the subsequent response of a charge travelling through the magnets, we developed an automated measurement program in Python that commands a 3-channel Gaussmeter and 3-channel motion controller via GPIB. A Hall Probe was mounted on two step-motors in order to have 2-dimensional movement. Beginning 30 mm before the magnet and ending 30 mm after, the field was measured. After each field reading, the value was used to calculate the subsequent bending radius and movement of a charge by

$$\frac{1}{\rho}[\mathrm{m}] = 0.2998\frac{B[\mathrm{T}]}{\beta E[\mathrm{GeV}]} \qquad (1)$$

where 1/ρ is the bending radius, B is magnetic field, β is the Beta Function, E is the electron beam energy (64 MeV), and 0.2998 accounts for the fundamental charge in a relativistic case. From the bending radius due to each field measurement, we calculated the lateral distance travelled in 1 mm longitudinally by a charge. The plot of field versus position for one of the bending magnets can be seen in Figure 1.

B. Electron Beam Preparations

The magnets were installed into a vacuum chamber in Beamline 2 of the ATF. The magnets were mounted on a step motor that can move perpendicular to the beam direction. A mirror was installed inside the vacuum chamber as well and aligned to receive two components of the edge radiation. From the mirror, the edge

radiation was directed out a window of the vacuum chamber to a 532 nm, 10 nm bandwidth filter that preceded a CCD camera. An approximation of this setup is shown in Figure 2.

Parameter	Value
Energy	64 MeV
Charge	400 pC
Energy spread	0.1%
Bunch Length	6 ps
Repetition Rate	1.5 Hz

Table I. Experimental electron beam parameters.

The electron beam was tuned until a clear image of several diffraction fringes was visible via the camera. The beam energy used was 64 MeV with energy spread of 0.1%. See Table I for all beam parameters.

III. Data Collection

In order to maintain conditions, all data was collected during one day, though beam tuning and optical alignment occurred over the preceding days. Beam emittance was changed by varying the current to the solenoid near the RF photocathode injector. For a constant dispersion value (0 Chirp, 0.1% energy spread, or on-crest acceleration in RF cavity), we varied current to solenoid by 1 A increments from 95 A to 110 A.

First, with the magnets in place, we changed emittance (solenoid current) and saved five camera images for each value. After each emittance change, the beam was realigned so that the entrance position into the bending magnets was the same. Second, the magnets were moved out of the beam path and the emittance was measured by the standard method for each solenoid current value. The method inserts fluorescent screens into the beam path to record beam size. For comparison purposes, four screen images from around the experimental setup were utilized as well as four screens from before the electron beam enters Beamline 2.

IV. Analysis

Analysis was done using Python with the exception of the use of existing Mathematica programs for the traditional emittance measurement calculation. The edge radiation diffraction pattern images were saved as ASC files. For each solenoid current level, the five corresponding images were read into arrays by pixel. A high number of x-rays was evident in the images. The method that proved most effective for removing the x-rays was to apply a median filter. The minimum level necessary was for every nine pixels (see Figure 3). Next, a standard python image contrast function was used to clarify the fringes against the background. A comparison of a raw image, median filtered image, and contrasted fringes can be seen in Figure 4.

Projection plots of the images were created based on a zoomed-in section of the fringes (see Figure 5). For each solenoid current value, the average of the projections was taken. The beam was parameterized by looking at the interpolation of the maxima and/or minima. Values for maxima minus minima (the envelope) and only the minima were compared and no significant difference observed. This result was not surprising because by observation alone the projections primarily show a difference in the minima levels for each emittance.

For calibration, parameterized values for edge radiation were compared to the emittance calculated from the fluorescent screen method. A plot of emittance according to edge radiation and emittance according to the traditional method versus solenoid current is seen in Figure 6.

V. Results and Discussion

We expect the emittance plots for the two methods versus solenoid current to reflect one another. The plots in Figure 6 do seem to be reflections, but their peaks do not align, indicating that the best emittance at a given solenoid current found by one method was not so for the other. This is problematic, particularly because we need the traditional method to calibrate the numeric output of the edge radiation method.

The most likely cause of this "misalignment" of the plots is the time separation between measurements. Because of having to move the magnets in and out of the beam path, it took time to collect the fluorescent screen data as well as to manually save five

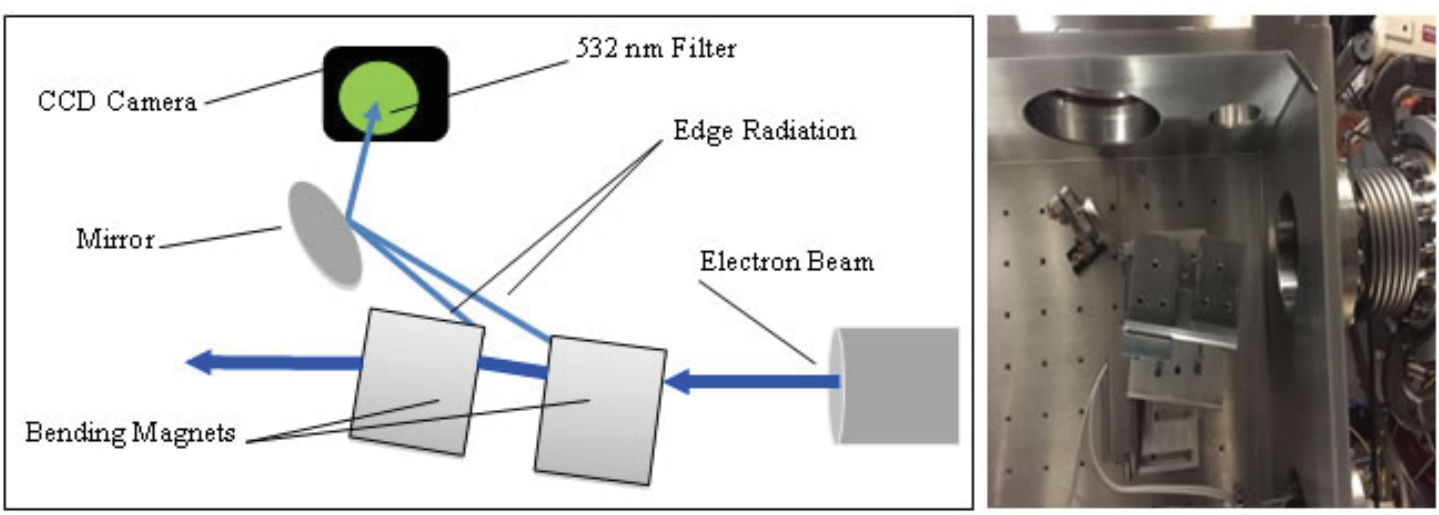

Figure 2. Left: The beam enters the first dipole magnet then continues to the second magnet where it is bent back to the original path. Edge radiation from 2 edges is reflected from the mirror to the filter, then camera, which detects the diffraction pattern.
Right: An image looking down into the vacuum chamber. The filter and camera are outside the chamber and so are not visible.

edge radiation images. The electron beam was unstable enough that the beam properties changed in this time lapse, likely due to factors such as the summer heat and humidity. Overall, the data appears to show that the edge radiation method can work; however, repetition of the experiment after developing faster/automated methods for collecting the data could help get more information from the edge radiation data.

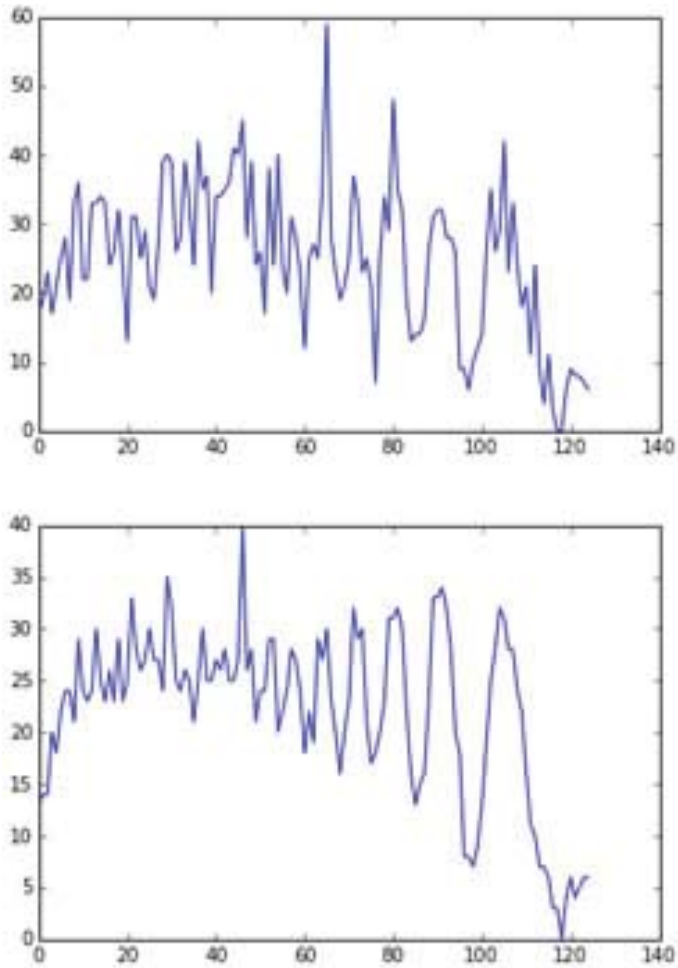

Figure 3. (top)Projection plot with no median filter. (bottom) Projection plot with 9 pixel median filter.

VI. Conclusion

Emittance can be measured via the interference of edge radiation from two bending magnets. We collected CCD images of edge radiation diffraction for various emittance levels of electron beam at the ATF. When compared to data from the standard measurement method, we found a definite correspondence between the two methods. However, the experiment needs to be repeated with more stable beam conditions and perhaps a more time-efficient method of data collection. When the edge radiation method is calibrated by the traditional emittance method, the resolution as well as the tolerance must be determined in order to instate edge radiation diffraction emittance measurements as a working diagnostic.

Overall, measurements of emittance by edge radiation diffraction are minimally invasive and can be applied to a single electron bunch. The method is simple, broadly applicable, and may aid future accelerator experiments that need specific bunch information.

VII. Acknowledgements

This project was supported in part by the U.S. Department of Energy, Office of Science, Office of Workforce Development for Teachers and Scientists (WDTS) under the Science Undergraduate Laboratory Internships Program (SULI).

Thank you to my project mentor, Christina Swinson, as well as Mikhail Fedurin and the rest of the staff at the ATF for welcoming me to the facility and showing me what it is to be a scientist. Thanks also to the Office of Educational Programs staff at BNL for their management of the summer programs.

VIII. References

http://www.bnl.gov/atf/

Chao, A.W., Mess, K.H., Tigner, M. and F. Zimmermann. Handbook of Accelerator Physics and Engineering. 2nd ed. Singapore: World Scientific Publishing Co., 2013.

G. Geloni et al., Nucl. Instr. Meth. A 605 (3), 409 (2009). Particle Beam Physics Laboratory (PBPL), UCLA. "Coherent Edge Radiation." http://pbpl.physics.ucla.edu/Research/Theory/CER/.

O. Chubar and P. Elleaume, in EPAC98 Conf. Proc. (1998).

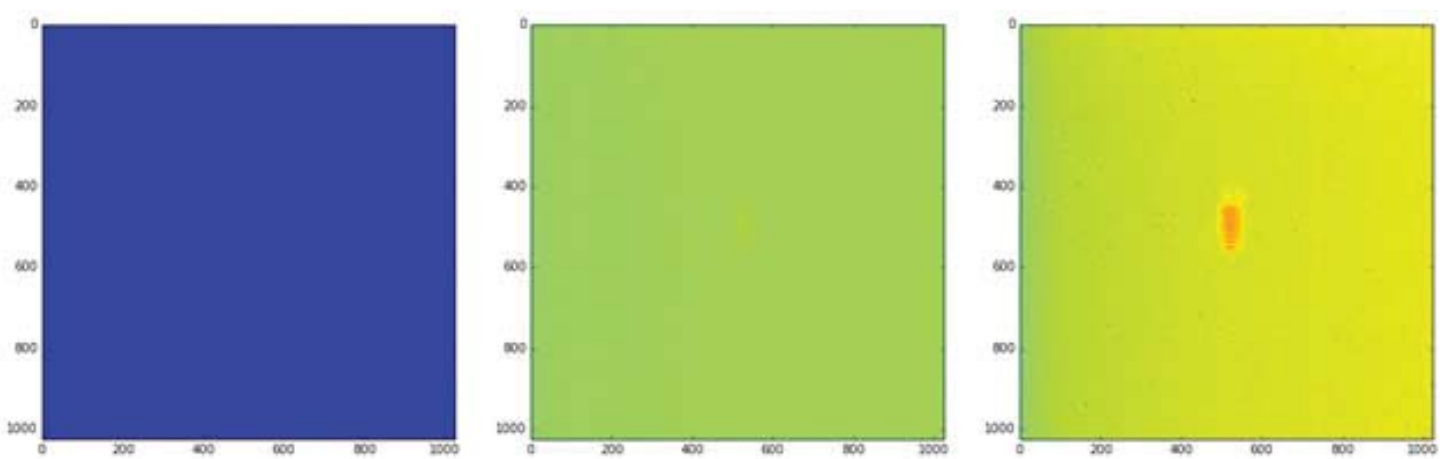

Figure 4. Left: The raw CCD camera image. Only x-rays are visible; fringe pattern not apparent. Center: The image after median filter is applied for every 9 pixels (highly filtered). Right: The image after a median filter and color contrast range applied.

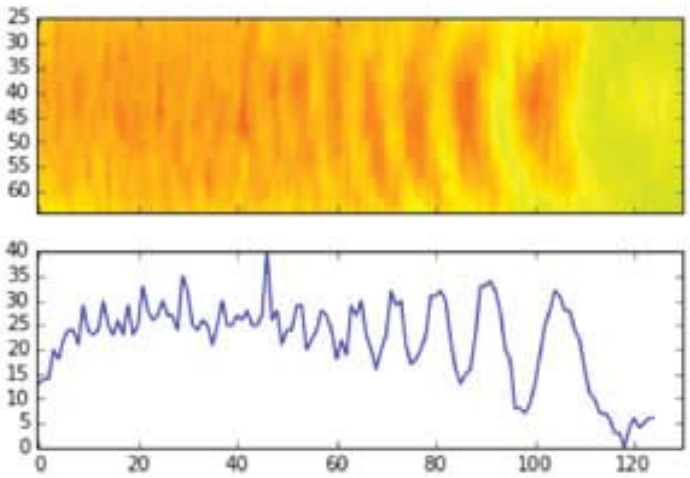

Figure 5. Upper: Diffraction pattern for solenoid current of 104 A. Lower: Projection of the pattern.

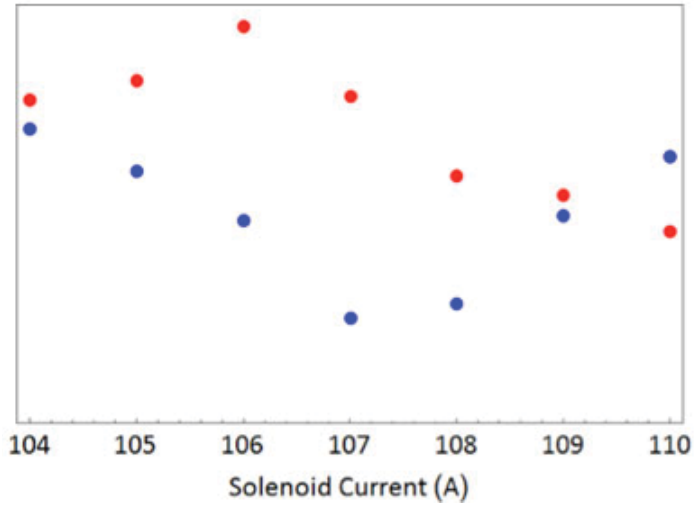

Figure 6. Plot of emittance via the edge radiation method (red) and the traditional method (blue) versus solenoid current.

Mechanical metrology testing for the Frontier Macromolecular Crystallography (FMX) Beamline and the Highly Automated Macromolecular Crystallography (AMX) Beamline at NSLS-II

Lauren Zipper
Mechanical Engineering, Binghamton University, Binghamton, NY 13902
Martin Fuchs
Photon Sciences, Brookhaven National Laboratory, Upton, NY 11973

Abstract

Macromolecular crystallography (MX) with synchrotron radiation is the leading technique to obtain 3D structures of biological molecules. At the National Synchrotron Light Source-II (NSLS-II), two MX beamlines, the Frontier Macromolecular Crystallography (FMX) beamline and the Highly Automated Macromolecular Crystallography (AMX) beamline, are being constructed. The FMX beamline will deliver a high photon flux of 1013 photons per second into a spot of 1 micron width. Due to its smaller beam spot, the requirements on the precision of FMX positioning systems are higher than that of AMX. My contributions include the testing of the mechanical precision of a goniometer and a 6 axis robot arm (TX 60) used as a sample mounter. At FMX, the goniometer, a crystal positioning instrument, needs to rotate crystals of down to a micrometer in size in an X-ray beam of the same size. Rotations are operated using the Experimental Physics and Industry Control System (EPICS), through a graphical user interface, the Control Systems Studio (CSS), an Eclipse-based collection of tools to monitor and operate large scale control systems. I have designed algorithms in MATLAB to analyze goniometer data to measure its sphere of confusion, the maximum deviation of its ideal position, which needs to be less than 100 nanometers. The robot arm (TX60) will allow for the auto-mounting of samples from a 24-puck dewar onto the goniometer. I have designed a three-axis sensor holder, using Autodesk Inventor, needed to perform repeatability tests necessary to verify the specifications of the TX60, which is specified to a repeatability of 30 microns. Using MATLAB, I have designed algorithms to analyze data collected during repeatability testing needed to avoid collisions with the goniometer during sample mounting.

I. Background

The scientific scope of the FMX and AMX beamlines is structural biology with applications of protein crystallography and x-ray diffraction. Proteins are the key building blocks of living organisms and to understand their functions, it is essential to know their structure. Distances of atoms in proteins are on the scale of Angstroms. X-rays have the wavelengths compatible with this length scale. X-rays cannot be used with lenses so x-rays are used with crystals in diffraction experiments. The size of the crystals used at these beamlines is on the scale of a few 100 down to one micron. The experiments results in diffraction patterns which are analyzed computational methods to obtain 3D structures of proteins. This process is shown in Figure 1.

X-rays are generated in the synchrotron by an undulator and have an energy range of 5-30 keV at FMX. The beamlines are used to focus and guide the x-rays while the end stations place the sample in the X-ray. The FMX and AMX end stations are the same for the purpose of the presented measurements. It is necessary to test the mechanical precision of the end station components using mechanical metrology. The two components I was tasked with testing include: the main goniometer and the robotic sample mounter. The goniometer is used to rotate crystal samples in the x-ray to obtain a diffraction image while the robotic sample mounter is used to mount the sample onto the goniometer.

II. Goniometer

The goniometer is needed to position and rotate the crystal in the x-ray beam. The proposed beamspot at FMX/AMX beamlines is on the order of one to a few tens of microns, therefore it is crucial that the goniometer operates without significant deviation of its initial position. To ensure, that the goniometer actually meets these requirements, it is necessary to measure its sphere of confusion, the maximum deviation from its ideal position when rotating by 360 degrees. Measurements were taken using a capacitive sensor manufactured by Lion Precision which determines the distance between the sensor and the measurement ball by the voltage between the two components. The data was collected with an oscilloscope and saved as .csv files to be analyzed with MATLAB algorithms.

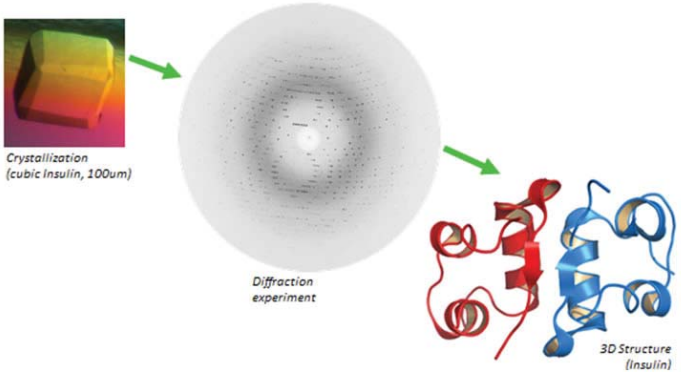

Figure 1. Protein structure obtained from diffraction and crystallization

III. Donaldson Ball Reversal

Before measuring the final stages of the main goniometers, it is crucial to establish measurement methods on a test goniometer. The two main components of the goniometer are the air bearing rotation axis and the centering translation stages. Errors seen when measuring the sphere of confusion are a combined error from these two main components. The sphere of confusion is analyzed when moving through a full rotation and a peak-peak deviation is acquired. The centering error, which has the form of a sine, can be minimized manually and the remainder can then be removed numerically. The sphere non-roundness error can be removed by measuring with the Donaldson Ball Reversal Method. The goniometer error when moving about the rotation axis is the one of interest. To measure the two independent errors of the goniometer and the metallic sphere the Donaldson Ball Reversal Method is used. To obtain the two errors, two measurements are needed and are taken on one side of the ball and then taken again 180 degrees opposite of the initial measurement while turning the sensor. One can then solve independently for the goniometer and the sphere error.

The Donaldson Ball Reversal Method is explained through Figure 2 and Equations 1-4 shown below.

$$E_{tot1}(\theta) = E_{Sphere}(\theta) + E_{Gonio}(\theta) \quad [1]$$

$$E_{tot2}(\theta) = E_{Sphere}(\theta) - E_{Gonio}(\theta) \quad [2]$$

$$E_{Sphere}(\theta) = (E_{tot1}(\theta) + E_{tot2}(\theta))/2 \quad [3]$$

$$E_{Gonio}(\theta) = (E_{tot1}(\theta) - E_{tot2}(\theta))/2 \quad [4]$$

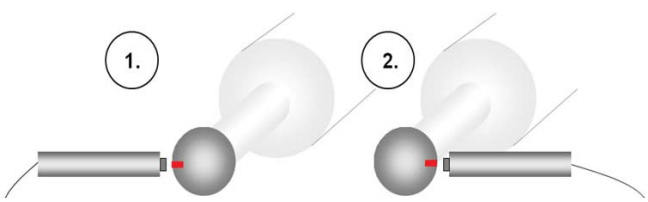

Figure 2. Donaldson Ball Reversal Method image courtesy Aline Mayer, 2011

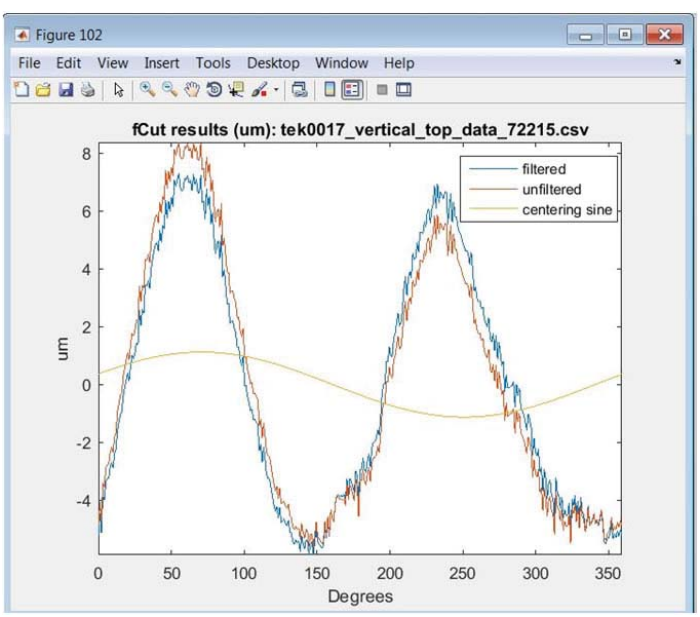

Figure 4. Centering sine removal in MATLAB from top vertical measurement

Here, $E_{tot1}(\theta)$ is the total error of the first side, $E_{tot2}(\theta)$ is the total error of the second side, $E_{Sphere}(\theta)$ is the sphere error and $E_{Gonio}(\theta)$ is the goniometer error. Measurements were taken on both vertical axes and both horizontal axis.

IV. Sphere of Confusion Analysis

To measure the sphere of confusion, two data sets must be acquired from the oscilloscope: the raw data of the position deviation and a calibration file, a repeated set of a given distance needed to convert voltage to microns (step size). Algorithms were used into isolate goniometer error in MATLAB by three main functions: um_per_volt_calib.m, which converts voltage to microns, fCut.m (Adrian Curtin 2010), which removes one cycle-centering error from ball roundness error and donaldson.m measures peak-peak deviation of goniometer error. I designed the first algorithm and two sub-functions within it, needed to find the minimum and maximum points in the calibration file. The conversion factor is obtained by dividing the step size by the voltage difference of

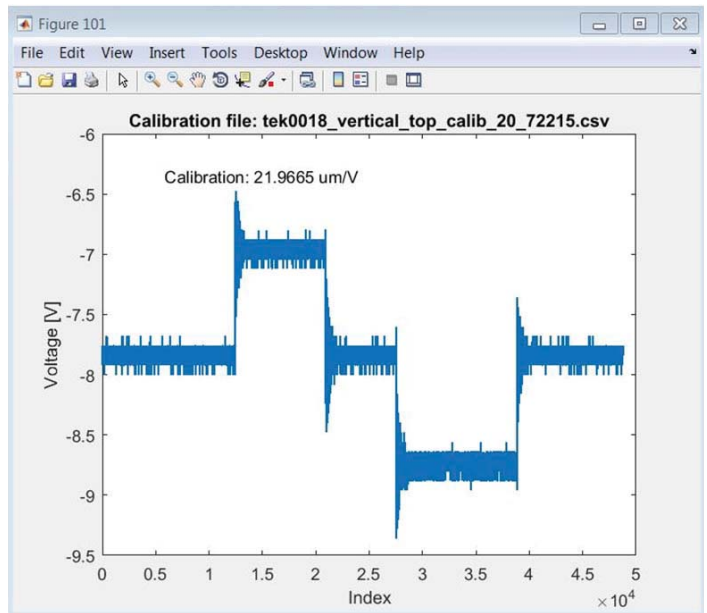

Figure 3. Calibration file and factor generated in MATLAB from top vertical measurement

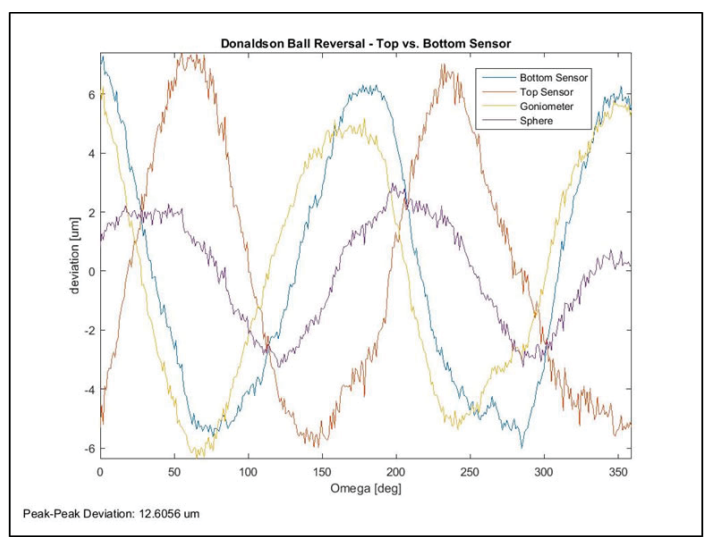

Figure 5. Donaldson Ball Reversal processed in MATLAB needed to analysis goniometer error (orange)

the minimum and maximum points. Figure 3 illustrates the calibration file of the top vertical axis. The second algorithm loads the raw data saved from oscilloscope into a .MAT file, cuts to useful range, bins data to average high frequency noise and finally remove the one-cycle centering error from ball roundness error with fCut. Figure 4 shows the result of the fCut. The third algorithm uses the Donaldson Ball Reversal Method and two paired data files to isolate the goniometer error. The paired vertical measurements are shown in Figure 4. The peak-to-peak deviation was measured to be 12.6 µm. These measurements established the method to measure the sphere of confusion.

V. Sample Mounter

The robotic sample mounter (Staubli TX60) is used to grab crystal pins in liquid nitrogen and mount them to the goniometer. The repeatability of the robot is specified by the vendor (Staubli) to a repeatability of 30 microns. This must be tested to avoid collisions with the goniometer during sample mounting. An experiment was designed to test the repeatability in which the robot would alternate between two positions. The first position is when the robot is positioned away from capacitive sensors to mimic the mounting of samples on the goniometer. The second position is when the robot is positioned within measuring distance to the capacitive sensors to mimic the gripper picking up the samples. Measurements were taken using the same equipment used to measure the sphere of confusion of the goniometer; however additional hardware and algorithms were needed to perform this experiment.

VI. Three Axis Sensor Holder

Repeatability of the robot was tested in all coordinate directions so it was necessary to position each sensor accordingly. I designed a three axis sensor holder using Autodesk Inventor which

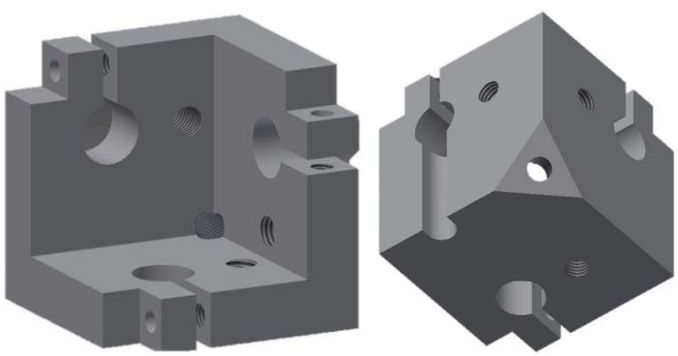

Figure 6 (left). Three axis sensor holder (front)
Figure 7 (right). Three axis sensor holder (back)

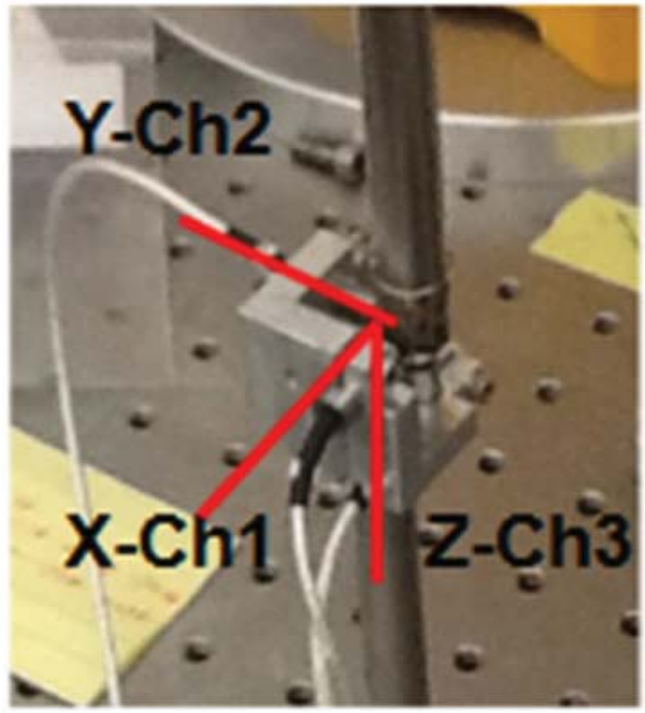

Figure 8. TX60 gripper with sphere inside sensor holder using testing

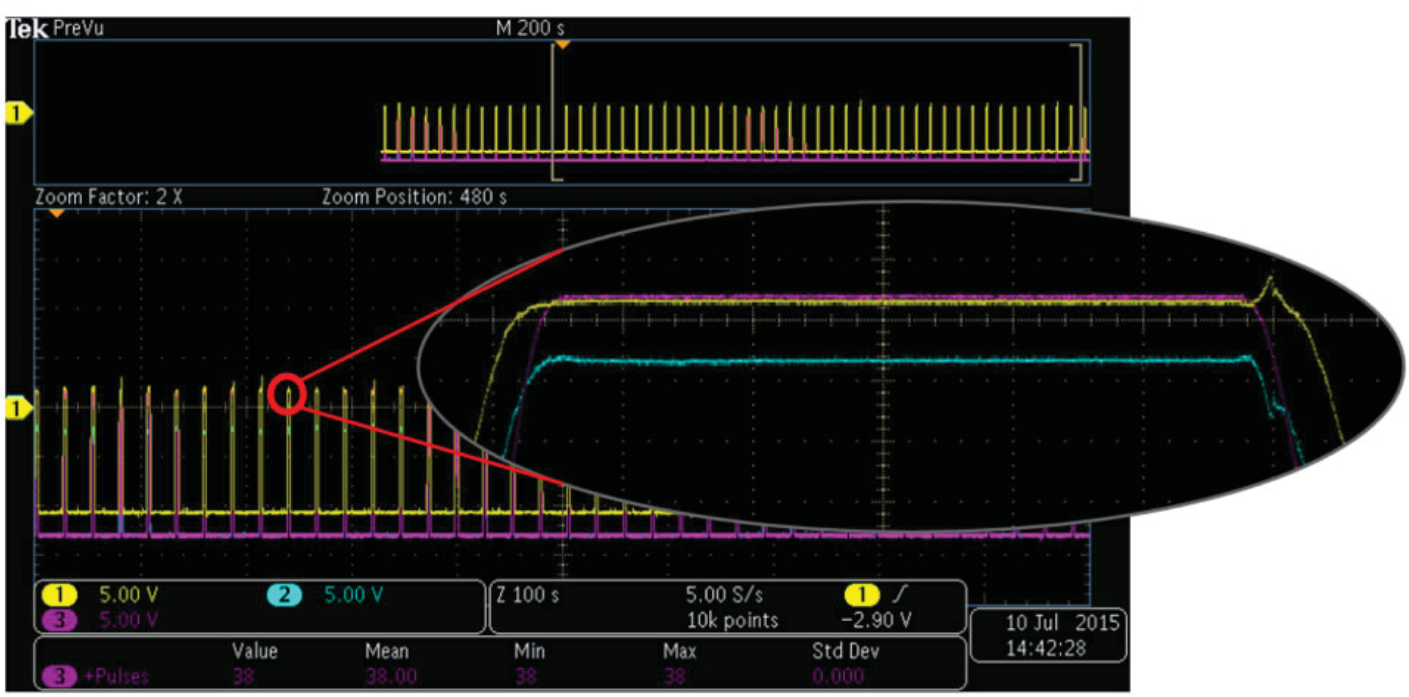

Figure 9. Repeatability raw data in oscilloscope with focus on individual peak

consists of an open face cube corner with holes on each face that holds the sensors. Design requirements include: each sensor of 18mm length to reach a sphere placed in the center at all equal distances, ability for a sensor (8mm diameter) to slide into a positioning hole and be tightened into place, mounting the holder on each face, and mounting the holder at the corner of the intersection of the faces. Figures 6 and 7 illustrate the design of the three axis holder in Autodesk Inventor. During the experiment the sphere was placed in the center of the cube with the TX60 gripper. Figure 8 shows the gripper in use with the three axis sensor holder in testing and the channels that belong to each sensor.

VII. Repeatability Analysis

To measure the repeatability, the raw data file and calibration file are analyzed with the algorithm I have developed called robot_repeatability.m. The algorithm loads data saved from the oscilloscope into a .MAT file, filters data and cuts it to useful ranges. The algorithm then automatically finds a peak for each approach of the robot gipper to the measuring position and determines the peak height by averaging the peak values to a single point. Figure 9 illustrates the raw data in the oscilloscope with a focus on an individual peak. The process is repeated for each channel. Voltages are then converted to micrometers and the final result is a plot of the number of mounts versus the distance of the gripper to the sensor in micrometers as shown in Figure 10. The maximum peak to peak variation is 29.6 µm, measured from Channel 3 in Z-direction, which shows that the robot is operating within the vendor's specifications.

VIII. Conclusions

In preparation for the testing of the final goniometer of the FMX and AMX beamlines, the sphere of confusion of a test goniometer was measured to be 12.6 µm peak to peak. The precision of this value is determined by the stability of the preliminary test setup and therefore was not determined here. The sensor precision, however, is 3 nm, therefore in a stable holder; this value assures that the method used to obtain the measurement is valid for applications of the main goniometer.

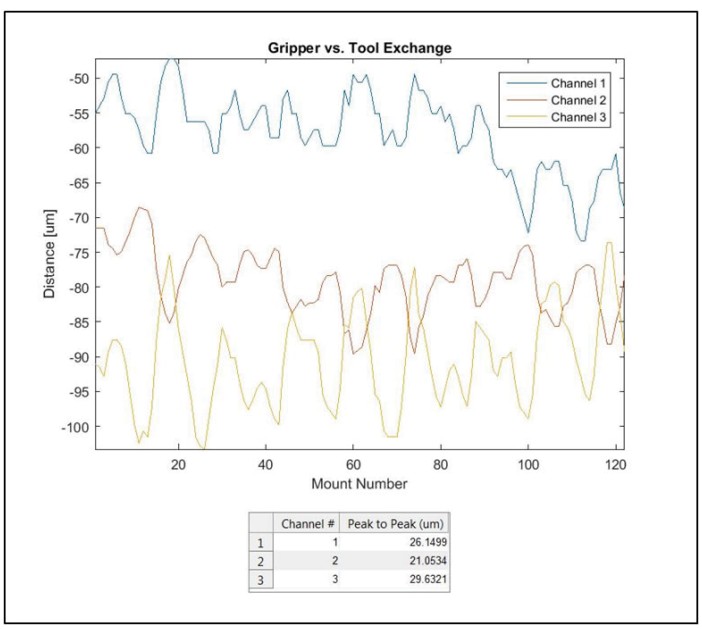

	Channel #	Peak to Peak (um)
1	1	26.1499
2	2	21.0534
3	3	29.6321

Figure 10. Data analysis from Robot Repeatability algorithm processed in MATLAB

The sample mounter will not collide with the goniometer during sample mounting as the robotic arm is operating within the specified repeatability of the sample mounter arm of 30 microns. The specified repeatability could be verified using the experiment described, the constructed three axis sensor holder and the robot repeatability algorithms established.

IX. References

[1]Curtin, Adrian. "fCut." Code Report. Paul Scherrer Institute, 2010.

[2]Donaldson, R.R. "A Simple Method for Separating Spindle Error from Test Ball Roundness." Annals of the CIRP 21.1 (1972): 125-126.

[3]Fuchs, M R, et al. "NSLS-II Biomedical Beamlines for Macromolecular Crystallography, FMX, and AMX, and for X-ray Scattering, LIX: Current Developments." 17th Pan-American Synchrotron Radiation Instrumentation Conference (SRI2013). Journal of Physics: Conference Series, 2014.

[4]Lion Precision. "Capacitive Sensors - Ungrounded Target." Vols. LT03-0022. March 2013.

Application containers as an alternative to virtualization

Joseph Zuhusky
Department of Physics, Boston College, Chestnut Hill, MA 02467
Antonio Wong
RHIC and ATLAS Computing Facility, Brookhaven National Laboratory, Upton, NY 11973

Abstract

The RHIC and ATLAS Computing Facility (RACF) at Brookhaven National Lab (BNL) provides support and computing services for scientists at BNL and abroad. The introduction of multi core CPUs in the mid2000s has led to widespread adoption of virtual computing environments that use these CPU resources flexibly and efficiently. Application isolation and resource control are easily achieved through the use of virtual computers. However, these virtualized computing environments require a hypervisormanaged, complete operating system (OS) within each virtual machine. A lightweight, alternative approach is to use Docker application containers. Containers share a single kernel with the host and only relevant application libraries, thus allowing for a smaller OS, lower overhead, and improved application performance. Docker containers have the potential to offer a more efficient way to distribute software across various computing environments. Primarily, this project benchmarks sample applications on bare metal (no virtual computer or container), virtual computers, and Docker containers and summarizes the results obtained. The second part of this project explores the characteristics of submitting Docker container jobs to a "High Throughput Computing" environment like HTCondor. As a result of using Docker containers, scientists and RACF staff will have more freedom in choosing a computing environment that fits their specific needs, while minimizing overhead associated with hardware resources.

I. Introduction and Background

The RHIC and ATLAS Computing Facility (RACF), at Brookhaven National Laboratory (BNL), provides computing services for experiments conducted at the Relativistic Heavy Ion Collider at BNL and the ATLAS experiment at the Large Hadron Collider at CERN in Geneva. Often times scientists rely on software that is incompatible with the hardware and operating systems currently used by the RACF. As a result, the scientists and RACF staff are forced to adapt to each others computational needs. An effective way to overcome these incompatibilities is for one partner to "virtualize" the computing environment of the other. Virtualization requires hardware and operating system (OS) overhead and this often yields a software performance penalty of about 510%. A new software technology called "Docker" offers an effective and alternative way to virtualize operating systems and run applications in that virtual environment. It does not require a virtual "guest OS" to be mounted onto the host. Rather it establishes protocols within the lightweight container, via the Docker engine, which allows for it to run by sharing the host's kernel while adhering to the principles of the virtualized OS environment. The analogy which is commonly used for Docker container is that of a shipping container. All sea ports in the world are capable of handling them. The entire software application is container inside it with all the necessary libraries and other software packages.

This project presents an investigation into how much Docker containers potentially reduces the software performance penalty associated with tradtional virtual machines. We benchmark the performance sample applications present the results obtained. The benchmarks are conducted on a few different computer processing units (processors or CPUs) and they run on bare metal, inside a virtual machine and inside a Docker container.

Scientists and their computer support counter parts are coupled as a result of the need for compatible computing environments between the two. Docker containers have the potential to decouple the relationship between scientists at BNL and CERN with the RACF team, while reducing software performance penalties associated with traditional virtualization. A decoupled relationship allows both groups to use whatever computing environments they want or need without having to take into account the needs of their counterparts, thus allowing experiments to be carried out more efficiently. Both groups in the relationship have the freedom to upgrade their hardware and operating systems as needed without having to do the same with their software.

II. Benchmark Description and Methods

A. CPU Generations & Descriptions

We began the project by benchmarking various CPU generations, more specifically, the performance of software running on those computers. Although Docker is only compatible with the newest CPU (hardware) generation, we benchmarked older hardware generations as well, for comparative purposes. This way, when we go to test the performance of Docker and the virtual machine, we can accurately gauge whether the performance of those environments is around what it should be; we needed to see if the newest CPU generation was performing at its best. The various CPU generations that we tested, in order from oldest to newest, are known by their codenames: "Nehalem", "Westmere", "Sandybridge", and "Ivybridge." Software executed inside Docker containers and virtual machines was only benchmarked on the Ivybridge CPU generation.

In order to test for differences in performance between traditional virtual machines and Docker containers, we ran the two software applications in each environment and compared those results to bare metal. We used isolated applications because they are not dependent on any external factors.

Isolated in the sense that the can run standalone with no external input/output or networking needs. We can install the applications, deploy them into the container and virtual machine (VM), and run them. This isolated nature of the software is important to our benchmarks because it limits the possibility of errors and lapses in performance occurring due to factors not within the con-

tainer or VM; these applications are controlled environments.

These processors (computer processing units or CPUs) inside the computers, which we are conducting the benchmarks on, are known as "multicore" CPUs. That means, although there is only one CPU chip, that chip can have multiple processes running on it without sacrificing an egregious amount of performance. Each core acts as an independent processor. Due to this feature, usually only a small overall penalty is associated with executing multiple programs.

B. HEPSPEC06

The first software application we ran was specifically designed for benchmarking CPU performance. This application is known as "HEPSPEC06" ("HS06") and it is a subset of the "SPEC06" CPU benchmarking set.1 The "HS06" software performs a set of calculations on the computer and returns a final score that rates the CPU's performance. That score is known as the "HS06" number. A higher score indicates better CPU performance. Because of virtualization overhead, CPU performance, and therefore software performance, is liable to a performance penalty. Using the HEPSPEC06 benchmark software offers a simple and direct way of judging the performance of various computing environments.

When running the HS06 benchmark, we allowed the machines to use only 16cores, even though most machines had many more. This is because the oldest machine we used only had 16 cores. This way we can simplify the comparison between CPUs. If this step had not been taken, then our analysis of the difference in performance between CPU generations would not only have to account for the novelty of CPU design, but also number of cores available; it does not make sense to compare a 16 core Nehalem machine to 40core Ivybridge machine. An HS06 number percore would have to be calculated. Therefore to keep things simpler, we exerted a handicap to all machines and only gave them access to 16 cores.

C. ATLAS

Although the HS06 tests are a good measure of CPU performance, the tests do not shed light on the performance of an actual scientific application. Therefore, it was necessary to benchmark the performance of another type application. The ATLAS application is a piece of simulation software provided to us from the ATLAS experiment being conducted at CERN in Geneva, Switzerland. Here we are simply measuring the total time it takes for the application to run in each environment. First, we tested the time it takes to run the application in an environment that the CPUs we are using on have other jobs submitted to them as well. Due to the multicore nature of the CPUs we are testing, this is what a normal computing environment looks like. Secondly, we tested the performance of the application in an environment with exclusive access to those machines. This is not a very realistic environment, but like the HS06 benchmarks, it gives us a clear picture as to how the performance of the application differs from processor to processor. In the latter examples, we ran one instance of the software at a time, and compared the results obtained.

Next we proceeded to execute six instances of the software at once and recorded the performance. Again, due to multicore capabilities, this type of execution is a reality. The reason for this test was to exert small amount stress to the hardware so we could get a better idea of the performance of each machine when running multiple instances of the application. We weren't expecting the time taken to run the software to sixfold (again due to the multicore technology available), but we were expecting a slight slip in performance. This type of test also brings us back to a more realistic computing environment. These multiprocess tests were performed only on the Ivybridge machine. We tested performance of bare metal, the VM, and the Docker container. Finally, to further study the capabilities of Docker containers, instead of running six instances of the application inside one container, we decided to run six Docker containers each running one instance of the application inside of it, and we compared the results. This was an enlightening exercise. However, we could not conduct a similar test that would run six VMs all at once.

D. HTCondor

Finally, after running both applications on various machines in all three environments, we decided to go ahead and try to run the same applications on a desktop computer, except this time the jobs would be submitted in the background as HTCondor jobs. Since computing jobs in the RACF are normally submitted via

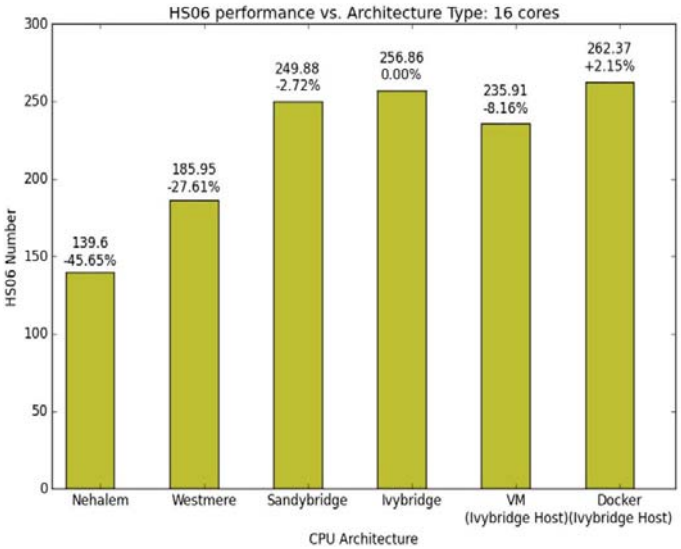

Figure 1. HS06 scores vs. CPU generation, VM and Docker container (16cores). % relative to Ivybridge performance.

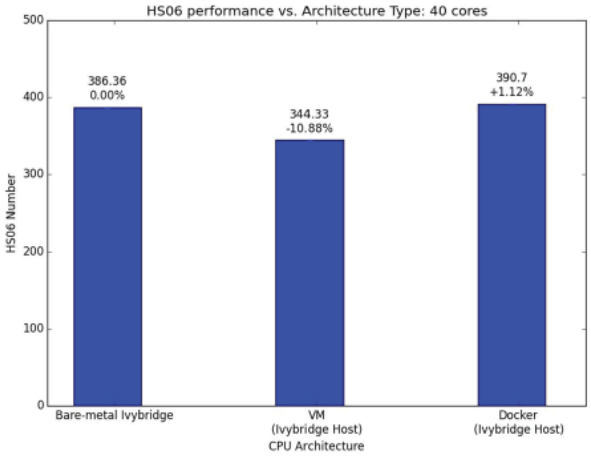

Figure 2. HS06 scores for Ivybridge CPU generation: bare metal, VM and Docker container (40cores). % relative to bare metal performance.

HTCondor, it would be rewarding and applicable if we could successfully run a Docker container, and an application inside of the container, as an HTCondor job.

III. Benchmark results

The initial HS06 results for the bare metal machines and the VM were what we expected. As seen in Figure 1, there is a performance curve across the CPU generations for bare metal that shows as CPU generation become newer, overall performance increases. The VM suffers ~8% application performance penalty or in this case an HS06 score penalty, which is exactly what we expect from a VM. However, the score for HEPSPEC06, when run inside the Docker container, is actually larger by ~2% than the same test that was run on bare metal. The most we can say from this benchmark is that Docker containers exhibit nearnative performance. A slightly larger HS06 number for Docker containers over bare metal is possibly due to an optimization that Docker makes. We do not currently know exactly what this optimization might be.

Because Docker is only compatible with the latest generation of CPUs, i.e. Ivybridge, we then performed the HEPSPEC06 benchmark again, only on the Ivybridge machine, running with the maximum number of cores for that machine (40). Figure 2 shows the results of this benchmark. Seen in Figure 2, the VM performance is ~11% less than that of bare metal, yet Docker still outperforms bare metal by ~1%. Here again, we can at most conclude that Docker exhibits nearnative performance, which is excellent.

In Figure 3, we present the preliminary results for our benchmark of the ATLAS application.

Figure 3 does not show the application performance running inside a Docker container. These tests are simply to see how the ATLAS application performs across the various CPU generations as well as within a VM, which again, was run on an Ivybridge host. The gold bars represent a normal computing environment. The relative performance in this environment is more unpredictable due to the fact that all machines could have different workloads at any given time. The red bars indicate an exclusive computing environment, i.e. only our applications are running on those machines. The data shown for an exclusive computing environment shows the performance curve with respect to CPU generation that we are expecting. The reader should also keep in mind here that a lesser value here is better; we are measuring time taken to run the application in its entirety and less time is indicative of better performance. VM performance here, relative to exclusive Ivybridge bare metal, is in the ballpark of what we expect for VM performance, that is ~5% worse than bare metal. Here that value is ~4.5%.

Finally, Figure 4 shows the ATLAS application performance when running on an Ivybridge CPU generation. The results shown are for the bare metal, virtual machine and Docker container environments. The gold bars here are the same as the red bars from Figure 3, i.e. an exclusive computing environment. ATLAS application performance inside a Docker container in this case produces the same relative results as we have seen in the previous HEPSPEC06 benchmarks. Docker containers again barely outperform bare metal machines by ~1% when running the same application. When six instances of the application are executed at once, the performance in the Docker container remains within 1% of native (bare metal) performance, while the VM slows down to be ~7% slower than native performance. The blue bars represent the average performance of six containers all running one instance of the application. The performance is still within ~1% of native speed. This is a fantastic result that highlights the extremely light weight nature of Docker containers.

IV. HTCondor Deployment

The RACF uses a high throughput computing software known as HTCondor to queue computing jobs. The ability to submit a Docker container job to HTCondor has a wide variety of applications and benefits. Namely, there will be reduced waiting times for jobs in the queue because of the new availability of any Linuxflavor OS on essentially any machine, and thus a smaller overall job run time, assuming close to native performance or small performance penalties. Overall job time will also decrease since the performance penalty associated with VMs will be significantly reduced by the deployment of Docker.

The main challenge with this part of the project was understanding the "docker" universe. An HTCondor "universe" is a way to specify, inside the HTCondor submit file, the job execution en-

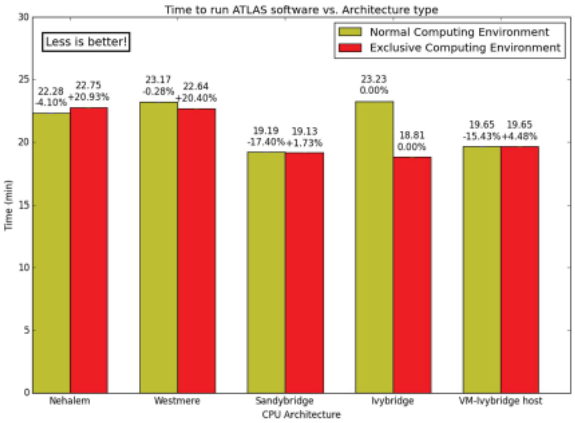

Figure 3. ATLAS average times for various CPU generations and VM, shown: normal and exclusive computing environments

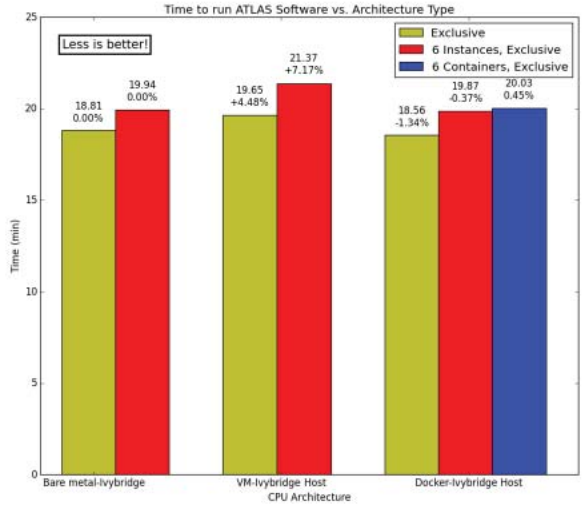

Figure 4. ATLAS avereage times for Ivybridge CPU generation: bare metal, VM, and Docker container. Gold: one instance of application, red: six instances, blue: six instances across six containers.

vironment. A “docker” universe job is very similar to a “vanilla” universe job. The “docker” universe specifies the job to run inside a Docker container on the execute machine. The execute machine must have Docker installed to be able to accept the job. The only difference between the “docker” and “vanilla” universes is that the Docker container, unlike the execute machine for the “vanilla” universe, does not have access to shared files. In a traditional Docker “run” command, which builds a container from a cached image, the user can specify what files from the host machine to mount into the container; the user is free to mount as many files as he or she likes. But due to the added layer of commands in the condor submit file, it is difficult to run the Docker specific commands that are needed when submitting a job via HTCondor. Essentially, there are no analogous “ClassAds” for traditional Docker commands. To reiterate, because of this, problems begin to arise when the user needs to put files from the host machine into the container so that he or she may run an application.

As a potential way around this issue, the Docker interface via HTCondor allows the user to transfer files into a scratch directory within the Docker container. Therefore, the user must specify all the directories to be transferred into the container using the traditional HTCondor file transfer mechanisms. From the scratch directory, the user has to specify, by executable script, exactly how to deploy those files throughout the container. If no file transfer mechanism is enabled, by default the Docker container mounts the file from which the HTCondor submit file was submitted. Another option is to specify the “remote_initialdir” or the remote working directory. This will simply mount that directory from the host execute machine, into the container. Either way, the user must do some organizational tasks once her or she actually gets the necessary files into the container.

Another issue that constrained our ability to easily run an application via these methods is who the user is within the container. Traditionally, Docker allows its users root access when running the container. However, when the job is submitted via HTCondor, the user inside the container is whomever submitted the file, and naturally, this cannot be root due to HTCondor’s security features.

In the end, we were successful in launching and running both sample applications inside a container as an HTCondor job. But we did have some serious poking around to do while using the “docker” universe. The main problems we faced were getting the exact files we needed exactly where we needed them inside the container, as well as navigating and setting up the container with the right file permissions so that we could execute the applications. Some tinkering with the Docker image we used beforehand was necessary to do some of this. But after sufficient tinkering, we were up and running and recorded benchmark results for both applications that were what we expected. Therefore, after a good deal of work on behalf of the user, the application should run smoothly via HTCondor.

In terms of recommendations when using HTCondor, here are a few. To get any files into the container, it is easiest to use the remote initial directory technique rather than the file transfer technique. As well, to anyone reading this who has experience with HTCondor, a mapping of the analogous Docker commands to HTCondor ClassAds would be extremely useful to a lot of users.

V. Conclusions

From our benchmark results, the most that we can conclude is that Docker containers offer a much lower performance penalty than virtual machines do. Considering the performance of the Docker containers over bare metal, we cannot accurately report an exact performance penalty. To come out and say that Docker containers are actually perform better than bare metal machine would be naive.

Therefore, the best we can conclude is the Docker containers exhibit nearnative performance, which is considerably better than virtual machines. Although, there is precedent for Docker containers outperforming bare metal machines. A similar study was done that concluded sometime Docker can outperform bare metal by ~12%.2

VI. Acknowledgements

I would like to first and foremost thank my mentor and advisor Tony Wong for his support and guidance over the course of my internship at BNL. I would also like to thank Will Strecker-Kellogg and Chris Hollowell, of the RACF, for their extensive help with this project. Further I would like to thank the Office of Educational Programs here at BNL for being wonderful hosts. This project was supported in part by the U.S. Department of Energy, Office of Science, Office of Workforce Development for Teachers and Scientists (WDTS) under the Science Undergraduate Laboratory Internships Programs (SULI). Finally, I would like to thank the entire RACF staff for their hospitality and encouragement during my internship.

VII. References

[1]www.spec.org

[2]Washbrook, Andrew John, and Gareth Douglas Roy. “Evaluation of containers as a virtualisation alternative for HEP workloads.” 21st International Conference on Computing in High Energy and Nuclear Physics (CHEP2015). Okinawa, Japan. Web. 20 July 2015 http://indico,cern.ch/event/304944/session/7/contribution/356/

[3]“Computing with HTCondor™.” HTCondor. N.p., n.d. Web. 06 Aug. 2015. <http://research.cs.wisc.edu/htcondor/>.

[4]“Docker.” Docker. N.p., n.d. Web. 06 Aug. 2015. <http://www.docker.com/>.